



The
University
Of
Sheffield.

**Effect of Hot Working and Heat Treatment Parameters on the Microstructure
and Properties of ZERON® 100 Superduplex Stainless Steel**

By:

Jamie A J Pennington

A thesis submitted in partial fulfilment of the requirements for the degree of
Doctor of Philosophy

The University of Sheffield
Faculty of Engineering
Department of Materials Science and Engineering

September 2018



Effect of Hot Working and Heat Treatment Parameters on the Microstructure and Properties of ZERON® 100 Superduplex Stainless Steel (Volume 1)

By:

Jamie A J Pennington

A thesis submitted in partial fulfilment of the requirements for the degree of
Doctor of Philosophy

The University of Sheffield
Faculty of Engineering
Department of Materials Science & Engineering

September 2018

Abstract

Duplex and superduplex stainless steels are high-alloy engineering materials whose annealed microstructure consists of approximately equal proportions of ferrite and austenite. This phase balance may however vary by as much as $\pm 20\%$ depending upon thermo-mechanical processing parameters. They are characterised by high resistance to stress corrosion cracking in Cl ion-containing environments, pitting and crevice corrosion. Their lower Ni contents and higher strength also confer economic and mechanical advantages over the super and common austenitic stainless grades, respectively.

The two-phase microstructure and high-alloy content of duplex and superduplex stainless steels however also present considerable challenges for thermo-mechanical processing including complex restorative behaviour in response to imposed deformation and the potential for the precipitation of deleterious tertiary phases. In order to optimize the performance (and address reported variability in quality) of high-integrity duplex and superduplex forged engineering components it is therefore necessary to understand the effects of thermo-mechanical process parameters on the microstructure evolution and subsequent mechanical properties of these alloys.

This work investigates the effect of variables typical of industrial forging processes on the microstructure, properties and the crystallographic texture of ZERON® 100, the first commercially available superduplex stainless steel. By contrast, much of the current research literature concerning duplex metallic materials has focused on non-industrially analogous processing parameters (heat treatment temperatures and cooling rates, for example) and unrepresentative service conditions. However, the conditions for the formation and the effects on material properties of the most common and deleterious tertiary duplex phases (e.g. σ and χ) are now well understood and avoided in industrial practice. Such methodologies therefore, although useful for the characterisation of tertiary precipitates and accordingly their effect on material properties, have limited applicability to the understanding of the complexities involved in thermo-mechanically processing duplex and superduplex stainless steel alloys.

A constitutive equation has been developed to describe the flow behaviour of ZERON® 100 and used as the basis of finite element simulations of the industrial forging process. These simulations have allowed for the identification of strain and temperature gradients developed throughout thermo-mechanical processing and also indicated potential areas of little-to-no grain refinement corresponding to ‘dead zones’ within forged components. High-fidelity replication of cooling curves calculated for specific locations within a thick-section forging during quenching and subsequent mechanical testing were also carried out. These mechanical tests, and EBSD analysis of commercially- and lab-processed material, confirmed the importance of the forging temperature in both the production of the starting billet material and finished product, chiefly due to its influence on the stability of grain boundary-pinning secondary austenite precipitates. Although the presence of chromium nitride tertiary precipitates have been demonstrated to embrittle the ferrite matrix, this work suggests primacy of the effect of ‘microstructure mechanics’ i.e. the refinement of the basic microstructure unit size, on impact toughness. The optimisation of the quality of duplex engineering forgings may therefore primarily be achieved through total thermo-mechanical process control in order that imposed deformation and heat treatment results in refinement of the ferrite matrix grain size.

Table of Contents

Abstract	iii
Table of Contents	iv
Nomenclature	vii
Acknowledgements	xi
1 Introduction	1
1.1 Background and Industrial Context	1
1.2 Problem Definition	3
1.3 Project Aim	3
1.4 Project Objectives	4
1.5 Thesis Outline	4
References	6
2 Stainless Steels and the ZERON® 100 Superduplex Stainless Steel Alloy	7
2.1 The Fe-Cr-Ni Alloy System	7
2.2 Ferritic Stainless Steels	9
2.3 Austenitic Stainless Steels	10
2.4 Martensitic Stainless Steels	11
2.5 Duplex Stainless Steels	11
2.6 Development of the ZERON® 100 Superduplex Stainless Steel Alloy	14
2.6.1 <i>Characteristics of ZERON® 100</i>	16
2.6.2 <i>Starting ZERON® 100 Billet Material</i>	17
2.7 Summary	18
References	19
3 Literature Review	20
3.1 The Precipitates and Corrosion of Duplex and Superduplex Stainless Steels	21
3.1.1 <i>The σ (sigma) Intermetallic Phase</i>	22
3.1.2 <i>Chromium Nitrides, Cr_xN</i>	25
3.1.3 <i>Secondary Austenite, γ_2</i>	29
3.2 Hot Deformation of Duplex and Superduplex Stainless Steels	31
3.2.1 <i>Flow behaviour of Duplex and Superduplex Stainless Steels</i>	33
3.2.2 <i>Constitutive Flow Modelling of Duplex and Superduplex Stainless Steels</i>	36
3.2.3 <i>Crystallographic Orientations in (Deformed) Duplex Metallic Materials</i>	41
3.3 Summary	44
References	46
4 Experimental Methodologies, Equipment Development & Starting Material	48
4.1 Elevated Temperature Uniaxial Compression Testing	48
4.1.1 <i>Experimental Work Conducted on the TMC</i>	50
4.1.1.1 <i>Axisymmetric Compression Tests for Flow Model Establishment</i>	50
4.1.1.2 <i>Industrially Analogous Axisymmetric Compression Tests</i>	86
4.2 Simulation of Metal Forming and the Finite Element Method	55
4.3 Electromagnetic Induction Heat Treatment Testing	56
4.3.1 <i>The Importance of Frequency</i>	56

4.3.2 <i>Advantages of Induction Heating</i>	57
4.3.3 <i>Operation of the Induction Heat Treatment Unit</i>	57
4.3.4 <i>Experimental Work Conducted on the ATPU</i>	60
4.3.4.1 <i>Design Development of the ATPU for Enhanced Cooling Control</i>	61
4.4 Electron Back Scatter Diffraction (EBSD)	83
4.4.1 <i>Descriptions of Crystallographic Orientation</i>	83
4.4.2 <i>EBSD Experimental Work</i>	86
4.5 Metallographic Preparation	89
4.5.1 <i>Electrolytic Etching</i>	90
4.6 Characterising the Starting ZERON® 100 Billet Material	91
4.6.1 <i>AFP vs. Standard ZERON® 100 Billet</i>	108
4.7 Summary	116
References	116
5 Development of Constitutive Flow Model	117
5.1 Experimental Data	118
5.2 Data Adjustments and Corrections	123
5.2.1 <i>Zero Offset Data Correction</i>	123
5.2.2 <i>Friction Correction</i>	126
5.3 Constitutive Equation Development and Isothermal Corrections	131
5.3.1 <i>Isothermal Flow Curves</i>	132
5.4 Characteristic Points on the Flow Curve	141
5.5 First Stage Constitutive Equations	147
5.6 Second Stage Constitutive Equations	155
5.7 Summary	162
References	170
6. Finite Element Method Simulations of ZERON® 100 Thermo-Mechanical Processing	171
6.1 Initial Simulation of the TMC Uniaxial Compression Testing	171
6.2 Simulation of the Open Die Forging Process	181
6.2.1 <i>Cogging</i>	185
6.2.2 <i>Upsetting</i>	191
6.3 Simulation of the Closed Die Forging Process	196
6.3.1 <i>Punching</i>	196
6.4 Summary	200
References	202
7 SEM-EBSD Analysis	203
7.1 Microstructure and Crystallography of ZERON® 100 Commercial Open Die Forging	204
7.1.1 <i>Weld Neck Position, C1</i>	205
7.1.2 <i>Close to Bore Inside Diameter, C3 Position</i>	221
7.1.3 <i>Flange Centre, C7 Position</i>	227
7.1.4 <i>Summary of the Localised Crystallography in the 16" Open Die Weld Neck Flange Forging</i>	232
7.2 Industrially Analogous Thermo-Mechanical Processing Tests	239

7.3 Summary	262
References	267
8 Thermal Simulation and Mechanical Testing	268
8.1 DEFORM™ FEM Quality Heat Treatment Model	269
<i>8.1.1 FEM Transient Heat Transfer Problem Principals and Set-up</i>	272
<i>8.1.2 Derived Cooling Curves</i>	279
8.2 Thermal Simulations and Mechanical Testing	282
<i>8.3.1 Impact Toughness and Hardness</i>	287
8.4 Summary	292
References	293
9 Conclusions and Further Work	294
9.1 Optimisation of the Thermo-Mechanical Processing of ZERON® 100	298
9.2 Recommendations for Further Work	304

Nomenclature

Symbol/Acronym	Description (units, where applicable)
α	Thermal diffusivity ($\text{cm}^2 \text{s}^{-1}$)
α	Temperature-independent equation constant (MPa^{-1})
α'	Cr-rich tertiary precipitate
β	Equation constant (MPa^{-1})
χ	Mo-rich intermetallic tertiary precipitate
δ	Ferrite
δ	Electromagnetic penetration (skin) depth (m)
ε	Strain
$\dot{\varepsilon}$	Strain rate (s^{-1})
$\bar{\varepsilon}$	Effective strain
$\dot{\bar{\varepsilon}}$	Effective strain rate (s^{-1})
ε_0	Initial plastic strain
ε_c	Critical strain
$\dot{\varepsilon}_{ij}$	Strain rate tensor
ε_p	Strain at peak stress
ε_r	Transient strain constant
ε_{xr}	Strain required to reach a fixed amount of softening
γ	Austenite
γ_2	Secondary austenite
λ	Wavelength (nm)
$\bar{\lambda}_\delta$	Average ferrite bandwidth (μm)
μ	Fictional coefficient
μ_0	Permeability of free space (H m^{-1})
μ_r	Relative magnetic permeability
ν	Degrees of freedom
π	Minimum work rate principle functional
θ	Bragg angle of incidence ($^\circ$)
ρ	Electrical resistivity (Ωm)
ρ	Density (kg m^{-3})
σ	Cr-rich intermetallic tertiary precipitate
σ	Stress (MPa)
$\bar{\sigma}$	Effective (von Mises) stress (MPa)
σ_0	Initial plastic stress (MPa)
$\sigma_{0.1}$	Stress at $\varepsilon = 0.1$ (MPa)
σ_d	Deviatoric stress tensor
σ_i	Intrinsic yield stress (MPa)
$\sigma_{i,j}$	Stress tensor component (MPa)
σ_m	Hydrostatic (mean) stress (MPa)
σ_p	Peak stress (MPa)
$\sigma_{ss(e)}$	Extrapolated steady state stress (MPa)
σ_y	Yield stress (MPa)
τ_{ij}	Shear stress component (MPa)
ΔH	Standard enthalpy (kJ mol^{-1})
Φ	Electromagnetic flux (Wb)

Ψ	Surface heat flux (W m^{-2})
d	Crystallographic planar spacing (\AA)
d	Average grain diameter (μm)
e	Error signal
f	Frequency (Hz)
f_{γ}	Fraction of austenite
f_{γ_2}	Fraction of secondary austenite
g	Acceleration due to gravity (m s^{-2})
h	Sample height (mm)
h	Heat transfer coefficient ($\text{W m}^{-2} \text{K}^{-1}$)
h_i	Instantaneous sample height (mm)
k	Critical value of von Mises yield criterion (MPa)
k	Thermal conductivity ($\text{W m}^{-1} \text{K}^{-1}$)
k	Material constant (Hall-Petch slope) ($\text{MPa mm}^{1/2}$)
m	Mass (kg)
n	Strain rate sensitivity
Q'	Convective heat flow (kJ s^{-1})
s	Standard deviation
s	Displacement (m)
t	Time (s)
u_i	Velocity component (m s^{-1})
v	Velocity (m s^{-1})
A	Temperature-independent equation constant
A	Sample area (mm^2)
A_1	Equation constant
A_2	Equation constant
AC	Alternating current (A)
AFP	Advanced Forging Product
A_i	Instantaneous sample area (mm^2)
A_i	Integral gain constant
AOD	Argon Oxygen Decarburisation
A_p	Controller proportional gain
ATPU	Advanced Thermal Processing Unit
B	Magnetic flux (T)
BCC	Body Centred Cubic
BCT	Body Centred Tetragonal
BEKD	Backscatter Electron Kikuchi Diffraction
BKD	Backscatter Kikuchi diffraction
C	Critical damage value for ductile fracture
C	Heat capacity matrix
CBL	Cut Back Limit
CDRX	Continuous DRX
CI	Confidence Interval
CL	Cockroft-Latham damage model
CNC	Computer Numeric Control
C_p	Specific heat capacity ($\text{J g}^{-1} \text{K}^{-1}$)
CPT	Critical Pitting Temperature
CPU	Central Processing Unit
CVN	Charpy V Notch
D	Sample diameter (mm)

DC	Direct current (A)
DRV	Dynamic recovery
DRX	Dynamic recrystallisation
DSS	Duplex Stainless Steel
Dt	Derivative time
E	Voltage (V)
E_T	Percussive energy of forging hammer (kgm)
EAF	Electric Arc Furnace
EBSD	Electron Back Scattered Detection
EBSP	Electron Back Scatter Pattern
F	Force (N)
F	Residual of the nodal force vector
FEA	Finite Element Analysis
FEM	Finite Element Method
FCC	Face Centred Cubic
FTTU	Fast Thermal Treatment Unit
G_1	Weight of forging hammer ram (N)
H	Magnetic field ($A\ m^{-1}$)
H	Conductivity matrix
H_1	Forging hammer ram drop height (m)
HAGB	High Angle Grain Boundary
HCP	Hexagonal Close Packed
HISC	Hydrogen-Induced Stress Cracking
HMI	Human Machine Interface
HV	Vickers Hardness
I	Electrical current (A)
IGBT	Insulated-Gate Bipolar Transistor
IPF	Inverse Pole Figure
J_1	First deviatoric stress tensor invariant
J_2	Second deviatoric stress tensor invariant
J_3	Third deviatoric stress tensor invariant
K	Penalty constant
K	Stiffness matrix
K_d	Derivative gain constant
K-M	Kocks-Mecking
K-S	Kurdjumov–Sachs orientation relationship
L	Billet longitudinal axis
LDVT	Linear Variable Displacement Transducer
MOSFET	Metal-Oxide-Semiconductor Field-Effect Transistor
MOUI	Multiple Operations User Interface
ND	Normal Direction
NR	Newton-Raphson root finding algorithm
P	Pressure (MPa)
Pb	Proportional band
PESR	Pressurised Electro-Slag Re-melting
PF	Pole Figure
PID	Proportional-Integral-Derivative control
PLC	Programmable Logic Control
PRE	Pitting Resistance Equivalency
PSC	Plane Strain Compression

PV	Process variable
Q	Heat source term (kJ)
\mathbf{Q}	Thermal load matrix
Q_{def}	Apparent hot deformation activation energy (kJ mol ⁻¹)
QHT	Quality Heat Treatment
R	Mo-rich intermetallic tertiary precipitate
R	Molar gas constant (J K ⁻¹ mol ⁻¹)
R	Electrical resistance (Ω)
R	Friction-corrected stress (MPa)
RCV	Recovery
RCX	Recrystallisation
RD	Rolling Direction
S	Standard error
S	Boundary surface of finite element domain
SCC	Stress Corrosion Cracking
SCE	Saturated Calomel Electrode
SDSS	Superduplex Stainless Steel
SEM	Scanning Electron Microscope
SFE	Stacking Fault Energy
SIBM	Strain-Induced Boundary Migration
SP	Setpoint
SSC	Sulphide Stress Cracking
SSCC	Sulphide Stress Corrosion Cracking
T	Temperature (K)
T_0	Initial temperature (K)
T_∞	Environmental temperature (K)
T_D	Deformation temperature (K)
TD	Transverse Direction
TEM	Transmission Electron Microscope
Ti	Integral time constant
TMC	Thermo-Mechanical Compression
TMTS	Thermo-Mechanical Treatment Simulator
T_s	Surface temperature
V	Sample volume (mm ³)
V_{20}	Volume at room temperature (mm ³)
V_i	Instantaneous sample volume (mm ³)
Z	Zener–Hollomon parameter

Acknowledgements

First and foremost, this work would not have been possible without the endless love, support and encouragement of my wife and inspiration, Natalie to whom I am eternally indebted, in awe of and love dearly – thanks for always stepping up and making it happen!

Inexpressible thanks also to my parents for the never-ending love, encouragement, support, advice, patience (and proof reading!). Starting, let alone finishing, this work would not have possible without the examples they, and my Grandparents Audrey and Vincent (the best engineer I ever knew), set and importance and value of hard work they all taught me.

The help and advice of my academic and industrial supervisors Prof. Brad Wynne and Dr. Glenn Byrne as well as financial support from the EPSRC is gratefully acknowledged.

I would also like to mention the invaluable help, encouragement and advice given by Mr. Glen McGrail and Dr. Isaac Sewell at Inductelec Ltd. which meant more to me that they will probably ever realise and who both continue to be an enormous influence and source of inspiration.

For my mum,

1.1 Background and Industrial Context

Duplex stainless steels (DSSs) are a group of important engineering alloys developed primarily as alternatives to the more ubiquitous single phase austenitic and ferritic grades. The characteristic two-phase, or duplex, microstructure of these steels is composed of approximately equal proportions of ferrite, δ and austenite, γ and achieved by specifying the correct balance of δ -stabilising elements such as, for example, Cr, Mo, Ti and Si and γ -stabilizing elements like Ni, N, C and Mn[1]. Common to all duplex steels however is a minimum wt.% Cr of approximately 20. The equilibrium thermodynamics of the two-phase duplex microstructure are discussed in more detail in Ch 2.

The two-phase microstructure contributes to the improvements in strength duplex stainless steels offer over equivalent single-phase austenitic grades. The grain size refinement[2] that can result from the presence of two equally-proportioned metallographic phases can also increase the toughness of duplex stainless steels as well. As with many metallic materials, the strength and toughness of DSSs can be enhanced further through appropriate thermo-mechanical processing to produce further grain size refinement of micro-duplex microstructures. The presence of relatively large separate volumes (and in approximately equal fractions) of ferrite and austenite in the duplex microstructure confer considerable advantage in terms of yield strength versus simple austenitic stainless steels. In contrast, as compared to ferritic stainless steel, the austenitic content of DSSs offers improved toughness and corrosion resistance, particularly in the heat affected zones of welded material[3].

Super duplex stainless steels (SDSSs) are a relatively recent addition to the DSS alloy category and offer improved resistance to corrosion over ‘standard’ DSSs, principally through their higher Cr, Mo and N contents which confer particularly good protection against localised pitting[4]. The increased concentrations of these elements however also necessitates greater austenite stabilizing element additions, such as Ni, in order to maintain the approximately equal balances of phases. Consequently, typical SDSSs can be expected to contain approximately 25Cr-7Ni-4Mo-0.2N wt.%[5][4]. The additional quantities of alloying elements mean that while technically adept, SDSSs do not always offer economical replacements for single phase

or standard duplex stainless steels. However, the increased strength they offer creates alternative opportunities to specify reduced section thicknesses, particularly when used in the form of welded or tubular components as for example in heat exchanger tube applications under aggressive nitric acid service conditions.

When produced under appropriately sensitive thermo-mechanical processing conditions, DSS and SDSS components are almost unmatched in their applicability to service in aggressive environments within the approximate temperature range -50 to 250°C. However, the highly alloyed two-phase microstructure, which provides such unique utility, is also responsible for these alloys' sensitivity to the precipitation of deleterious tertiary phases which can significantly impact material properties[6]. Much research has already been focused on understanding the thermodynamics behind these phase transformations, particularly in relation to the intermetallic Cr- and Mo-rich σ and χ phases[7][8], respectively, since their presence in the microstructure has been shown to embrittle catastrophically and also reduce corrosion resistance. These phases are however generally formed in temperature ranges outside those typically encountered in service or forging and quality heat treatment. Furthermore, the large body of research focused upon them has led to a general refinement of industrial practices such that their presence is largely now avoided in modern commercial thermo-mechanical processing[9]. Other phases, in particular Cr-nitrides, have also been strongly associated with a deleterious impact upon the toughness of high N-bearing SDSSs[10]. However, the factors influencing nitride formation are much less well understood and in particular the association of thermo-mechanical processing conditions to SDSS microstructure morphology and the influence this can play in their formation is unclear. Cr-nitrides also pose another problem in terms of their complex and poorly understood formation kinetics; limited research into this phenomenon has suggested that different types of Cr-nitrides can form in SDSSs, in different regions of the microstructure, during isothermal heat treatments and also during fast cooling from elevated soak temperatures[11].

The mechanical and anti-corrosion superiority, as well as improvements in weldability and the economic competitiveness of their relatively low Ni content, have seen SDSSs expand from oil and gas into other demanding applications such as water purification through thermal desalination and reverse osmosis as well as phosphoric acid (H_3PO_4) production plant[12]. However, oil and gas industrial use remains a key application, and SDSSs are commonly

encountered in subsea pipework systems (particularly weld neck flanges as well as swivel ring hub and body assemblies) with associated risers, manifolds, pressure vessels, valves and heat exchangers. Furthermore, a combination of oversupply and the development of competing technologies for the extraction of fossil fuels has led to a recent period of volatility in oil and gas market prices. This has subsequently stimulated an industry-wide drive towards increased process efficiency. Consequently, improved component performance and lifetimes in increasingly challenging and marginal conditions are being actively sought. Production of components with optimum material properties, achievable through optimized microstructures from well-defined thermo-mechanical processing parameters, for operation in these conditions is therefore of great importance.

1.2 Problem Definition

It is clear that the production of SDSSs components requires careful control of thermo-mechanical processing parameters in order to produce the desired material and mechanical properties. However, as demands on these components increase, a more fundamental and in-depth understanding of the relationship between these parameters and their effect on the microstructure is required. While research into certain aspects of the duplex microstructure has resulted in a detailed body of work on specific limitations of SDSSs and strategies for their mitigation, clear and important gaps in this knowledge still persist. At present, a comprehensive and fundamental multi-scale understanding of the relationship between microstructure evolution of SDSSs and thermo-mechanical processing parameters has yet to be established. Furthermore, a link to the optimisation of industrial forging and final quality heat treatment procedures, in order to improve the material properties of SDSS components based on such a fundamental understanding, also needs to be made. It is within this context that the research presented here has been undertaken in order to fill these knowledge gaps and to contribute to the field of study.

1.3 Project Aim

To investigate the microstructure evolution and commercially-reported variability in mechanical properties of ZERON® 100 (UNS S 32760) through industrially-analogous thermo-mechanical testing and metallographic analysis in order that fundamental

understanding of the complex process metallurgy may be deepened and strategies developed to optimise the production of forged SDSS engineering components.

1.4 Project Objectives

1. Develop a constitutive equation to model the flow behaviour of ZERON® 100 super duplex stainless steel, based on isothermal uniaxial compression test data.
2. Simulate, using the finite element method (underpinned by the above-mentioned flow model), commercial forging and heat treatment operations.
3. Associate observable microstructure evolution, morphologies and mechanical properties with macro-scale processing parameters, principally temperature, strain and strain rate.
4. Investigate any potential micro-scale orientation relationships with meso-scale features such as material flow patterns and mechanical properties in test samples from both commercial forging and lab-scale experimentation.

1.5 Thesis Outline

This thesis will seek to address each of these objectives and in order to do so, the following structure has been adopted:

- Chapter 2 The ZERON® 100 SDSS alloy:

This chapter presents background information on the development, production and utilisation of stainless steels generally and the specific SDSS used for this study, including general thermodynamic consideration of the duplex microstructure as well as an outline of the typical thermo-mechanical processing route a ZERON® 100 forging undergoes. Characterisation of as-received billet starting material is also presented and the two ZERON® 100 material variants, AFP and ‘standard product’, are also compared.

- Chapter 3 Literature Review:

Analysis of the relevant theoretical background to this work and establishment of the current state of understanding pertaining to duplex alloys and their thermo-mechanical processing is presented in this chapter. Methodologies used in this work are also compared to and analysed in the context of those detailed in other similar works.

- Chapter 4 Experimental Methodologies:

This chapter covers detailed explanations of the theoretical underpinning and operation of the main experimental methods and apparatus used in this study including; axisymmetric compression testing, metallographic preparation for optical and electron microscopy, crystallographic orientation and texture analysis through scanning electron microscope (SEM) - electron back-scattered detection (EBSD), finite element analysis computer simulation and proportional integral derivative (PID)-controlled induction heat treatment.

- Chapter 5 Axisymmetric Compression Testing and Constitutive Equation Development:

The plasticity of ZERON® 100 is investigated in this chapter; data and models developed from this are used to analyse the flow behaviour of ZERON® 100 under the testing conditions described and underpin the subsequent development of the FEM computer simulations of industrial-scale thermo-mechanical processing.

- Chapter 6 Finite Element Method (FEM) Computer Simulation of Commercial Thermo-Mechanical Processing:

This chapter covers the FEM computer simulation of industrial forging operations using DEFORM™, a commercially available simulation tool designed to analyse various forming and heat treatment processes. Specific attention is focused on identifying areas of accumulated strain and the development of temperature gradients within the forging throughout the processing route by which a weld neck flange component is produced.

- Chapter 7 SEM-EBSD Analysis:

SEM-EBSD analysis data including identification as well as evidence of dynamic recrystallization/recovery within the duplex microstructure and analysis of the orientation relationships between the phases is presented in this chapter. Samples of material from impact toughness specimens taken from specific locations in an open die forged weld neck flange as well as laboratory-processed samples are analysed and compared.

- Chapter 8 Thermal Simulation and Mechanical Testing:

This chapter begins with the derivation of location-specific cooling curves from within a 16” (406.4 mm) ZERON® 100 weld neck flange forging through FEM analysis of the final quality heat treatment operation. These cooling curves are then interpolated and simulated using induction heat treatment equipment (following initial experimental equipment verification, benchmarking and adaption) and assessed in terms of associated mechanical properties.

- Chapter 9 Conclusions and Recommendations for Further Work:

This final chapter provides a critical summary of the key observations from the preceding chapters. The main themes of the investigation are drawn together and synthesised in terms of potential thermo-mechanical processing optimisation in the production of ZERON® 100 forgings. Key areas and themes, relating to this processing optimisation, that could be usefully investigated through follow-on future research from this work are also considered.

REFERENCES

- [1] R. Gunn, Ed., *Duplex stainless steels : microstructure, properties and applications*. Woodhead Publishing, 1997.
- [2] M. Abe, A. Hiura, K. Ishida, and T. Nishizawa, “Grain Growth in Duplex Stainless Steels,” *Tetsu-to-Hagane*, vol. 70, no. 15, pp. 2025–2032, Nov. 1984.
- [3] T. Kuroda, K. Ikeuchi, and Y. Kitagawa, “Role of Austenite in Weld Toughness of Super Duplex Stainless Steel,” *Weld. World*, vol. 49, no. 5–6, pp. 29–33, May 2005.
- [4] J.-O. Nilsson, “Super duplex stainless steels,” *Mater. Sci. Technol.*, vol. 8, pp. 685–700, 1992.
- [5] M. Pohl, O. Storz, and T. Glogowski, “Effect of intermetallic precipitations on the properties of duplex stainless steel,” *Mater. Charact.*, vol. 58, no. 1, pp. 65–71, 2007.
- [6] J. O. Nilsson and A. Wilson, “Influence of isothermal phase transformations on toughness and pitting corrosion of super duplex stainless steel SAF 2507,” *Mater. Sci. Technol.*, vol. 9, no. 7, pp. 545–554, Jul. 1993.
- [7] A. F. M. Pérez, R. Sandström, I. Calliari, and F. A. R. Valdés, “Sigma phase precipitation on welded SAF 2205 Duplex Stainless Steels after isothermal heat treatment,” *MRS Proc.*, vol. 1611, pp. imrc2013-4a-054, Jul. 2014.
- [8] I. Calliari, M. Pellizzari, and E. Ramous, “Precipitation of secondary phases in super duplex stainless steel ZERON100 isothermally aged,” *Materials Science and Technology*, vol. 27, pp. 928–932, 2011.
- [9] A. M. Elhoud, N. C. Renton, and W. F. Deans, “The effect of manufacturing variables on the corrosion resistance of a super duplex stainless steel,” *Int. J. Adv. Manuf. Technol.*, vol. 52, no. 5–8, pp. 451–461, Feb. 2011.

- [10] M. Knyazeva and M. Pohl, "Duplex Steels. Part II: Carbides and Nitrides," *Metallogr. Microstruct. Anal.*, vol. 2, no. 5, pp. 343–351, Oct. 2013.
- [11] E. Bettini, U. Kivisäkk, C. Leygraf, and J. Pan, "Study of corrosion behavior of a 2507 super duplex stainless steel: influence of quenched-in and isothermal nitrides," *Int. J. Electrochem. Sc.*, vol. 9, no. 6, pp. 61–80, 2013.
- [12] P. Boillot and J. Peultier, "Use of Stainless Steels in the Industry: Recent and Future Developments," *Procedia Eng.*, vol. 83, pp. 309–321, 2014.

Chapter 2: Stainless Steels and the ZERON® 100 Superduplex Stainless Steel Alloy

Stainless steel is a general term used to describe a wide range of metallic materials which can be broadly characterised as Fe-based alloys containing $\geq 12\text{wt.}\%$ Cr and are thus able to form a thin passivating surface film of chromium oxide. This chromium oxide layer provides resistance to corrosion in aqueous environments and oxidation at high temperatures. Stainless steels encompass a great diversity of chemical compositions, material properties and microstructures and have been the subject of previous extensive studies [1][2]. It therefore suffices here to briefly review the main sub-categories of stainless steel in order to contextualise duplex stainless steels. A brief discussion of the development of super duplex stainless steels with specific reference to the ZERON® 100 alloy will also be presented.

2.1 The Fe-Cr-Ni Alloy System

At their most basic, stainless steels are simply pseudo-binary Fe-Cr alloys (Fig. 2.1) containing three discrete phases; the body centred cubic (BCC) high and low temperature Fe allotropes ferrite, $\delta\text{-Fe}$ and $\alpha\text{-Fe}$, respectively (as noted below, referred to as δ in Fig. 2.1), the face centred cubic (FCC) Fe-allotrope austenite, $\gamma\text{-Fe}$ and a high-Cr phase, σ . Duplex stainless steels are composed of a continuous ferrite matrix that constitutes the first solid phase to form upon freezing of the melt[3]. The research literature is however inconsistent in the labelling of ferrite, and instances of reference to both the α and δ allotropes can be found. For the purposes of consistency, and because it is the first to form at high temperature, the duplex ferrite phase is herein referred to as $\delta\text{-Fe}$.

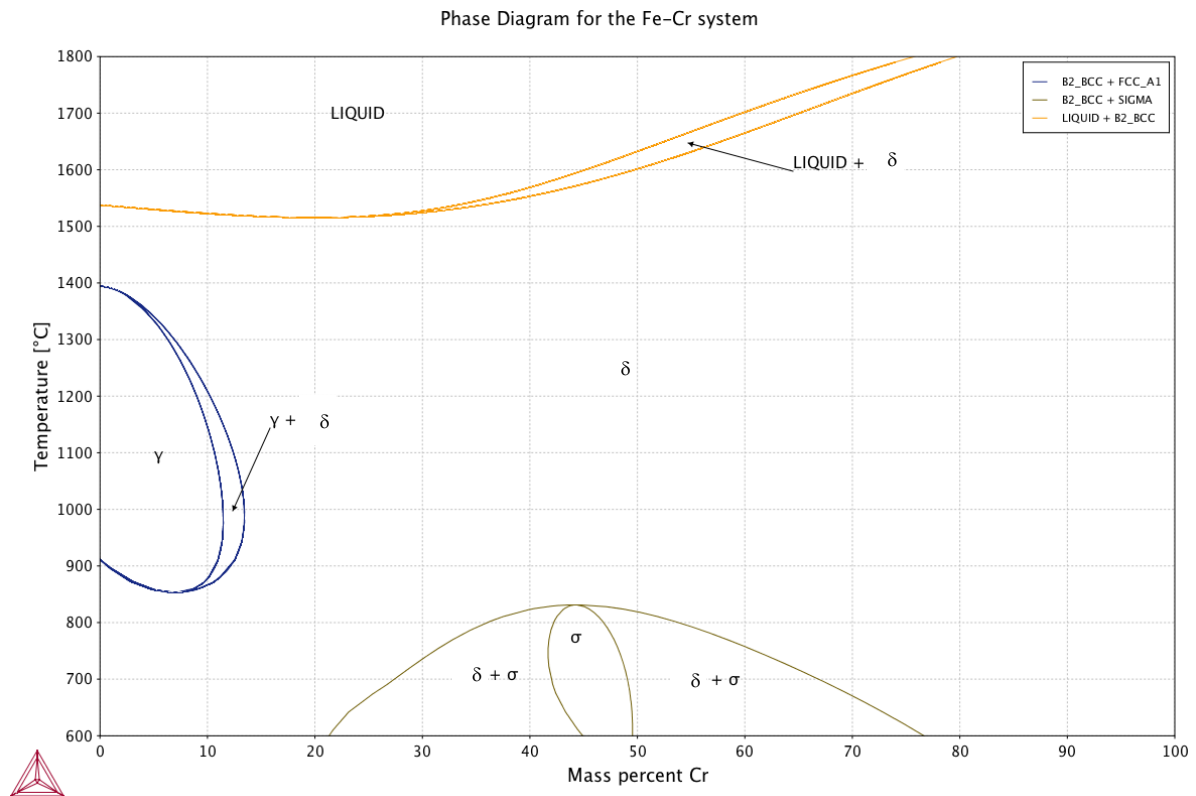


Fig. 2.1 Equilibrium phase diagram for the pseudo-binary Fe-Cr alloy system as calculated using Thermo-Calc® and the FEDEMO database

The 'γ loop' indicated in Fig. 2.1 can be stabilised at lower temperatures through the addition of Ni to the Fe-Cr alloy system (Fig. 2.2) and thus by varying the elemental proportions in this ternary system fully ferritic, austenitic or a combination of both (duplex) microstructures can be produced[4]. Martensitic stainless steels can also be produced via the diffusionless, strain-induced shear transformation[5] through suitable coiling to room temperature of their elevated temperature austenitic structure.

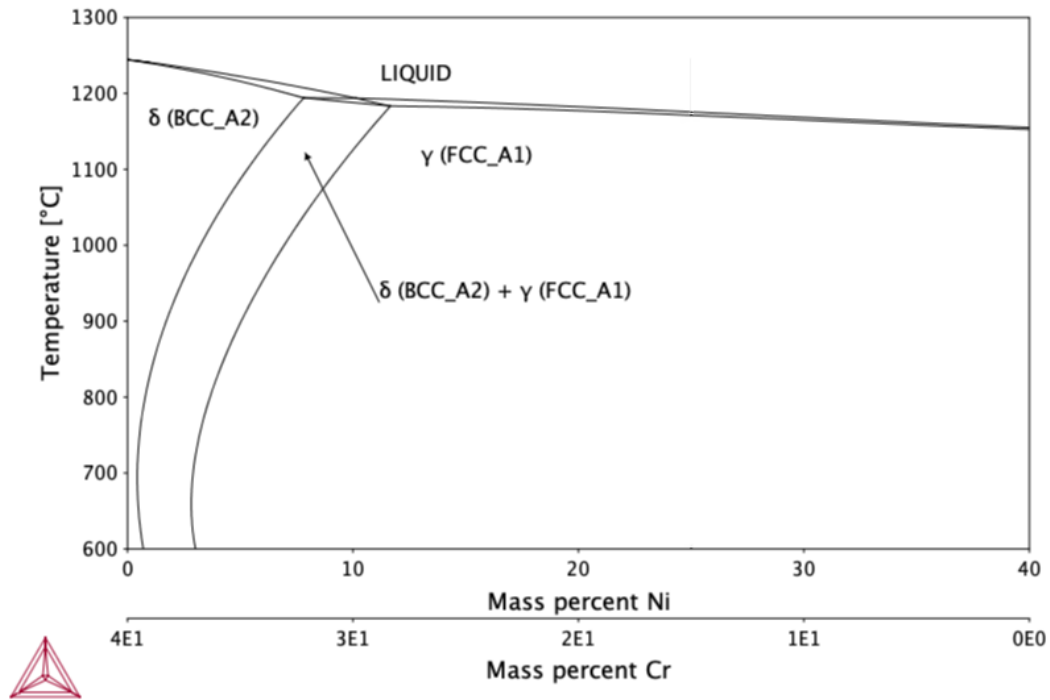


Fig. 2.2 Pseudo binary phase diagram for the Fe-Cr-Ni alloy system at 60 wt.% Fe calculated using Thermo-Calc® CALPHAD software and the FEDemo database

2.2 Ferritic Stainless Steels

Ferritic stainless steels (as designated by the 400 series of AISI standard grades) are popular in engineering applications largely as a result of the economic advantages their low Ni contents offer. Historically, type 430 (the basic 17 wt.% Cr stainless steel) has seen the most ubiquitous deployment with its user-specifiable Cr contents from 14 to 18 wt.% providing a choice of properties from improved weldability, strength and impact resistance to corrosion resistance particularly in nitric acid[6]. They can achieve comparable mechanical properties to mild steel (typical tensile strengths for annealed AISI type 400 material can be expected to fall within the range 470 – 550 MPa)[7], albeit with improved corrosion resistance due to their Cr contents (from a minimum of ca. 12wt.% up to a maximum 30 wt.%) and as such are preferred for thin sheet applications, e.g. high-strength shell and tube heat exchangers and pressure vessels[8]. The low Ni content of these stainless steels means their corrosion resistance is however generally not comparable to the austenitic grades.

Despite their high strengths, the ferritic grades are however prone to brittle fracture with much work indicating that increasing the Cr content (to promote greater corrosion resistance,

especially in mild service environments) of the ferritic alloy also acts to increase the ductile-to-brittle-transition-temperature, below which the material is regarded as having low impact strength. Mo and Nb additions (0.12 – 1.0 wt.%) are often added to enhance creep resistance, heat resistance, toughness and formability. Nb availability also allows for preferential combination with C and N, Nb[CN], to suppress the formation of chromium nitrides or complex chromium carbides and so helps to avoid the corrosion resistance depletion associated with high temperature sensitization[9].

2.3 Austenitic Stainless Steels

The general Cr and Ni compositions of the austenitic stainless steels (the AISI 300 series) are in the range 13 – 25 wt.% and 8 – 20 wt.%, respectively[6]. Austenitic stainless steels account for the majority of global stainless steel production and are commonly encountered in medical, flue gas clean-up plant and paper bleaching applications[10]. The standard stainless grades 304 and 316 are both examples of austenitics. Relative to the other stainless grades, austenitics offer high ductility and low yield strength. Their resistance to corrosion in a variety of media, as conferred by high Ni contents, means austenitic stainless steels are generally preferred for severe acid service corrosion and resistance to Cl pitting and stress corrosion cracking (SCC). Austenitic stainless steels are also relatively easy to weld (important for field fabrication) and as such have found ubiquitous application in the off-shore oil and gas and nuclear industries where weld quality in piping is of critical importance[11].

As with ferritics, additional alloying elements such as Nb and Mo can be added to austenitic stainless steels (up to ca. 0.8 wt.%) with the effect that the austenitic lattice is strained to such an extent that, in combination with the grain refining effect (due to the formation of fine precipitates of niobium-carbide or niobium carbonitride) the yield strength can be significantly increased. Mo and Nb are also capable of ‘mopping-up’ excess carbon and nitrogen and therefore minimizing the precipitation of complex chromium carbides, Cr[CN], during heat treatment or welding which in turn prevents local loss of chromium in the matrix that can lead to inter-granular corrosion, pitting corrosion or welding difficulties[9][12].

2.4 Martensitic Stainless Steels

Martensitic stainless steels can in effect be considered a subgroup of the ferritic grades; their Cr and Ni contents are typically in the range 12 – 13 wt.% and ≤ 4 wt.%, respectively. The metastable martensite transformation usually occurs upon cooling from hot working in the austenitic phase temperature range and produces a hard and strong microstructure with moderate corrosion resistance[3]. Martensitic stainless steels have many important uses in hygiene-critical applications such as surgical and dental implants since they can be machined to a smooth, easy to clean surface finish which makes microbial attachment and growth difficult. They are also utilized as turbine blades and CNC-milled, single piece axial compressor blisks (portmanteau of bladed disk) in hydro-electric and gas power generation applications due to their strength.

Extremely close control of alloy content is however required to adjust down the martensite transformation temperature, principally such that components may be easily machined in the austenitic temperature range then transformed at sub-ambient temperatures. This tight composition control however generally limits use to highly specialised, low-volume military applications. Increasing use of precipitation hardened martensitic stainless steel grades has arisen from alloying combinations of Cu and Nb in a low-C martensitic matrix to give very high levels of hardness while maintaining the stabilization effect and corrosion cracking resistance through the prevention of Cr-carbide precipitation[13]. These effects are typically achieved through the addition of ca. 0.7 wt.% Nb in the presence of ca. 2% Cu.

2.5 Duplex Stainless Steels

The duplex stainless steel (DSS) family of alloys are characterised by their combination of high strength to weight ratio, good resistance to SCC and two-phase microstructure (Fig. 2.3), in which both the ferritic and austenitic components are ‘stainless’ (i.e. of chemical composition > 12 wt.% Cr) and present in approximately equal volume fractions[14]. Their development and increasing prevalence as engineering materials has been in large part driven by the economic advantages they offer over super austenitic stainless steels and high-nickel alloys for applications in aggressive service conditions containing Cl^- ions, H_2S and CO_2 [15], despite the remarkably high corrosion resistance and elevated temperature strength of these alternative alloys. The cost-effectiveness is largely a factor of the lower Ni contents in DSS alloys.

Phase equilibria calculations illustrate that the first phase to form upon cooling below the alloy's *liquidus* temperature is ferrite, assuming the BCC crystal lattice structure (Fig. 2.4). Ferrite, or δ -Fe is, as noted above, the high temperature allotrope of Fe and a solid solution containing ca. 0.025% C. Upon further cooling below the *solidus* temperature the second Fe allotrope, austenite (γ -Fe) forms from the ferrite phase. Austenite is another solid solution of Fe-C, albeit with FCC crystal structure and lower stacking fault energy than ferrite, and contains a maximum of ca. 2.14% dissolved C.

The ferrite-austenite duplex structure enhances the resistance to sensitization, with welds of thickness 1 – 90 mm in operational service produced by all common arc techniques[16]. Importantly, the duplex structure also retards the propagation of stress corrosion cracks (SCCs) and therefore DSSs (in the annealed condition) are preferred to certain lower grade austenitics in service environments containing the simultaneous presence of a tensile stress and a specific corrosive medium[17]. The susceptibility of DSSs to SCC, and particularly sulphide SCC (SSCC, commonly also referred to as sulphide stress cracking, SSC)[18], has been shown to be strongly dependent on temperature. Additionally, high-Cr duplex alloys in the heavily cold worked condition are considerably more susceptible to SSCC than solution annealed alloys[19].

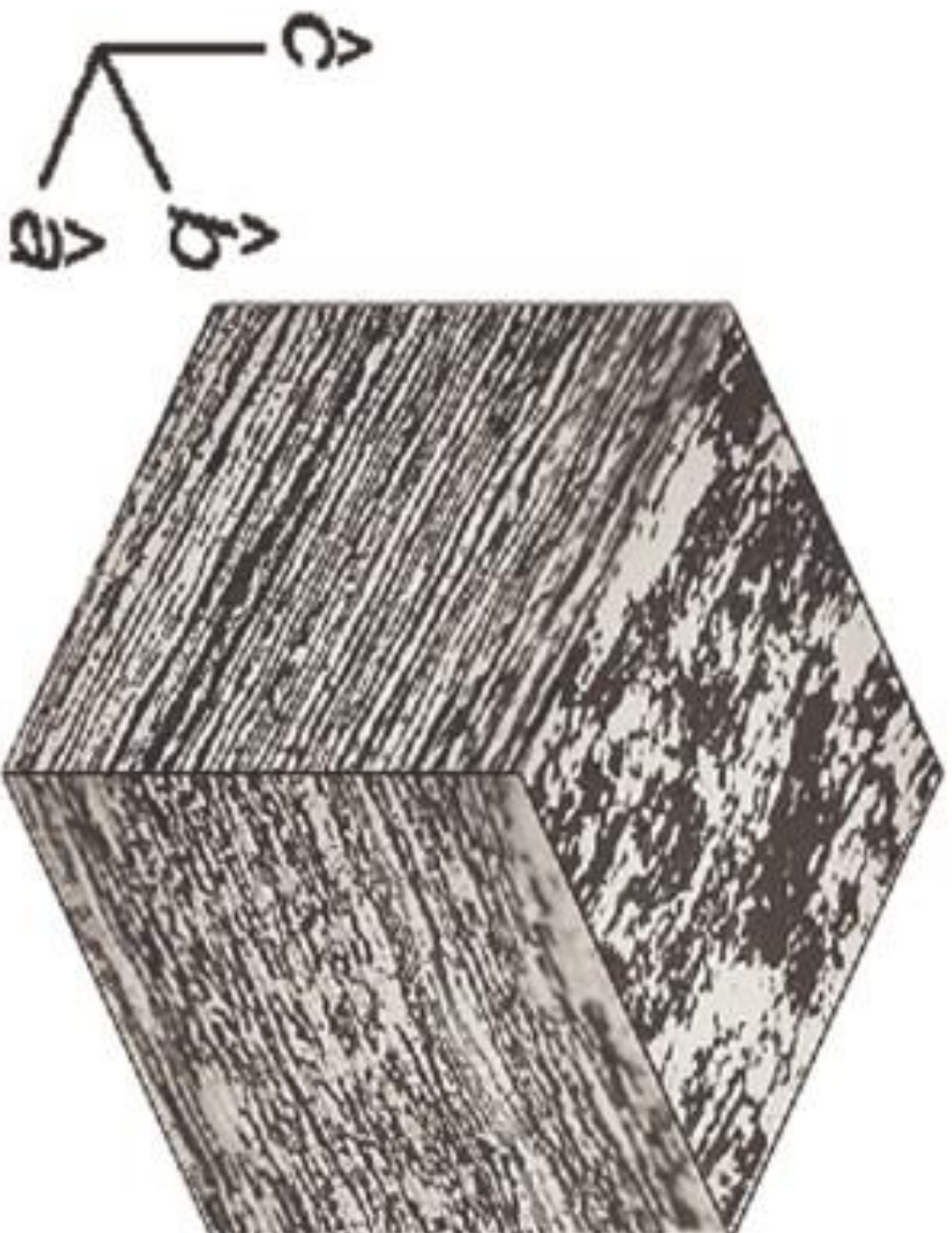


Fig. 2.3 Microstructure of a block of as-received SDSS showing a 3D spatial distribution of ferrite (dark) and austenite (light) phases[20]

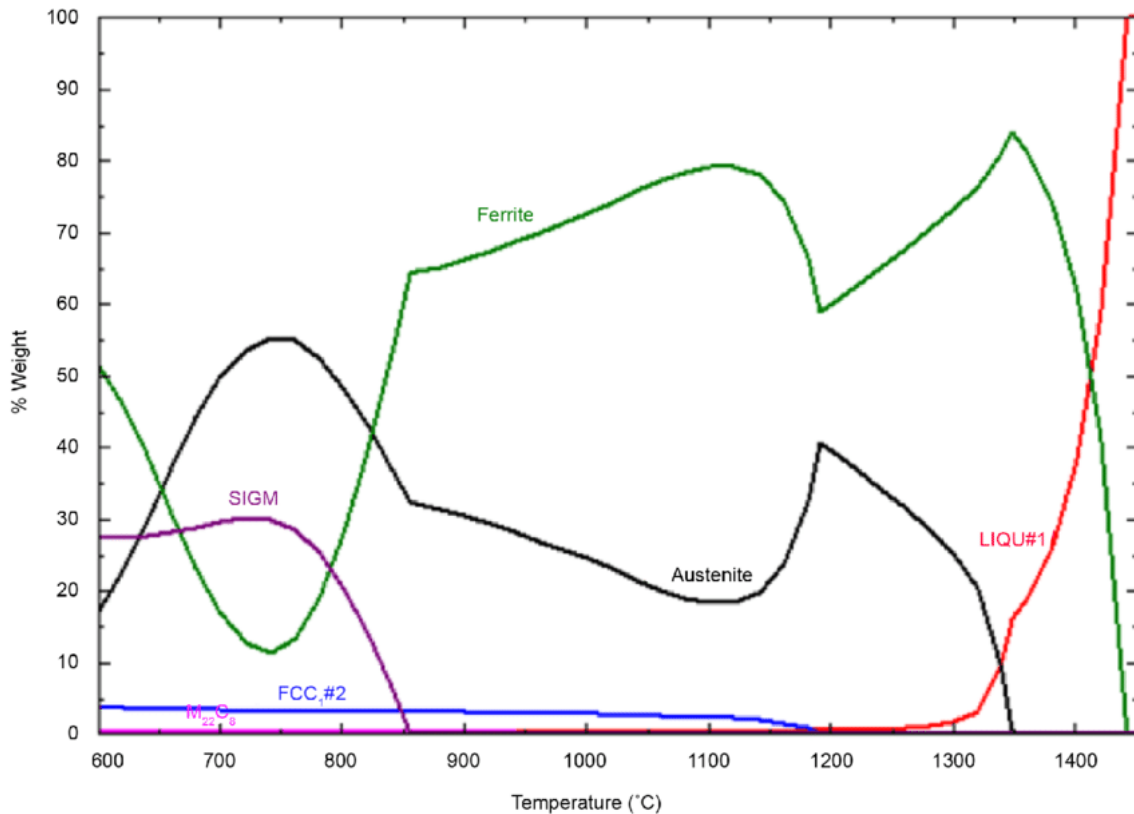


Fig. 2.4 Equilibrium phase diagram for the duplex and tertiary phases in a typical duplex stainless steel, adapted from Ref. [21]

The development of DSS to offer improved pitting and stress corrosion resistance has led to the designation ‘super duplex stainless steels’ (SDSSs), defined as having pitting resistance equivalency (PRE) > 40, where

$$PRE_N = \text{wt.\%Cr} + 3.3(\text{wt.\%Mo}) + 16(\text{wt.\%N}) \quad \text{Eqn. 2.1}$$

And generally, Cr contents > 24 wt.%. $PRE_N > 40$ is recognized as the minimum level of alloying required to resist crevice corrosion in seawater by the Norwegian oil and gas NORSOK standard[22]. DSS Cr contents are generally around 22 wt.% by comparison.

2.6 Development of the ZERON® 100 Superduplex Stainless Steel Alloy

The increasing depletion of ‘conventional’ oil and gas reserves over previous decades has precipitated an expansion in both the exploration for new reservoirs and techniques to maximise the recovery from marginal wells. In both cases, increasingly challenging service

conditions are often encountered and the performance envelope of the materials, such as duplex stainless steels, utilised in subsea pipework systems (particularly weld neck flanges as well as swivel ring hub and body assemblies) with associated risers, manifolds, pressure vessels, valves and heat exchangers, has sought to be expanded. The suitability of duplex stainless steels to the demands associated with offshore oil and gas production has also led to their deployment in other aggressive environment applications such as water purification through thermal desalination and seawater reverse osmosis as well as phosphoric acid (H₃PO₄) production plant, flue gas desulphurisation and the process and petrochemical refinement industries[15].

Duplex stainless steels such as ZERON® 25 (based on the 25Cr-6Ni-2Mo alloy system) achieved considerable success after development in the late 1970s and early 1980s for application in sea water injection lift and firewater pump castings. However, with the move to increasingly harsh environments detailed above, the impetus to develop new alloys with improved localised corrosion resistance as well as optimised mechanical properties such as toughness, ductility, proof strength, formability as well as weldability grew. ZERON® 100 was the first of the ‘super’ duplex stainless steels (SDSSs) developed to satisfy these requirements in 1991 by Weir Materials (UK) Ltd. from Mather & Platt Machinery (UK) Ltd.’s investigations in the late 1980’s into the effect of Mn and N additions (up to 4 and 0.03 wt.%, respectively) on the mechanical properties and phase transformations of ZERON® 25[23]. ZERON® 100 (covered by UNS S 32760 for wrought products and UNS J 93380 for castings) (25 wt.%Cr, 7 wt.%Ni, 3.5 wt.%Mo, 0.25 wt.%N) is produced, stocked and processed into a variety of product forms, namely plate, bar, pipe, hot isostatically pressed powder and, with particular pertinence to this work, bossed weld neck flange forgings[17]. The typical maximum elemental chemical composition of wrought ZERON® 100 is shown in Table 2.1.

Table 2.1 Maximum elemental compositions (wt.%) of wrought ZERON® 100 (UNS S 32760, F55)

Cr	Ni	Mo	W	Cu	N	Si	C	Mn	P	S	Fe
26.0	8.0	4.0	1.0	1.0	0.3	1.0	0.03	1.0	0.03	0.01	Bal.

2.6.1 Characteristics of ZERON® 100

ZERON® 100 offers comparable fracture toughness and localised corrosion resistance in Cl⁻ ion and H₂S- containing environments to the highly alloyed super austenitic grades, however it also combines yield stresses in the range 550 - 600 MPa. This high strength allows for the specification of thinner wall thicknesses in, for example, ZERON® 100 pipes and vessels and offsets the higher material cost than commonly deployed regular austenitic stainless steels such as 316 and 304. The W- and Cu-bearing content of ZERON® 100 also offers elevated resistance to corrosion in the presence of halides, acids and alkalis. The high strength of ZERON® 100 also compares well to equivalent properties achievable in the ferritic grades of stainless steel.

It is important to note however that limitations arise in the application of SDSSs and DSSs above approximately 250°C due to the brittleness of the ferrite phase in the presence of myriad intermetallic, carbide and nitride third phases such as σ , R, χ and α' (Fig. 2.4) which precipitate at elevated temperatures chiefly as a result of high alloy contents. Precipitation of the α' phase (also referred to as 475 embrittlement) in particular produces a substantial loss in toughness taking ca. 6 hours at 475°C (as compared to 10³ hours at 330°C) and generally limits DSS & SDSS use to below 300°C[24]. An effect of the Si, W, Mo and Cr in the chemical compositions of DSSs is to stabilise the phase fields of these deleterious inter-metallic, carbide and nitride tertiary phases to higher temperatures and shorter times as illustrated in Fig. 2.5.

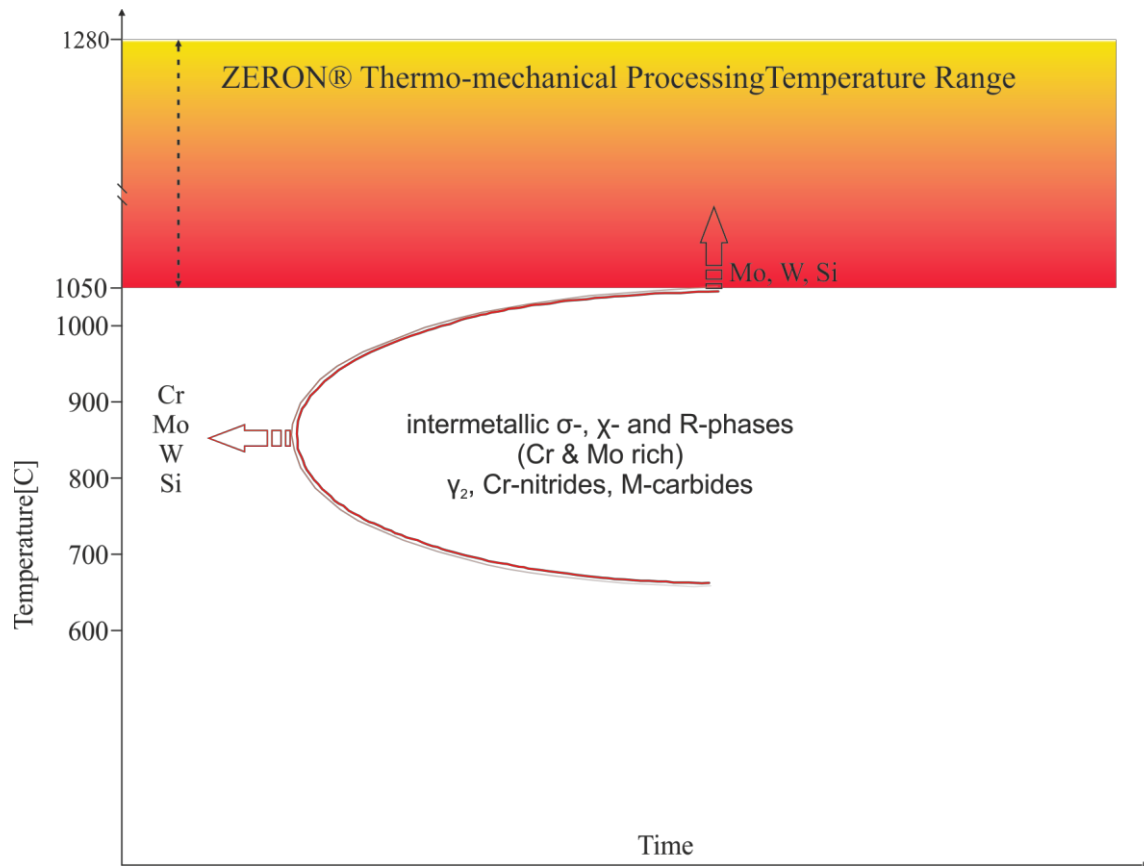


Fig. 2.5 Schematic time-temperature transformation curve indicating the conditions for precipitation of tertiary phases in wrought DSS microstructures. The stabilizing effect of alloying elements in extending the envelope of the temperature - time stability field in which these phases precipitate is indicated by the arrows.

2.6.2 Starting ZERON® 100 Billet Material

This work focuses on the ‘downstream’ thermo-mechanical processing of ZERON® 100 SDSS, and while a detailed investigation of the steel making processes undertaken to produce this material is beyond its scope, it suffices to summarise below the production of the starting billet upon which much of the experimental work conducted herein has been carried out.

ZERON® 100 starting billet stock can be produced through rotary forging of cast ingots. Unless otherwise stated, work detailed herein has been carried out on circular-section billets forged from cast ingots in a GFM RF100 rotary forging machine at Böhler Edelstahl (Austria) GmbH & Co. KG and supplied by NeoNickel (Blackburn, UK) Ltd./Rolled Alloys Inc. The Böhler Edelstahl GFM RF100 rotary forge is configured with four, two-tonne, diagonally

opposed, flywheel-driven hammers and is capable of accepting a maximum ingot diameter of 1000 mm.

Rotary forging of ingots into billets is typically achieved in a five – eight pass cogging operation followed by solution heat treatment at 1100°C and water quenching. Ingot casting was carried out (also at Böhler Edelstahl) through conventional electric steel making processes; melting a scrap charge in an electric arc furnace (EAF) and argon oxygen decarburization (AOD) of the melt followed by homogenization heat treatment. This production process is illustrated schematically below in Fig. 2.6

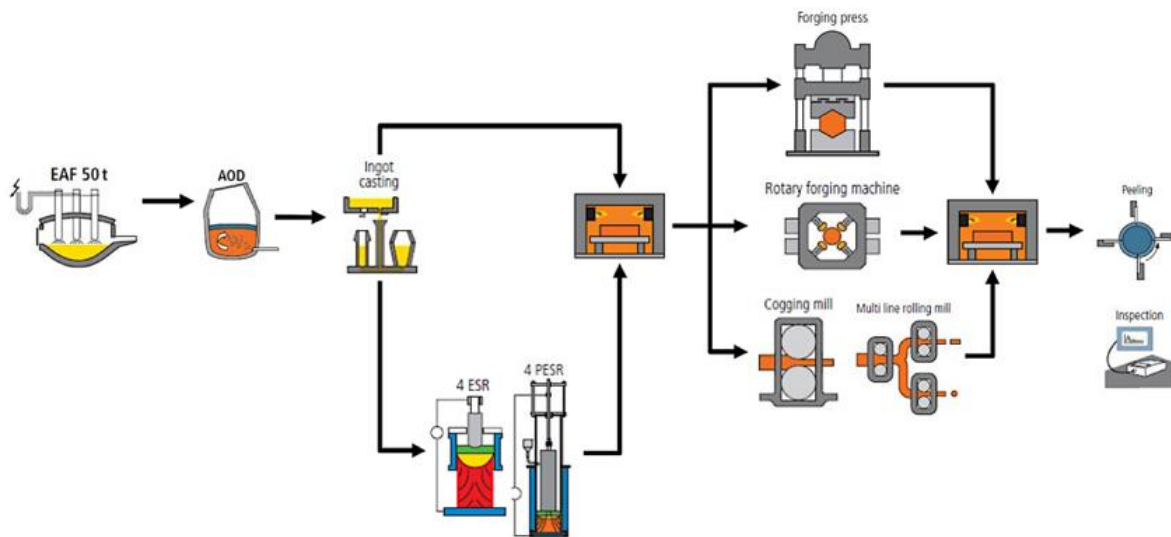


Fig. 2.6 Schematic illustration of the (duplex stainless) steel making process for both the ‘standard’ duplex and superduplex products as well as ZERON® 100 AFP through incorporation of additional (P)ESR operations.

An alternative to standard ingot casting in the billet production process is (pressurized) electroslag re-melting, (P)ESR, used to produce the AFP (Advanced Forging Product)-branded ZERON® 100 material and developed to produce a more chemically homogenous ingot structure, with greater grain size refinement as compared to the standard product.

2.7 Summary

This chapter has provided a general introduction to the Fe-Cr-Ni stainless steel alloy family and briefly outlined the main constituent grades within it as a means of contextualising DSSs. The DSS grade has been explored in detail with specific focus on the subsequent development of higher alloy, more corrosion resistant SDSSs. ZERON® 100, the first of the SDSSs

developed and the material upon which the following work presented here is based, was also introduced in detail. As part of this characterisation the quantitative metallographic techniques used extensively in subsequent chapters of this work have been introduced and explored.

REFERENCES

- [1] K.H. Lo, C.H. Shek, J.K.L. Lai, Recent developments in stainless steels, *Mater. Sci. Eng. R Reports*. 65 (2009) 39–104. doi:10.1016/j.mser.2009.03.001.
- [2] H.K.D.H. Bhadeshia, R.W.K. Honeycombe, *Steels : microstructure and properties*, 3rd ed., Elsevier, Butterworth-Heinemann, Oxford, 2006.
- [3] A.O. Humphreys, *Low Temperature Fracture Behaviour of the Superduplex Stainless Steel ZERON 100*, University of Birmingham, 1997.
- [4] R. Gunn, ed., *Duplex stainless steels : microstructure, properties and applications*, Woodhead Publishing, 1997.
- [5] J. Talonen, H. Hänninen, P. Nenonen, G. Pape, Effect of strain rate on the strain-induced $\gamma \rightarrow \alpha'$ -martensite transformation and mechanical properties of austenitic stainless steels, *Metall. Mater. Trans. A*. 36 (2005) 421–432. doi:10.1007/s11661-005-0313-y.
- [6] A.J. Sedriks, *Electrochemical Society., Corrosion of stainless steels*, Wiley, 1979.
- [7] J. Demo, ed., *Structure, Constitution, and General Characteristics of Wrought Ferritic Stainless Steels*, ASTM International, West Conshohocken, PA , 1977. doi:10.1520/STP619-EB.
- [8] A.K. Khare, *American Society for Metals. N.W. Pennsylvania Chapter., Ferritic steels for high-temperature applications : proceedings of an ASM International Conference on Production, Fabrication, Properties, and Application of Ferritic Steels for High-Temperature Applications*, Warren, Pennsylvania, 6-8 October 1981, American Society for Metals, Ohio, 1983.
- [9] A.J. Deardo, Niobium in modern steels, *Int. Mater. Rev.* 48 (2003) 371–402. doi:10.1179/095066003225008833.
- [10] T. Sourmail, Precipitation in creep resistant austenitic stainless steels, *Mater. Sci. Technol.* 17 (2001) 1–14. doi:10.1179/026708301101508972.
- [11] B.T. Lu, Z.K. Chen, J.L. Luo, B.M. Patchett, Z.H. Xu, Pitting and stress corrosion cracking behavior in welded austenitic stainless steel, *Electrochim. Acta*. 50 (2005) 1391–1403. doi:10.1016/j.electacta.2004.08.036.
- [12] K. Sugimoto, Y. Sawada, The role of molybdenum additions to austenitic stainless steels in the inhibition of pitting in acid chloride solutions, *Corros. Sci.* 17 (1977) 425–445. doi:10.1016/0010-938X(77)90032-4.
- [13] C. Bathias, R.M. Pelloux, Fatigue crack propagation in martensitic and austenitic steels, *Metall. Trans.* 4 (1973) 1265–1273. doi:10.1007/BF02644521.
- [14] J.-O. Nilsson, Super duplex stainless steels, *Mater. Sci. Technol.* 8 (1992) 685–700. doi:10.1179/mst.1992.8.8.685.
- [15] R.A. Lula, *American Society for Metals., Duplex stainless steels*, ASM, 1983.
- [16] R. Francis, G. Warburton, A model for corrosion of the depleted zones around sigma precipitates produced during welding of superduplex stainless steels, in: *Stainl. Steel World Conf. Corros. Alloy., The Hague, 1999*: pp. 711–720.
- [17] R. Francis, G. Byrne, G. Warburton, The Corrosion of Superduplex Stainless Steel in Different Types of Seawater, in: *Corros. Conf. Expo, NACE International, Houston, Texas, 2011*: pp. 3333–3341.
- [18] A.A. El-yazgi, D. Hardie, The embrittlement of a duplex stainless steel by hydrogen in a variety of environments, *Corros. Sci.* 38 (1996) 735–744. doi:10.1016/0010-938X(95)00162-D.
- [19] R. Francis, G. Warburton, *The corrosion of ZERON 100 in oil and gas production environments*, Manchester, 2008.
- [20] M. ElMassalami, I. Palatnik-de-Sousa, M.C.L. Areiza, J.M.A. Rebello, A. Elzubair, On the magnetic anisotropy of superduplex stainless steel, *J. Magn. Magn. Mater.* 323 (2011) 2403–2407. doi:10.1016/j.jmmm.2011.05.007.
- [21] S.-H. Jeon, S.-T. Kim, J.-S. Kim, J.-S. Kim, K.-T. Kim, Y.-S. Park, Effects of Copper Addition on the Precipitation of Chromium Nitrides and the Associated Pitting Corrosion Resistance of the Hyper Duplex Stainless Steels, *Mater. Trans.* 53 (2012) 2129–2134. doi:10.2320/matertrans.M2012277.
- [22] *NORSOK M-001 Rev 4, Materials Selection*, Oslo, 2004.
- [23] C.V. Roscoe, *Structure-Property Relationships in a Series of Duplex Stainless Steels*, University of Manchester, 1987.
- [24] S.S.M. Tavares, R.F. de Noronha, M.R. da Silva, J.M. Neto, S. Pairis, 475 °C Embrittlement in a duplex stainless steel UNS S31803, *Mater. Res.* 4 (2001) 237–240. doi:10.1590/S1516-14392001000400003.

Chapter 3: Literature Review

A summary characterisation of duplex and super duplex stainless steels (DSSs and SDSSs) and their development (with specific reference to ZERON® 100, UNS S 32760), as well as the other main sub-categories of the stainless steel alloy family has been presented previously in Ch. 2. In this chapter critical consideration is focused upon the general body of research concerning DSSs and SDSSs pertinent to the scope, aims and methodologies of this work.

Due to their importance and applicability as engineering materials, SDSSs, and DSSs in general, have been the subject of a great deal of varied research interest. This extensive body of research has greatly informed and underlined design guidance and industrial practice as to the safe application and suitable service environments of duplex material. The most common engineering applications into which DSSs and SDSSs are deployed (predominately aggressive service environments such as subsea oil and gas, power generation, flue gas desulphurisation, acid pressure vessels and heat exchangers) has, not unsurprisingly, led to a disproportionate focus on the joining of these alloys and their corrosion resistance. The key area of corrosion resistance will be explored generally in this chapter however, particular attention will be focused upon that research which relates the industrially analogous thermo-mechanical processing of SDSS to the development of microstructure morphology (and associated mathematical/computer modelling thereof).

As noted above, DSSs and SDSSs were originally developed for, and to this day are still commonly found in, aggressive service environments; principally the offshore oil and gas, marine, petrochemical and process industries. Corrosion resistance (and therefore by extension, the potential to increase service life) is thus a key focus for research related to these alloys and is often evaluated as a function of the parameters of typical post-forming quality heat treatment processes (overwhelmingly soak time and temperature). A critical summary of the principal themes and outcomes of this work is presented below and structured in accordance with those key tertiary precipitates identified as particularly deleterious to material properties and which also, due to the thermodynamics of their formation, are worthy of particular consideration in relation to the scope and methodologies of this work. Following this, a critical evaluation of the research work with explicit emphasis upon the mechanical evaluation of DSS and SDSS is presented. In accordance with the computer simulation, replication and evaluation of the bulk

forming of ZERON® 100 subsequently presented in this work, research pertaining to the evaluation of the flow characteristics of DSSs and SDSSs will also be subject to particular consideration as well as those studies which have attempted to analyse the microstructure development of DSS and SDSS alloys in terms of the forming processes to which they have been subjected.

3.1 The Precipitates and Corrosion of Duplex and Superduplex Stainless Steels

Much of the corrosion-focused research related to DSSs and SDSSs concerns the formation, characterisation and effects on material performance of the Cr-rich, crystallographically tetragonal, eutectoid σ (sigma) intermetallic phase. This phase is generally found to precipitate isothermally during ageing in the approximate temperature range 650 - 900°C and attracts considerable special attention in the research literature due to the highly deleterious effect on material performance (both corrosion resistance and mechanical properties) it is associated with. The σ intermetallic is however, only one of a large number of potential tertiary precipitates which may be formed in duplex and superduplex alloys systems during their thermo-mechanical processing (as has been discussed previously in Ch. 2, and summarised in Figs. 2.4 & 2.5). The thermodynamics of, particularly, σ phase formation have been investigated and reviewed extensively[1],[2], however considerable research has also been conducted into the χ (chi), Cr_xN (chromium nitride), M_{23}C_6 (M-carbide), secondary austenite (γ_2) and α' (alpha prime, or so-called 475°C embrittlement) phases as well[3],[4]. In common with σ , these phases have been shown generally to form at temperatures < 1000°C through, primarily, elemental (mainly Cr, Ni, Mo, N) depletion of the surrounding matrix, thereby increasing susceptibility to localised pitting corrosion. In addition to their reduction of the resistance to corrosion of DSSs and SDSSs, the most commonly noted effect of impaired mechanical performance caused by these deleterious tertiary precipitates is reduced toughness as a result of matrix embrittlement[1]. Inasmuch as stainless steels in general have been so extensively studied, these, and many other various precipitates, are well characterised and it has been widely reported that their precipitation results in across-the-board property changes. These changes almost invariably adversely affect the performance of not only duplex but all sub-categories (e.g. austenitic, martensitic etc.) of stainless steel.

3.1.1 The σ (Sigma) Intermetallic Phase

Simplification of the Fe-Cr-Ni ternary phase diagram into a pseudo-binary Cr-Ni phase diagram at ca. 70% (Fig. 2.2) Fe shows that the formation of σ is via the eutectoidal decomposition of ferritic matrix phase[5] according to the reaction $\delta \rightarrow \gamma_2 + \sigma$, between 600 and 1000°C, with the fastest rate of precipitation suggested to occur between ca. 850 and 900°C[6]. Further, it has also been suggested that this formation occurs as, initially, nucleation on ferrite – austenite interfaces then growth via ferritic decomposition in a cellular morphology. Contrastingly however, it has also been suggested that the formation of σ phase is the culmination of a complex precipitation sequence involving precursor χ and nitride particles[2] and despite such a large body of work, no one complete, definitive description has yet emerged. Qualitative chemical analyses have shown that chromium, molybdenum, and silicon are enriched in the σ phase thereby predisposing its precipitation in the SDSS versus DSS grades due to their compositional enrichment in these elements. The intra-granular precipitation of σ phase well as the myriad other tertiary intermetallic, carbide and nitride phases noted above occurs in the duplex ferrite phase due to its higher rate of diffusion, especially so at elevated temperature and its reduced solubility at low temperatures.

The σ phase is perhaps deserving of particularly great scrutiny due to the large volume fraction it can occupy (particularly in comparison with the other intermetallic χ phase) and the associated diminution of both corrosion resistance and mechanical properties it is widely agreed to produce[7],[8]; at volume fractions of ca. 4% σ , wrought super duplex products can be expected to return impact toughness results (as determined through the Charpy V-notch, CVN impact toughness mechanical test) as low as < 30 J[9]. Further to this, assumed ‘elementally lean’ areas of the duplex microstructure surrounding σ particles (commonly precipitated under artificial isothermal aging conditions around 850 - 950°C) become susceptible to localised pitting in the common aqueous acidic media (e.g. FeCl_3 or $\text{AlCl}_3 \cdot 6\text{H}_2\text{O}$) used in corrosion testing. Just as the CVN notched bar impact toughness test is most commonly used to determine the impairment of mechanical properties, the critical pitting temperature (CPT) test, which measures corrosion resistance, (ASTM G48-11) is generally employed to empirically determine the minimum temperature (°C) needed to produce pitting attack at least 0.025 mm (0.001 in.) deep (excluding specimen edge attack)[10]. The significance of the CPT is in the identification of the minimum temperature at which pitting of

the sample occurs, with design code acceptance criteria generally in the range 40 - 50°C (dependent on region and the specific guidance used). To conduct the CPT test, samples are generally ground flat (using a coarse, ca. P 120, SiC grit paper) and the edges bevelled. The samples are then exposed initially for 24 hours at a given start temperature, T_0 (dependent on the required design code stipulated minimum), removed, washed, dried and weighed. If no significant weight loss (ca. 0.0001 g/cm²) is observed the samples are tested for a further 24 hours at $T_0 + 5^\circ\text{C}$ and so on until pitting occurs. In the case of a σ -bearing duplex material, the CPT has been shown to be directly related to its presence in much of the time-temperature space[1] (albeit in conjunction with other tertiary phases such as secondary austenite, Cr₂N and χ which accommodate the crucial alloying elements chromium, molybdenum and nitrogen). Typically, CPTs of ca. 80°C have been shown to be expected in unaged superduplex material and also superduplex material aged to short times outside the temperature range 850 - 950°C. However, this has been shown to reduce by as much as 35°C under, for example, aging conditions of 600 s at 800°C[11]. The complex precipitation and transformation behaviour in these alloy systems means sole attribution to the presence of σ phase is too simplistic to account for this behaviour in CPT.

The ASTM G48-11 CPT corrosion test commonly adopted in the literature due to its ubiquity in industrial practice. The CPT test has been used successfully as a means of ranking materials in order of resistance to pitting attack since it is relatively simple to initialise and run, doesn't require a high level of operator skill and produces easily interpretable results. It is however, a relatively coarse and empirical measure of a duplex alloy's ability to resist pitting corrosion. Although a full evaluation of the measures by which resistance to corrosion in DSSs and SDSSs can be assessed is beyond the scope of this work, for completeness however, it suffices to note that the pitting temperature of stainless steels can also be determined electrochemically though, for example, the methodology established in the ASTM G150-13 testing standard to determine a potential independent CPT[12]. This test is designed to establish a pitting potential range since the measured pitting potential at a given temperature varies due to the random nature of the pitting initiation process, where the pitting potential is generally shown to decrease with increasing temperature. In contrast to the discretised nature of ASTM G48-11 test methodology, the potentiostatic technique for the establishment of the CPT requires continuous heating of a sample at 0.0167 °C/s (1°C/min) after submersion and stabilisation in a test cell configuration composed of 1M NaCl(aq) electrolyte, initially at 0°C. Prior to commencing the

temperature scan the specimen is anodically polarized to, and held at, a constant potential above the pitting potential range (ca. 700 mV, versus saturated calomel electrode (SCE) at 25°C). The current is monitored during the temperature scan, and the CPT is defined as the temperature at which the current increases rapidly. The ASTM G150-13 test standard defines this for practical reasons as the temperature at which the current density exceeds 100 $\mu\text{A}/\text{cm}^2$ for a period of 60 s. The potentiostatic method of electrochemically determining the CPT of a DSS, although a more complicated test to set up and run, as well as necessitating higher operator skill and specialist testing equipment, removes much of the qualitative assessment inherent in the ASTM G48-11 methodology and provides a more quantitative assessment of CPT through changes in current density which can be very accurately measured. Studies of the effects of annealing temperature and time on corrosion resistance using this potentiostatic methodology to determine CPT suggest that, in accordance with CPT determination based on the ASTM G48-11 methodology, isothermal aging in the range ca. 600 - 850°C can produce drastic drops in the CPTs in duplex material (i.e. increase susceptibility to pitting corrosion) with the lowest CPTs recorded for material aged to longest times[11],[13]. It is unlikely however, due to the relatively wide range of temperatures and long times to which isothermal aging is generally conducted in studies on DSS and SDSS material, that σ phase precipitation alone is responsible for decreased CPT and many of the other deleterious tertiary precipitates noted previously (particularly Cr-nitrides) are likely to also play a significant role due to localised sensitisation effects[14].

Despite the precipitation of σ phase being influenced to a large extent by heat treatment temperature, it is important to note that much of the research into the corrosion of duplex material is based around methodologies conspicuously non-analogous with common industrial practice; in particular isothermal formation at aging temperatures and times unrepresentative of commercial thermo-mechanical processing or service conditions[15]. These studies do however highlight the catastrophic effect on performance that even a small amount of σ precipitation can produce and underscore the importance of its avoidance through elevated soak temperatures and aversion of isothermal ageing conditions in service. The final quality heat treatment operation for the typical thermo-mechanical processing of SDSSs is carried out in the approximate temperature range 1080 - 1120°C where thermodynamic equilibria indicates stability of only the duplex austenite and ferrite phases (Fig. 2.4). Sigma phase, and indeed many other deleterious intermetallics, carbides and nitrides form at significantly lower

temperatures, as noted above. Those studies orientated more around the cooling rate(s) upon quenching after heat treatment have broadly allowed for the improvement of industrial practice through identification of a critical cooling rate of ca. 0.4 K s^{-1} below which the formation of around 1% σ can be expected[16],[17]. Additionally, studies replicating and analysing the effects of heat treatments at the higher end of the commercial (rather than laboratory) soak temperature range have shown how the high temperatures increase in the duplex ferritic volume fraction (albeit diluted in Cr, Mo and Nb) thus helping to suppress intra-granular σ formation[7]. It has been suggested however, that a predominance of the ferrite phase in the duplex microstructure resulting from elevated annealing temperatures (ca. $> 1060^\circ\text{C}$) may actually lower corrosion resistance, as evidenced by lower CPTs[18], due to the dilution of the key alloying elements in this phase. Further studies[19] investigating the effects of more industrially analogous elevated temperature annealing on UNS S 32750 material also suggest relative elemental depletion of the duplex ferrite phase at temperatures $> 1080^\circ\text{C}$ and subsequent lowering of the CPT. This impairment in resistance to pitting corrosion at higher annealing temperatures is explained by the lowering of the ferrite PRE_N and supported by electron microscopy showing a transition in the sites at which pits form; above 1080°C metastable pits are mainly distributed in the ferrite phase whereas annealing at temperatures in the range $1030 - 1050^\circ\text{C}$ result in most of the metastable pits forming in the austenite phase [13],[19].

3.1.2 Chromium Nitrides, Cr_xN

While cooling sufficiently rapidly from elevated soak temperatures may have been demonstrated to help avoid σ formation, other studies of DSS and SDSS material heat treatments have shown that these conditions may also prefer the formation of alternative deleterious phases such as the Cr_2N -type Cr-nitride and underline the difficulties in thermo-mechanically processing such complex alloys[20]. With nitrogen contents in SDSSs of ca. 0.2% and minimum Cr contents of 25%, the precipitation of Cr-nitrides is an important consideration and has become an increasing focus of research, having previously been overlooked due to the perceived primacy of the effect the intermetallic σ phase has on mechanical properties and corrosion resistance. Chromium nitrides are generally of the stoichiometric form Cr_2N (although a cubic CrN-type chromium nitride has also been observed, albeit far less frequently and reportedly with little or no adverse effect on toughness

and corrosion properties[21]. The most commonly encountered Cr₂N-type chromium nitrides have been observed to assume the hexagonal close packed (HCP) crystal lattice arrangement and can be rich in Cr, Mo, and V and depleted in Ni and Cu, relative to the surrounding ferritic matrix. These particles have been observed to precipitate both isothermally along ferrite (δ) – ferrite (δ) grain boundaries and ferrite (δ) – austenite (γ) interphases in the approximate temperature range 700 - 900°C (so-called ‘isothermal nitrides’) and also intra-granularly under non-equilibrium cooling conditions from temperatures > 1000°C (termed ‘quenched – in’ nitrides). It is suggested that rapid cooling from annealing temperatures in excess of ca. 1000°C does not provide enough time for the nitrogen present in the ferrite phase of the duplex microstructure to diffuse into the austenite, resulting in a solid solution super saturated in nitrogen and thus the subsequent precipitation of finely dispersed, very small intra-granular Cr-nitride particles[22]. Other studies[8] into the precipitation of Cr-nitrides have termed the isothermal formation of Cr-nitrides discontinuous (cellular) precipitation. In common with the previously discussed σ phase, the mechanism for discontinuous Cr-nitride precipitation is not wholly agreed upon, although a widely accepted mechanism suggests that supersaturation of nitrogen in the surrounding matrix drives cellular growth however, as the degree of nitrogen supersaturation reduces, the driving force for cell growth will gradually also decrease and thus reduce the migration rate of the cell front over time, with this front being enriched in chromium relative to the surrounding matrix. Extending this somewhat, a detailed SEM/TEM-based investigation[23] into the relationship between chromium nitride and secondary austenite precipitation in various DSSs and SDSSs proposed a co-operative precipitation mechanism for these two phases at the ferrite – austenite interphases; it is suggested that heterogeneous nucleation of high-coherency M₂N-type nitrides occurs at Kurdjumov-Sachs (K-S) orientated δ/γ interphases followed by growth into the δ grain due to the nitrogen supersaturation from intra-granular nitride dissolution and the low solubility (as well as faster diffusivity) on this side of the boundary. As nitride precipitation proceeds, austenitic stabilizing elements (Ni and Cu) are rejected into, while ferrite stabilizing elements (Cr and Mo) are taken from, the surrounding matrix, thereby creating favorable conditions for γ_2 precipitation. At longer times the γ_2 growth reaches primacy and the nitrides are left behind on the original δ/γ interphases, eventually becoming unstable and dissolving after their co-operative precipitation with the γ_2 . The mechanism of cooperative growth of nitrides and γ_2 is active just at the beginning of the precipitation, then with increasing time, the γ_2 continues to grow alone. Support for this mechanism of precipitation is provided by earlier SEM observations of the simultaneous

precipitation of Cr-nitrides and γ_2 at interphase boundaries after aging solution annealed SAF - 2507 SDSS extruded bars at 850°C for 10 min[1].

Many of the studies in the literature relating to Cr-nitrides are concerned with the isothermal formation of chromium nitrides and again, in a similar manner to the discussion of the σ phase above, do not have immediate relevance to industrial thermo-mechanical processing where the precipitation of these nitrides during continuous cooling is likely to be of more relevance. The precipitation of Cr_2N is generally agreed by most studies to be detrimental to mechanical (in particular toughness) and corrosion properties. It is also reported that the impairment to corrosion resistance caused by the presence of Cr-nitrides arises due a ‘sensitization – type’ effect from the formation of chromium depleted zones in the areas surrounding the particles. Cr_2N type Cr-nitrides have been proposed[23] to precipitate in ‘rod-like’ morphologies from the ferrite by nucleation and growth with the predominate orientation relationship to the ferrite matrix:

$$(110)_{\delta} \parallel (0001)_{\text{Cr-nitride}}$$

$$[111]_{\delta} \parallel [1101]_{\text{Cr-nitride}}$$

Here it can be seen that the closest packed planes of each phase are parallel (equivalent to the BCC – HCP Burgers orientation relationship).

Cr_2N particles are generally found to be of the order 50 – 250 nm in size and thus necessitate identification through transmission electron microscopy (TEM), however studies based on the SEM-EBSD technique have also managed to identify nitrides of both the CrN and Cr_2N stoichiometry[24]. The variation in Cr-nitride particle size has been reported to be associated with the conditions under which they precipitate, with isothermal aging to longer times generally responsible for producing larger, and less finely dispersed, particles than continuous cooling. It is important to stress again at this point, as was noted previously for the σ -phase, the methodologies employed by many of the studies focused on Cr-nitrides are targeted specifically towards their formation for characterization purposes. As such, heat treatments at artificially low temperatures and to extended times are commonly adopted as well as prior thermal processing techniques unlikely to be encountered in the commercial production of wrought DSS and SDSS products or indeed subsequent ‘downstream’ metallurgical processing

operations. Despite a generally acknowledged deleterious effect on material properties caused by the presence of Cr-nitrides in the duplex microstructure, it appears that this effect is largely dependent upon the size and dispersion of the precipitates; rapid water quenching following 10 minutes of soaking at 1125°C to produce finely dispersed, nano-sized (ca. 50 – 100 nm), ‘quenched – in’ nitride particles within ferrite grains has been shown to have a negligible effect on the corrosion resistance of SAF 2507 (UNS S 32750) SDSS material[22], as determined through potentiodynamic polarization measurements up to 0.8 V_{Ag/AgCl} in 90°C 1M NaCl(aq) to obtain the CPT. Conversely, under the same test conditions, samples of the same SDSS material aged for 10 minutes at 800°C prior to water quenching and containing 80 – 250 nm sized ‘isothermal’ Cr-nitrides didn’t exhibit any passivity. Indeed, a sharp rise in current density was recorded at applied potentials as low as 0.08 V_{Ag/AgCl}. However, due to the low aging temperature at which these ‘isothermal’ nitrides were precipitated it is acknowledged that small amounts of σ phase also contributed to this decrease of the CPT.

A final point to note on Cr-nitride precipitates in the duplex microstructure concerns their identification following metallographic preparation techniques (grinding, polishing and etching) and microscopy. Recommended practice to reveal the presence of intra-granular chromium nitrides is through the use of a 10% oxalic acid (CHO₂)₂ solution electrolyte, the methodology of which is discussed in further detail in Ch. 4.5.1. Technical guidance indicates however, that oxalic acid may exaggerate the apparent size of precipitates and potentially should not be used for quantitative assessment. By attaching the sample of duplex material to the positive pole of a source of direct electric current and applying a constant voltage for a period of time (ca. 8 – 15 s) at a potential within a specified range (ca. 3 – 5 V), a high density of small etching pits in the ferrite phase may be revealed through accelerated localized corrosion where the material is affected by nitride precipitates. This is therefore a method that, although not making them directly visible, provides indirect evidence for the presence of intragranular nitrides. The possibility exists however, in using this preparation technique, for ‘over etching’ which may cause excessive pitting of the sample and lead to the ‘false positive’ identification of the prior existence of Cr - nitride precipitates

3.1.3 Secondary Austenite, γ_2

Distinction between secondary austenite and intra-granular primary austenite within the duplex microstructure is not consistent in the literature with no standardized, widely-adopted nomenclature. It is suggested that a specially adapted electrolytic etching technique[23] may be adopted to distinguish between primary (noted as γ_1 below for clarity) and secondary austenite due to the compositional differences between these two phases and subsequently the formation of a clear ‘step’ where γ_2 has grown from γ_1 and can be distinguished in secondary electron mode SEM. This technique however, limits identification to primary intra-granular austenite exhibiting a film of γ_2 on the periphery. As will be discussed in detail in subsequent chapters, experimental SEM-EBSD investigations conducted as part of this work illustrate that crystallographic orientations and morphological differences can also be employed as methods for discrimination.

It is suggested[25] that secondary austenite refers to any austenite that forms upon reheating, as well as that which can also be formed by growth of the former primary austenite islands. It seems likely that the unstandardized classification and difficulty of precise identification of this particular tertiary duplex precipitate may be largely responsible for the comparative absence of research into its characterization and effects on material properties. For example, it is suggested that the differentiation of γ_2 formed by diffusion and shear, or shear followed by diffusion is difficult since no well-defined relationship between formation temperature, formation mechanism, composition, and orientation relation can be deduced from experimental data[26].

It is noted that there at least three distinguishable mechanisms/processes by which γ_2 can form[4]; the previously mentioned eutectoid decomposition ($\delta \rightarrow \sigma + \gamma_2$), Widmanstätten precipitation and via a shear process resembling that of martensite formation. These processes appear to have a thermal dependence whereby below ca. 650°C γ_2 forms isothermally via the shear mechanism and above this temperature precipitation is in the form of Widmanstätten precipitates. It is the Widmanstätten-type γ_2 precipitates that appear to assume the K-S relationship with the ferrite matrix; $(111_{\gamma_2}) \parallel (\bar{1}10_{\delta})$, $[1\bar{1}0_{\gamma_2}] \parallel [111_{\delta}]$ [26].

Direct decomposition of ferrite to (primary) austenite, γ_1 ($\delta \rightarrow \gamma_1$) occurs under cooling below the *solidus* at very high temperatures (ca. $> 1300^\circ\text{C}$) and forms the basis of the duplex microstructure. This austenite phase forms large grains within the ferrite matrix and is commonly seen in isotropically orientated lath-like (also referred to as ‘stringer’) morphologies, parallel to the primary forming axis (rolling, forging, extrusion etc.) or principal stresses (Fig. 2.3). Secondary austenite precipitates are primarily identified by their much smaller sizes, relative to γ_1 grains, and also secondarily, their acicular morphologies (although small and more equiaxed γ_2 precipitates are also commonly encountered). In common with the above noted other undesirable phases caused by inappropriate heat treatment of duplex material, secondary austenite precipitates have been linked to a drastic decrease in corrosion resistance which may also reduce the toughness[27]. Secondary austenite precipitates of Widmanstätten needle morphology have been shown to form as a result of quenching from elevated (ca. 1300°C) solution annealing temperatures, analogous to the previously noted ‘quenched – in’ Cr-nitrides. Parallels can also be drawn between the second type of nitrides noted above as ‘isothermal’[22], and γ_2 precipitates formed by heating up slowly through a temperature range around 1000°C to annealing temperatures below 1150°C . These γ_2 precipitates assume in the same Widmanstätten needle-like morphology as the high temperature quenched γ_2 precipitates however, it is noted that this temperature is a function of the duplex material’s chemical composition[26].

The principal deleterious effect of secondary austenite, both the eutectoid and Widmanstätten morphology type precipitates, has been noted as reducing duplex material’s resistance to corrosion. However, in contrast to, for example, the noted effects of Cr-nitrides or σ intermetallic precipitates, it is suggested that γ_2 can be expected to possess the toughness generally observed in primary austenite[1] and (as explored below) may act to strengthen the more ductile α matrix when precipitated intra-granularly. Despite similar mechanical properties to the primary phase, Widmanstätten γ_2 has however been shown to be compositional different, specifically in terms of Ni content. This higher Ni content in Widmanstätten γ_2 than ferrite has been suggested to indicate that formation is accompanied by diffusion.

3.2 Hot Deformation of Duplex and Superduplex Stainless Steels

The variety of products into which duplex material is manufactured necessitates a range of hot working processes. Additionally, increasing implementation of DSSs as structural materials in nuclear storage container applications has led to the introduction of cold working as routine industrial practice[28]. Commonly encountered DSS and SDSS subsea pipework systems (particularly weld neck flanges as well as swivel ring hub and body assemblies) with associated risers, manifolds, pressure vessels, valves and heat exchangers are produced through various open and closed die hot forging, deep drawing, extrusion, wire drawing and ring rolling operations. In all cases these operations result in permanent shape change of the metallic material through greater or lesser amounts of induced plastic strain. In metal forming the plastic deformation to affect shape change of the metallic workpiece is generally considered large, with little or no material removal and high applied stresses (tensile and/or compressive) [29]. It is also common in the production of duplex engineering components for the manufacturing processes to consist of several, sequential bulk metal forming operations such as rolling and wire drawing or open die upsetting, piercing and ring rolling to produce high tensile cable and seamless rings, respectively. The production of a ZERON® 100 weld neck flange itself, as will be discussed in detail in subsequent chapters, requires a series of open die hot forging operations including upsetting and cogging. During hot forming operations the working of the microstructure, in addition to producing the desired general bulk, or even near-net, change in shape, will also importantly tend to improve the mechanical properties of the workpiece such as, for example, increasing ductility, toughness and yield strength through grain size refinement. It is noted, for example, that bulk ultra-grain refinement ($< 1 \mu\text{m}$) achieved through severe plastic deformation in polycrystalline duplex materials can produce superior combinations of properties including improved corrosion resistance[30]. In essence, hot working operations are carried out to achieve the mechanical purpose of producing a desired component shape change, however, the deformation required to realize this has the advantage of significantly improving the material properties by refining the, usually coarse, prior microstructure.

There are inherent similarities between many of the various metal forming processes, however, due to their complexity, a categorisation based on, for example, the nature of the applied load, or indeed any other of the possible myriad parameters, would produce an extremely complex

taxonomy that is not particularly well suited for pedagogical use. For the purposes of establishing the scope of this work, attention is focused herein on studies with obvious applications to bulk metal, as opposed to sheet metal, forming i.e. replication of the deformation modes analogous to the shaping of bodies with concentrated mass where the orthogonal dimensions (x -, y - and z -) of the bodies are broadly similar in size, rather than those similar to sheet metal operations where bodies are formed with initially large planar extensions and small extensions in the third direction[29].

Further, due to the importance of the constitutive flow stress behaviour of the metallic work piece in predicting and analysing the effects of hot working, and the absence of any such detailed prior investigations for the ZERON® 100 alloy specifically, this section will largely concentrate on studies which have attempted to characterise the complex stress – strain relationship of, broadly similar, DSS and SDSS alloys, both metallographically and analytically. It was also noted above that microstructure evolution is integrally linked to metal forming operations and as such, in addition to mechanical characterisation of duplex material's flow behaviour, special consideration will also be given to those studies which have attempted to relate the complex microstructure morphology and development that occurs during the hot deformation of DSSs and SDSSs to imposed processing parameters, principally strain, temperature and strain rate. In many cases however,[31],[32],[33],[34] it is common to see the flow behaviour of DSSs at high temperature described almost exclusively in terms of the generalised hot working relationship between peak stress and strain rate[35] developed to characterise the general recrystallization behaviour of single phase materials under hot rolling schedules:

$$\dot{\epsilon} = A(\sinh \alpha\sigma)^n \exp\left(-\frac{Q_{def}}{RT}\right) \quad \text{Eqn. 3.1}$$

Where, as will be explored in greater detail in Ch. 5, A and n are the temperature-independent model constants, α the inverse of the stress (MPa^{-1}) associated with power-law breakdown (also temperature-independent), Q_{def} the activation energy for hot working (kJ mol^{-1}), $\dot{\epsilon}$ (s^{-1}) and σ (MPa) the true strain rate and true stress involved, respectively, T the temperature (K) and R the molar gas constant ($\text{kJ mol}^{-1} \text{K}^{-1}$).

Since the flow stress depends on both temperature and strain rate, the Zener–Hollomon parameter, Z can be defined which combines these factors and is used to describe the shape of flow stress curves:

$$Z = \dot{\epsilon} \exp\left(-\frac{Q_{\text{def}}}{RT}\right) \quad \text{Eqn. 3.2}$$

As a final introductory observation regarding the body of work concerning the hot deformation of the duplex and superduplex stainless grades, it is clear that much literary attention is paid to two particular members of these classes; SAF - 2507 (UNS S 32750, EN 1.4410) SDSS and SAF - 2205 (UNS S 31803, EN 1.4462) DSS. SAF - 2205 and SAF – 2507 are tradenames for duplex and superduplex grades, respectively, produced by (or under licence from) Sandvik AB, Sweden[4]. Investigations into the micro- and macro-scale behaviour of ZERON® 100 under industrially analogous hot working strain, strain rate and temperature regimes are conspicuously less apparent, and therefore underline the overall novel value of the investigations subsequently presented in this work. To further frame the following review of the current state of the art and understanding of forming DSSs and SDSSs, it is also important to note that the deformation modes most commonly employed to investigate the plastic deformation of DSSs and SDSSs (high-pressure torsion, plane-strain compression and tension, for example) produce large equivalent true strains and strain rates, consonant with industrial operations like rolling, drawing and extrusion. In contrast, and as shall be demonstrated in subsequent chapters of this work, open die forging (and uniaxial compression, its highest fidelity experimental proxy) results in much less severe bulk plastic deformation and associated anisotropy of the duplex microstructure. Characterisation of the flow behaviour is therefore much less straightforward in such instances and the competing variables of dynamic recrystallization and dynamic recovery on microstructure response cannot be as easily delineated. Investigations employing experimental methodologies analogous to the industrial open die forging of ZERON® 100 engineering components are, as a result, therefore largely absent from the current body of work.

3.2.1 Flow behaviour of Duplex and Superduplex Stainless Steels

The complex microstructure of duplex material and its morphology makes prediction of phase volume fraction, transformational driving forces and stability under hot deformation conditions

extremely complicated and can lead to, for example, wide variations between calculated and observed ferrite content at high temperature and strain regimes[36]. Such variable (and difficult to predict) volume fractions of ferrite under conditions of hot deformation can have significant impact on the flow behaviour of duplex material due its difference in stacking fault energy (SFE) to the austenitic component of the duplex microstructure. The difference in SFE between the two microstructure components in DSSs and SDSSs is extremely important since it is this property which is largely responsible for the nature of the flow response exhibited under imposed deformation and its in-depth consideration is conspicuously absent from a large part of the research literature. In general, the recovery (RCV) behaviour displayed by crystalline metallic materials in response to plastic deformation occurs as a result of dislocation rearrangement (as a well as mutual annihilation) leading to the formation of cellular, sub-grain dislocation structures and, consequently, the release of energy. In materials of low SFE, the ability for dislocations to ‘climb’ out of their glide planes – an important process in RCV – is reduced and hence the recovery of a small fraction of the external work expended in deforming the metal is inhibited[37]. It is of particular relevance in this case to note that austenite is a very low SFE material and therefore only very little climb and rearrangement of dislocations can take place as a result of plastic deformation. Instead, austenite (and other similarly low SFE materials) undergoes recrystallization (RCX) in response to plastic deformation whereby, at some critical strain, new, generally equiaxed and strain-free small grains with low dislocation density are nucleated and grow in substitution of the former deformed grains.

These highly simplified descriptions of the RCX and RCV processes are commonly observed under post forming (at high strain rate) cooling or subsequent annealing reheat treatments and hence termed ‘static’. In the case of RCX, this is the microstructure basis for the classic decrease in strength and increase in ductility certain metallic materials, for example copper and aluminium alloys, exhibit when heat treated. However, RCX and RCV can also occur during hot working schedules and so are termed dynamic recovery and recrystallization (DRV and DRX, respectively). The characteristic high ductility of ferrite during hot working[33] is a consequence of its high SFE allowing for DRV whereby dislocations can easily climb or cross slip leading to the formation of polygonised sub-grains which become larger and more ‘perfect’ at increasing temperature and decreasing strain rate and stress. Conversely the previously noted low SFE of austenite reduces the mobility of dislocations and thus limits DRV. Instead, after exceeding some critical strain, DRX can take place whereby many of the dislocations are

eliminated through the nucleation and growth of new ‘defect-free’ grains and a characteristic flow softening shape is observed in the flow curve after peak stress.

In general, it has been well established that the duplex ferrite phase softens by extended DRV after some amount of work hardening during high temperature plastic deformation, leading to the formation of a complex network of sub-grain boundaries composed of a mix of higher- and lower-angle walls characterised by misorientation angles $< 20^\circ$ [38] while the austenitic phase (and other low SFE materials in general such as single phase austenitic stainless grades) soften by DRX. It therefore becomes apparent, that under conditions of high temperature deformation of duplex material, a complex interaction occurs between the, previously noted, variable ferrite/austenite phase ratio, the partitioning of strain between these two phases and the associated predominate dynamic microstructure restoration mechanisms. It is important to note that the mismatching mechanical deformation behaviour between the duplex phases (ultimately resulting in stress and strain partitioning) can also affect microstructure corrosion and SCC susceptibility[39].

A generalised description of this mechanical behaviour duality in duplex material, as manifest in flow curve profiles, has been proposed based on high strain rate ($1 - 10 \text{ s}^{-1}$), hot torsion testing to equivalent true strains as great as $\varepsilon = 4.0$ of non-commercial duplex and super duplex alloys[40]; it is suggested that at low deformation temperatures in the range $900 - 1000^\circ\text{C}$ an increased γ volume fraction decreases the material ductility as expressed by a rapid work hardening response up to peak stress followed by extended flow softening. Evolution of the flow curve shape is seen in the high ductility temperature range $1000 - 1200^\circ\text{C}$ where, in contrast to low temperature behavior, similar stress variations in the work hardening region preceding peak stress and the flow softening region succeeding it are exhibited. In general, this DRV-type softening response flow curve exhibits only a mild peak and small difference between this and the onset of steady state stress-strain invariance. Microstructure observations suggest that this curve profile results from ‘continuous’ dynamic recrystallization as new ferrite grains form through the growth of sub-grain dislocation networks and sub-boundary misorientation. SEM-EBSD analysis[41], as will be explored in further detail below, of ferrite deformation substructures confirmed that, during hot torsional deformation, ferrite grains become progressively subdivided into roughly equiaxed crystallites, bounded partly by low-

angle and partly by high-angle non-crystallographic boundaries, which appeared to form via the extended dynamic recovery mechanism.

In contrast, the rapid rise to peak stress and following extended softening in the flow curves produced from lower temperature plastic deformation of duplex metallic material is generally associated with the influence of the additional increase in intra-granular precipitation of K-S orientated hard γ_2 particles within the soft ferrite matrix of the duplex microstructure. The coherency between the additional austenite precipitates and the ferrite matrix increases the degree of interaction with dislocations and thus inhibits deformation of the ferrite resulting in the higher yield stresses and work hardening rates observed in the flow curve profiles. Confirmation of the coherence of K-S orientated γ_2 precipitates in the δ matrix has been demonstrated in numerous studies on the precipitation behavior of thermo-mechanically processed DSSs and SDSSs[4], [8], [42].

3.2.2 Constitutive Flow Modelling of Duplex and Superduplex Stainless Steels

As noted above, the main microstructural mechanisms that influence and determine the hot workability response of SDSSs and DSSs have been quite extensively investigated. However, the complexity of their interactions as functions of temperature and strain rate has meant that some important features, such as the modelling of the flow stress variation with strain, remain essentially only qualitatively addressed[43].

Eqn. 3.1 has been successfully applied to the correlation of hot deformation behavior of Ni and Cu-alloys as well as 18/8 (Grade 304) stainless steel in which DRX has been shown to be the rate-controlling dynamic restoration process[35]. Additionally, derivation of the Q_{def} term in Eqn. 3.1, and differences in this value between different materials under torsion (ca. 17 – 24 kJ mol.⁻¹ for Cu, Ni and 18/8 vs. 7 – 10 kJ mol.⁻¹ for Al) has allowed DRV to be identified as the rate-controlling process in the hot deformation of Al-alloys versus DRX in other materials such as Cu and Ni-alloys. This is further supported by observations of well-developed subgrains during hot torsion of aluminum suggesting, as is also the case in creep, DRV is the rate-controlling process.

Importantly however, these are single phase metallic materials, and in contrast to DSSs and SDSSs, the volume fraction or chemical composition of this phase does not change during hot deformation as a function of temperature. This not being the case in DSSs and SDSSs, the result is a differential portioning of strain as a derivative of relative volume fraction, itself a function of temperature. The reporting of a single value of Q_{def} as a mechanical property of state over a range of temperatures, in which the dominate restoration process likely transitions between DRV and DRX (as a result of the SFE difference between the changing majority metallic phase), may therefore be somewhat too simplistic and makes the direct applicability of Eqn. 3.1 to accurately describe duplex material's flow behavior questionable [33], [44].

It was noted above that the a DRV response is characterized by attainment of steady state at high strains and that beyond the onset of DRX flow stress reaches a peak before gradual softening. Complications in the analysis of flow curves whose profiles are influenced by both the DRV and DRX restorative mechanisms arise therefore due to the relative position of the peak in the flow stress which can shift as a function of the Zener–Hollomon parameter (Eqn. 3.2). Further development of the work leading to Eqn. 3.1 has produced a set of equations ultimately allowing the continuous changing shape of the flow stress curves to be described in terms of Z [45] and through which the characteristic effects of DRX on the flow curve profile may be incorporated, once the ‘non-recrystallising’ flow stress curve has been modelled. This approach requires that a series of characteristic points (along with the associated values of strain and strain rate) be found and from which it is possible to extrapolate and then model a continuous flow curve, rather than a series of discrete points. To do this, it is shown that description of the extrapolated curve (i.e. the flow stress curve which would have been achieved if dynamic recrystallisation had not taken place) is first necessary, followed by subtraction of the effect of dynamic recrystallisation from the extrapolated curve. The extrapolated curve is described through:

$$\sigma = \sigma_0 + (\sigma_{\text{ss}(e)} - \sigma_0) \sqrt{(1 - \exp[-\varepsilon/\varepsilon_r])} \quad \text{Eqn. 3.3}$$

Where σ_0 and $\sigma_{\text{ss}(e)}$ are two of the previously noted characteristic points found from the experimental flow stress curve and ε_r is the ‘transient strain constant’ which effectively defines the curvature of the flow stress curve between σ_0 and $\sigma_{\text{ss}(e)}$ where the equation saturates. It is indicated that ε_r can be found though the relation:

$$\varepsilon_r = -0.1 \ln[1 - (\sigma_{0.1} - \sigma_0)/(\sigma_{ss(e)} - \sigma_0)^2] \quad \text{Eqn. 3.4}$$

Where $\sigma_{0.1}$ is another, previously noted, characteristic point. Once the ‘non-recrystallizing’ flow stress curve has been modelled it is then possible to subtract from it the effect of recrystallisation, by using an equation of the form:

$$\Delta\sigma = \Delta\sigma_s(1 - \exp[-(\varepsilon - \varepsilon_c)/(\varepsilon_{xr} - \varepsilon_c)]^p) \quad \text{Eqn. 3.5}$$

Where $\Delta\sigma$ is the difference between the ‘DRV’ and ‘DRX’ curves in terms of stress at any strain, $\Delta\sigma_s$ is the difference between the two curves once both curves have reached steady state, and ε_{xr} is the strain required to reach a fixed amount of softening, measured in terms of $\Delta\sigma/\Delta\sigma_s$ which effectively defines the rate of softening as a result of DRX.

This methodology[45] presents obvious application to the analysis of DSS and SDSS material flow curves due to the incorporation of the softening effects of DRX on the shape and the general saturation of the model at high strains as a result of DRV. The application of this methodology to the interpretation/modelling of experimental flow stress data from the uniaxial hot compression of ZERON® 100 SDSS material will be explored in greater detail in Ch. 5.

For the purposes of completeness however, it is important to note particular examples of work into development of constitutive equations for prediction of the flow behaviour of DSSs whereby development of the use of Eqn. 3.1 into a more detailed family of constitutive relationships able to describe the particular straining behaviour of this material has been proposed. This approach, based on load transfer from δ to γ during torsion of wrought 2205 DSS has been shown to have good agreement with experimental data and suggests an alternative, more detailed and comprehensive model may be able to capture the suggested sequential effects of DRV and DRX from strain partitioning between the soft δ and hard γ phases[43].

The basis of this model arises from the analysis of the high temperature response of DSSs which clearly demonstrate that the hot workability of these materials is critically influenced by their particular microstructure composed of a harder phase (austenite) that coexists within a

softer one (ferrite). The composite model proposed, in its simplest form, is based on equations that arise from the rule of mixtures applied under the Taylor hypothesis of uniform strain (where the hard and soft zones deform in parallel relative to the applied load with the same strain rate):

$$\sigma_{\text{DSS}} = f_{\gamma}\sigma_{\gamma} + (1 - f_{\gamma})\sigma_{\delta} \quad \text{Eqn. 3.6}$$

$$\varepsilon_{\text{DSS}} = f_{\gamma}\varepsilon_{\gamma} + (1 - f_{\gamma})\varepsilon_{\delta} \quad \text{Eqn. 3.7}$$

Where f is the volume fraction of the duplex phase indicated by the preceding subscript. Differentiating Eqn. 3.7 with respect to time i.e. $d\varepsilon_{\text{DSS}}/dt$, under the uniform stress condition applied to the whole structure where the austenitic and ferritic phases are effectively in series [46] (and also assuming no significant variation in f_{γ}), leads to:

$$\dot{\varepsilon}_{\text{DSS}} = (1 - f_{\gamma})\dot{\varepsilon}_{\delta} + f_{\gamma}\dot{\varepsilon}_{\gamma} \quad \text{Eqn. 3.8}$$

For true, as opposed to engineering, strains, Eqn. 3.7 can be rewritten as:

$$\varepsilon_{\text{DSS}} = \ln[f_{\gamma}\varepsilon_{\gamma} + (1 - f_{\gamma})\varepsilon_{\delta}] \quad \text{Eqn. 3.9}$$

This reduces to the form of Eqn. 3.7 at low strains. Calculating the flow stress of DSS from the law of mixtures based on the Taylor hypothesis has been suggested as applicable to describe wrought DSS material behavior of the steady-state flow stress under plane strain compression mode and peak stress in torsion[46]. In comparing the calculated flow stresses obtained from Eqn. 3.6 and those from the application of the constitutive equations Eqns. 3.1 & 3.2 for the same deformation conditions it was shown[46] that the peak stress in tension, σ_{t} was higher than steady state flow stress under the plane strain compression (PSC) mode condition, σ_{c} at 1000 °C, but both agree relatively well with the result from applying Eqn. 3.6 and the data in the literature for ferrite and austenite single phase materials. At increasing temperatures, the differences between σ_{t} and σ_{c} decrease, and a close fit to the flow stress values as predicted by Eqn. 3.6 is obtained.

Where complexities in the shape of flow curves for composite duplex materials under certain deformation modes arise, consideration should be given to the relative orientation of the microstructure; the widely reported[46] agreement of constitutive models based on Eqns. 3.1 & 3.2, and indeed on the law of mixtures (of the type Eqn. 3.6), with PSC experimental data can be explained by the relatively simple parallel alignment of planar-linear austenite ‘lathes’ in a ferrite matrix along the rolling direction of wrought plate material, giving rise to the uniform strain condition. In particular, this explains the applicability of the law-of-mixtures composite model expressed in Eqn. 3.6. However, a more complex situation arises under alternative deformation modes such as torsion[47]. Lower than predicted macroscopic flow stresses at low strains may be potentially indicative of greater plastic deformation of the ferrite phase than the austenite phase, thereby allowing ferrite to control early-stage deformation behavior with no transmission of strain across the $\delta - \gamma$ interphase boundary occurring. In terms of the microscopic stress state and configuration of the duplex phases, at the onset of deformation the plates or ‘lathes’ of austenite are generally aligned along the sample axis, according to the way in which the samples were machined out. In this orientation they are parallel to the maximum shear stress and form an angle of 45° with respect to the direction of the principal stress in torsion and correspond to an intermediate state between the parallel uniform strain and series uniform stress conditions. As deformation continues beyond yield and up to peak stress the austenite grains become inclined at approximately 45° to the longitudinal axis (along which the maximum shear stress in torsion is aligned) putting them parallel to the direction of torsional principal stress and explaining why the flow stress value at the peak of the flow curve is well described by Eqn. 3.6[46].

The rule of mixtures may be used to describe the overall flow based on the volume fraction of the duplex phases, and therefore, also to estimate the volume fraction of these phases from the material flow behavior. However, it is suggested that the effect of the coherency between γ particles and the α matrix may also be important to consider and more difficult to evaluate[40]. Interphase coherency has been suggested to play an important role in the partitioning of strain between the two duplex phases since austenite particles formed by the solid-state transformation $\delta \rightarrow \gamma$ are coherent and thereby increase the degree of interaction with glide dislocations, acting to inhibit deformation of the softer ferrite matrix and thereby increase the yield stress and work hardening rate during the early stages of deformation. This effect continues to be important as long as δ/γ coherence is maintained. However, γ particles have

little effect on material strength once coherence has been lost. Where γ particles are coherent strain appears to be partitioned fairly equally between the duplex phases. However, strain transfer from the softer matrix becomes less effective across incoherent interphases and the ferrite is forced carry more of the deformation. Strain accumulation in the ferrite has also been shown to occur under cold working schedules where higher local strain hot spots have been observed after 20% cold rolling[28]. Furthermore, correspondence of the above noted load transfer from δ to γ during the progression of hot torsion is echoed after 40% cold rolling where strain localisation was shown to intensify in austenite grains, indicating the predominate accommodation of plastic deformation at higher strains.

3.2.3 Crystallographic Orientations in (Deformed) Duplex Metallic Materials

The electron backscatter diffraction (EBSD) technique is well established electron microscopy tool and allows for precise textural mapping of the microstructure and crystallographic phases in metallic materials as well as identification of misorientation gradients associated with localized plastic strain.

Crystallographic analysis of duplex and superduplex material is notably less well represented in the literature relative to studies based on corrosion and mechanical testing as well as more standard optical and electron microcopy, pertinent examples of which have been noted and discussed above. This discrepancy may be explained, in part, by the technical difficulty in correctly indexing the potential myriad discrete phases which can form in the duplex microstructure. For illustration, the crystallographic geometric parameters for EBSD phase identification of the most commonly occurring tertiary phases in duplex and superduplex material are presented in Table 3.1[24]. Identification of DSS and SDSS EBSPs using a minimum of 4 – 6 Kikuchi bands can result in inaccurate and impractically lengthy automatic indexing times when ca. > 2 crystallographic phases (e.g. HCP, FCC & BCC) are specified in the SEM-EBSD acquisition software. In addition, the disparity in volume occupied between the primary austenite and ferrite duplex phases and the other tertiary phases (common examples of which have been discussed above and are noted in Table 3.1) produces further technical difficulty in applying SEM-EBSD to duplex material; high-resolution step sizes of the order 50 – 75 nm are required to capture the presence of, for example, χ , Cr_2N and CrN phases over a scan area < 100 μm^2 , even when the presence and volume of these phases have been produced

under artificial aging conditions[24]. Conversely, much coarser step sizes (as great as 3 μm) have been employed to obtain large EBSD maps (ca. 5 mm^2) and provide information about the duplex phase ratio, grain structure and crystallographic texture[41]. Such variation in the EBSD scan parameters limits the ability of this technique to be applied to the simultaneous analysis of bulk crystalline anisotropy and localized microstructure evolution as a result of thermo-mechanical processing, without technically difficult and time-intensive repetitive high- and low-resolution scans over the same sample area. Further examples of the application of crystallographic analysis to the study of DSSs and SDSSs can also be found in the somewhat more basic characterization of as-received wrought material[30] where datum metrics, such as average grain size and the identification and spacing of austenite twin boundaries, prior to experimentation are established.

Table 3.1 Parameters of common phases in duplex material used in SEM-EBSD identification

Phase	a (Å)	b(Å)	c(Å)	α(°)	β(°)	γ(°)	Space group
Ferrite	2.87	2.87	2.87	90	90	90	229
Austenite	3.66	3.66	3.66	90	90	90	225
Cr_2N	4.75	4.75	4.43	90	90	120	162
CrN	2.97	4.12	2.88	90	90	90	59
σ	8.80	8.80	4.56	90	90	90	136
χ	8.92	8.92	8.92	90	90	90	217
Cr_{23}C_6	10.6	10.6	10.6	90	90	90	62

Where crystallographic analysis and data have been applied to the study of, specifically, the hot deformation behavior of DSSs and SDSSs, it has been possible to confirm (as will also be demonstrated later in Ch. 7 of this work) the existence of the typical simple BCC shear texture in the duplex ferrite phase, whereby at high strains in the range $\varepsilon = 0.5 - 1.0$ slip generally occurs in the $\langle 111 \rangle$ -type directions and on $\{110\}$ -type planes. Similar, albeit somewhat weaker than for the duplex ferritic phase, texture components have also been observed from high-strain hot torsion in the austenitic duplex phase where ODFs using the Bunge angular notation indicate rather well-defined texture components located along the $\{111\} \langle uvw \rangle$ fiber as well as situated on the $\{hkl\} \langle 110 \rangle$ fiber in the Euler space. This has been suggested to

indicate that plastic deformation during the hot torsion of SAF – 2205-type DSS appears to largely occur via crystallographic slip in both phases[41]. Contrastingly however, under alternative experimental processing regimes to hot torsion testing, the existence of any corresponding deformation texture is questioned[48]; upset forging of several different compositions of nitrogen-alloyed DSSs to size reductions of ca. 16 - 62% has been suggested as ineffective in inducing ferrite deformation texture with no indication of the presence of the BCC duplex fiber texture $\langle 111 \rangle$ & $\langle 100 \rangle$ associated with uniaxial compression. Instead, in this instance, it was reported that ferrite grains tended to cluster around the particular orientations [113], [115], [117] and [122] albeit with overall weak texturing of ca. 2.163 max intensity. Although components of the BCC duplex fiber deformation texture can be found in IPF data from uniaxial compression of ZERON® 100 material presented subsequently in this work (Ch. 7), a commonality can be seen in the weakness of the texture suggesting that, in general, open die hot forging as replicated by experimentally analogous uniaxial compression, is not conducive to the inducement of strong crystallographic texture (at least in as much as any texture can form through a ca. half-height size reduction). The observed improvement in hardness of certain alloy compositions by forging are therefore not attributed to crystallographic anisotropy but instead classic micro-mechanical evolution and compositional increases in nitrogen content linked to austenite phase stabilization. Where impact toughness increased after forging in other compositionally different DSSs, it was shown that the volume fraction of ferrite had increased from the as-received material and furthermore, that the greatest grain size refinement (from a reduction in size of 48%) correlated to the greatest impact toughness.

In addition to ODF textures in duplex and super duplex material, crystallographic analyses applied to misorientations across austenite-ferrite grain (and ferrite sub-grain) boundaries also indicate confirmation of, on average, more strain partitioning into the ferrite phase versus the austenite phase for a given nominal strain level under high temperature torsion testing[41], [43]. Such analyses of crystallographic misorientations within the ferrite deformation substructure (at ca. $\varepsilon = 1.0$) have been suggested to resemble strain-induced boundary migration (SIBM) driven by the differences in the stored energy between the regions separated by large-angle boundary segments where some ferrite sub-grains become converted to ‘crystallites’ which remain approximately equiaxed and partly bounded by low-angle and also high-angle boundaries. Further, it is also suggested based on this formation of ‘recrystallized’

ferrite ‘crystallites’ through the coalescence of low-angle sub-grain boundaries, that an ‘extended DRV’ mechanism, alternatively termed ‘continuous dynamic recrystallization’ (CDRX), might be predominantly responsible for this high SFE material substructure.

It is important to note however, that due to, in part, the limited number of crystallographic analyses focused on the high temperature deformation of DSSs and SDSSs (versus, for example, those focused on fracture mechanics, tribology or joining) a complete picture has yet to emerge. The softening of the austenitic phase through DRX[49], as noted above, is in fact suggested to be inhibited in two phase alloys and in addition, rather than an alternative term, the CDRX mechanism can be distinguished from ‘extended DRV’ in terms of the relative amounts of low- and high-angle boundaries in the microstructure [50].

3.3 Summary

Due to the merits offered by the two-phase microstructure combining higher strength than austenitic steels with a higher toughness than ferritic steels and excellent corrosion resistance, duplex steels have become ubiquitous engineering materials for aggressive service environments and hence the subject of a great deal of in depth, and varied research interest, as has been demonstrated above. Focus here has been given to those studies with the greatest relevance to the scope and methods of this work and as such a fully comprehensive review of the myriad aspects of duplex metallic material has by no means been presented.

The temperature range for commercial hot forging DSSs and SDSSs is broadly supported by the careful survey of the literature presented above where, below 1000°C the precipitation of brittle phases such as σ and Cr-nitrides have been demonstrated and temperatures in excess of 1200°C prefer the formation of ferrite from austenite and result in undesirable formability and mechanical properties. The thermodynamics of the many potential deleterious tertiary precipitates in the duplex microstructure are extremely complicated. The avoidance of catastrophic failure from the presence of σ phase through specific thermomechanical processing parameters has been extensively investigated and is now broadly understood. However, the secondary effects on mechanical performance and corrosion resistance resulting from, for example, alteration of δ/γ volume fractions and potential subsequent precipitation of Cr_2N and γ_2 etc. through rapid quenching or extended higher temperature quality heat

treatments means an essentially precipitate-free microstructure cannot be expected in certain section thickness components due to the physical limits imposed by thermal conductivity and elemental diffusivity ranges[51]. It is important to emphasize again that although much work has been conducted into the characterization of duplex material's precipitates, the industrial applicability of much of this work is somewhat limited. Low temperature isothermal aging and quasi-equilibrium cooling rates allow for straightforward identification of deleterious precipitates however, they are unrepresentative of common industrial quality heat treatment practice and assessments of the diminution they can cause to material properties should be considered in terms of the often artificially high volumes they occupy. Where a specific reduction of material properties has been identified as related to the presence/effects of a particular deleterious tertiary precipitate, it is often likely to be the case that account needs to be taken of the contributions from other precipitates.

The microstructure evolution of the deformed duplex microstructure is relatively under-investigated as compared to the corrosion resistance, deleterious precipitates and joining of, specifically, SAF – 2205 and SAF – 2507 DSS and SDSS. However, a picture of strain partitioning between the ferritic and austenitic phases appears generally accepted. The differences in SFE energy between these two phases leads to different flow behavior as determined by the DRV and DRX mechanisms. It is, however, not clear as to the extent to which these two mechanisms act to influence the overall profile of the flow curve. Their relationship to the principal variables of hot deformation (temperature and strain rate) is also still a subject of some uncertainty and complicated further by the simultaneous effects of these variables on the duplex δ/γ volume fraction. It has also been shown that the application of the rule of mixtures to modelling the flow behaviour of duplex material has resulted in close agreement to experimental stress-strain data. However, the subtraction of the effect of DRX from an extrapolated, 'non- recrystallizing' DRV curve, which would otherwise exhibit very little stress variation between peak and steady state invariance, may be another potentially alternative approach to the development of a constitutive flow model.

It was also noted above that interphase coherency may, at least in part, contribute to DSS and SDSS flow behaviour. This is likely to be an additional or further softening mechanism to the previously discussed effects of DRV and DRX and arises from the loss of δ/γ coherency which takes place during deformation. As with many other aspects of the duplex alloy system

demonstrated above, no wholly agreed upon explanation exists due to the complexity of the interactions between the many thermomechanical, thermodynamic, elemental, crystallographic and microstructure variables, all of which need to be considered.

REFERENCES

- [1] J. O. Nilsson and A. Wilson, "Influence of isothermal phase transformations on toughness and pitting corrosion of super duplex stainless steel SAF 2507," *Mater. Sci. Technol.*, vol. 9, no. 7, pp. 545–554, Jul. 1993.
- [2] H. Sieurin and R. Sandström, "Sigma phase precipitation in duplex stainless steel 2205," *Mater. Sci. Eng. A*, vol. 444, no. 1–2, pp. 271–276, Jan. 2007.
- [3] I. Calliari, M. Pellizzari, and E. Ramous, "Precipitation of secondary phases in super duplex stainless steel ZERON100 isothermally aged," *Materials Science and Technology*, vol. 27, pp. 928–932, 2011.
- [4] J.-O. Nilsson, "Super duplex stainless steels," *Mater. Sci. Technol.*, vol. 8, pp. 685–700, 1992.
- [5] A. Momeni and K. Dehghani, "Hot working behavior of 2205 austenite-ferrite duplex stainless steel characterized by constitutive equations and processing maps," *Mater. Sci. Eng. A*, vol. 528, no. 3, pp. 1448–1454, 2011.
- [6] M. Pohl, O. Storz, and T. Glogowski, "Effect of intermetallic precipitations on the properties of duplex stainless steel," *Mater. Charact.*, vol. 58, no. 1, pp. 65–71, 2007.
- [7] T. . Chen and J. . Yang, "Effects of solution treatment and continuous cooling on σ -phase precipitation in a 2205 duplex stainless steel," *Mater. Sci. Eng. A*, vol. 311, no. 1–2, pp. 28–41, Jul. 2001.
- [8] K. H. Lo, C. H. Shek, and J. K. L. Lai, "Recent developments in stainless steels," *Materials Science and Engineering: R: Reports*, vol. 65, pp. 39–104, 2009.
- [9] S. Topolska and J. Labanowski, "Impact-toughness investigations of duplex stainless steels," *Mater. Tehnol.*, vol. 49, no. 4, pp. 481–486, Aug. 2015.
- [10] ASTM G48-11, "Standard test methods for pitting and crevice corrosion resistance of stainless steels and related alloys by use of ferric Chloride solution," *ASTM Int.*, vol. 03, no. 2009, pp. 1–10, 2003.
- [11] L. Zhang, Y. Jiang, B. Deng, W. Zhang, J. Xu, and J. Li, "Effect of aging on the corrosion resistance of 2101 lean duplex stainless steel," *Mater. Charact.*, vol. 60, no. 12, pp. 1522–1528, 2009.
- [12] ASTM G150-13, "Standard Test Method for Electrochemical Critical Pitting Temperature Testing of Stainless Steels BT - Standard Test Method for Electrochemical Critical Pitting Temperature Testing of Stainless Steels," *ASTM Int.*, 2013.
- [13] N. Ebrahimi, M. Momeni, M. H. Moayed, and A. Davoodi, "Correlation between critical pitting temperature and degree of sensitisation on alloy 2205 duplex stainless steel," *Corros. Sci.*, vol. 53, no. 2, pp. 637–644, 2011.
- [14] V. S. Moura, L. D. Lima, J. M. Pardal, A. Y. Kina, R. R. A. Corte, and S. S. M. Tavares, "Influence of microstructure on the corrosion resistance of the duplex stainless steel UNS S31803," *Mater. Charact.*, vol. 59, no. 8, pp. 1127–1132, 2008.
- [15] N. Lopez, M. Cid, and M. Puiggali, "Influence of σ -phase on mechanical properties and corrosion resistance of duplex stainless steels," *Corros. Sci.*, vol. 41, no. 8, pp. 1615–1631, Aug. 1999.
- [16] I. Calliari, E. Ramous, and P. Bassani, "Phase Transformation in Duplex Stainless Steels after Isothermal Treatments, Continuous Cooling and Cold Working," *Mater. Sci. Forum*, vol. 638–642, pp. 2986–2991, Jan. 2010.
- [17] K. W. Chan and S. C. Tjong, "Effect of Secondary Phase Precipitation on the Corrosion Behavior of Duplex Stainless Steels," *Mater. (Basel, Switzerland)*, vol. 7, no. 7, pp. 5268–5304, Jul. 2014.
- [18] L. F. Garfias-Mesias, J. M. Sykes, and C. D. S. Tuck, "The effect of phase compositions on the pitting corrosion of 25 Cr duplex stainless steel in chloride solutions," *Corros. Sci.*, vol. 38, no. 8, pp. 1319–1330, Aug. 1996.
- [19] H. Tan, Y. Jiang, B. Deng, T. Sun, J. Xu, and J. Li, "Effect of annealing temperature on the pitting corrosion resistance of super duplex stainless steel UNS S32750," *Mater. Charact.*, vol. 60, no. 9, pp. 1049–1054, Sep. 2009.
- [20] N. Pettersson, R. F. A. Pettersson, and S. Wessman, "Precipitation of Chromium Nitrides in the Super Duplex Stainless Steel 2507," *Metall. Mater. Trans. A*, vol. 46, no. 3, pp. 1062–1072, 2015.
- [21] M. Knyazeva and M. Pohl, "Duplex Steels. Part II: Carbides and Nitrides," *Metall. Microstruct. Anal.*, vol. 2, no. 5, pp. 343–351, Oct. 2013.
- [22] E. Bettini, U. Kivisäkk, C. Leygraf, and J. Pan, "Study of corrosion behavior of a 2507 super duplex stainless steel: influence of quenched-in and isothermal nitrides," *Int. J. Electrochem. Sc.*, vol. 9, no. 6, pp. 61–80, 2013.
- [23] A. J. Ramirez, J. C. Lippold, and S. D. Brandi, "The relationship between chromium nitride and secondary austenite precipitation in duplex stainless steels," *Metallurgical and Materials Transactions A*, vol. 34, no. 8, pp. 1575–1597, 2003.
- [24] C. Örnek and D. L. Engelberg, "Correlative EBSD and SKPFM characterisation of microstructure development to assist determination of corrosion propensity in grade 2205 duplex stainless steel," *J. Mater. Sci.*, vol. 51, no. 4, pp. 1931–1948, Feb. 2016.
- [25] J. M. Pardal, S. S. M. Tavares, M. C. Fonseca, J. A. de Souza, R. R. A. Côte, and H. F. G. de Abreu, "Influence of the grain size on deleterious phase precipitation in superduplex stainless steel UNS S32750," *Mater. Charact.*, vol. 60, pp. 165–172, 2009.
- [26] J.-O. Nilsson, L. Karlsson, and J.-O. Andersson, "Secondary austenite formation and its relation to pitting corrosion in duplex stainless steel weld metal," *Mater. Sci. Technol.*, vol. 11, no. 3, pp. 276–283, 1995.

- [27] R. . Perren *et al.*, “Corrosion resistance of super duplex stainless steels in chloride ion containing environments: investigations by means of a new microelectrochemical method: II. Influence of precipitates,” *Corros. Sci.*, vol. 43, no. 4, pp. 727–745, Apr. 2001.
- [28] C. Örnek and D. L. Engelberg, “Towards understanding the effect of deformation mode on stress corrosion cracking susceptibility of grade 2205 duplex stainless steel,” *Mater. Sci. Eng. A*, vol. 666, pp. 269–279, 2016.
- [29] H. S. Valberg, *Applied Metal Forming: Including FEM Analysis*. Cambridge University Press, 2010.
- [30] Y. Cao *et al.*, “Concurrent microstructural evolution of ferrite and austenite in a duplex stainless steel processed by high-pressure torsion,” *Acta Mater.*, vol. 63, pp. 16–29, 2014.
- [31] Y. Han, D. Zou, Z. Chen, G. Fan, and W. Zhang, “Investigation on hot deformation behavior of 00Cr23Ni4N duplex stainless steel under medium-high strain rates,” *Mater. Charact.*, vol. 62, no. 2, pp. 198–203, 2011.
- [32] J. Cabrera, “Hot deformation of duplex stainless steels,” *Journal of Materials Processing Technology*, vol. 143–144, pp. 321–325, 2003.
- [33] M. Faccoli and R. Roberti, “Study of hot deformation behaviour of 2205 duplex stainless steel through hot tension tests,” *Jouranal Mater. Sci.*, vol. 48, pp. 4196–5203, 2013.
- [34] Y. Yang and B. Yan, “The microstructure and flow behavior of 2205 duplex stainless steels during high temperature compression deformation,” *Mater. Sci. Eng. A*, vol. 579, pp. 194–201, Sep. 2013.
- [35] C. M. Sellars and W. J. McTegart, “On the mechanism of hot deformation,” *Acta Metallurgica*, vol. 14, no. 9. Pergamon, pp. 1136–1138, 01-Sep-1966.
- [36] T. Maki, “Stainless steel: Progress in thermomechanical treatment,” *Curr. Opin. Solid State Mater. Sci.*, vol. 2, no. 3, pp. 290–295, 1997.
- [37] R. W. Cahn and P. Haasen, *Physical Metallurgy*. 1996.
- [38] P. Cizek and B. P. Wynne, “A mechanism of ferrite softening in a duplex stainless steel deformed in hot torsion,” *Mater. Sci. Eng. A*, vol. 230, no. 1–2, pp. 88–94, 1997.
- [39] C. Örnek, P. Reccagni, U. Kivisäkk, E. Bettini, D. L. Engelberg, and J. Pan, “Hydrogen embrittlement of super duplex stainless steel – Towards understanding the effects of microstructure and strain,” *Int. J. Hydrogen Energy*, vol. 43, no. 27, pp. 12543–12555, 2018.
- [40] O. Balancin, W. A. M. Hoffmann, and J. J. Jonas, “Influence of microstructure on the flow behaviour of duplex stainless steels at high temperature,” *Metall. Mater. Trans. A*, vol. 31A, pp. 1354–1364, 2000.
- [41] P. Cizek, B. P. Wynne, and W. M. Rainforth, “EBSD investigation of the microstructure and texture characteristics of hot deformed duplex stainless steel,” *J. Microsc.*, vol. 222, no. 2, pp. 85–96, 2006.
- [42] Z. Zhang *et al.*, “Microstructural characterization and electron backscatter diffraction analysis across the welded interface of duplex stainless steel,” *Appl. Surf. Sci.*, vol. 413, pp. 327–343, 2017.
- [43] S. Spigarelli, M. El Mehtedi, P. Ricci, and C. Mapelli, “Constitutive equations for prediction of the flow behaviour of duplex stainless steels,” *Mater. Sci. Eng. A*, vol. 527, no. 16–17, pp. 4218–4228, Jun. 2010.
- [44] J. M. Cabrera, A. Mateo, L. Llanes, J. M. Prado, and M. Anglada, “Hot deformation of duplex stainless steels,” *J. Mater. Process. Technol.*, vol. 143–144, pp. 321–325, 2003.
- [45] S. B. Davenport, N. J. Silk, C. N. Sparks, and C. M. Sellars, “Development of Constitutive Equations for Modelling of Hot Rolling,” *Mater. Sci. Technol.*, vol. 16, no. May, pp. 539–546, May 2000.
- [46] A. Iza-Mendia, A. Pinol-Juez, J. J. Urcola, and I. Gutierrez, “Microstructural and mechanical behaviour of a duplex stainless steel under hot working conditions,” *Metall. Mater. Trans. A*, vol. 29A, pp. 2975–2986, 1998.
- [47] L. Duprez, B. C. De Cooman, and N. Akdut, “Flow stress and ductility of duplex stainless steel during high-temperature torsion deformation,” *Metall. Mater. Trans. A*, vol. 33, no. 7, pp. 1931–1938, Jul. 2002.
- [48] P. Chandramohan, S. S. M. Nazirudccn, and S. S. Rninakrishnan, “Hot forging of nitrogen alloyed duplex stainless steels,” *J. Mater. Sci. Technol.*, vol. 23, no. 1, pp. 111–117, 2007.
- [49] A. Dehghan-Manshadi, M. R. Barnett, and P. D. Hodgson, “Microstructural evolution during hot deformation of duplex stainless steel,” *Mater. Sci. Technol.*, vol. 23, no. 12, pp. 1478–1484, Dec. 2007.
- [50] Y. Liu, H. Yan, X. Wang, and M. Yan, “Effect of hot deformation mode on the microstructure evolution of lean duplex stainless steel 2101,” *Mater. Sci. Eng. A*, vol. 575, pp. 41–47, 2013.
- [51] E. Angelini, B. De Benedetti, and F. Rosalbino, “Microstructural evolution and localized corrosion resistance of an aged superduplex stainless steel,” *Corros. Sci.*, vol. 46, pp. 1351–1367, 2004.

Chapter 4 Experimental Methodologies, Equipment Development & Starting Materials

Initially to determine the key functional relationship between flow stress and strain, temperature, and strain rate for the given superduplex microstructure it was necessary to conduct elevated temperature uniaxial cylindrical compression tests to establish the isotropic flow (or *effective*) stress and workability (or *formability*) of the material. A robust flow model derived from these data then allows for the subsequent development of equations to describe this behaviour which in turn form the basis upon which the Finite Element Analysis (FEA) of industrial thermo-mechanical processing depends; yield criterion, flow hardening and temperature-dependent constitutive relations between stress and strain during plastic flow.

4.1 Elevated Temperature Uniaxial Compression Testing

Uniaxial compression testing required the use of a servo-hydraulic experimental rig to facilitate the nominally isothermal deformation of various test samples to a specified total equivalent true strain under closely controlled strain rates. This last testing parameter is especially important due to the tendency of metal behaviour to become increasingly sensitive to strain rate at high temperatures.

The Servotest Testing Systems Ltd. Thermo-Mechanical Treatment Simulator (TMTS) or Thermo-Mechanical Compression (TMC) machine allows for the laboratory-scale replication and investigation of forging and rolling metal forming processes due to its capacity to deform in two modes; axisymmetric and plain strain compression, respectively. In addition to forgings, use of the TMC therefore makes simulation of long and flat products possible as well.

The TMC machine's capabilities are illustrated in Table 4.1 and main components are illustrated schematically in Fig. 4.1 below

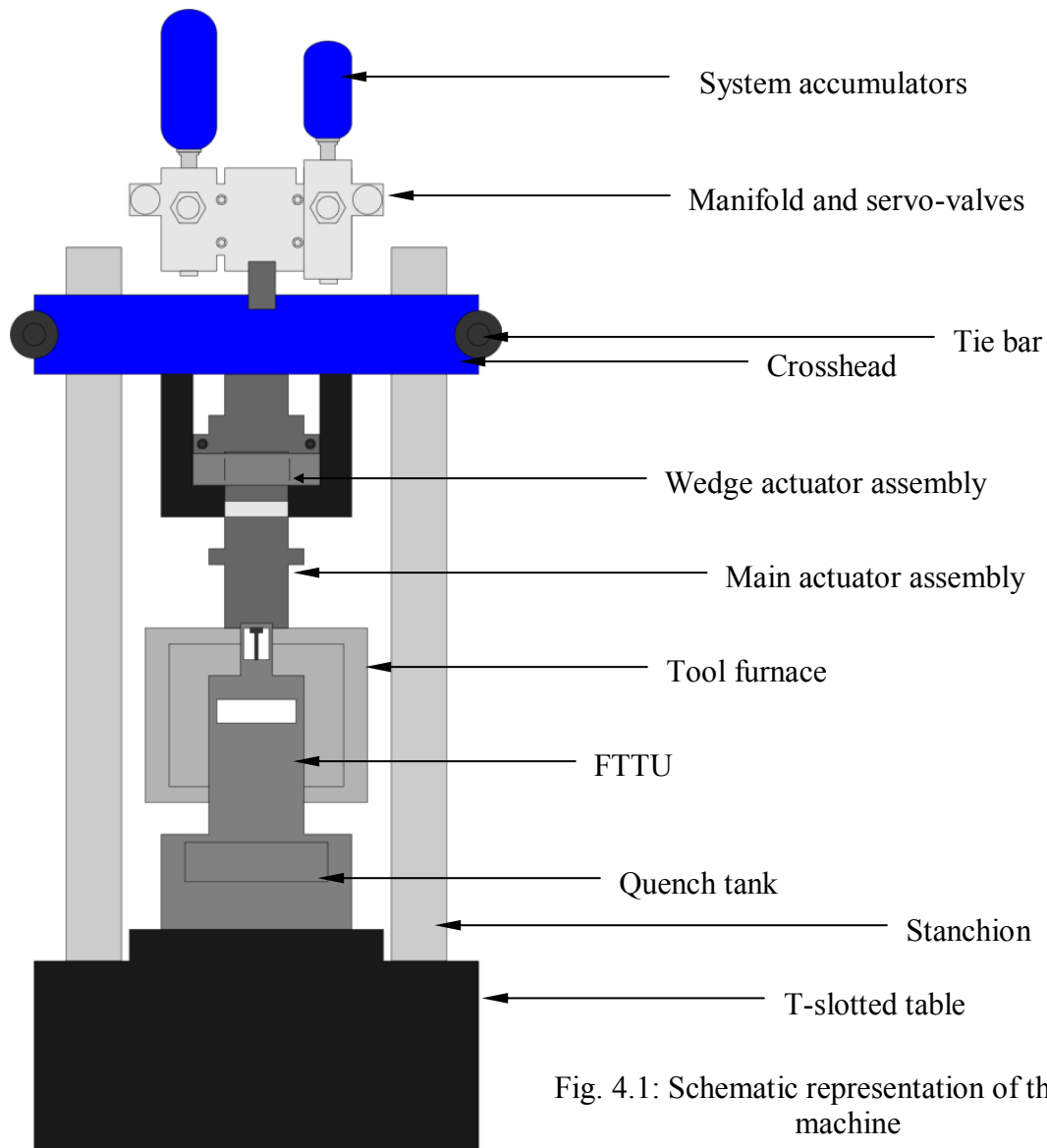


Table 4.1: TMC machine specifications

Max. load (kN)	500
Max. displacement rate (mm/s)	3000
Max. tool displacement (mm)	100
Max. pre-deformation temperature (°C)	1200 (via induction-heated Fast Thermal Treatment Unit, FTTU)
Max. tool temperature (°C)	1050 (via refractory-lined, resistance-heated tool furnace)

Uniaxial compression testing on the TMC is carried out under nominally isothermal conditions, at a specified constant strain rate, $\dot{\epsilon}$. A cylindrical sample of standard dimensions ($h = 15$ mm, $D = 10$ mm) (Fig. 4.2) is transferred via a servo-hydraulically controlled linear robot manipulator into the FTTU for preheating to the specified deformation temperature, T_D . The sample is then held in the FTTU at T_D to ensure thermal homogenisation before the manipulator transfers it into the tool furnace where it is compressed between two platens to the specified total equivalent true strain (whilst still being held in place by the robot manipulator). Fig. 4.3 illustrates the compression of a sample inside the TMC's tool furnace. The sample is then transferred out of the tool furnace and returned to the FTTU for the specified post-deformation heat treatment. The FTTU's integrated water/mist and forced air allow the sample temperature to be closely controlled immediately after deformation has finished.

4.1.1 Experimental Work Conducted on the TMC

Two discrete sets of uniaxial compression tests were conducted on the TMC and are detailed below. In both sets of tests initial sample dimensions were constant (as illustrated in Fig. 4.2) and the samples were all compressed to a total true strain of ca. 0.69, or an engineering strain of 0.5 (half height reduction). The temperature vs. time schematic plots of these tests are presented in subsequent chapters as part of the discussion and analysis of the test data. These data were acquired from the TMC in the form of instantaneous measurements of top tool velocity, sample temperature and load as a function of the main actuator displacement. During the compression stroke the applied force is measured as a function of the displacement s , giving the instantaneous tool (or compression) velocity, v as the time derivative of displacement, i.e. $v = ds/dt$. The force required to compress the cylinder is measured against the displacement giving the load-stroke curve, $F = f(s)$ from which the true stress vs. strain flow curves can be calculated.

4.1.1.1 Axisymmetric Compression Tests for Flow Model Establishment

Cylindrical samples (Fig. 4.2) were machined from a billet of AFP ZERON® 100, parallel to its longitudinal axis. Nine separate uniaxial compression tests were carried out on these samples at three strain rates and three deformation temperatures. The experimental matrix for this series of uniaxial compression tests, organised by strain rate (s^{-1}), is listed in Table 4.2. In all instances the samples were heated to the deformation temperature in the FTTU at the same

rate (ca. 5°C/s) and the tool furnace was maintained at the maximum attainable temperature, 1050°C. The samples were lubricated with boron nitride to prevent the samples from sticking to the die by minimising metallic contact and thus excessive barrelling of the sample during compression.

Table 4.2 Experimental matrix of TMC operational variables for uniaxial compression tests to determine the flow behaviour of ZERON® 100

Test #	Strain rate [s^{-1}]	Deformation Temperature, T_D		
		T_{D1} [°C]	T_{D2} [°C]	T_{D3} [°C]
1 - 3	0.01	1050	1125	1200
4 - 6	0.1	1050	1125	1200
7 - 9	1	1050	1125	1200

Each sample was held at its respective deformation temperature in the FTTU for 1 minute to ensure thermal homogenisation prior to transfer into the tool furnace for compression.

4.1.1.2 Industrially Analogous Axisymmetric Compression Tests

A series of industrially-analogous thermo-mechanical processing tests were carried out on 15mm x 10mm cylindrical samples machined from a 350mm dia. ZERON® 100 AFP billet, parallel to the longitudinal axis, L . (Fig. 4.2)

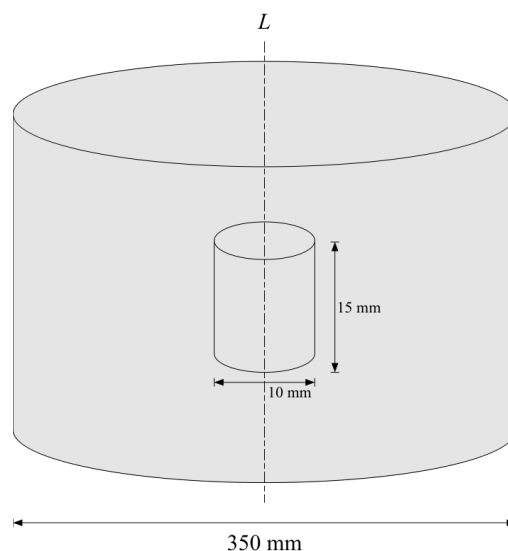


Fig. 4.2: Schematic of an example test sample, prior to upsetting and heat treatment, and its relative orientation to the billet from which it was machined.

Samples were upset at different temperatures then subjected to heat treatment, also at different temperatures. The strain rate of the upsetting remained constant throughout the tests and each sample was compressed to a total true strain of ca. 0.69. The intermediate cooling between upsetting and heat treatment was also varied. These combinations of experimental variables are listed in Table 4.3.

The industrial open die forging process to produce weld neck flange components in ZERON® 100, and from which the experimental parameters were informed is illustrated in Fig. 4.3.

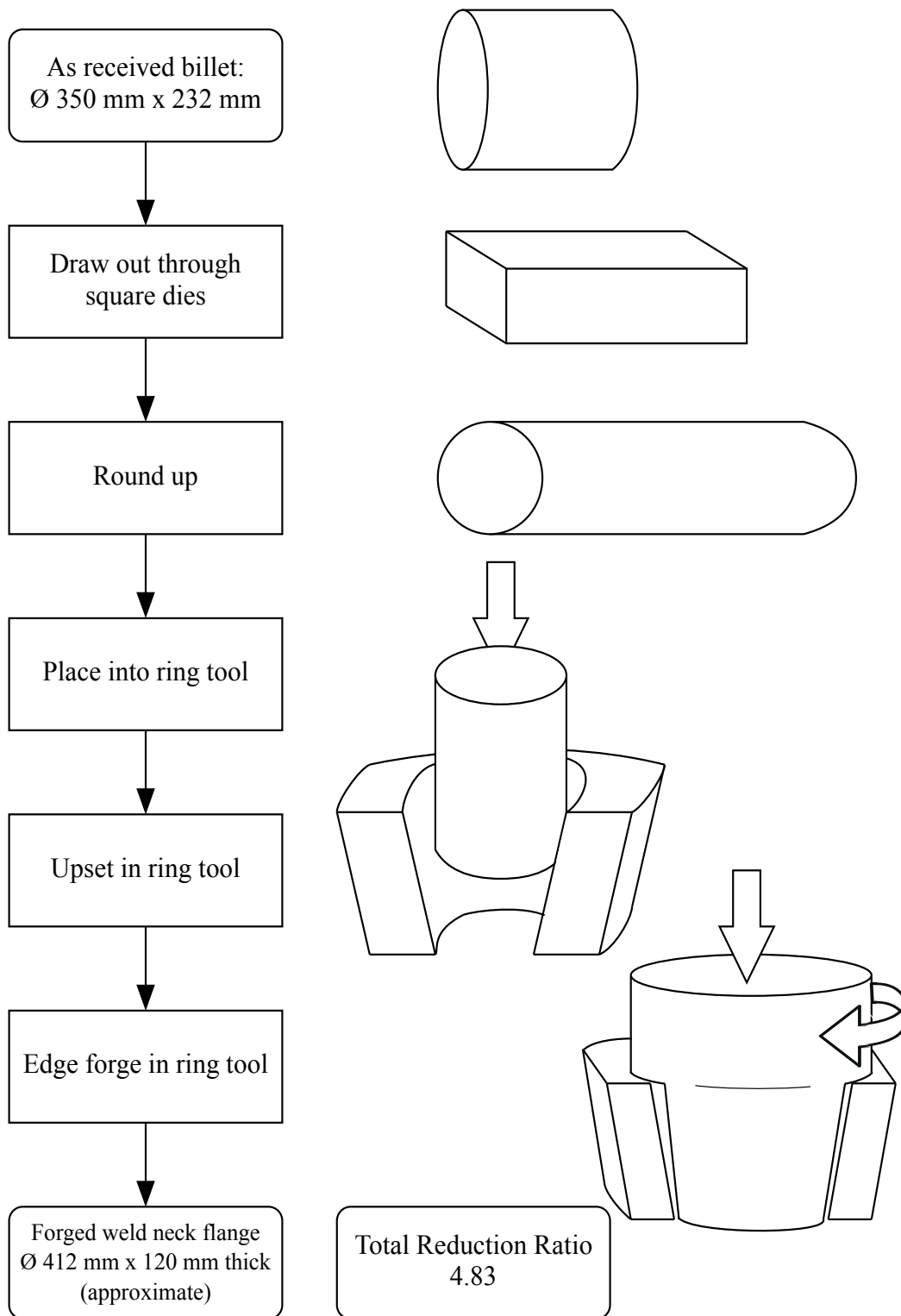


Fig.4.3: The commercial open die forging process for the manufacture of weld neck flange components in ZERON® 100 (as indicated by the commercial forging

Table 4.3: Experimental matrix for the industrially-analogous thermo-mechanical processing tests

Test #	T_D (°C)	Strain rate (s ⁻¹)	Total true strain	Post-upsetting cooling	Heat treatment temperature (°C)
6	1050			air	1120
8	1050			air	1080
5	1200			air	1120
7	1200			air	1080
2	1050			water	1120
4	1050	0.1	0.69	water	1080
1	1200			water	1120
3	1200			water	1080
10	1050			controlled reheat	1120
12	1050			controlled reheat	1080
9	1200			controlled reheat	1120
11	1200			controlled reheat	1080

In all cases above, the heating rate to the high and low forging and heat treatment temperatures was constant and the samples were soaked at these respective temperatures prior to upsetting and quenching (after the heat treatment operation) for 1 minute.

After forging, standard industrial practice is to let the component air cool and then subject it to a final quality heat treatment. The forging process is specified to only take place within the approximate temperature range 1050°C – 1280°C. Subsequent heat treatment is carried out at soak temperatures of either 1120 or 1080 ± 10°C, after loading the forging at room temperature into a furnace below 500°C, ramping to soak temperature at approximately 150°C/h and holding at this temperature for a minimum of 9h. Following soaking, the sample is quenched in an agitated water tank after having been transferred from the furnace in approximately 45s. Immersion time in the quench tank is approximately 10 min. / inch (23.6 s/mm) section thickness. The heat treatment process flow diagram is illustrated in Fig. 4.4.

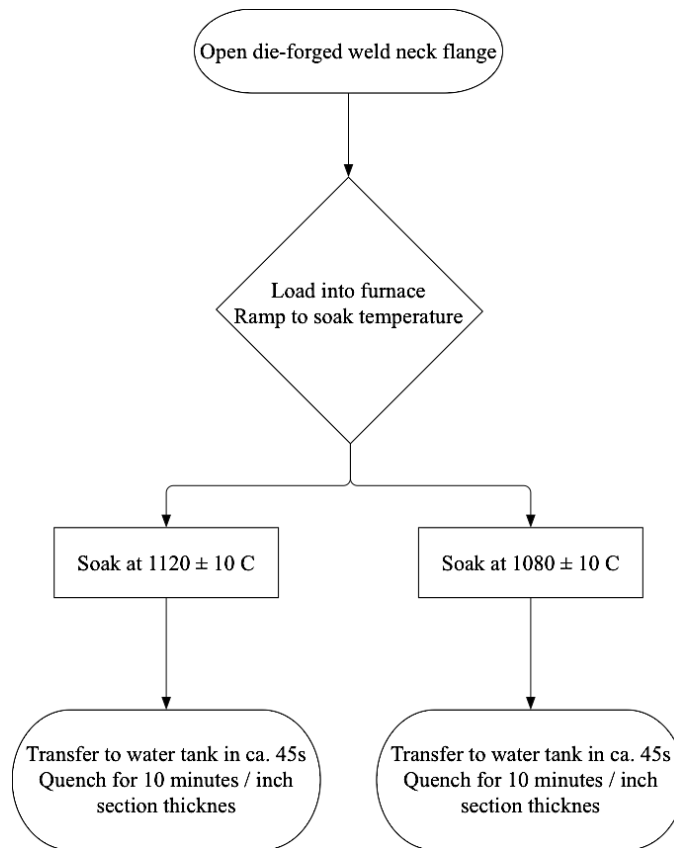


Fig. 4.4: The final quality heat treatment process

4.2 Simulation of Metal Forming and the Finite Element Method

Key to application of the finite element method (FEM) is the concept of discretisation, whereby a finite number of points (or nodes) are defined in the domain of a function (or functions). The value of the function(s), and derivatives as appropriate, are then evaluated at these points, for a prescribed set of boundary conditions. In the application of the FEM to metal forming, these functions describe the yield criterion, constitutive relations and flow hardening rules of a given material in response to force and displacement[1].

The basis of the construction of all finite element models, including those used throughout this work is, as noted above, the identification of a number of finite points in the domain of a function or functions and the specification of the value of their associated derivative(s) at each of these nodal points. In this way, continuous functions within each element (described uniquely by the nodal points defining each element) locally approximate the function or functions.

Discretisation in this way allows the sub-division of an initially unstrained body into a collection of small elements, inter-connected throughout at the nodal points and hence the domain of the function(s) can be approximated to a finite collection of sub-domains represented by these *finite elements*. In this way the elastic behaviour of each of the finite elements in the assembly can be used to describe the global behaviour of the body under stress.

Once defined, the general procedure to find the solution to the established element equation(s) requires assemblage of these element equations into a matrix or matrices from which a numerical solution to the global equation(s) can be found.

4.3 Electromagnetic Induction Heat Treatment Testing

The fundamental basis of induction heating relies on the production of time-varying magnetic field to induce a current, I in a conductive workpiece. This current produces a power loss equivalent to I^2R , where R is the electrical resistance in the circuit, which is responsible for generating heat in the workpiece. The power electronics architecture responsible for the production of an excitation current in a solenoid work-head coil (commonly formed by copper windings around the workpiece) which generates the time-varying magnetic field, relies on solid state power semiconductors, principally MOSFETS and IGBTs (depending on application and desired frequency range). These devices are characterised by very low forward conducting voltage drops and switching times on the order of ns (10^{-9} s) and allow for the generation of magnetic field frequencies, f in the range 50kHz – 10 MHz.

4.3.1 The Importance of Frequency

Frequency relates to current penetration into the workpiece and controls the depth of heating. In general terms, low frequency magnetic fields penetrate deeper into the workpiece than higher ones and therefore allow the induced current also to flow deep within the workpiece too. However, there is a limiting depth at half-thickness in the workpiece beyond which the field should not be allowed to penetrate further. At greater depths than this the field in the opposing direction will cause it to be cancelled out and no current will be induced.

High frequencies only produce induction heating at the surface of the workpiece and therefore require close control of the applied power to avoid the development of steep thermal gradients, ΔT if a homogenous temperature distribution is required. The penetration depth of the magnetic field into the workpiece as a function of frequency, $\delta(f)$ is described as,

$$\delta = \sqrt{\frac{2\rho}{\mu_r f}} \quad (\text{Eqn. 4.1})$$

Where,

μ_r = relative magnetic permeability

ρ = electrical resistivity of the workpiece (Ωm)

f = frequency (Hz)

Eqn. 4.1 illustrates that the only way to actively control the penetration depth is to modulate the frequency since the resistivity and permeability of the workpiece are fixed by its material properties. The penetration, or skin, depth into the workpiece is defined as the depth at which the current has reduced to e^{-1} of its surface value[5].

4.3.2 Advantages of Induction Heating

In comparison to alternative methods (electro- and non-electro-), induction heating, when coupled to a suitably sensitively feedback controller, offers several advantages for the heat treatment of metallic materials. Principal amongst these are the quality of heating achievable through the instantaneous power control with continuous variability. Continual modulation of the power in the time-domain allows for very close control of the available heat. Furthermore, very high power densities can be achieved in the workpiece without the need for conduction, making it the hottest part of the system and thereby reducing the time required to achieve a desired temperature. This has considerable benefit in terms of material wastage through oxidation and carburisation.

4.3.3 Operation of the Induction Heat Treatment Unit

The Inductelec (Sheffield, UK) Ltd. PID controlled UT-18kW induction heater installation (herein referred to as the Advanced Thermal Processing Unit, ATPU) allows for the replication

of complex, industrially-analogous thermal cycles programmable via a Human-Machine Interface (HMI) integrated into the inverter which in turn connects to the induction heater work head and coil. Surface temperature of the workpiece is monitored via a spot-welded K-type thermocouple and a pyrometer. Contact between the workpiece and coil is avoided by locating the workpiece inside height-adjustable spring-loaded ceramic pins. The design of the ATPU is illustrated in Fig. 4.5

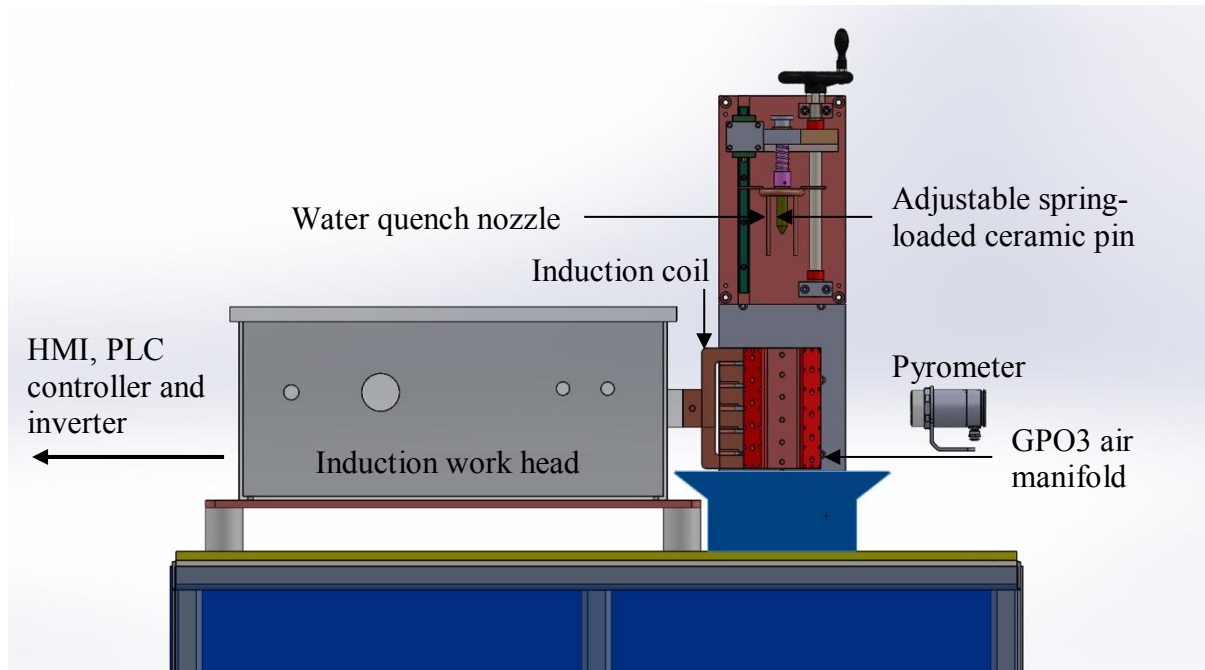


Fig. 4.5: ATPU configuration. For clarity the 18 kW inverter and integrated HMI/PID controller have been omitted. A second ceramic pin is located in the centre of the coil at the bottom (not shown) and the height adjustable top pin (shown) allows for suspension of varying workpiece geometries within the coil without contacting against it. Detail of the induction coil (with only one turn included for clarity) is shown in Fig. 4.5

The copper load (induction coil) has a large time-varying AC current set up in it by imposing a sinusoidal AC voltage across it. This current then creates a time-varying magnetic field, H that can be defined for a solenoid of n windings as,

$$H = \frac{nI}{l} \quad (\text{Eqn. 4.2})$$

Where,

l = length of the core (m)

The magnetic field in turn creates a time-varying magnetic flux density, B described by

$$B = \mu_0\mu_r H \quad (\text{Eqn. 4.3})$$

An induction solenoid coil (as described above) is illustrated schematically in Fig. 4.6

A voltage will be induced around any conductive object placed in this magnetic field, as illustrated by the workpiece placed inside the single-turn induction coil in Fig. 4.6. This voltage is equal to the rate of change of magnetic flux in the workpiece[6],

$$E = \frac{d\Phi}{dt} \quad (\text{Eqn. 4.4})$$

Where, the magnetic flux in the workpiece, of surface area A , is,

$$\Phi = BA \quad (\text{Eqn. 4.5})$$

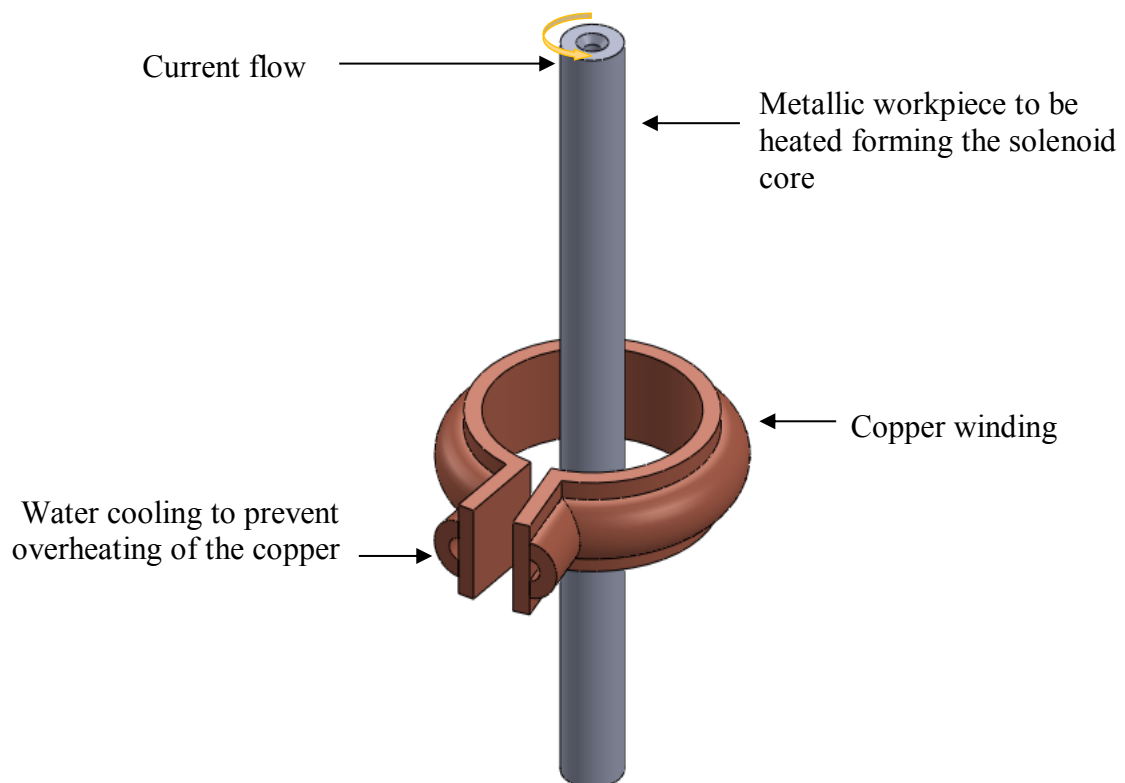


Fig. 4.6: Induction coil and workpiece. For clarity only one turn of the coil is shown; the ATPU has six turns

The cylindrical geometry of the conductive workpiece means the voltage causes current to flow around the outside, normal to the flow of current that would be produced in resistance heating between two electrodes on the top and bottom faces of the workpiece. However, in the same manner as resistive heating, it is this induced current that causes I^2R losses (heat generation, or Joule heating) in the workpiece.

4.3.4 Experimental Work Conducted on the ATPU

Initial calibration, verification and benchmarking trials were carried out on the ATPU using a high-carbon tool steel sample to replicate a relatively simple *quasi*-tempering thermal cycle. This series of initial tests was used to establish the thermal heterogeneity between the surface and the centre of the sample that arises as a consequence of thermal conductivity phenomena and the inductive heating skin effect (noted above). These initial tempering experiments illustrated the improved experimental accuracy achievable through recording temperature from the centre of the sample via an embedded, mineral-insulated thermocouple, rather than using a thermocouple spot welded to the surface of the sample. Additionally, a process control advantage was also demonstrated through these initial verification experiments by embedding the thermocouple inside the sample, away from direct exposure to the air blast cooling system.

As well as calibration and verification, the initial tempering simulations also served to establish the physical limitation of the ATPU's original cooling system design. In order to accurately simulate the computer-modelled cooling rates from specific points within a thick section weld neck flange forging, redesign and reprogramming of the ATPU was proven to be necessary through these initial experiments,

The DEFORMTM FEM software tool was used to model the QHT process, the final step in the thermal-mechanical processing of ZERON® 100 weld neck flange forgings. The operation was modelled as a transient heat transfer problem and solved over the time domain in which the thermally homogenised forging was transferred through air out of the soak furnace and immersed in a quenching tank to rapidly cool. Cooling curves for specific locations (named C1, C3 & C7) within the forging were generated through extraction of time-temperature data from the corresponding mesh elements. Through redesign of the cooling system and reprogramming of the PID control algorithm it was possible to accurately replicate the cooling rates in these positions within the ZERON® 100 forged flange (Fig 4.25a) component using

samples of the same material taken from as-received billet. These samples were also supplemented by ‘interrupted’ testing whereby the cooling profiles at the C1 and C3 locations were simulated for the transfer through air part of the QHT operation and then immediately quenched in order that the ‘thermal state’ immediately prior to immersion in water was captured. Samples subject to thermal simulation in the ATPU were impact toughness and hardness tested in order to correlate cooling rate to mechanical properties.

4.3.4.1 Design Development of the ATPU for Enhanced Cooling Control

Prior to replicating the thermal profiles calculated for the C1, C3 and C7 positions in the 16” ZERON® 100 weld neck flange during the quality heat treatment operation, it was first necessary to validate the ATPU experimental apparatus. The following sections therefore detail the tests carried out to determine the operational capability of the ATPU and then subsequently the redesign and PLC reprogramming necessary to achieve the required process control and cooling rates necessary to produce high fidelity analogues of the data outputted by the previously detailed DEFORM™ FEM thermal simulations. A necessary part of this will therefore require a superficial discussion of basic negative feedback in closed loop process control. However, only inasmuch as it directly relates to the operation of the ATPU since an extensive treatment of the wide variety of methods for control system design and the functioning of the discrete elements therein is beyond the scope of this text.

The key elements of the original ATPU experimental rig setup are detailed below wherein a 12 mm² x 150 mm sample was placed inside the output inductor (work-head coil, Fig. 4.7) with a K-type thermocouple spot welded on the sample surface to record temperature and feed back into the ATPU’s PLC input module.

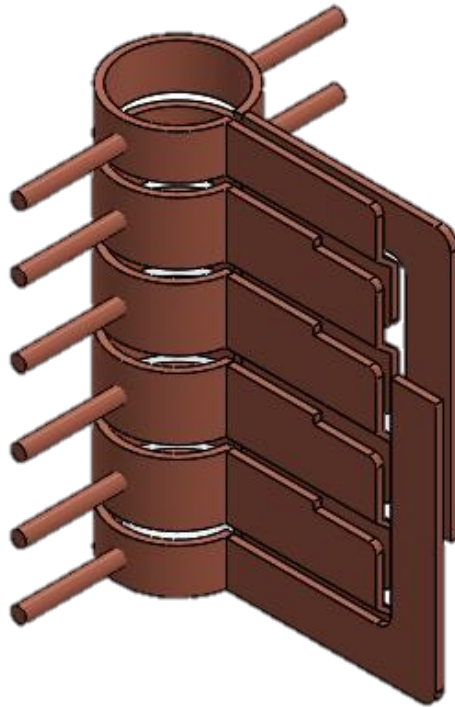


Fig. 4.7 Isometric view of the six turn, contra-wound ATPU work-head inductor. The sample illustrated in Fig. 8.9 is inserted into the coil longitudinally and held in place by two adjustable spring-loaded ceramic pins (not shown for clarity) which prevents shorting from accidental contact between the energised coil and sample during testing.

A high-carbon tool steel test sample was used for initial ATPU calibration trails using a simulated *quasi* tempering thermal cycle (Fig. 8.14). Surrounding the work-head coil (Fig. 8.10) were two polyester-glass laminate GPO3 brackets (suitable for high frequency and voltage applications) each housing 10 pneumatic fittings into which ¼" OD polyethylene air-line tubing, running from to the 4 – 20 mA P-valve, terminated. The 4 – 20 mA P-valve position is controlled by the PLC output and thereby a proportionate volume of compressed air can be blown through the fittings onto the sample inside the coil to cool it. The coil shown above in Fig. 8.10 is reproduced again below (including coil blocks connecting the inductor and workhead) in Fig. 8.11 with the surrounding polyester-glass laminate brackets including the holes into which the pneumatic fittings were inserted and held in place (the air-lines and fittings are not shown for clarity).

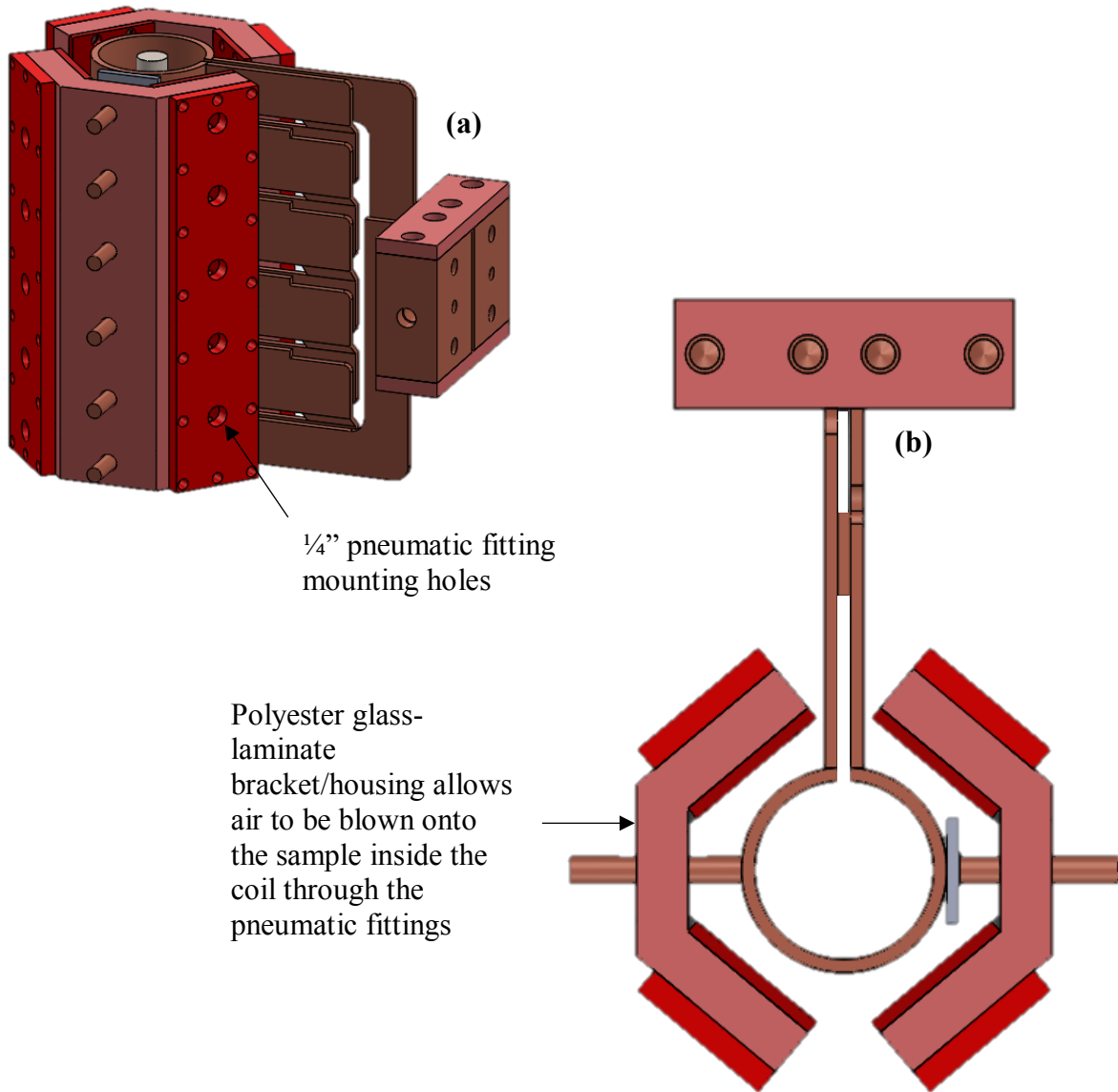


Fig. 4.8 ATPU output inductor and surrounding polyester-glass laminate bracket/housing for pneumatic fittings shown in **a** isometric and **b** plan view

To achieve more rapid rates of cooling than would otherwise be achievable through air blown onto the sample through the pneumatic fittings, a quench system situated above the coil allows water to be 'showered' through copper piping onto the top of the sample. Unlike the air-cooling system controlled through P-valve position outputted from the PLC, the water quench system is controlled by a normally closed direct-acting two-way solenoid valve. When the coil inside this solenoid valve is energised, the ferro-magnetic ferrite core plunger (and attached seal) is pulled against the action of a spring into the coil and thereby opens the cavity between the inlet and outlet ports and allows water to flow into the quench ring, around and down through the piping onto the sample (Fig. 8.12). PLC programming allows manual selection of the cooling

medium (air or water) to be used when the various setpoints defining a given thermal cycle to be replicated are entered into the HMI unit.

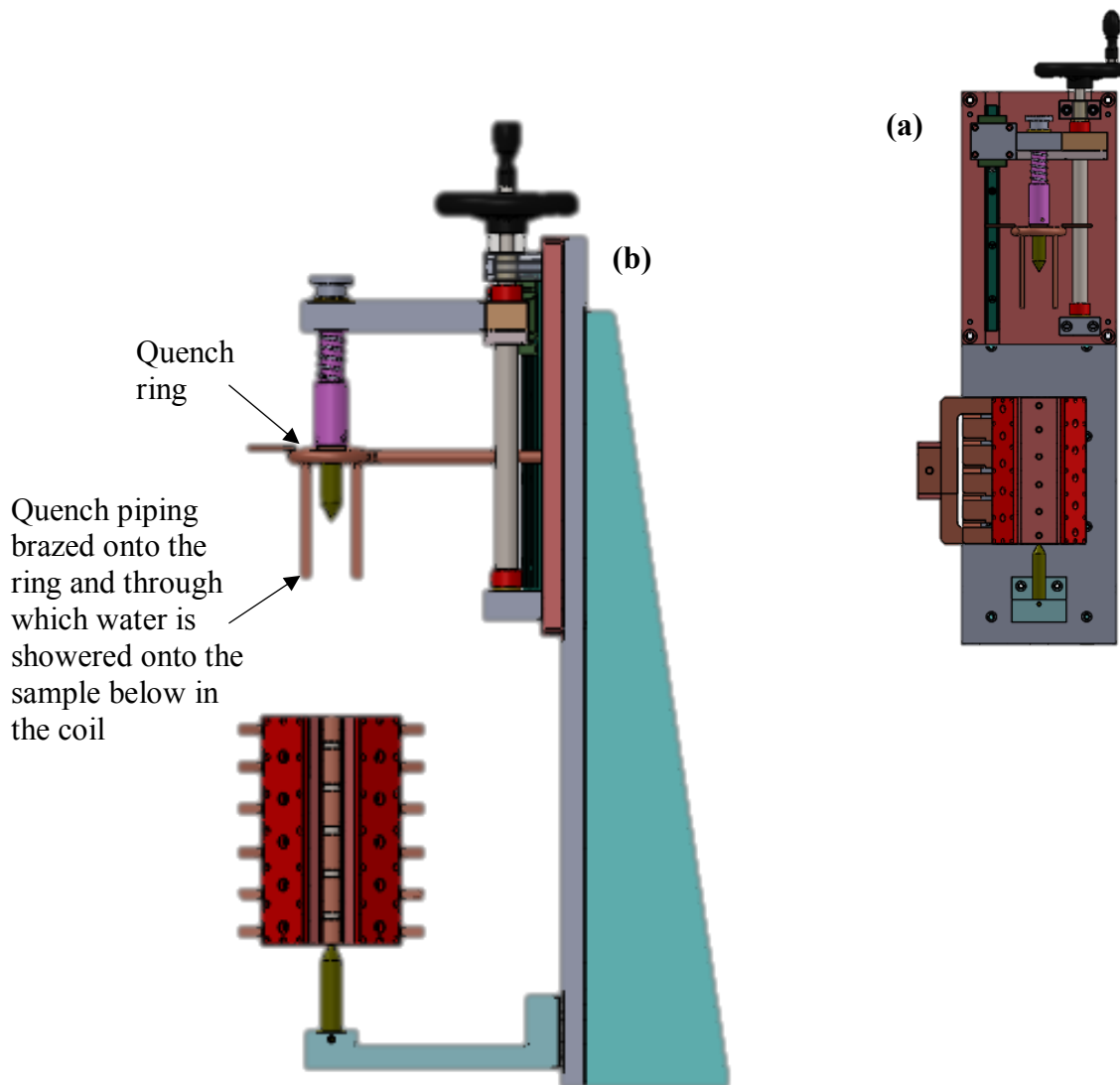


Fig. 4.9 Detailed view of the ATPU output inductor and polyester-glass laminate bracket/housing for the pneumatic fittings with surrounding sample clamping system and water quench assembly shown in **a** front and **b** side elevation.

Fig. 4.10 below is a photo of the ATPU showing the inductor coil, GPO3 brackets, top ceramic pin and pneumatic fittings in details, as illustrated previously in Figs. 4.7 - 4.9

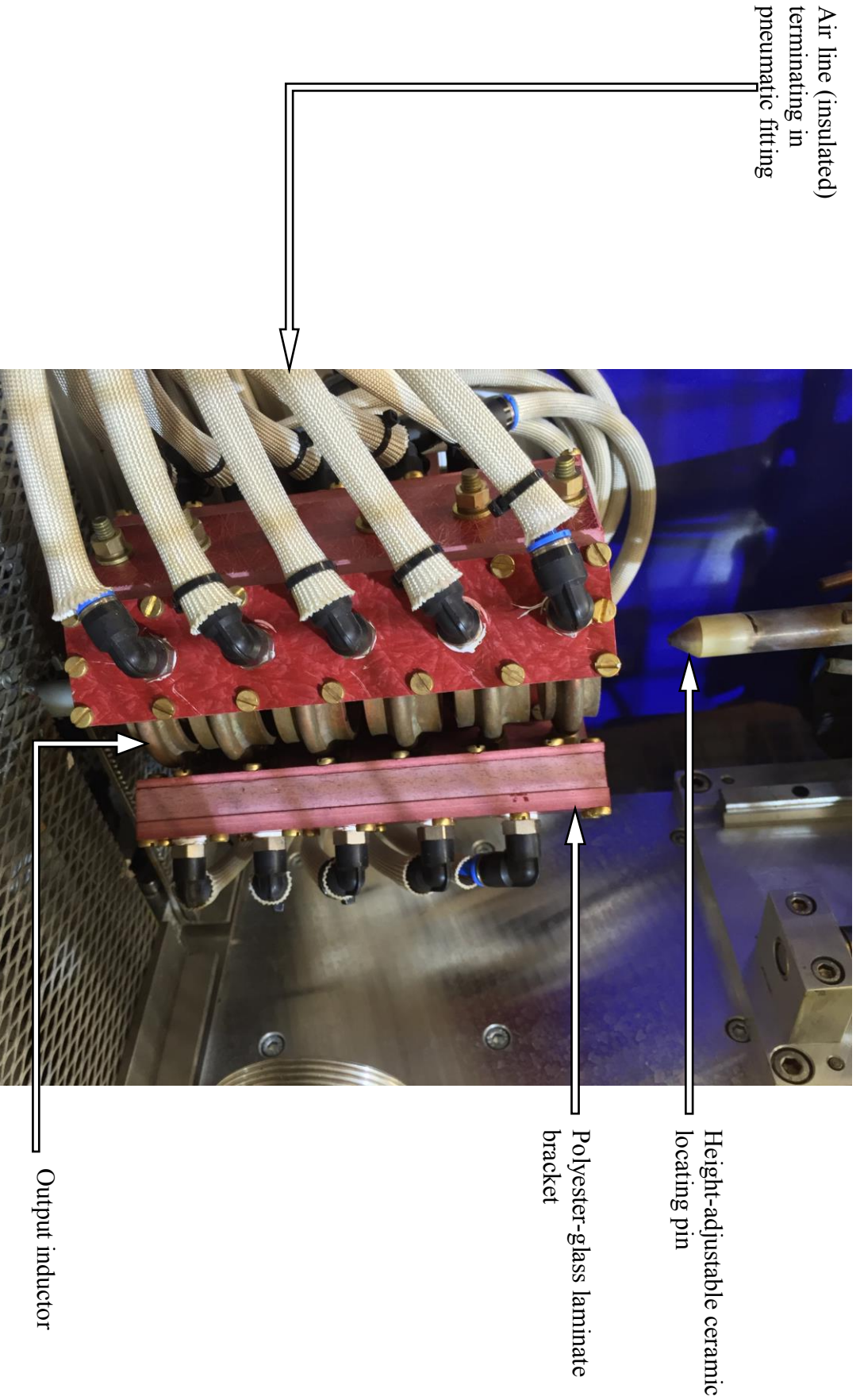


Fig. 4.10 Detail of the ATPU enclosure showing the coil, GPO3 brackets, top sialon sample locating pin, pneumatic fitting and air lines

The time-temperature profile of the first trial calibration ‘tempering’ run on the ATPU, configured as described above, is plotted in Fig. 4.11 and overlaid on top of the ‘target’ temperature-time output as described by the ‘Setpoint’ dataset.

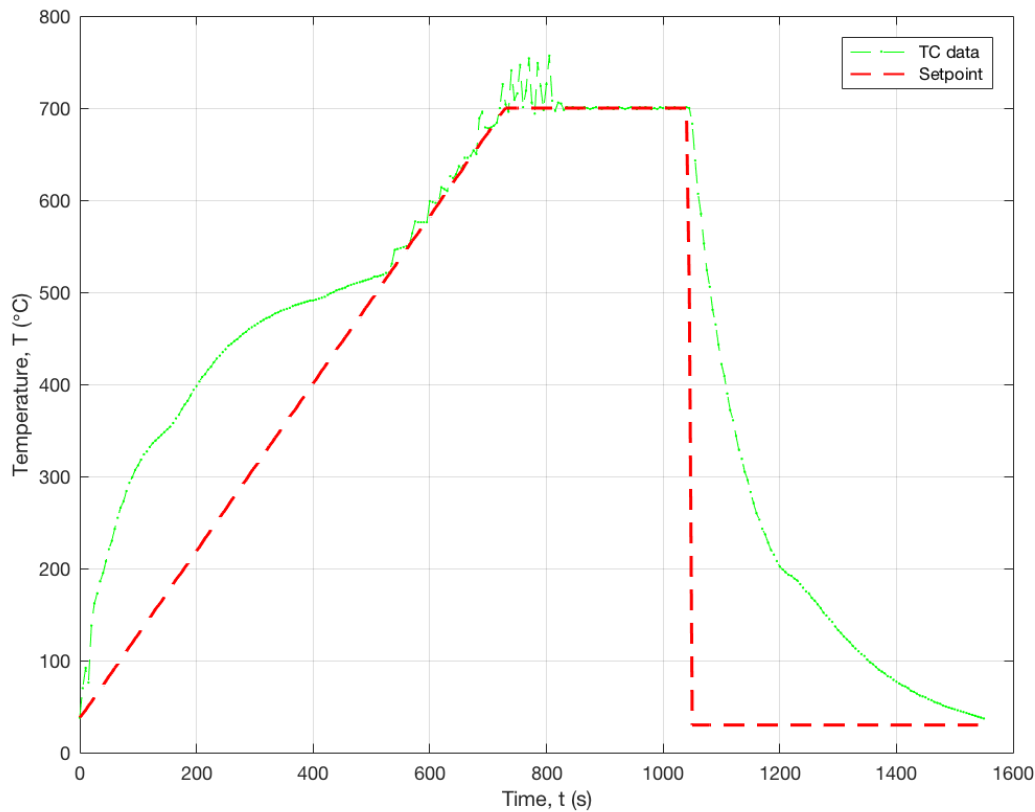


Fig. 4.11 Initial calibration test on the ATPU through basic tempering thermal cycle where a high C-steel was heated at ca. 10°C/s to 700°C and held for 5 minutes, then rapidly quenched back to room temperature.

Assessment of the results of the initial thermal cycle reveals a significant overshoot of set point during the initial part of the ramp to dwell followed by stabilization, albeit with oscillations. Further temperature oscillations upon the assumption of dwell are also present, albeit dampened by the end of the test segment. Programming an infinite cooling rate and specifying ‘air only’ allowed for an initial assessment of the achievable cooling rate via this quenchant to be made. Clearly, as the temperature of the sample decreases the rate at which the ATPU is able to cool it also decreases. Observations of the sample during thermal cycling also indicated a potential source of experimental error from the likely disparity between the temperature recorded on the surface of the sample and the bulk temperature during the thermal cycle. Consideration of the conduction of heat from the skin depth layer of the sample, in which the

majority of induced current flows (and thus I^2R heating losses are developed), indicates the likely existence of thermal heterogeneity due to the development of temperature gradients from the surface to the centre.

To assess this potential source of systematic experimental error (and thus minimise in the replication of the thermal profile from the FE model) the same basic tempering thermal cycle illustrated in Fig. 4.12 was repeated with temperature data gathered from both a surface spot welded K-type thermocouple as before as well as the addition of an embedded K-type thermocouple in the centre of the sample (half-height, half-thickness).

The $T = f(t)$ profiles of this sampling location verification trial, as recorded through two thermocouples centrally embedded and spot welded onto the surface of the sample, respectively (for the initial *quasi* tempering thermal cycle of the high-C steel sample) are illustrated below in Fig. 8.15

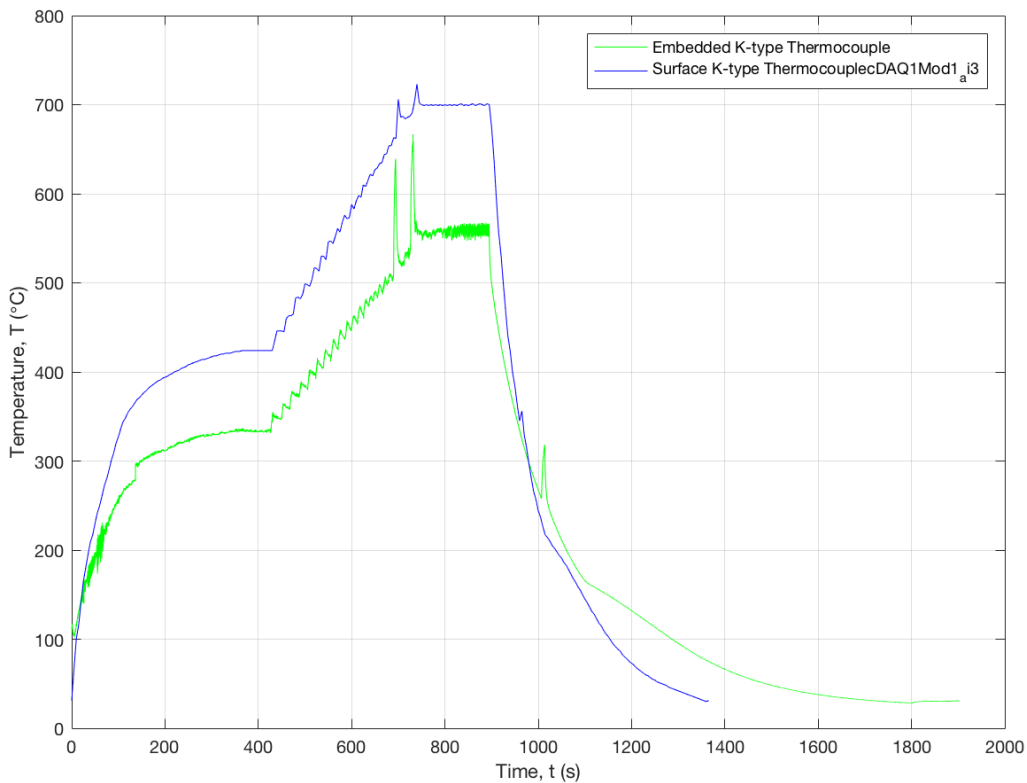


Fig. 4.12 Example $T-t$ data output from *quasi* tempering thermal cycle as recorded by surface and embedded K-type thermocouples

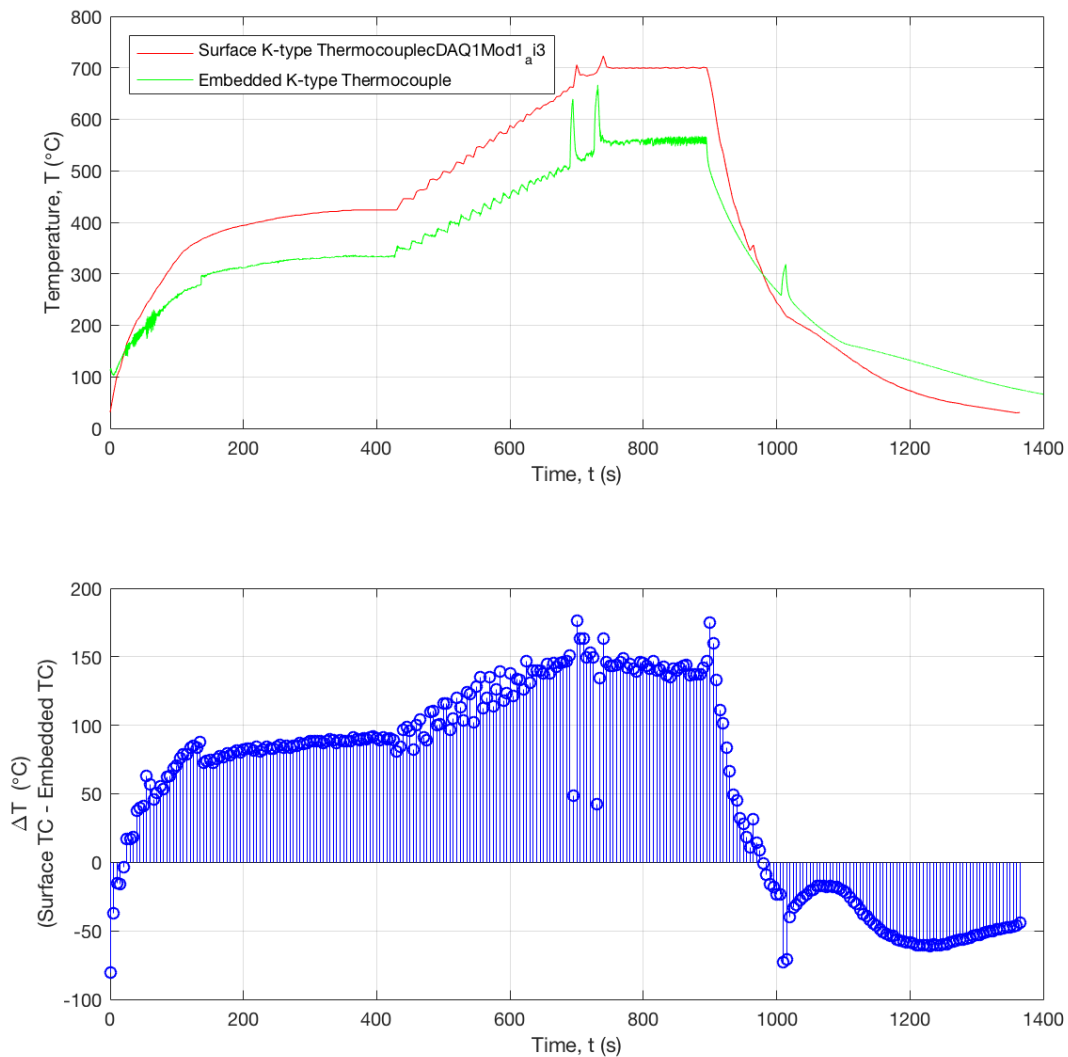


Fig. 4.13 Replication of the T-t profile from *quasi* tempering thermal cycle as recorded by surface and embedded K-type thermocouples and quantification of ΔT between these two thermocouples as indicated by the stem plot.

Fig. 4.12 indicates a clear disparity between the temperatures recorded at the surface and at the centre of the sample. The ATPU was controlled during this thermal cycle through the embedded K-type thermocouple in the centre of the sample. The disparity between the temperatures recorded at the two thermocouple locations is quantified in Fig. 4.13 where the stem plot indicates size of the temperature difference, ΔT between the surface and centre of the sample. Additionally, similarly poor process control parameters (i.e. inappropriately tuned PID algorithm) are evident in this thermal simulation as in the initial calibration test. Although the setpoint data has been omitted on Fig. 4.12 for clarity, it is clear that a large overshoot occurs

upon commencement of the thermal cycle potentially due to incorrectly specified power deration of the induction generator. Further, the same oscillations during the ramp to and hold at dwell temperature are also evident, additionally indicative of incorrectly specified P and D terms (set too low and too high, respectively). Correct configuration of the PID algorithm is discussed in further detail below.

Fig. 4.13 confirmed the suspected thermal heterogeneity within the sample, allowing for the identification of a ca. 50 - 150°C temperature difference between the surface and centre of the sample, depending on specific point within the thermal cycle. Trialling of the experimental set-up of the ATPU in this way informed the change in methodology from recoding sample temperature from a sport welded surface thermocouple to an embedded thermocouple in the centre of the sample.

The move to embedding the K-type thermocouple in the centre of the sample, as well as providing a higher fidelity indication of the bulk material temperature had the additional methodological advantage of moving the hot junction of the thermal couple away from direct contact with the air blown onto the surface of the sample thus reducing the sensitivity to extreme temperature change and thereby acting to stabilise some of the oscillations previously noted about the setpoint target temperatures. Furthermore, by locating the thermocouple hot junction at the maximum possible distance away from the skin depth of the material the opposite effect of severe temperature ‘spiking’ when power was supplied form the generator was able to be somewhat suppressed. Again, this helped in damped the oscillatory temperatures in the sample above and below the setpoint target, ultimately allowing for more accurate tracking of the setpoint.

In order to approximate the interpolated cooling curves derived from the FEM model with as high fidelity as possible it was however necessary to also adjust the PID controller algorithm, the details of which, in addition to a cursory summary of closed loop control, are outlined below.

Programmable logic control (PLC) is used to monitor inputs and control output based on a series of pre-programmed ‘rules’ to automate a process. A PLC unit consists of input modules, a central processing unit (CPU) and output modules or points (Fig. 4.14). The input is capable of accepting a variety of digital and analogue signals from various field sensors (for example

and pertinent to this case, thermocouples, voltage and current) and converting them into logic signals which can in turn be processed by the CPU. The CPU then makes decisions and executes control instructions based on the above-mentioned pre-programmed rules held in its memory. The control instructions are passed to the output modules and converted into digital or analogue signals that can be used to control a variety of field devices (or actuators) via transducers. Operator interfacing devices (i.e. HMI units) allow information to be displayed and new control parameters to be entered in real time.

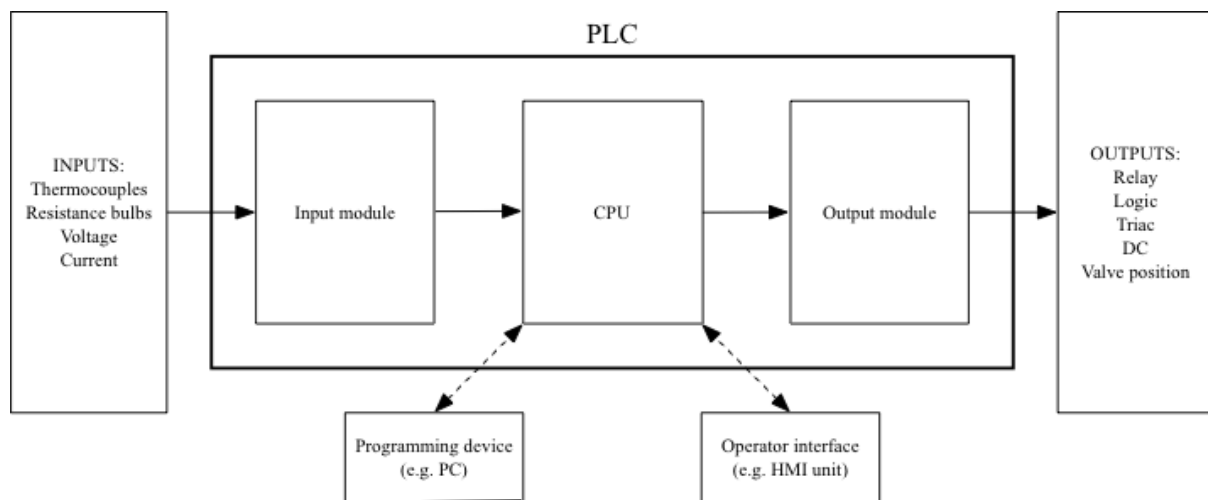


Fig. 4.14 Schematic layout and operation of a PLC unit as employed in the ATPU

During a thermal cycle (the ramp portion(s), for the purposes of illustration here), if the recorded sample temperature ('process variable', PV in general control systems terminology) sufficiently trails the corresponding setpoint temperature such that a large-enough change in the error signal is produced, the PID-controlled output signal (+ve in this case) provides a command voltage signal to the inverter unit, which itself generates proportionate amount of power. Conversely, if the sample temperature is too high, the PID control output (now -ve) initiates corrective action by, in the case of the ATPU, proportionally opening the 4 – 20 mA P-valve to provide a variable amount of air cooling.

The decision making by the PLC's CPU (control output) is determined by programming a series of ladder logic elements, or 'blocks', wherein the specific P, I & D terms for the control algorithm may be specified. The PID algorithm produces an output control signal (via the PLC output module) through the summation of the P, I and D terms.

The most basic feedback system control mode is *proportional*, P-control whereby any corrective action taken is proportional to the error and can be expressed as:

$$y = A_P e \quad \text{Eqn. 4.6}$$

Where y is the PV to be controlled (sample temperature in this case), A_P is the proportional gain of the controller and e is the error signal. To maintain control of the output using only P-control requires the maintenance of a steady state error (also known as the *proportional offset*).

In process control applications like the ATPU, the gain, A_P is specified by the width of the proportional band, Pb or temperature error (as a percentage of the total temperature range, or the display range, required to produce full heating power i.e. 18 kW). The Pb may be used in conjunction with high and low cutback limits (CBL, in setpoint units) above and below a setpoint, respectively. For example, for a given ramp to dwell schedule, full power supplied from the generator at start-up is proportionally reduced upon attainment of the low CBL by movement of the Pb up to control around the setpoints (Fig. 4.15)

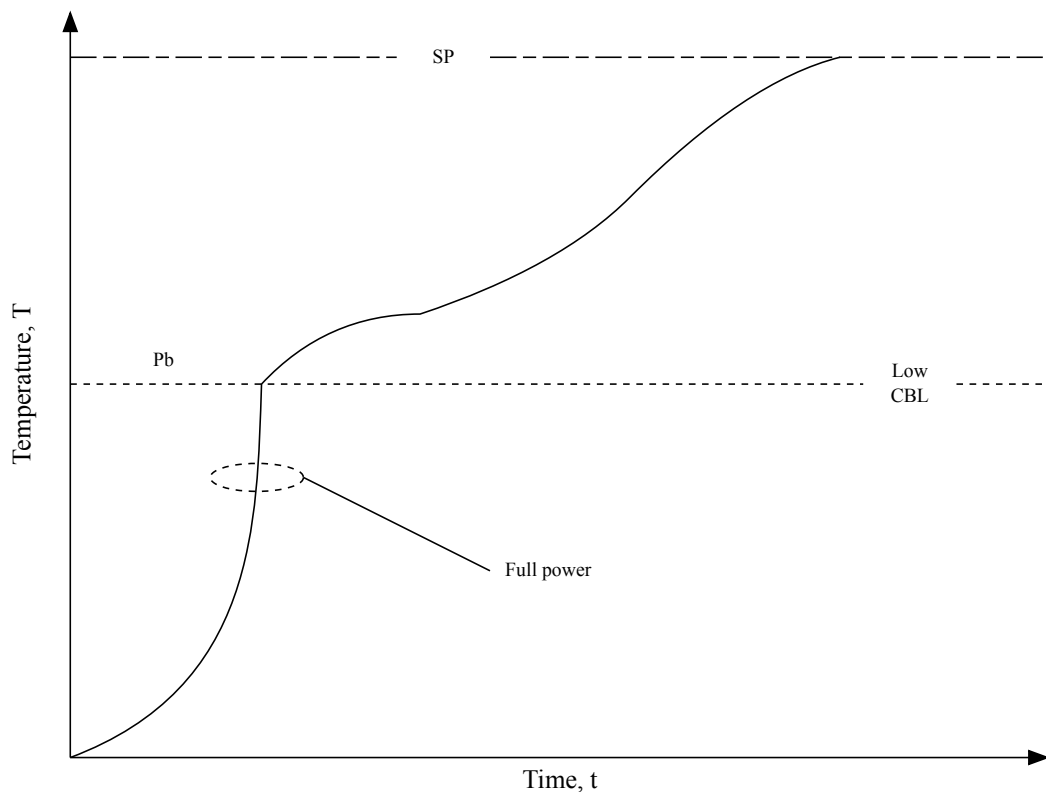


Fig. 4.15 Schematic illustration of one term P-control used in conjunction with CBLs

Application of Eqn. 4.6 implies that A_P should be as high possible for good P-control. However, the inherent limitation in P-control becomes apparent since the gain is increased, and hence also the tendency towards instability (oscillation of the PV) as the P_b is narrowed. Excessive narrowing of the P_b can ultimately lead to simple on/off control. It is therefore necessary to add a second compensating term to the basic P-control mode.

In cases where the transient response is controlled sufficiently, movement of the P_b about a (stationary or dwell) setpoint to reduce the steady state error can be obtained by integrating e (Eqn. 4.7) to obtain the I term. The I term is specified by the integral time constant, T_i . T_i is the time taken for the P_b to move its own length. The integral increases progressively with time until the error signal has decayed to zero indicating control continues to increase as long as error is present with the correction, and therefore y , being proportional to this time integral (Eqn. 4.7).

$$y = A_i \int e \, dt \qquad \text{Eqn. 4.7}$$

Where A_i is the integral gain constant, usually in s^{-1} or ms^{-1} . schematic plot of the PV response to two term (P+ I) control is shown in Fig. 4.16

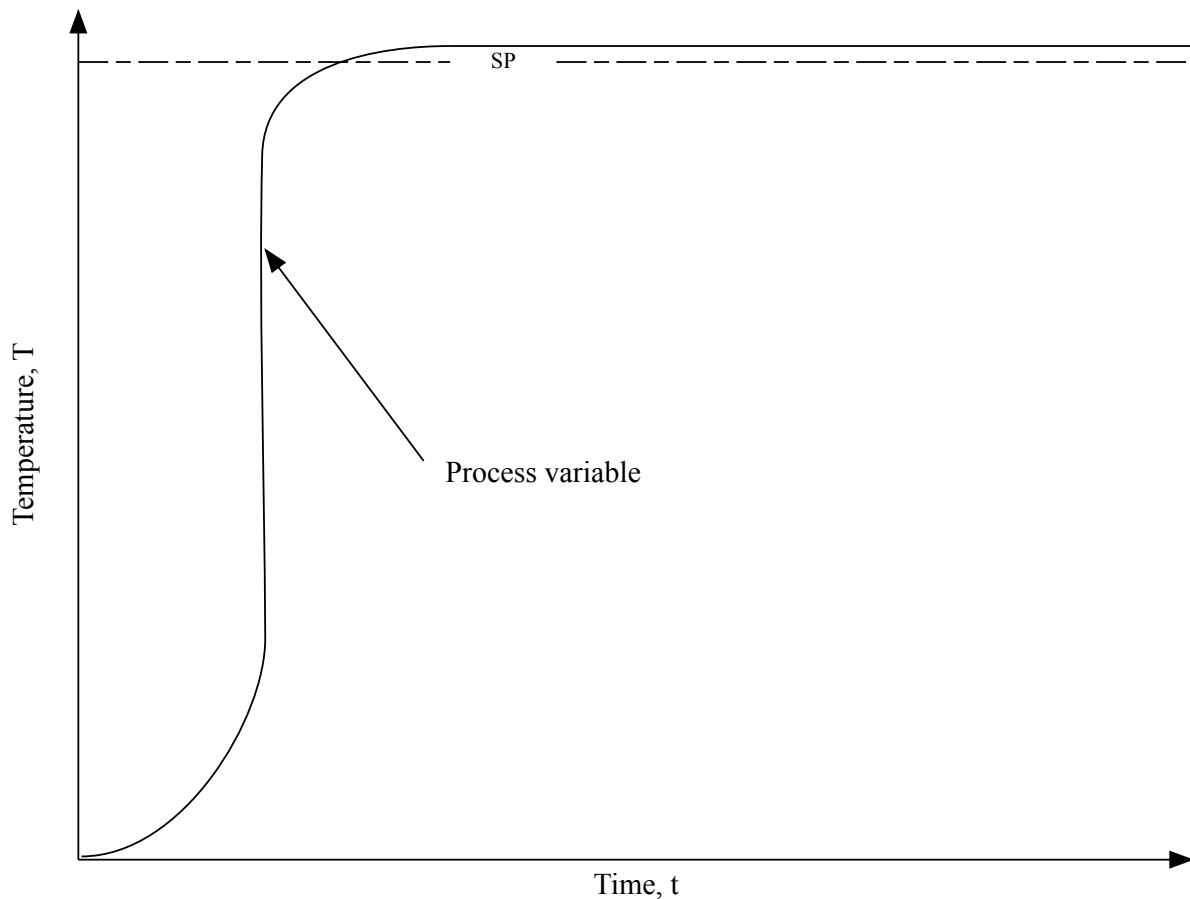


Fig. 4.16 Schematic plot of PV (temperature) for a two term (P + I) controller

P + I control may be employed, and tuned, to improve the steady state response of a control system. However, a third term must be considered if improvements in transient performance are sought. This is the D or derivative term. Derivative control makes corrections that are proportional to the rate of change of the error signal, i.e. de/dt and is given by the equation:

$$y = K_d \frac{de}{dt} \tag{Eqn. 4.8}$$

Where K_d is the derivative gain constant, in s or ms (depending on the PLC's CPU).

Due to its sensitivity to de/dt , derivative control can be thought of as anticipatory since significant corrections are produced before the magnitude of the error becomes too large. In specific temperature control systems such as the ATPU, instead of differentiating the error signal, the rate of change of the temperature command signal may be differentiated in order to obtain the requisite dT/dt . The heating power required to inductively raise the temperature of

the sample (i.e. through internal I^2R losses and neglecting the effects of radiative, convective etc. losses) is proportional to dT/dt and therefore this signal can be used to predict the required future heating power. This is referred to as Derivative time, Dt (or Differential feed forward, D Ffwd in some instances).

Since the D term acts antagonistically to changes in the controlled output, it can also stabilize a closed-loop control system by dampening the tendency towards oscillation. It is instructive to analogise Dt (s or ms) as a 'speed limit' above which changes in the PV cannot occur. If the temperature (PV) changes faster than specified by this Dt 'limit', *derivative action* takes place.

Derivative control is useful in the control of sudden input or load changes to a system due to the production of a control signal from changes in the error signal. It may not however be used alone since, by definition, it is unable to respond to steady state error. Instead therefore it must be used in conjunction with P or P + I control. The advantage of incorporating the D term in process control is illustrated schematically in Fig. 4.17.

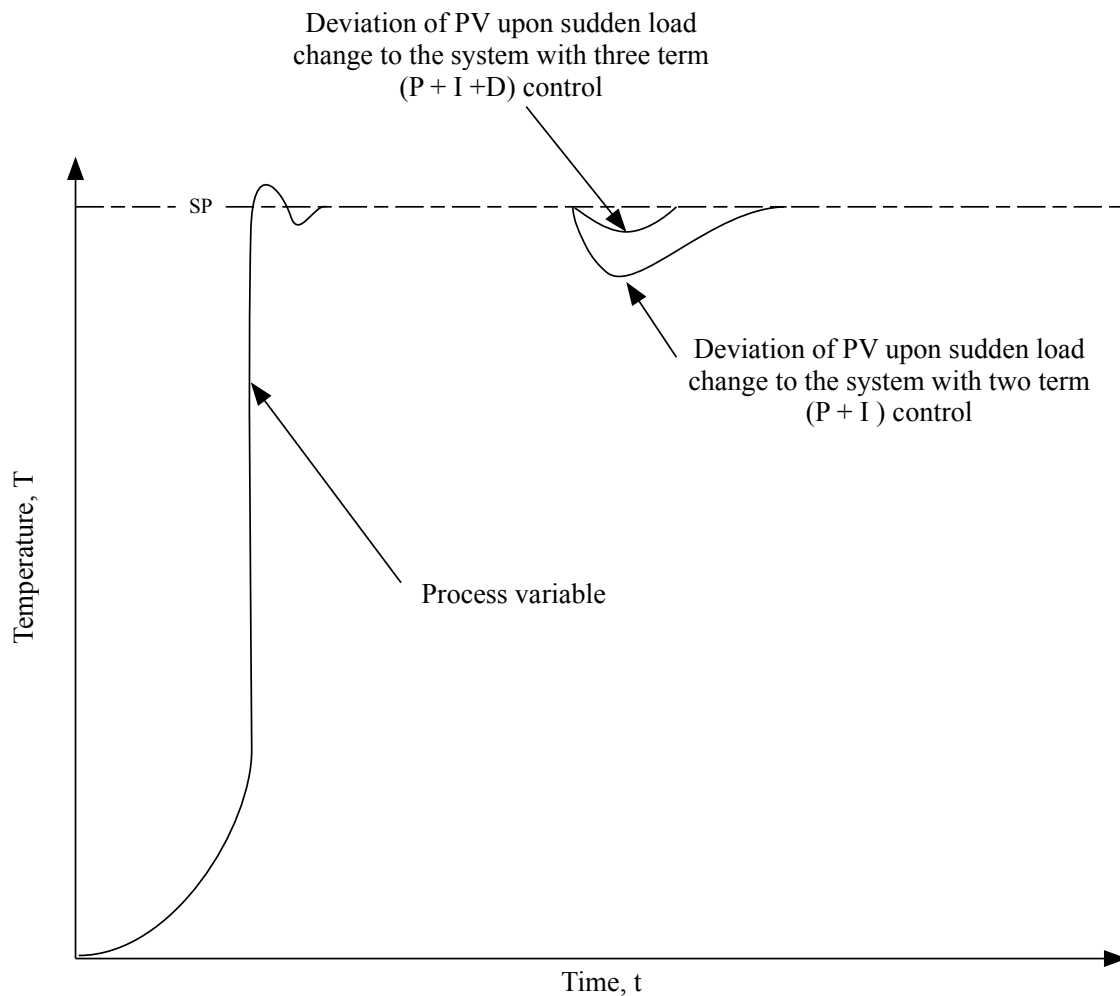


Fig. 4.17 Schematic illustration of the advantage and action of three term (P+I+D) control

Optimisation of the above described P, I and D terms to improve upon the process control demonstrated in Figs. 4.15 – 4.17 required manual tuning of the PID algorithm. In very simplistic and qualitative terms, reducing the system's tendency towards oscillation and thereby increasing control can generally be achieved by increasing P_b and T_i and decreasing D_t .

To achieve a high fidelity between the K-type-recorded sample temperature and the setpoints defining the required cooling curves from the FEA model the D_t value was adjusted within experimentally determined high and low bounds to find the optimum setting such that the correct initial heating rate with a low error signal was produced. This adjusted D_t setting also acted to reduce the temperature overshoot at the commencement of dwell.

Conversely however, by setting D_t too low an insufficiently fast initial cooling rate is produced while the opposite is true when D_t is specified too high. Achieving fidelity to the SPs during

both the ramp and cooling portions of the thermal cycle therefore required extensive and careful iterative adjustment of Dt , in combination with T_i to maintain progressive increase of the control output signal since more air flow (and ultimately mist) was required to achieve the required dT/dt as the sample temperature fell.

With changing sample temperature comes variable thermal losses which act to increase the error signal as dT/dt rises/falls. By adjusting T_i (initially to at least the frequency of one oscillation about SP), this increase in control output signal provides variable power/cooling to control dT/dt by acting to limit the size of error signal.

Adjustments to the P_b value also affect the temperature accuracy, particularly oscillations about the SPs during ramping and dwelling phases of the thermal cycle when this value was set too high. Correspondingly, specifying P_b too low resulted in achievement of desired temperature too slowly.

It may be seen then that considerable ‘fine tuning’ of the ATPUs process controls was required to achieve an acceptable level fidelity between sample temperature and SP. This proved to be particularly so when attempting to replicate the transition from the end of the ‘linear’ air cool phase of the cooling curve from the C1 location. Fig. 4.18 & Fig. 4.19 provide examples to illustrate the effect on temperature accuracy that the iterative process of manually tuning the PID algorithm had.

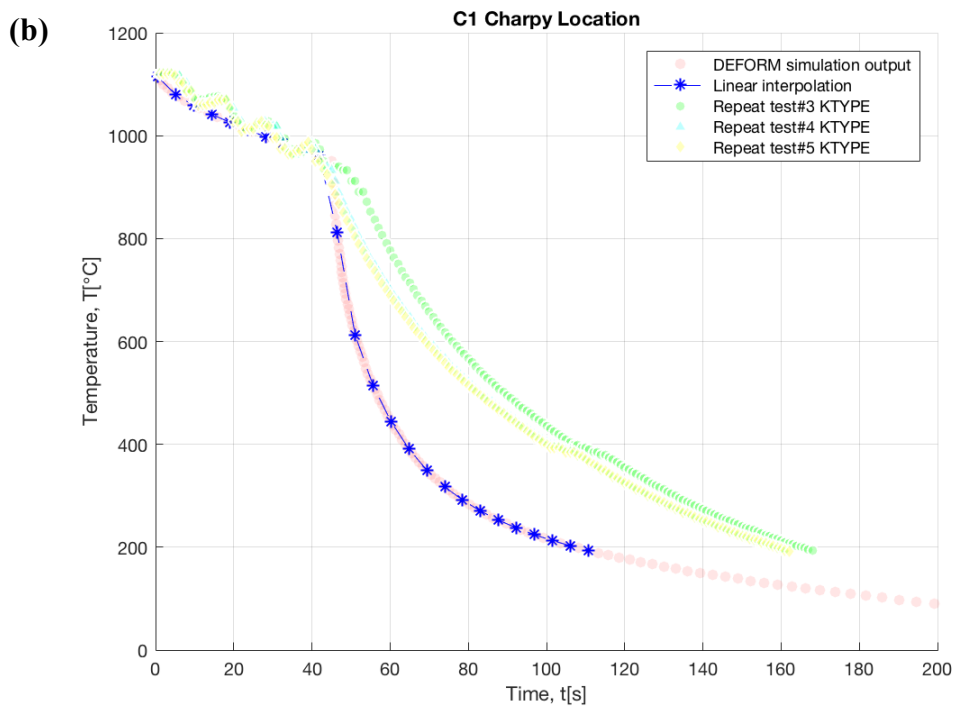
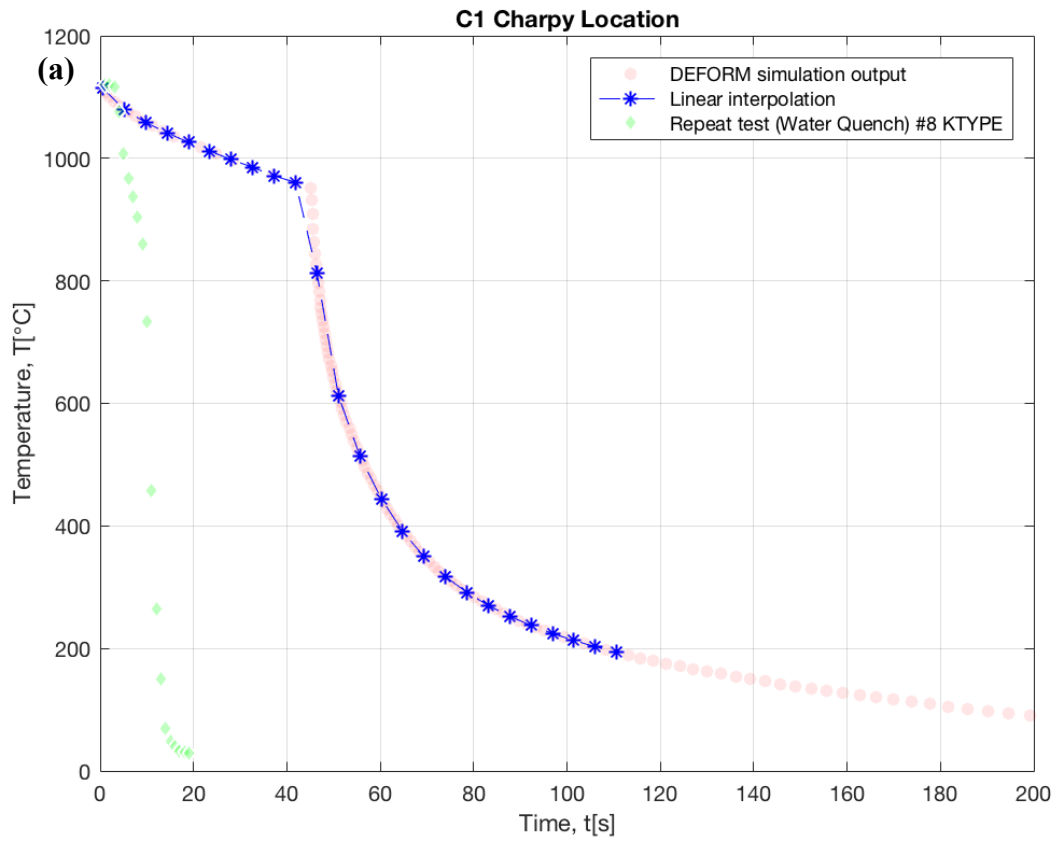


Fig. 4.18 Iterative adjustment of the ATPU controller algorithm to achieve high fidelity replication of the modelled cooling rate at the C1 location **a** with water quench only (to illustrate achievable upper cooling rate **b** with air-only control – note oscillations about, and slow cooling rate after, the linear air cool

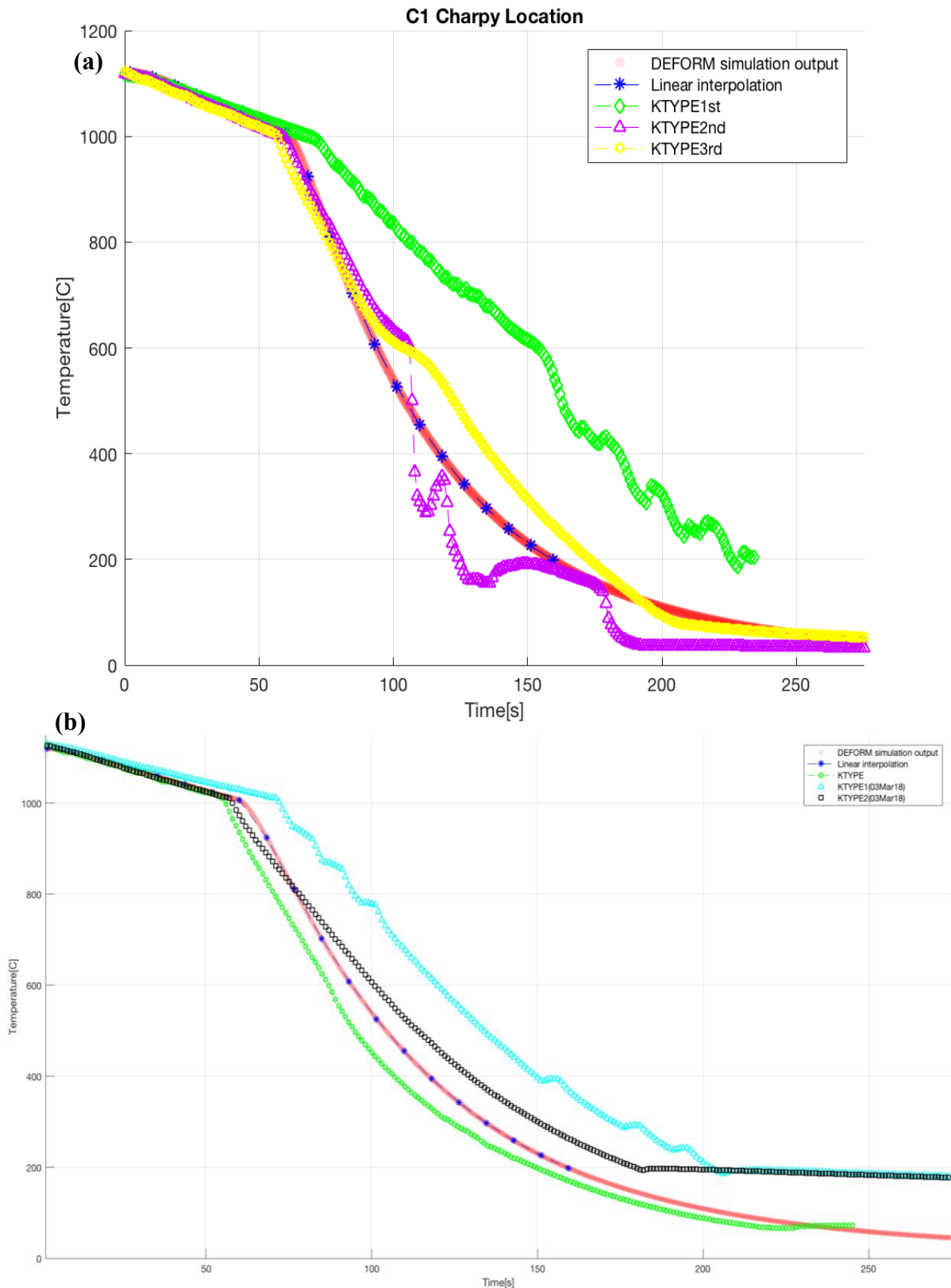


Fig. 4.19 Incremental improvements to the fidelity between sample temperature and C1 location SPs through PID tuning **a** note the removal of oscillations during the first section of the cooling profile **b** further improvement to the control of the sample cooling rate with the green markers illustrating the closest achieved approximation to the SPs

Incremental improvement in the approximation of the desired cooling curve profile can be observed from Fig. 4.18 to Fig. 4.19. The cooling rate achievable via water quenching the sample is illustrated for reference in Fig. 4.18a and although rapid provides no way to control the cooling rate as was required. The K-type dataset displayed in green in Fig. 4.19b represented the closest approximation to the interpolated cooling curve from the FEA model that could be achieved by manually tuning the ATPU's PID algorithm, and in effect defines the physical limit of the controllable cooling rate achievable through the configuration detailed above.

To improve the fidelity between the sample temperature and the interpolated cooling curves, the ATPU's cooling system was redesigned to incorporate atomising mist nozzles in order that the FEA model data of the QHT operation could be better physically simulated.

To achieve both faster, and controllable cooling rates the ATPU's original ¼" pneumatic airline fittings were adapted to incorporate pressure fed, external mix flat spray pattern fine atomizing nozzles capable of achieving flow rates of 3 – 33 l/hr. from air and liquid pressure of 0.2 – 3.0 and 0.4 – 6.3 bar, respectively (dependent upon specific hardware assembly). Adaptation of the cooling system in this way also required redesign of the GPO3 brackets surrounding the coil previously illustrated in Figs. 4.8 – 4.10.

External mixing of the liquid streams occurs outside the nozzle with the independence of the air and liquid allowing flow rates to be independently controlled and precisely metered. Finer atomization can be produced by increasing the air flow rate with in-line flow restrictors. Flat fan, wide angle (80° - 90°) spray patterns may be produced in this new configuration of the ATPU and were aimed onto the sample through the gaps in the coil (Fig. 4.7). In addition to facilitating a faster cooling rate, this had the added advantage of providing more homogenous cooling than was previously achievable by showering water top-down onto the sample through the quench ring and piping.

Forcing the cooling air through the smaller, specifically positioned, nozzle apertures greatly improved the cooling efficiency over the previously used ¼" (19.05 mm) pneumatic fittings. When combined with water, the resulting mist cooling is much more efficient than with air alone. To maintain close control of the sample temperature with this much improved capability

of the ATPU it was found necessary to increase the width of the Pb to much larger values while also reducing the value of Dt to reduce temperature oscillations and overcooling, particularly around SPs defining the transition from slower to faster cooling. The configuration of the new cooling system triggers the mist action ((by opening the solenoid water valve) only when a signal ≥ 16.8 mA from the P-valve is read by the PLC controller (indicating operation at 80% of full capacity).

The ATPU's redesigned cooling system composed of nozzle, in-line flow restrictors and new position-adjustable brackets are illustrated in Fig. 4.20 & Fig. 4.21

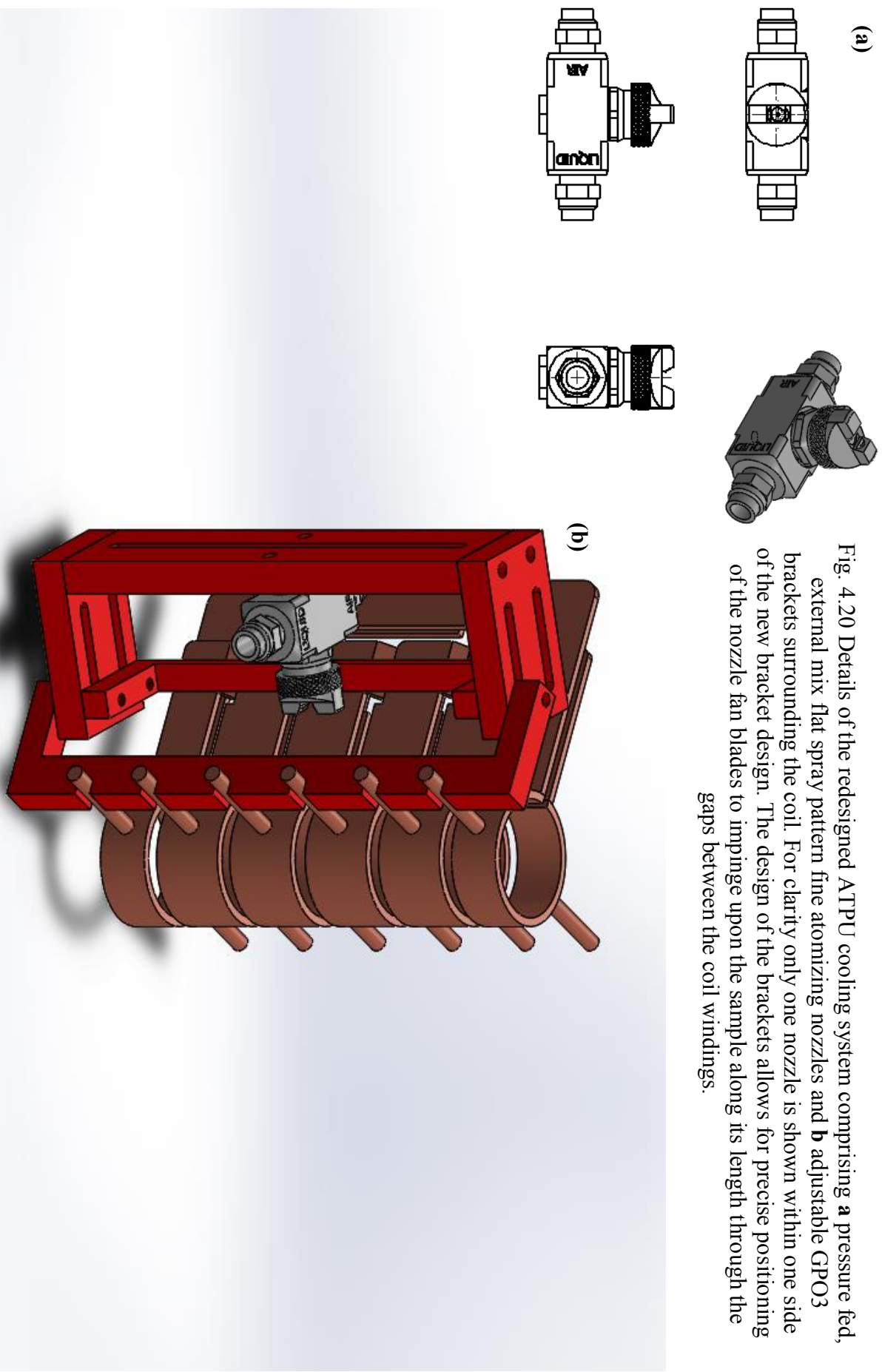
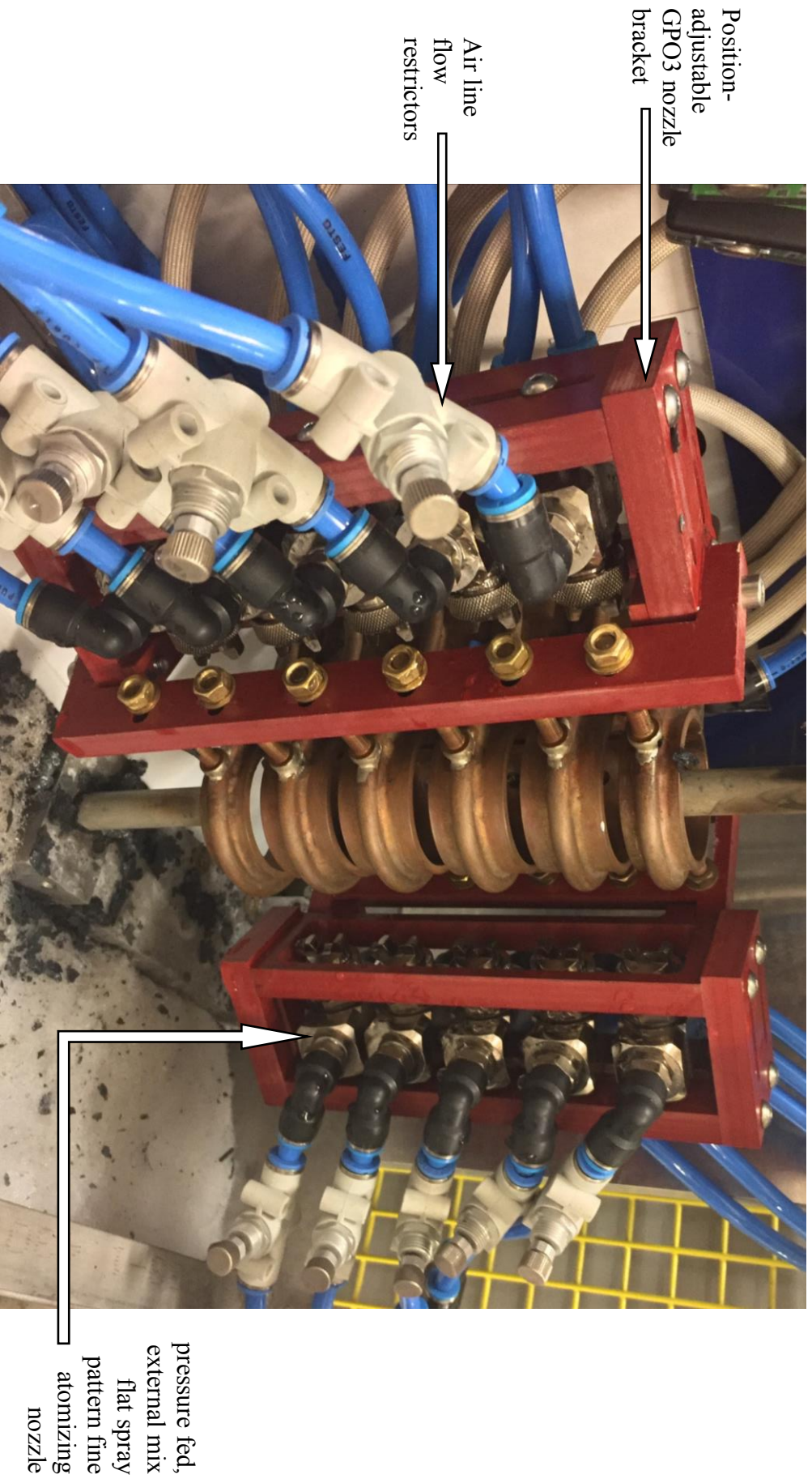


Fig. 4.20 Details of the redesigned ATPU cooling system comprising **a** pressure fed, external mix flat spray pattern fine atomizing nozzles and **b** adjustable GPO3 brackets surrounding the coil. For clarity only one nozzle is shown within one side of the new bracket design. The design of the brackets allows for precise positioning of the nozzle fan blades to impinge upon the sample along its length through the gaps between the coil windings.



4.21 Detail of the redesigned ATPU air/water mist cooling system

4.4 Electron Back Scatter Diffraction (EBSD)

EBSD is a scanning electron microscope (SEM)-based material analysis technique used to determine local crystallographic information about bulk crystalline or polycrystalline microstructures. The capability to automate data collection and mapping of sample texture has meant EBSD has become an extremely important tool in metallographic investigations. Alternative acronyms to EBSD include backscatter Kikuchi diffraction (BKD) and backscatter electron Kikuchi diffraction (BEKD), in reference to the patterns formed by backscattered electrons diffracted (when incident upon the angled surface of a sample) onto a scintillating screen/detector.

EBSD is a well-established SEM accessory and used routinely today in many contexts, not only metallography, to provide crystallographic information. Development of automated indexing of EBSPs and the high spatial resolutions achievable have been key to the wide scale adoption of EBSD to characterise grain boundaries, determine crystal orientation and discriminate between crystallographic phases thus allowing a complete quantitative representation of microstructure to be established.

4.4.1 Descriptions of Crystallographic Orientation

Using the unit reference sphere (a hypothetical sphere of radius, $r = 1$ having the same origin as, and surrounding, a single crystal) it is possible to describe a three-dimensional crystallographic direction or plane normal as two-dimensional point. This two-dimensional planar representation of three-dimensional crystal orientation uses projection onto the unit reference sphere. The stereographic projection is used specifically for crystalline metallic materials and of which pole figures and inverse pole figures are derivatives. Use of the stereographic projection maintains the angular relationships within the crystal.

The stereographic projection allows angular relationships between crystallographic plane normals or directions to be represented in two dimensions; it provides a graphic means by which the relationships between directions and planes in two crystallographic phases can be assessed. To construct the stereographic projection, crystal poles are spherically projected onto the reference sphere with the plane of projection lying on the sphere's equator. The equator defines the 'primitive circle' of the sphere and poles falling in the northern hemisphere of the

sphere project onto this primitive circle. Poles on the primitive circle project onto themselves. Figure 4.22 below schematically presents the $\{100\}$ poles of an idealised cubic single crystal in the stereographic projection, projected onto the equatorial plane in the unit sphere.

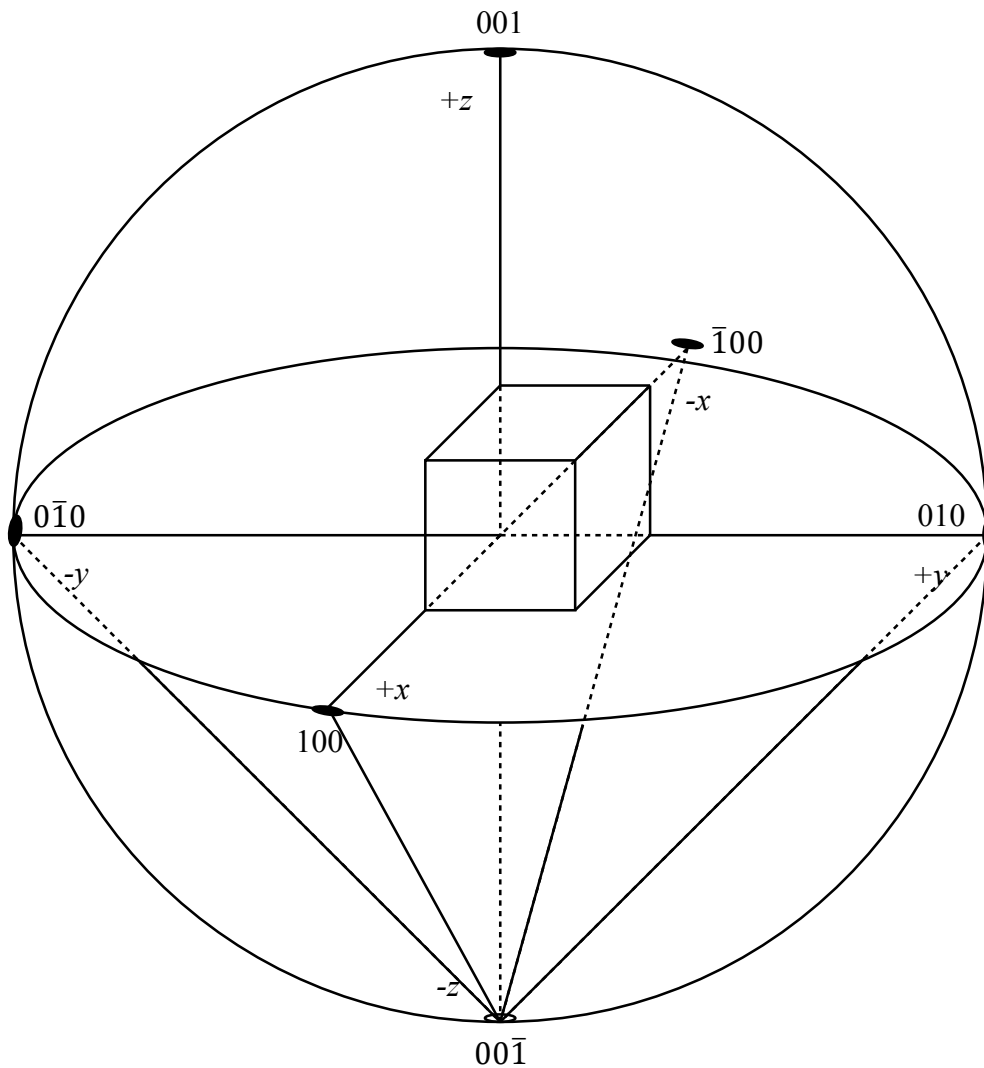


Fig. 4.22 Cubic crystal at the centre of the stereographic sphere. The z -axis is in the direction of the north pole and x - and y -axes are in the equatorial plane (the stereographic plane of projection). Normals to the $\{100\}$ crystal faces are shown and the $\{hkl\}$ indices of their intersections with the sphere.

The orientation of crystal co-ordinate system in the co-ordinate system of the sample is represented in a pole figure, PF; in effect a stereographic ‘contour map’. ‘Peaks’ in this map indicate the orientation of a particular crystal plane (or set of planes), with the intensity or frequency of the contours (contour spacing) indicating the degree of preferred orientation relative to a random distribution (in unit multiples of uniform density, mud).

Ferro-silicon alloys used in electrical transformer cores provide a classic example of PF geometry. Rolled and recrystallised polycrystalline iron-silicon exhibits a strong texture whereby the $\langle 100 \rangle$ crystal directions align parallel to the rolling direction, RD. In a $\{100\}$ orientated PF where the $\{100\}$ planes of all the crystallites lie parallel to the sheet surface, these $\{100\}$ plane will be indicated by tightly clustered contour ‘peaks’ at the centre of the PF (i.e. normal to the sheet surface) and also orthogonally to this, along the RD and transverse direction, TD[11]. An example of such an $\{100\}$ PF will appear as shown below in Fig. 4.23 where the RD is denoted X0 and the TD as Y0.

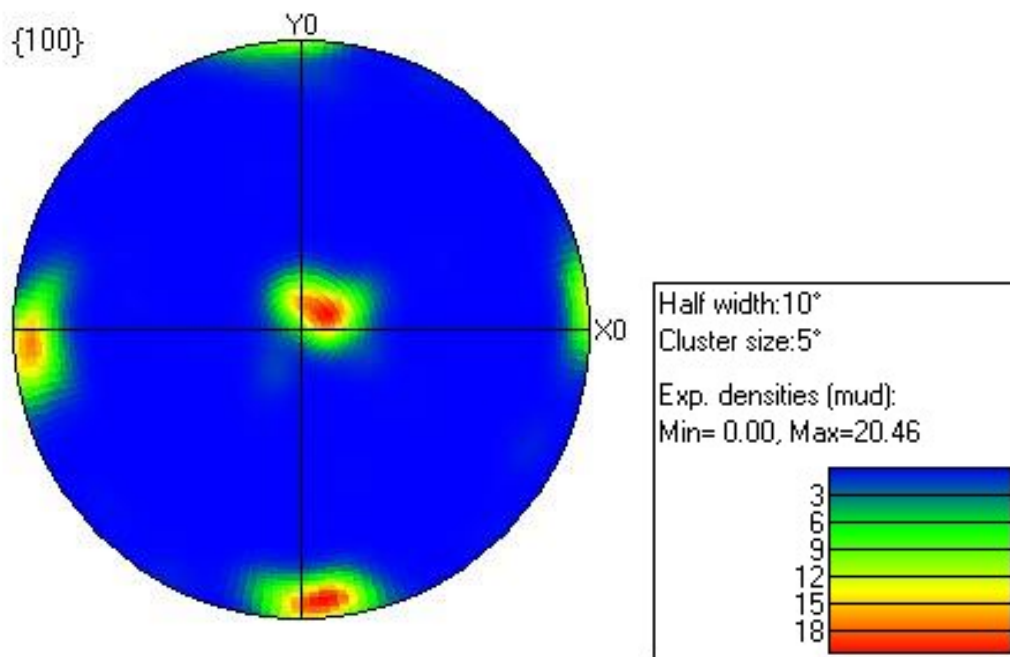


Fig. 4.23 $\{100\}$ -orientated PF in which the $\{100\}$ crystal planes lie closely, but not perfectly parallel, to the sheet surface and equally, the $\langle 100 \rangle$ directions lie closely, but not perfectly parallel, to the RD and TD.

Fig. 4.23 presents a simple, easily recognisable strong single texture. However, PFs prepared by recording experimental backscattered electron diffraction patterns from polycrystalline isotropic metallic material in a scanning electron microscope often represent rather more complicated textures. These textures may consist of more than one component whereby more than one set of directions and planes are aligned to varying degrees parallel to the sheet plane and along the RD and TDs. For example, if the $\{100\}$ planes from a different material were more randomly orientated (i.e. weaker textured) with respect to the surface of the sheet in Fig. 4.23 above, the contour lines representing the distribution of the $\{100\}$ plane normals may instead extend out across the RD and TDs.

In contrast to the stereographic projection, in the equal area projection equal areas on the reference sphere are represented by equal areas in the projection. This has obvious applicability for the measurement of population densities and specifically with reference to this work, the distribution of grain orientations within a polycrystalline metallic material. Using the equal area projection, a random distribution of orientations appears as a uniform density of poles versus a distorted distribution on the stereographic projection. However, angles between great circles on the sphere are not preserved in the equal area projection.

The orientation of a sample's co-ordinate system can also be projected into the crystal co-ordinate system in a representation known as the inverse pole figure, IPF rather than in the PF representation where, vice versa, the orientation of the crystal co-ordinate system is represented in the sample co-ordinate system. In the IPF therefore the orientation is defined by the axes of the sample co-ordinate system, i.e. RD, TD and normal direction, ND and the reference system is defined by the crystal co-ordinate system. The stereographic projection for the cubic system is made up of 24 of each of right-handed and left-handed unit triangles, with a single one of these unit triangles usually used for an IPF (single according to crystal symmetry it is not necessary to show the entire PF). IPFs are often used for axisymmetric cubic crystal samples since the axes plotted are mirror symmetry planes for the sample. In the case of cubic crystal symmetry and for the purposes of representing FCC and BCC materials in this work, the well-known unit triangle with apices $\langle 100 \rangle$, $\langle 110 \rangle$ and $\langle 111 \rangle$ is used[10].

4.4.2 EBSD Experimental Work

EBSD scans were performed on ZERON® 100 samples taken from commercial forgings and experimental material. In all cases EBSD scans were performed on a FEI Co. Sirion FEG-SEM. The optimised working distance between the tilted sample and the incident electron beam was 14mm and an accelerating voltage of 15 keV and spot size 5 were used. A fully automatic HKL Technology (now Oxford Instruments plc.) Channel5 EBSD detector system was fitted to the SEM and allowed for imaging, diffraction pattern acquisition and indexing, phase identification, and post processing orientation mapping, stereographic representations (pole figures) and inverse pole figure production.

The EBSD scans were performed on specimens sectioned and prepared from standard Charpy V-notch samples taken parallel to the axial direction of the forging from three positions in a 16 ³/₄ inch (425.45 mm) weld neck flange forging as illustrated in Fig. 4.24.

The standard Charpy V-notch sample and the approximate locations these samples are taken from in the weld neck flange forging (Fig. 4.25) are illustrated in Figs. 4.25(a) and 4.25(b)

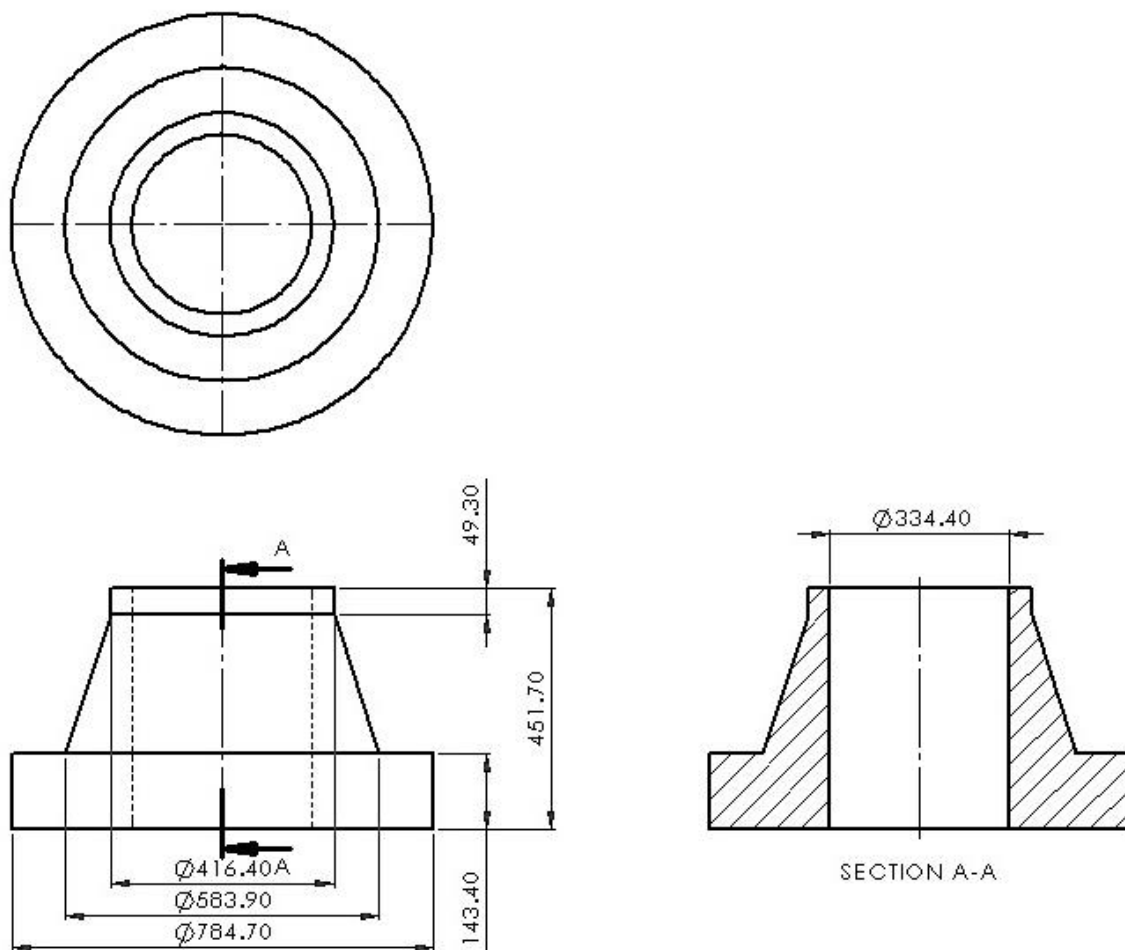


Fig. 4.24 16 ³/₄ " (425.45 mm) weld neck flange forging (all dimensions in mm). The 'rough' component illustrated here is machined to the final geometrical specification after forging. The piercing operation to form the bore can be performed as part of the forging process using a punch or machined out subsequently. Regardless of the method of material removal, the bore is always formed prior to heat treatment.

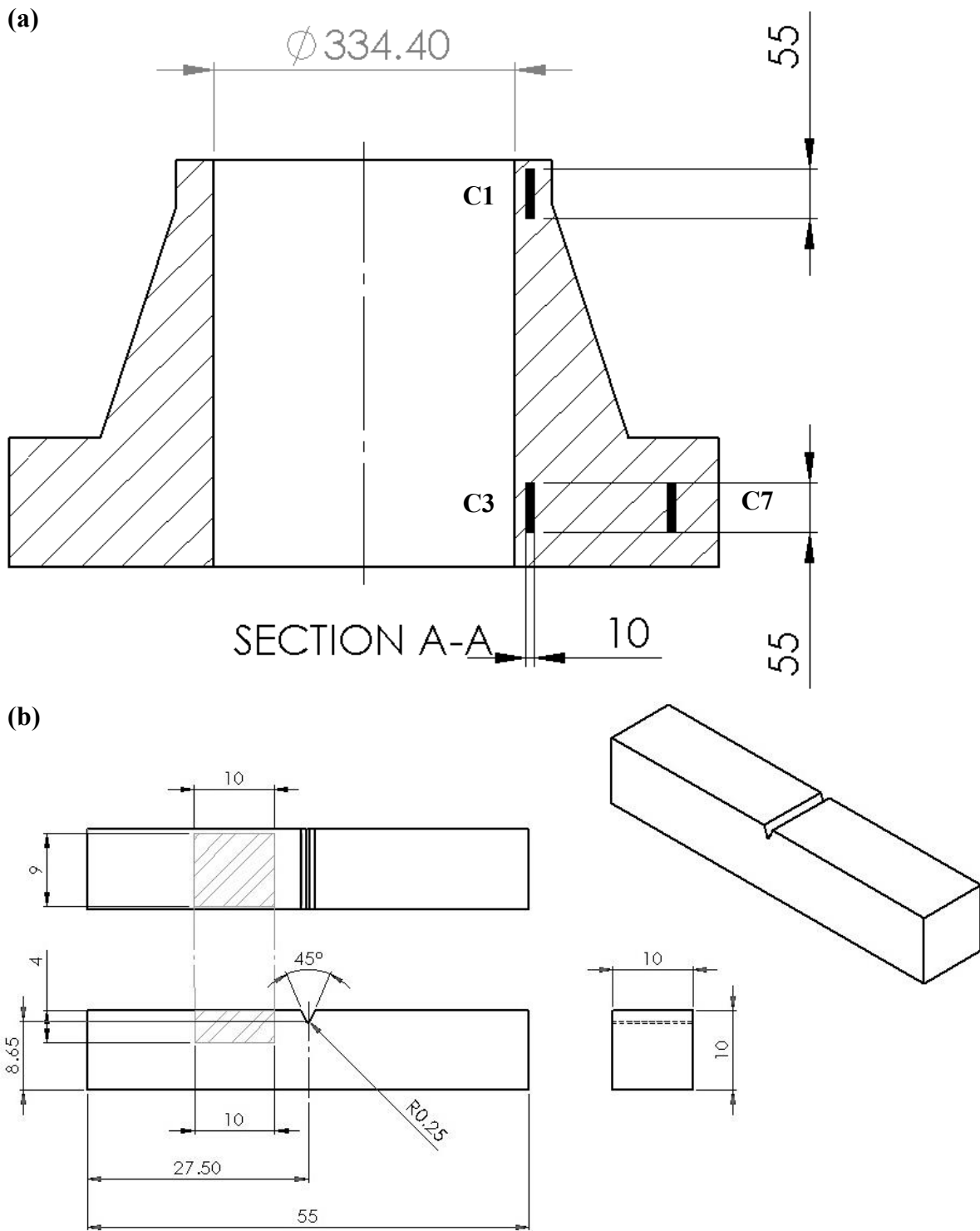


Fig. 4.25 The orientation and location in the **a** weld neck flange forging from which the Charpy V-notch impact toughness samples were taken and **b** ASTM standard Charpy V-notch impact toughness samples from which the EBSD samples were sectioned.

The Charpy impact resistance specimens subject to EBSD analysis were removed from the neck of the forging (C1) in the axial direction, close to the bore inside diameter (C3) in the axial direction and in the centre of the flange (C7), also in the axial direction (Fig. 4.25 a).

Specimens subjected to EBSD analysis from the industrially analogous axisymmetric compression tests were removed from the compressed TMC samples parallel to the forging axis. The subsequently produced EBSD specimens were prepared and orientated such that the scanned specimen face corresponded with the highest-strain central area of the TMC sample (Fig. 4.26).

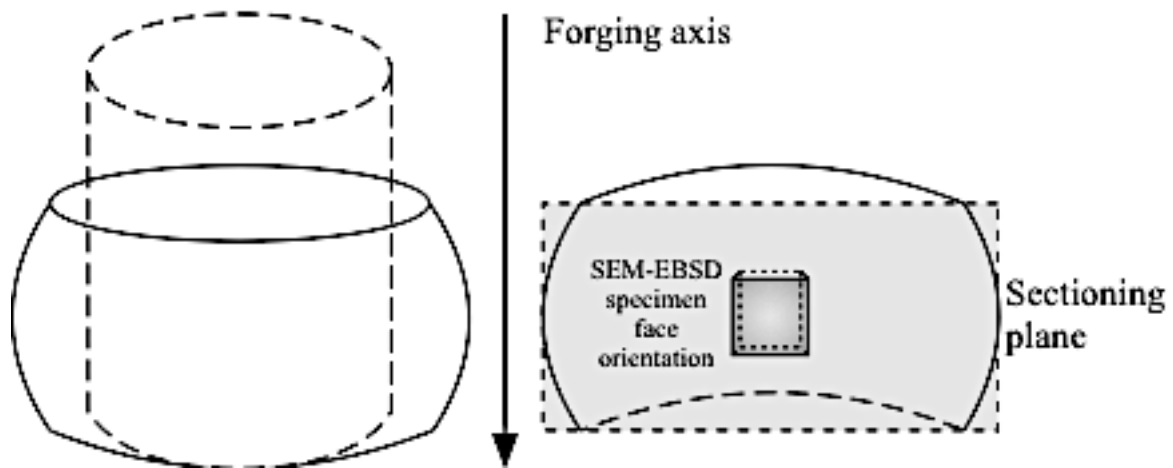


Fig. 4.26 Orientation of the EBSD specimens taken from the TMC samples used in the industrially analogous axisymmetric compression tests

4.5 Metallographic Preparation

Standard metallographic preparation techniques were followed for the production of all optical and electron micrographs included in this work. Sectioning of samples to the required dimensions for microscopy was performed on a Struers Inc. Secotom-50; a benchtop cut-off saw with movable cutting table, motorised cutting wheel positioning and variable speed in conjunction with Buehler Inc. AcuThin™ rubber-bonded abrasive sectioning blades.

Sectioned samples were hot compression mounted in a graphite and mineral filled conductive phenolic thermoset and initially ground flat using incrementally finer SiC grit papers over the range P800 – P2400 (depending on the nature of prior sectioning). Following grinding, the

samples were polished to a mirror finish using progressively finer monocrystalline diamond suspensions over the range 6 μm – 1 μm with long napped, synthetic nylon/rayon polishing cloths. Final stage polishing to remove superficial mechanical damage specifically for EBSD analysis was conducted using Buehler MicroPolish™ 0.05 μm alumina oxide suspension. Acetone ($\text{C}_3\text{H}_6\text{O}$) was used for degreasing between each stage of the preparation process and also in post-preparation ultrasonic baths immediately prior to microscopy.

4.5.1 Electrolytic Etching

Electrolytic etching was employed to enhance the phase contrast between the duplex austenitic and ferritic phases for the purposes of optical microscopy. The electrolytic etching procedure employed for the purposes of this work was performed as direct current electrolysis with the metallographically prepared specimen as the anode. The cathode material used was a stainless steel of comparable chemical composition to the sample. Electrical connection to the sample surface was made by contacting with a wire/thin bar-type probe cathode.

Electrolytic etching generally provides more reproducible and consistent results than chemical- and colour etching alternatives, however uneven etching of the specimen surface can often occur, generally with heavier etching near edges due to localised difference in surface current density.

Voltage and time parameters for electrolysis were established by trial and error, and depended on factors such as progressive electrolyte concentration dilution (during etching of multiple samples), cathode material and area, geometry of the electrochemical cell, and specimen surface area. They were however typically of the order 1.5 – 3.5 V for contact time of 5 - 10 s.

Aqueous solutions of 40% sodium hydroxide (NaOH) and 10% oxalic acid ($\text{C}_2\text{H}_2\text{O}_4$) were used sequentially in a two-step procedure (with intermediate washing of the sample) as etchants to colour ferrite and intermetallic phases and delineate microstructure, respectively. Oxalic acid was also used for the purposes of intergranular chromium nitride precipitation detection.

The apparatus configuration to achieve the above described electrolytic etching is illustrated schematically in Fig. 4.27 below.

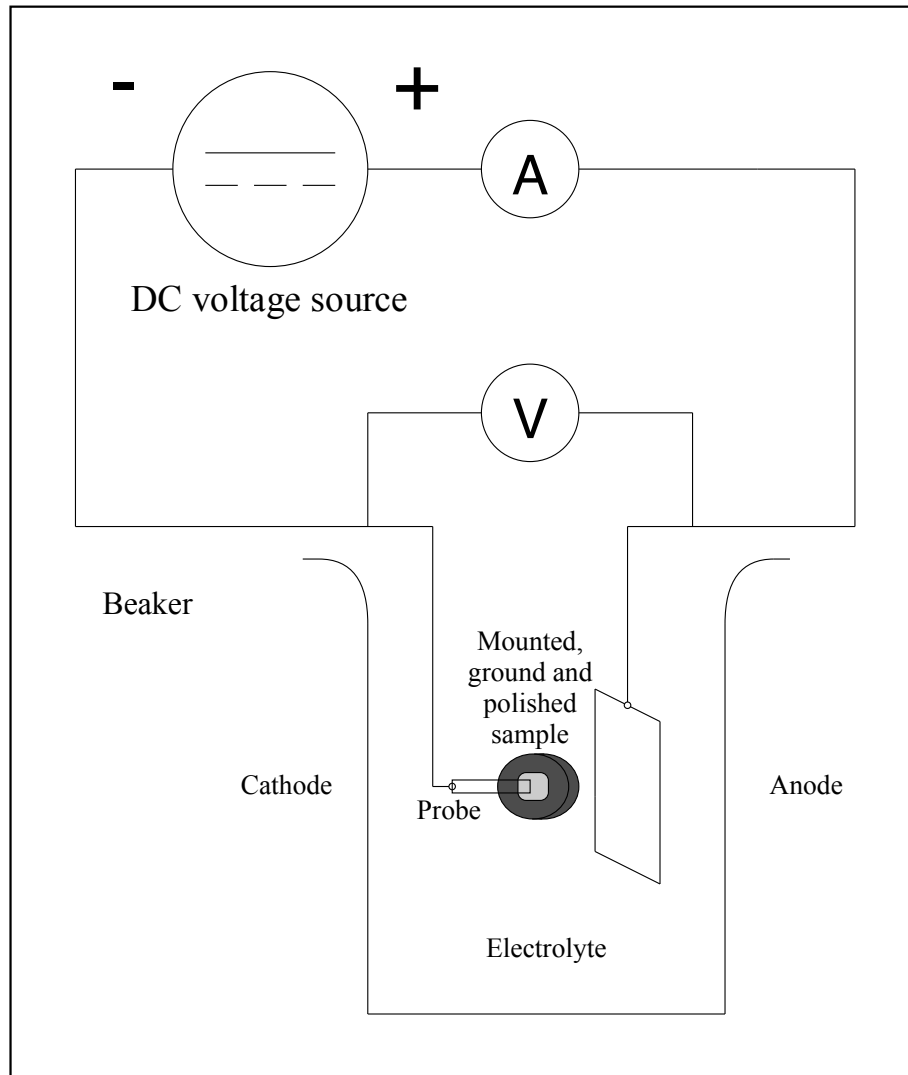


Fig. 4.27 Experimental set-up for electrolytic etching of a super duplex stainless steel sample. The electrolyte solutions used (not indicated above) were, sequentially, NaOH(aq) and C₂H₂O₄(aq) with intermediary rinsing in deionised water.

4.6 Characterising the Starting ZERON® 100 Billet Material

ZERON® 100 AFP as received 250 mm diameter billet starting material was characterised through analysis of eight ca. 1200 x 900 μm² micrograph ‘fields’ from each of 4 off 12 mm² cross sectional area x 150 mm length (parallel to the billet’s longitudinal axis) samples. The optical photo micrograph surfaces lay parallel to the *L* axis indicated in Fig. 4.28 which schematically illustrates the positions of the samples in relation to the orientation of the billet. The 12 mm² x 150 mm samples machined from the billet were subsequently used for the thermal simulation experiments detailed in Ch. 8 and then machined down into the standard dimensions for Charpy V-notch impact toughness tests.

16 off 12 mm² x 150 mm samples were taken from the billet to be used in the thermal simulation and mechanical testing work in Ch. 8. Characterisation of the billet was based on analysis of 8 ‘fields’ on each of four of these samples (shaded grey in Fig 2.7a) selected for their representative locations across the diameter of the billet and from which it was assumed average ferrite bandwidth, $\bar{\lambda}_\delta$ and volume fraction austenite, f_γ would be representative of the bulk material. The optical micrograph fields were cited at approximate equal spacings along the centreline length of the sample (Fig. 4.28). Fig. 2.29 shows an example of these eight ‘fields’ from one of the four 12 mm² x 150 mm samples.

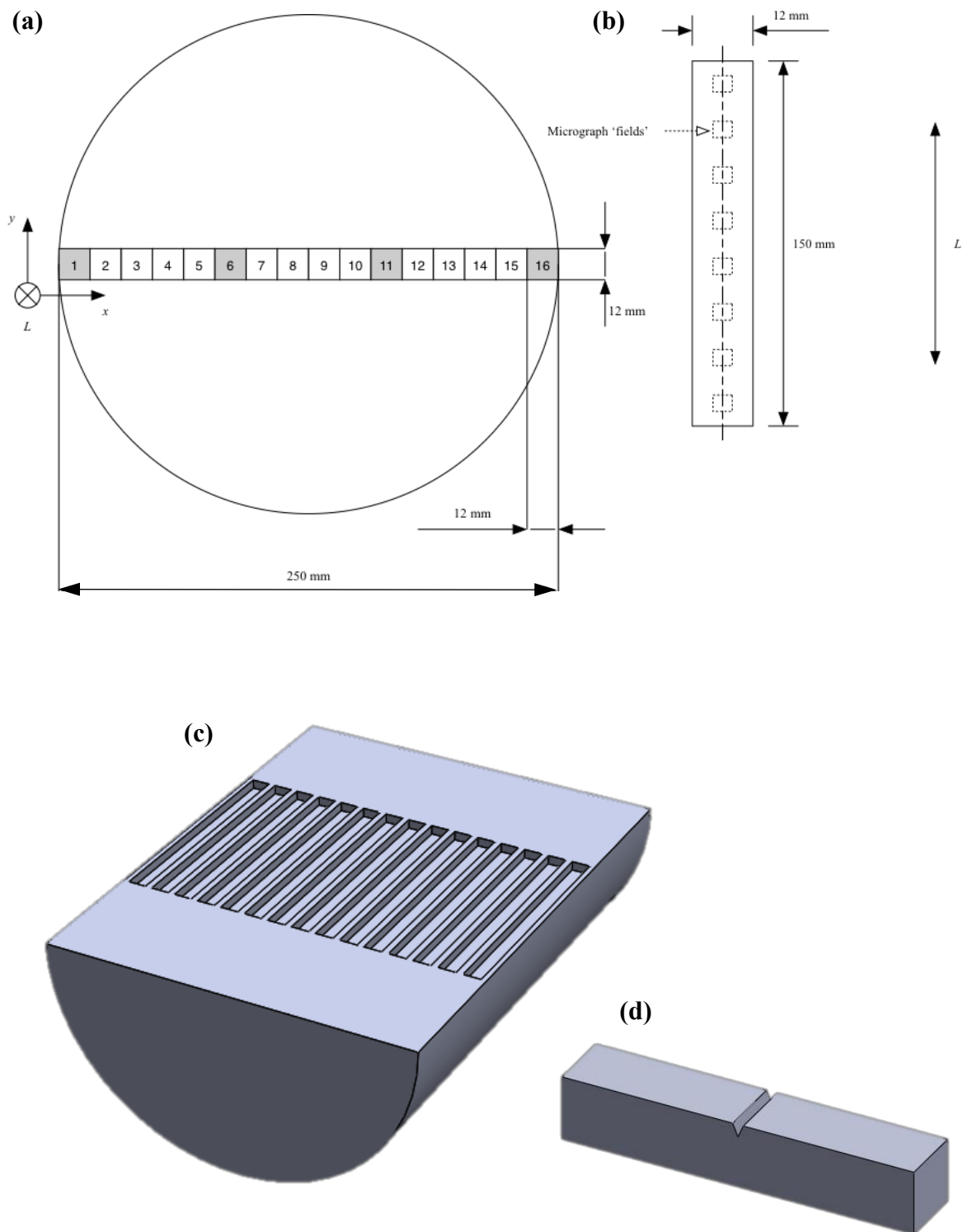


Fig. 4.28 ZERON® 100 AFP Ø 250 mm billet starting material **a** 2-D schematic elevation view of the billet face showing the locations from where the samples were taken NOT TO SCALE **b** schematic 2-D plan view of a sample showing approximate locations of micrograph fields NOT TO SCALE **c** 3-D representation of the billet shown in section view with the sectioning plane parallel to the sample face on which the micrographs were taken **d** 3-D representation of a sample machined to final dimensions prior to impact toughness testing

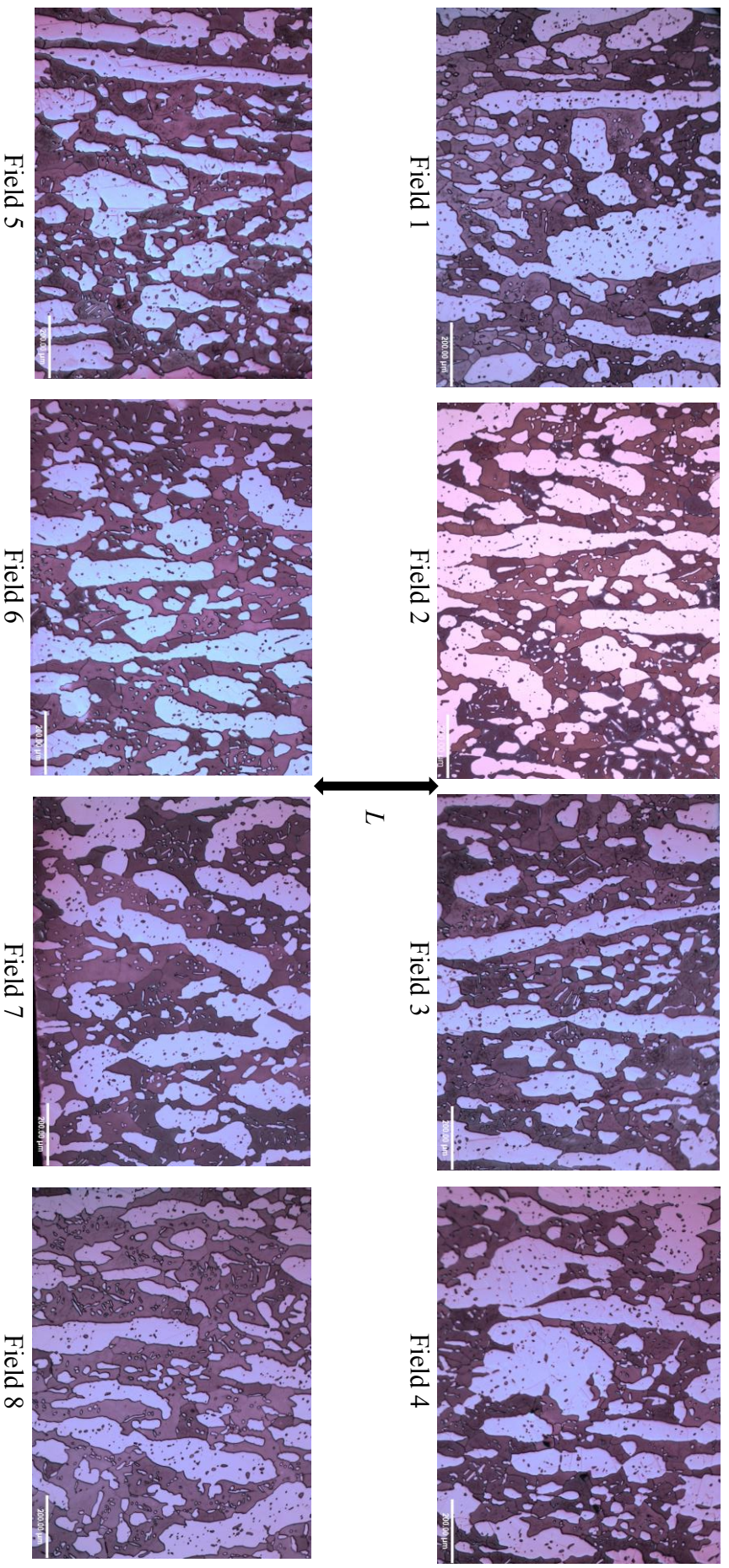


Fig. 4.29 Example optical photo micrographs of the ZERON® 100 AFP billet starting material. The orientation of the corresponding longitudinal axis of the billet is also indicated by the arrow.

The alignment of the primary austenite ‘lathes’ parallel to the billet’s L -axis is clearly demonstrated in Fig. 4.29 and indicates the strong ‘macro-texture’ developed in the material through the primary steel making process whereby a typical cast ingot is converted into billet for subsequent ‘downstream’ processing operations, such as open die forging to form bossed blanks from which weld neck flange components are ultimately machined to specification. In subsequent chapters of this work the difficulty of ‘disrupting’ or refining this bulk ‘primary macro-texture’ through commercial open die forging process will be demonstrated.

Characterisation of the starting material was carried out through programmatic image analysis of the micrographic fields taken from the 4 off 12 mm² cross sectional area x 150 mm length samples. The MATLABTM image analysis programme developed to automate this process is based on the input of data derived from binarization of the micrographs and subsequent ‘interaction’ of the image pixels with superimposed grid lines. The average ferrite bandwidth, $\bar{\lambda}_\delta$ is a commonly quoted microstructure metric for duplex and superduplex material and indicates the spacing between the austenite grains. Its determination was carried out in accordance with the intercept procedure and involves an arithmetic count of the number of grain boundary intersections with a test line, per unit length of test line, to calculate the mean lineal intercept length. The applicability of the methodology to calculate average grain size to the determination of $\bar{\lambda}_\delta$ in duplex material is detailed in the DNV – RP – F112 Recommended Practice Offshore Code[12] which provides proven technology and sound engineering practice as well as guidance for the higher-level Offshore Service Specifications and Offshore Standards. DNV – RP – F112 recommends superimposition of four or five parallel lines over a micrograph along which the length of the line falling in each ferrite unit is measured, where the total number of measurements should be > 50 and the magnification used (ca. 50 x – 1000 x) for measurement chosen such that typically 10 – 15 microstructure ‘units’ are intersected by each line. Additionally, it is also recommended that measurement be carried out in a minimum of four different fields in the area of interest (i.e. on each test specimen and location to be examined) and that the value of $\bar{\lambda}_\delta$ to be reported should be the average of all the measured values in the fields. It is acknowledged the average ferrite bandwidth microstructure metric quoted here includes potentially multiple individual ferrite grains in each ‘unit of bandwidth’. In this work, the focus was on understanding how to minimise this bandwidth. In most part, this is due to industrially processed material having ferrite grain sizes in excess of the average bandwidth (see Ch. 7 for confirmation of this through EBSD investigations). Therefore, the

focus of this work was the development of a robust image analysis routine that yielded accurate measurement of ferrite bandwidth, rather than concentrating on differentiation between individual grains of ferrite.

Statistical analysis to describe the accuracy of the measurements was based on calculation of the standard deviation, s from $\bar{\lambda}_\delta$ in each of the fields of measurement for n intercept line measurements

$$s = \frac{\sum(\lambda_\delta - \bar{\lambda}_\delta)^2}{n-1} \quad \text{Eqn. 4.9}$$

From the standard deviation, the standard error of the sample mean can be calculated:

$$S(\bar{\lambda}_\delta) = \frac{s}{\sqrt{n}} \quad \text{Eqn. 4.10}$$

Using these statistical parameters, and the t -distribution to account for the error introduced by using the sample standard deviation rather than the population standard deviation to determine the standard error of the mean, a 95% Confidence Interval (CI) for $\bar{\lambda}_\delta$ is reported by:

$$\bar{\lambda}_\delta \pm t_{(95, n-1)} S(\bar{\lambda}_\delta) \quad \text{Eqn. 4.11}$$

Where the $t_{(95, n-1)}$ variable indicates the t value at 95% CI determined from the shape of the t -distribution as a function of the number of degrees of freedom, $n - 1$. The value $t_{(95, n-1)}$ takes for a range of n values is indicated below in Table 4.4 for demonstrative purposes:

Table 4.4 Example of values of t for 95% confidence limits $t_{(95, n-1)}$ as a function of the number of degrees of freedom, $\nu = n-1$.

ν	$t_{(95, n-1)}$
1	12.706
2	4.303
3	3.182
4	2.776
5	2.571
6	2.447
7	2.365
8	2.306
9	2.262
10	2.228

Binarization of the micrographs (Fig. 4.31) was achieved through use of the various image pre-processing algorithms provided in MATLABTM's Image Processing Toolbox, primarily *a posteriori* correction of shading artefacts arising as a result of uneven illumination from incident microscope light on not-perfectly-planar sample surfaces. Enhancement of micrograph images in this way, through a series of pre-processing steps prior to analysis, was extremely important for high fidelity binarization of micrographs. This was due to the inherent unevenness (and thus shading) produced as a result of the manual grinding and polishing of the sample surface (prior to electrochemical etching), themselves necessary preparation techniques due to the difference in hardness of the two duplex phases.

To achieve the requisite uniformity in micrograph background illumination an approach was taken whereby an approximation of the background was created as a separate image and then 'subtracted' from the original micrograph. This subtractive approach to addressing shading inhomogeneity required the use of a user-defined iterative *morphological opening* function with the effect that all 'objects' (grains) in the micrograph which could not completely contain a structuring element (sized appropriately such that an arbitrarily defined disk shape of radius proportional to iteration number could not fit entirely inside the austenite grains) were removed. By rendering the background approximation created in this way as a surface plot (creation of coloured parametric surfaces enabling mathematical functions to be viewed over a rectangular region) it is possible to identify where the illumination in the micrograph varies. After subtracting the background image from the original it was often required to adjust the contrast of the processed image by saturating a percentage of the data (ca. 1%) at both low and high intensities and stretching the intensity values to fill the dynamic range[13].

High-fidelity binarization of the processed micrograph image is then possible once any background noise is removed. Noise reduction was performed through an *area opening* function which removed all connected 'objects' having fewer than n user definable non-negative, integer-valued, numeric scalar pixels from the binary image and produced another binary image. The default connectivity is specified as a numeric scalar (by default 8 for 2-D connectivities). Examples of uncorrected micrograph background illumination and a surface plot of background illumination variation in are shown in Figs. 4.30a & 4.30b, respectively.

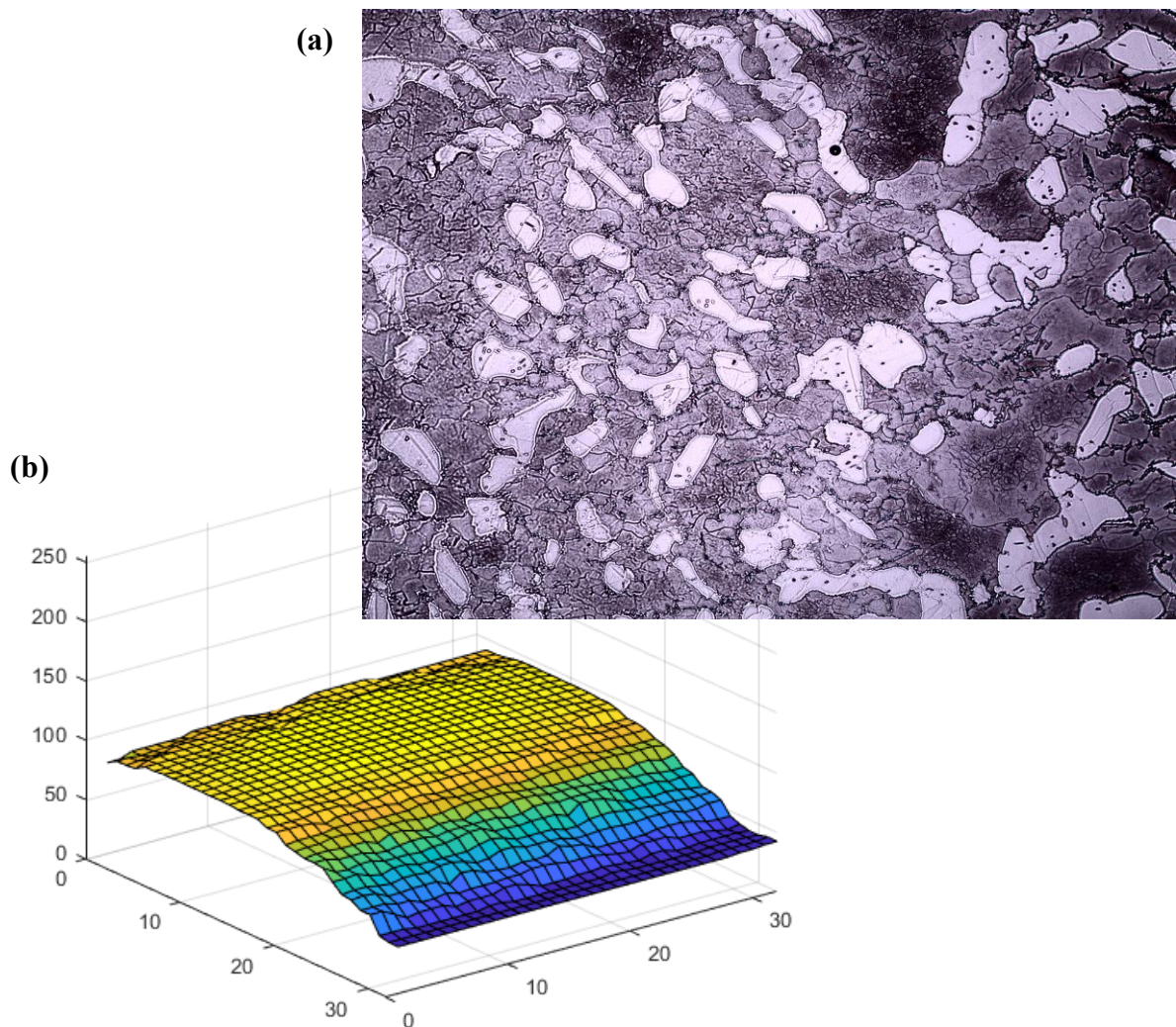


Fig. 4.30 Optical light micrographs often suffer from inhomogeneity of background illumination making binarization of a 'raw' micrograph image very difficult and necessitating image pre-processing operations. The differential shading can be clearly seen here with the highest intensity light reflected from, approximately, around and to the immediate left of the centre. The edges of the image are appreciably darker as can be seen in the differences in shading of the primary austenite grains in the centre and top-right of the image **b** Surface plot of the variation in intensity of the background pixels in a micrograph (*note not 2.9a*) with reversed y -axis (meaning pixels at the bottom of the image appear at the front of the surface plot.) $[0, 0]$ therefore represents the upper-left corner of the image and the highest part of the surface indicates that the 'brightest' pixels occur near the middle rows of the image. The lowest pixel values occur at the bottom of the image.

Through the noise reduction and background illumination corrections described above, it is possible, with a high degree of fidelity, to binarize micrographs, whereby the value of each pixel (representing its brightness) is stored as an 8-bit integer (the *byte image*) and thus leads

to a range of possible values from 0 to 255. 0 was taken as black and assigned to all pixels corresponding to the ferrite phase and 255 was white, thus representing pixels in the austenite phase. Analysis (according to DNV – RP – F112 as described above) was then performed on the binary images in order to determine the characteristic parameters $\bar{\lambda}_\delta$ and f_γ .

The values of each pixel along each overlaid gridline on a binarized image can be programmatically determined and are illustrated for one example grid line in Fig. 4.32b. The pixel value data along each grid line were then imported into MATLAB™ as tab delimited .txt files (containing displacement along the grid line and corresponding pixel value). However, to categorise and analyse the data correctly it was necessary to apply the following logical conditions so that the correct spacing intervals along the grid lines were calculated for only the ferrite, not ferrite and/or austenite, bandwidth.

Four options exist into which the line data can be characterised, dependent upon which phase the imposed grid line starts and finishes in. Since all images are of the type binary 8-bit, this can be determined from the first and last y -axis grey values where; white (austenite) = 255 and black (ferrite) = 0.

1. The grid line starts and ends in the austenite phase; $yData(1) = 255 == yData(end)$;
2. The line starts in the austenite and ends in the ferrite phase; $yData(1) = 255 \sim yData(end) == 0$;
3. The line starts and ends in the ferrite phase; $yData(1) = 0 == yData(end)$;
4. The line starts in the ferrite and ends in the austenite phase; $yData(1) = 0 \sim yData(end) == 255$;

By applying these logical conditions in a conditional if, else if, else programmatic loop, the spacings of the ferrite grains were identified and $\bar{\lambda}_\delta$ (for each grid line) calculated by taking the length of grid line as the final x -axis value of distance (μm) (Fig. 4.32b), i.e. $L_{gridline} = xData(end)$;

The overall $\bar{\lambda}_\delta$ for the micrograph was then simply taken as the arithmetic mean of all the $\bar{\lambda}_\delta$ values calculated for each grid line. The associated error reported for the $\bar{\lambda}_\delta$ values was then calculated as described above, with the value of $t_{(95,n-1)}$ determined by the number of grid lines imposed on the micrograph image, typically in the range 8 – 11 in order to comfortably exceed the recommended criteria detailed in DNV – RP – F112 (noted above).

Fig. 4.32 however illustrates the inherent problem in relying solely on imposed grid lines in one orientation (horizontal in this case) for highly anisotropic material; the top grid line in Fig. 4.32a intersects the same primary austenite grain in the top left-hand side of the image three times and therefore risks violating the assumption of independent measurements. Therefore, in characterising the ZERON® 100 billet starting material measurements were taken along both horizontally and vertically orientated grid lines (in both cases following the same procedures outlined previously) with the reported values of $\bar{\lambda}_\delta$ below taken as the mean of the individual $\bar{\lambda}_\delta$ measurements for the horizontal and vertical gridlines. It is however important to stress, as noted before, that in strongly isotropic material, like the ZERON® 100 starting billet analysed here, calculations derived from gridlines lying normal to the predominate direction of anisotropy are likely to contain inherent (albeit systematic) error due to the measurement of the same features more than once. The importance in sizing and orientating the overlaid grid lines appropriately is therefore clearly underlined by the example illustrated in Fig. 4.32

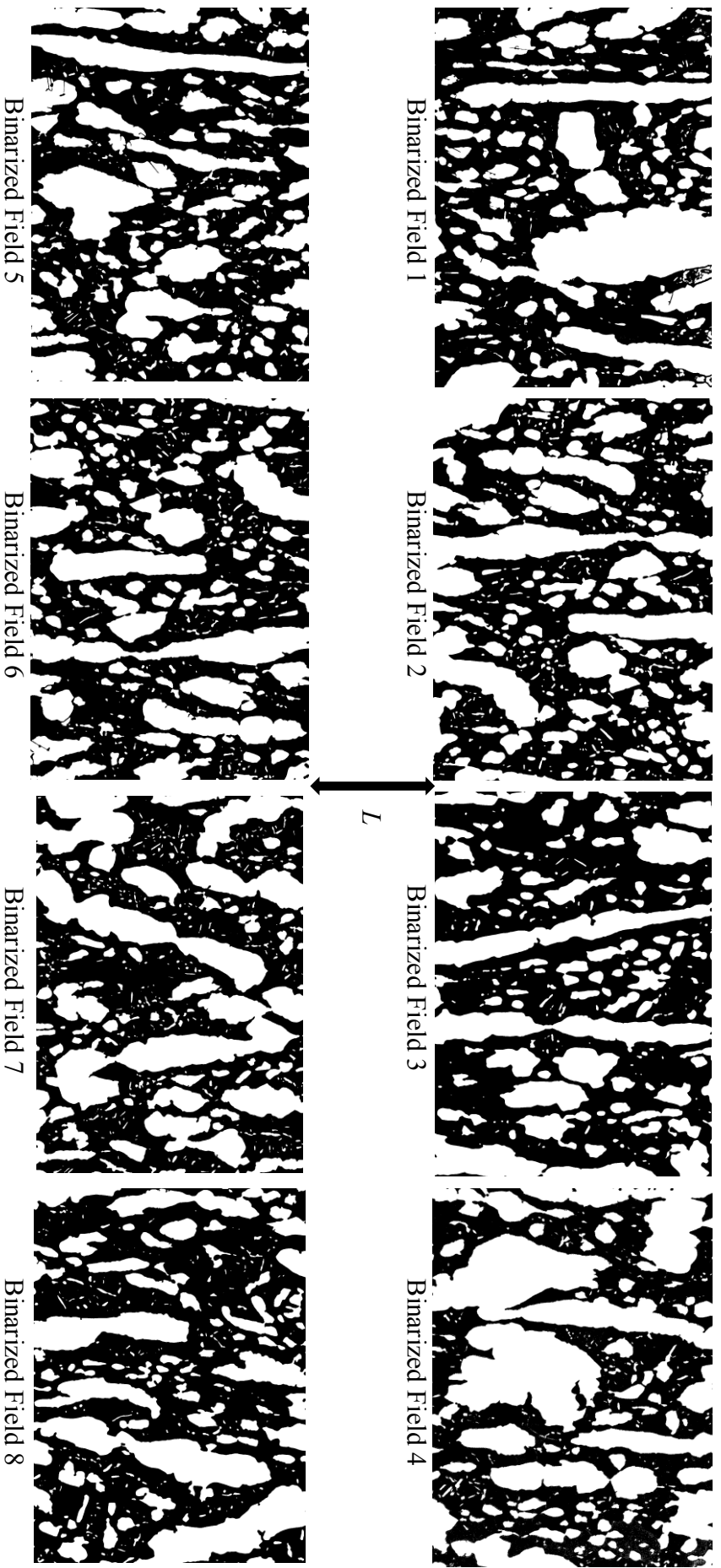


Fig. 4.31 Example *binarized* optical photo micrographs (from Fig. 2.8) of the AFP ZERON® 100 billet starting material. The orientation of the corresponding longitudinal axis of the billet is also indicated by the arrow.

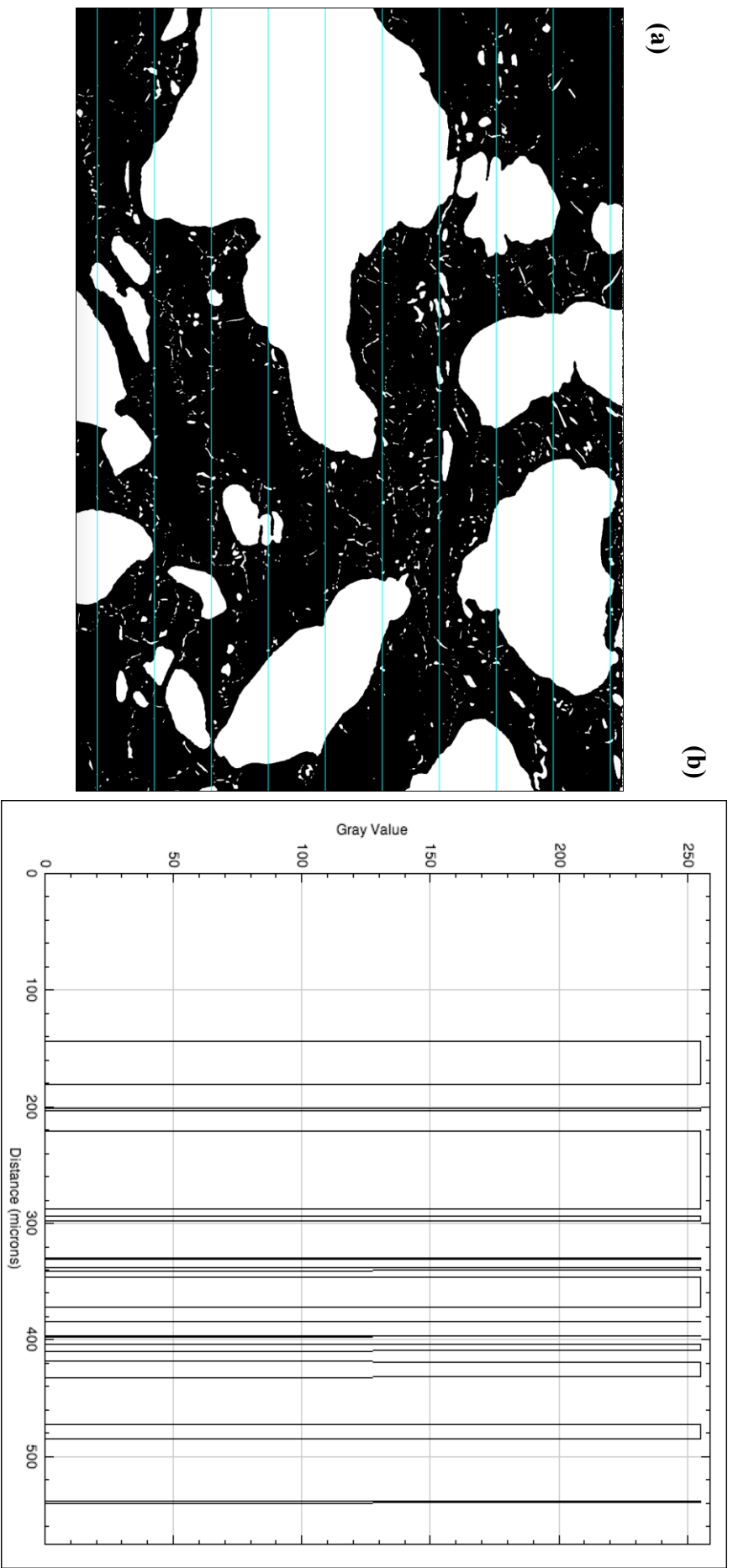


Fig. 4.32 Determination of average ferrite bandwidth **a** an example of another binarized micrograph on ZERON®'s duplex microstructure is overlaid with horizontal grid lines and **b** the binary pixel grey values (0 or 255) along the length of the top line (in microns). λ_{δ} calculated from this micrograph (using the binarization and pixel values along overlaid grid lines methods described) is: $29.7 \pm 9.2 \mu\text{m}$. Note however this is an example and not a micrograph taken from the billet starting material described above. The graph indicates that, in accordance with DNV – RP – F112 guidelines, 13 'microstructure units' are intersected by the line.

In addition to the $\bar{\lambda}_\delta$ microstructure parameter, the f_γ was calculated for each of the micrographic fields used as data to characterise the starting material billet. However, rather than adopting a similar grid-based point counting approach as in the calculation of $\bar{\lambda}_\delta$, high fidelity binarization of the micrographs (achievable through the detailed image correction procedures outlined previously) allowed for the rapid and highly accurate automatic identification of the austenite phase grains and thus determination of the f_γ parameter.

Automatic analysis of the particles in an image in this way is achieved by scanning the binary images until the 'edge' of an object (in this case an austenite grain) is detected, i.e. a change recorded in neighbouring pixel values from 0 to 255. This edge is 'followed' and traced-out until the starting point is reached again and the 2-D 'path' outlined. The number of pixels contained within the outline boundary are measured and then filled to make them invisible as the scan resumes until the end of the image or selected region is reached. This operation is illustrated below in Fig. 4.33.

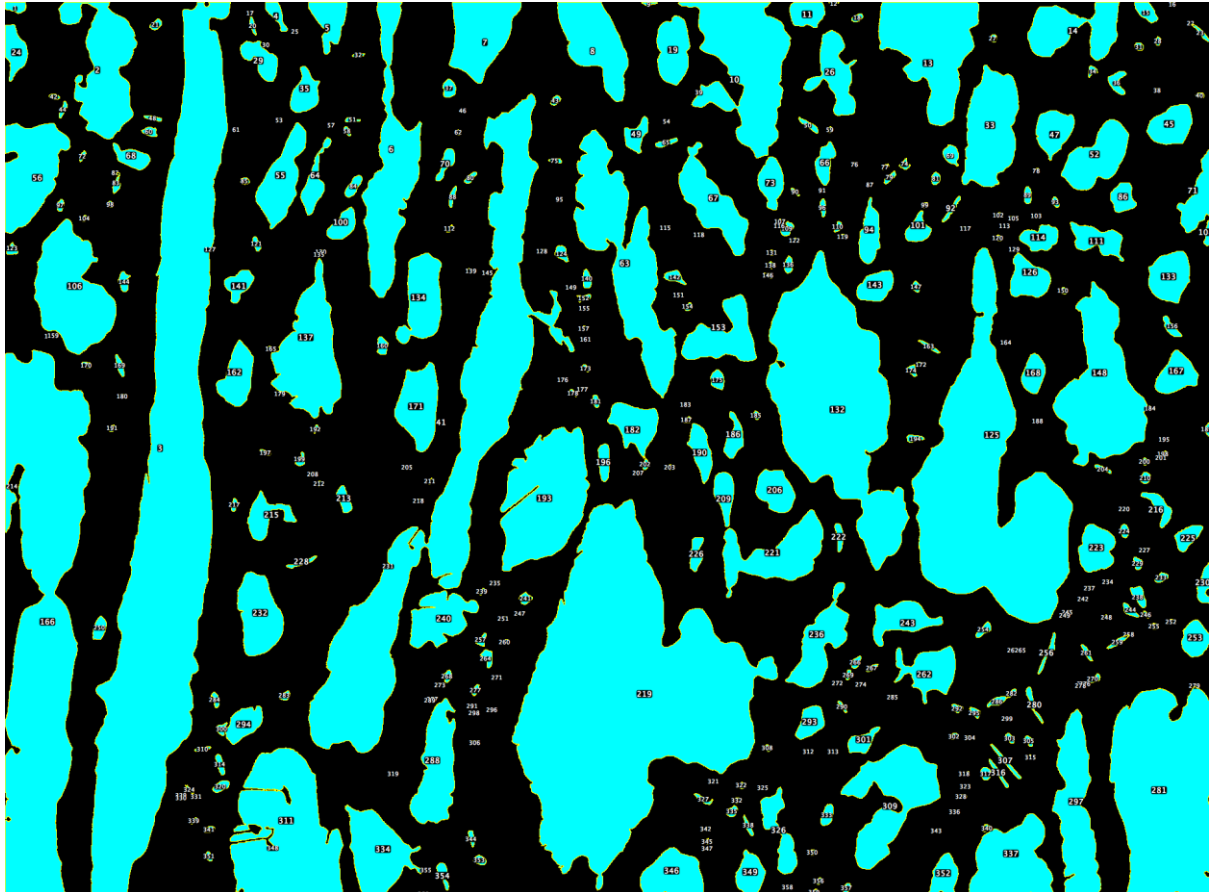


Fig. 4.33 Binarized field 5 (see Fig. 2.10) subjected to particle analysis whereby the white austenite (particle) boundaries have been identified and the pixels they enclose calculated and subsequently recoloured blue.

The pixels recoloured in blue in Fig. 4.33 are referenced against the total number of pixels in the image and thus the f_{γ} parameter calculated. Furthermore, by specifying a threshold size of particle (in pixels^2 , or μm^2 for appropriately scaled images) outside which particles with size (area) are ignored, it is possible to determine the % of γ_2 within the austenite phase. Of course, although γ_2 particles are commonly identified by their small size, this is not an exclusively accurate identification method. As noted elsewhere in subsequent chapters of this work, the existence of the K-S crystallographic relationship between an austenite particle and the surrounding ferrite matrix can alternatively be used to uniquely identify γ_2 particles. However, as a first approximation using the techniques/functions of image analysis, a size thresholding approach was adopted here. This is illustrated below in Fig. 4.34 (note again, not from the startling billet material) taken from a highly strained region at the centre of a uniaxially compressed ZERON® 100 cylindrical sample. In this case although the same measuring procedure detailed previously is followed, the binarized image is not shown with the overlaid

‘particle counts’ mask as in Fig. 4.33. Instead the ferrite matrix is again coloured black and the primary austenite grains excluded on the basis of the size thresholding criteria.

It is important to note that this ‘size thresholding’ image analysis method to identify and quantify the f_{γ_2} parameter is somewhat of a ‘coarse tool’ and contains an acknowledged inherent systematic error whereby, in statistical terms, a ‘false positive’ may be given in the identification of small primary austenite particles which may have sheared-off during the buckling of primary austenite grains as a result of thermo-mechanical processing. The nature of systematic error in measurement of experimental data means that however, the potential inclusion of small primary austenite particles in the f_{γ_2} count is a consistent, reproducible inaccuracy which will act to increase the actual value of f_{γ_2} .

The characteristic microstructure data from the eight example fields presented in Figs. 4.29 and 4.31 are given below in Table 4.5

Table 4.5 Characteristic microstructure data for the example micrographs presented quoted to three significant figures

Field #	Horiz. Grid line λ_δ (μm)	Vert. Grid line λ_δ (μm)	Field $\bar{\lambda}_\alpha$ (μm)	Field f_δ (%)	Field f_γ (%)	Field f_{γ_2} (%)
1	49.2 ± 4.27	59.4 ± 17.4	54.3 ± 10.9	56.1	43.9	1.13
2	40.3 ± 5.00	52.1 ± 6.9	46.2 ± 5.95	56.1	43.9	2.20
3	57.5 ± 10.4	95.5 ± 14.3	76.5 ± 12.4	38.4	61.6	1.10
4	54.0 ± 9.85	57.6 ± 20.8	55.8 ± 15.3	44.6	55.4	1.74
5	48.9 ± 10.1	58.6 ± 11.2	50.7 ± 10.7	52.5	41.5	1.33
6	38.6 ± 4.67	78.4 ± 20.6	58.5 ± 12.6	58.8	41.2	2.05
7	42.9 ± 7.90	64.1 ± 22.1	53.5 ± 15.0	55.3	44.7	2.27
8	46.1 ± 6.52	85.3 ± 17.5	65.7 ± 12.0	60.7	39.3	1.69
	45.3 ± 6.99	70.5 ± 15.7				

As noted, the example data presented above relates to the micrographs presented in Fig. 4.29 & Fig. 4.31 and is included here for illustrative purposes to demonstrate the techniques and quantitative metallographic processes adopted throughout this work for the determination of duplex microstructure metrics. When averaged over the four samples selected for billet starting material characterisation, the same quantitative metallographic approach as above indicated

$\bar{\lambda}_\delta = 57.9 \pm 11.4 \mu\text{m}$. Further, the duplex phase balance (%) was $f_\delta = 52.8$ and $f_\gamma = 47.2 \pm 6.17$, of which $f_{\gamma_2} = 1.68 \pm 0.51$.

Ref. [12] tentatively suggests a ferrite bandwidth of 30 microns to be the upper limit of acceptability for fine phase distributions in duplex microstructures as a risk reducing measure against the propagation of HISC through the ferrite phase. The processing route(s) required to produce such a refined ferrite bandwidth in industrial-sized engineering components (ca. \varnothing 400 mm & 225 mm section thickness) are however not indicated. Discussions with the industrial supply chain involved in the production of superduplex engineered components also indicate there is very little understanding of optimisation of the manufacturing process with most practices adopting similar methodologies as for ‘standard’ Q&T steels or single-phase stainless steels.

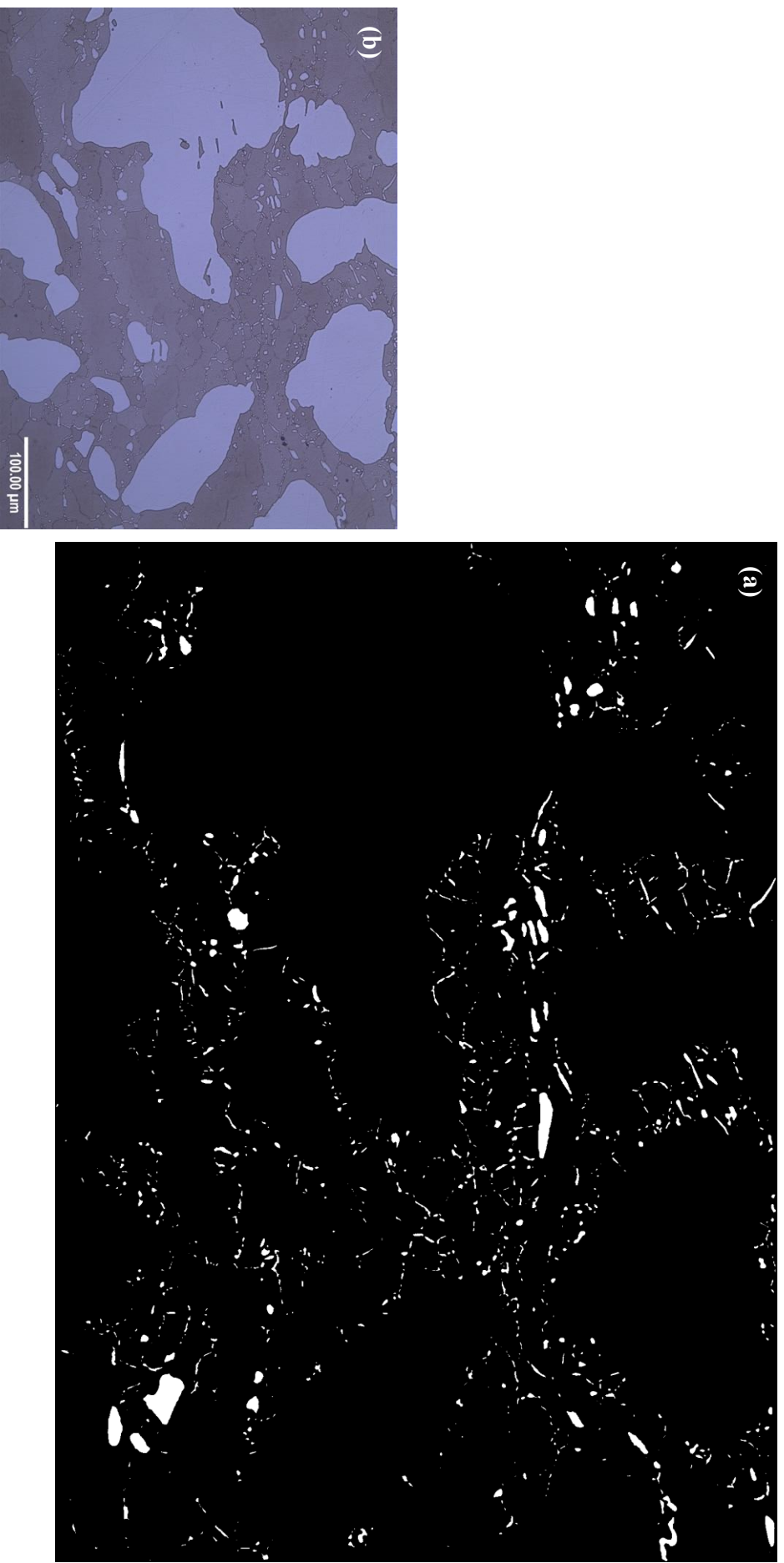


Fig. 4.34 Image analysis techniques applied to the identification and measurement of γ_2 **a** binarized micrograph image specified to include only the reformed austenite precipitates by limiting the upper particle size area threshold to $250 \mu\text{m}^2$ **b** original $20 \times$ optical micrograph taken from a high strain region in the centre of a uniaxially compressed ZERON® 100 sample. The reformed austenite precipitates identified in this example by the 'size thresholding' method account for 1.53% of the total austenitic volume fraction.

Note the difference in the reported margin of error at a 95% CI for measurements of $\bar{\lambda}_\delta$ taken along horizontally versus vertically orientated gridlines in Table 4.4. This difference again highlights the difficulty in applying the linear intercept method for grain size determination to this strongly anisotropic ZERON® 100 billet starting material; due to the size and elongation of the primary austenite particles along the L -axis, horizontally orientated lines tend to intersect any large particles with approximately equal extensions in the x - and L - axes more than once over approximately similar spacings. Conversely, vertically orientated lines tend to intersect primary austenite grains with large extensions in the L -axis only once with large spacing, but also intersect several smaller γ_2 particles (with small spacing) resulting in a wide interval of measurements and thus ultimately leading to a large standard error.

4.6.1 AFP vs. Standard ZERON® 100 Billet

Characterisation of the two ZERON® 100 material variants was conducted on two \varnothing 250 mm ZERON® 100 billets produced according to Fig. 2.6; one via the ‘conventional’ electric steel making process (EAF + AOD), the other billet was AFP material (produced by (P)ESR). Herein the AFP billet is referred to as 1B and the standard material billet as 2B.

Billet 1B was subject to a reduction ratio of 4.16:1 in the GFM RF100 and solution heat treatment soak time at 1100°C of 1 hr 56 min. The EAF + AOD billet (2B) received more work however with a reduction ratio of 4.5:1, followed by a soak time of 6 hr 12 min. at 1100°C. The chemical compositions of the billets are indicated below in Table 4.6

Table 4.6 Chemical compositions of the two different ZERON® 100 material variants (billets 1B and 2B) in the solution annealed condition

<i>Chemical Composition</i> (wt.%)	<i>Billet ID</i>	
	1B (AFP)	2B (standard product)
C	0.017	0.015
Si	0.23	0.31
Mn	0.46	0.48
P	0.021	0.025
S	0.0008	0.0003
Cr	25.42	25.03
Mo	3.72	3.58
Ni	7.21	7.21
W	0.54	0.56
Cu	0.58	0.58
Al	0.007	-
N	0.23	0.22
Fe	Balance	Balance

Sample locations at the centre, outside edge and mid-radius of the billets were examined to capture the assumed axial microstructure symmetry imparted to the billet by the four diagonally opposed hammers of the rotatory forging machine as the ingots are rounded-down to 250mm diameter billets.

For both billets, a reduction in and f_{γ} (%) is seen at the surface of the billet, relative to the centre, however the data from billet 2B suggests that there may be an intermediary increase in f_{γ} between the centre and billet mid-point (Fig. 4.34). Although further sampling of billet 2B at intermediate distances along the radius is needed to corroborate this trend more fully, it is pertinent to note that billet 2B is standard product ZERON® 100. Standard product billets are generally characterized by greater segregation, porosity and more irregular distribution of inclusions compared to AFP material. The increase in the fraction of austenite in the centre of billet 2B, compared to the centre, may therefore possibly be related localized chemical heterogeneity from the ingot casting.

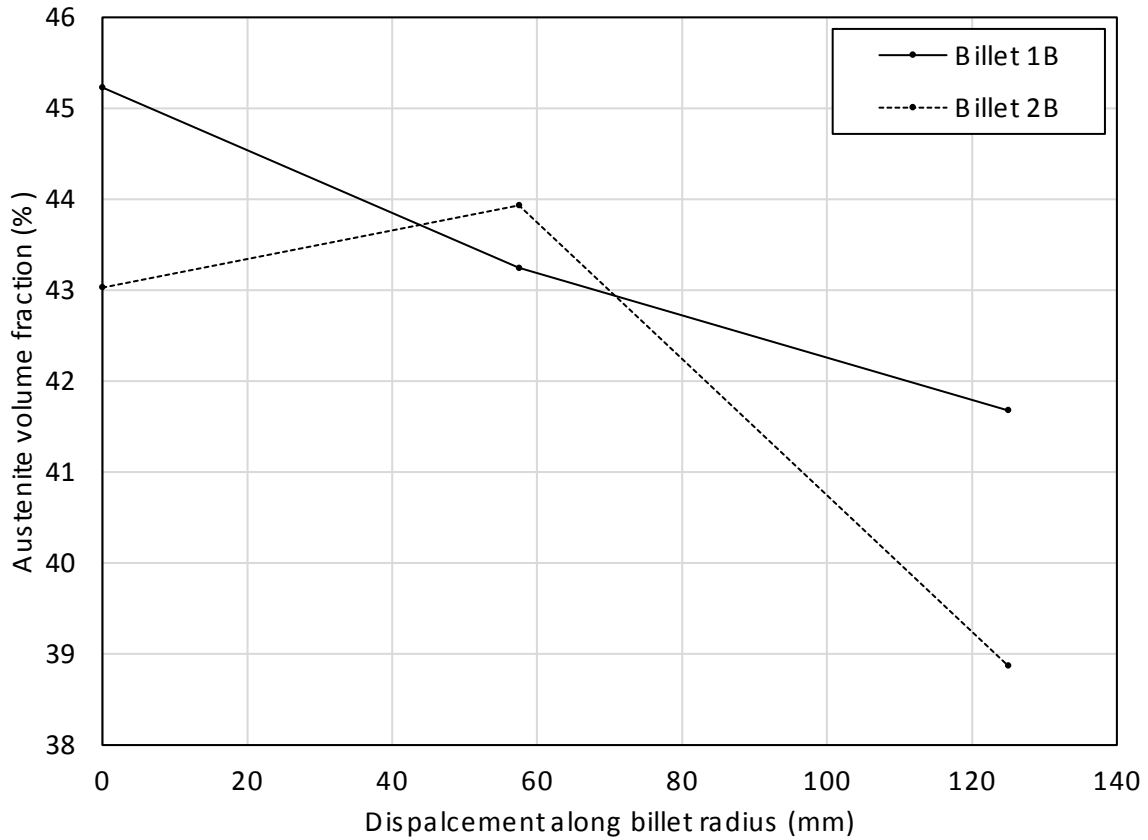


Fig. 4.34: Variation in total f_{γ} ($\gamma_1 + \gamma_2$) from the centre to the outside edge of the AFP and standard product ZERON® 100 billets

In addition to phase balance, a further key metric in the quantitative characterization of AFP and standard ZERON® 100 billet starting material is the refinement of the microstructure. The refinement of the microstructures of billets 1B and 2B, as determined by $\bar{\lambda}_{\delta}$ as a function of displacement along the radius, is presented in Fig. 4.35. The f_{γ_2} in the two billets, as a function of sample radial position is presented in Fig. 4.36

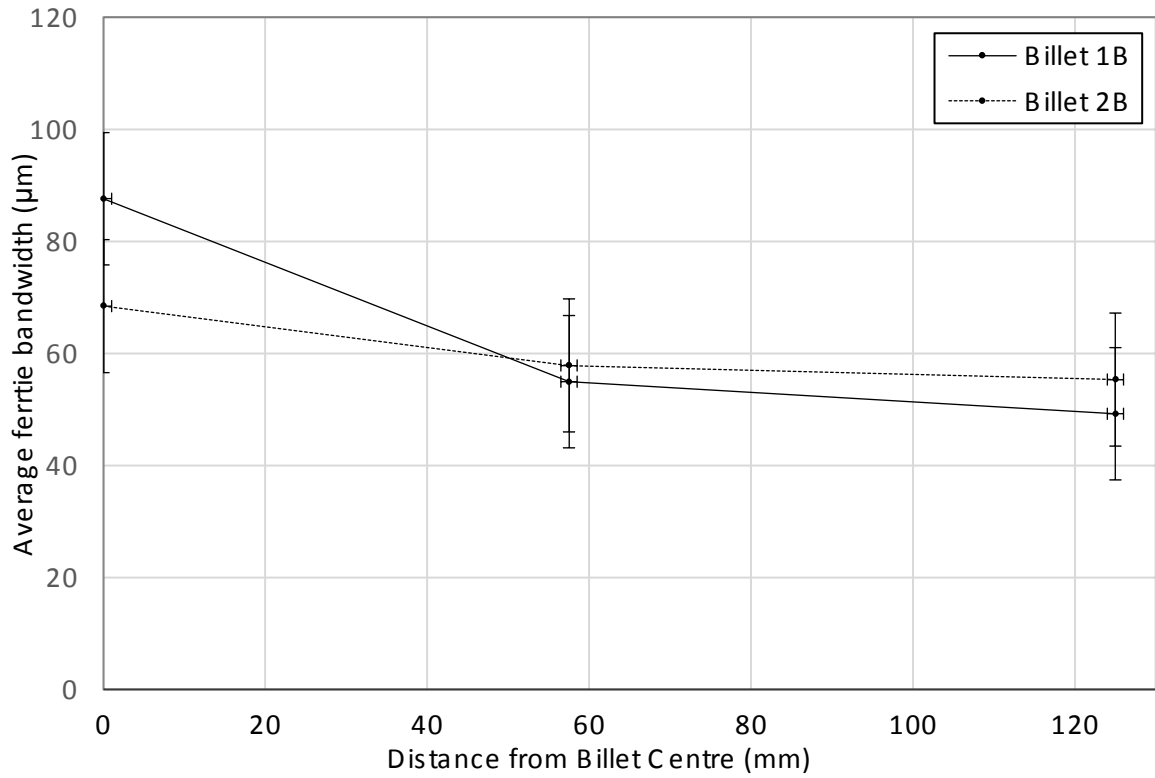


Fig. 4.35 $\bar{\lambda}_{\delta}$ as a function of displacement along the radius from the centre of ZERON® 100 AFP and standard material billets.

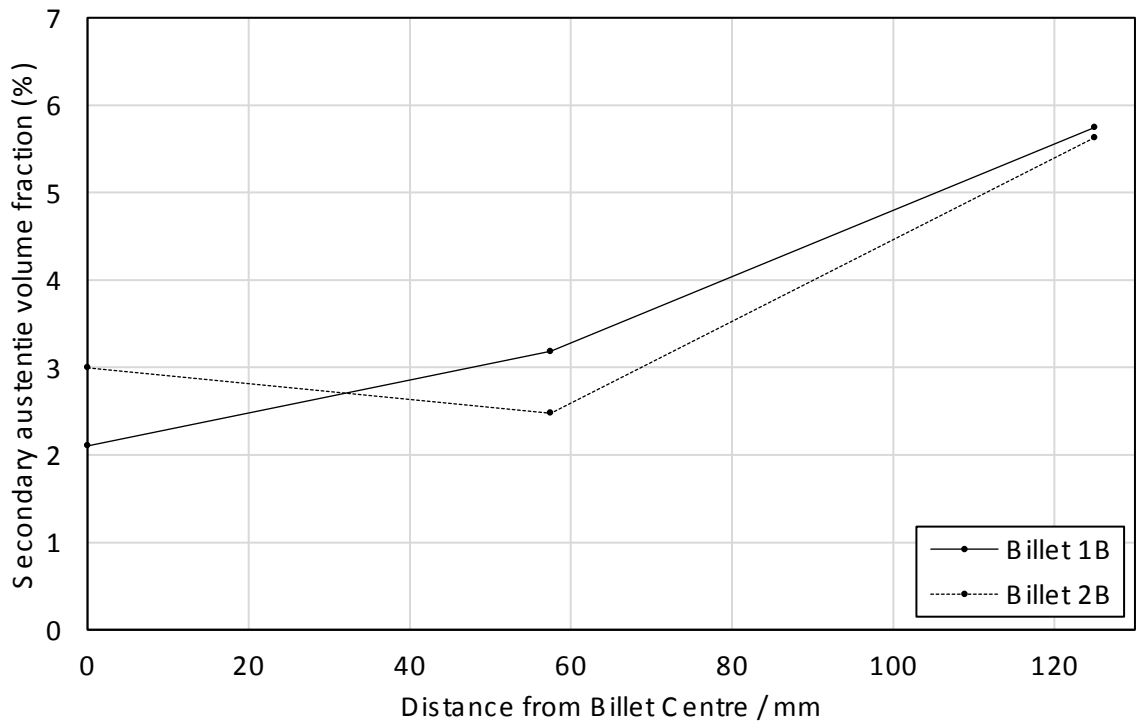


Fig. 4.36 f_{γ_2} as a function of displacement along the radius from the centre of ZERON® 100 AFP and standard material billets.

Fig 4.35 & 4.36 indicate that a refinement of the microstructure is found in both billets with increasing distance from the centre; the fraction of γ_2 increases, while $\bar{\lambda}_\delta$ is shown to decrease. It is notable however that despite being subject to a greater forging reduction ratio and longer time at temperature during solution annealing, the fraction of reformed austenite at the surface of billet 2B is essentially identical to that at the surface of billet 1B. The production process of the AFP billet (1B) is therefore likely to play a significant role in producing its refined microstructure.

The AFP billet production route is generally favoured due to the cleaner (lower number of inclusions and interstitial elements) and more homogenized steel ingots produced. However, Fig. 4.35 & 4.36 also suggest that a refined microstructure may also be produced (versus the conventional ingot casting production route) which has important benefits in terms of resistance to hydrogen induced stress corrosion (HISC) cracking. As a consequence, production methods that result in starting material with reduced basic microstructure unit size, i.e. short ferrite mean free paths, are advantageous in terms of the critical mechanical property of toughness. Recommended design practice [12] also indicates how HISC cracks generally propagate in straight cleavage through the ferrite phase. Therefore, by developing as short as possible a free ferrite path along which cleavage can occur, i.e. minimisation of the ferrite bandwidth, the toughness of the microstructure is enhanced and greater resistance to HISC imparted.

The microstructures of the two ZERON® 100 billets (AFP and standard material) are presented below in Fig. 4.37 and Fig. 4.38, respectively. In Ch. 7 and Ch.9 of this work, equivalent high and low temperature billet microstructures are discussed in terms of suitability as starting material for secondary forging operations. In a high temperature equivalent billet microstructure, as will be explored in detail later, forming is carried out at temperatures above that of the subsequent solution heat treatment. The γ_2 precipitates that form upon the immediate cooling of the billet after cogging in the GFM pin the refined ferrite grain boundaries formed during working. However, since they precipitate upon cooling from above the solution heat treatment temperature, they remain thermally stable and do not dissolve when reheated to this lower temperature. This allows for the retention of the deformation-induced ferrite grain refinement in the high temperature equivalent billet microstructure and thus confers advantages in terms of toughness. It is suggested this high temperature equivalent billet microstructure

represents the optimum starting material for secondary forming operations. The presence of obvious allotriomorphic γ_2 precipitates decorating generally refined ferrite grain boundary structures in Fig. 4.37 is believed to indicate the presence of this high temperature equivalent microstructure in the AFP billet. However, since the exact thermo-mechanical processing schedule in the steelmaker's GFM RF100 rotary forging machine is not known, it is unclear to what extent this microstructure has been produced as a result of high temperature forming of the billet or as a consequence of the prior (P)ESR casting process which reduces segregation, porosity and the irregular distribution of inclusions in AFP material.

Conversely, Fig. 4.38 is believed to indicate the presence of low temperature equivalent billet microstructure whereby, broadly, pre-solution heat treatment forming of the billet has been carried out at a sufficiently low temperature such that the γ_2 precipitates that form upon cooling after cogging in the GFM are dissolved at the higher solution heat treatment temperature. This 'unpins' the ferrite grains leaving them free to coarsen and the work imparted in the forming of the billet is lost. Note the comparatively fewer instances of allotriomorphic γ_2 precipitates in Fig. 4.38 vs. Fig. 4.37. This is somewhat supported by the quantitative metallography in Fig. 4.34 – Fig. 4.35 however the error bounds and comparatively coarse sampling intervals/frequency necessitate further, higher resolution, investigation to confirm this with more confidence.

As with the AFP billet, it is unclear as to the extent the assumed low temperature equivalent billet microstructure in the standard product is a function of the steelmaker's thermo-mechanical processing of the ingot into billet or the ingot casting process. However, it is suggested that, all other factors being equal, forged components from this billet would be less tough than those from the AFP material.



Fig 4.37 Billet 1B microstructure (ZERON® 100 AFP)



400µm

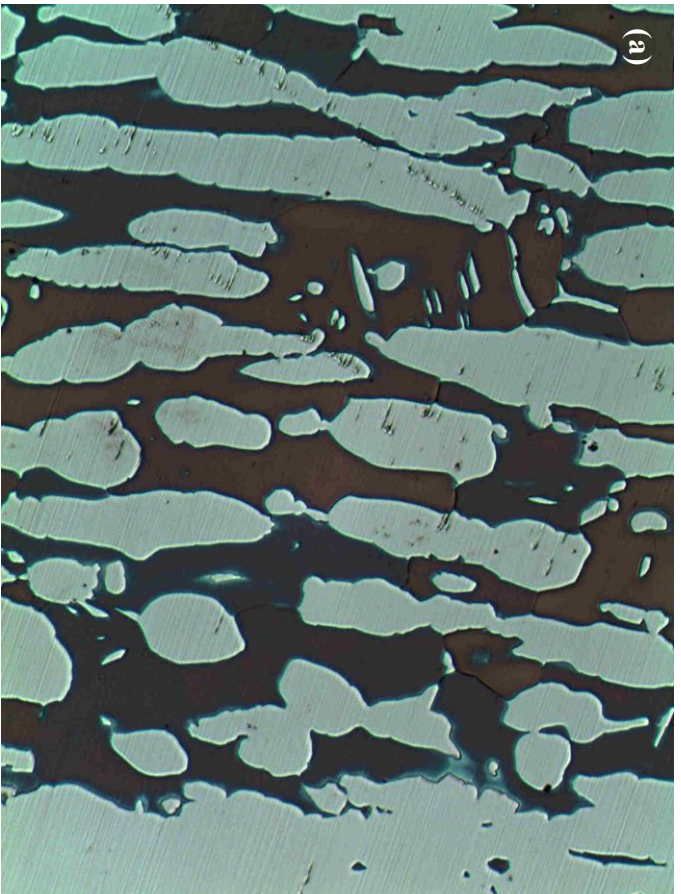


Fig. 4.38 Billet 2B microstructure (ZERON® 100 standard product)



400 μm

ZERON® 100 is produced in two variants; AFP and ‘standard material’. The work above, conducted at the outset of this project, investigated the metallographic differences between these two materials. Inhomogeneity was shown to exist to a degree within the billets of both materials. However, despite lower forging reduction ratio and less time at solution treatment temperature, the AFP billet exhibited generally higher f_{γ} (%) and essentially similar $\bar{\lambda}_{\delta}$ to the standard material billet. These microstructure metrics are generally indicative of good corrosion resistance and toughness properties and, considering the difference in thermo-mechanical processing parameters, prefer the AFP product as the starting material of choice for ‘downstream’ secondary thermo-mechanical processing operations.

4.7 Summary

The operation and theoretical basis of the main equipment and techniques used in this work have been detailed above. In doing so it is hoped that the justification for their use is clear. Greater detail on the various theoretical fundamentals covered here can be found in the indicated references. Where additional, minor experimental techniques are indicated in subsequent chapters of this work, brief summaries are also provided. Characterisation of the starting material upon which subsequent experimental work detailed in later chapters has also been presented. As part of this characterisation the quantitative metallographic techniques used extensively in subsequent chapters of this work have been introduced and explored.

REFERENCES

- [1] D. Rees, *Basic Engineering Plasticity: An Introduction with Engineering and Manufacturing Applications*. 2006.
- [2] H. S. Valberg, *Applied Metal Forming: Including FEM Analysis*. Cambridge University Press, 2010.
- [3] R. W. Evans and P. J. Scharning, “Axisymmetric compression test and hot working properties of alloys,” *Mater. Sci. Technol.*, vol. 17, no. 8, pp. 995–1004, Aug. 2001.
- [4] S. Kobayashi, S.-I. Oh, and T. Altan, “Metal Forming and the Finite-Element Method,” *J. Mater. Shap. Technol.*, vol. 8, no. 1, p. 377, 1989.
- [5] J. Davies and P. Simpson, *Induction Heating Handbook*. Maidenhead: McGraw-Hill, 1979.
- [6] V. Rudnev, D. Loveless, R. L. Cook, and M. Black, “Handbook of Induction Heating,” *Marcel Dekker, New York*, p. 796, 2003.
- [7] R. C. Dorf and R. H. Bishop, *Modern control systems*. Pearson Prentice Hall, 2011.
- [8] R. C. Weyrick, *Fundamentals of automatic control*. McGraw-Hill, 1975.
- [9] D. S. MacKenzie and G. E. Totten, *Analytical characterization of aluminum, steel, and superalloys*. Taylor & Francis, 2006.
- [10] O. Engler and V. Randle, *Introduction to Texture Analysis: Macrotexture, Microtexture, and orientation mapping*. 2008.
- [11] C. Hammond, *The Basics of Crystallography and Diffraction*. Oxford: Oxford University Press, 2015.
- [12] “DNVGL-RP-F112 Design of duplex stainless steel subsea equipment exposed to cathodic protection,” Høvik, 2017.
- [13] O. Marques, *Practical Image and Video Processing Using MATLAB®*. Hoboken, NJ, USA: John Wiley & Sons, Inc., 2011.

Chapter 5: Development of Constitutive Flow Model

The following chapter details the data evaluation from the axisymmetric compression tests carried out in this work in order to establish a constitutive flow model for the ZERON® 100 alloy. The testing parameters chosen were outlined in Ch. 4 and reflect a balance between industrial reproducibility and the operational capacity of the TMC.

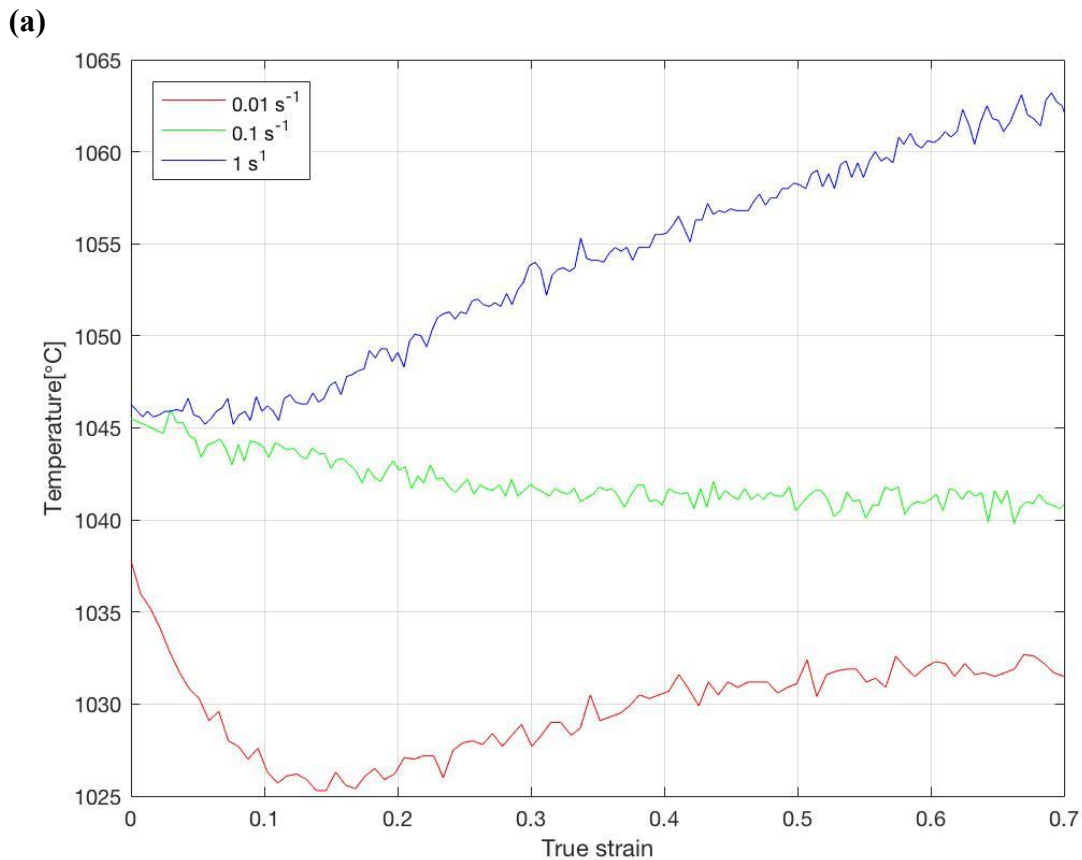
No quantitative analysis (numerical or analytical) of the flow behaviour of the ZERON® 100 alloy has been previously undertaken, and for the forging of a weld neck flange component the understanding of the development of strain penetration in the workpiece and the associated strain rates and heat transfers is anecdotal. Furthermore, no specification is made as to the minimum capacity of the forging hammer or the number of hammer blows the workpiece should receive during a given operation for optimum die fill, material properties etc. The specified industrial thermo-mechanical processing range of ZERON® 100 is 1050 – 1280°C. This work represents the first controlled lab-scale replication of the open die upsetting process and provides a novel approach to modelling the complex softening mechanisms arising from the deformation of the two-phase duplex microstructure.

The data outputted from the TMC are first corrected to account for any compliance in the machine (as well as drift from the calibrated zero position and minor variations in sample dimensions due to thermal expansion, lubrication, imperfect alignment on the bottom anvil tool by the robotic manipulator etc.) then subsequently adjusted for the effects of friction and non-isothermal compression. From this processed data a value of activation energy for deformation, Q_{def} (kJ mol.⁻¹) is calculated and validated for a range of friction coefficients by comparison with similarly reported values in the literature. A constitutive equation is subsequently developed relating the flow stress as a function of strain, strain rate and temperature. Several constitutive models exist that can be used to describe the flow behaviour of metallic materials as have been explored in Ch. 3. Davenport et al. extending the work of Shi et al.[1], [2], developed a methodology for deriving first and second stage constitutive equations for material which displays flow behaviour characteristic of both dynamic recovery (DRV) and dynamic recrystallization (DRX). Due to the difference in stacking fault energy (SFE) between ZERON® 100's duplex ferritic and austenitic phases, flow behaviour influenced by both DRV

and DRX was observed and as such this methodology was taken as the basis for the subsequent data analysis and flow model development.

5.1 Experimental Data

The temperature data as recorded by the embedded N-type thermocouple in the cylindrical TMC sample is presented in Fig. 5.1 and arranged according to the three deformation test temperatures at which the experiments were carried out (Table 4.2). The temperature changes experienced during the tests are normalised by plotting against the true strain to which all the samples were deformed.



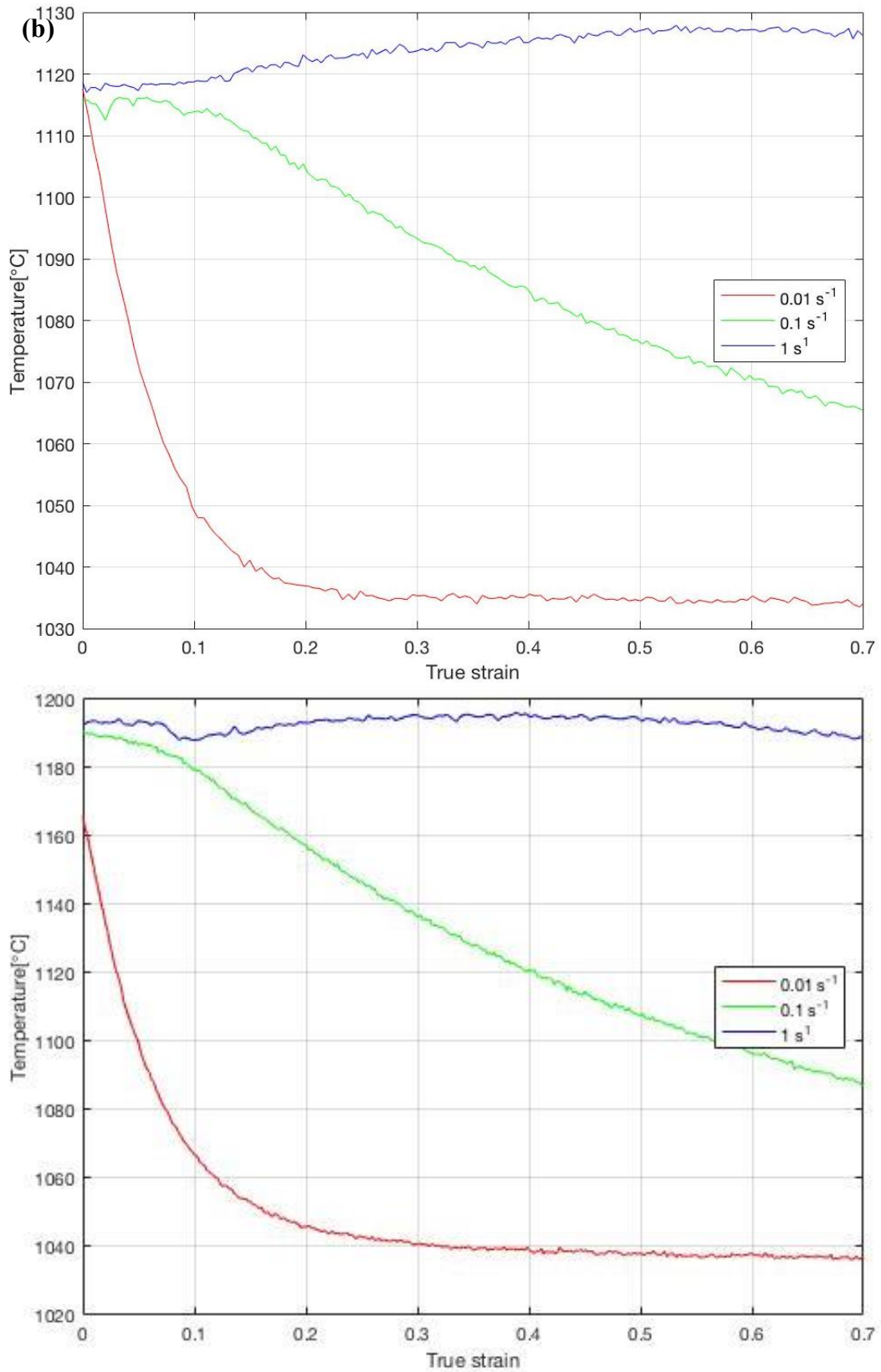


Fig. 5.1 Temperature profiles as functions of strain, recorded in the TMC samples during the uniaxial compression tests at **a** 1050°C, **b** 1125°C and **c** 1200°C

At all test temperatures, Fig. 5.1 indicates cooling occurs in the sample at the slowest strain rate; likely the result of a die chill effect due to the long contact time between the workpiece and top tool. In Figs. 5.1b & c there was a large difference in initial sample temperature and tool temperature, since the latter was limited by the maximum attainable temperature of the tool furnace (1050°C). At these higher temperatures (1125°C and 1200°C) contact times as short as ca. 7s (0.1 s⁻¹ strain rate tests) between workpiece and tooling is enough to cause large temperature drops in the range 55 – 115°C. Conversely, a consistent increase in sample temperature is observed during rapid compression (tests at a strain rate of 1 s⁻¹) at all test temperatures and is likely the result of adiabatic heating, since deformation of the sample occurs in < 1s and therefore very little of the system's energy is able to be transferred as heat to the surroundings.

For the slowest strain rate tests (0.01 s⁻¹) at these higher temperatures (1125°C and 1200°C) contact time increases by orders of magnitude and is demonstrated to be sufficient for quasi thermal equilibrium to be reached between the tooling and the sample. Such large decreases in sample temperature during compression complicate the evaluation of the material flow stress, as is discussed later, and in certain instances necessitated neglect of these data.

Fig. 5.2 shows an example of the full raw data output from the TMC for the three uniaxial compression tests conducted at 1125°C in the strain rate range 1 – 0.01 s⁻¹. Whereas only the temperature change in the sample during the deformation portion of these tests were shown in Fig. 5.1, Fig. 5.2 illustrates the change in temperature of the sample during the full test, from initial heating in the FTTU to final water quenching after deformation. The load – displacement curves are also plotted in Fig. 5.2 from which the true stress – strain curves can be calculated. It can also be seen from Fig. 5.2 that tool velocity can be expressed as the time derivative of tool displacement, i.e. $v = ds/dt$ and that this velocity decreases throughout the compression stroke in order to maintain the constant true strain rate indicated in the tool velocity vs. displacement plots.

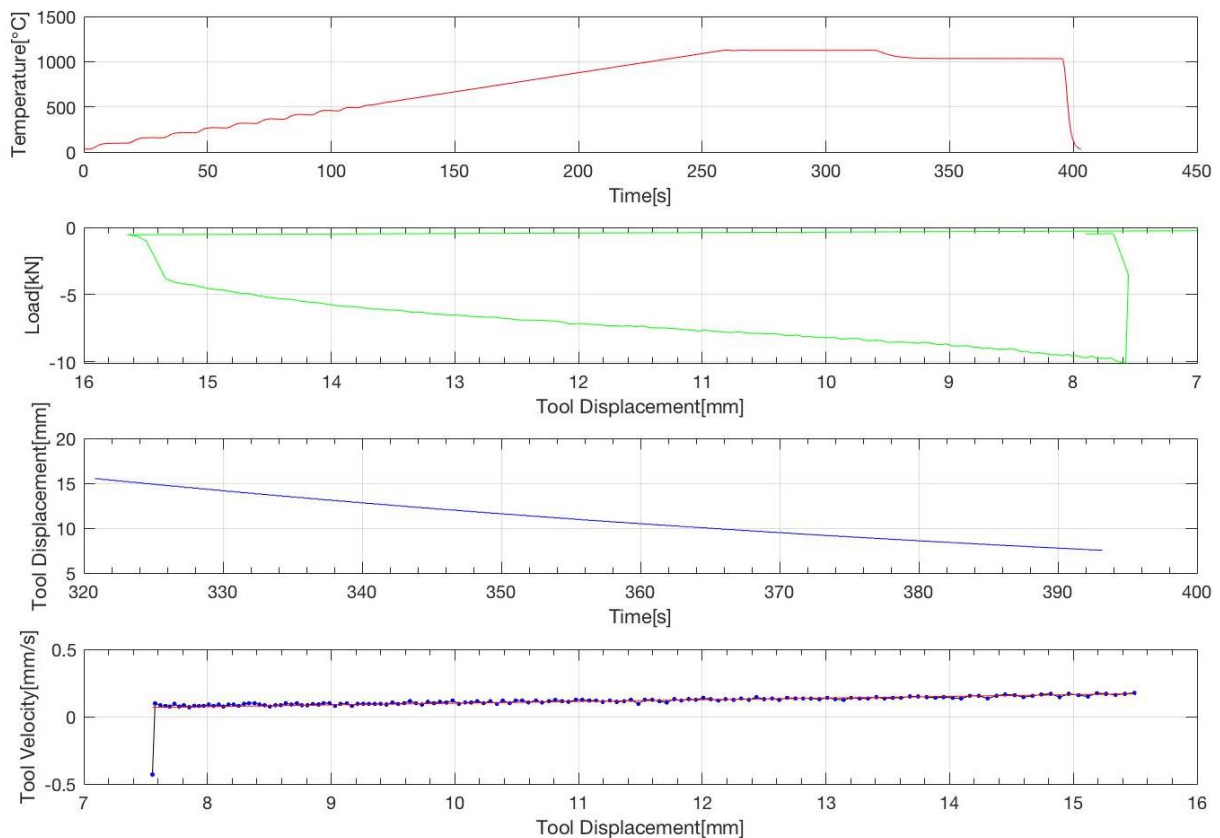
Figs. 5.2a-5.2c show examples of the full raw data output from the TMC for the three uniaxial compression tests conducted at 1125°C in the strain rate range 1 – 0.01 s⁻¹. This includes the Time-Temperature data from the embedded thermocouple in the cylindrical sample over the whole test, the load-displacement (or stroke) of the TMC’s top tool, the speed of the top tool (tool displacement – time plot) and the strain rate as derived from the tool velocity (dv/dt) – tool displacement plot.

The experimental matrix for this series of uniaxial compression tests, organised by strain rate (s⁻¹) from Ch. 4 is reproduced for reference below in Table 5.1

Table 5.1 Experimental matrix of TMC operational variables for uniaxial compression tests to determine the flow behaviour of ZERON® 100

Test #	Strain rate [s ⁻¹]	Deformation Temperature, T_D		
		T_{D1} [°C]	T_{D2} [°C]	T_{D3} [°C]
1 - 3	0.01	1050	1125	1200
4 - 6	0.1	1050	1125	1200
7 - 9	1	1050	1125	1200

(a)



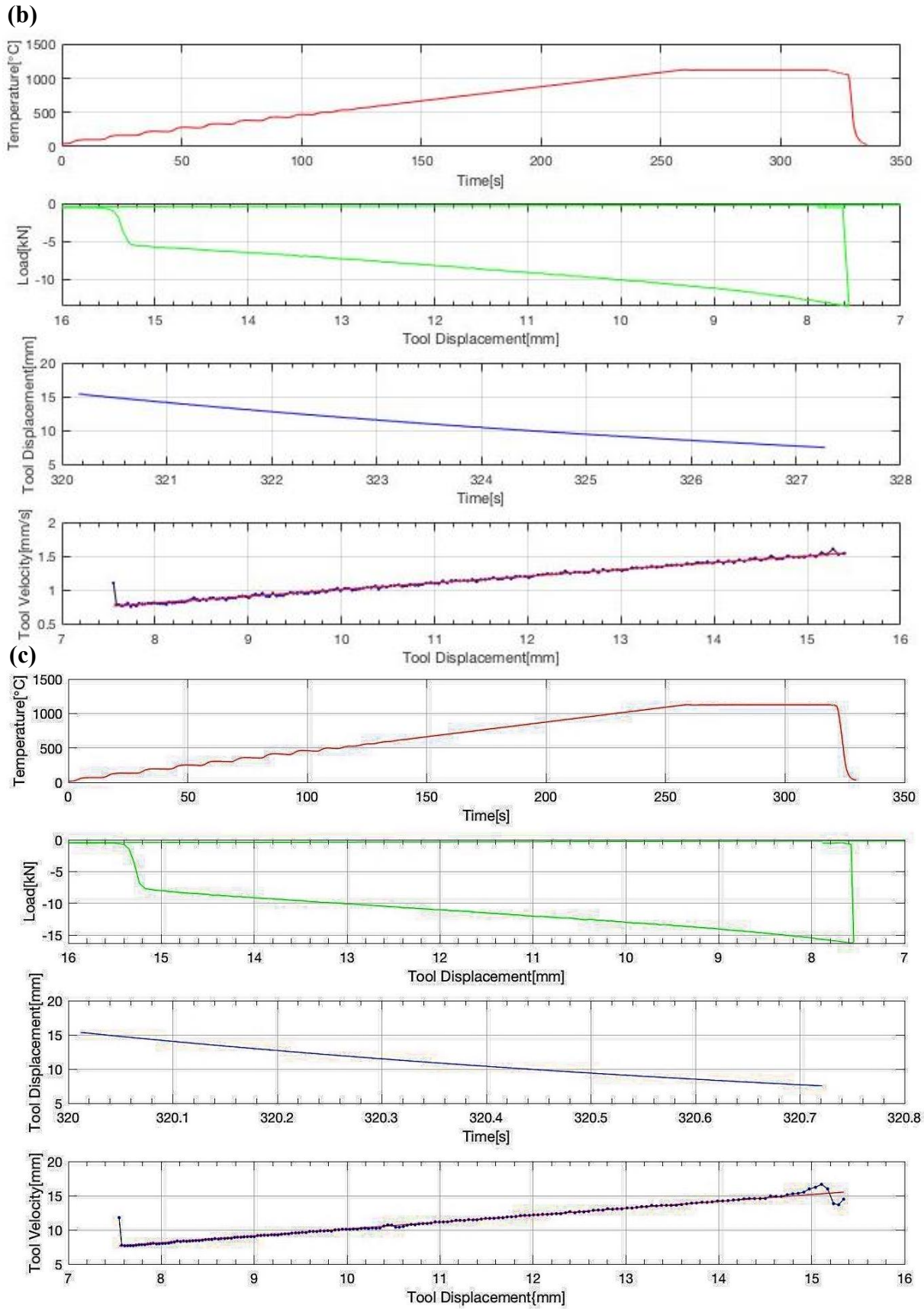


Fig. 5.2 Raw TMC data for uniaxial compression tests at 1125°C and strain rates **a** 0.01 s^{-1} **b** 0.1 s^{-1} **c** 1 s^{-1}

5.2 Data Adjustments and Corrections

Before the data derived from the uniaxial compression tests can be analysed and a flow model developed, certain post processing is required in order to correct for the effects of non-isothermal compression, friction during compression (which causes the sample to barrel) and to establish a datum point for the onset of compression. This last adjustment to the data is herein referred to as the ‘zero offset’.

5.2.1 Zero Offset Data Correction

The zero offset correction is performed on the raw load – displacement data, as exemplified in Fig. 5.2, prior to the calculation of true stress – strain plots. The correction is achieved through the establishment of the linear-elastic response of the material to imposed deformation before the onset of yielding; a straight line is programmatically fitted through two points identified as defining the instant contact is made between the top tool and the sample and the sample’s point of yield. The extrapolated point of intersection between this line and the zero load ‘noise’ in the load cell (Fig. 5.3) is then taken as the true datum point for the onset of the compression test and this value is subtracted from all subsequent values to zero-offset the data (Fig. 5.4).

This correction, while in some instances only minor, is important nevertheless since it accounts for any drift that may occur during testing, after initially zeroing the positions of the TMC’s wedge and tooling. Any distortion in the data to the load – displacement position at the onset of compression from either ‘background noise’ in the load cell, machine compliance, geometric misalignment of the sample on the anvil by the robot manipulator or initial dispersion of excess lubricant between the sample and tooling is also removed via this zero-offset correction.

For illustration, zero offsetting of the data from test nos. 5 and 8 is shown below in Figs. 5.3 and 5.4.

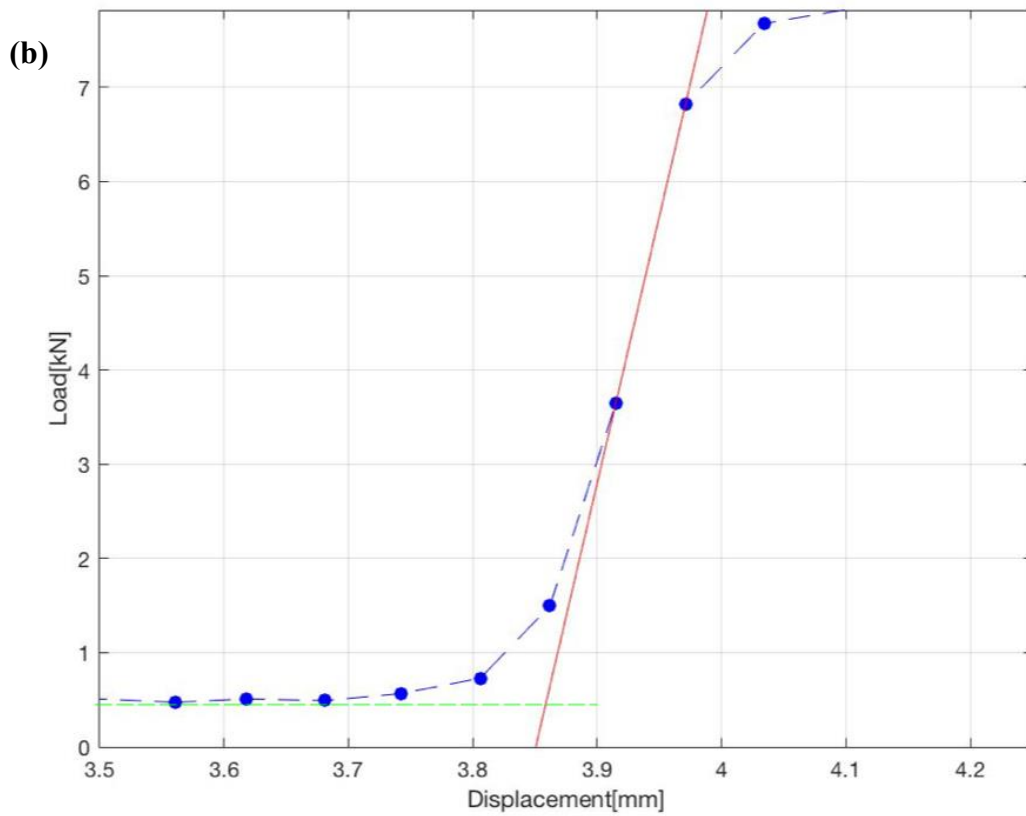
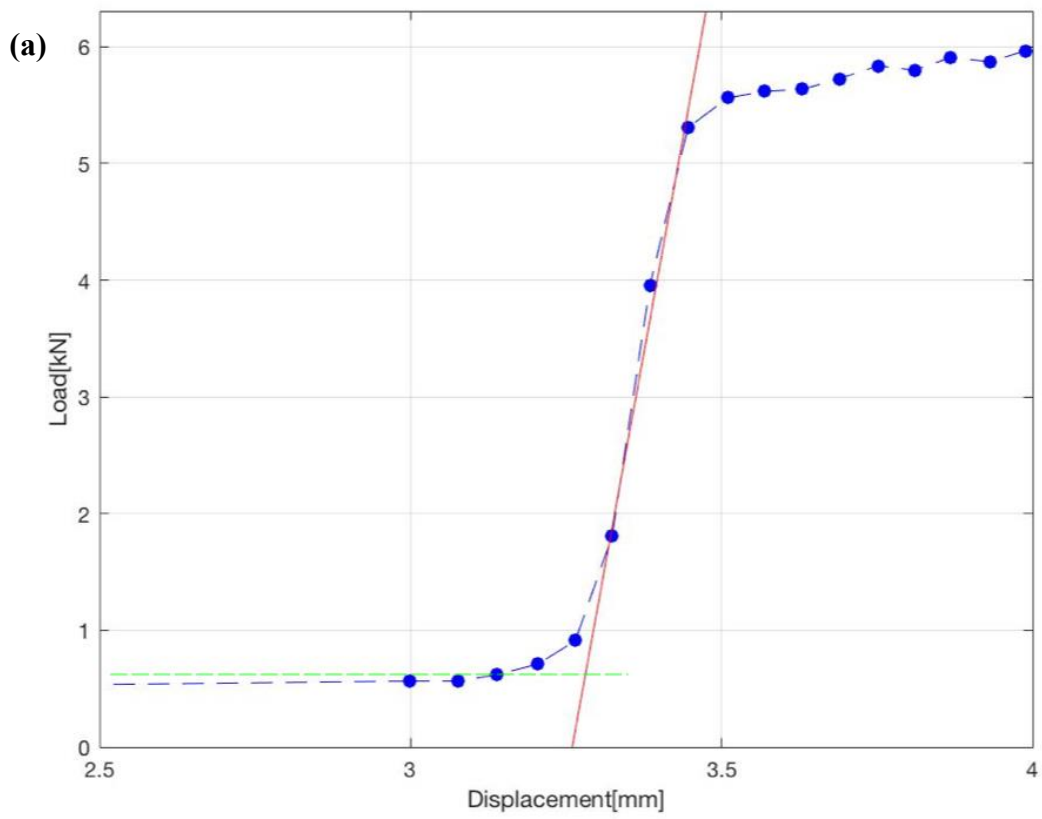


Fig. 5.3 Datum point establishment for tests at 1125°C **a** 0.1 s⁻¹ **b** 1 s⁻¹ strain rates

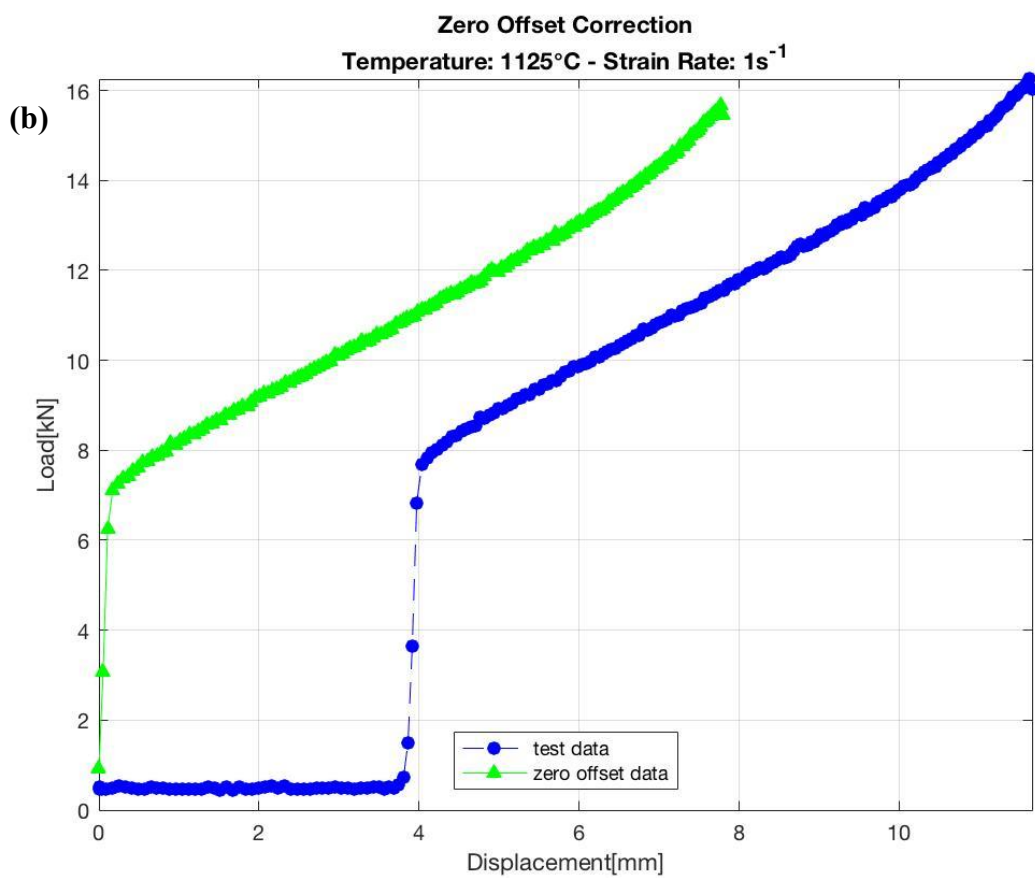
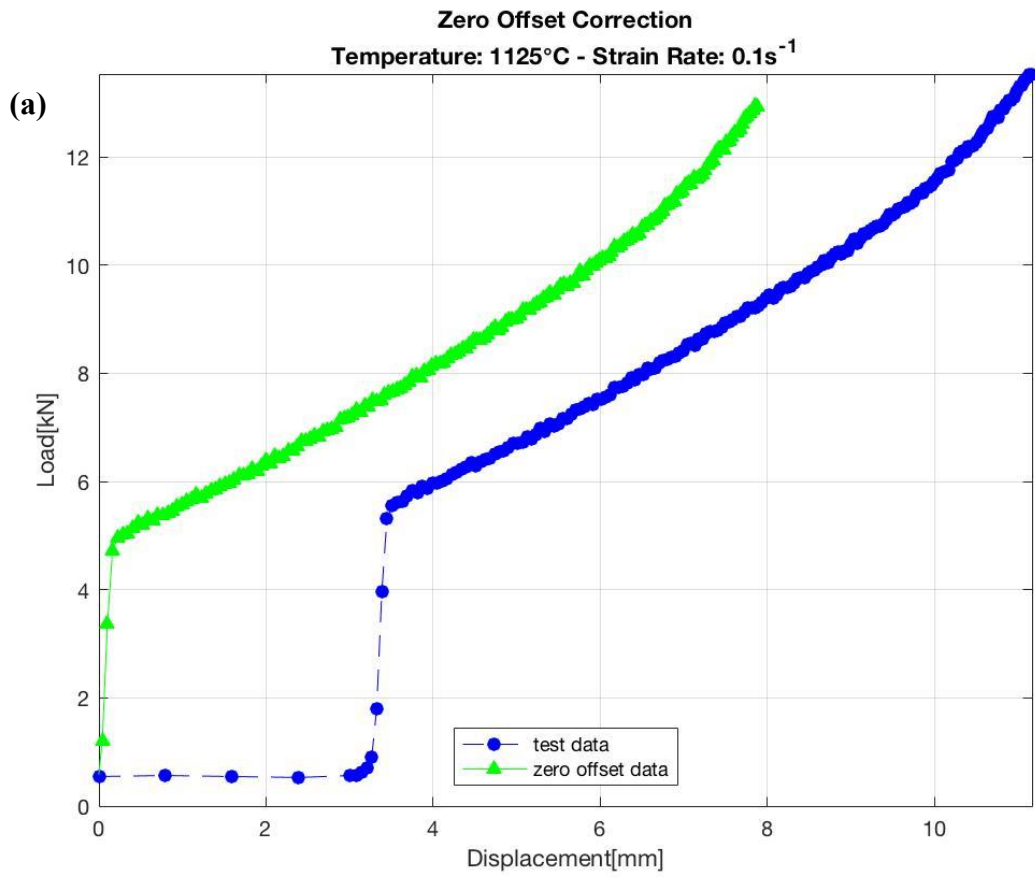


Fig. 5.4 Corrected and uncorrected TMC uniaxial compression load - displacement data

5.2.2 Friction Correction

The coefficient of friction for hot forming operations, μ can vary a great deal and depends upon a range of processing conditions including temperature, lubricant(s), workpiece and tooling materials, workpiece and tooling surface finishes. This frictional coefficient arises from the imperfect metal – metal surface contact on the micro scale and acts to impede relative motion between such surfaces. Friction also acts to increase the required load for deformation and can lead to inhomogeneities in the workpiece, commonly referred to as ‘dead zones’ where very little straining occurs. Coulomb’s law allows for a simplified assumption of the complex interfacial mechanics between the tooling and workpiece:

$$\mu = \frac{\tau_i}{P} \quad \text{Eqn. 5.1}$$

Where, τ_i is the interfacial shear stress and P is the mean pressure (or stress normal) at the interface.

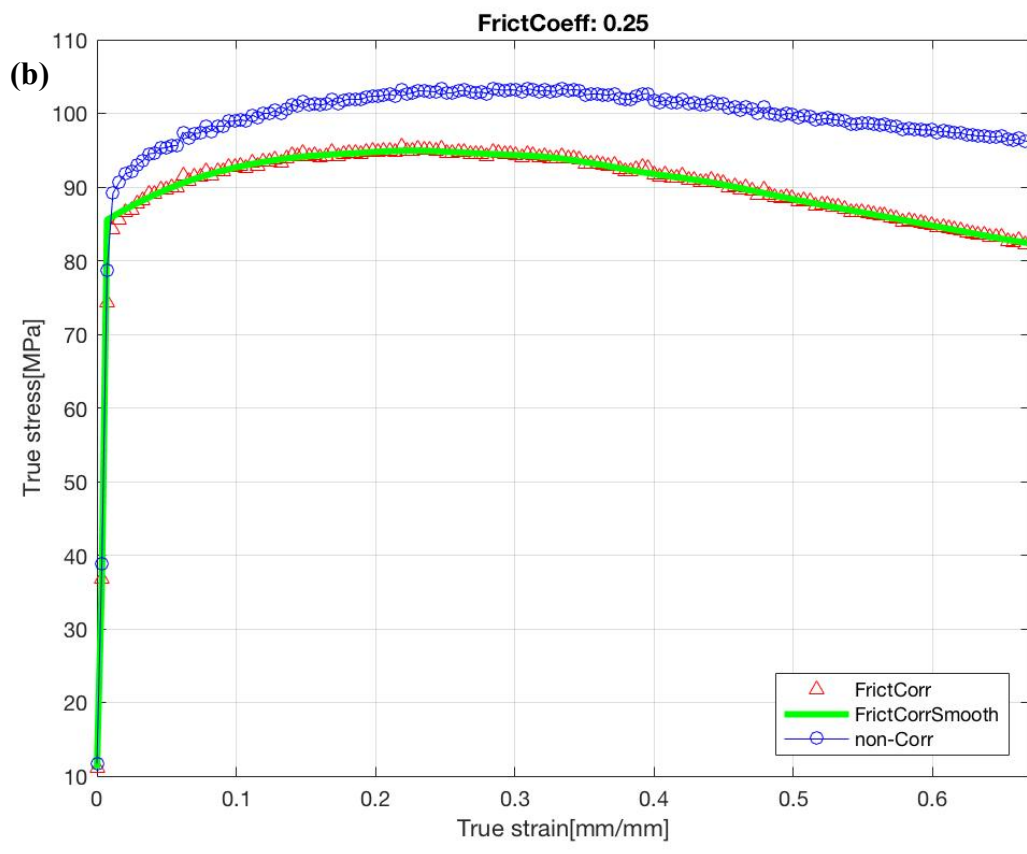
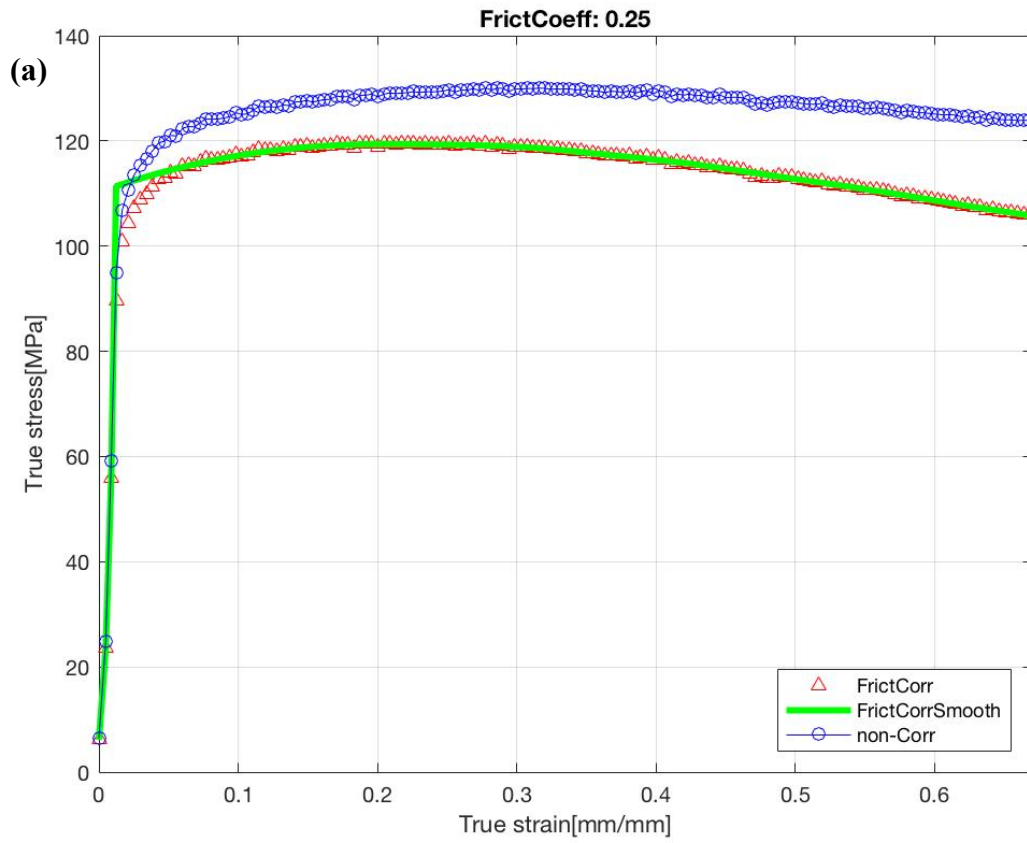
Average values of friction coefficients for lubricated open die hot forging of steels are widely reported[3] and can be aggregated into the approximate range 0.2 – 0.35. The uniaxial compression data were therefore corrected according to a 4 x1 vector of values, [0.2, 0.25, 0.3, 0.35] on this range and validated through comparison of the subsequently derived values of Q_{def} to values reported in the literature for comparable super duplex alloys, lubricants and thermo-mechanical processing parameters. It was found that a friction coefficient of 0.25 provided the best agreement between Q_{def} for ZERON® 100 under uniaxial compression, subject to the processing parameters previously described, and comparable reported values for SAF – 2507 (UNS S 32750). A value for the friction coefficient of 0.25 was optimised through comparison of the FEM-predicted areas of highest and lowest strain and micrographs taken from these corresponding areas of the compressed samples which clearly show almost complete retention of the as-received macro-orientation of the starting microstructure in the low strain, dead-zones and high levels of isotropic grain refinement in the highly-strained centre regions (Figs. 6.3 – 6.8). This indicated fidelity between the coefficient chosen and the frictional effects during compression

The friction coefficient can be used to correct the value of true stress and strain calculated from the zero-offset load – displacement data through Eqn. 5.2,[4].

$$R = \frac{P}{\left[\frac{h_i}{\mu d}\right]^2 \exp\left(\left[\frac{\mu d_i}{h_i}\right] - \left[\frac{\mu d_i}{h_i}\right] - 1\right)} \quad \text{Eqn. 5.2}$$

Where R is the true stress (MPa), h_i and d_i are the instantaneous sample height and diameter (mm), respectively, and d is the initial sample diameter (mm). Examples of the friction corrected and uncorrected true stress – strain curves for the tests conducted over the range of deformation temperatures at constant 1 s^{-1} and 0.1 s^{-1} strain rates are plotted below in Figs. 5.5 and 5.6, respectively.

After the friction correction has been applied the data are further smoothed programmatically through a robust local regression using weighted linear least squares and a 2nd degree polynomial model that assigns lower weight to outliers in the regression. This method assigns zero weight to data outside six mean absolute deviations. The span of the moving average in this method is set to 15% where, in this case, the span is a percentage of the total number of data points, less than or equal to 1.



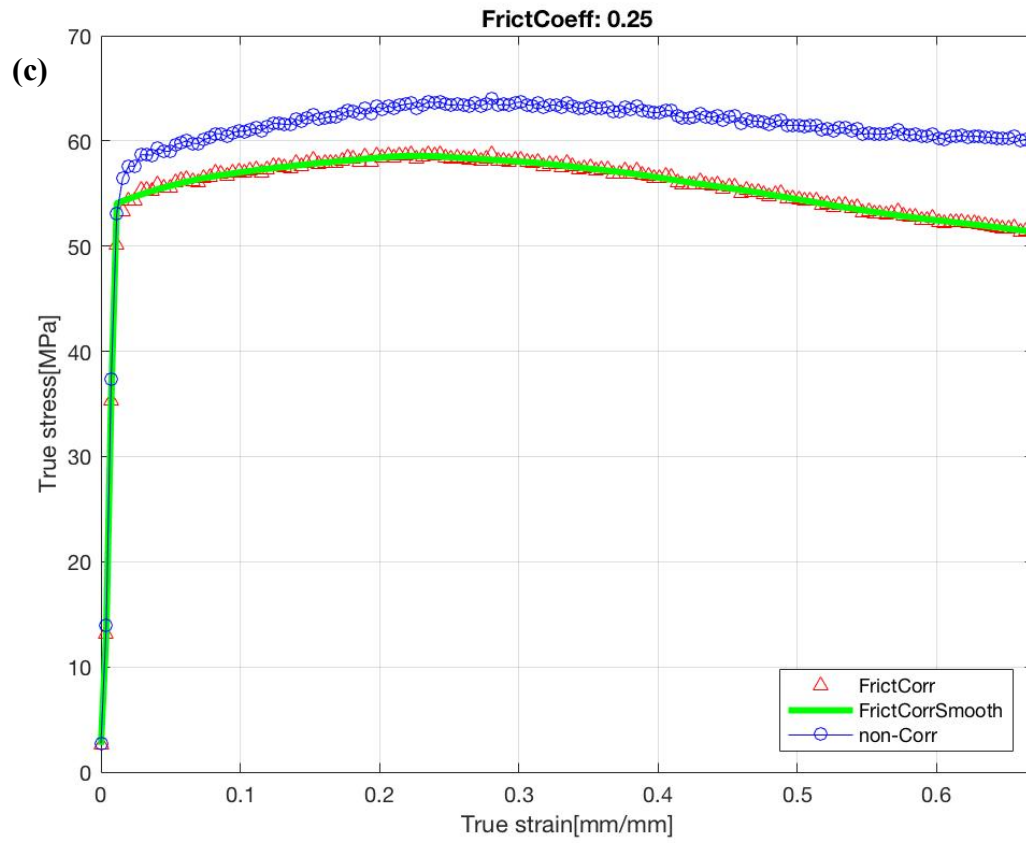
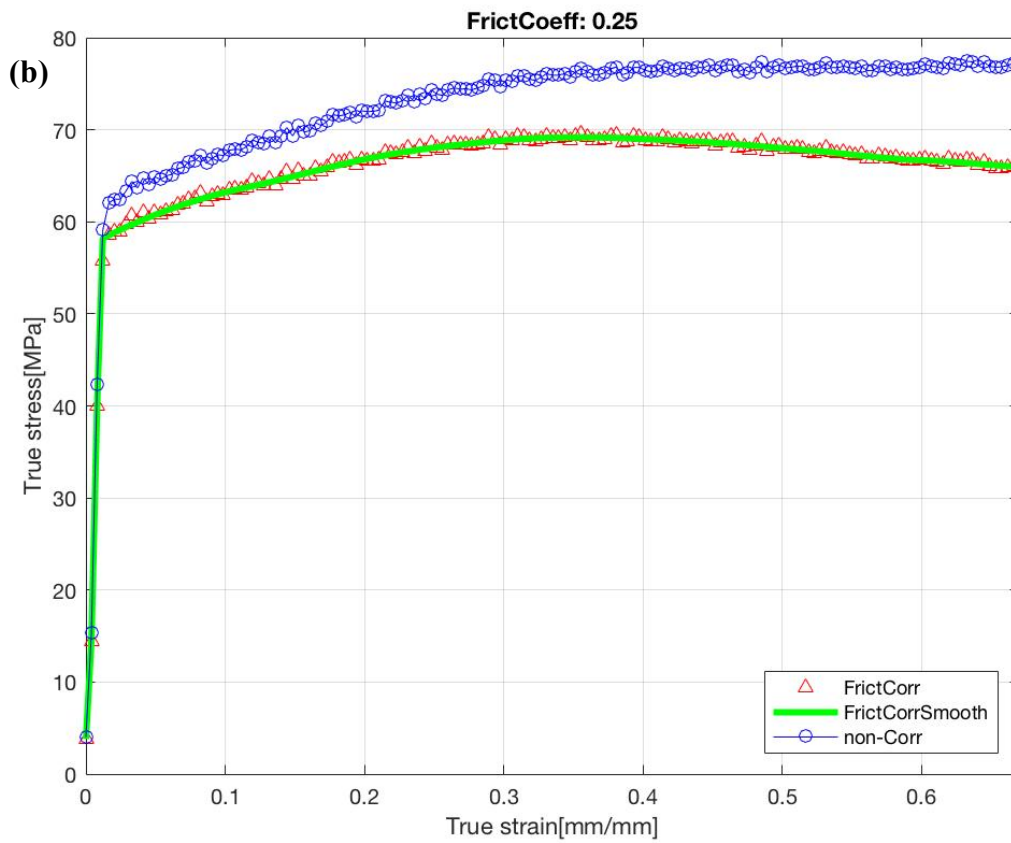
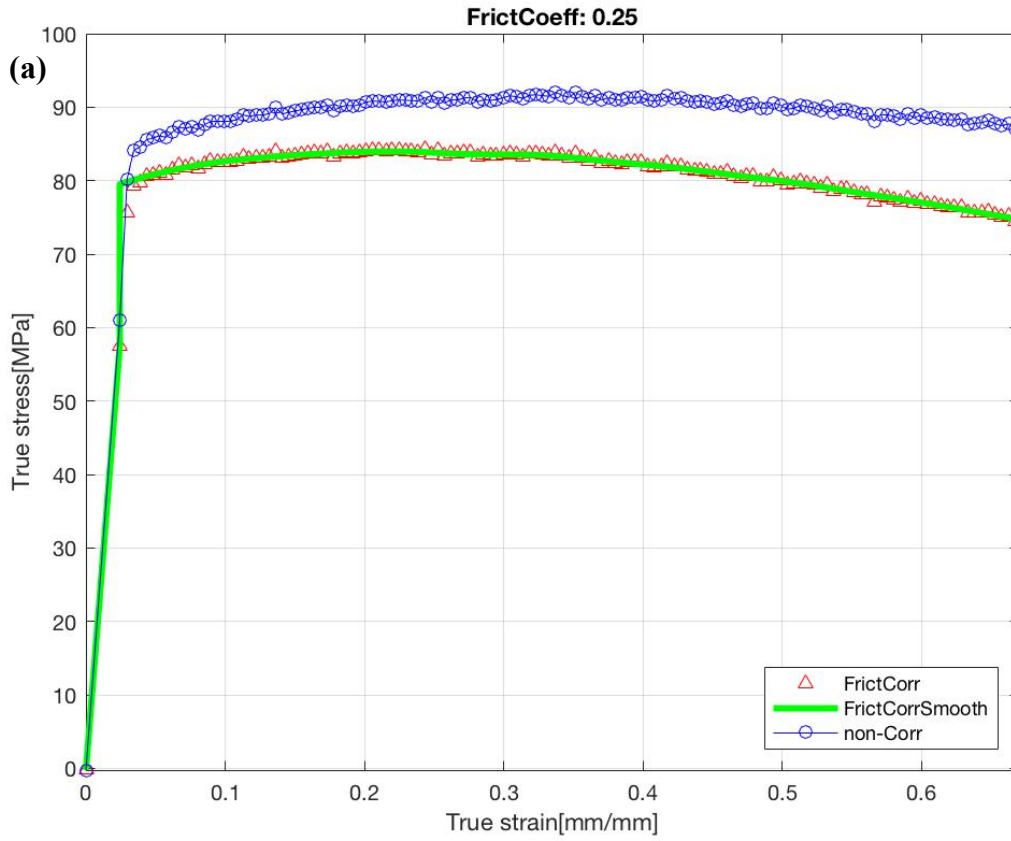


Fig. 5.5 Friction corrected (using $\mu = 0.25$) and uncorrected true stress – strain curves for uniaxial compression tests conducted at a constant 1 s^{-1} strain rate and **a** 1050°C **b** 1125°C and **c** 1200°C



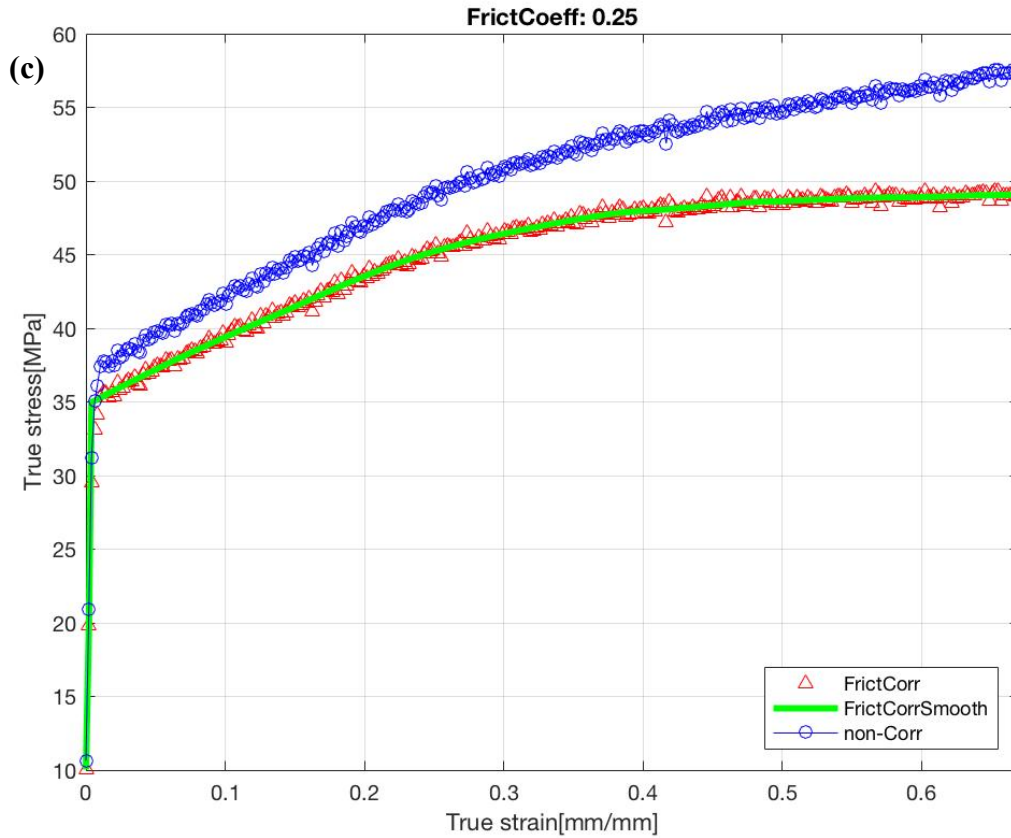


Fig. 5.6 Friction corrected (using $\mu = 0.25$) and uncorrected true stress – strain curves for uniaxial compression tests conducted at a constant 0.1 s^{-1} strain rate and **a** 1050°C **b** 1125°C and **c** 1200°C

5.3 Constitutive Equation Development and Isothermal Corrections

Formulation of a constitutive flow model requires the development of two sets of equations. The first set relate flow stress to a temperature-compensated function of strain rate through the Zener – Hollomon parameter, Z

$$Z = \dot{\varepsilon} \exp\left(\frac{Q_{\text{def}}}{RT}\right) \quad \text{Eqn. 5.3}$$

Where T is the absolute temperature (K) and R is the molar gas constant ($8.314 \text{ J K}^{-1} \text{ mol}^{-1}$).

These equations are defined for a discrete series of strain offsets ($\varepsilon_1, \varepsilon_2, \dots, \varepsilon_n$) along the flow curve. The second stage equations build upon the first set, however they allow for continuous flow curves to be described in terms of Z and ε .

Before the first stage constitutive equations can be developed however, it is necessary to first temperature correct the flow curves, examples of which were shown in Fig. 5.4, for the effects of non-isothermal compression. As demonstrated in Fig. 5.1, the temperature drop in the samples under certain strain rates and deformation temperatures was large and therefore the flow stress curves need to be further corrected to reflect those that would have been produced if the deformations had been isothermal since such heat transfers are likely to distort the true shape of the stress–strain curves. Adiabatic heating effects were also identified in Fig. 5.1 and these too can produce material softening effects which distort the shape of the curves, ultimately leading to misrepresentative second stage equations.

5.3.1 Isothermal Flow Curves

The activation energy for deformation, Q_{def} is required to perform the above-mentioned isothermal corrections to the flow curves, and while there are general benchmark values for many grades of common plain carbon, high strength and micro alloyed steels, such information is not readily available for more exotic, complex and high-alloy systems such as duplex and superduplex stainless steels. Certain values have been published for similar super duplex material, principally SAF – 2507[5],[6] however this work presents the first such characterisation of ZERON® 100 through analogous processing parameters to industrial forging.

To calculate Q_{def} a 25 x 1 vector of incremental strains was defined in the range $\varepsilon_y - \varepsilon_n$ where ε_y corresponds to plastic strain $\varepsilon = 0$ and ε_n is the total true strain to which the sample was compressed, 0.69 in this case. For each strain offset a graph of $\ln(\dot{\varepsilon}) = f(\sigma)$ is plotted, as illustrated in Fig. 5.7 below for the exemplar ca. 0.22 and 0.55 strain offsets.

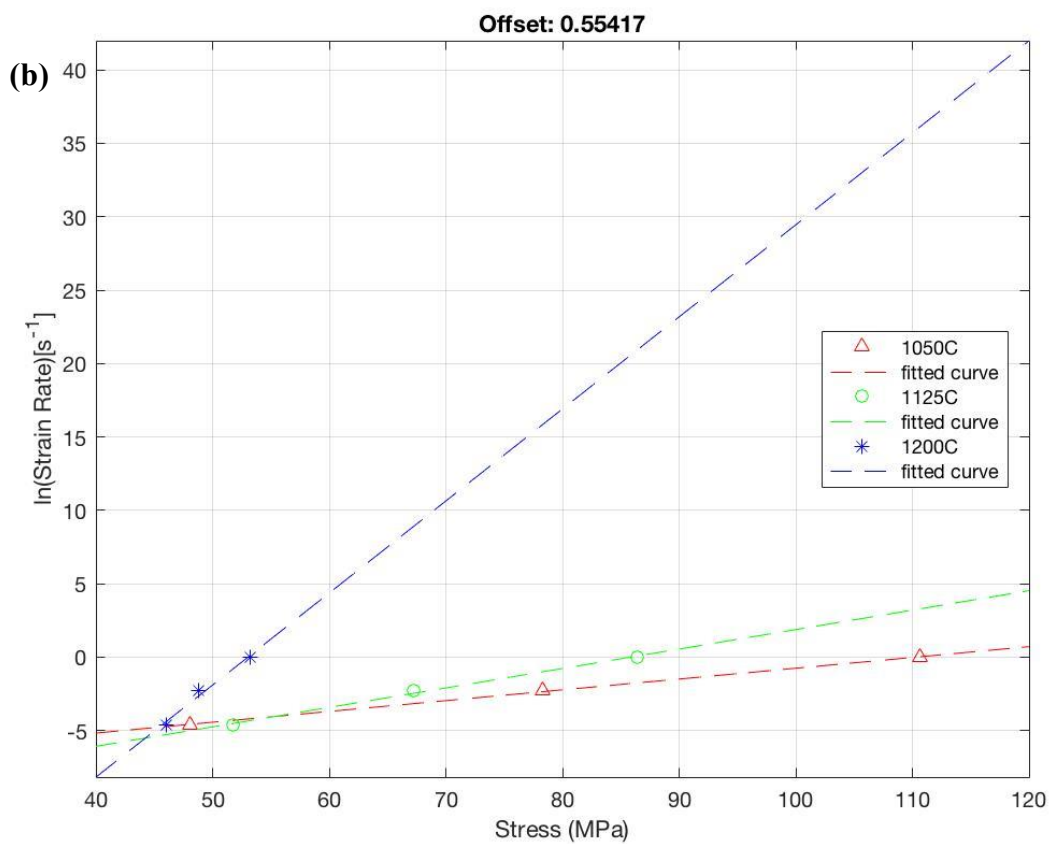
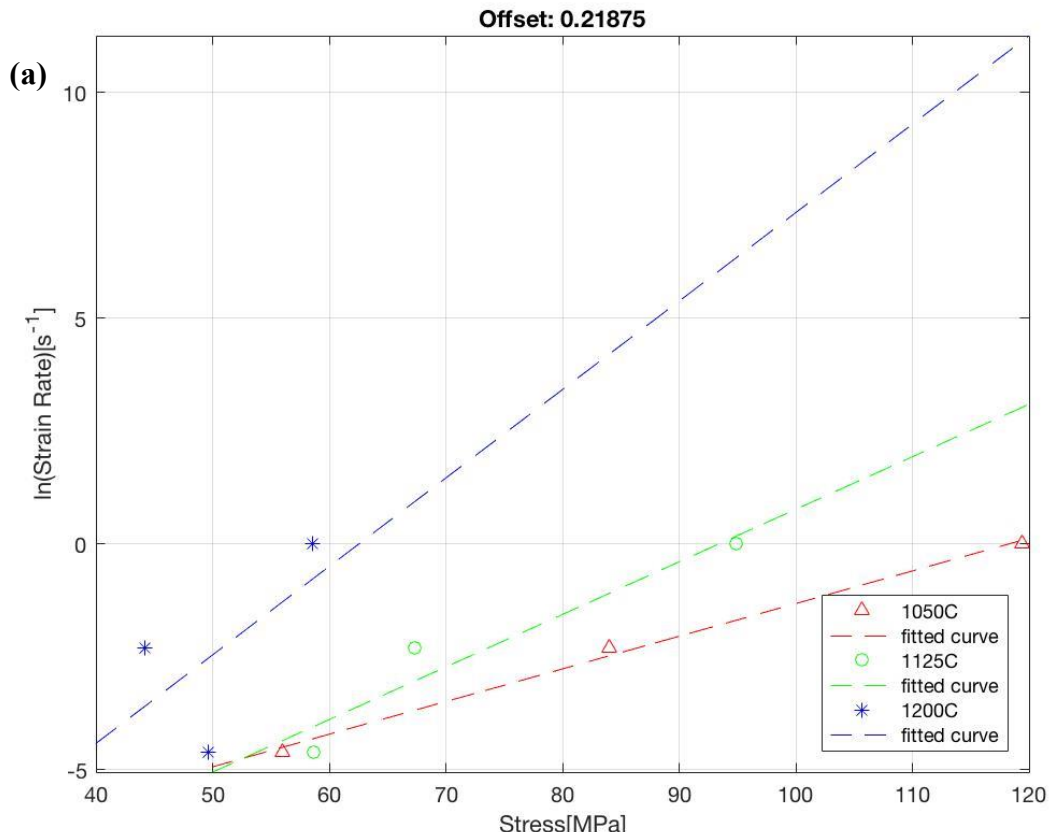


Fig. 5.7 Instantaneous values of $\ln(\text{strain rate})$ vs. stress at strain, ϵ offsets **a** 0.22 and **b** 0.55

The linear fits applied to the data in Fig. 5.7 allow for the extrapolation of instantaneous \ln (strain rate) and temperature values at points of equal stress. It is recommended[1] that three points of equal stress, on a 50 MPa interval are chosen at which \ln (strain rate) can be extrapolated, however, as is clear from the data presented in Figs. 5.5 and 5.6 relating to the tests at constant 0.1 and 1 s⁻¹ strain rates and deformation temperatures of 1050°C, 1125°C and 1200°C, no three such values of stress, all within the yield – peak range, on a 50 MPa interval can be found.

For the purposes of model robustness three points of equal stress on a smaller interval were chosen (75, 81.5 and 88 MPa) since the instantaneous temperature data from the tests correspond specifically to calculated values of true stress and therefore the closer the agreement between recorded data and the chosen points of equal stress the more accurate the temperature data. Even when reducing down to a smaller stress interval however, there were instances where the chosen values fell outside the range of experimental data between yield and peak stress for certain combinations of strain rate and deformation temperature test parameters; such is the range of data accumulated over the selected testing parameters of strain rate and deformation temperature.

This limitation is highlighted in Tables 5.2 and 5.3 where the difference between the chosen points of equal stress and closest matches to these points (in excess of the yield) in the experimental data are indicated in the δ columns. Values of instantaneous temperature corresponding to the points of equal stress were only selected where this difference could be minimised as much as possible. Even so, it is clear from Figs. 5.6 and 5.7 that 75 MPa is well below the yield stress for tests carried out at the highest deformation temperature. This is also the case for all tests at the slowest strain rate over the full range of deformation temperatures. As noted previously, the long contact time between the tooling and sample at the slowest strain rate caused a significant ‘die chill’ effect, especially when the sample was preheated to the higher temperatures and is likely to have distorted the flow response of the material under these conditions. It was therefore decided that only data from the faster strain rates (0.1 and 1 s⁻¹) and medium – low temperatures (1125 and 1050°C) would be included in further formulation of the flow model.

Table 5.2 Equal stress point 81.5 MPa

δ	σ_i [MPa]	T_{nominal} [°C]	$\dot{\epsilon}$ [s ⁻¹]	T_i [°C]	T_i [K]	$1/T_i$ [K ⁻¹]
0.06	81.44	1050	0.1	1042.1	1315.25	0.0007603
12.32	69.17	1125	0.1	1088.8	1361.95	0.0007342
32.01	49.48	1200	0.1	1085.4	1358.55	0.0007361

Table 5.3 Equal Stress Point 88 MPa

δ	σ_i [MPa]	T_{nominal} [°C]	$\dot{\epsilon}$ [s ⁻¹]	T_i [°C]	T_i [K]	$1/T_i$ [K ⁻¹]
12.41	100.41	1050	1	1064.9	1338.05	0.0007474
0.05	88.05	1125	1	1127.4	1400.55	0.0007140
29.42	58.58	1200	1	1193.6	1466.75	0.0006818

Despite discarding data from the slowest strain rate and highest temperature tests, as previously above noted in Ch. 5.1, the range covered in the points of equal stress chosen (tables 5.2 and 5.3) still includes values very close to (and slightly below) yield under certain combinations of test parameters (Fig. 5.5 and 5.6). Accepting this limitation however as a function of data derived from conducting as industrially analogous tests as possible, the value of activation energy can be determined from the average of the gradient of the lines fitting the data points shown in Fig. 5.7, for all 25 chosen strain offsets. The approach adopted in selecting a small interval of equal stress points and selecting data only from tests at 0.1 and 1 s⁻¹ strain rates and 1125 and 1050°C temperatures produces line gradients that are approximately the same for all stresses and at each strain increment, as shown in Fig. 5.8

It should be noted however, that this approach of curve fitting between two data points in a series does not allow for proper assessment of scatter in the data; since the gradients of the lines in Fig. 5.8 are constant for all stresses at each strain increment, a uniform Q_{def} may be inferred, however without an additional data point it is unclear whether this consistency remains within the scatter of the data and therefore if there is a change in Q_{def} (and hence the micromechanics of deformation) outside the range of testing parameters examined here.

For a frictional coefficient of 0.25, the approach detailed above yielded an average value of $Q_{\text{def}} = 439.83 \text{ kJ mol}^{-1}$

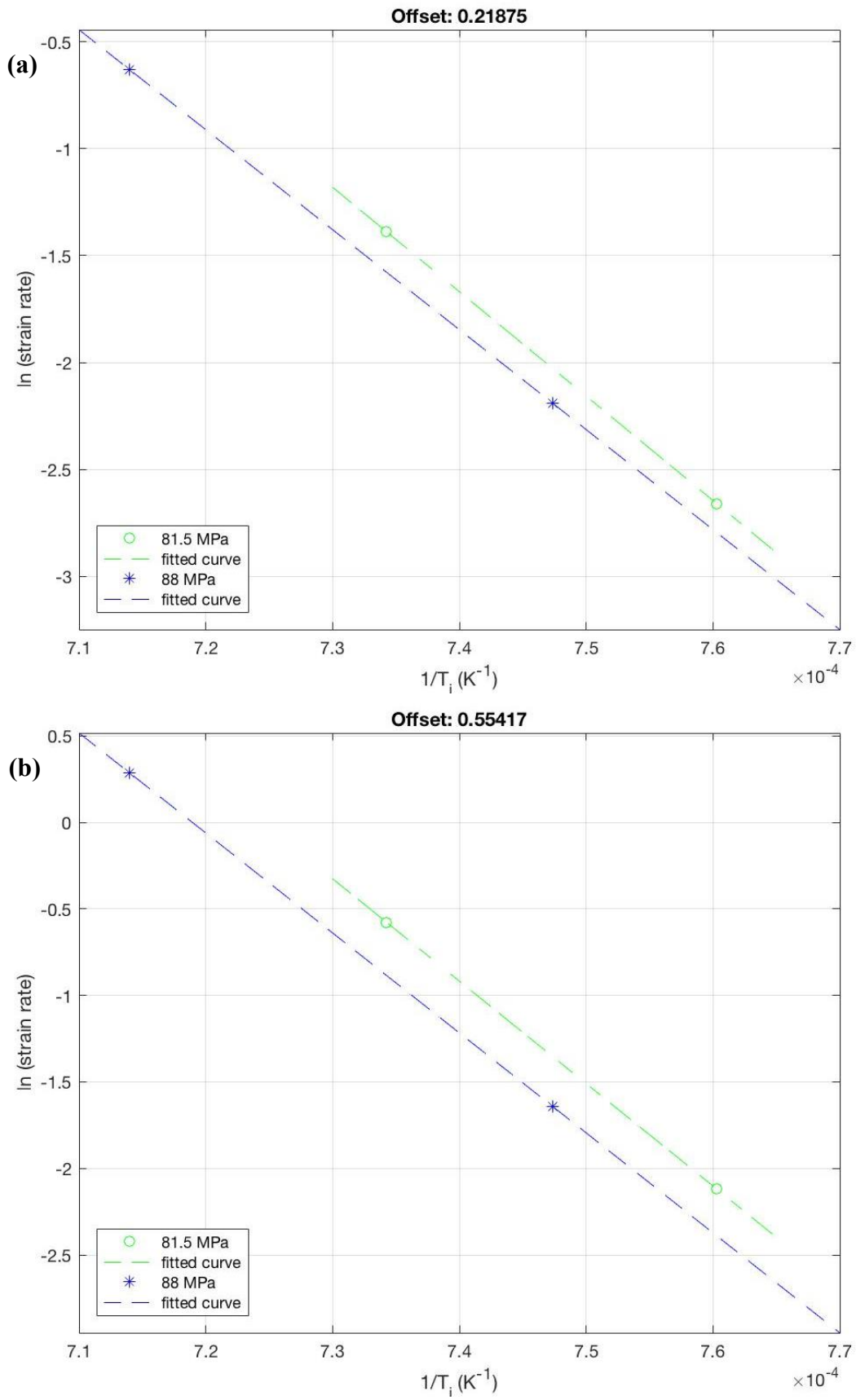
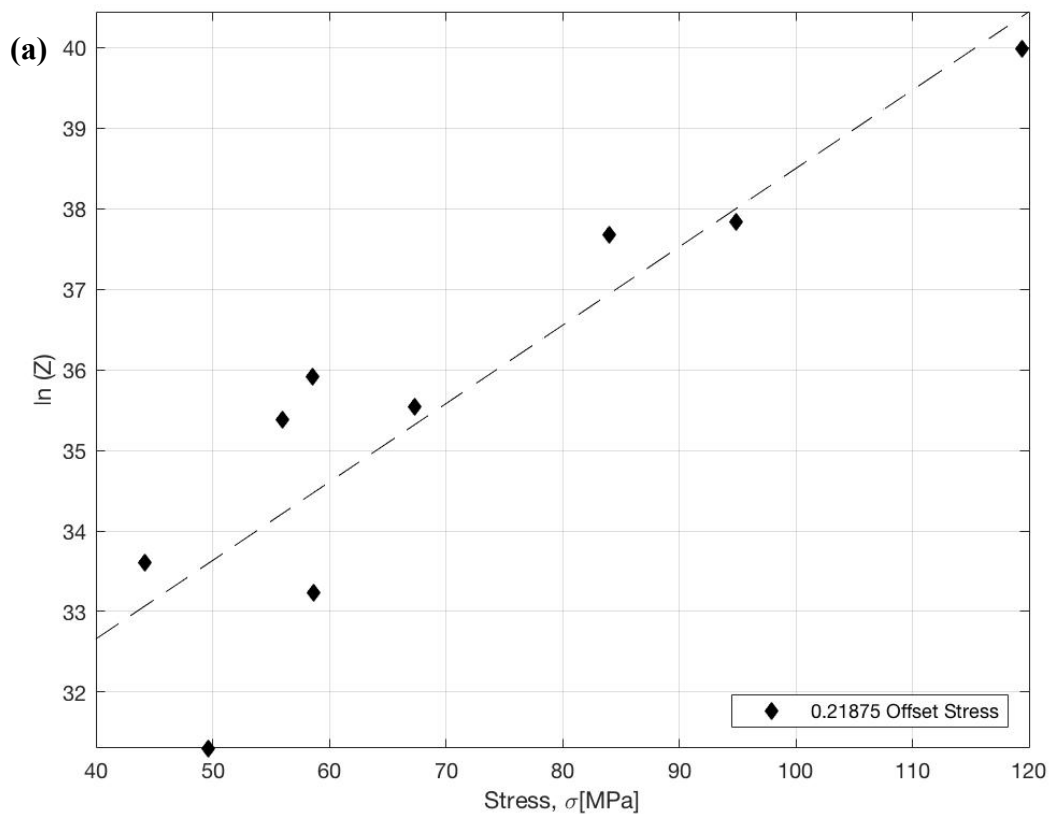


Fig. 5.8 Interpolated \ln strain rate vs. inverse temperature taken from Fig.5.7 at approximate strain offsets of **a** 0.22 and **b** 0.55

Isothermal correction of the flow stress data also requires the determination of another first stage constitutive equation parameter, β which allows for the dependence of flow stress on Z to be described in exponential form at high stresses (Eqn. 5.4).

$$Z = A \exp(\beta\sigma) \tag{Eqn. 5.4}$$

Where A is a model coefficient and β can be found by plotting $\ln(Z) = f(\sigma)$ and averaging the gradient of the fitted curves. For the testing parameters described nine discrete values of Z can be defined and the logs plotted against the stresses at each of the defined offset stresses discussed in 4.3.1. These plots are shown below in Fig. 5.9 for approximate offsets 0.22 and 0.55



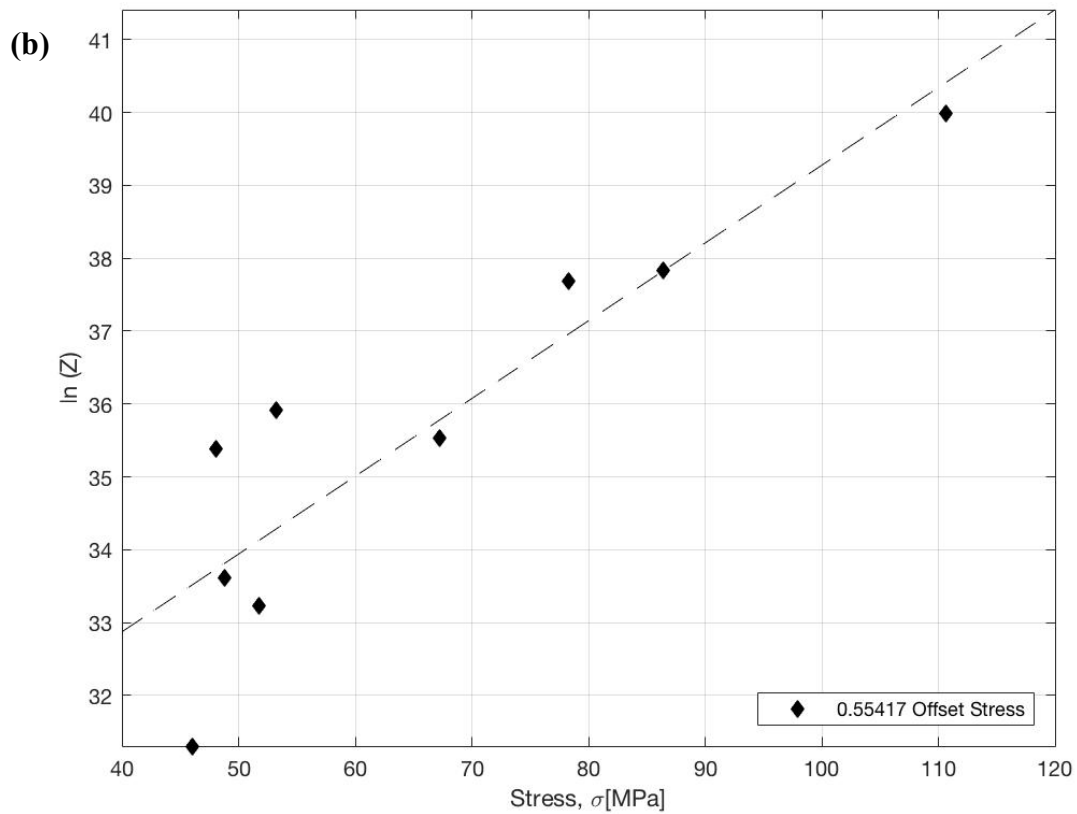


Fig. 5.9 Plots of $\ln(Z)$ vs. stress for offset strains of ca. **a** 0.22 and **b** 0.55

Each value of β is only valid for a particular value of strain, at which the first stage constitutive equation describes the stress. It is therefore necessary to define β as a function of strain from which β values to greater strains than those tested to in this work can be extrapolated. The resultant curve can then be applied to the range of testing parameters for ZERON®100 discussed above. The plot of $\beta = f(\epsilon)$ is shown below in Fig. 5.10.

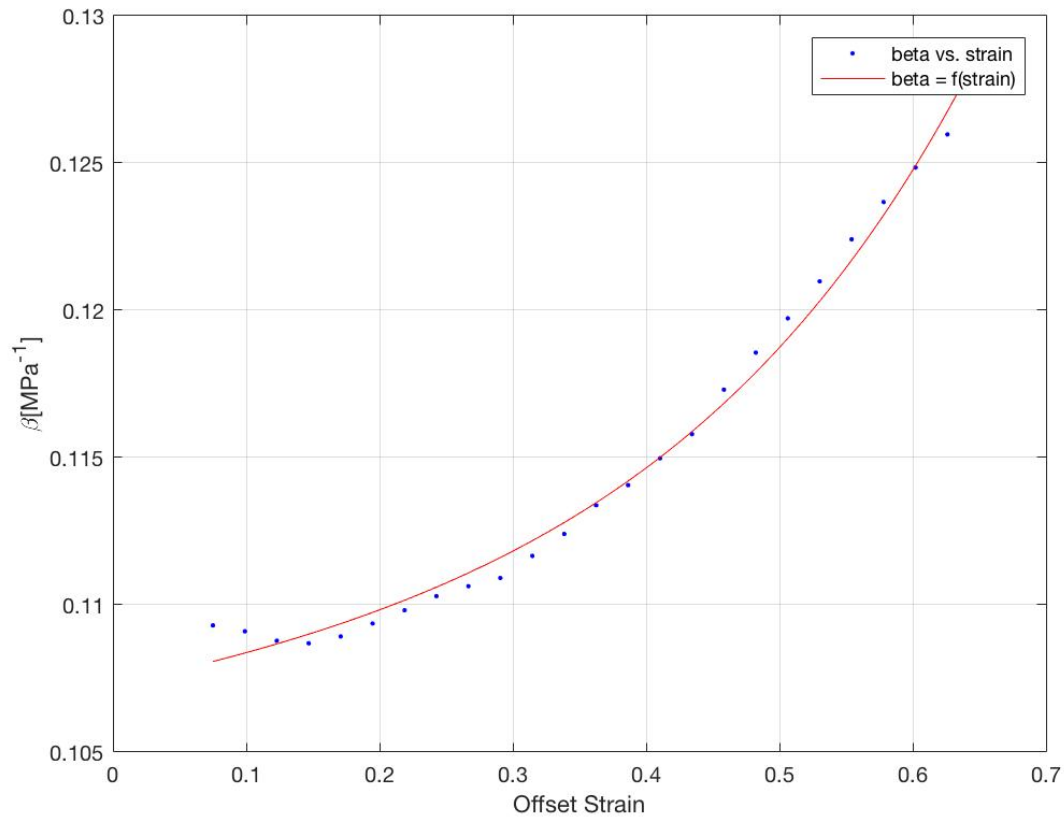


Fig. 5.10

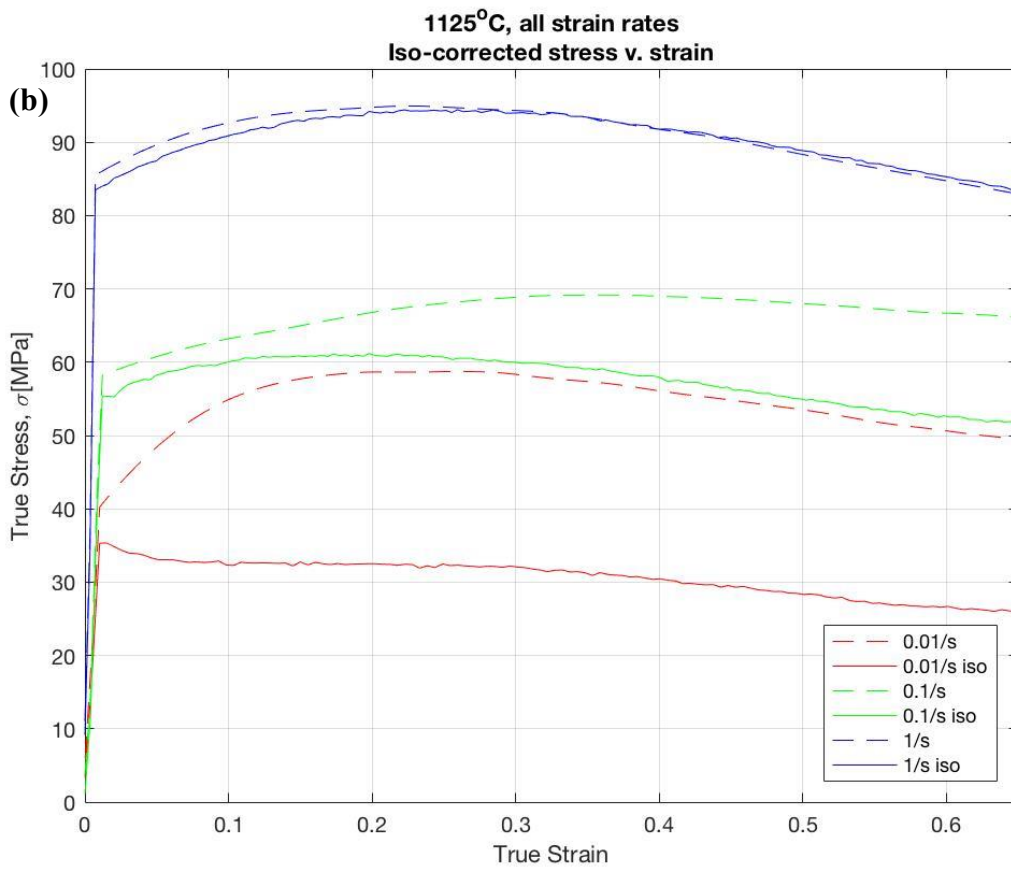
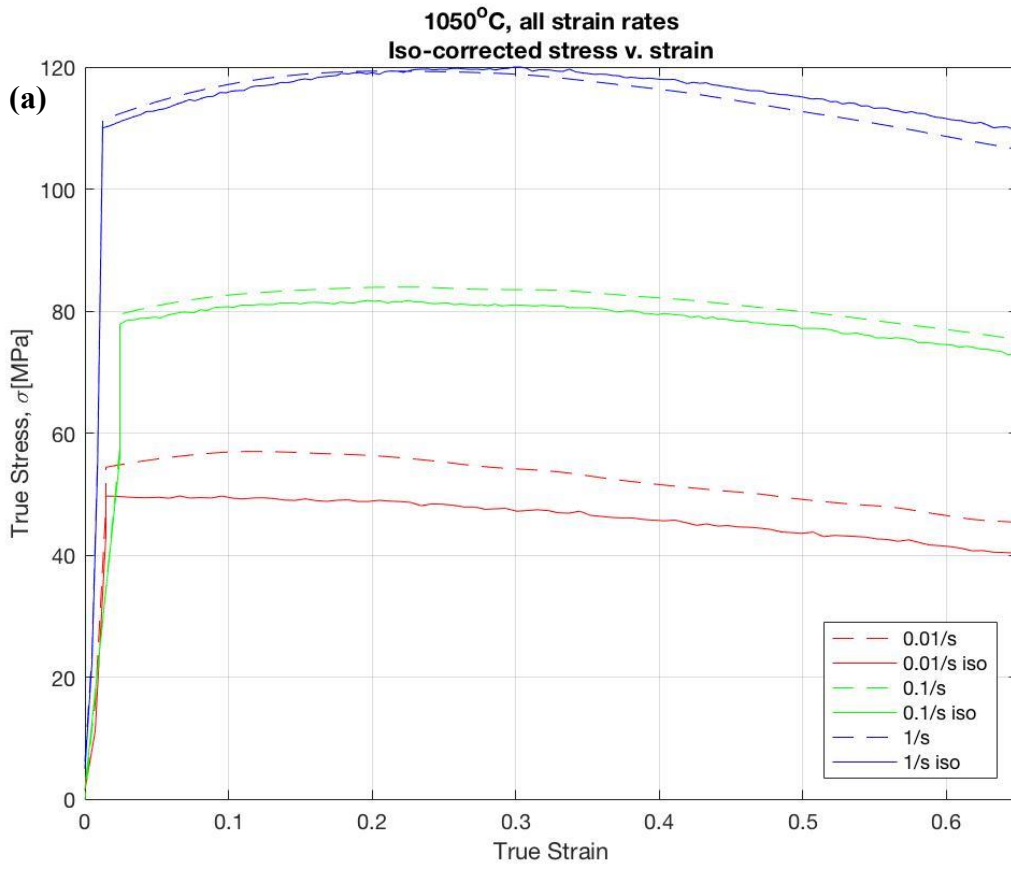
The fit in Fig. 5.10 is described by a two-term exponential function, given in Eqn. 5.5 below. The degree-of-freedom adjusted coefficient of determination (or adjusted R^2) was calculated as 0.991, suggesting a good agreement between the data and Eqn. 5.5.

$$\beta = a \exp(b\varepsilon) + c \exp(d\varepsilon) \quad \text{Eqn. 5.5}$$

Where a , b , c and d are model coefficients equal to 0.09359, -0.01669, 0.002006 and 3.437, respectively. With beta defined in terms of strain and a value of Q_{def} determined, it is now possible to isothermally correct each data point in the flow stress curves according to Eqn. 5.6

$$\sigma_2 = \sigma_1 + \frac{Q_{\text{def}}}{\beta R} \left(\frac{1}{T_2} - \frac{1}{T_1} \right) \quad \text{Eqn. 5.6}$$

Where σ_1 and T_1 are the instantaneous experimental values of stress and temperature (MPa and K, respectively), T_2 is the nominal isothermal test temperature (K) and σ_1 is the corrected isothermal stress (MPa). Using Eqn. 5.6, complete isothermal stress-curves are derived and presented in Fig. 5.11.



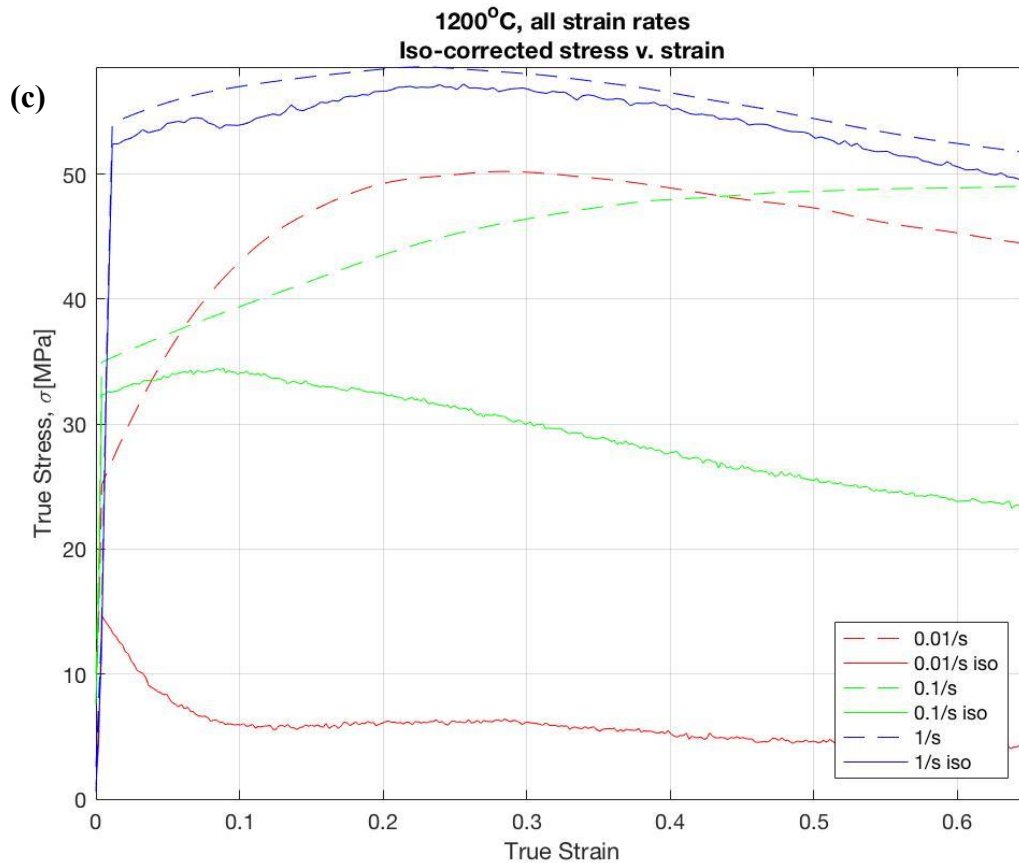


Fig. 5.11 Isothermally corrected stress – strain curves for uniaxial compression tests at 0.01, 0.1 and 1 s⁻¹ strain rate and **a** 1050°C deformation temperature **b** 1125°C deformation temperature and **c** 1200°C deformation temperature

Due to the large drop in temperature of the samples during testing at the highest temperature and slowest strain rate, considerable divergence is shown between the stress calculated from the experimental data and the stress after isothermal correction in Fig 5.11a and b. As in the previous determination of Q_{def} , the distortion this temperature drop causes in the representation of the flow behaviour of ZERON® 100 under these conditions necessitates neglect of these data for further development of second stage constitutive equations through the identification of characteristic points on the flow curves.

5.4 Characteristic Points on the Flow Curve

At this point it is possible to express a first-stage constitutive equation to describe the dependence on Z of the elevated (ca. > 55 MPa) flow stress using an exponential equation of the type indicated in Eqn. 5.4. However, a second stage equation is needed if the flow

behaviour is to be modelled as a continuous curve, rather than a set of discrete points. The determination of such a second stage constitutive equation requires the identification of a series of characteristic stress, strain points along the now zero-offset, friction corrected and isothermal experimental flow stress curves. These characteristic points are outlined below in Table 5.4.

Table 5.4 Characteristic points along the flow curve needed for the derivation of second stage constitutive equations

Characteristic Point		Description
(i)	σ_0	Stress at the onset of plastic strain
(ii)	$\sigma_{0.1}$	Stress at $\varepsilon = 0.1$
(iii)	σ_p	Peak stress (and corresponding ε_p)
(iv)	σ_{ss}	The onset of stress-strain invariance

In order to incorporate the effects of dynamic recrystallization into a second stage constitutive equation a further characteristic point, $\sigma_{ss(\varepsilon)}$ must be discerned which indicates the onset of steady state conditions in the flow curve extrapolated from the test data to describe the flow behaviour of material which does not dynamically recrystallize. These characteristic points are illustrated in relation to an idealised flow stress curve schematically in Fig. 5.12 below.

It is important to note there that steady state stress-strain invariance was unachievable under certain test conditions of temperature and strain rate under discussion here. Indeed it is noted[7] that the amount of strain required to reach steady state is much larger for material undergoing extended dynamic recovery or continuous dynamic recrystallization (CDRX), e.g. $\varepsilon = 20$, than for lower SFE material in which discontinuous dynamic recrystallisation (DDRX) occurs, e.g. $\varepsilon = 0.5$. Such potentially large strains would be unachievable in uniaxial compression and are most commonly reported for torsional deformation[8], [9].

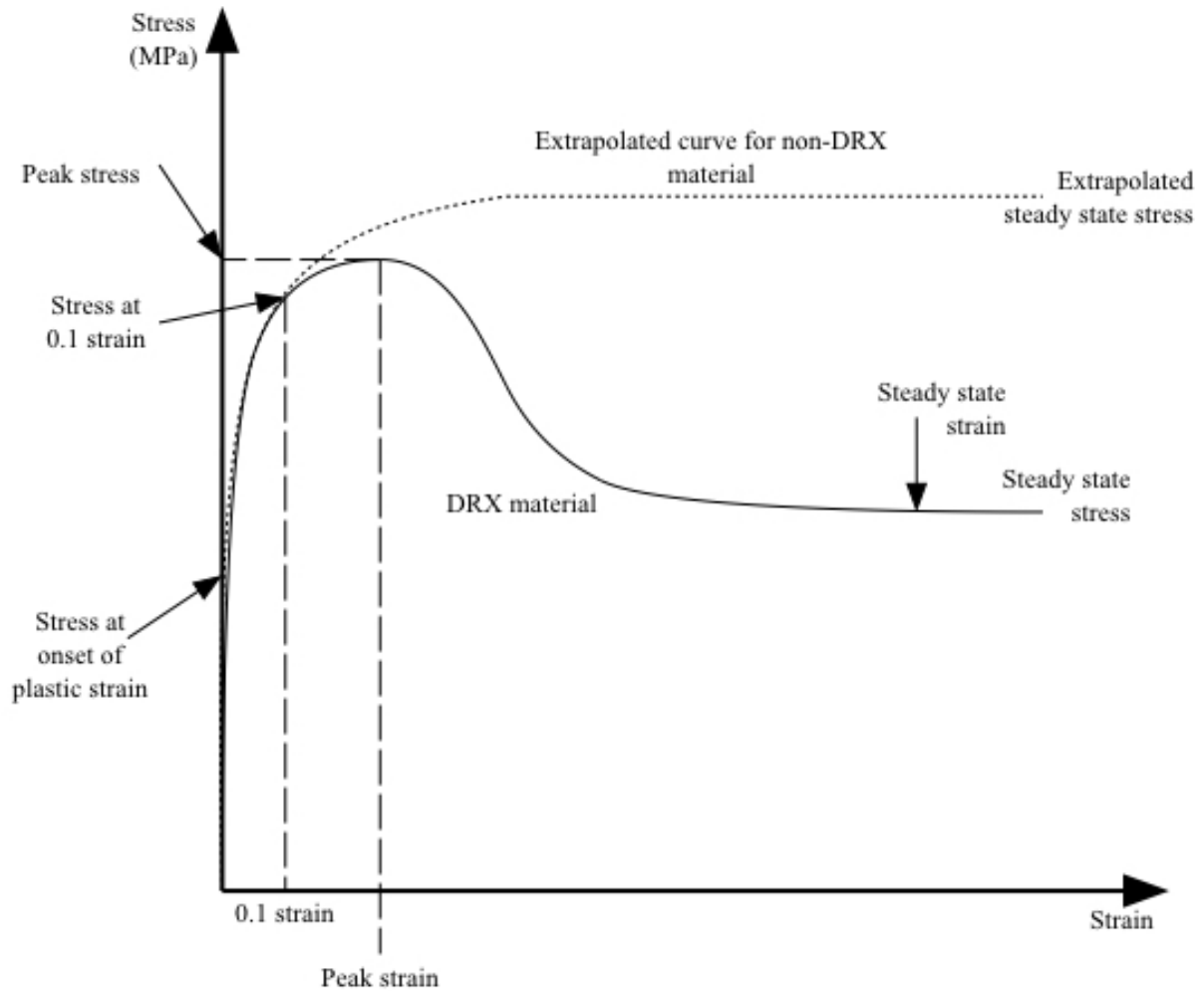


Fig. 5.12 Characteristic points on a flow curve for DRX material illustrated schematically

The value of the fifth characteristic point, $\sigma_{ss(\epsilon)}$ was determined by means of a Kocks-Mecking plot whereby the isothermal flow curves are differentiated with respect to strain and the derivatives plotted against stress. The linear portion of this differential curve is then extrapolated and its point of intersection on the abscissa corresponds to the extrapolated steady state value of flow stress; the characteristic point $\sigma_{ss(\epsilon)}$. For illustrative purposes, the Kocks-Mecking plot for the uniaxial compression test at 1125°C at 0.1 s⁻¹ constant true strain rate is shown below in Fig. 5.13. Fig. 5.13a shows the associated flow curve for this test and from which the yield point is shown to be ca. 55 MPa, with a total temperature drop, ΔT of ca. 52°C as the sample is compressed. Fig. 5.13b shows the derivative, $d\sigma/d\epsilon$ from Fig. 5.13a vs. the equivalent true stress to create the Kocks-Mecking plot.

From the flow data (Fig. 5.13a) the onset of plastic strain and the peak stress are determined and compared for validity against values determined programmatically from the derivative (Fig. 5.14a) values in the Kocks-Mecking plot. Using these values as lower and upper subset bounds, respectively, of the flow data required to determine $\sigma_{ss(\epsilon)}$, a first order polynomial (of the form $d\sigma/d\epsilon = m\sigma + \sigma_{ss(\epsilon)}$) linear regression is applied to the data points on the Kocks-Mecking (K-M) plot between yield and up to ca. $0.82\sigma_p$ (Fig. 5.14b).

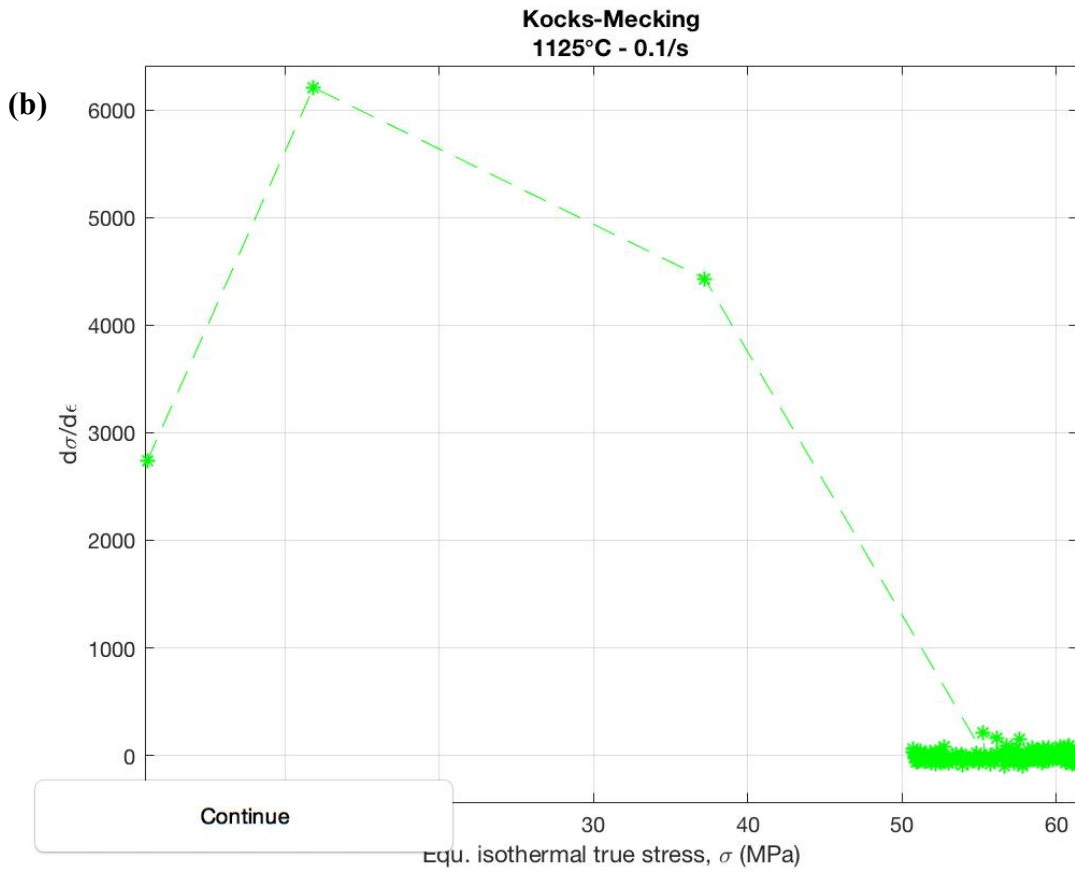
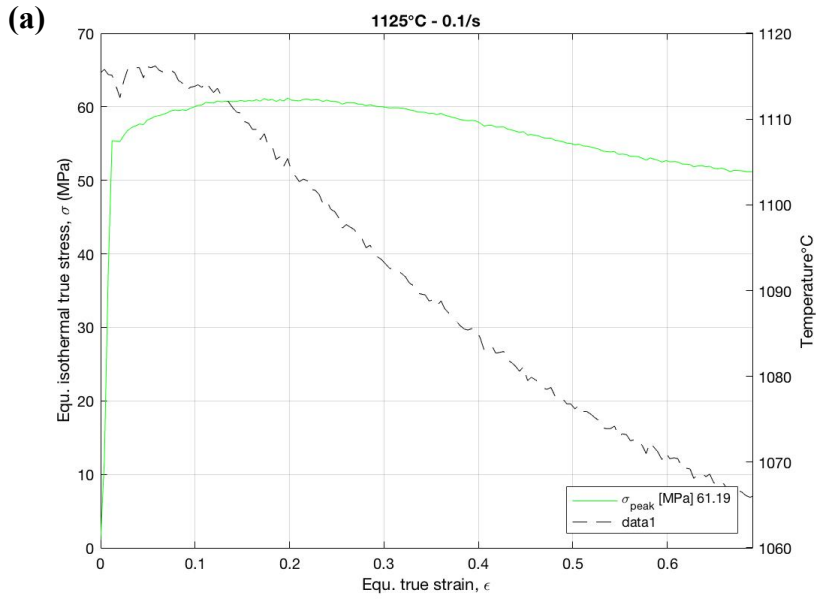


Fig. 5.13 Kocks-Mecking **a** based on flow curve from the uniaxial compression test at 1125°C at 0.1 s⁻¹ constant true strain rate and **b** plot of $d\sigma/d\epsilon$ vs. σ

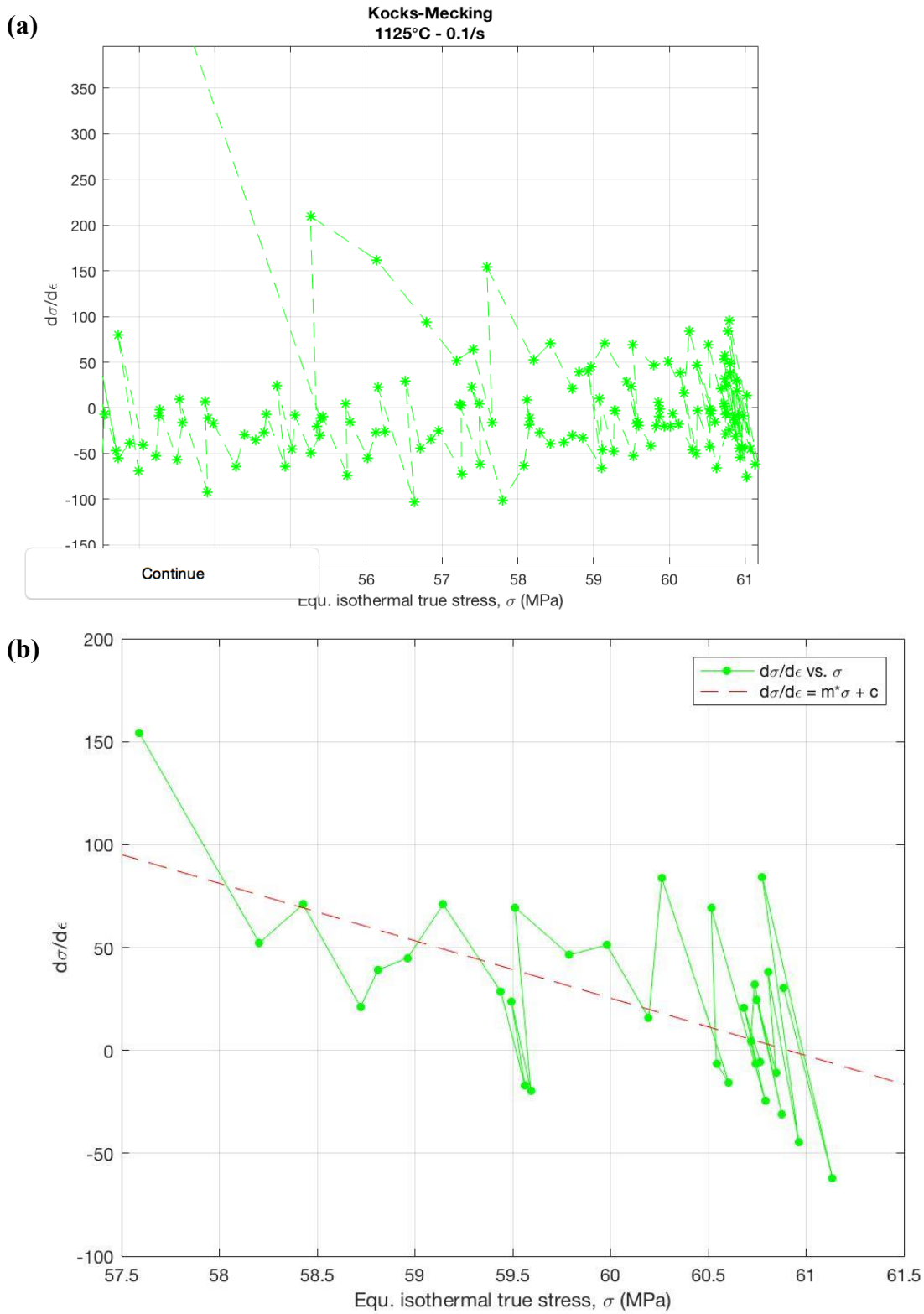


Fig. 5.14 Processed the Kocks-Mecking plot data **a** rescaled K-M plot **b** linear curve fit through the data subset defined between the onset of plastic strain and $0.82\sigma_p$

In order to determine the root of $f(\sigma)$, the algorithm (using a combination of bisection, secant, and inverse quadratic interpolation methods) begins at $\sigma(0)$ and tries to locate a point $\sigma(1)$ where $f(\sigma)$ has the opposite sign of $f(\sigma)$ at $\sigma(0)$. The programme then iteratively shrinks the interval where $f(\sigma)$ changes sign to reach a solution. The function $f(\sigma)$ is specified in the computer code as an anonymised handle and in the case of Fig. 5.14 above this was determined to be $\sigma_{ss(e)} = 60.91$ MPa.

At this point $\sigma_{ss(e)}$ (and other characteristic points, Table 5.2) values can be determined accurately and programmatically from all the flow curves corresponding to the discrete test conditions of deformation temperature and constant strain rate (outlined in Table 4.2) over which the flow behaviour of ZERON® 100 was investigated. Note however, as previously indicated, the sample temperature drop associated with tests conducted at the highest temperature and slowest constant strain rate caused such considerable divergence between the stress calculated from the experimental data and the stress after isothermal correction, that abandonment of these data was necessary and thus determination of characteristic points along their associated flow curves not undertaken.

5.5 First-Stage Constitutive Equations

Although the characteristic points of first-stage constitutive equations described above form the basis of the development of a set of second-stage constitutive equations which describe continuous flow curves in terms of Z and $\dot{\epsilon}$, a first-stage constitutive equation, approximating to a power law at low stresses and to an exponential law at higher stresses, is the hyperbolic sine relationship (Eqn. 5.7) and is typically encountered in computer modelling (of, for example, forming processes such as forging and extrusion) using the FEM.

$$Z = A[\sinh(\alpha\sigma)]^n \quad \text{Eqn. 5.7}$$

Where, A and α are constants and the exponent n is the strain rate sensitivity defined as

$$\partial \ln \sigma / \partial \ln \dot{\epsilon} |_{\epsilon, T}. \quad \text{Eqn. 5.8}$$

Eqn. 5.7 describes the relationship between Z and σ , however only for a point of constant strain and therefore each of the model coefficients are only valid for one characteristic point on the

flow curve. Furthermore, the relationship between α and n can be described by:

$$\alpha = \frac{\beta}{n} \quad \text{Eqn. 5.9}$$

Determination of the β coefficient as a function of strain was discussed previously (Eqn. 5.5) and therefore values of α can be determined for each characteristic point, and though a $\ln - \ln$ plot of Z as a function of $[\sinh(\alpha\sigma)]$, the values of n and A can also be calculated. This leads ultimately to the expression of the first-stage, phenomenological constitutive equation describing the relationship between σ and Z as [10]:

$$\sigma = \left(\frac{1}{\alpha}\right) \sinh^{-1} \left(\frac{Z}{A}\right)^{1/n} \quad \text{Eqn. 5.10}$$

In the case of the experimental data derived from the isothermal uniaxial compression of ZERON® 100 over the temperature and constant strain rate ranges indicated previously, the correspondence to Eqn. 5.10 is demonstrated below, along with an exemplar determination of the model coefficients A , α and n .

At low stresses the dependence of the Z parameter on flow stress may be described by a power law of the form Eqn. 5.11

$$Z = \dot{\epsilon} \exp\left(\frac{Q_{\text{def}}}{RT}\right) = A_1 \sigma^n \quad \text{Eqn. 5.11}$$

From which the strain rate sensitivity exponent, n can be determined empirically by programmatically applying a first order polynomial fit to Eqn. 5.12 over a range of offset stresses which cover the strain to which the samples were tested.

$$\ln Z = n \ln \sigma + \ln A_1 \quad \text{Eqn. 5.12}$$

Figs. 5.15 & 5.16 below indicate the $\ln - \ln$ plots of $Z = f(\sigma)$ from Eqn. 5.11 for the example offset equivalent true stresses at ca. 0.22 and 0.55 strain (as were also used as examples previously in Figs. 5.7, 5.8 & 5.9)

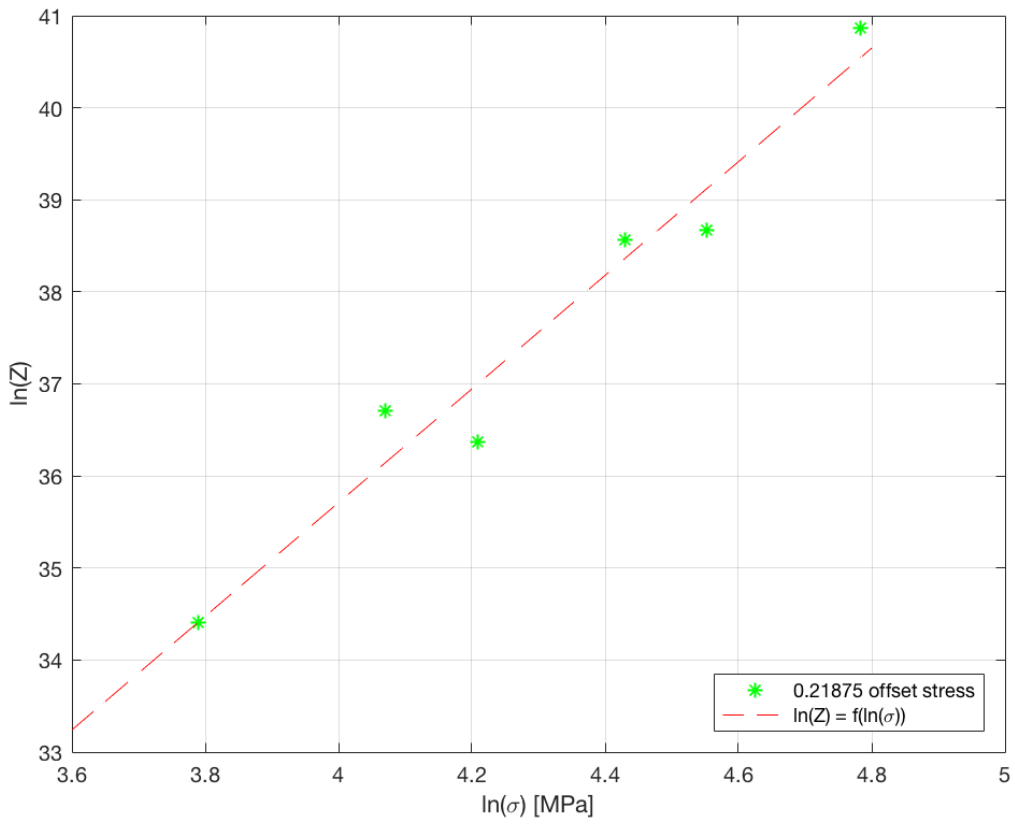


Fig. 5.15 Plot of Eqn. 5.11 for a strain offset ca. 0.22

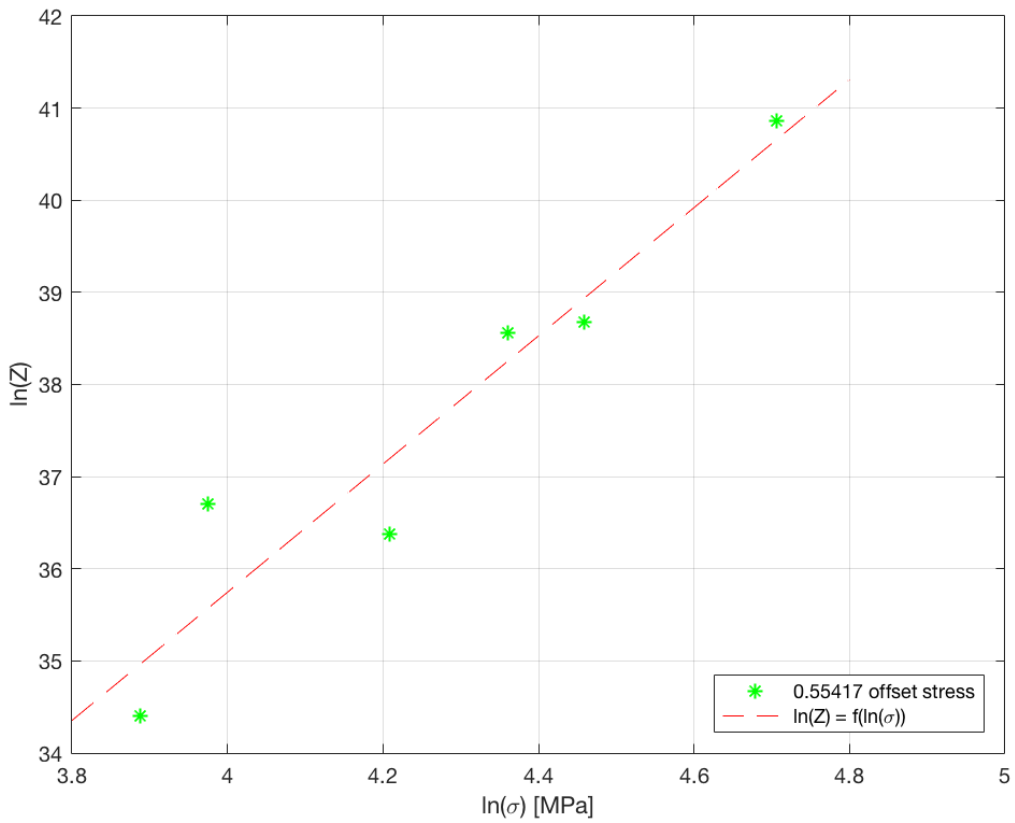


Fig. 5.16 Plot of Eqn. 5.11 for a strain offset ca. 0.55

By averaging the gradient of the plotted function $f(\ln[\sigma])$ over a range stresses at offset equivalent true strains from the onset of plasticity to a half-height compression ($\varepsilon \approx 0.69$) the n term in Eqns.5.9 & 5.10 was determined to be 6.5

The α model coefficient can be determined in a similarly empirical manner from the decomposition of the general constitutive equation (Eqn. 5.9) at high stress into the exponential relation of Z to σ .

$$Z = \dot{\varepsilon} \exp\left(\frac{Q_{\text{def}}}{RT}\right) = A_2 \exp[\beta\sigma] \quad \text{Eqn. 5.13}$$

Noting the relationship between the α and β coefficients identified in Eqn. 5.9, a similar procedure to the determination of the strain rate sensitivity exponent can be adopted to find α from Eqn. 5.13

$$\ln Z = \beta\sigma + \ln A_2 \quad \text{Eqn. 5.14}$$

Figs. 5.17 & 5.18 below indicate the \ln – normal plots of $\ln(Z) = f(\sigma)$ from Eqn. 5.14, again for the example stresses at offset equivalent true strains of ca. 0.22 and 0.55

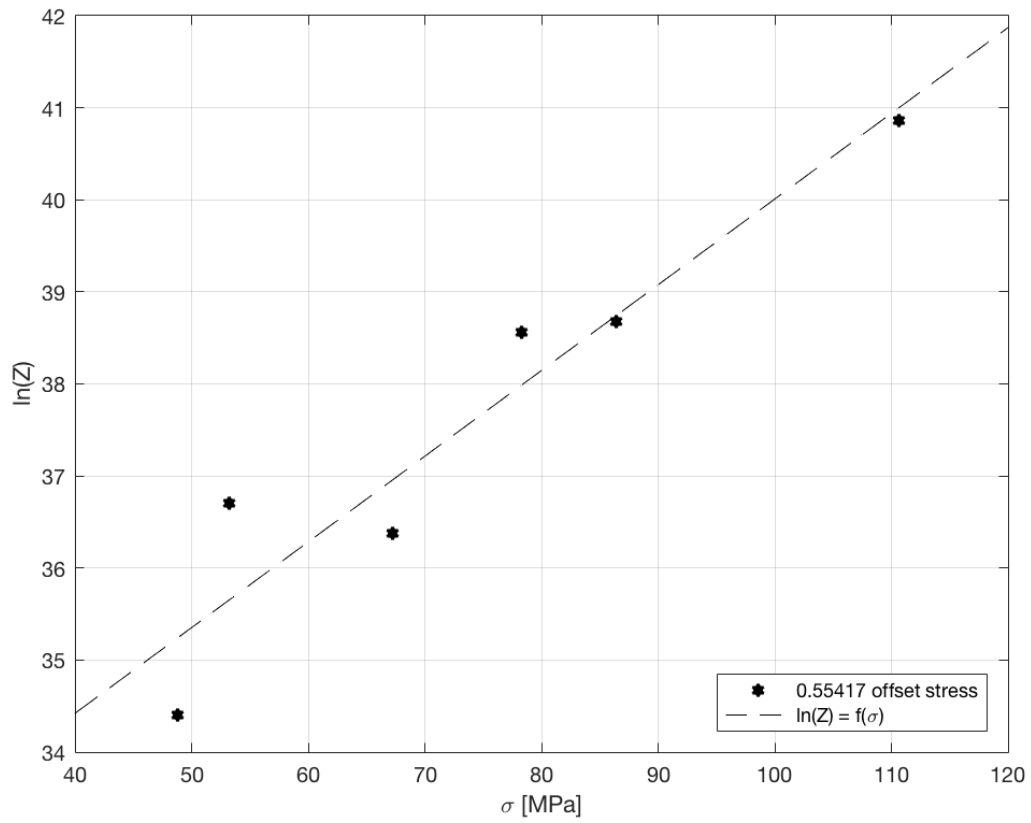


Fig. 5.17 Plot of Eqn. 5.13 for a strain offset ca. 0.55

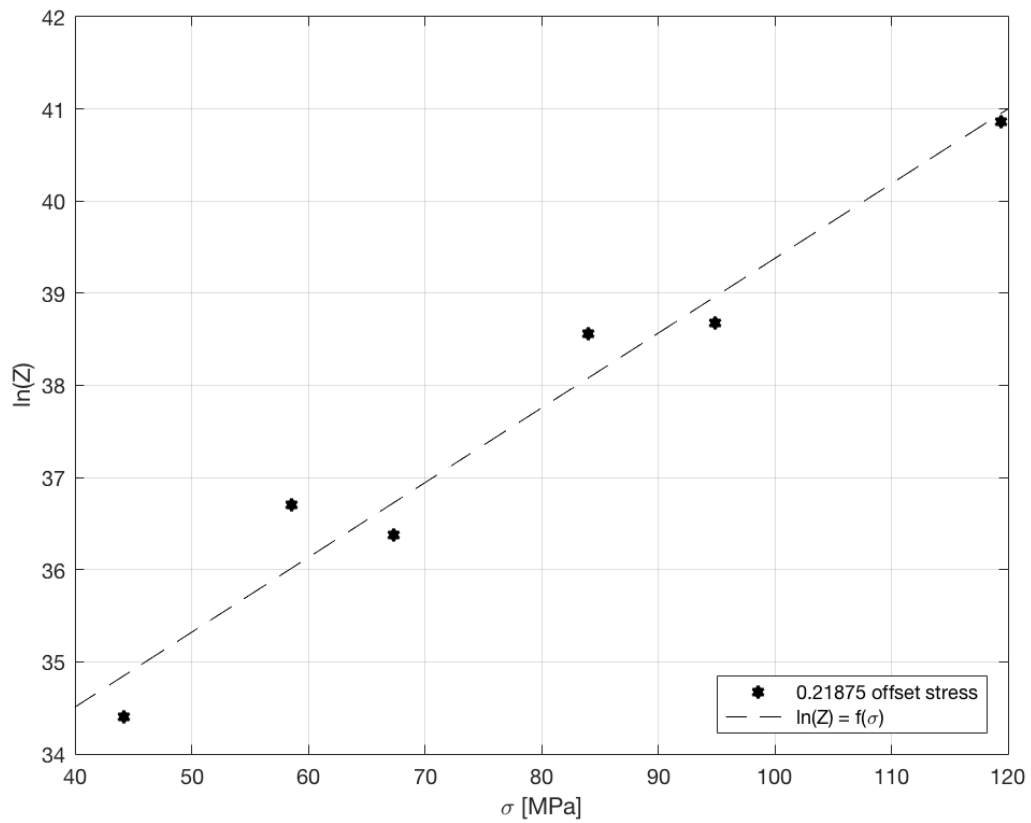


Fig. 5.18 Plot of Eqn. 5.13 for a strain offset ca. 0.22

By averaging the gradient of the plotted function $f(\sigma)$, as demonstrated in Figs. 5.17 & 5.18, over the range of offset equivalent true stresses corresponding to range of equivalent true strains from the onset of plasticity (ε_0) to a half-height compression ($\varepsilon \approx 0.69$), and then solving Eqn. 5.8, the α coefficient in Eqn. 5.9 was calculated as 0.0113 MPa^{-1} .

Finally, the remaining unknown model coefficient, A from Eqns. 5.7 & 5.10 was determined from Eqn. 5.15

$$\ln Z = n \ln(\sinh[\alpha\sigma]) + \ln A \quad \text{Eqn. 5.15}$$

Figs. 5.19 & 5.20 show example plots of $\ln(Z) = f(\sinh[\alpha\sigma])$ for stresses at offset strains of, again, ca. 0.22 and 0.55.

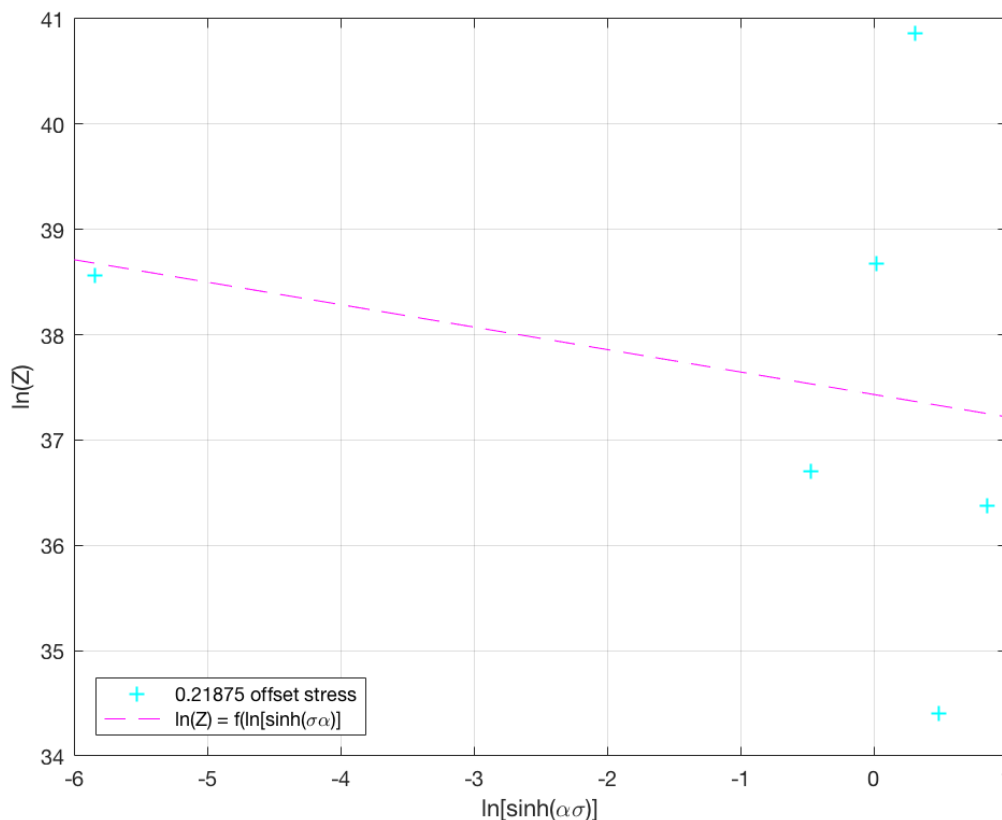


Fig. 5.19 $\ln(Z) = f(\sinh[\alpha\sigma])$ for stresses at a strain offset of ca. 0.22

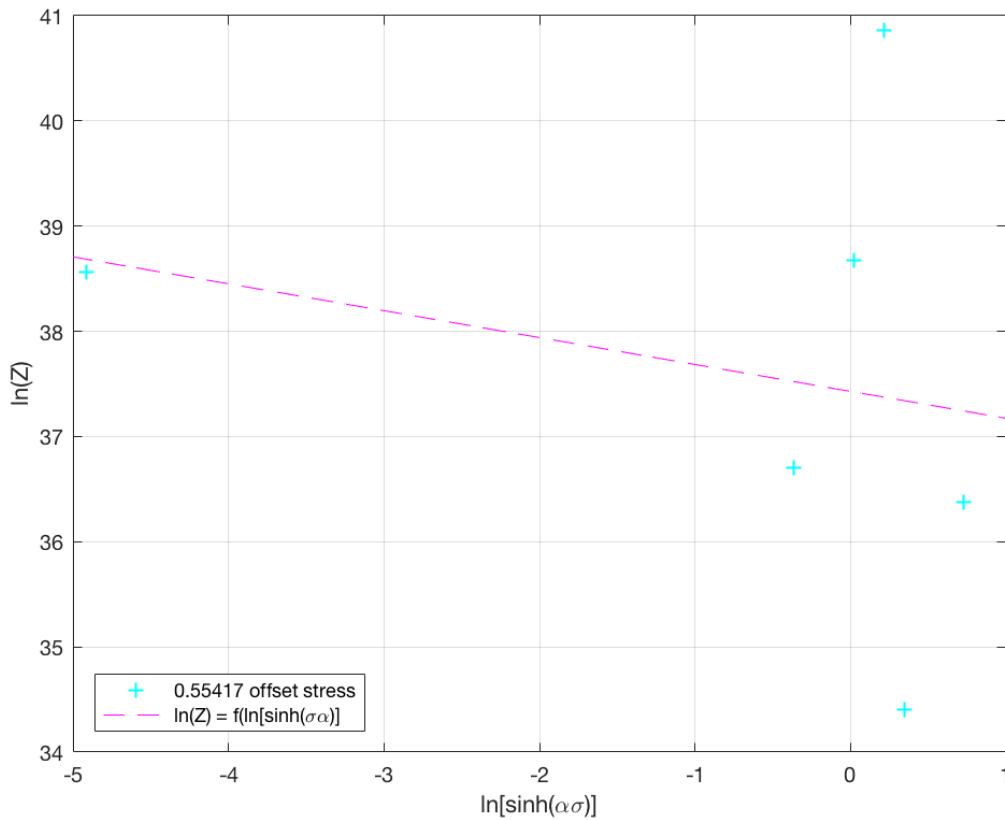


Fig. 5.20 $\ln(Z) = f(\sinh[\alpha\sigma])$ for stresses at a strain offset of ca. 0.55

Taking the average of this plotted function over the range of offset stresses corresponding to the maximum strain to which the samples were compressed produces a value for the A coefficient of 1.8×10^{16} .

Combining the above determined model coefficients allows the expression of the first stage constitutive equation (Eqn. 5.9) as:

$$\sigma = \left(\frac{1}{0.0113}\right) \sinh^{-1} \left(\frac{Z}{1.8 \times 10^{16}}\right)^{1/6.5} \quad \text{Eqn. 5.16}$$

Eqn. 5.16 allows for description of the dependence of ZERON® 100's flow stress on temperature and strain rate (as associated by the Zener – Hollomon parameter). Validation of the above work in deriving the model coefficients for the first stage constitutive equation is presented in Table 5.5 where the obtained parameters above can be compared against equivalent published data for other duplex and super duplex materials (cast and wrought products) deformed, variously, in uniaxial, plane strain compression (PSC) and tension modes.

Table 5.5 Comparative published values for first stage constitutive flow model coefficients (* indicates data from present study)

n	Equation Parameter α [MPa ⁻¹]	A	Q_{def} [kJ mol ⁻¹]	Material	Mode of Deformation	Reference
4.2	0.0139		450	2304 (hot rolled)	PSC	[11]
3.8	0.008		380	2304 (as cast)	PSC	[12]
6.9	0.009	1.5×10^{22}	569	2205	Uniaxial	[13]
4	0.007		438	2507	compression Uniaxial	[13]
4.9	0.014	8.4×10^{14}	430	2205	compression Tensile	[6]
6.5	0.0113	1.8×10^{16}	439	ZERON® 100	Uniaxial	*
6.6	0.012	1.5×10^{20}	461	2205 (hot rolled)	compression Uniaxial	[5]

5.6 Second Stage Constitutive Equations

As previously noted, the first-stage constitutive equations detailed above only define non-continuous, discretised points on the flow stress curve and therefore a further set of equations are required if the flow curves are to be described continuously in terms of Z and ε ; these are the second-stage constitutive equations.

Davenport et al.[1] note that the extrapolated curve indicated schematically in Fig. 5.12 as representative of material which does not undergo DRX can be described by:

$$\sigma = \sigma_0 + (\sigma_{ss(e)} - \sigma_0)\sqrt{(1 - \exp[-\varepsilon/\varepsilon_r])} \quad \text{Eqn. 5.17}$$

Where the term ε_r (the transient strain constant) defines the curvature of the flow curve between the onset of plastic straining and saturation. To a first approximation, this transient strain constant is given as:

$$\varepsilon_r = -0.1 \ln[1 - (\sigma_{0.1} - \sigma_0)/(\sigma_{ss(e)} - \sigma_0)^2] \quad \text{Eqn. 5.18}$$

In order to fully define the above continuous second stage equations in terms of Z and ε it is necessary to describe the characteristic points in these equations as functions of Z . The determination of the characteristic points on the flow curve (Table 5.2) used in the second stage constitutive equations as functions of Z is outlined below.

The dependence of σ_0 of Z is indicated in Fig. 5.21

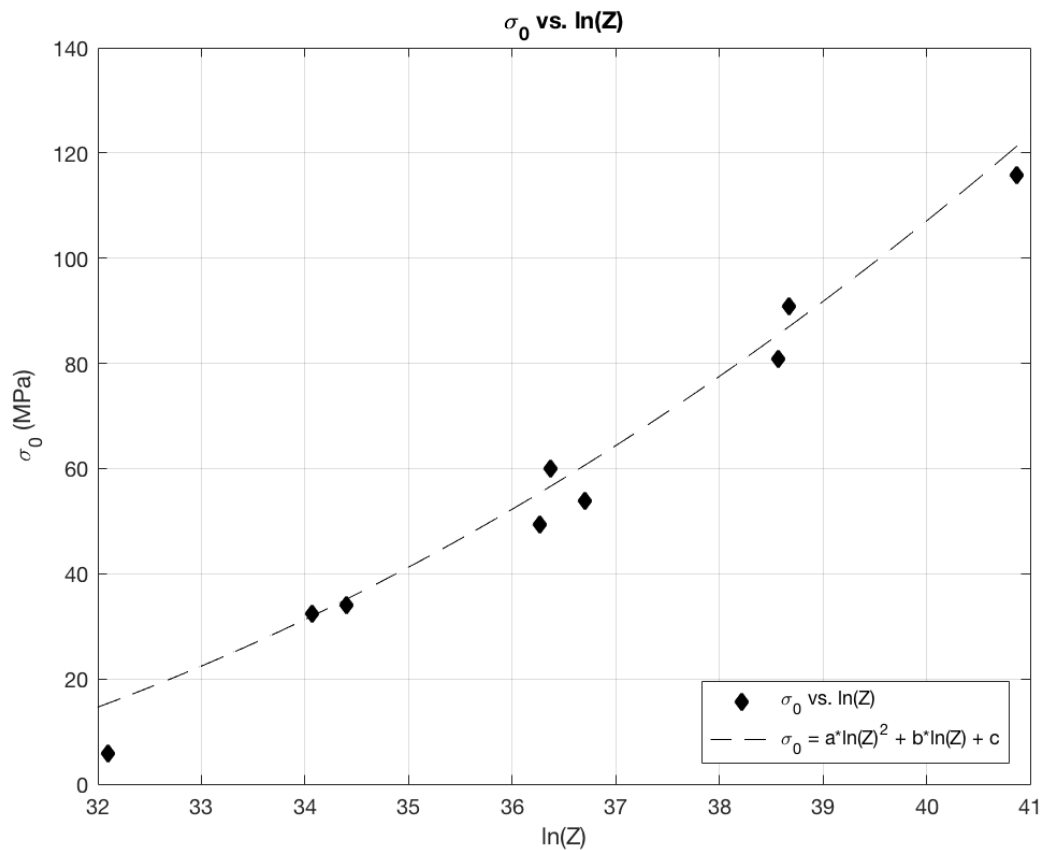


Fig. 5.21 Characteristic point σ_0 as a function of $\ln(Z)$

As an indication of the correctness of fit of the model describing the dependence of σ_0 on Z shown in Fig. 5.21, a residual plot is presented below in Fig. 5.22. The residuals, r shown in Fig. 5.22 are defined as the differences between the response data and the fit to the response data at each predictor value. Mathematically, this can be expressed as:

$$r = y - \hat{y} \tag{Eqn. 5.19}$$

Where the residual for a specific predictor value is the difference between the response value y and the predicted response value \hat{y} .

Assuming a high fidelity fit between model and data, the residuals should approximate to random errors and therefore, random residual behaviour can be taken as indicative of a good fit between model and data.

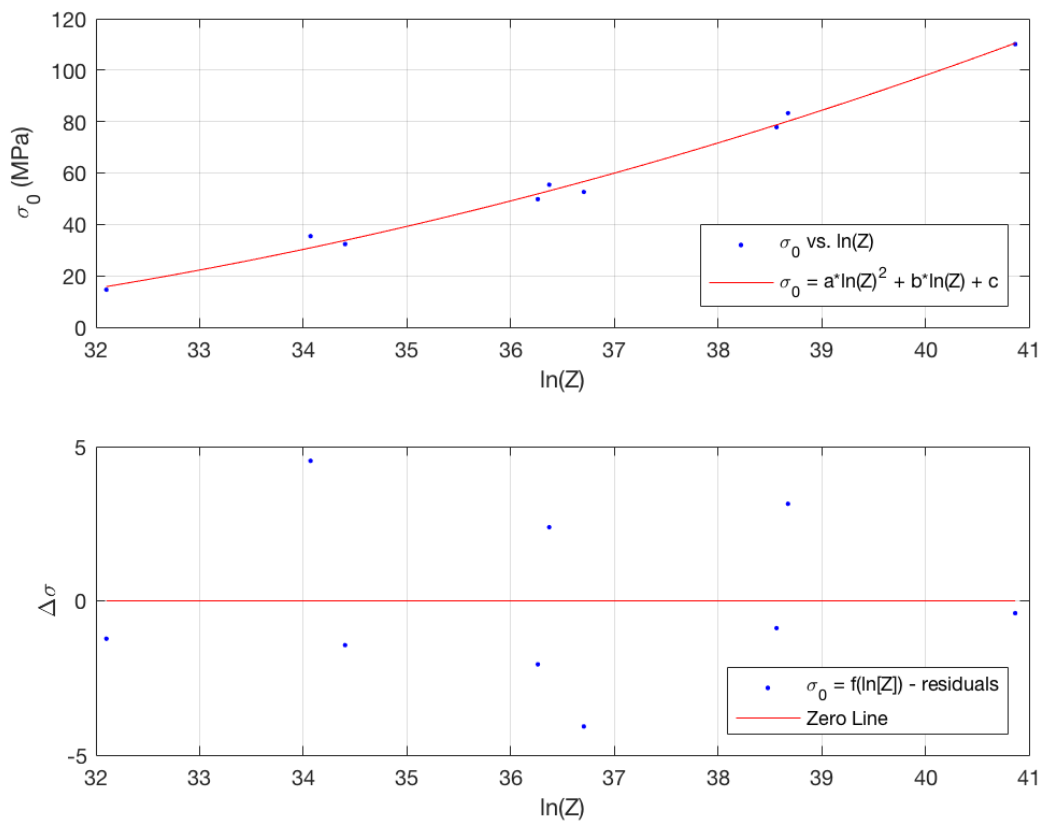


Fig. 5.22 Residuals plot for the second order polynomial model fit of σ_0 to $\ln(Z)$

The residuals indicated in Fig. 5.22 and goodness of fit statistics indicate a good correspondence between the second order polynomial model $\sigma_0 = 0.4639 \ln(Z)^2 - 23.0490 \ln(Z) + 277.6879$ and the data.

This same approach is repeated below to find the function that describes the dependence of the next characteristic point on the flow curve, $\sigma_{0.1}$ on Z , as indicated in Fig. 5.23

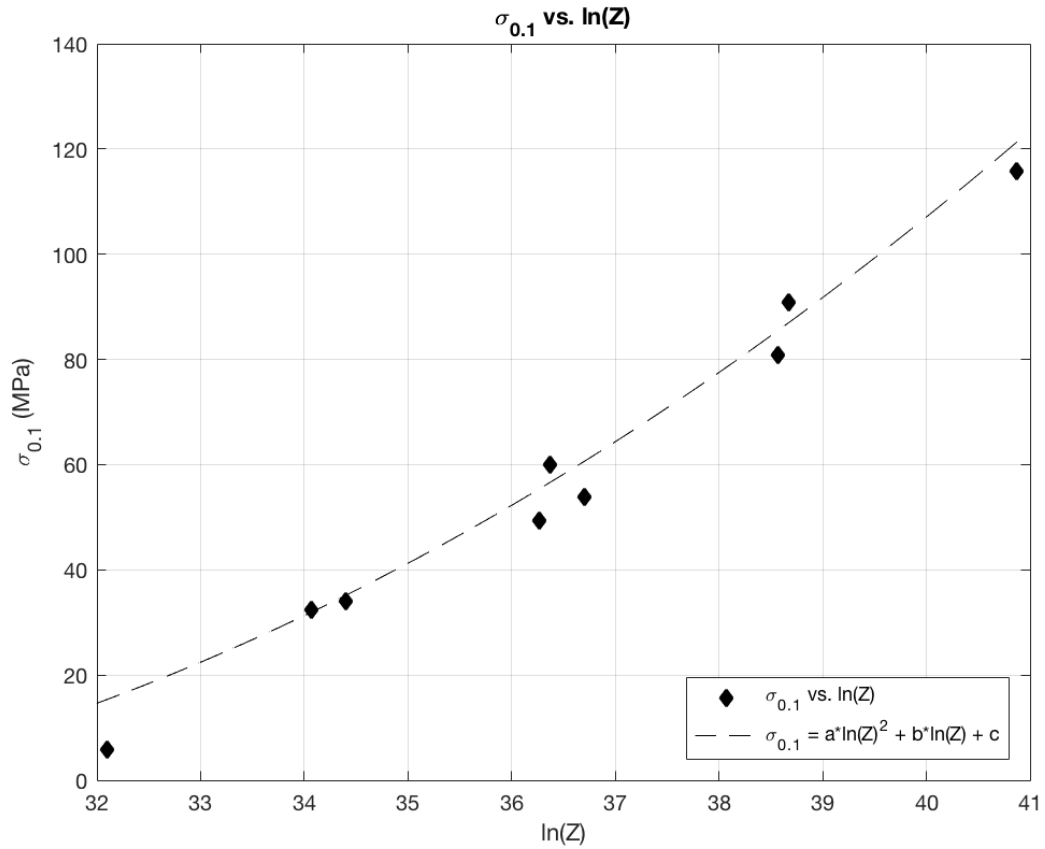


Fig. 5.23 Characteristic point $\sigma_{0.1}$ as a function of $\ln(Z)$

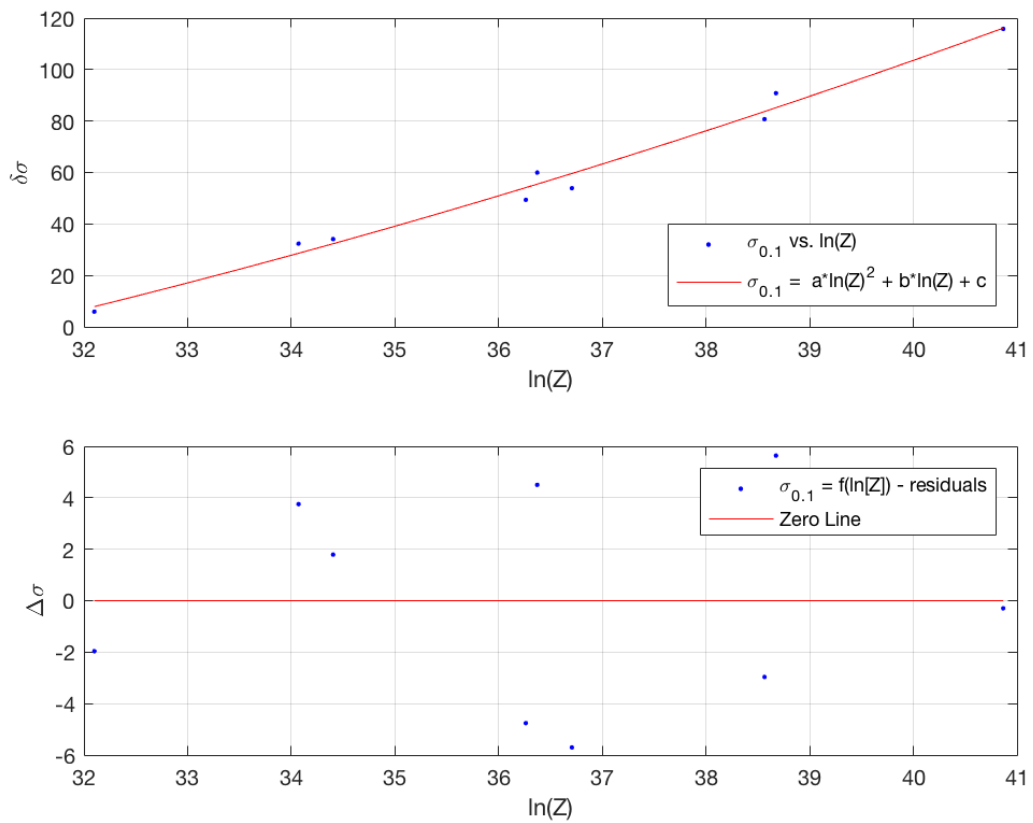


Fig. 5.24 Residuals plot for the second order polynomial model fit of σ_0 to $\ln(Z)$

Figs. 5.23 & 5.24 indicate, again, that a second order polynomial function describes well the dependence of σ_0 on $\ln(Z)$. In this instance, the function is given as $\sigma_{0,1} = 0.2682 \ln(Z)^2 - 7.226 \ln(Z) - 36.56$. The residuals in Fig. 5.24 appear randomly scattered relative to the fit (the zero line) indicating a good correspondence between the model and the data.

Finally, a linear (first order polynomial) model was found to best describe the relationship between the extrapolated point of stress-strain invariance, as determined through the K-M plots detailed previously, and Z . This is illustrated below in Figs. 5.25 & 5.26

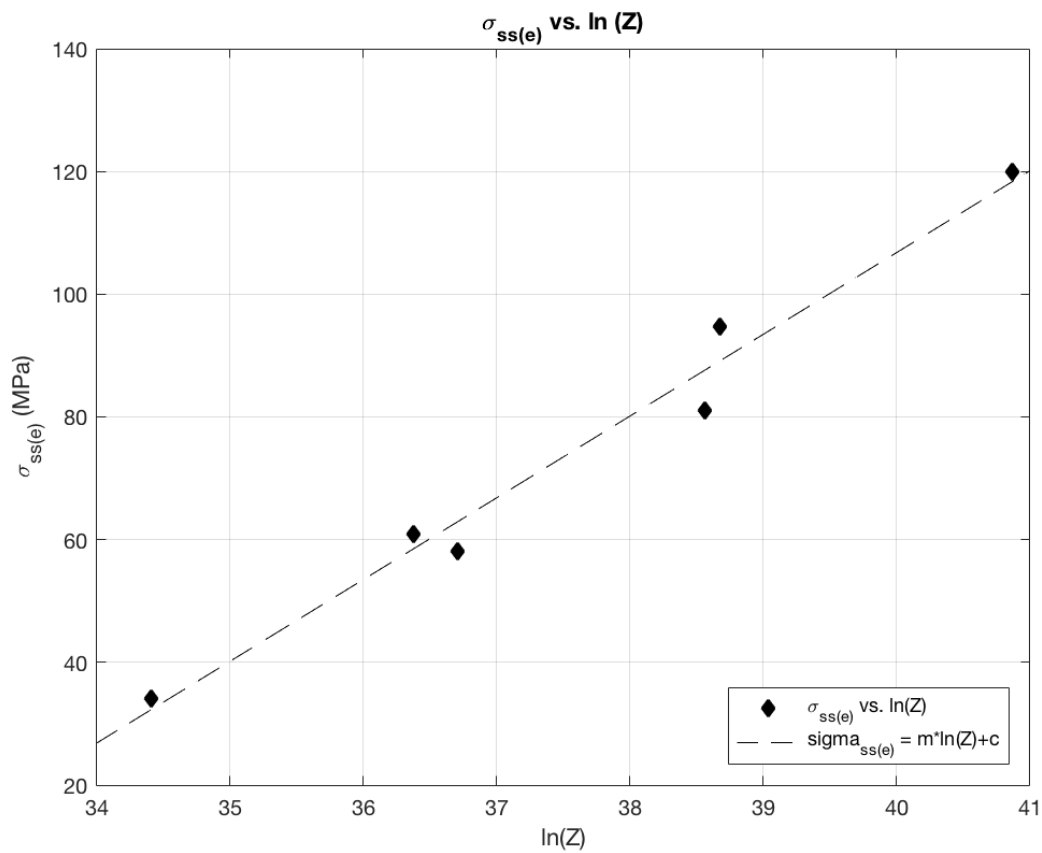


Fig. 5.25 The characteristic point defining the onset of stress-strain invariance as a function of $\ln(Z)$

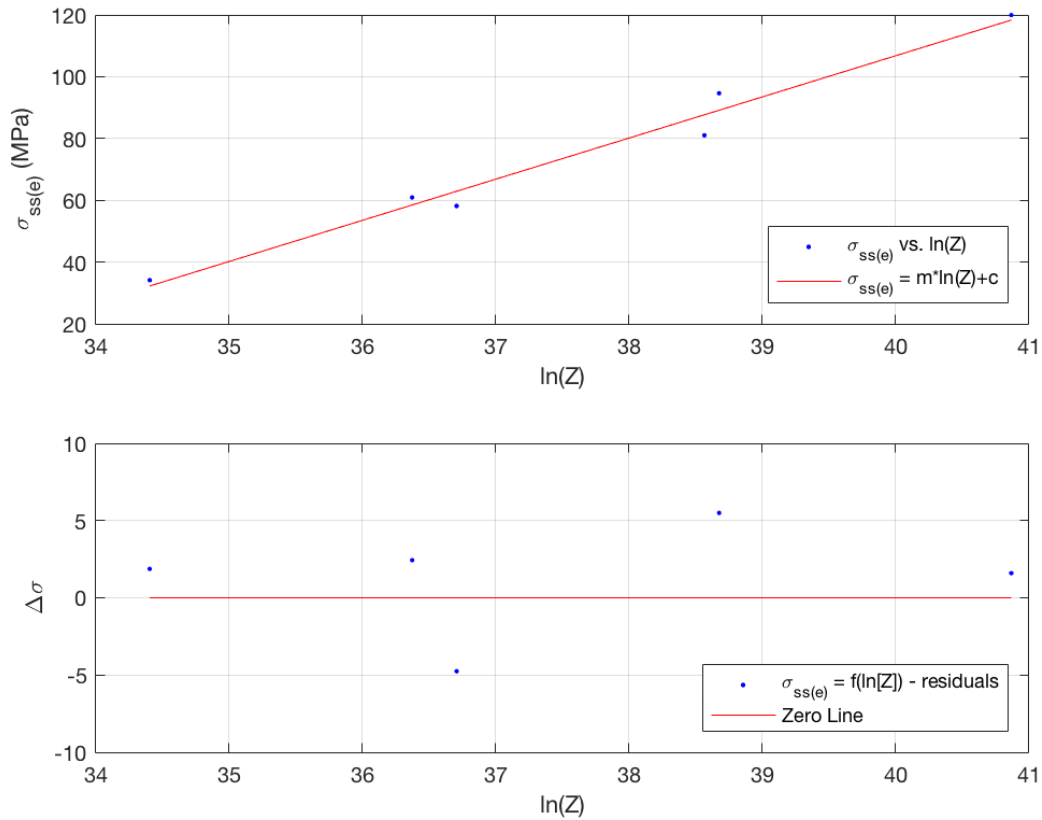


Fig. 5.26 Residuals plot for the linear fit of $\sigma_{ss(e)}$ to $\ln(Z)$

The random scattering of the residuals in Fig. 5.26 about the zero line indicate a good agreement between the model, in this case $\sigma_{ss} = 13.32 \ln(Z) - 426$ and the data.

At this point, with the characteristic points on the flow curve defined in terms of functions of Z it is possible to use Eqns. 5.16 & 5.17 to plot modelled flow curves and compare their fidelity to the data derived from the uniaxial compression experiments. In this way, the appropriateness of the derived Eqns. 5.16 & 5.17 in describing the flow behaviour of ZERON® 100 can be validated.

Figs. 5.27 - 5.29 indicate the modelled flow response at the strain rates 0.1 s^{-1} and 1 s^{-1} for isothermal uniaxial compression at 1050°C , 1125°C and 1 s^{-1} at 1200°C . Note the omission of test data and modelled fits for the 0.01 s^{-1} test parameter at all temperatures due to the previously discussed divergence between the stress calculated from the experimental data and the stress after isothermal correction as a result of the convective/radiative heat transfer caused by temperature differences between the samples and tool furnace and conductive losses from excessive (ca. 70 s) contact time between the thermally heterogeneous dies and samples.

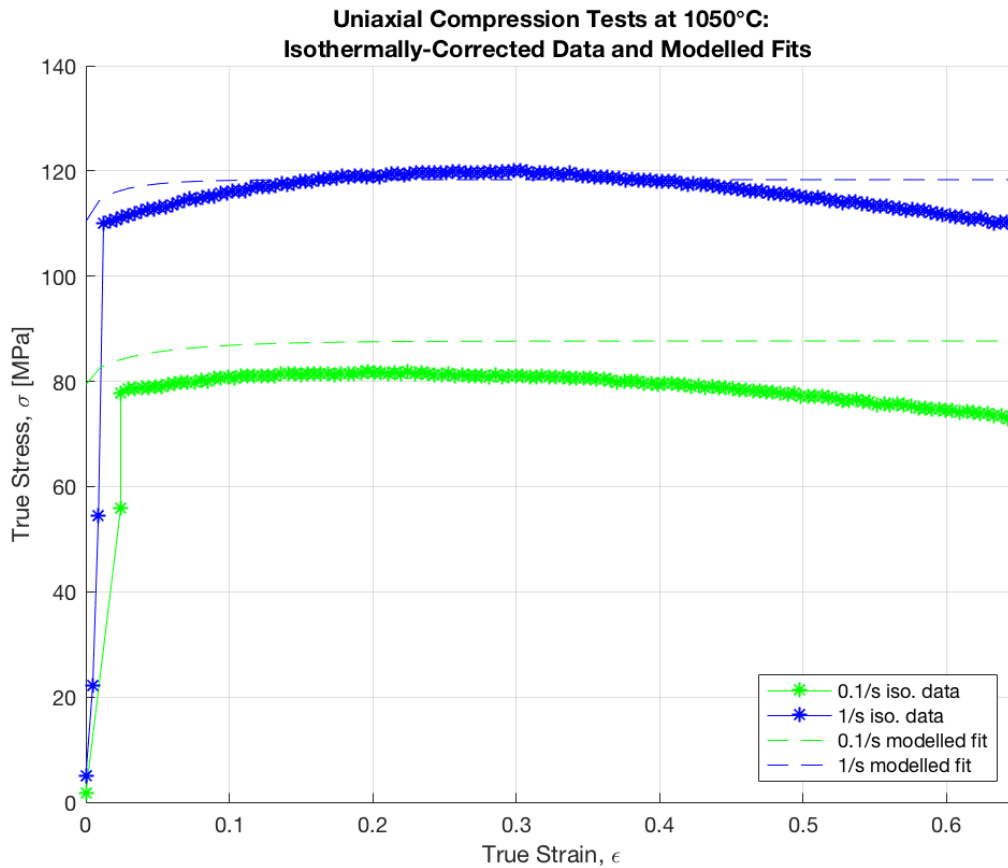


Fig. 5.27 Corrected data & second-stage constitutive flow modelling at 1050°C and 0.1 and 1 s⁻¹ strain rates

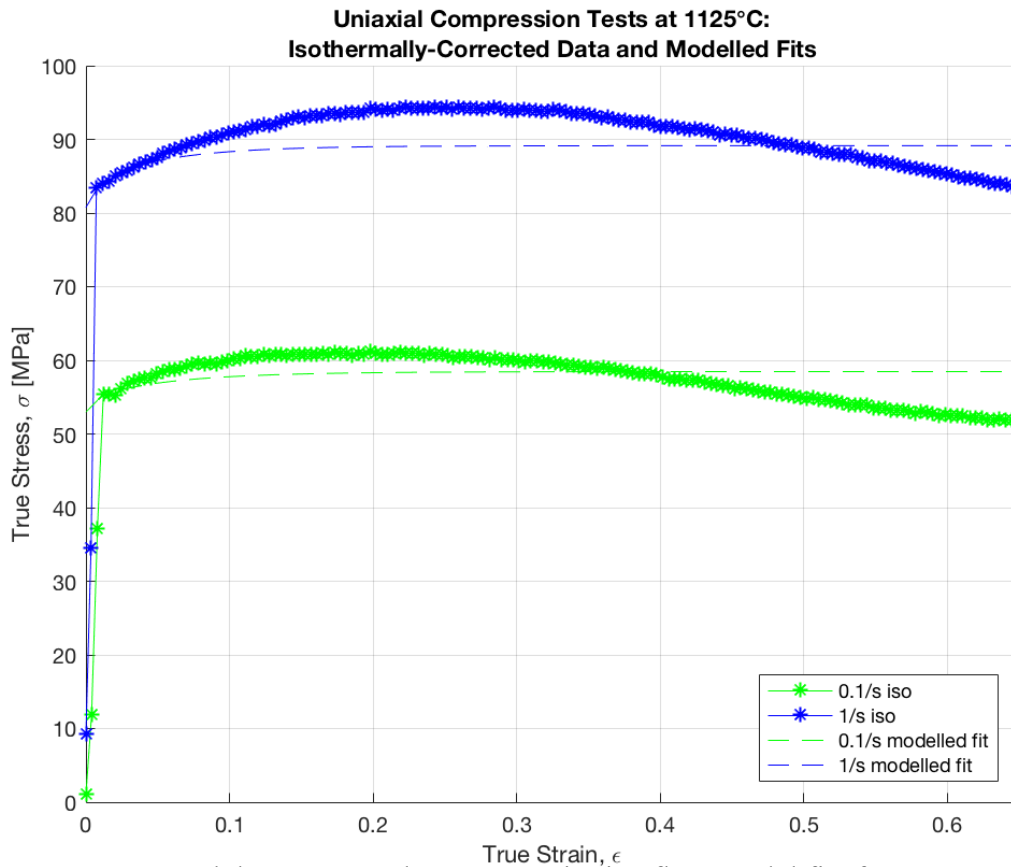


Fig. 5.28 Corrected data & second-stage constitutive flow model fits for tests at 1125°C and 0.1 and 1 s⁻¹ strain rates

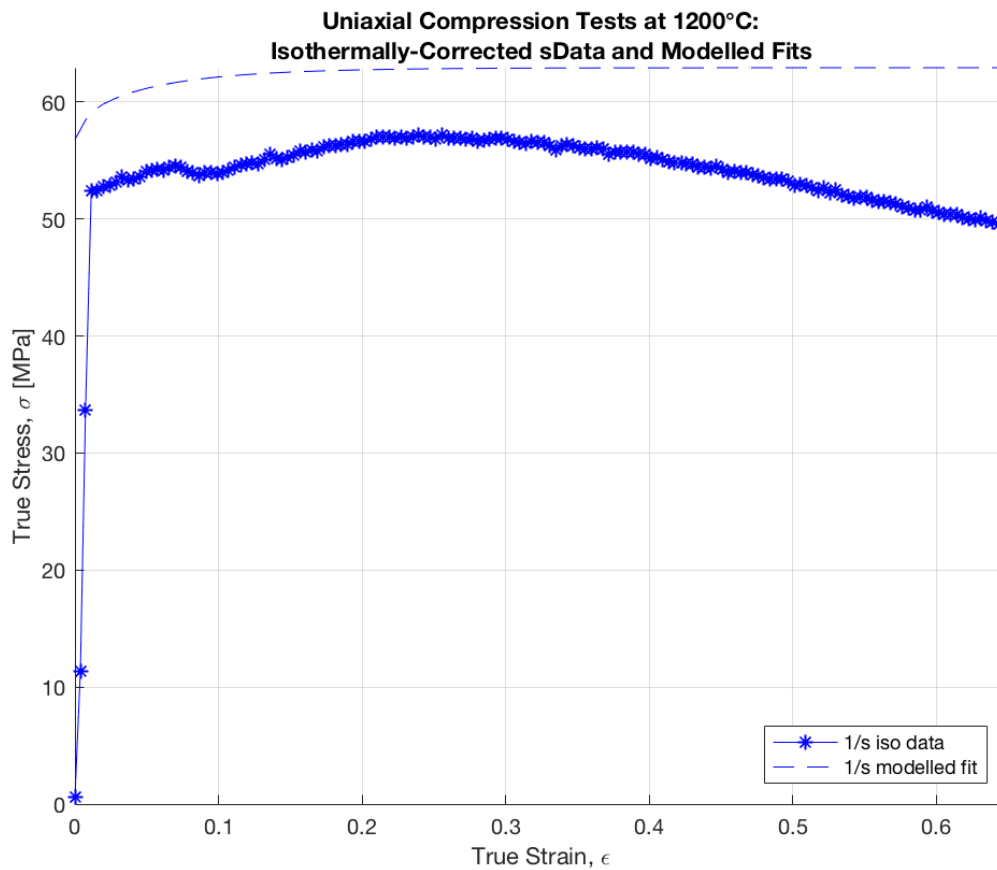


Fig. 5.29 Corrected data & second-stage constitutive flow model fits for test at 1200°C and 1 s⁻¹ strain rate

5.7 Summary

Data has been presented from the nominally isothermal uniaxial compression of wrought ZERON® 100 material at constant true strain rates. A complex deformation response is exhibited and for which discrete and continuous constitutive flow models have been developed in an attempt to describe this behaviour.

The coefficient values calculated for the first stage, discrete general constitutive equation were compared against published data available in the literature (Table 5.3) as a means of verification. This first –stage constitutive equation (Eqn. 5.15)[14], provides a description of the fundamental parameters affecting the flow relation $\sigma(T, \epsilon, \dot{\epsilon})$ in the high Z regime and in following chapters of this work will be used, in part, in the specifications of a material model in the FEA of the thermo-mechanical processing operations through which a 16” ZERON® 100 weld neck flange component is produced.

This material model should specify the flow curve of the workpiece material being deformed, necessitating the FEA program to perform interpolation between the available data. To avoid interpolation errors therefor a constitutive equation derived from data over a wide range of test conditions, representative of those encountered in the simulated process, is optimal. It is therefore important at this point to note the limitations of the model presented here due to the demonstrated complexities in flow behaviour of ZERON® 100 material at extremes of temperature and strain rate and the ultimately limited processing window represented by the final data presented in Figs. 5.28 – 5.30.

It was noted previously that the TMC's tool furnace and tooling is capable of achieving a maximum temperature of 1050°C and thus large temperature differences were shown (Fig. 5.1) to arise between the dies and samples pre-heated in the FTTU. These temperature differences are likely to be a significant factor acting to affect and complicate the plastic response due to the importance of temperature on flow behaviour. At the slowest strain rate the samples were in contact with the tooling for ca. 70 s and as such, in this extreme case, conductive thermal losses will have a significant impact on the exhibited flow behaviour. Indeed, for nominal isothermal uniaxial compression at 1125°C and 1200°C, temperature decreases during deformation in the range ca. 50 - 120°C can be seen (Fig 5.1b & 5.1c). Such temperature changes will invariably act to affect the duplex phase balance, and therefore by extension are likely to also influence the amount of strain partitioning between ferrite and austenite and in turn prejudicing the predominance of the DRV vs. DRX softening mechanisms.

Assessment of the constitutive equations presented above suggests a reasonable approximation to the flow behaviour of ZERON® 100, albeit *importantly within a limited processing window of temperature and strain rate*. Further development of the constitutive equations through a $\Delta\sigma$ correction as described in Eqn. 3.5 to capture the apparent decrease in stress after the peak presents an obvious opportunity to extend this work by accounting for the presumed increase in the rate of dynamic recrystallization leading to this flow softening. It is however appropriate at this point to consider the purpose of a constitutive equation to be able to generally describe flow behaviour over a range of temperatures and strain rates and, conflictingly, the incapability to this end of an 'overfitted model'. Further development of the constitutive equations to better fit the flow data effectively should be considered against the accuracy of the experimental data.

These experimental data are subject to servo-hydraulic, PID etc. machine effects inherent in the design and operation of the TMC. In addition, the accuracy of the tool furnace's recorded temperature and equivalence to that of the tooling inside are also likely to affect the accuracy of the data. As a consequence of the test geometry, frictional effects (as manifest in the 'barrelling' of the sample) may well have also introduced artefacts into the data for which the correction applied in Eqn. 5.2 is too simplistic. Finally, and perhaps most importantly, the previously noted microstructure effects have a significant impact on the accuracy of the data due, but not limited to, the constantly variable phase balance (and thus associated level of strain partitioning, tertiary precipitation etc.). These microstructure effects will also likely be further complicated by the through-thickness inhomogeneity in the billet, as demonstrated in Ch. 2. Starting ferrite bandwidths and duplex phase proportions in the TMC samples were shown to vary with displacement along the radius from the centre of the billet suggesting that the flow behaviour may be, in part at least, also influenced by the origin of the test sample.

The microstructures, as prepared and micrographed according to the methodologies outlined in Ch. 2.6.2.1 and Ch. 4.5, of the uniaxial compression test samples are illustrated below in Fig. 5.30 and Fig. 5.31. In Fig. 5.30 & Fig. 5.31, those samples corresponding to deformation at 1050°C and 1125°C and strain rates of 0.1 s⁻¹ and 1 s⁻¹ are presented since the constitutive equations developed above most closely describe the flow data from these tests.

Microstructures are also presented in Fig. 5.32. These micrographs were taken from the sample compressed at 1200°C and 1s⁻¹ strain rate, since the corrected flow data and associated constitutive mode for this test condition, illustrated in Fig. 5.29, show some agreement, albeit with less fidelity than indicated in Fig. 5.28 & Fig. 5.27.

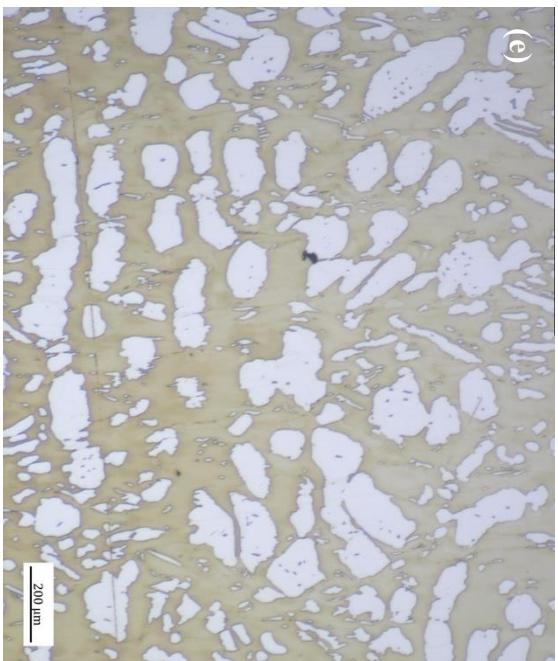
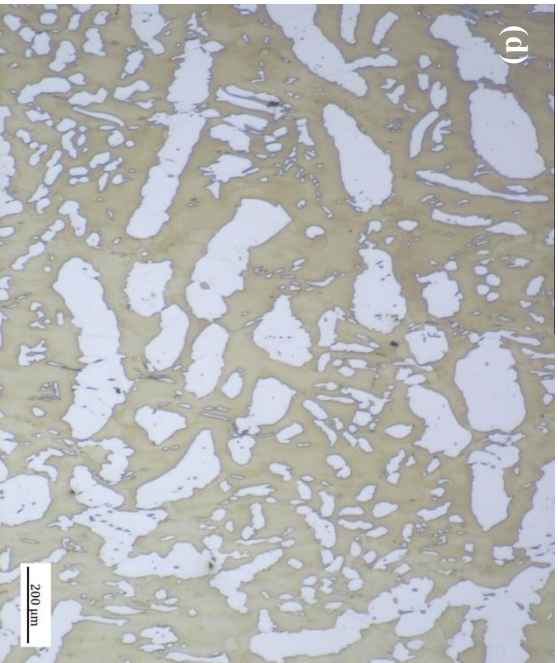
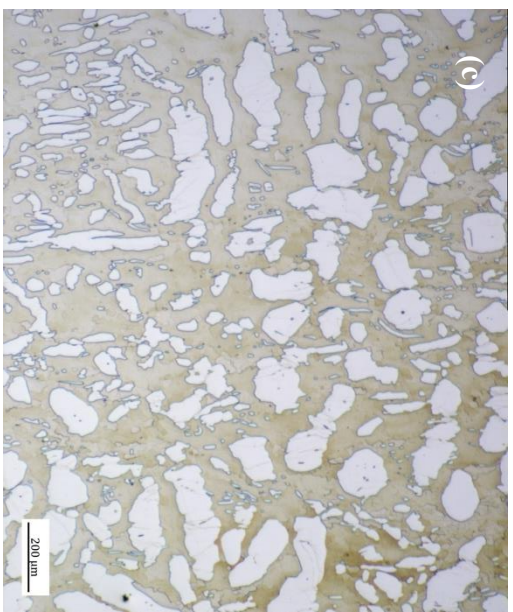
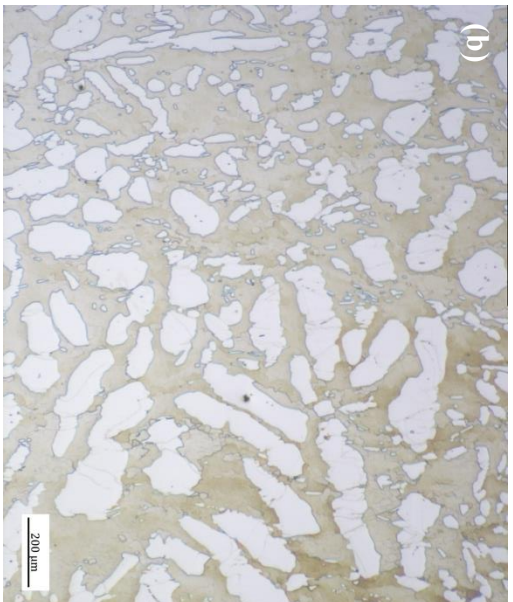
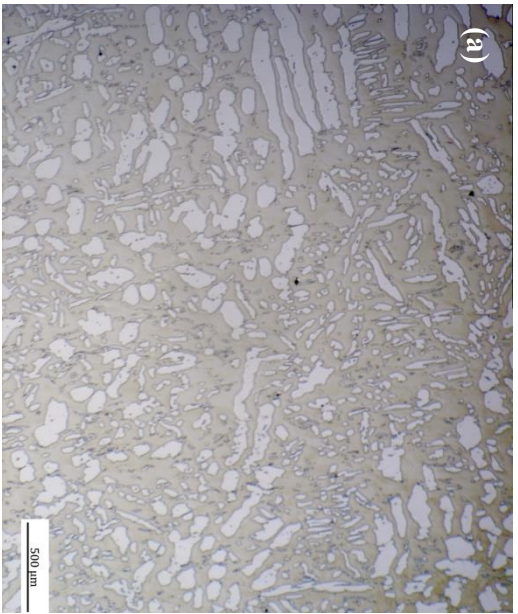


Fig. 5.30 Micrographs from nominally isothermal uniaxial compression at 1050°C and **a** – **c** strain rate, $\dot{\epsilon} = 0.1$ and **d** – **e** strain rate, $\dot{\epsilon} = 1$

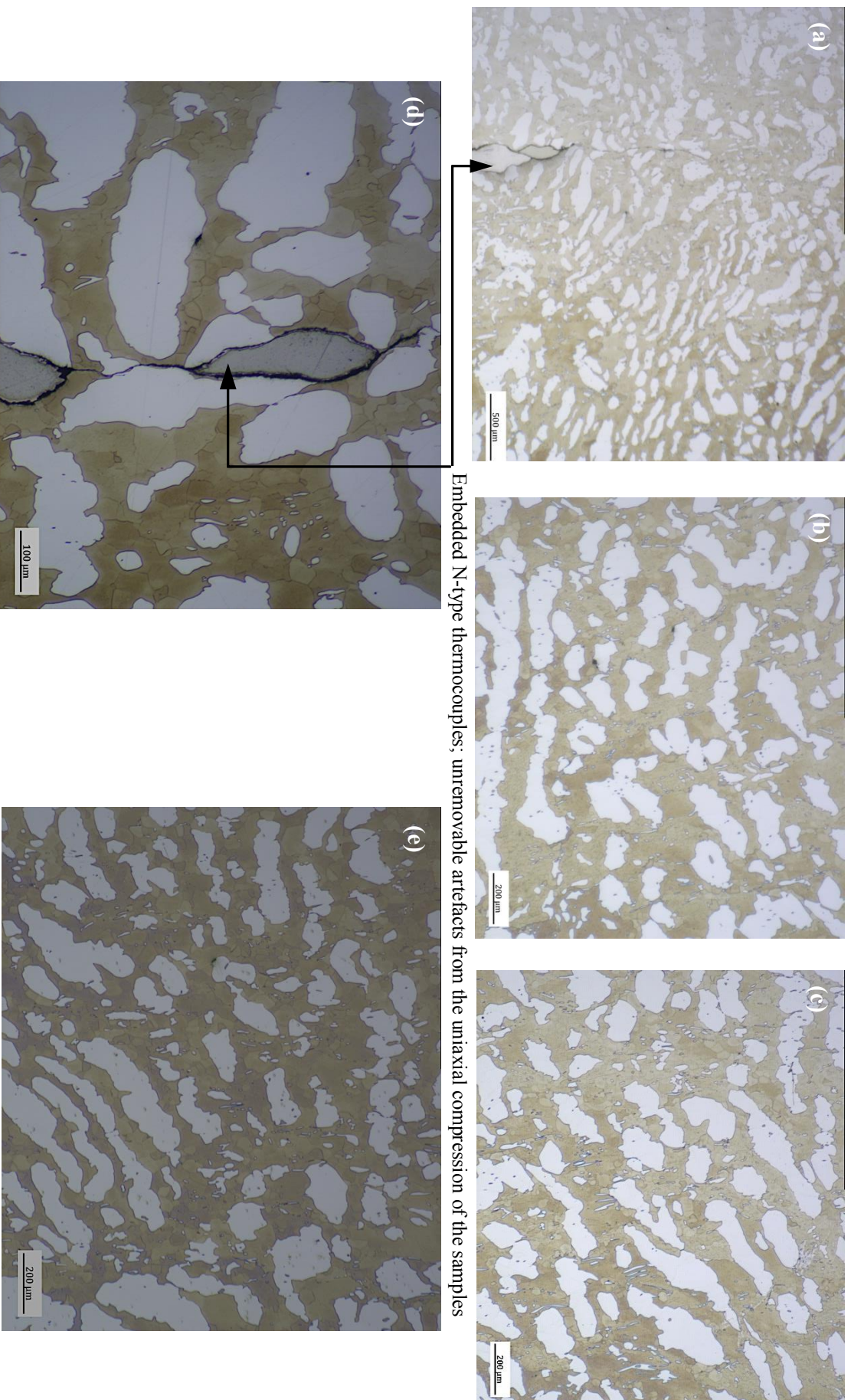


Fig. 5.31 Micrographs from nominally isothermal uniaxial compression at 1125°C and **a** – **c** strain rate, $\dot{\epsilon} = 0.1$ and **d** – **e** strain rate, $\dot{\epsilon} = 1$

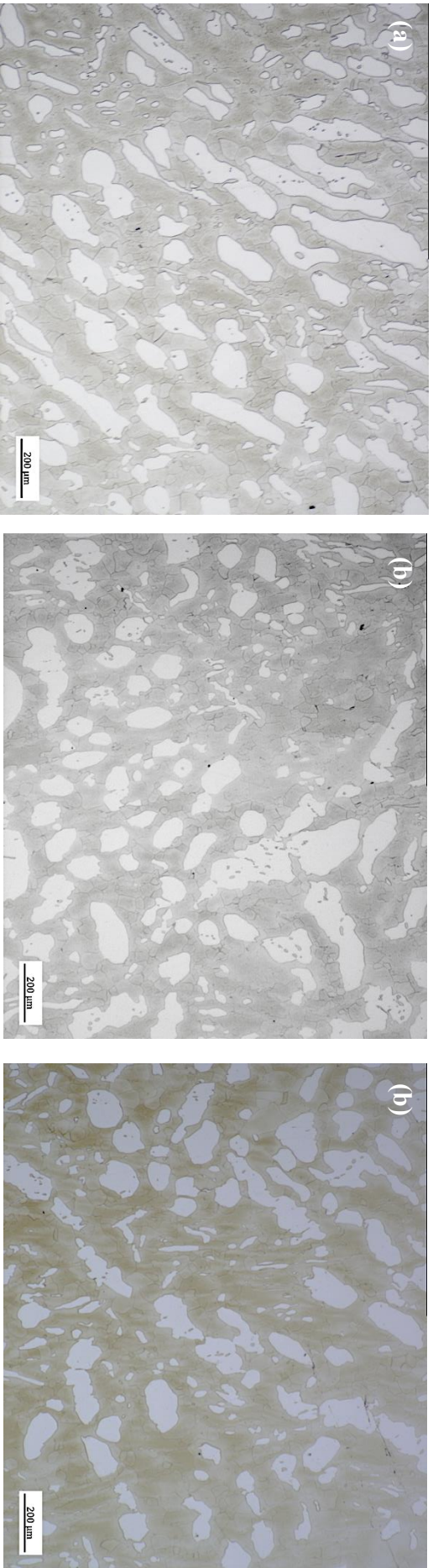


Fig. 5.32 Micrographs from nominally isothermal uniaxial compression at 1200°C and constant strain rate, $\dot{\epsilon} = 1$

The conductive heat loss from the samples to the tooling during slow compression at the higher deformation temperatures makes general evaluation of the flow behaviour difficult, as has been previously discussed. However, the data presented in Fig. 5.11a where the closest approximation to thermal homogeneity was achieved (and isothermal corrections for adiabatic heating etc. made to negate temperature effects) provides an opportunity for a general, albeit somewhat limited, characterisation of the stress-strain response.

At 1050°C a predominately austenitic duplex microstructure is predicted by equilibrium thermodynamics. The low SFE of austenite reduces the rate at which recovery occurs and instead the build-up of lattice strain leads to the initiation of new ‘defect-free’ recrystallised grains. When this process occurs during deformation it is termed dynamic recrystallisation (DRX)[15]. However, the typical stress-strain behaviour of austenite, as characterised by work hardening to peak stress followed by decreasing stress with increasing strain until steady state is reached, is not immediately apparent. Instead, at a constant strain rate of 0.01 s⁻¹, following the rapid attainment of peak stress, the profile of the flow curve appears to approximate to strain invariance (albeit with slight work softening). This behaviour may be interpreted as the balance of ‘equal and opposite’ work hardening and recovery dislocation events.

As strain rate increases to 0.1s⁻¹ and 1s⁻¹, a marked change in the stress-strain curves is seen whereby the peak stress and associated strain increase. These stress-strain curves also indicate more work hardening occurs at faster strain rates. The duplex microstructure complicates the interpretation of this trend[16] due to a possible difference in the sensitivity of austenite and ferrite to strain rate potentially causing a disproportionate distribution of the load between them as strain rate increases[9]. The extensive twinning in the austenite phase deformed at 1s⁻¹ strain rate (Fig. 5.33) suggests that the increase in work hardening seen at the fastest strain rate is accompanied by a subsequent increase in DRX. The parallelism of these ‘perfect’ twins indicates likely formation as a response to DRX during uniaxial compression, as opposed to being artefacts from the steel making process through which the as received billet was produced and out of which the TMC samples were machined. In the latter case, the twins would have deformed during compression rather than forming (in ‘perfectly parallel alignment’) as a result. Confirmation of the precise nature of these twins and thus the likelihood of their formation as a result of DRX required analysis of EBSD misorientation data, of the type presented subsequently in Ch. 7.

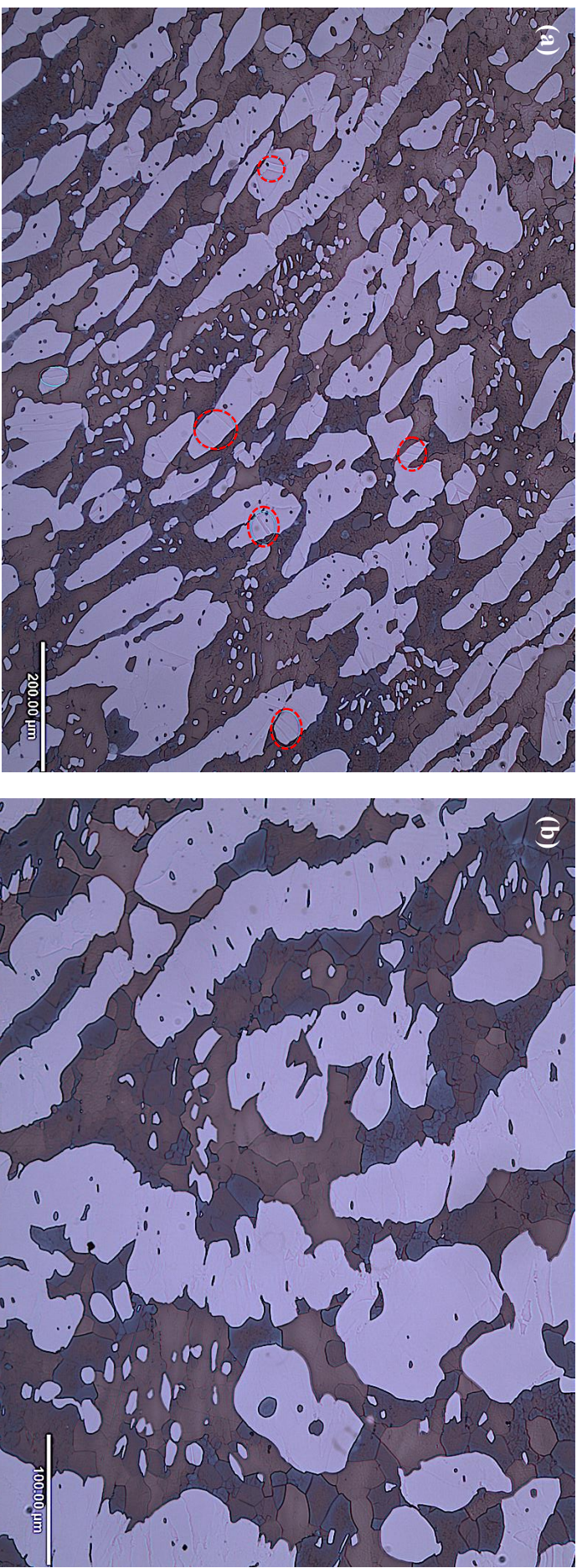


Fig. 5.33 Extensive twinning in the uniaxial compression samples deformed at 1050°C and 1 s^{-1} strain rate **a** examples of the numerous, presumed DRX, twins are circled in blue **b** higher ($\times 20$) magnification showing the twins in greater detail

REFERENCES

- [1] S. B. Davenport, N. J. Silk, C. N. Sparks, and C. M. Sellars, "Development of Constitutive Equations for Modelling of Hot Rolling," *Mater. Sci. Technol.*, vol. 16, no. May, pp. 539–546, May 2000.
- [2] H. Shi, A. J. McLaren, C. M. Sellars, R. Shahani, and R. Bolingbroke, "Constitutive equations for high temperature flow stress of aluminium alloys," *Mater. Sci. Technol.*, vol. 13, no. 3, pp. 210–216, Mar. 1997.
- [3] S. L. Semiatin, "Workability in Forging," in *Handbook of Workability and Process Design*, 2003, pp. 187–207.
- [4] B. Roebuck, J. D. Lord, M. Brooks, M. S. Loveday, C. M. Sellars, and R. W. Evans, "Measurement of flow stress in hot axisymmetric compression tests," *Mater. High Temp.*, vol. 23, no. 2, pp. 59–83, Jan. 2006.
- [5] Y. Yang and B. Yan, "The microstructure and flow behavior of 2205 duplex stainless steels during high temperature compression deformation," *Mater. Sci. Eng. A*, vol. 579, pp. 194–201, Sep. 2013.
- [6] M. Faccoli and R. Roberti, "Study of hot deformation behaviour of 2205 duplex stainless steel through hot tension tests," *Journal Mater. Sci.*, vol. 48, pp. 4196–5203, 2013.
- [7] F. Montheillet, "Modelling discontinuous and continuous dynamic recrystallization," in *J.J. Jonas Symposium on Thermomechanical Processing of Steel*, 2000, pp. 297–310.
- [8] Y. C. Lin and X.-M. Chen, "A critical review of experimental results and constitutive descriptions for metals and alloys in hot working," *Mater. Des.*, vol. 32, no. 4, pp. 1733–1759, Apr. 2011.
- [9] L. Duprez, B. C. De Cooman, and N. Akdut, "Flow stress and ductility of duplex stainless steel during high-temperature torsion deformation," *Metall. Mater. Trans. A*, vol. 33, no. 7, pp. 1931–1938, Jul. 2002.
- [10] S. L. Semiatin and T. Altan, "Measurement and interpretation of flow stress data for the simulation of metal forming processes," Wright-Patterson Air Force Base, OH, 2010.
- [11] A. Iza-Mendia, A. Pinol-Juez, J. J. Urcola, and I. Gutierrez, "Microstructural and mechanical behaviour of a duplex stainless steel under hot working conditions," *Metall. Mater. Trans. A*, vol. 29A, pp. 2975–2986, 1998.
- [12] A. Iza-Mendia and I. Gutierrez, "Factors affecting the hot workability of duplex stainless steels," in *Duplex 2007 International Conference & Expo.*, 2007.
- [13] J. M. Cabrera, A. Mateo, L. Llanes, J. M. Prado, and M. Anglada, "Hot deformation of duplex stainless steels," *J. Mater. Process. Technol.*, vol. 143–144, pp. 321–325, 2003.
- [14] C. M. Sellars and W. J. McTegart, "On the mechanism of hot deformation," *Acta Metallurgica*, vol. 14, no. 9, Pergamon, pp. 1136–1138, 01-Sep-1966.
- [15] P. M. Hodgson, J. J. Jonas, and C. H. J. Davies, "Modeling of hot and warm working of steels," in *Handbook of Thermal Process Modeling of Steels*, C. H. Gur and J. Pan, Eds. Boca Raton: CRC Press, 2009, pp. 225–264.
- [16] E. Evangelista, H. J. McQueen, M. Niewczas, and M. Cabibbo, "Hot workability of 2304 and 2205 duplex stainless steels," *Can. Metall. Q.*, vol. 43, no. 3, pp. 339–353, Jan. 2004.

Chapter 6: Finite Element Method Simulations of ZERON® 100 Thermo-Mechanical Processing

The mathematical basis of the finite element method (FEM) as applied to metal forming processes was introduced in Ch.4. The ability of the commercially available, and industrially ubiquitous, DEFORM™ FEM-based engineering software system has been used to analyse the thermo-mechanical manufacturing processes through which ZERON® 100 weld neck flange components are produced. DEFORM™ is specially designed to handle large deformations with its automatic remeshing algorithms maintaining mesh quality and special formulations for large deformation and changing contact conditions. In particular, this chapter details the work undertaken to investigate the evolution of thermal and strain profiles within a ZERON® 100 forging as a result of various open- and closed-die forging and heat treatment processes.

The FEM simulation in DEFORM™ of the final QHT operation is detailed separately in Ch. 8, as part of the experimental process through which location-specific cooling rates in the forging were replicated and assessed in terms of effects upon impact toughness.

Initial DEFORM™ FEM simulations of the TMC uniaxial compression testing, through which the data to establish the constitutive equations were derived, are detailed below.

6.1 Initial Simulation of the TMC Uniaxial Compression Testing

Finite element simulation of the experimental uniaxial compression tests (lab-scale analogues of open die upsetting) detailed in Table 4.2 was carried out as means of seeking to validate the constitutive equations developed to describe the flow behaviour of ZERON® 100 (and detailed previously in Ch. 5).

Simulations of the TMC uniaxial compression tests in DEFORM™ were carried out as 2-D, single blow deformations. The movement of the top tool was specified as a hydraulic press, controlled by a constant average strain rate. As per Ch. 5, a constant friction coefficient of 0.25 was used. A stopping criteria of 7.5 mm displacement between the tools was specified in correspondence to half-height compression of the samples. A mesh of ca. 2500 elements was used to cover the sample.

Results from FEM simulation of the TMC uniaxial compression tests may be summarised in terms of the strain profile developed within the, initially, cylindrical, samples as illustrated schematically in Fig. 6.1. and may be compared to low magnification micrographs in Fig. 6.2

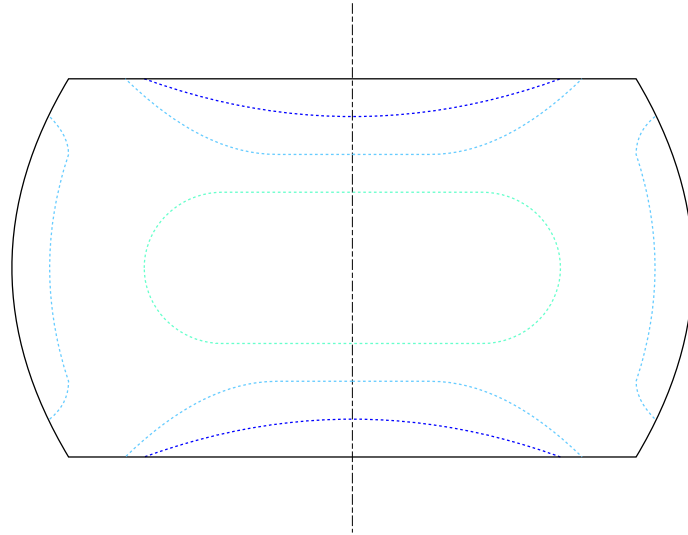


Fig. 6.1 Generalised strain profile as indicated by finite element analysis of the uniaxial compression TMC samples. At all compression temperatures, the highest strain regions are observed at the centre of the sample and around laterally expanded 'sides' (as indicated by the turquoise dashed lines). Conversely, the least strain is observed in 'dead zones' located in the areas of the sample where, or close to, direct contact with the tools has occurred. These 'dead zones' are indicated by dark blue dashed lines.



Fig. 6.2 Panoramic low magnification micrograph of a TMC sample uniaxially compressed at a constant true strain rate of 0.1 s^{-1} , to a total true strain of 0.69 at a nominally isothermal temperature of 1200°C . Note the correspondence to the schematic strain profile in Fig. 6.2 where the as-received anisotropy of the billet has been disrupted in the high-strain central and edge regions of the sample. The as-received elongation of the austenite lathes is however essentially retained from the billet in the low-strain dead zones predicted by the FEM simulation

The correspondence between the generalised strain profile, as predicated by the FEM simulations, illustrated in Fig. 6.1 and the example microstructure morphology evident in Fig. 6.2 is, superficially at least, indicative of a reasonable approximation of the input process parameters and material model to the behaviour of the ZERON® 100 sample under the testing conditions.

The simulation data for the uniaxial compression of the \varnothing 10 mm x 15 mm cylindrical sample to a true strain of 0.69 at a constant strain rate of 1 s^{-1} and a nominally isothermal temperature of 1050°C is illustrated below in Fig. 6.3. The evolution of the effective strain state variable is indicated by the colour bar.

In addition to low magnification panoramas, high magnification optical micrographs were also taken of the compressed TMC samples used for the derivation of the constitutive flow equations. Examples of these micrographs are shown in Fig. 6.4 in relation to the strain profile data generated in DEFORM™ for the corresponding test parameters. Comparison of the DEFORM™ strain data and the microstructure morphology in Fig. 6.4a, 6.4b and 6.4d suggests that a refined and extensively sub-structured ferritic matrix may be expected with $\bar{\lambda}_\delta$ as small as $10.1 - 17.7 \mu\text{m}$ in regions where strains of ca. 1 – 1.8 have been experienced at approximate temperatures of 1050°C and strain rates of 1 s^{-1} .

The adjusted experimental flow curve for the uniaxial compression test at 1050°C and 1 s^{-1} , as well as indicating a reasonable agreement with the constitutive flow model also exhibits a profile indicative of a flow softening response after peak stress has been achieved at ca. 0.3 strain. Since austenite is indicated to be the majority duplex phase at this temperature, it is suggested that the DRX mechanism may in large part be responsible for the decrease in stress with increasing strain after the peak of the flow curve. The high instances of observable twins at the centre of the compressed sample where strains in excess of ca. 0.6 are indicated (Fig. 6.4a & Fig. 6.4e) is cited as evidence in support of this. The mixed twin boundary morphology observed (straight and bent) suggests the occurrence of both RCX and DRX where twins formed during static recrystallization or static annealing during the prior forming of the billet were plastically deformed during uniaxial compression in the TMC[1]. In addition, new DRX twins are generated as a softening response to this secondary plastic deformation after the achievement of a critical level of strain > 0.3 .

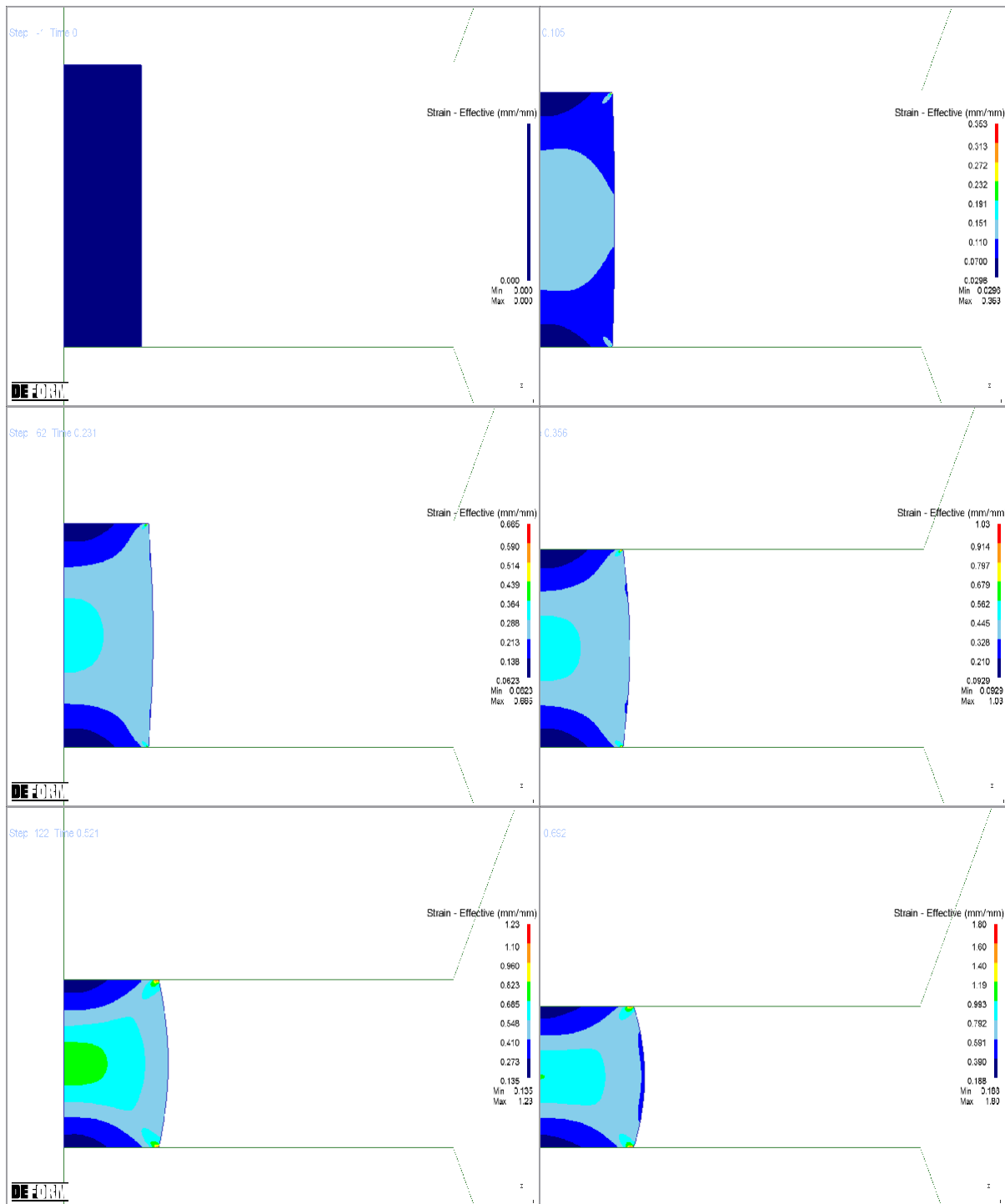


Fig. 6.3 FEM-predicted evolution of the effective strain profile within the uniaxially compressed TMC sample for the nominally isothermal test at 1050°C and constant true strain rate of 1 s⁻¹.

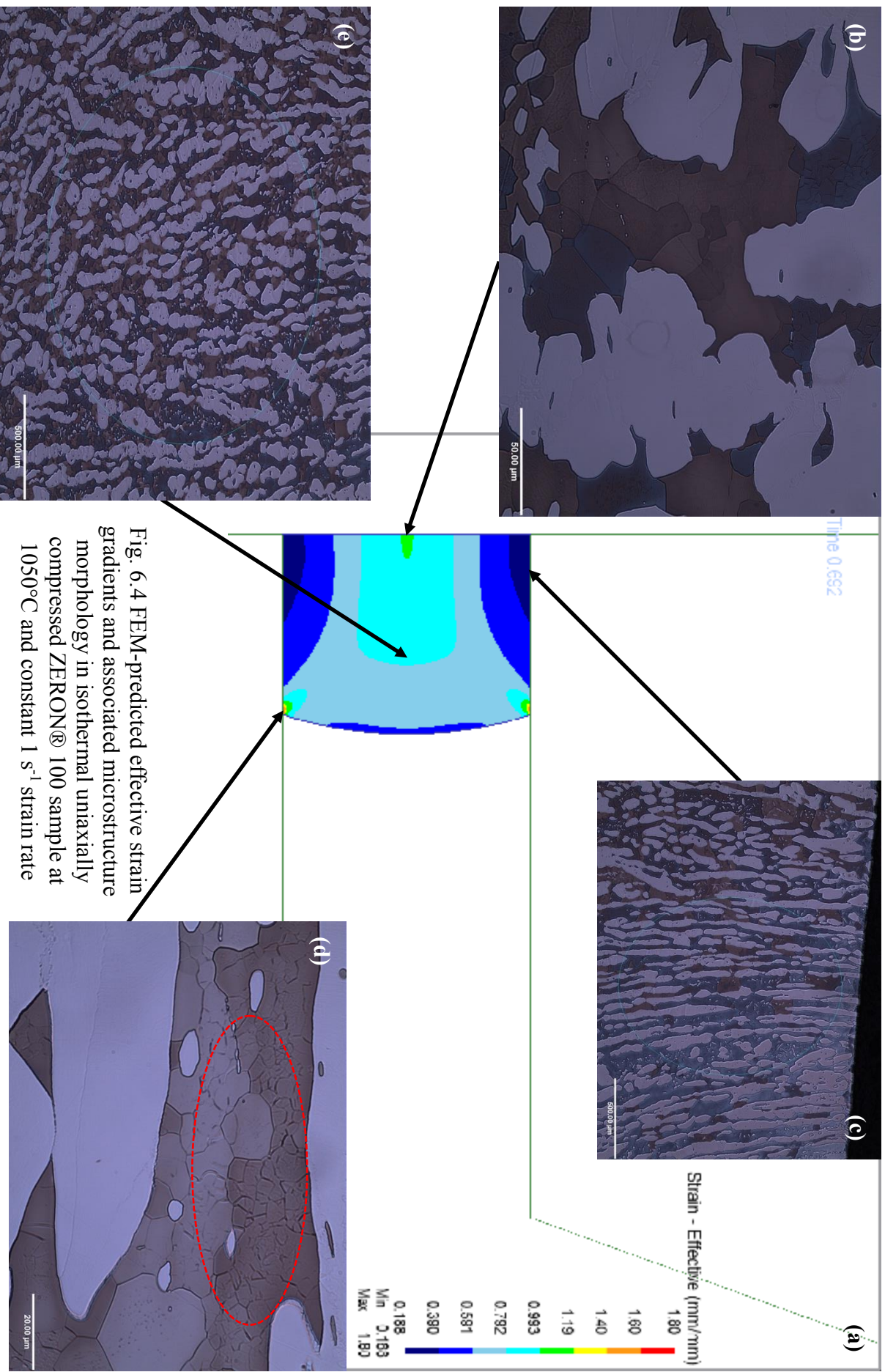


Fig. 6.4 FEM-predicted effective strain gradients and associated microstructure morphology in isothermal uniaxially compressed ZERON® 100 sample at 1050°C and constant 1 s^{-1} strain rate

The adjusted experimental flow curve for the uniaxial compression test at 1125°C and 1 s⁻¹, as well as also indicating, broadly, approximate agreement with the constitutive flow model, exhibits the classic profile of a material exhibiting flow softening through DRX in response to imposed plastic deformation. As with the uniaxial compression test above conducted at 1050°C and 1 s⁻¹ strain rate, the FEM simulation data for this next test are indicated below in Fig. 6.5. Again, the development of the strain profile in the sample throughout the displacement of the TMC's top tool is illustrated.

Broad similarities with the generalised grain profile in Fig. 6.1 can be seen, whereby the sample material in the 'dead zones' directly underneath/above the TMC tooling is predicted to experience very little effective true strain penetration. In support of this, the isotropic elongation of the austenite lathes is again seen in the micrograph (Fig. 6.6b) taken of the equivalent position in the sample. This is suggested to indicate very little refinement or evolution of the as received starting billet microstructure.

In other, high-strain, areas of the sample a refinement of the ferrite matrix can be observed, as was also indicated in Fig. 6.5. Minimum $\bar{\lambda}_\delta$ as small as 9.3 – 19.1 µm is indicated in regions strained to ca. 0.98 – 1.77. Equilibrium thermodynamic calculations (Fig. 2.4) indicate an increased volume fraction of ferrite in the duplex microstructure at 1125°C vs. 1050°C. Comparison of the micrographs in Figs. 6.4b & 6.4d with Figs. 6.6c & 6.6d is however interpreted as indicating greater accommodation of the flow softening exhibited in the experimental stress-strain curve by DRV processes at higher temperatures due to well-developed, and broadly increased equi-axiality of the obvious, circled red, ferrite cellular substructures[2]. Additionally, Fig. 6.7 taken from the highly-strained areas of the sample, indicates a high density of non-parallel, bent twins in the austenite grains (as well as instances of morphologically similar straight twins as also noted above in Fig. 6.4). This mixed twin morphology is likely to arise both as a result of distortion of pre-existing recrystallisation twins during subsequent plastic deformation as well as the dynamic generation of new twins during uniaxial compression. In comparison to Fig. 6.4 it is suggested that a displayed greater ferrite refinement and higher density of non-parallel austenite twins indicates the enhanced role of the DRV restoration mechanism in the displayed flow softening behaviour.

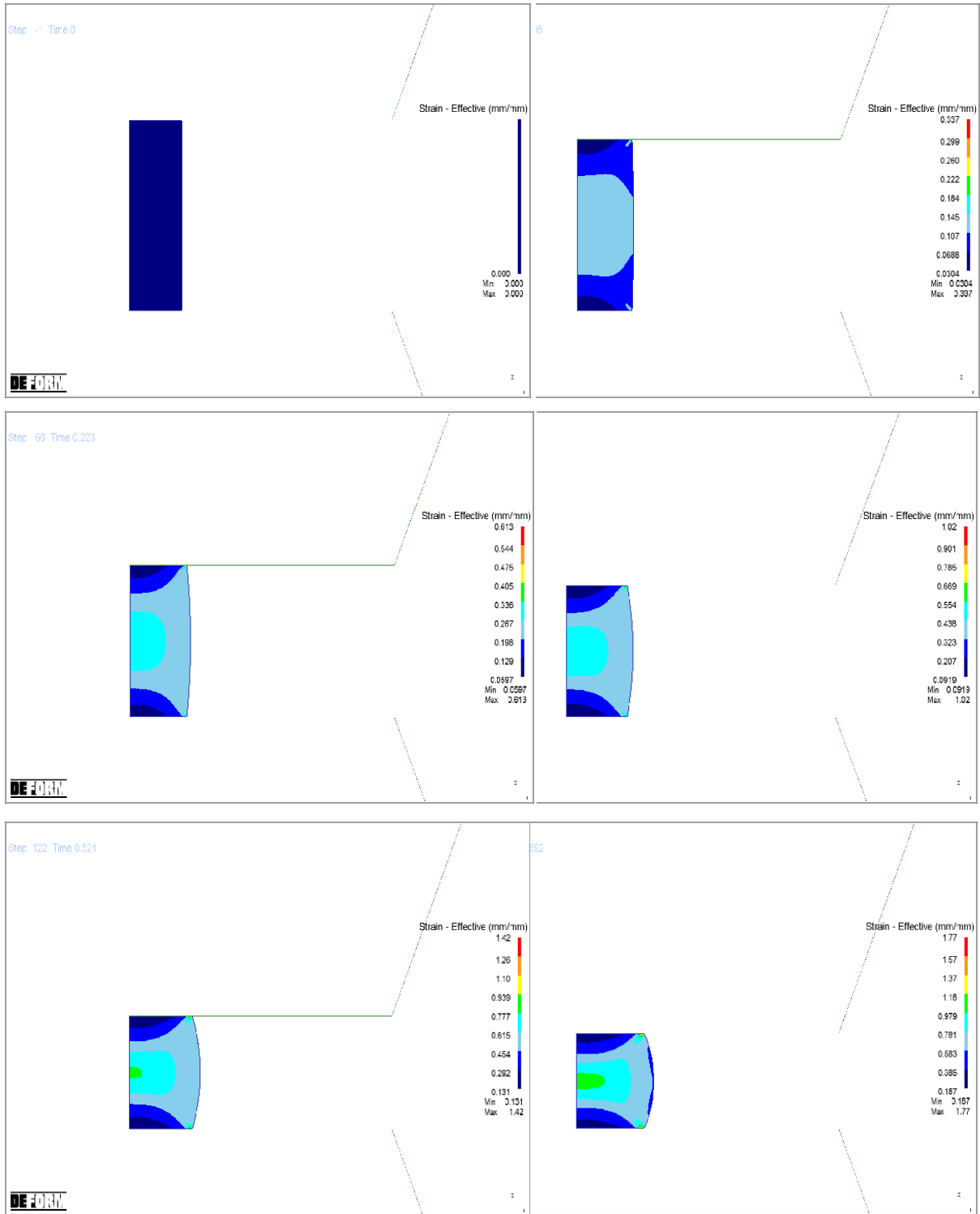


Fig. 6.5 FEM-predicted evolution of the effective strain profile within the uniaxially compressed TMC sample for the nominally isothermal test at 1125°C and constant true strain rate of 1 s⁻¹.

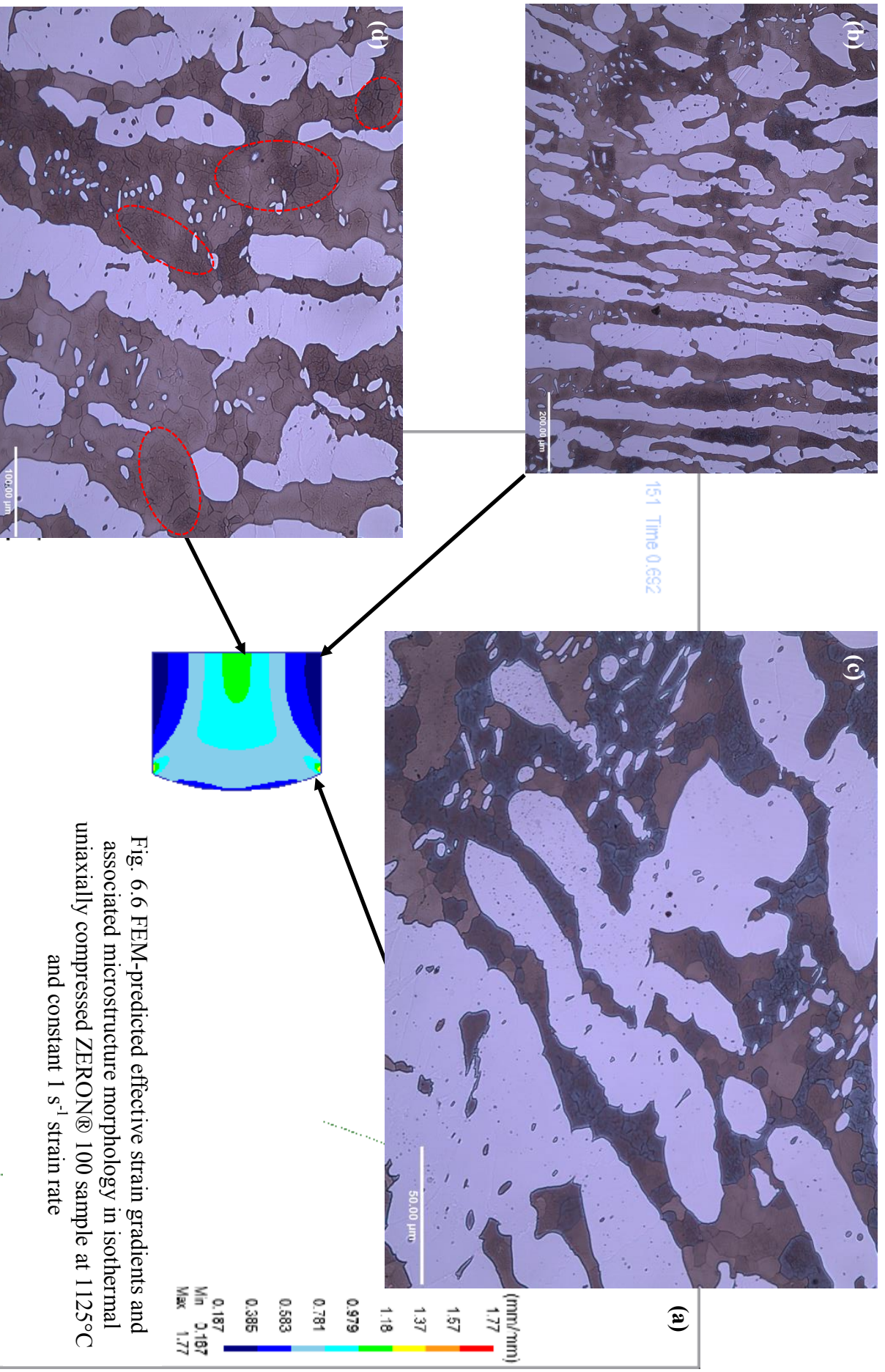


Fig. 6.6 FEM-predicted effective strain gradients and associated microstructure morphology in isothermal uniaxially compressed ZERON® 100 sample at 1125°C and constant 1 s⁻¹ strain rate

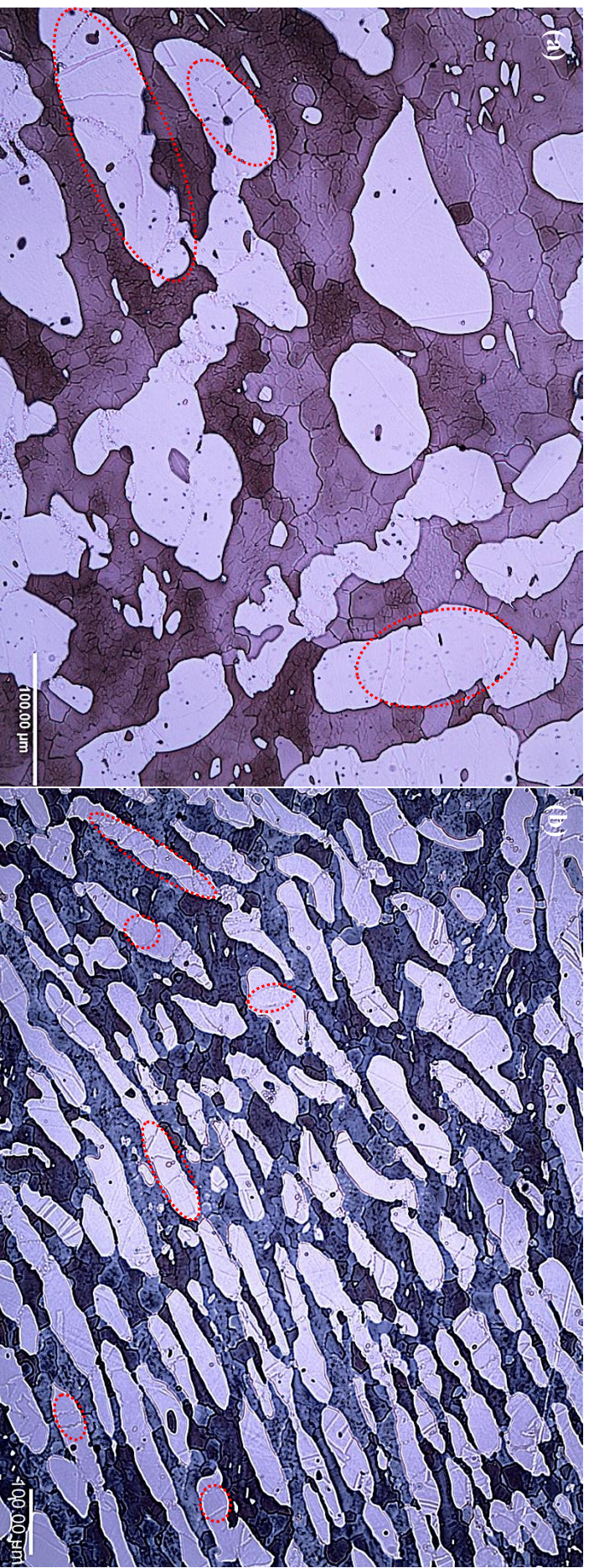


Fig. 6.7 Mixed austenite recrystallisation twin morphologies in the high-strain regions of the TMC test sample uniaxially compressed nominally isothermally at 1125°C and 1 s⁻¹ strain rate. A polarizing filter has been used to accentuate the presence of the twins. However, without orientation data as generated through EBSD analysis, this cannot be confirmed and it is acknowledged that these morphologies may instead be standard grain boundaries. Note **a** the refined and generally equiaxed ferrite matrix as well as **b** the mixed morphology of the austenite recrystallization twins (especially multiple instances of non-parallel bent boundaries circled in red).

6.2 Simulation of the Open Die Forging Process

The general open die forging process through which 16” flanged pipe connection forgings are manufactured was illustrated schematically earlier. Briefly, the initially circular section billet is drawn out square and then rounded up back into an approximately circular section again in an attempt to increase the amount of work done prior to upsetting and edge forged in the ring tool to produce the characteristic flanged forging shape. It was through this process that the forging from which the mechanical data presented in Table 7.1 was obtained.

The DEFORMTM multiple operations (MO) interface was introduced with the release of v.11.0 in 2014 and supports automatic sequencing of multiple step manufacturing processes, with obvious application to the above described open die forging sequence. The basic approach to the FEM remains unchanged however, and as detailed in Ch. 4, can be briefly summarised as follows:

- Divide the workpiece into small regions (the elemental mesh).
- Calculate the resistance to deformation of each element.
- Assemble behavioural equations of each individual element to get complete behaviour of the workpiece.
- Simulate the complete operation as a series of very short increments:
 - In all simulations detailed in this work, one increment, or solution time step, was typically specified to represent less than 1% of the complete process time
 - Workpiece shape, temperature and material properties are updated after each step
 - Workpiece resistance to deformation at step $t + 1$ is based on calculated properties from step t
 - Typically, thousands of increments are specified to simulate a single operation
- Iterate over each increment for all other operations in the total forming process.

The DEFORMTM user interface (UI) operation editor provides a graphical environment to browse and to edit multiple operations. Each operation in the above manufacturing process was specified through either the single-/multi-hit forming or 3D cogging pre-defined templates. These templates, available in the operation browser require customizable input data (geometry, tool/workpiece movement, meshing, material, boundary conditions, inter-object data,

positioning, friction, heat transfer, simulation step definition and stopping controls) for the description of single impression and repeated blow forming operations.

The structure and definition of scheduled MOs is fundamentally different to the simulation of single operations in previous releases of DEFROM™. On second and subsequent operations the stopping condition must be known in advance. However, the workpiece shape is not necessarily known in advance and new dies/tooling may need to be imported. Depending on the specifics of the forming operations in the manufacturing process, some information must be read from the primary operation, however other information must be defined new for each subsequent operation. Additionally, workpiece – tooling positioning and boundary condition generation must be scheduled to allow for workpiece shape changes during operations and potentially ambiguous behaviour to, for example, changes in environment temperature from operation to operation.

The first ‘operation’ in the open die forging process indicated previously was modelled in DEFROM™ as a 3-D (by default) cogging operation. Indicated billet dimensions of \varnothing 350 mm x 233 mm were used to define the workpiece primitive for which a mesh of ca. 95,000 tetrahedral elements and 18300 nodes was defined (Fig. 6.8).

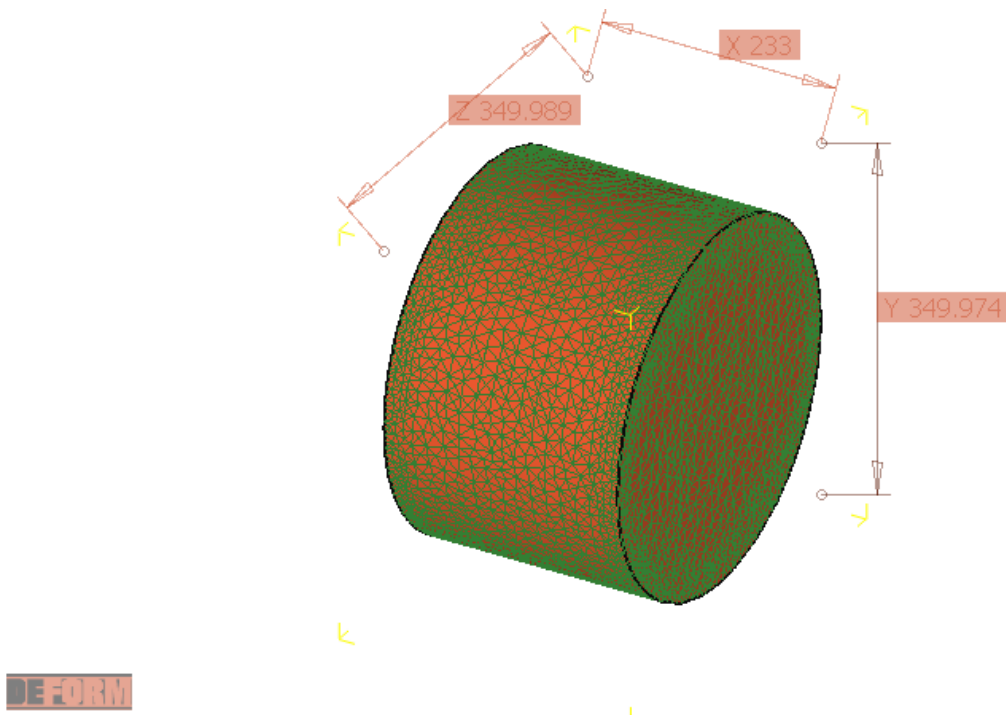


Fig. 6.8 FEM elemental mesh of the as-received \varnothing 350 mm ZERON® 100 billet prior to open die forging into a weld neck flange component. The shape of the mesh boundary is defined by the shape of the workpiece. Element edges are always defined with straight lines in the DEFORM™ meshing algorithm.

The number and size of elements are critical considerations in the specification of any FEM mesh. Not only is the geometric resolution of the problem defined through these parameters, the computational load is also significantly affected; for a given forming process increasing the number of elements generally increases the calculation time. Additionally, in MOs, the size of features to be formed in subsequent operations complicates the meshing processes and must be considered in specifying the element size in the initial mesh since anything smaller than the size of the smallest element will not be resolved.

State variables such as temperature, effective true strain rate and stress are averaged over each element in the mesh from the values calculated at the nodal points. Increased numbers of elements therefore provide a smoother representation of the actual solution. Sharper gradients across elements, where the difference between the averaged and peak value can be large, are generally produced as element size is increased.

Prior to presentation of the data from the FEM modelling of the open die forging processes through which the 16” weld neck flange was manufactured, it is important to note several key

limitations in both the set-up and running of the simulation since the accuracy of the presented solution is largely dependent on the quality and fidelity of the input data.

Limited information from the forge shop where the 16” ZERON® 100 weld neck flange forging was manufactured indicated that after the draw-out-square and round-up cogging operations, prior to upsetting the billet into the ring tool, the diameter of the billet had been reduced to 260 mm and the length increased to 422 mm. However, no further information was available as regards the tooling geometry, the number of blows the billet received in each operation, the lubricant(s) used, the temperature of the tooling or the number of intermediate reheats conducted during forging. The forging hammer was indicated as 60 c.w.t however, no dimensions of the frame assembly were available nor whether the action of the ram was gravity or power drop (and thus by extension the magnitude of the striking velocity, the pressure acting on the ram cylinder in the downstroke or the surface area of the ram cylinder). In the absence of the above information estimations were made based on available, albeit limited, comparable data in the literature. The total blow energy E_T (of the assumed gravity drop hammer) was calculated as equal to the kinetic energy of the ram generated solely through free-fall velocity, or:

$$E_T = \frac{m_1 V_1^2}{2} = \frac{G_1 V_1^2}{2g} = G_1 H_1 \quad \text{Eqn. 6.1}$$

Where, m_1 is the mass of the dropping ram, V_1 is the velocity of the ram at the start of deformation, G_1 is the weight of the ram, g is the acceleration due to gravity (9.81 m s^{-2}), and H_1 is the height of the ram drop[3]. Finally, and perhaps most importantly, it is also pertinent to revisit the limitations of the constitutive equation developed in Ch. 5 to describe the flow behaviour of ZERON® 100. The equation was shown to have general agreement with the experimental data over a limited range of processing conditions. Application of this equation to the DEFORM™ material model therefore requires extensive interpolation, with associated errors, to find solutions over the expanded range of, for example, strain rates, strains and temperatures that occur in commercial open die forging.

6.2.1 Cogging

The set-up of the cogging simulation is detailed below. However, repeated crashing when attempting to run 3-D cogging simulations as MOs with hammer die action revealed an underlying instability in the software for which a solution was under development, albeit not available at the time of writing. Consequently, the separate draw-out-square and round-up cogging operations were instead simulated as one single operation where the die action was specified at a constant speed (75 mm s^{-1}) and controlled by the attainment of a billet cross section reduction to 260 mm (the indicated billet diameter prior to upsetting in the ring tool).

In the available 3-D cogging template, passes, composed of an auto-calculated number of 'bites' from the top and bottom dies, along the billet are specified by cycle time, i.e. the total time lapse between two successive bites. In a typical cogging operation, it is the summation of:

Bite Deformation + Bite Decompression Time + Bite Dwell Time + Bite Heat Transfer.

Decompression Time is the time lapse before dwelling is started and after deformation is completed. During this time both top dies and bottom dies are in contact with the billet. Dwell Time is the time lapse between decompression time and the commencement of the next bite. During this time only the bottom die is in contact with the billet. In a case where the forging stroke is reached before the completion of the cycle time, the remaining time of the cycle has been considered as Heat Transfer during which neither die will be in contact with the billet. A bite cycle is illustrated schematically below in Fig. 6.9.

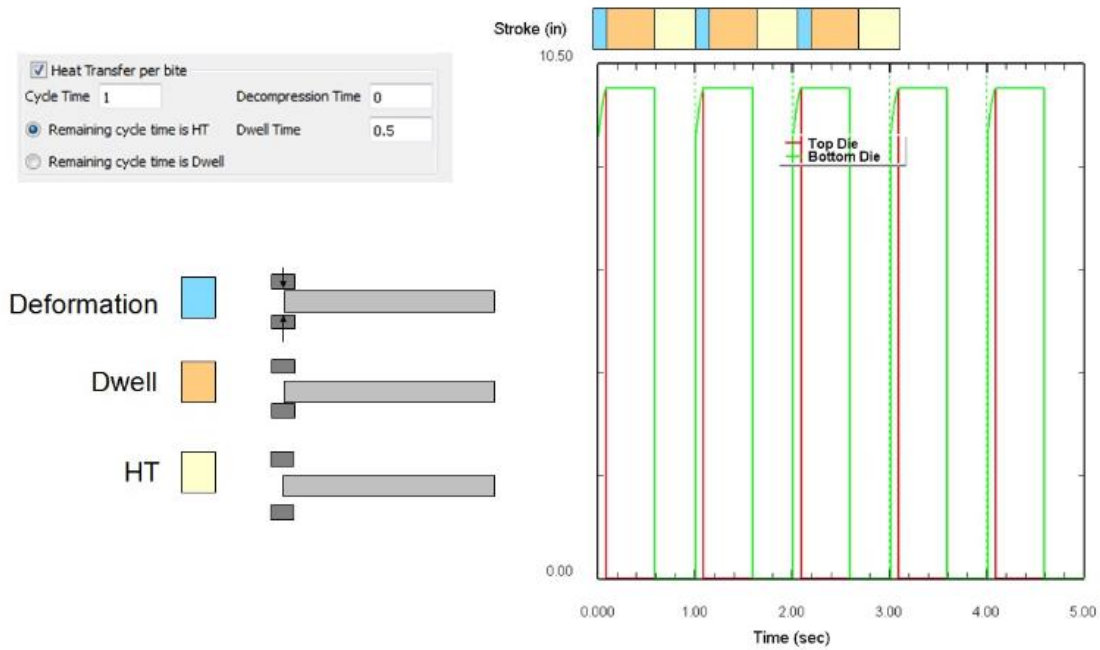


Fig. 6.9 Schematic illustration of the DEFROM™ cogging bite cycle

Cogging can be very lengthy process during which the billet temperature drops below the specified minimum forging temperature (1050°C) at certain point. By enabling the adaptive reheat option in the cogging template, the system automatically reheats the billet to a specified forging temperature (1280°C) and continues the cogging process. Adaptive reheat only takes place between passes. The reheating process was specified to be triggered when the average temperature of the surface nodes in the mesh fell below the assigned triggering temperature. In this way the billet temperature is maintained within the specified window. However, since the triggering temperature for reheating is auto-calculated by the system, the number of reheats performed during the actual forging operation and the temperature variation experienced by the billet are likely to be different. This has obvious and important to note associated impacts on potential discrepancy between simulated and physical flow stresses.

A complete bite cycle in the cogging process (as detailed above) is illustrated in 3-D representation below (Fig. 6.10), albeit viewed in the *y*-plane, where the tooling and manipulators used are both shown. The parameters for the cogging operation are specified in the pass table during the initial problem definition (Fig. 6.11)

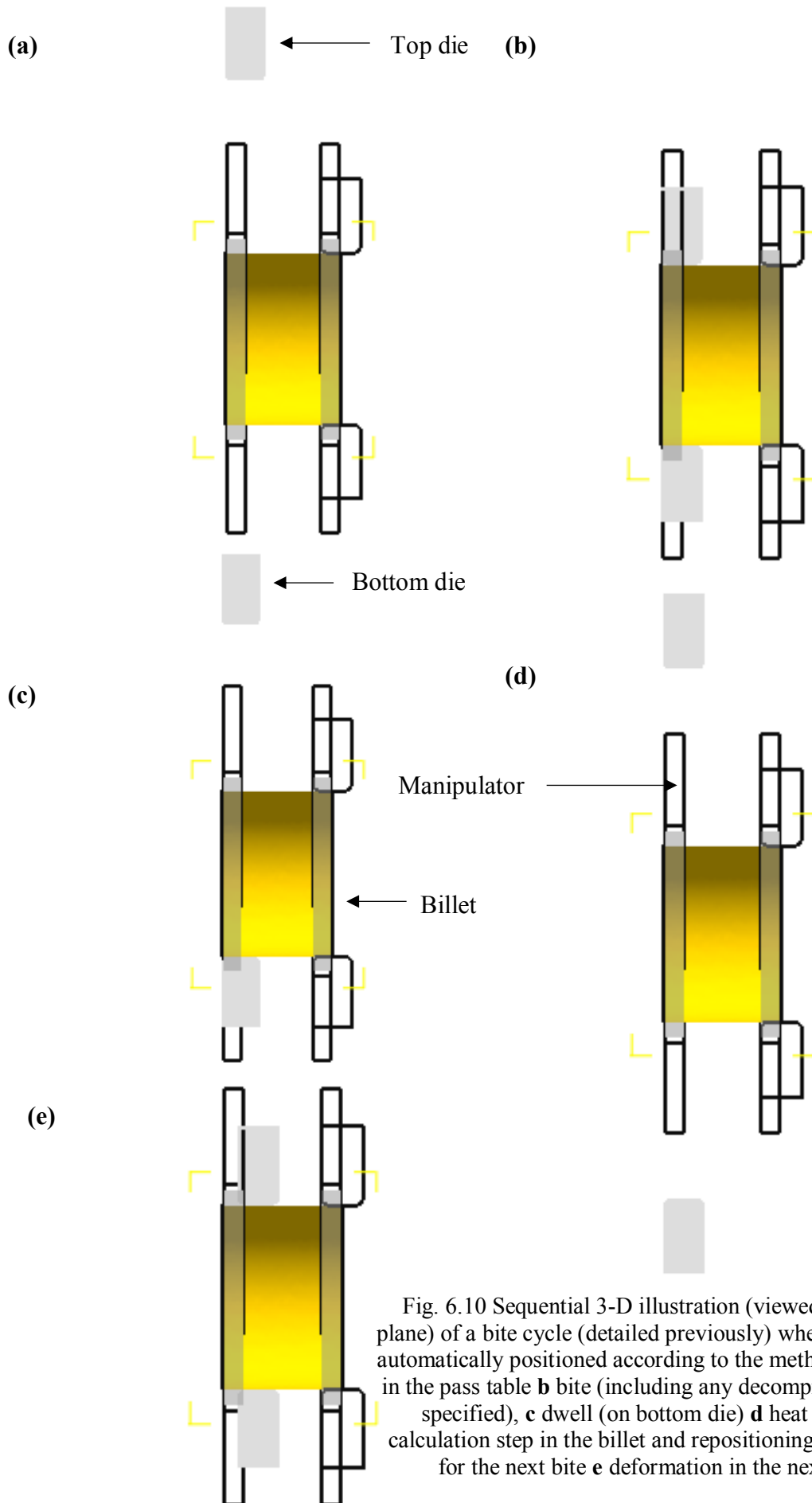


Fig. 6.10 Sequential 3-D illustration (viewed in the y-plane) of a bite cycle (detailed previously) where **a** dies are automatically positioned according to the method specified in the pass table **b** bite (including any decompression time specified), **c** dwell (on bottom die) **d** heat transfer calculation step in the billet and repositioning of the dies for the next bite **e** deformation in the next bite

	1	2	3	4	5	6	7	8
Auto-calculate Bites	<input checked="" type="checkbox"/>							
Number of Bites	1	1	1	1	1	1	1	1
Axial Feed per bite	30	30	30	30	30	30	30	30
Cross-section thickness	260	260	260	260	260	260	260	260
Movement Direction	+X							
Rotation per bite (Deg)	0	0	0	0	0	0	0	0
Rotation per pass (Deg)	45	45	45	45	45	45	45	45
Dwell Time before pass	0	0	0	0	0	0	0	0
Transfer time before pass	10	0	0	0	0	0	0	0
Die positioning method	3-ofst							
Die start position	40	-40	-40	-40	-40	-40	-40	-40
Die stop position	0	0	0	0	0	0	0	0
Bites to skip	0	0	0	0	0	0	0	0

Fig. 6.11 Example DEFORM™ 3-D cogging template pass table. In the simulation shown below four passes (not the eight indicated here) with a 90° rotation / bite were specified to achieve a roughly square sectioned billet. Auto-calculation of bites allows the system to determine the number of bites in a pass from the die geometry, billet length and axial feed per bite.

The data from the simulation of the cogging operation is illustrated below in Fig. 6.12, however for brevity only a brief selection of the ca. 1800 simulation steps have been shown. The data are plotted in terms of the effective strain state variable (as indicated by the colour contours).

Interactive slicing (a DEFORM™ post-processor data analysis and display feature) is used in Fig. 6.13 to illustrate the sub-surface extent of the indicated strain profile developed in Fig. 6.12.

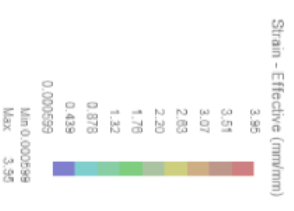
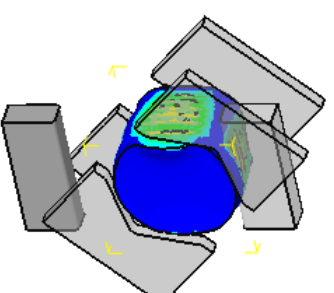
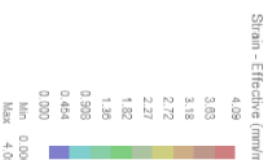
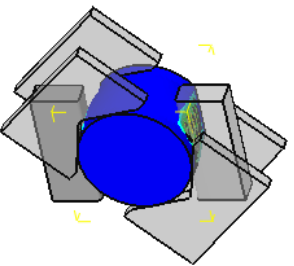
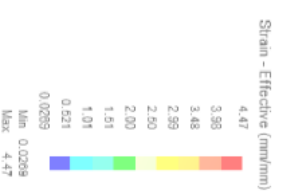
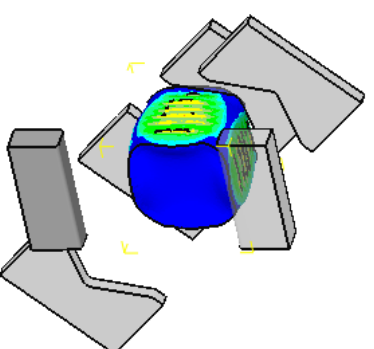


Fig. 6.12 Development of strain in the ZERON® 100 billet as it is clogged from \varnothing 350 mm to ca. 260 mm cross sectional length and approximately square profile (isometric view). This cross-section thickness is determined by the parameters specified in the pass table (Fig. 6.14) which also determine the simulation stopping criteria



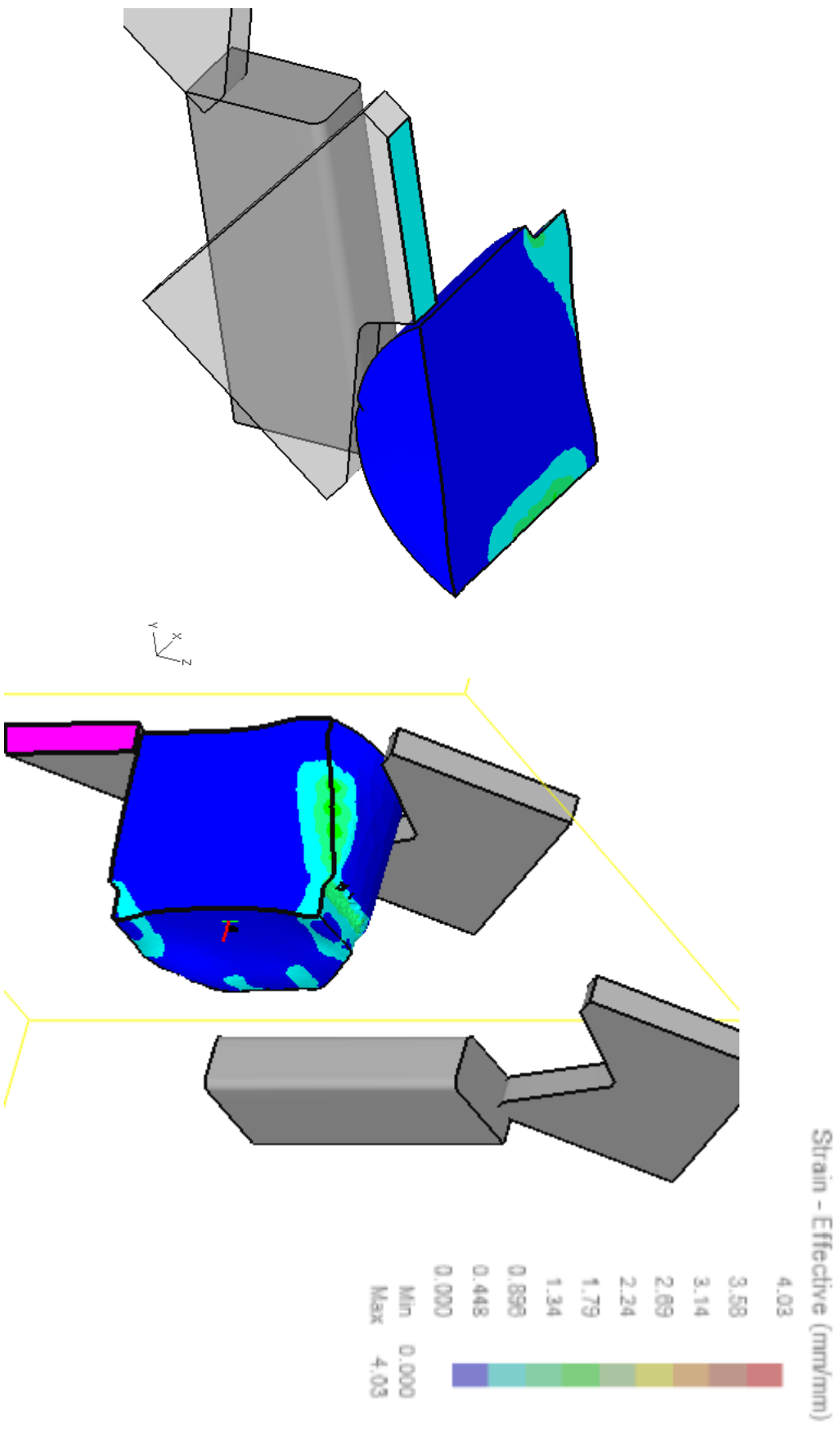


Fig. 6.13 Section view through the billet as the cogging passes are conducted

Although the ‘draw-out-square’ and ‘round-up’ cogging processes were modelled as a single operation (due to the noted limitations of the software and available process information), the same indicated billet section thickness was achieved, albeit through the approximation of a circular- to-square rather than circular-to-square-back-to-circular cross-sectional area.

The simulation indicates a superficial-at-best impartation of strain into the billet through cogging, with negligible penetration into the bulk material, as illustrated by the sectioned views of the billet in the x - y plane along the normal (z -) direction (Fig. 6.13).

Even when the noted limitations of the simulation as an analogue of the actual forging operation are considered, large volumes of the workpiece microstructure are therefore assumed to be essentially unchanged from as-received after the billet has been cogged. This suggests that the upsetting into the ring tool operation is chiefly responsible for imparting the work through which significant microstructure refinement in the forging is affected. The set-up and simulation of this multi-blow upset forming operation is detailed in the next section below.

6.2.2 Upsetting

The upset into the ring tool operation simulation was defined as a uniaxial 2-D multi-blow hammer forging operation. In axisymmetric mode, the problem is modelled in cross-section with respect to the central axis. Therefore, the model requires the deforming geometry to be axially symmetric and in the first quadrant and fourth quadrant (i.e. $x > 0$). In addition, it is assumed that the flow in every radial plane is identical. Use of the 2-D multi-blow template allows the forging operation to be set up without having to manually restart after each blow and, similarly, in comparison to the pass table in 3-D cogging operations (Fig. 6.11), a blow table allows the number of blows to be defined. Therefore, for every blow the percentage of blow, energy, reheating and separate dwelling time need only be defined once during the problem set up. In DEFORMTM's MO UI, advanced features like adaptive process controls and blow efficiency can be defined as functions. The adaptive reheating was also used in the multi-blow upsetting simulation in order that the workpiece was kept within the specified temperature window throughout the operation. Again, the system triggered reheating when an average of the surface node temperatures fell below the specified temperature and was allowed to soak the billet for 5 minutes at 1280°C before forging continued.

It is again important to highlight the approximate and limited nature of this multi-blow upsetting operation simulation, since, as mentioned before, little-to-no information was available as regards the forging hammer capacity, geometry, efficiency, number of blows delivered to the workpiece, temperature of the die(s) or the geometry of the ring tool. It is also important to note that the upsetting simulation presented here was not run in series after the previous cogging operation due to underlying software instability when inheriting the billet between operations after it had been cogged. In order, therefore, to simulate this final operation to form the characteristic ‘top hat’ weld neck flange profile a discrete, independent upset simulation was performed. Clearly, the strain profile history from the cogging of the billet could therefore not be developed in the upsetting operation, and the resultant data presented are likely to be somewhat under-representative of that in the final forged component. The data from the upset simulation is presented below in Fig. 6.14 and again plotted in terms of strain.

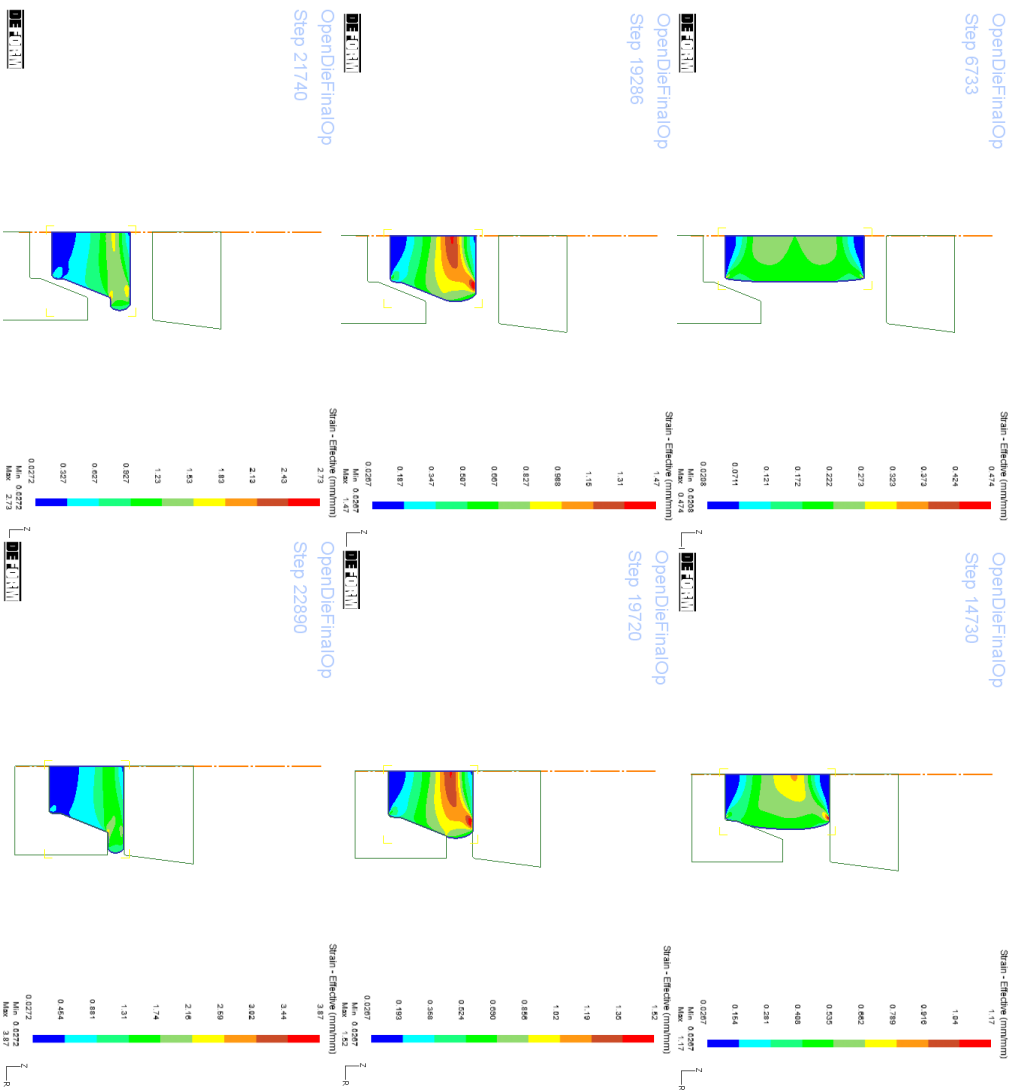


Fig. 6.14 Open die upset into the ring tool to form the weld neck flange shape

The data presented above in Fig. 6.15 indicate an inhomogeneous distribution of strains within the forging. The highest strains (and therefore assumed greatest microstructure refinement) appears to be concentrated in the flange area of the forging where the greatest material flow has occurred as well as in the centre of the forging. Fig. 6.15 also suggests very little strain impartation into areas of the forging in close proximity to the tooling, in a similar manner to development of the ‘dead zones’ noted above in the simulation of the uniaxial compression tests on the TMC (Fig. 6.1 & Fig. 6.5). It is however also important to consider the additive nature of true (rather than engineering) strains[4] and therefore the sum of the strains indicated in the previous cogging operation as well as in this last upset operation need to be considered when assessing the total strain in the manufacture process.

Considerable lack of strain penetration can be seen in the forging in the areas around the C1 position which contrastingly exhibited the best mechanical properties. This approximate C1 location, as detailed in Ch. 8, is however the fastest cooling during quenching after the quality heat treatment and thus suggests the existence of a more complex relationship between mechanical properties and strain, likely influenced by temperature and starting microstructure too. Finally, it should also be noted that the starting geometry of the billet specified in Fig. 6.7 was different from that indicated in the forging schedule (although the dimensions were noted as approximate). The billet length needed to be extended to allow enough material for the formation of the required flange thickness indicated. This is possibly because of specification of unrepresentative tooling geometry, hammer capacity, friction coefficient etc. in the simulation however, it may also indicate inaccurate dimensional information supplied by the forge shop and highlights the difficulty in working with limited information available concerning the details of a forming process.

Fig. 6.15 below shows the simulation output of the open die upset using the flownet post-processing tool available in DEFROM™. The flownet traces a pattern through the deformation states of the workpiece. However, in contrast to the finite element mesh, the flownet pattern stays intact while the remeshing takes place and thereby gives a graphic approximation of grain flow patterns. This can be thought of as similar to a macro etch and allows a cross section of the workpiece to be viewed at various stages throughout the forming process.

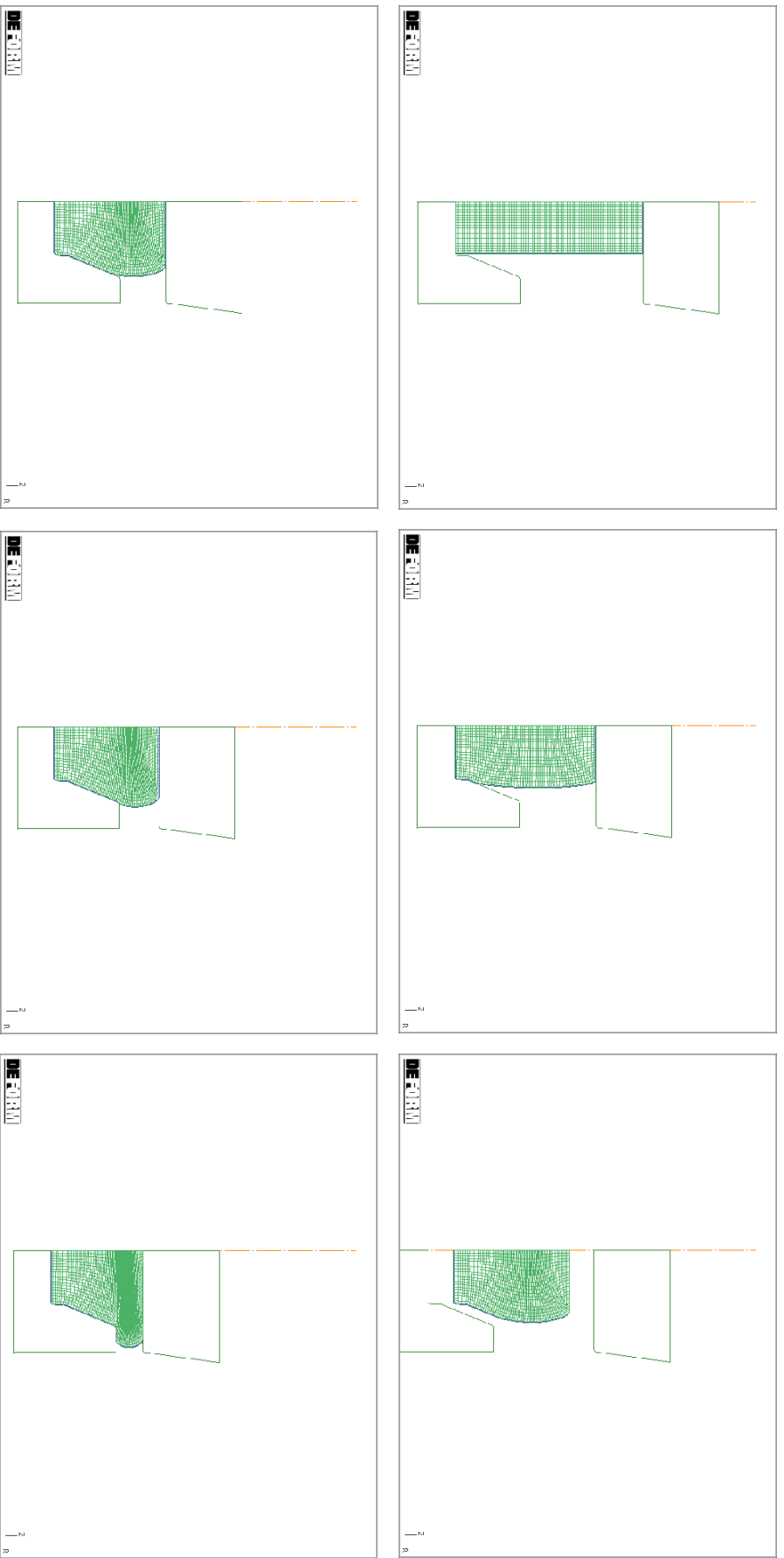


Fig. 6.15 Flownet tracking of the billet deformation throughout the open die forging clearly shows that non-uniform, localised deformation is concentrated around the centre of the workpiece. Comparison of the data here with the strain (Fig. 6.17) and the micrographs (Figs. 6.4, 6.6 & 6.7) suggest these should be the areas of greatest ferritic grain refinement in the matrix and $\langle 111 \rangle 60^\circ$ austenite RCX twinning.

6.3 Simulation of the Closed Die Forging Process

In addition to the open die forging process above, closed die forging has also been used to manufacture ZERON® 100 weld neck flanges, albeit with no available associated mechanical data and in smaller sizes. In this process the starting billet is first upset (open die) and then stamped in a 20-tonne counterblow closed die hammer to forge the component (for which documentation including die dimensions were available and hammer energy calculated as per Eqn. 6.1). The flash formed is trimmed off in a deburring press afterwards. The forming of the bore in the weld neck flange components would normally be achieved through a CNC machining operation after forging however, it was believed that greater material properties could be achieved by forming this bore with a punching operation as part of the forging process.

Using the 2-D axisymmetric multi-blow forming and heat transfer templates in the MO UI, this complete forming process was simulated with the workpiece inherited along operations and thus a more accurate estimation of the total strain provided than for the previous open die forging where two discrete operations had to be simulated. The data from this simulation is presented below and compared against the final results from a similar simulation where the punching operation was omitted.

6.3.1 Punching

Simulation of the formation of the bore through the punching operation incorporated a damage criterion based on an available modified Cockcroft-Latham (CL) model (Eqn.6.2), specifiable as default DEFORM™, under the assumption that plastic fracture (and thus mesh element deletion) occurs when the damage exceeds a critical value, C .

$$\int_0^{\bar{\epsilon}} (\sigma^*/\bar{\sigma}) d\bar{\epsilon} = C \quad \text{Eqn. 6.2}$$

where $\bar{\sigma}$ is the effective stress, $\bar{\epsilon}$ is the effective strain in the fracture and $(\sigma^*/\bar{\sigma})$ is non-dimensional factor of stress concentration. Normally the CL model is used in controlling the many modes of fracture common to cold rolling and should be determined experimentally. Several values of critical damage were available in the literature[5],[6] and from which a first approximation was made and iteratively adjusted. It is however important to note that not all

these values were not determined under conditions analogous to the hot punching of SDSS forgings (modelling wire drawn high carbon steel for example) and therefore further experimentation is needed to accurately determine a more representative figure for the hot plastic fracturing of superduplex stainless steel. DEFORMTM also offers several other alternative methods to trim or remove material including direct geometry editing, Boolean operations and material shearing. To prevent numerical insatiability arising from the excessive distortion of the FE mesh during material separation and removal in the punching operation, a damaged-based element deletion criterion was applied to the remeshing algorithm. Additionally, it was found that the specification of mesh windows helped to prevent the excessive elemental distortion responsible for the generation of negative Jacobian errors. The mesh windows are illustrated in Fig. 6.16 and allow the mesh generator to use the problem behaviour to automatically refine the mesh. The points picked around the workpiece define the areas for mesh refinement which are stored in the database and the information used when the remeshing criterion is triggered.

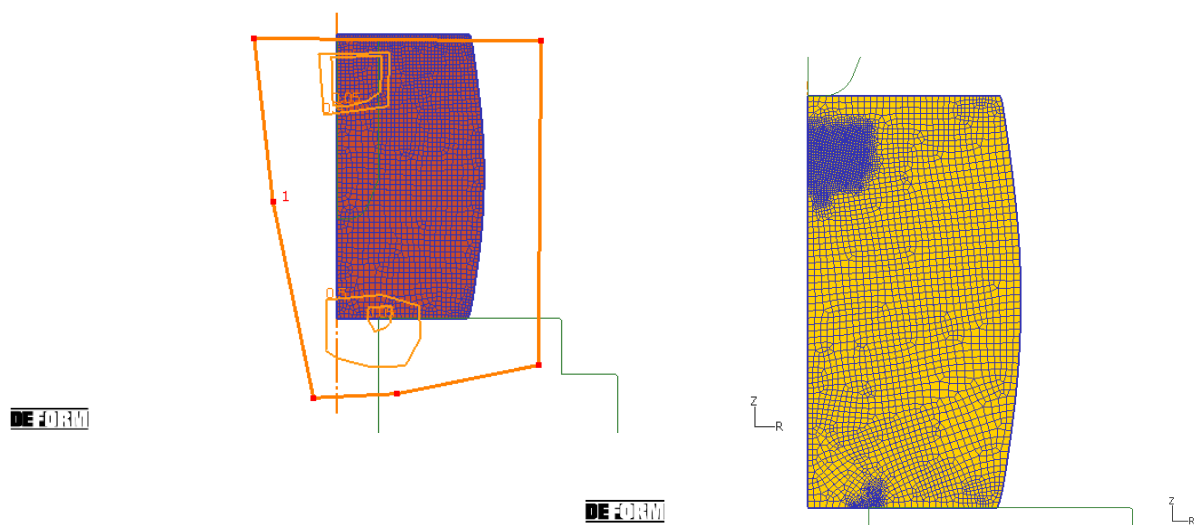


Fig. 6.16 Mesh windows for the punch operation **a** window 5 (1.0 element size) establishes default element size. The smallest windows (0.05 and 0.01 element sizes) take precedence over the larger surrounding windows (0.5 element size) **b** the element size refinement resulting from the mesh windows, concentrated around the (stationary) bottom die and moving with the punch

A selection (for brevity) of simulation data for the upsetting of the billet and subsequent punching and stamping operations in the closed die forging process are presented below in Fig. 6.17. Comparison between the final strains and deformation in the punched and un-punched closed die forgings is also made in Fig. 6.18.

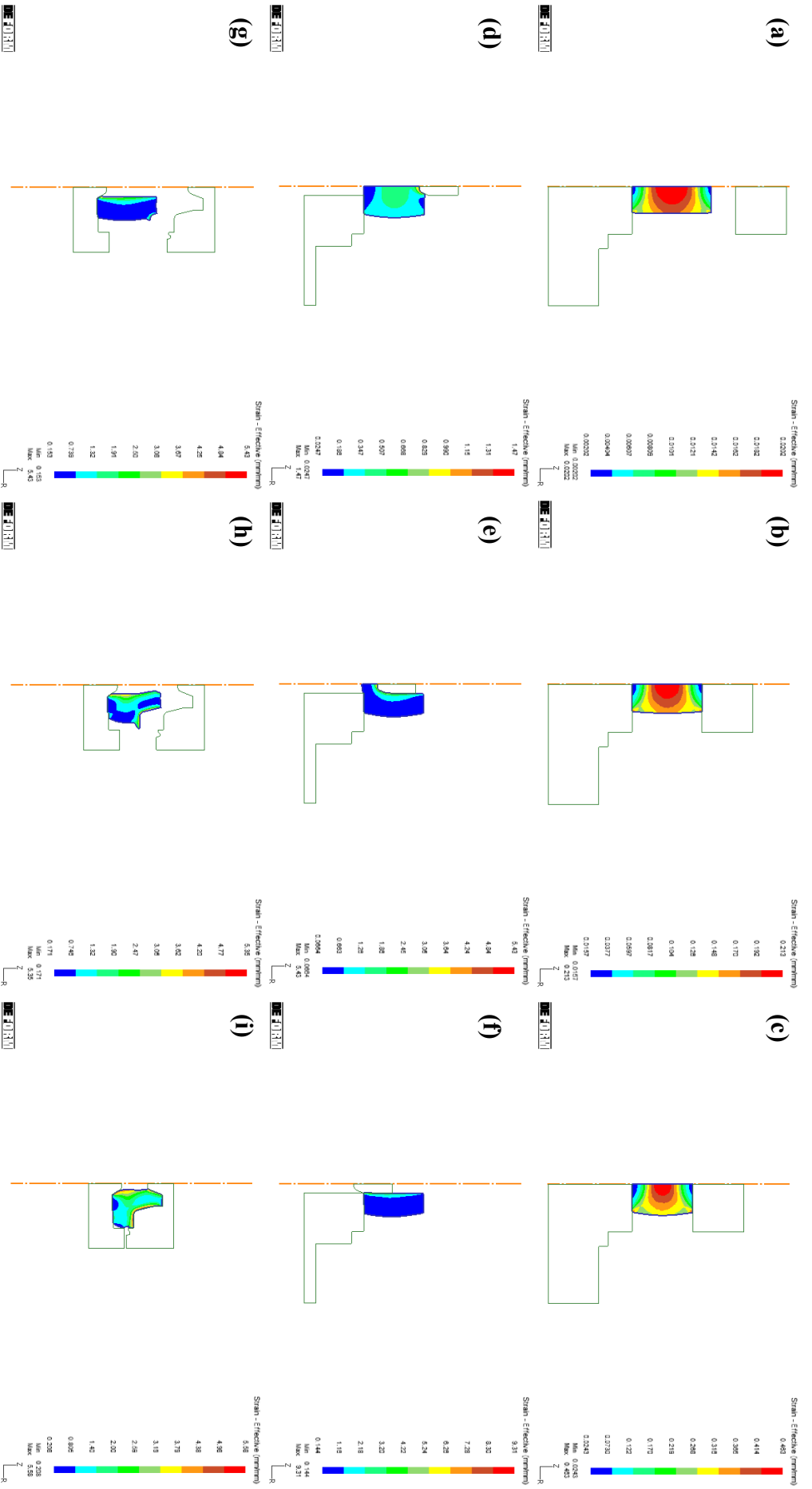


Fig. 6.17 Selected steps in the MO simulation of the closed die forging process plotted with the strain state variable **a** – **c** upsetting **d** – **f** punching **g** – **i** stamping

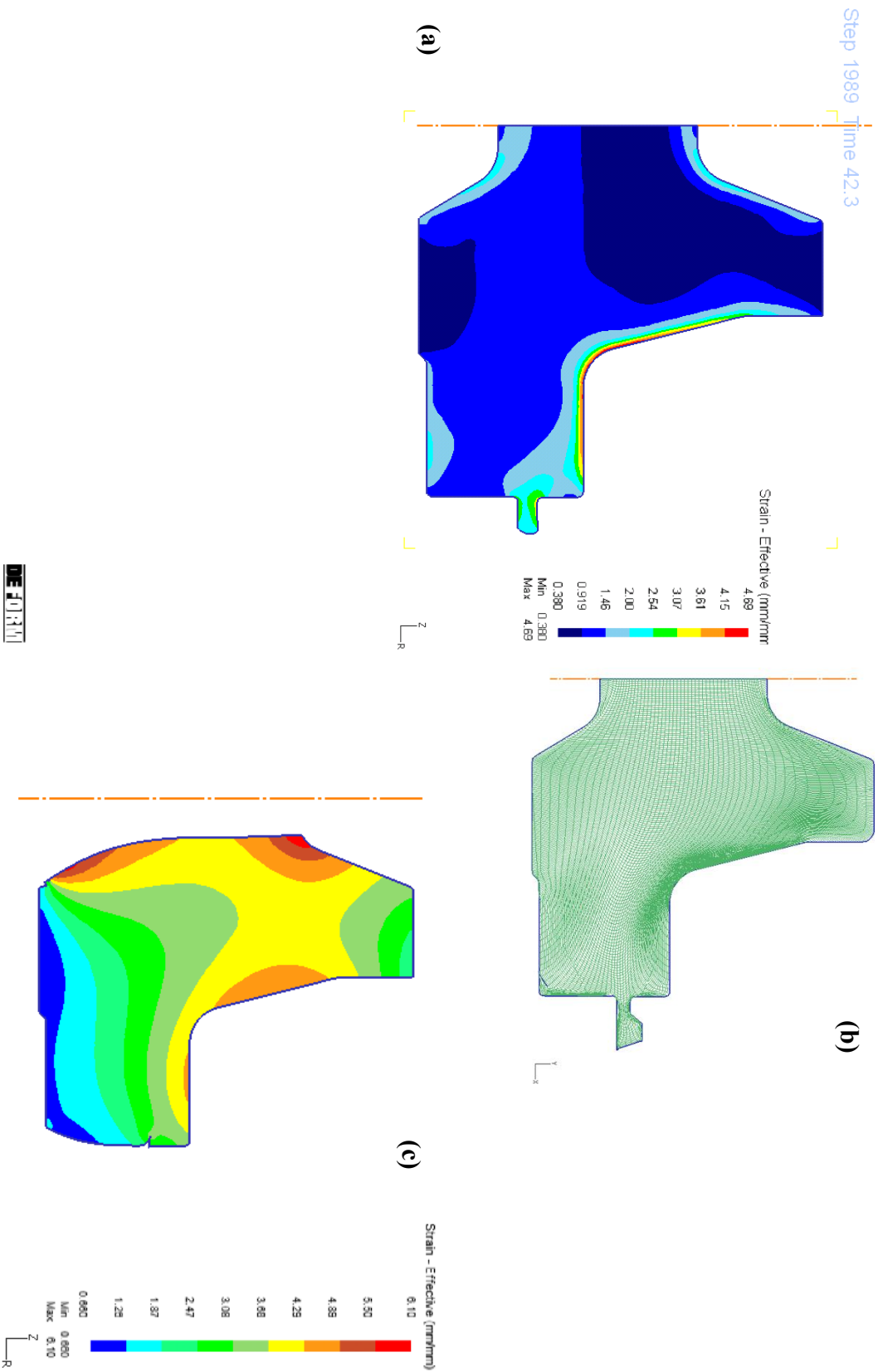


Fig. 6.18 Comparison of the strain and flowmet data in the **a – b** un-punched and **c** punched closed die forgings

6.4 Summary

Simulation of the open die forging process for the production of ZERON® 100 weld neck flanges suggests the development of heterogeneous and highly localised strains within the workpiece. The extremely limited available information from the forge shop greatly complicated the set-up of this simulation and software limitations meant the cogging and upsetting into the ring tool operations had to be simulated discretely without inheritance of prior thermo-mechanical processing history in the work piece. Because of these limitations (in addition to the previously noted restricted temperature, strain and strain rate applicability of the material model) the data produced from these simulations cannot therefore be viewed with high confidence. However, they do indicate an extremely superficial impartation of strain into the billet by cogging to the quoted dimensions. To work the billet more before forming the weld neck flange profile, an extended series of upsets, drawing-out and rounding up operations may therefore be more effective. The use of the flownet post-processing analysis tool in the final operation of the open die forging process (upsetting into the ring tool) suggests the greatest grain flow occurs across the C3 and C7 positions (Fig. 6.15). However, it is important to consider the effect this may produce in terms of the orientation of the Charpy V-notch crack tip and thus the direction of crack propagation. Assuming the austenite grains from the starting billet material are broadly orientated parallel to the longitudinal axis of the weld neck flange and thus normal to the V-notch, the excessive grain flow indicated in these positions may act to orientate them more parallel to the direction of crack propagation and thus limit their effectiveness in retarding cracking. Comparisons may be drawn here with the micrographic and simulation data from the TMC samples presented earlier, where the orientation of the austenite grains was shown to have broadly aligned along the direction of material flow in the high-strain regions in the corners of these samples (Fig. 6.2 & Fig. 6.7). It is noted that (HISC) cracks generally propagate in straight cleavage through the ferrite phase and that the crack may be arrested by the austenite phase depending on crack size and stress level[7]. The design criteria specifying minimum and average impact toughness acceptance criteria from the testing of longitudinally oriented Charpy samples from these locations in the forging may therefore be inherently biased and potentially partly responsible for the reported variation in properties (detailed further in Table 7.1).

The closed die forging process (incorporating a punching operation) was shown to cause greater straining of the workpiece, likely as a result of the restriction of lateral material flow in the

impression dies. Without comparable mechanical data from the closed- and open-die forged flanges, it is difficult to assess the difference in properties these two different methods of forging may have produced. However, when compared to the simulation data from the same closed die process, albeit without the punching-out of the bore, a higher straining can be seen in the typically under-worked internal areas of the forging, next to the bore. Assuming that this higher strain does not cause an undesirable re-orientation of the austenite grains, it is suggested that forming the bore through a punching operation during the closed die forging process represents the optimum manufacturing route. Evaluation of the punched forging in Fig. 6.18 also indicates somewhat incomplete die fill after the specified 17 blows and therefore it is also suggested (assuming a reasonable approximation of the hammer energy, die temperature, frictional coefficient etc. has been made) that a minimum of a least 20 blows during the impression die stamping operation are specified. It is however important to stress again the limitations of and assumptions made in the above simulations of the forging processes and thus that the data presented should only be viewed as guidance in the optimisation of the manufacturing process.

Temperature is an important parameter to control during the forging not only due to its effect on flow stress but also, as has been noted in Ch. 2 (and will be explored in greater detail in subsequent chapters), in terms of the thermodynamic stability of the γ_2 precipitates and the subsequent effect they have during the quality heat treatment in retaining the grain refinement from hot working. In the above simulations, the adaptive reheating features of the DEFORMTM process simulation tool have been employed to ensure the workpiece does not cool below the minimum temperature specified. However, as will be discussed further in Ch.7 and Ch. 9, it is suggested that this minimum temperature should not be lower than that of the subsequent quality heat treatment. As a consequence, extremely close control of the thermo-mechanical processing is recommended (not least to avoid the issue relating to Fig. 6.18 noted above). The adaptive reheating was set to trigger when an average of the surface node temperatures fell below the allowable minimum (1050°C) in an attempt to replicate the forge shop practice of measuring work piece temperature during forming with a pyrometer. Analysis of the simulation data indicated that under this criteria reheating occurred very frequently towards the latter stages of operations requiring many hammer blows. The temperature at which the forging is carried out, as noted above, is proposed to be of paramount importance and therefore it is suggested that adequate pre-heating of the tooling is also likely to be highly significant. The

geometry and distribution of thermal mass in the workpiece makes maintenance of homogeneously high temperatures very difficult. However, assuming a sub-optimal, equivalent low temperature starting microstructure in the billet prior to forging, such frequent reheating may be required to ensure adequate retention of the grain refinement through the precipitation of thermally-stable grain boundary-pinning secondary austenite particles.

The route to optimisation of the thermo-mechanical processing of ZERON®100 forgings involves incremental adjustments to ensure the optimum conditions at each step. The data presented in this chapter underline this; open die forging may be improved through extended draw-out and rounding-up operations prior to upsetting. Closed die forging appears to offer an improvement again over open die forging, and through the inclusion of a punching operation to form the bore in the weld neck flange, this process may be incrementally improved in terms of the predicated material properties output. Close process control of temperature and workpiece-die lubrication/filling should also be ensured as a means of optimisation of the thermo-mechanical processing through incremental improvement.

REFERENCES

- [1] F. C. Liu and T. W. Nelson, "Twining and dynamic recrystallization in austenitic Alloy 718 during friction welding," *Mater. Charact.*, vol. 140, pp. 39–44, Jun. 2018.
- [2] C. Ouchi and T. Okita, "Dynamic Recovery and Static Recrystallization of 1.8 % Al Steel in Hot Deformation*."
- [3] G. E. Dieter, H. a. Kuhn, and S. L. Semiatin, *Handbook of Workability and Process Design*. 2003.
- [4] H. S. Valberg, *Applied Metal Forming: Including FEM Analysis*. Cambridge University Press, 2010.
- [5] S. Benesova, J. Krnac, R. Wludzik, and J. W. Pilarczyk, "Application of cockroft-latham criterion in FEM analysis of wire fracture in conventional drawing of high-carbon steel wire," in *2008 Conference Proceedings of the Wire Association International, Inc.: Wire Expo*, 2008, pp. 24–38.
- [6] P. Wai Myint, S. Hagihara, T. Tanaka, S. Taketomi, and Y. Tadano, "Determination of the Values of Critical Ductile Fracture Criteria to Predict Fracture Initiation in Punching Processes," *J. Manuf. Mater. Process.*, vol. 1, no. 2, pp. 12–25, Oct. 2017.
- [7] "DNVGL-RP-F112 Design of duplex stainless steel subsea equipment exposed to cathodic protection," Høvik, 2017.

Chapter 7: SEM-EBSD Analysis

The crystallography of ZERON® 100 was investigated by means of SEM - EBSD, the underlying methodology of which was detailed previously. Specimens subject to SEM - EBSD investigation were prepared from Charpy V-notch impact toughness samples, themselves taken from specific locations in a commercial open die 16” weld neck flange forging and for which corresponding mechanical data were also available. Prior studies concerned with crystallographic investigations of duplex and superduplex material have almost exclusively been based on laboratory scale thermo-mechanically processed material. In this study EBSD analysis of industrially processed material was carried out, for which impact toughness data was available thereby allowing direct analysis of the crystallographic basis for differences in location-specific mechanical performance within a single engineered component.

SEM – EBSD specimens were also prepared from the samples produced through industrially analogous axisymmetric compression tests on the TMC and for which complete thermo-mechanical processing data (load, displacement, temperature etc.) had been recorded throughout both the compression and heat treatment segments of the experiments.

The following chapter is therefore ordered according to the thermo-mechanical processing to which these two discrete sets of SEM – EBSD specimens were subject. In all cases, the specimens were prepared according to the same metallographic procedure (Ch. 4.5) and sectioned to standard dimensions as specified by the holder used attach to the motorised stage in the SEM.

7.1 Microstructure and Crystallography of ZERON® 100 Commercial Open Die Forging

Three Charpy samples were taken from each of the three locations within the forging, all parallel to the axial direction; the neck, close to the bore inside diameter and the centre of the flange, respectively. These three locations were labelled C1, C3 and C7, respectively and this labelling system was also applied to the EBSD specimens prepared from these Charpy samples.

The mechanical data for the C1, C3 and C7 positions samples are listed below in Table 7.1

Table 7.1 Mechanical data for the Charpy V-notch impact toughness samples from which EBSD specimens were prepared. The minimum acceptance level is the lowest admissible toughness in any of the three tests. The mean acceptance level is the minimum admissible toughness averaged over the three tests.

	<i>C1</i> <i>Weld neck</i>	<i>C3</i> <i>Bore ID</i>	<i>C7</i> <i>Flange centre body</i>
Minimum acceptance level (J)		35	
Mean acceptance level (J)		45	
Test # 1 (J)	60	16	39
Test # 2 (J)	88	17	36
Test # 3 (J)	67	21	41
Mean (J)	72	18	39

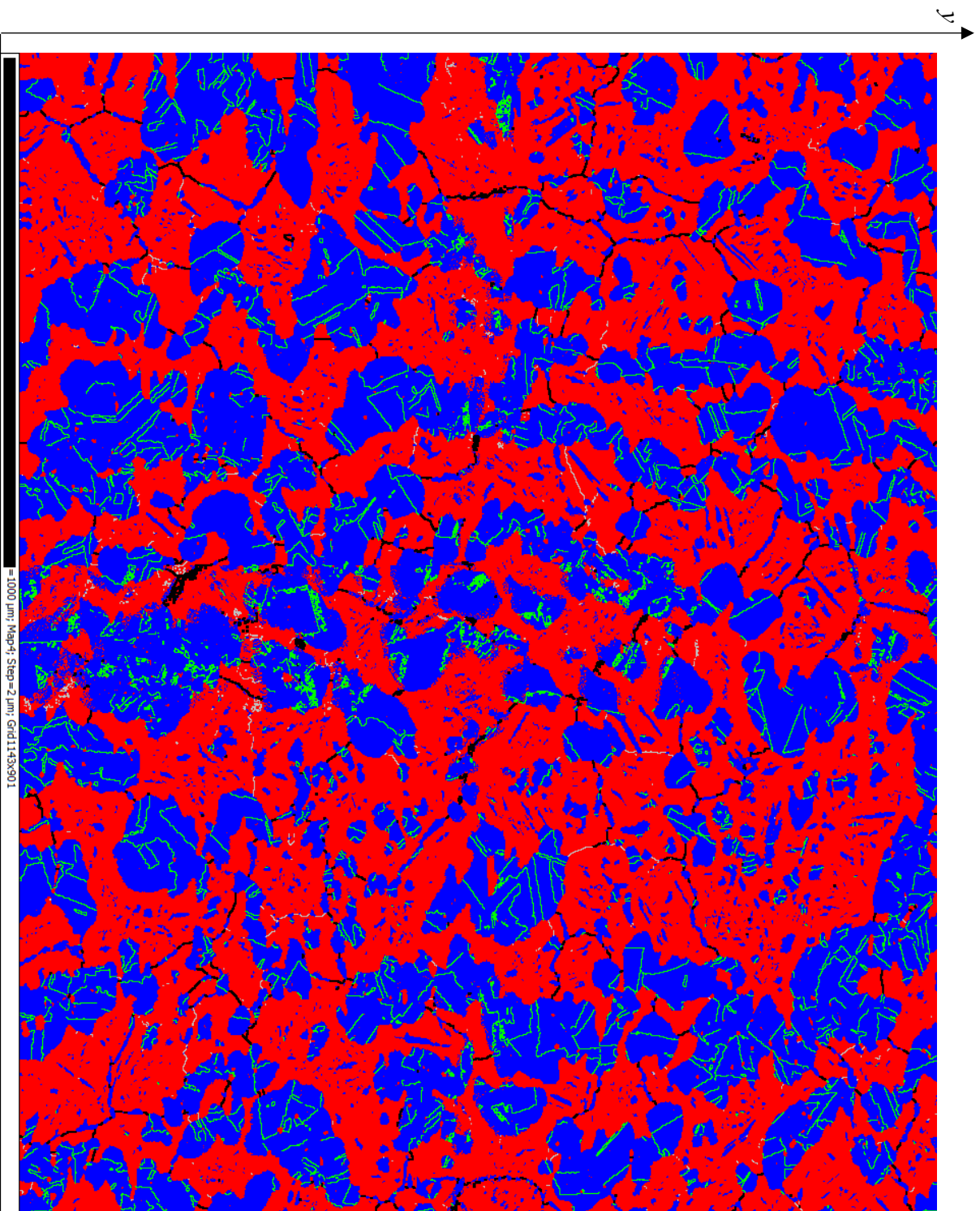
Three samples were taken from each position and tested individually. The DNV-OS-F101 Offshore Standard stipulates that the overall positional toughness as averaged over the three tests should be no lower than 45 J with no one impact toughness result below 35 J at -46°C. This is indicated in Table 7.1 for reference by the minimum and mean acceptance levels.

A marked difference is apparent from Table 7.1 in the impact toughness properties as a function of position within the forging. The underlying crystallography of the forging microstructure in these three discrete positions is therefore presented in the following first part of this chapter.

Particular focus is given to the crystallography of the ferrite phase since HISC cracks generally propagate in straight cleavage through the ferrite phase with the result that the mean free ferrite path becomes an important consideration in duplex/super duplex design codes, especially as they pertain to fabrication techniques[1].

7.1.1 Weld Neck Position, C1

The crystallographic phase map of the EBSD specimen prepared from the C1 Charpy sample is presented below in Fig. 7.1. The data forming the map in Fig. 7.1 was generated from four separate, overlapping scans carried out sequentially and covering an area of approximately 4 mm². The overlap between adjacent scanned areas was approximately 5%. The step size was set comparatively large at 2 μm to maximize the scanned area in the time available, however due to large average microstructure unit size, this was more than sufficient to allow for a minimum of 10 data points per grain. This large average microstructure unit size illustrated in Fig. 7.2 were IPF colouring in the sample *y*-direction has been used to illustrate the individual ferritic matrix grains. Examples of the grain dimensions along the *x*- and *y*- axis are also included



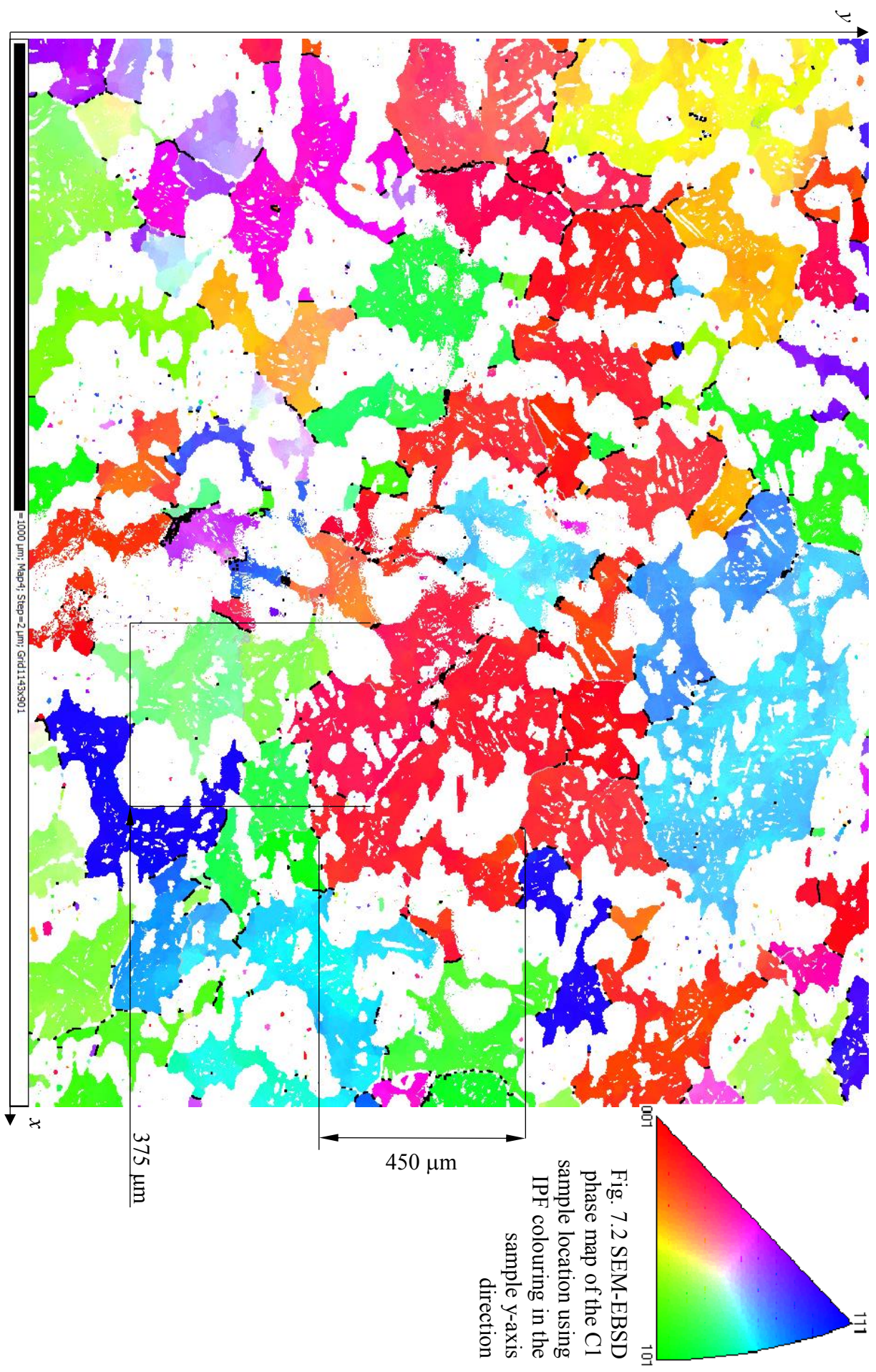
= 1000 μm ; Map#1; Step=2 μm ; Grid1143x901

Forging axis \leftarrow

Charpy V-notch orientation \triangle

Fig. 7.1 SEM-EBSD phase map of the C1 sample location microstructure from the commercial open die weld neck flange forging

- Red = ferrite
- Blue = austenite
- Black = grain boundaries
- Green = $\langle 111 \rangle > 60^\circ$ twin boundaries



In Fig. 7.1 The ferritic matrix phase is coloured red and the austenite phase is blue. Also shown in Fig. 7.1, as the green-coloured lines within the austenite grains, are the $\Sigma 3$ annealing twin boundaries. As in other close-packed cubic material, the major part of the twin interface is parallel to the $\{111\}$ planes. These annealing twins are known to form during the recrystallization of deformed cubic-close packed metals; γ -Fe in this case, however, the phenomenon is also observed in other FCC metals such as α -Brass, Ni and Cu[2]. In contrast to the lenticular shape of mechanical twins, annealing twins are characterised by their parallel banded appearance since their formation is not deformation-driven. Instead, their shape is determined by the minimisation of interfacial energy during the recrystallization process.

The phase balance of the microstructure shown in Fig. 7.1, as indicated from the EBSD statistics, was 52.8% ferrite vs. 47.2% austenite. The major ferritic phase forming the microstructure matrix is focused on in isolation in Fig. 7.2 where inverse pole figure (IPF) colouring in the sample y -axis direction has been used to indicate the crystallographic orientation of the ferrite grains with respect to the major axis along which the forging was upset.

The x - and y -axis orientation of Fig. 7.2 relative to the Charpy V-notch tip and the forging axis remains the same as indicated in Fig. 7.1.

The textural representation of Fig. 7.2 is shown through the inverse pole figure (IPF) in Fig. 7.3a where the occurrence of contours indicates the frequency with which the various direction $\langle uvw \rangle$ coincide with the indicated specimen axis. Texture, or preferred orientation, can also be represented through the stereographic projection and illustrated by means of pole figures (PFs), Fig. 7.3b.

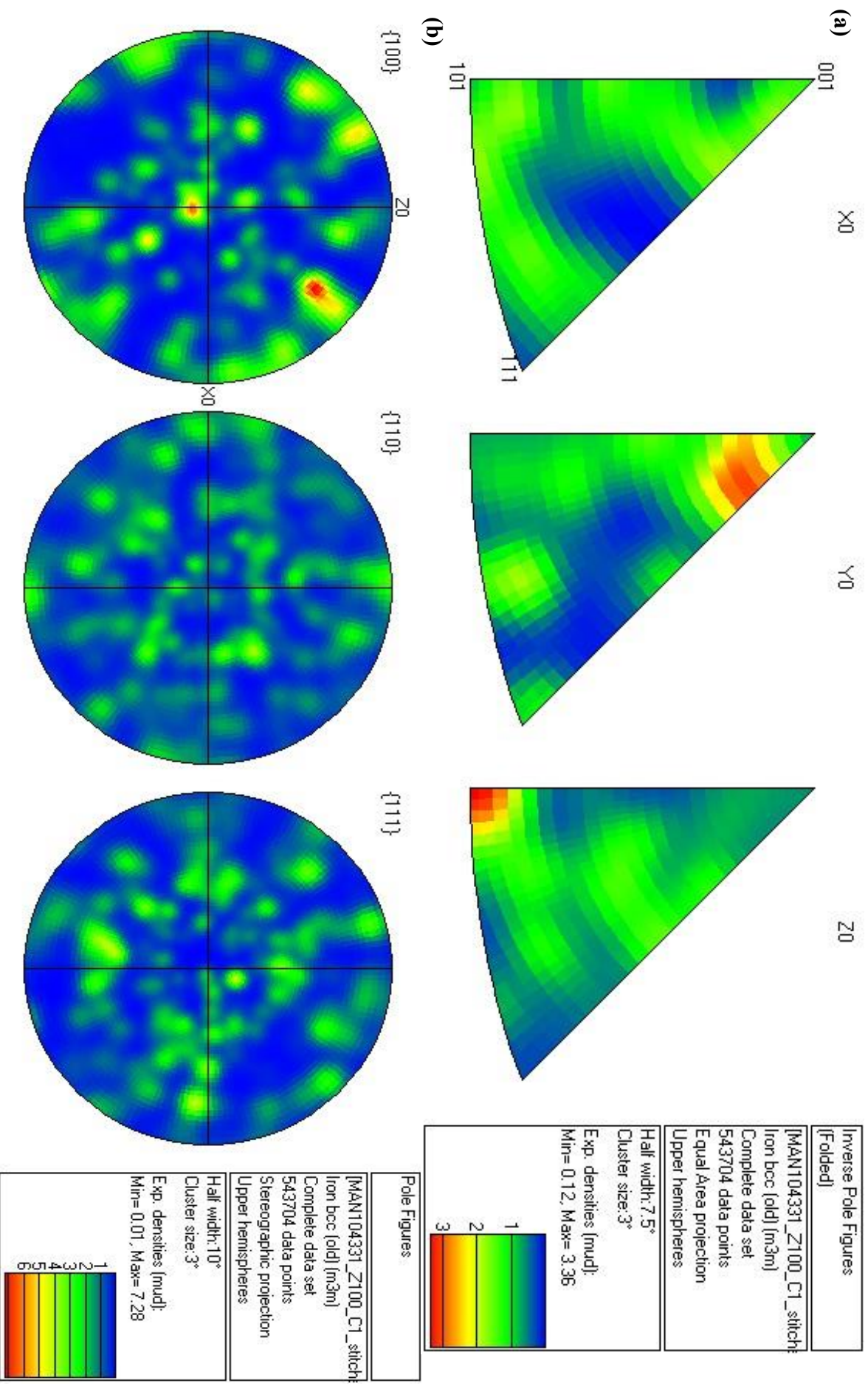


Fig. 7.3 Representation of texture in the duplex BCC Fe phase through **a** IPF and **b** PF (orientated parallel to the specimen y-axis)

The contours in the Y0 sample direction (Fig. 7.3a) suggest one part of the of the duplex fibre texture, $\langle 100 \rangle$ has formed parallel to the forging axis. For BCC metals in general, uniaxial compression or upsetting has been shown to lead to the formation of the duplex fibre texture $\langle 111 \rangle + \langle 100 \rangle$ [3].

It should however be noted that Fig. 7.2 clearly indicates the comparatively large microstructure unit size resulting from the forging process, as compared to the typically much higher grain refinement exhibited after, for example, a rolling operation. Certain ferrite grains can be seen to have sizes/diameters on the order of ca. 400 – 500 μm and as such the identification of the $\langle 100 \rangle$ texture in Fig. 7.3 should be regarded with some caution since, despite scanning a specimen area of almost 1 mm^2 , only a small number of grains have actually been sampled. This small population size is indicated by the expected densities (mud) in the legends on Fig. 7.3

Fig 7.3b provides further evidence of the previously noted development of a weak component of the fibre texture as evidenced by the $\langle 100 \rangle$ contours in the Y0 orientated IPF (Fig. 7.3a). In the left-hand side PF, the steepest contours in the centre suggest a clustering of $\{100\}$ plane normals closely, but not perfectly parallel to the forging axis. The second steep contour in this PF is consequently a projection of $\{100\}$ plane normals along the transverse direction.

In addition to crystallographic texture, the EBSD analysis carried out on the specimens taken from the Charpy samples also provided grain boundary data. These are presented in Fig. 7.6 below where various line styles have been used to differentiate between grain boundary angles. For clarity, the red colouring used to identify the ferrite phase in Fig. 7.1 has been omitted. Axes orientation remain consistent with Fig. 7.1. Discussion of the misorientation angle distributions for the ferrite boundaries is presented later in this chapter as a comparison between the data from the three sample locations within the forging.

The presence of a component of the $\langle 100 \rangle$ fibre texture was shown to have formed, albeit weakly, in the BCC phase of the duplex ferrite-austenite microstructure. BCC grains highly representative of this preferred orientation were defined as a discrete subset within this population in order that the crystallographic relationship between the microstructure matrix and the associated reformed FCC austenite particle (which can be seen to have precipitated intra-granularly) could be defined.

In ferrous metallurgy the Kurdjumov-Sachs (K-S) orientation relationship (Fig. 7.4) is well defined for the shear transformation to BCT martensite (α' -Fe) from FCC (γ -Fe) crystallographic structures[4], and has potential application in the case of ZERON® 100 material and the precipitation of inter-granular secondary austenite particles on ferrite-ferrite matrix boundaries. The K-S orientation relationship requires that the $\{111\}$ planes in the γ -Fe phase are orientated parallel to the $\{110\}$ α' -Fe phases and the $\langle 110 \rangle$ γ -Fe directions are parallel to the $\langle 111 \rangle$ α' -Fe direction. This relationship be expressed as:

$$\{111\}_{\gamma} \parallel \{110\}_{\alpha'}$$

$$\langle 1\bar{1}0 \rangle_{\gamma} \parallel \langle 1\bar{1}1 \rangle_{\alpha'}$$

The K-S relationship is illustrated schematically below in Fig. 7.4

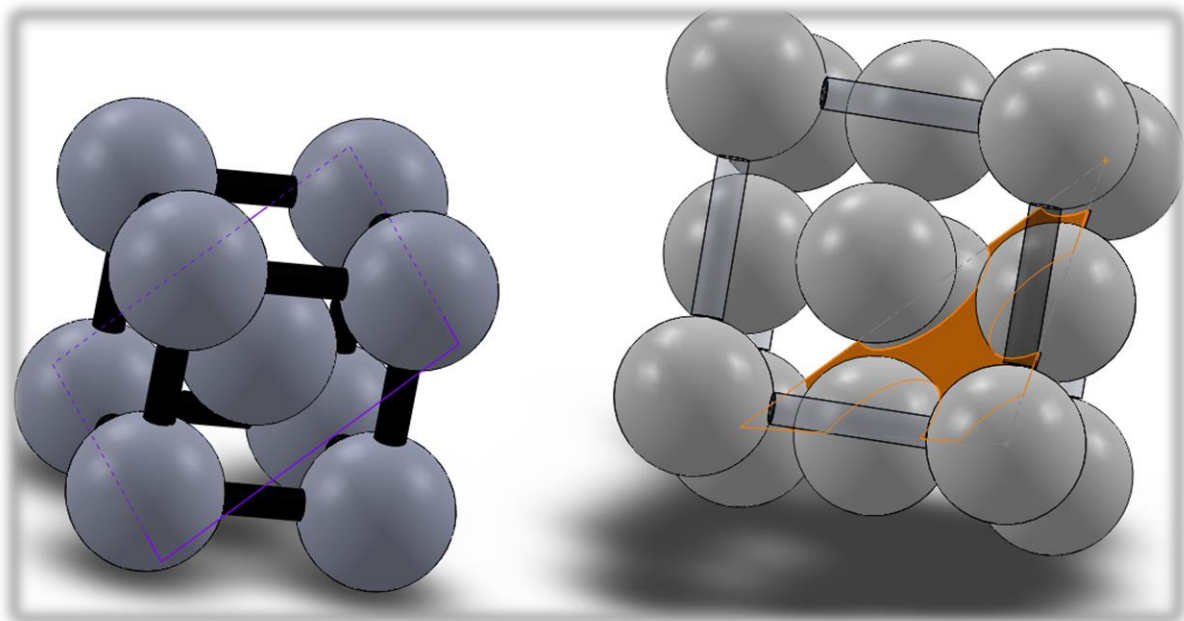


Fig. 7.4 The K-S relationship where a $\{111\}$ plane (outlined in purple) in the BCC structure (left side) is parallel to a $\{111\}$ plane (coloured orange) in the FCC structure (on the right side)

The occurrences of K-S relationships in the microstructure of the C1 location is shown below in Fig. 7.5 & 7.6. In this presentation of the EBSD data, orthogonal consistency is maintained with Fig. 7.2 whereby the major upsetting axis is orientated parallel to the y-axis in the sheet plane. In illustrating the instances of the K-S relationship, the red colouring of for the BCC phase used in Fig. 7.1 has been removed for clarity. Furthermore, the green lines indicating the presence of the $\langle 111 \rangle$ 60° twin boundaries in the FCC phase have also been removed. Grain

boundaries in the matrix are however shown to indicate the presence of δ -Fe - δ -Fe boundaries, where; misorientations $> 2^\circ$ are represented by silver lines and black lines indicate the presence of misorientations $> 15^\circ$. Occurrences of special K-S orientation relationship between the FCC and BCC phases are highlighted by the presence of green lines.

Analysis of the microstructure data in terms of the phase orientation relationships in this way provides a novel method of discrimination between the primary and secondary FCC phase; secondary austenite has characteristically been identified as small particles precipitating intra-granularly, within the large grains of the ferrite matrix or particles, or inter-granularly along former ferrite-ferrite grain boundaries. Certain ambiguity can therefore arise in heavily deformed microstructures between similarly sized buckled/sheared primary austenite and reformed austenite particles. This is illustrated below in Fig. 7.6 where the presence of the K-S orientation relationship between certain small FCC phase particles and the surrounding BCC matrix identifies them as reformed austenite, in contrast to other similarly sized and shaped primary FCC particles where the same orientation relationship between the BCC matrix phase is not observed.

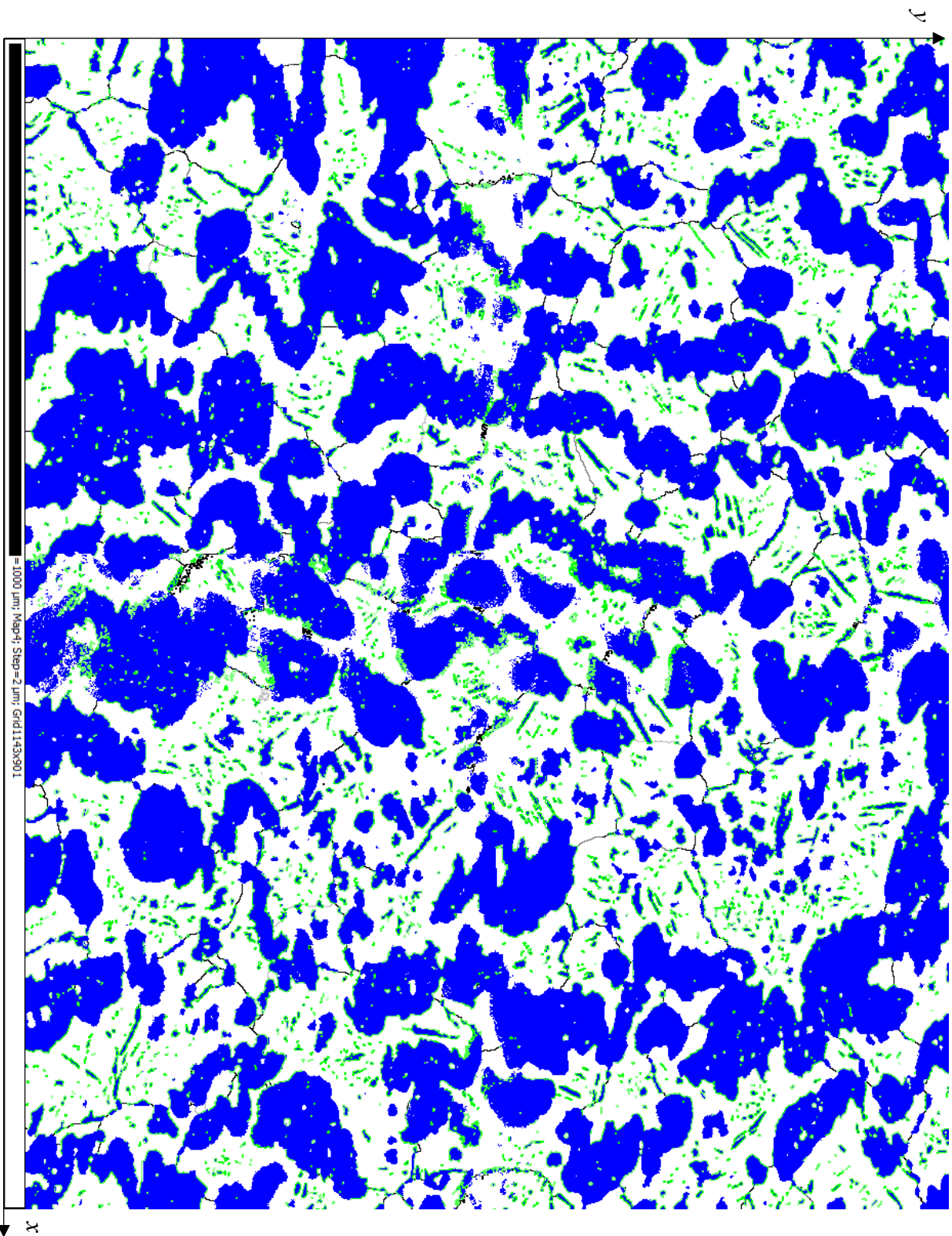


Fig. 7.5 K-S orientation relationships in the CI location microstructure. Occurrences of the special K-S relationship between the FCC and BCC phases in the microstructure are indicated by the green lines. Grain boundaries and sub-grain boundaries in the BCC phase are also indicated by the black, grey and silver lines as discussed above

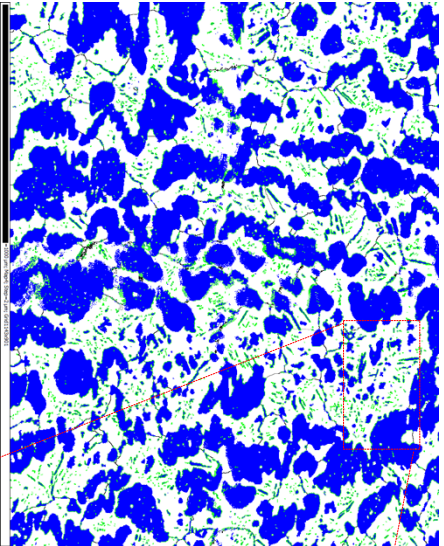
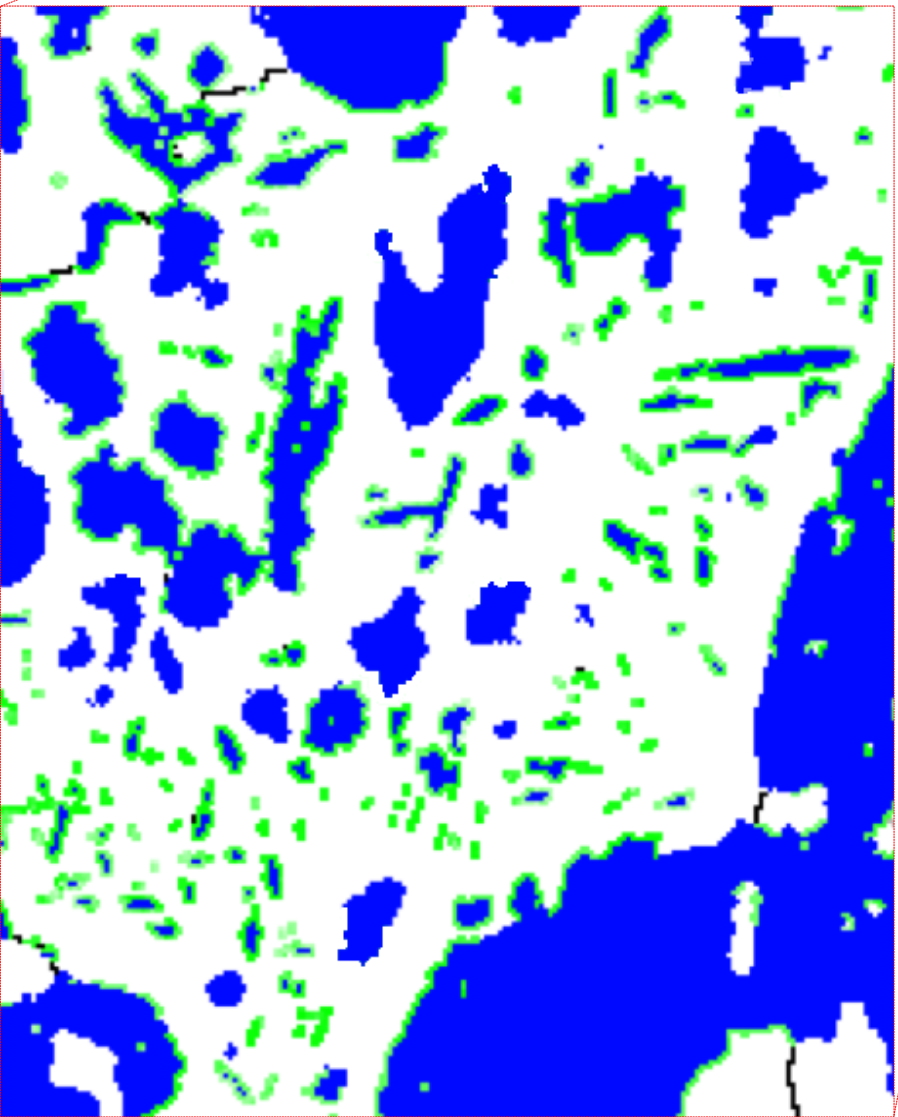


Fig. 7.6 Enlarged section of the C1 location microstructure (shown in relation to its position within Fig. 7.7) in which discernment can be made between reformed and primary austenite particles of similar morphology due to the presence of the K-S orientation relationship with the surrounding ferritic matrix (indicated by the green lines).



The K-S relationship is demonstrated further in instances of inter-granular reformed austenite precipitation, seen to occur almost exclusively along high angle ($> 15^\circ$) δ - δ grain boundaries. Here special misorientations can be seen to occur that satisfy the K-S relationship across both sides of a grain boundary separating two dissimilarly orientated ferrite grains hence allowing bi-directional growth of austenite precipitates from the grain boundary. This phenomenon is demonstrated in Fig. 7.7 where a subset of the data presented in Fig. 7.5 is shown and defines an inter-granular reformed austenite precipitate (white) satisfying the K-S relationship with two dissimilarly orientated ferrite grains across both sides of the grain boundary. Orthogonal consistency with Fig. 7.1 is maintained in Fig. 7.7 and the same line colour scheme to define grain the δ -Fe - δ -Fe boundaries and sub-grain boundaries as well as phase interfaces that satisfy the K-S orientation as Fig. 7.5 & 7.6 is also used.

The insets in Fig. 7.7 shows a high magnification of the area around which the subset noted above is defined. The symmetry between the phases in this subset is illustrated in Fig. 7.8 where non-contoured, scattered data is presented in PF format. The PFs are orientated such that the $\{110\}$ planes of the δ -Fe and the $\{111\}$ planes of the γ -Fe phases are lie closely parallel to the sheet surface, with the major upsetting axis of forging (Y0) lying transversally to this.

Confirmation of the K-S relationship between the austenitic and ferrite phases is provided by the correspondence of the scattered data (from all grains covered in the subset) in the $\{110\}$ δ -Fe and $\{111\}$ γ -Fe PFs. This is emphasised by the dashed red squares and blue circles enclosing the parallel orientations in these phases, respectively. Fig. 7.8a shows the $\{111\}$ γ -Fe PF in reduced contrast such that its superimposition over the $\{110\}$ δ -Fe PF (Fig. 7.8b) allows for identification of these parallel close packed planes through their corresponding positions. The $\{111\}$ γ -Fe PF is shown superimposed over the $\{110\}$ δ -Fe PF in Fig. 7.6b.

The K-S relationship also requires $\langle 111 \rangle_\alpha \parallel \langle 110 \rangle_\gamma$. In the same manner as Fig. 7.8, comparison and superimposition of the $\{110\}$ γ -Fe and the $\{111\}$ δ -Fe PFs (Fig. 7.9) indicates the correspondence of these common close packed directions, as can be seen by the positions of the scattered data along the common great circle (dashed grey line). For confirmation, the $\{110\}$ γ -Fe PF is shown superimposed over the $\{111\}$ δ -Fe PF in Fig. 7.9b.

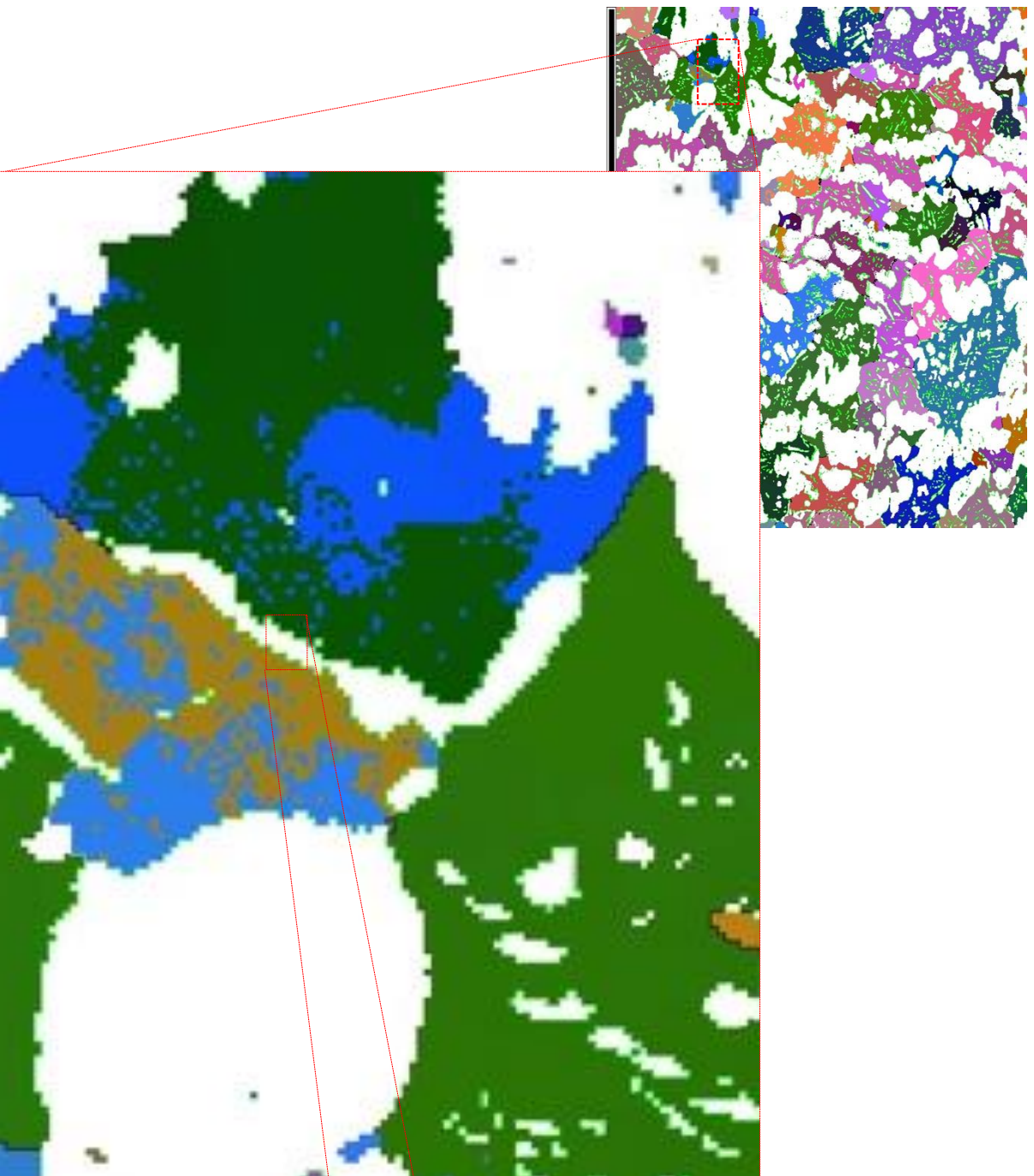


Fig. 7.7 Data subset defining the special K-S relationship (lime green) interface along occurring between an intergranular austenite precipitate (white) and dissimilarly orientated δ -Fe grains

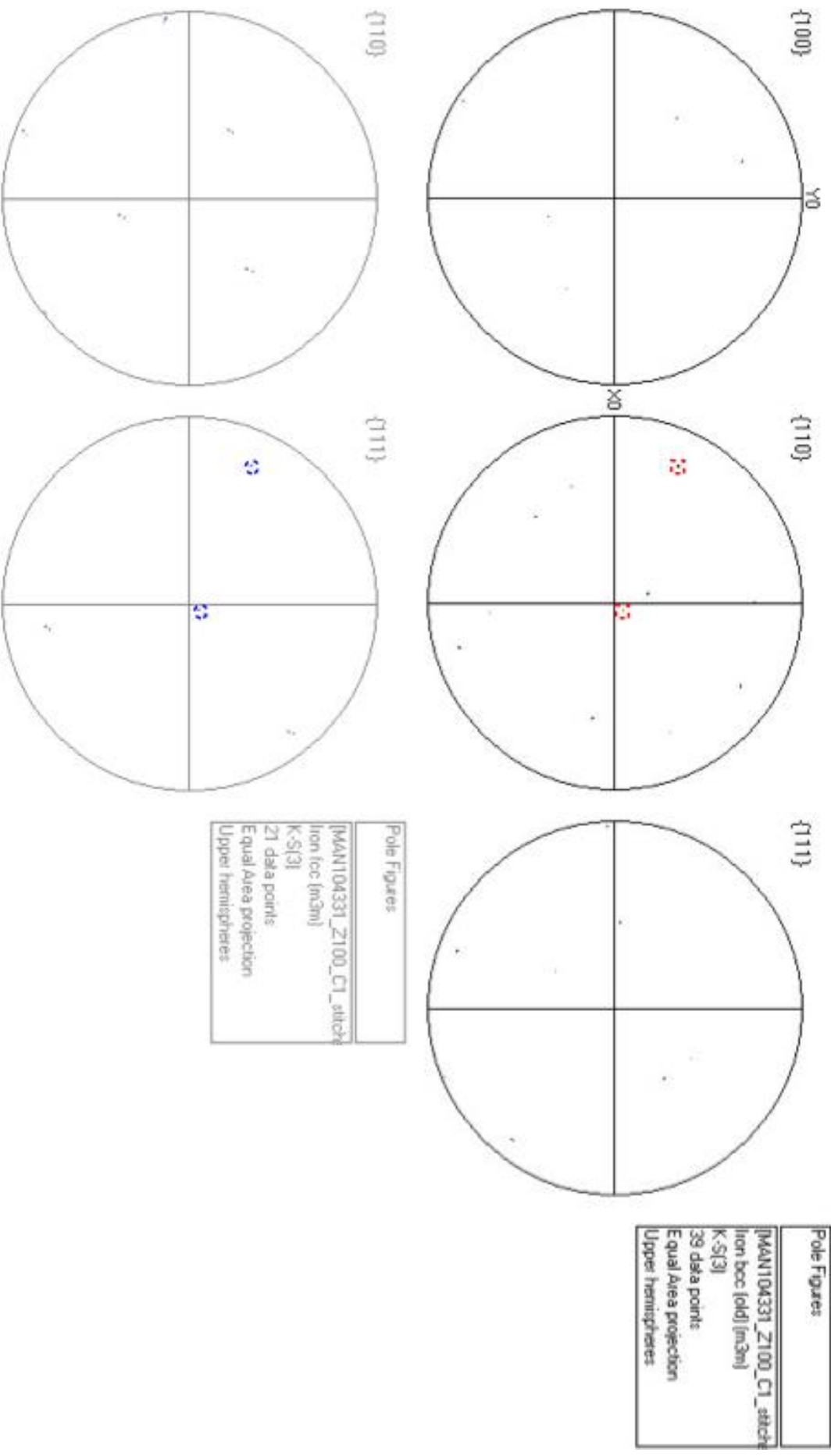


Fig. 7.8a α -Fe and γ -Fe PFs for the data set defined above in Fig. 7.9

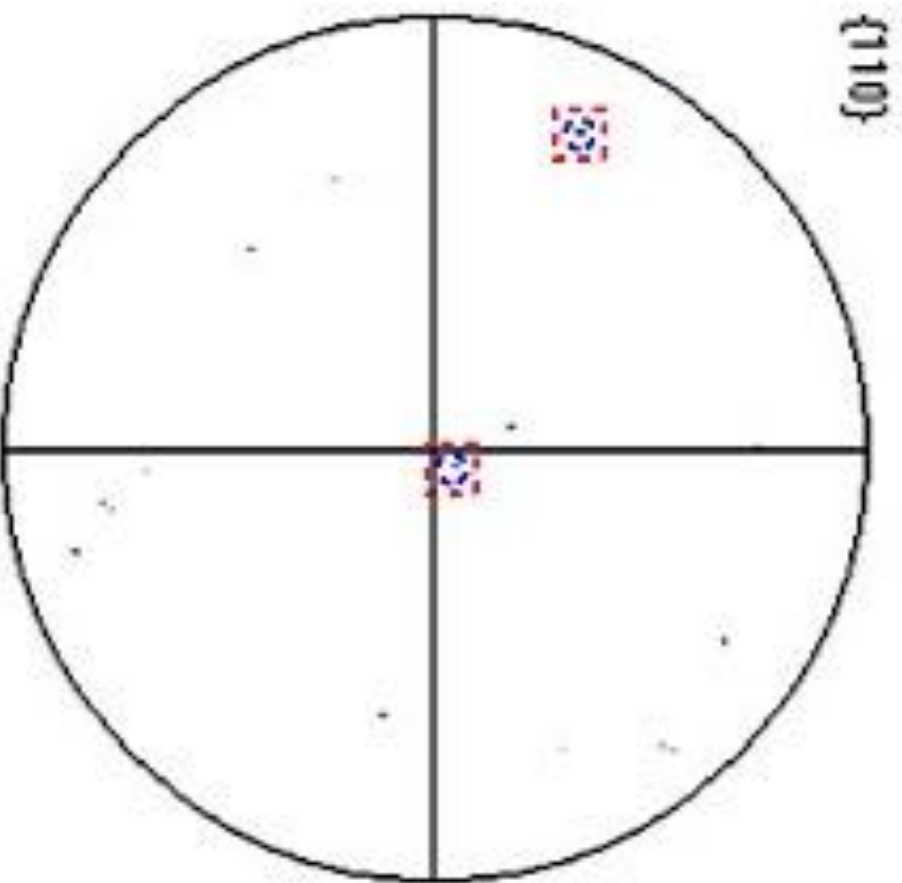


Fig. 7.8b $\{111\}$ γ -Fe PF superimposed on top of $\{110\}$ δ -Fe. Note the correspondence in position of the red squares and blue circles from Fig. 7.8a indicating the parallelism of the $\{110\}$ planes in the δ -Fe either side of the grain boundary, and the $\{111\}$ planes of the intra-granular γ -Fe precipitate, respectively.

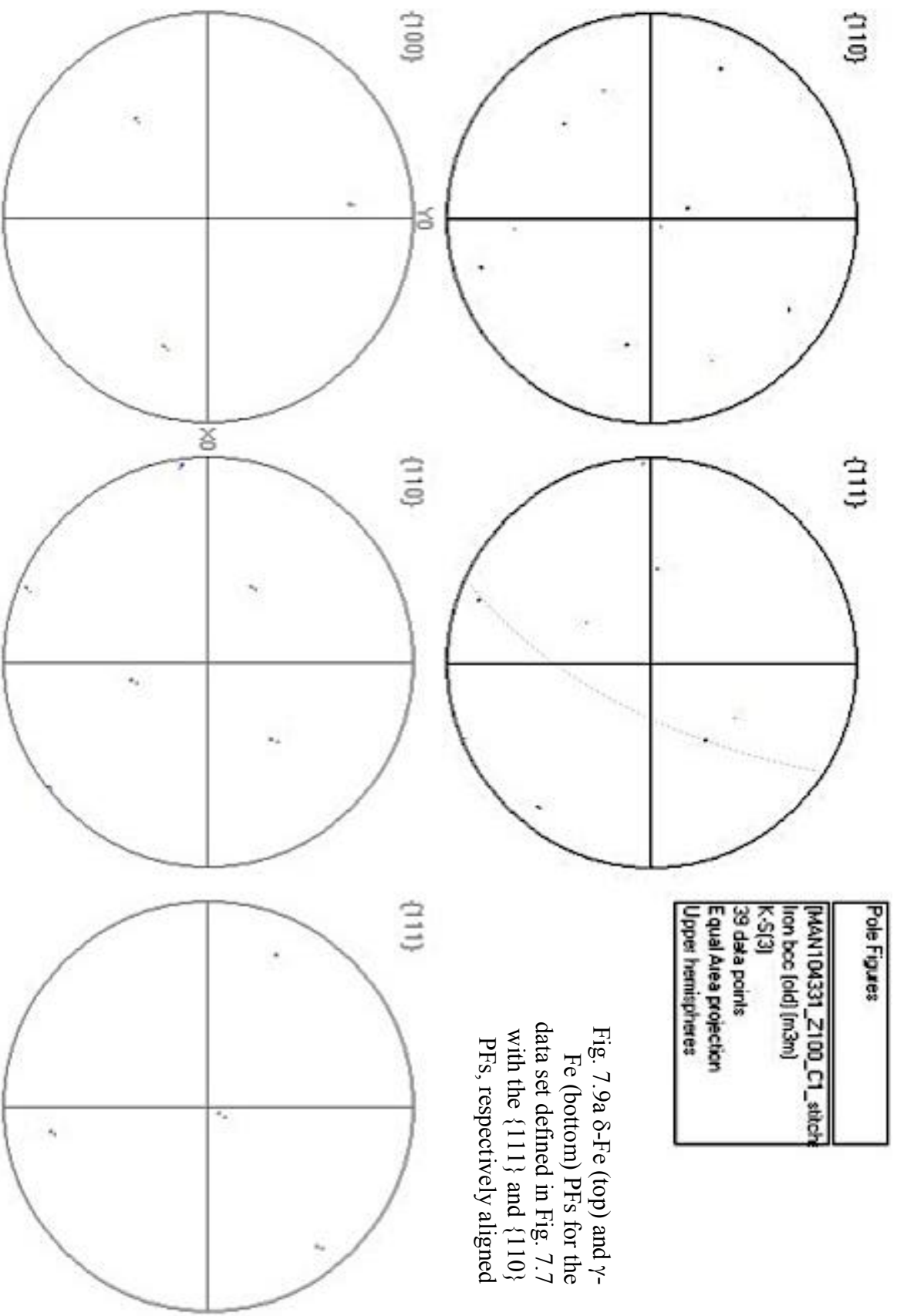


Fig. 7.9a δ-Fe (top) and γ-Fe (bottom) PFs for the data set defined in Fig. 7.7 with the {111} and {110} PFs, respectively aligned

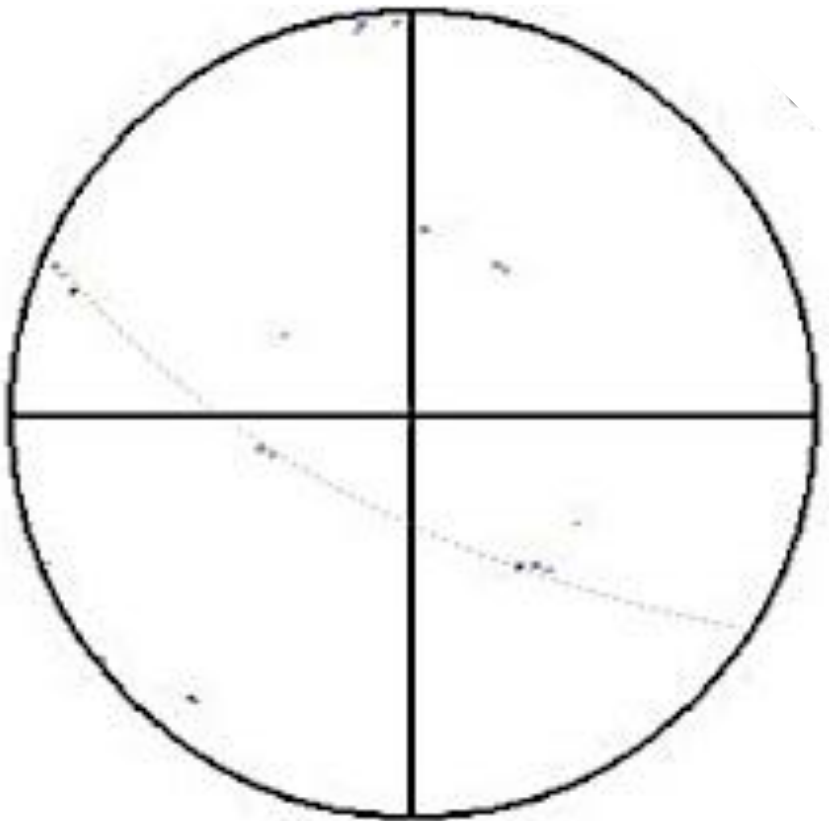


Fig. 7.9b $\{110\}$ γ -Fe PF data superimposed on top of $\{111\}$ δ -Fe PF data (as shown in Fig. 7.11a). Note the correspondence in position of the blue scattered data from the γ -F phase on the same great circle (grey dashed line) along which the black scattered data from the δ -Fe phase lies, thus indicating the parallelism of these two close packed directions.

7.1.2 Close to Bore Inside Diameter, C3 Position

The C3 position in the forging was the worst performing mechanically. As previously described for the C1 position, the data for the C3 position was collected through sequential scans with approximately 5% overlap to maximise coverage of the specimen surface. The step size specified was 0.75 μm .

The scan data indicate the phase balance for this specimen to be 51.7% ferrite and 48.3% austenite. The ferrite phase is coloured red in Fig. 7.10 and the austenite phase is coloured blue. The presence of characteristic $\langle 111 \rangle 60^\circ$ annealing twins in the austenite phase is indicated by the green lines. It should also be noted that in contrast to Fig. 7.1, the axis along which the forging was upset corresponds to the specimen x -axis and the orientation of the Charpy V-notch is parallel to the specimen y -axis in Fig. 7.10.

Fig. 7.13 shows the ferrite phase in the duplex microstructure using IPF colouring. For clarity colouring of the austenite phase has been removed. As noted for the C1 position data, the colouring in Fig. 7.11 demonstrates the coarseness of the microstructure refinement produced by the forging process; the ferritic matrix phase can be seen to form basic microstructure units of size on the order 260 – 625 μm . These measurements are indicated by the arrows in Fig. 7.11 in directions parallel to the major axis along which the forging was upset and also parallel to orientation of the Charpy V-notch, i.e. the direction of crack propagation. Delineation between grains at grain boundaries (defined as misorientations $> 15^\circ$) in Fig. 7.11 is denoted by the black lines. A certain amount of mis-indexing of BCC in FCC Fe grains is also evidenced by the black phase boundary lines in Fig. 7.11 and likely occurred as a result of pseudo-symmetry effects, arising from the close similarities between weak EBSPs generated by these two cubic phases in certain similar orientations.

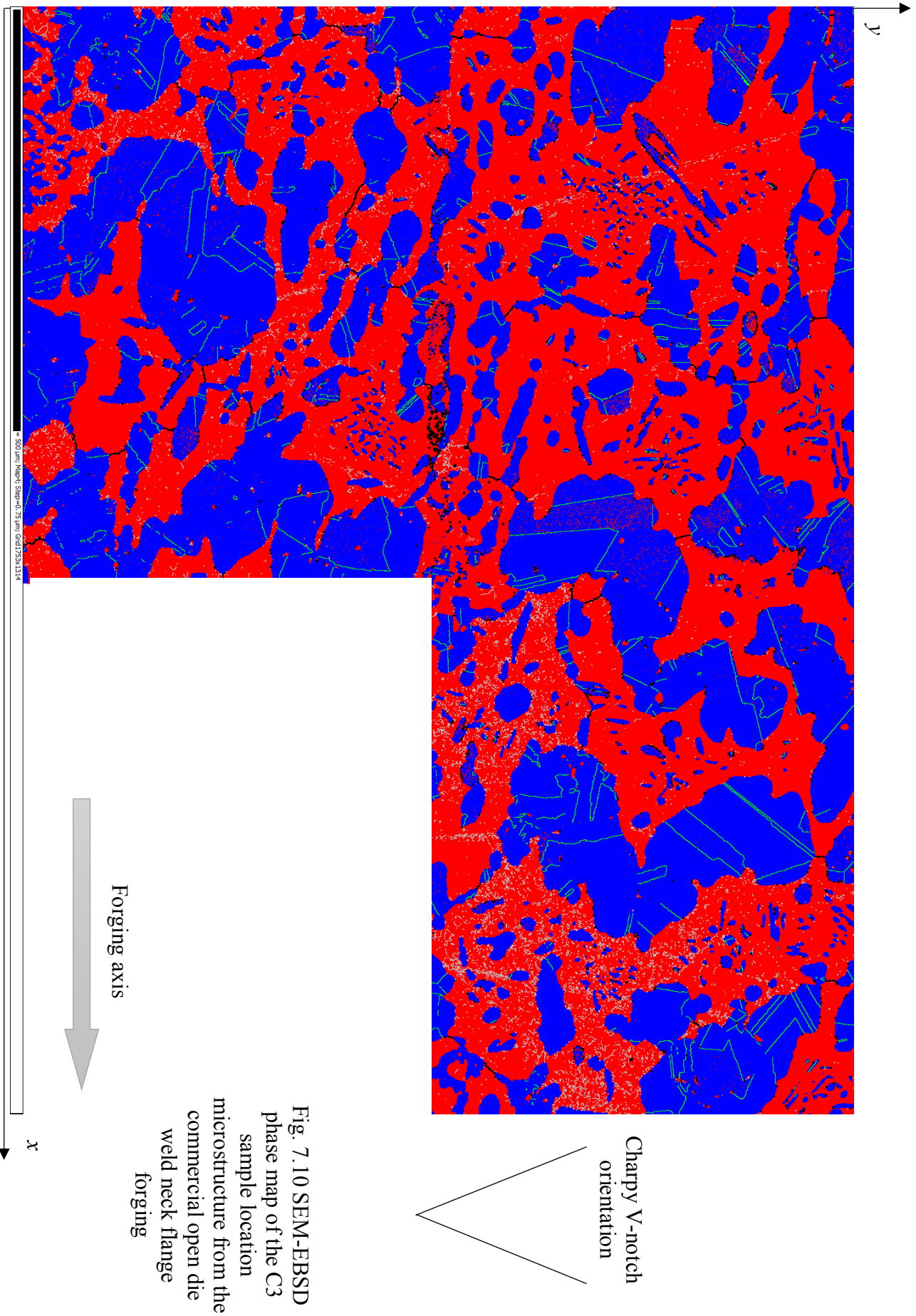


Fig. 7.10 SEM-EBSD phase map of the C3 sample location microstructure from the commercial open die weld neck flange forging

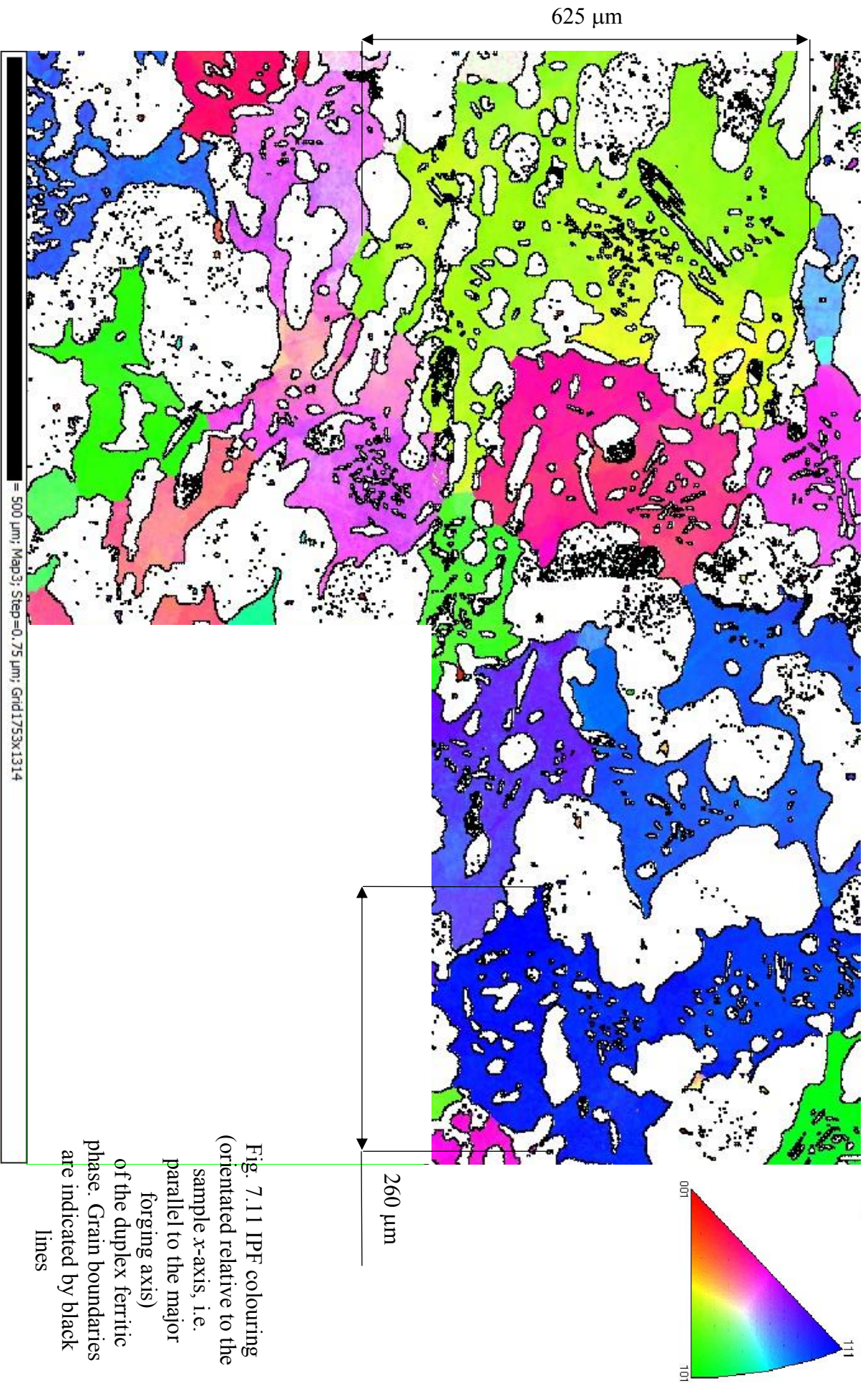


Fig. 7.11 IPF colouring (orientated relative to the sample x-axis, i.e. parallel to the major forging axis) of the duplex ferritic phase. Grain boundaries are indicated by black lines

Texture in the C3 position specimen is represented in the IPFs displayed in Fig. 7.12. The contours in the X0 IPF (orientated parallel to the specimen x -axis, i.e. along the major axis the forging was upset) suggest the occurrence, albeit weakly, of the $\langle 111 \rangle$ part of the duplex fibre texture, $\langle 111 \rangle + \langle 100 \rangle$ commonly seen to occur parallel to the uniaxial compression axis in BCC metals. In the C1 position the other, $\langle 100 \rangle$, part of the duplex texture was seen parallel to the axis of compression. However, strength of the contours in the IPFs is indicated relative to a random distribution, in terms of multiples of uniform density (mud), and the legend suggests that, at most, the occurrence of a $\langle 111 \rangle$ component of the duplex uniaxial compression texture in the FCC Fe is ca. only three times more likely than that of a random distribution of texture.

In the $\{100\}$ PF shown in Fig. 7.13, there is some evidence of a similar component of the fibre texture seen in the comparable pole figure for the ferrite phase in the C1 position (Fig 7.3b). The contours in this PF suggest a clustering, and slight rotation of the (100) plane normal about the forging axis parallel to the sheet surface, and the corresponding clustering of the [100] direction closely along Y0 axis (the axis along which the Charpy V-notch is orientated in this position), with approximately equal rotation about the X0 axis

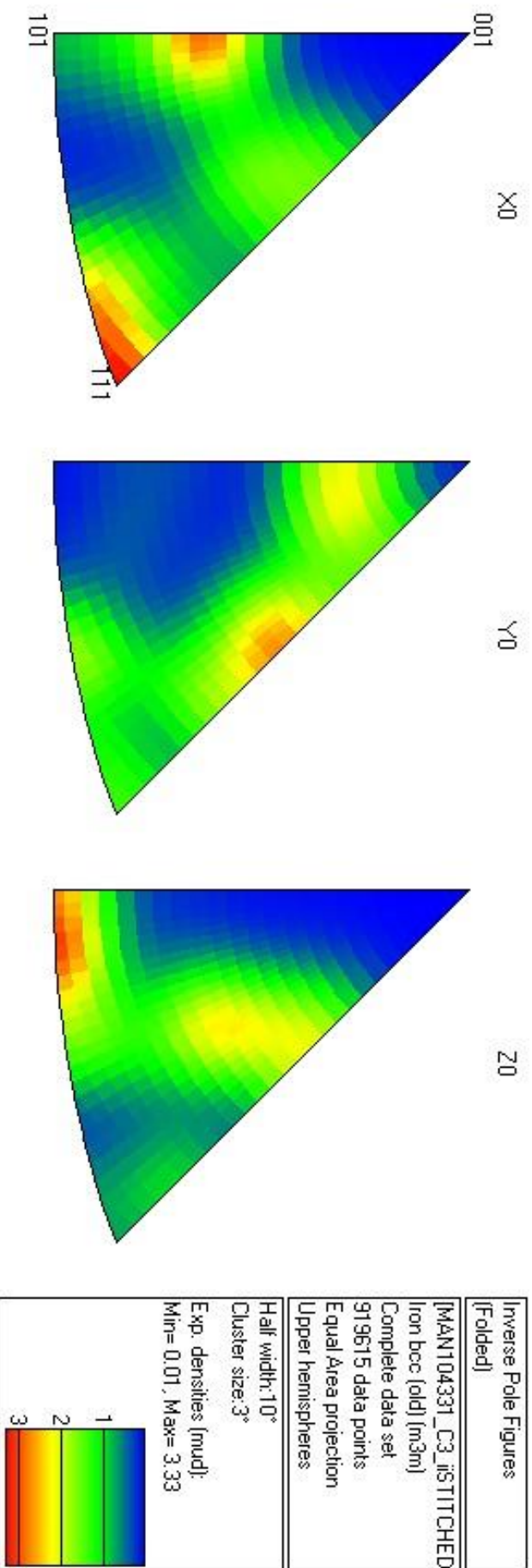


Fig. 7.12 IPF representation of the ferritic matrix texture in the C3 position in the open-die 16" weld neck flange forging

Clustering from 111 X0 IPF

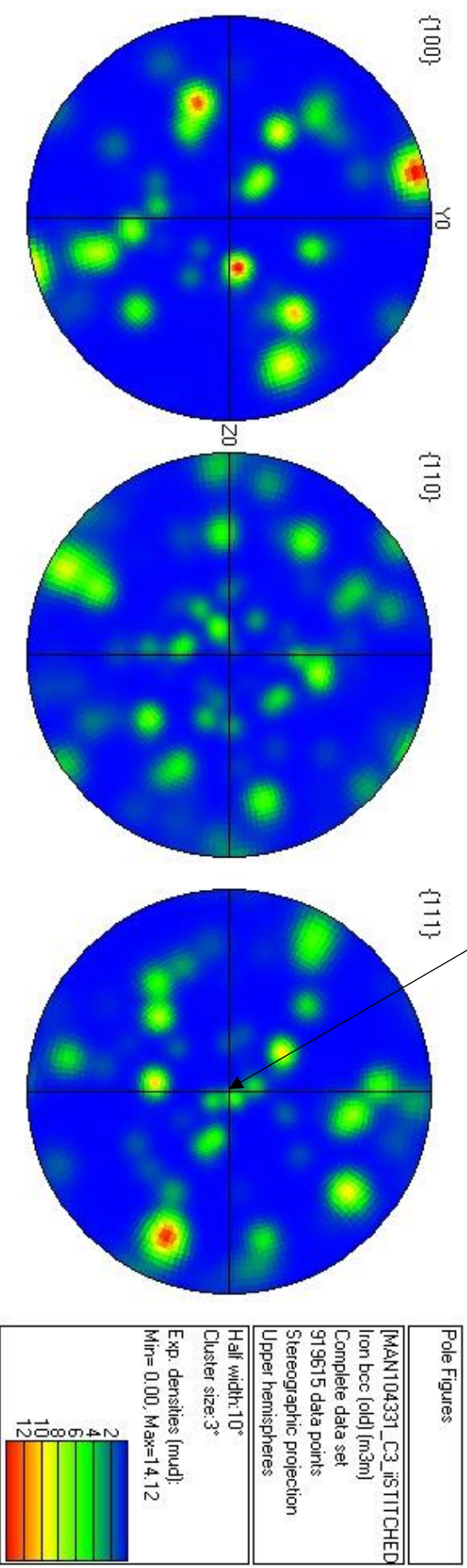


Fig. 7.13 Pole figures for the duplex ferrite phase in the C3 forging position where, in the left side PF, the {100} planes lie closely parallel to the sheet surface, i.e. along the axis the forging was upset and the <100> directions lying close to the Y0 and Z0 directions.

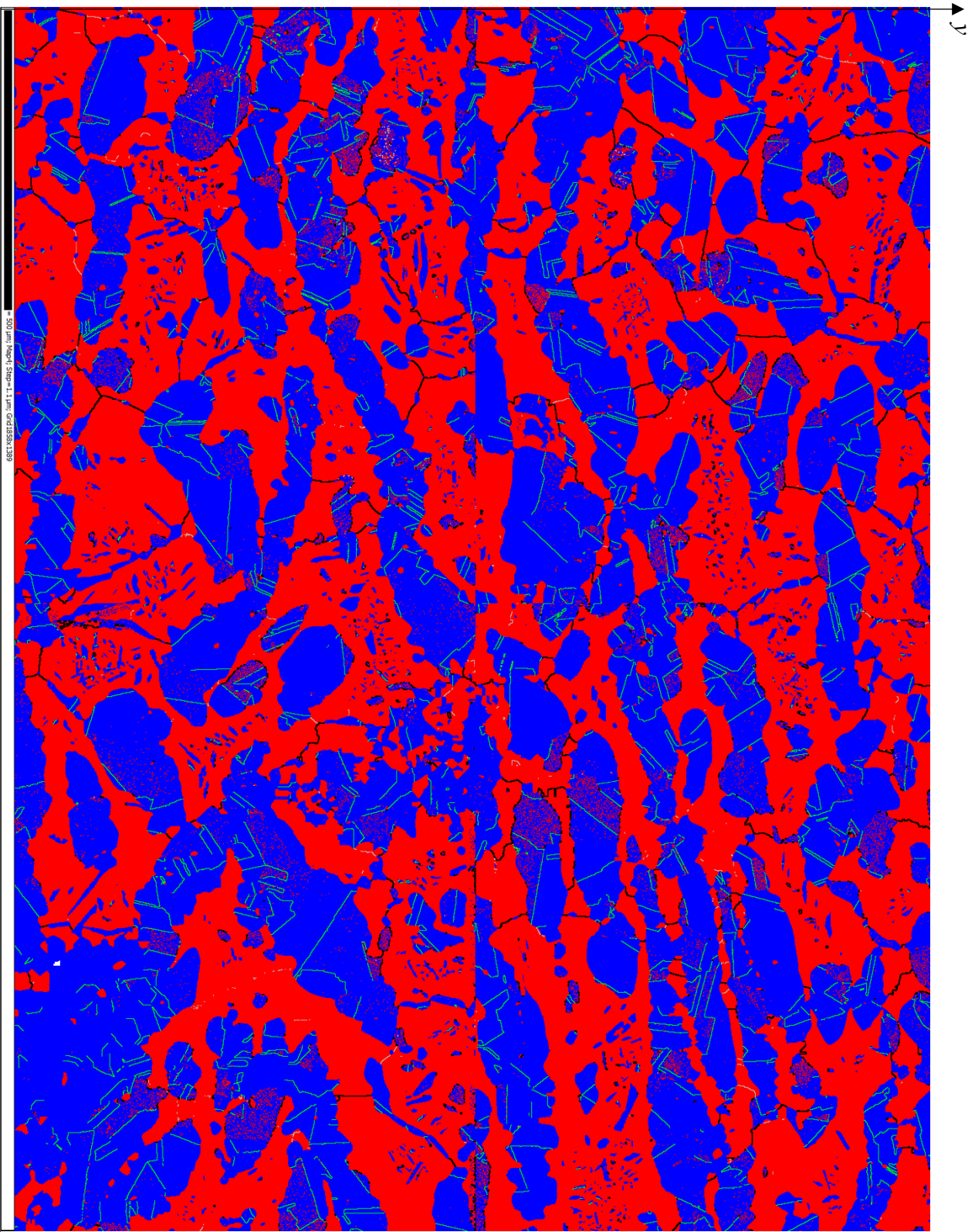
7.1.3 Flange Centre, C7 Position

Table 7.1 indicates that the averaged toughness recorded at the C7 position fell below the minimum mean permissible value, despite all three tests producing impact toughness results above the minimum individual value of 35 J. In this regard, the C7 and C3 positions in the forging share the most similar mechanical properties.

As with the data presented for the C1 and C3 locations, the scan of the C7 specimen surface presented in Fig. 7.14 is composed of four sequential scans with an approximate overlap of 5%. In total, an area approximately 3.15 mm² of the surface of the C7 specimen was scanned, with a step size of 1.1 µm. The scan data indicate the phase balance in the C7 position to be 49.6% ferrite and 50.4% austenite. In Fig. 7.16 the BCC ferritic matrix is coloured red and the FCC austenitic phase is coloured blue (to maintain consistency with the presentation of data from the C1 and C3 positions).

Characteristic $\langle 111 \rangle$ 60° annealing twins in the austenite phase are again indicated by the green lines in Fig. 7.16. As indicated in Fig. 7.12 for the C3 specimen, the axis along which the forging was upset again also corresponds to the specimen *x*-axis in the C7 specimen, and the orientation of the Charpy V-notch is parallel to the specimen *y*-axis. This orthogonal alignment is indicated on Fig. 7.14.

Fig. 7.15 shows the scanned surface of the C7 specimen using IPF colouring for the ferritic matrix, in the direction of the specimen *x*-axis, i.e. parallel to the axis along which the forging was upset. Again, as in Fig. 7.13, ferritic grain boundaries $> 15^\circ$ in the ferrite matrix are indicated by black lines and silver lines denote misorientations $> 2^\circ$. Using the IPF colouration in this way again illustrates the large size of the basic ferrite microstructure unit; on the order of ca. 500 µm when measured along the specimen *x*-axis. As in Fig. 7.1 illustrating the microstructure morphology in the C1 position, the orientation of the large primary austenite lath-like grains can be seen broadly to be aligned parallel to the forging axis. This may be interpreted as indicative of some retention of the as-received starting billet microstructure morphology in the final forged component.



Charpy V-notch orientation

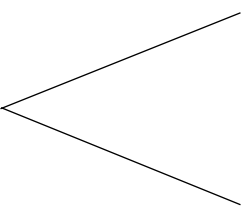


Fig. 7.14 SEM-EBSD phase map of the C7 sample location microstructure from the commercial open die 16" weld neck flange forging

Forging axis



x



The texture of the ferrite matrix in C7 specimen is illustrated in Fig. 7.16 where the X0 PF indicates the weak presence of the $\langle 111 \rangle$ component (aligned closely to the forming axis) of the duplex $\langle 111 \rangle + \langle 100 \rangle$ texture characteristic of BCC metals subject to uniaxial compression. The indication in Fig. 7.16a of a clustering of $\langle 111 \rangle$ crystal directions almost parallel to the X0 forming axis is however shown to be only ca. 2 – 2.5 times more likely than that of a random distribution of directions. This is likely to be largely a function of the coarse ferrite grain size (Fig. 7.15) and consequently, the relatively small number of grains covered by the scan step size of 1.1 μm . The texture indicated therefore may be attributable to a small number of strongly orientated grains rather than representative of the general bulk anisotropy. This limitation is indicative of the difficulty in balancing the antagonistic experimental parameters of high-resolution data derived from appropriately small step sizes (i.e. small enough to detect potential tertiary phase precipitates) and scan areas that are sufficiently large so as to be statistically representative of the bulk material.

This weak indication of texture in the BCC phase is however reinforced by the $\{111\}$ PF (Fig. 7.16b) where the $\{111\}$ planes are orientated parallel to the sheet surface and which can be observed to seemingly indicate the same small clustering of $\langle 111 \rangle$ directions lying slightly rotated about the X0 (major forming) axis. Correspondingly, the (001) stereographic projection shown in the $\{100\}$ PF (Fig. 7.16b) also indicates the potential presence of several $\{111\}$ plane normals, again with the noted rotation about the x -axis.

In contrast to the BCC ferrite phase, the presence of texture, however weak, is not observed in the other duplex FCC austenite phase, largely as a result of the orientation mismatches across the large number of $\langle 111 \rangle$ 60° intra-granular annealing twin boundaries (illustrated by the green lines in Fig. 7.14).

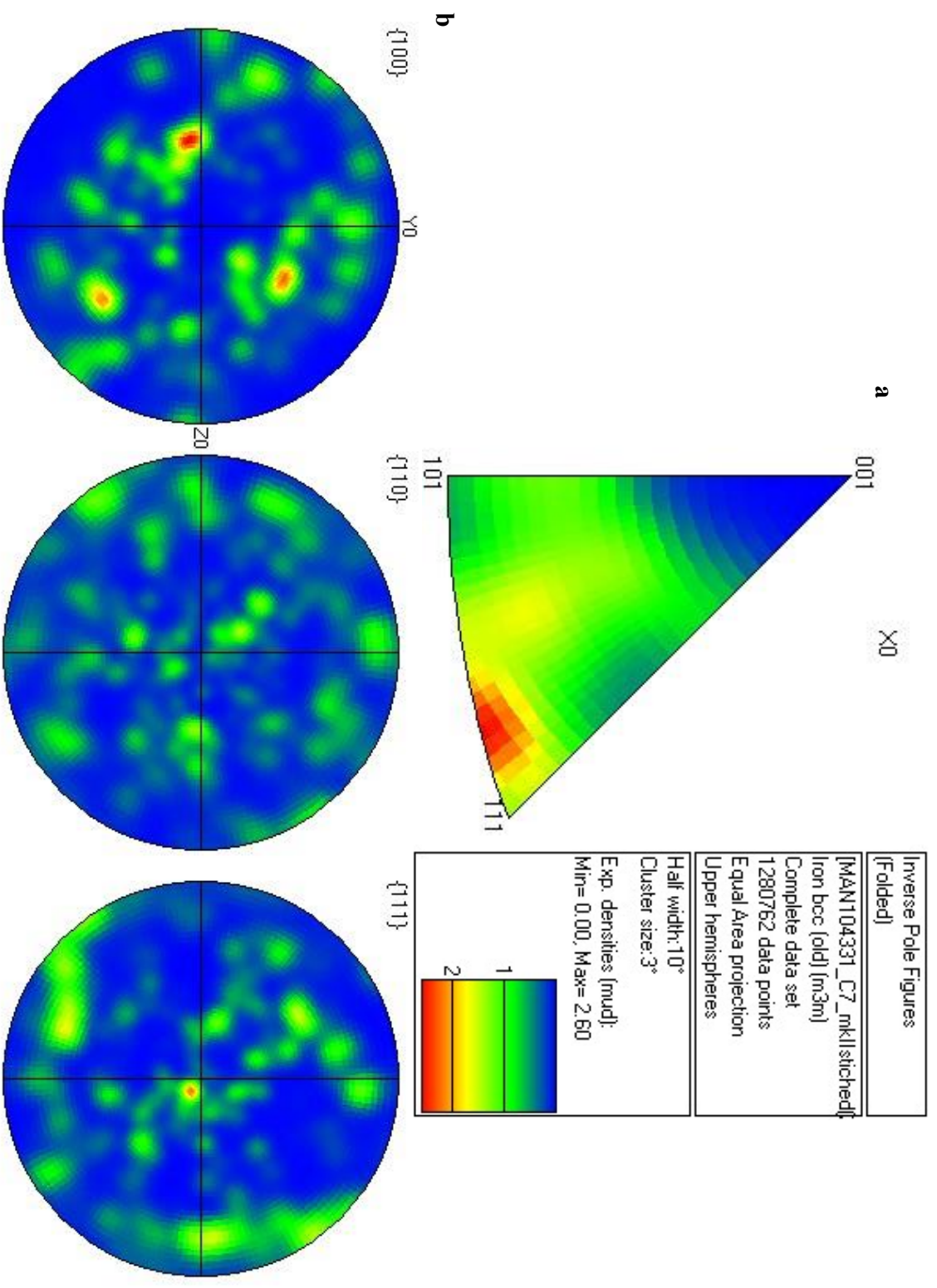


Fig. 7.16 Texture in the duplex BCC Fe phase in the scanned area of specimen C7 represented in **a** IPF and **b** PF formats. Note the presence of the $\langle 111 \rangle$ fibre indicated by the sharp contour in the $\{111\}$ PF

7.1.4 Summary of the Localised Crystallography in the 16" Open Die Weld Neck Flange Forging

The preceding three sub-sections of this chapter have presented a general summary of the crystallography of the 16" open die weld neck flange forging in three specific locations. A notable observation can be made from the data presented above when considering the substructure of the BCC Fe matrix in the three different positions in the forging. The greater volume of ferrite sub grain boundaries ($< 15^\circ$, and more specifically $\leq 5^\circ$) in the C3 position than the C1 and C7 positions is superficially apparent from comparison of Figs. 7.1, 7.10 & 7.14. This observation is however confirmed and quantified in Fig. 7.19 below where the relative frequencies of the misorientation distributions ($^\circ$) in the BCC Fe are plotted for each location in the forging.

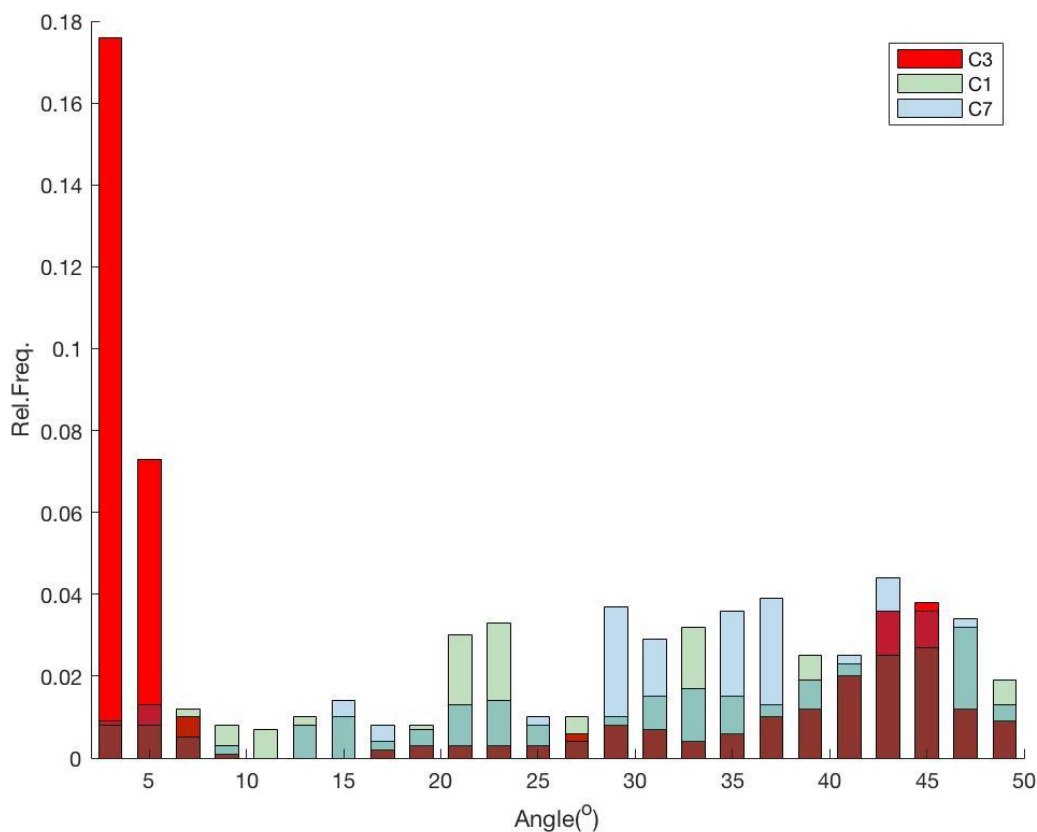


Fig. 7.17 BCC Fe misorientation distribution for the three locations in the forging

Fig. 7.17 demonstrates that the greatest relative frequency of low angle sub grain boundaries in the duplex BCC Fe matrix occur in the C3 position within the forging. This is also the location from which the least tough Charpy V-notch specimens were taken and suggests a potential correspondence between poor mechanical properties and the occurrence of ferritic substructure in the microstructure.

Further to this observation, in both C3 and C7 positions the same $\langle 111 \rangle$ component of the duplex $\langle 111 \rangle + \langle 100 \rangle$ deformation texture associated with the uniaxial compression of BCC metals was seen to have formed in the bulk duplex BCC Fe matrix and was aligned parallel to the major forming axis. Conversely, in the C1 forging location, from where the Charpy V-notch samples produced impact toughness values that exceeded specification, the $\langle 100 \rangle$ component of the duplex $\langle 111 \rangle + \langle 100 \rangle$ deformation texture was seen in the overall BCC Fe duplex phase data. Upon first impression, this observation suggests that the $\langle 111 \rangle$ fibre rather than the $\langle 100 \rangle$ fibre may play a role in the low impact toughness. This, however, is unexpected since the (100) plane is the nominal cleavage plane for BCC metals and thus a $\langle 100 \rangle$ fibre texture would be expected to produce a lower resistance to crack propagation when the V-notch is orientated perpendicular to the major forging axis.

It is however judicious to note at this point the limitations of the data sets presented above when drawing conclusions about location-specific texture within the 16" open die weld neck flange forging. As was indicated previously, the lack of grain refinement resulting from the open-die forging process has resulted in a component with a comparatively very large basic microstructure unit size; the ferrite matrix has been shown to have average grain size on the order ca. 250 – 800 μm (Figs. 7.11 & 7.15). Consequently, despite the large number of data points collected during the EBSD scans, the number of unique grains indexed was relatively small and therefore the scan area needs to be much expanded to have confidence in the observations above. In reflecting on the relative lack of grain refinement in the forging, it seems likely that as much as crystallographic orientation may play a part in determining mechanical properties, impact toughness will be strongly influenced by the large ferrite mean free paths for crack propagation presented by essentially unrefined basic microstructure matrix units.

Of final note however concerning the analysis of the commercially thermo-mechanically processed ZERON® 100 material (and as will be explored further in the following section), certain microstructure similarities can be observed in the data from the C3 and C7 positions (Fig. 7. 10 & Fig. 7.14); precipitation of γ_2 particles appears largely intra-granular with very little allotriomorphic austenite decorating the ferrite grain or sub grain boundaries (especially so in the C3 position). Conversely, the microstructure in the C1, although by no means devoid of intra-granular γ_2 , appears to contain more ferrite – ferrite grain boundary precipitation. As

will be discussed in detail below, these microstructure differences in these different locations may be indicative of thermal heterogeneity within the forging during deformation, i.e. the material in the C1 position was hotter than that in the C3 position, potentially as a result of cyclic cooling and intermediate reheating as the workpiece was forged. Without appropriate data (pyrometry, thermocouple etc.) and records of the forging schedule from the forge shop however, this is difficult to confirm.

Optical metallographic analysis of the material subject to EBSD appear to support this qualitative assessment of the C1 and C3 EBSD microstructure data where the greatest volume fraction of γ_2 was calculated in the C1 sample the precipitates of which were also, on average, the least circular, i.e. of elongated, needle-like, allotriomorphic morphology. It is inferred that this elongated acicular morphology is largely a product of the growth along ferrite grain boundaries of the allotriomorphic precipitates. Conversely, the least tough Charpy sample (from the C3 location within the forging) had the smallest fraction of reformed austenite and these precipitates were, on average the most circular, i.e. equiaxed morphology. The proportion of γ determined to be γ_2 precipitates and associated circularity at the three test positions within the 16" weld neck flange forging are plotted against impact toughness in Fig. 7.18.

Optical micrography of the C3 specimens subject to SEM-EBSD analysis adds a further interesting dimension to the interpretation of mechanical behaviour as a function of location within the commercial forging. In Fig. 7.21 the obvious dark mottled/speckled areas suggest the potential precipitation of Cr-nitrides within the ferrite matrix (as revealed by the electrochemical etching procedure outlined in Ch. 4.5). The embrittling nature of these tertiary precipitates has been well documented (Ch. 3.1.2) and in combination with the above noted large ferrite mean free paths (as a result of coarse matrix grain size) and possibly even the higher density of low angle sub-grain boundaries (relative to the C1 and C7 positions, Fig. 7.19), may have contributed to the low impact toughness test score. No evidence of Cr-nitrides was however found through EBSD analysis of the sample and therefore it is important to note that this 'pitting' identified in Fig. 7.19 may also be an idiosyncratic artefact of the etching process, i.e. 'over-etching' in areas of high current density. Since Cr-nitrides are nano-sized their detection through micron step size EBSD scans designed to capture data from large areas for the purposes of texture analysis is inappropriate. Additionally, the 'pitting' noted in Fig. 7.19 results from the electrochemical dissolution of Cr-nitrites by the oxalic acid.

Spectrographic analysis e.g. EDS would therefore not necessarily indicate high concentrations of N or Cr in these areas.

Fig. 7.20 shows optical micrographs from the C1-location specimen, the toughest of the three taken from the commercial 16'' flange forging. Again, the same obvious dark mottled/speckled areas as in Fig. 7.19 can be seen. Note however, that these areas correspond to the most 'highly etched' areas of the sample surface (blue arrows in Fig. 7.20a) suggesting possible corroboration of the above noted possible effect of over etching.

Since the C1 position Charpy samples were the much tougher than the C3 samples it would appear to follow that the potential Cr-nitride precipitation identified in Figs. 7.19 and 7.20 does not embrittle the duplex ferrite matrix so much as to be solely attributable for dramatically reducing impact toughness. Instead it is suggested that a nitrated duplex microstructure may even be tolerable in terms of impact toughness if sufficient matrix grain size refinement can be achieved, i.e. through the pinning effect of intra-granular γ_2 precipitates which may also confer additional crack retardation properties. Avoidance of Cr-nitride precipitation in the duplex microstructure should be regarded as optimum thermomechanical processing practice. However, the physical limitations imposed by section thickness, cooling rate, chemical composition and thermodynamics means this may not always be possible. Figs. 7.19 & 7.20 in combination with the data presented in Table 7.1 challenge the reported primacy ascribed to the deleterious effect of Cr-nitride precipitation, as noted in Ch. 3.1.2. Instead the data and analyses in this work suggest an incremental, combinational deleterious effect on impact toughness where Cr-nitride precipitation occurs in concert with sub-optimal microstructure unit sizes.

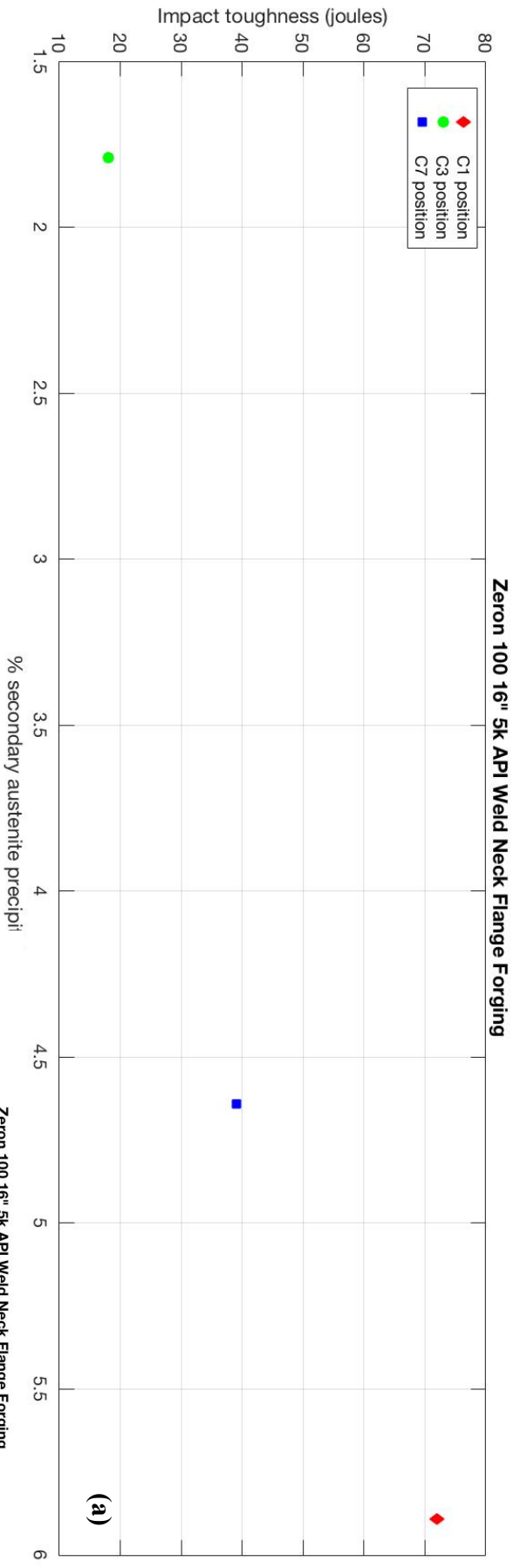


Fig. 7.18 Impact toughness in the Charpy test locations as functions of γ_2 parameters **a** the toughest Charpy sample (from C1 position within the forging) had the greatest fraction of γ_2 **b** these precipitates were also, on average, the least circular, i.e. elongated, needle-like morphology.

Conversely, the least tough Charpy sample (from the C3 location within the forging) had the smallest fraction of γ_2 and these precipitates were, on average the most circular, i.e. equiaxed morphology

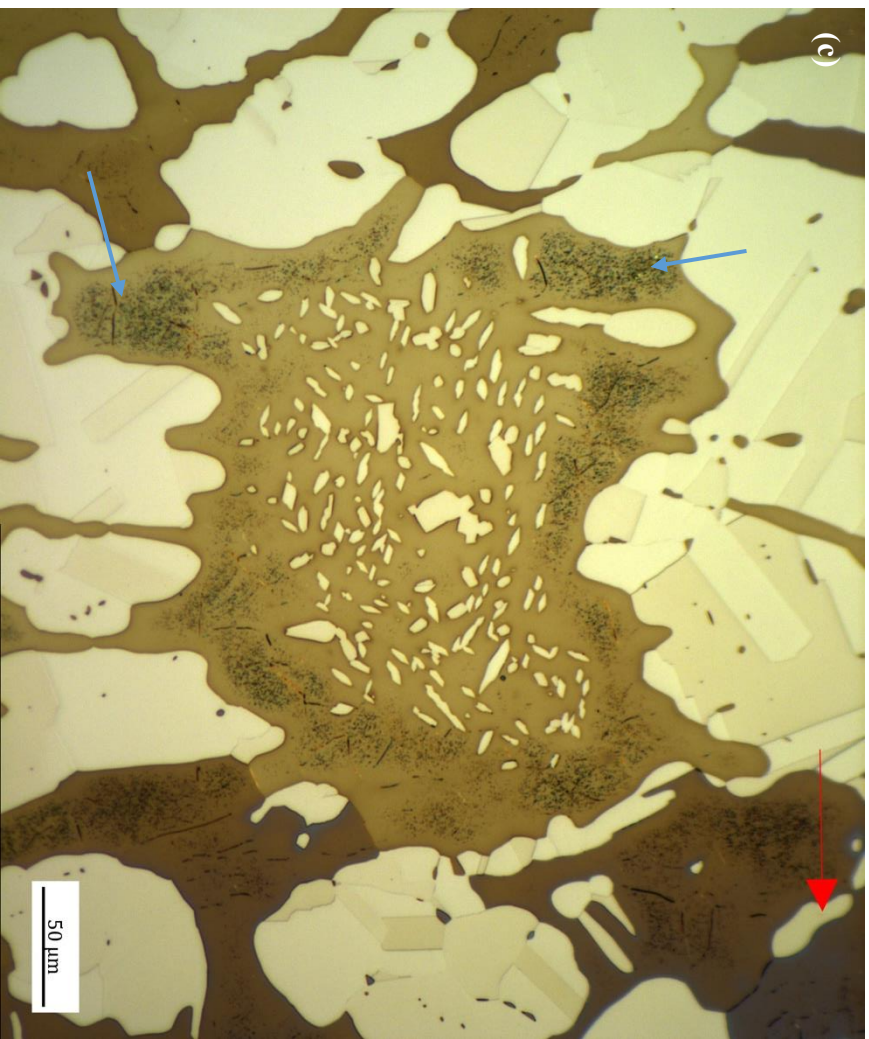
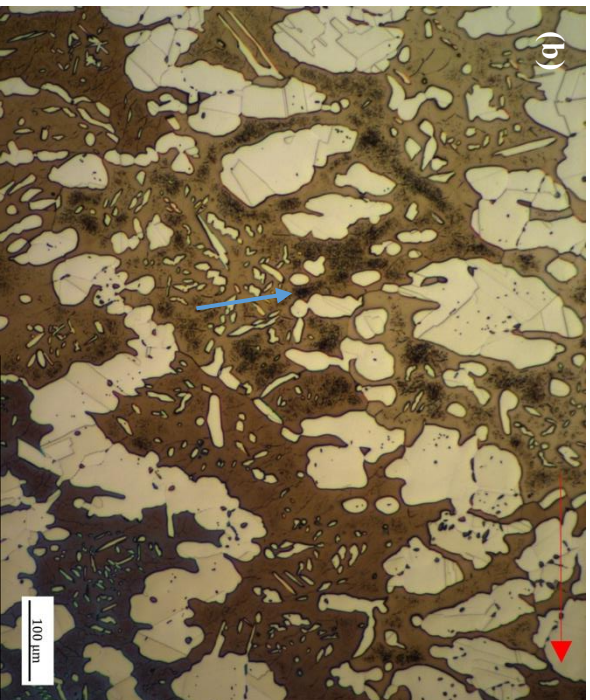
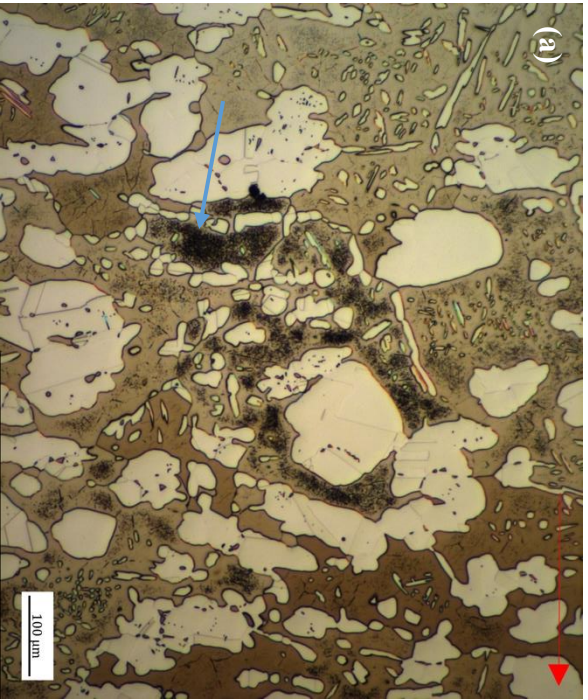


Fig. 7.19 Optical micrographs of the C3 impact toughness specimens subjected to the SEM-EBSD analysis detailed above. The red arrows indicate the direction of the major longitudinal axis along which the forging was upset and therefore the direction perpendicular to that of crack propagation. Blue arrows point to the obvious dark mottled/speckled areas potentially indicative of Cr-nitride precreation

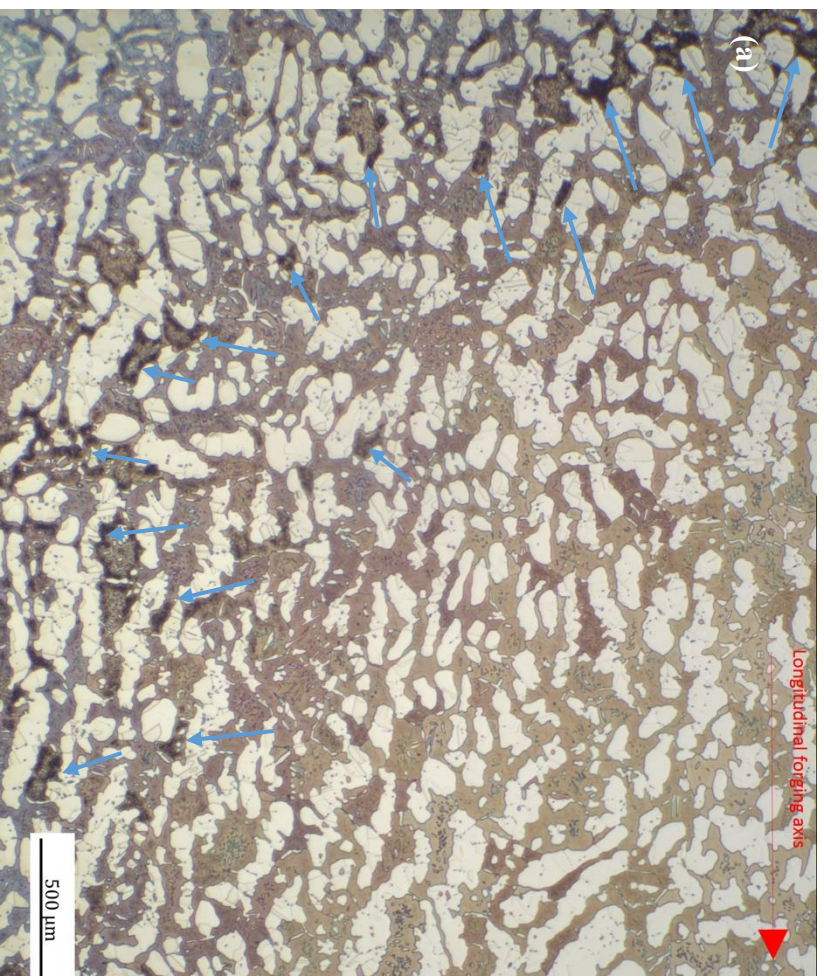
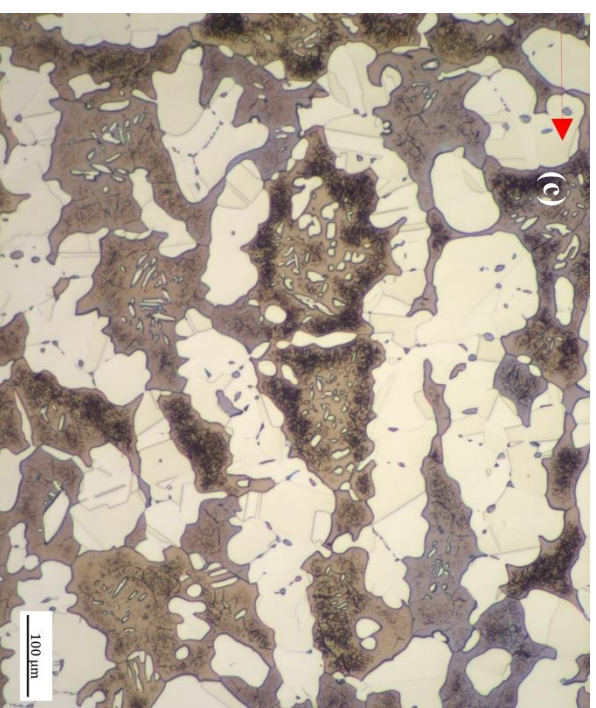
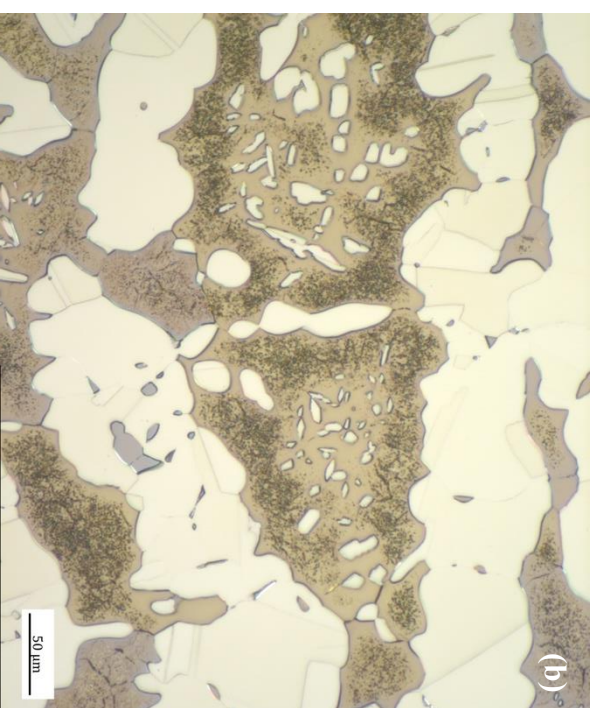


Fig. 7.20 Optical micrographs of the C1 impact toughness specimens subjected to the SEM-EBSD analysis detailed above. The red arrows indicate the direction of the major longitudinal axis along which the forging was upset and therefore the direction perpendicular to that of crack propagation. Blue arrows point to the obvious dark mottled/speckled areas potentially indicative of Cr-nitride precreation



7.2 Industrially Analogous Thermo-Mechanical Processing Tests

As described in Table 4.3, a series of industrially analogous tests were carried out on the TMC machine under the objective to replicate with as high fidelity as possible, the commercial open die forging process through which billet starting stock material is converted into a bossed forging and from then subject to final QHT. A total of 12 industrially analogous tests were carried out from which four samples were subject to crystallographic analysis via SEM-EBSD. With reference to Table 4.3, these were the samples from test numbers 3,4,7 & 8. The time – temperature profiles of these four tests are illustrated schematically below in Figs. 7.21 – 7.24. The selection of these particular four tests allowed for the capture of both the high and low temperature deformation microstructure immediately after uniaxial compression (experimental correspondence to open die forging) via water quenching (test nos. 3 & 4) and comparison with the effects of allowing the sample to air-cool under *quasi*-equilibrium conditions (test nos. 7 & 8), again between deforming (forging) and quality heat treatment.

The high and low forging temperatures were specified as 1200 and 1050°C, respectively since these temperatures represent, in the case of 1200°C, the best compromise between the upper limit of the commercial forging temperature range (1280°C) and the reliable operational capacity of the TMC, and in the case of 1050°C, the lower limit of the commercial forging temperature range (below which the work piece is required to be reheated before forging can continue). The quality heat treatment (QHT) temperature post-deformation was kept constant across the four tests at 1080°C and represents the lower of the two temperatures used for QHT in industrial practice. The higher temperature also used in the QHT of ZERON® 100 forgings is 1120°C. The lower QHT temperature has been previously tentatively specified in commercial practice in an attempt to prejudice the formation of a greater volume fraction of austenite such that the microstructure's capacity to absorb nitrogen, as it is rejected from solution within the ferrite phase at high temperature, during the water quench is improved and the formation of Cr-nitrides less likely. It is also hypothesised that a higher austenite volume fraction than ferrite would infer greater corrosion resistance. Quantitative metallographic measurement on the data here however indicate such a prejudice towards greater f_{γ} from QHT at 1080°C may not necessarily be achieved.

Deformation during the industrially analogous thermo-mechanical tests was carried out at a constant strain rate of 0.1 s^{-1} and to a constant true strain of 0.69 (i.e. a half-height compression of the test sample). The TMC test samples dimensions' have been considered previously in Ch. 4 & Ch. 5 and were taken from the as-received, 250 mm diameter AFP ZERON® 100 billet (detailed and characterised in Ch. 2.) parallel to its L -axis.

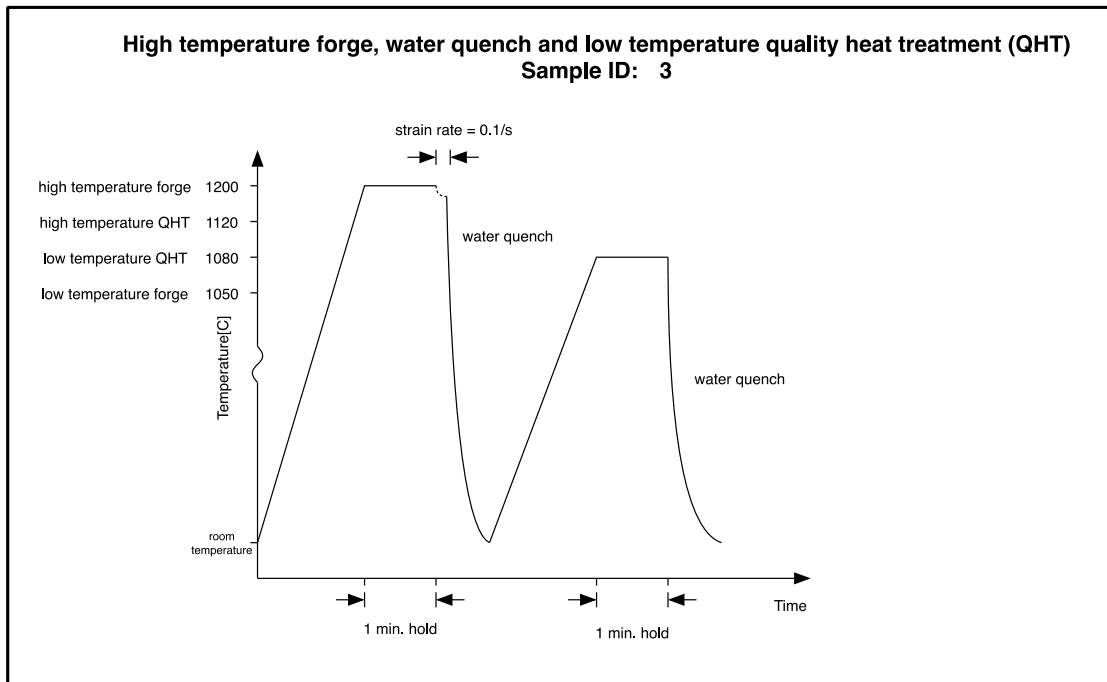


Fig. 7.21 Time-temperature profile for test # 3; compression at 1200°C (high temperature forge), water quench, reheat to and soak at 1080°C (low temperature QHT) and then water quench to room temperature.

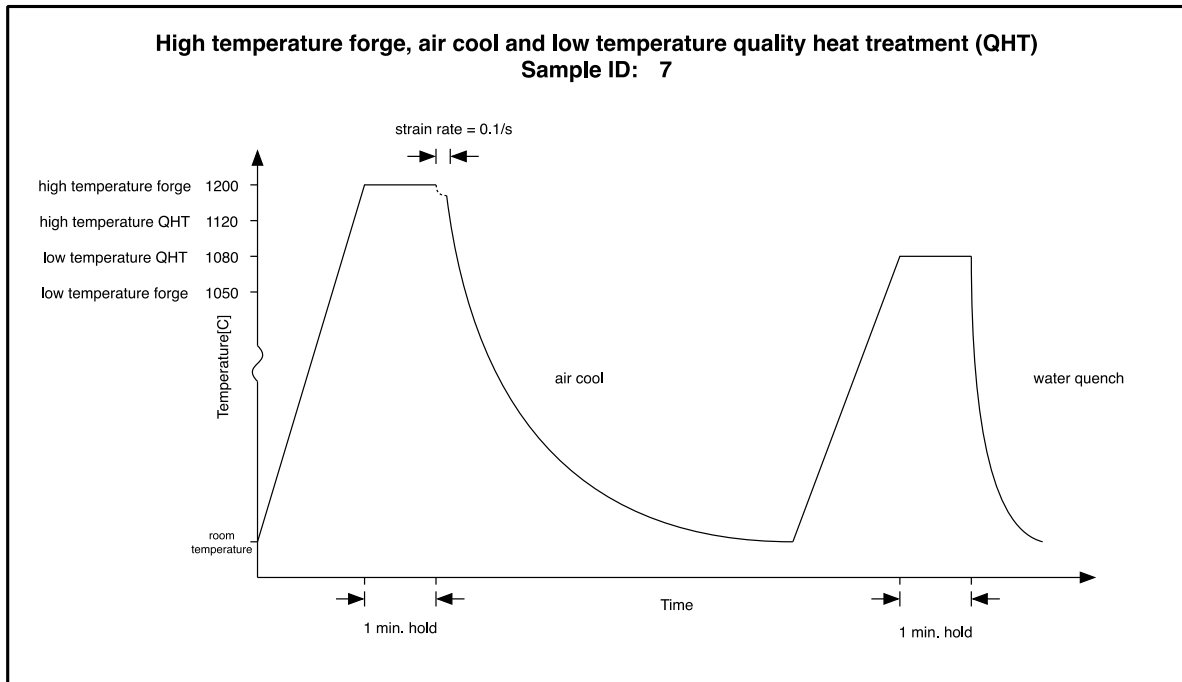


Fig 7.22 Time-temperature profile for test # 7; compression at 1200°C (high temperature forge), *quasi-equilibrium* air cool, reheat to and soak at 1080°C (low temperature QHT) and then water quench to room temperature.

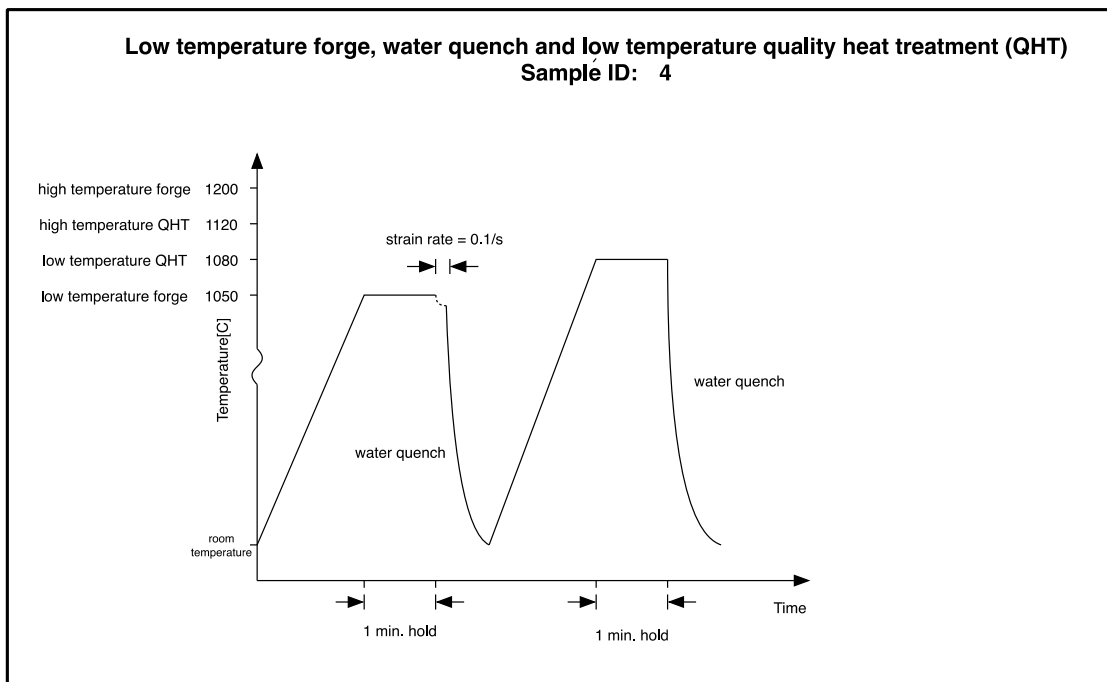


Fig 7.23 Time-temperature profile for test # 4; compression at 1050°C (high temperature forge), water quench, reheat to and soak at 1080°C (low temperature QHT) and then water quench to room temperature.

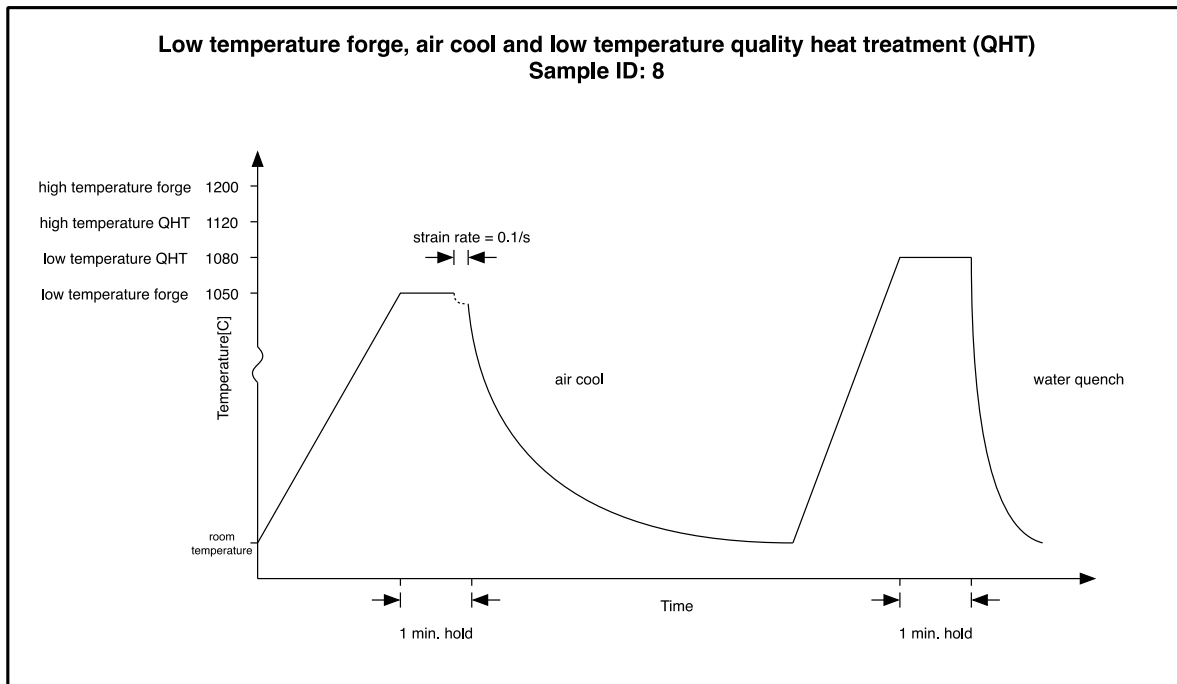


Fig 7.24 Time-temperature profile for test # 8; compression at 1050°C (low temperature forge), *quasi-equilibrium* air cool, reheat to and soak at 1080°C (low temperature QHT) and then water quench to room temperature.

The phase map of the surface of the sample from test # 3 is presented below in Fig. 7.25. In continuation of the convention followed above, the BCC ferrite phase coloured red and the FCC austenite phase is coloured blue. The sub-grain structure in the ferrite phase is indicated by the presence of silver coloured lines depicting low angle grain boundaries ($> 2^\circ$ misorientation), while black lines represent higher angle boundaries ($> 15^\circ$). The indicated phase proportions from the EBSD data are 39.4% austenite and 60.6% ferrite. Image analysis of several optical micrographs of the same sample surface at lower magnification than Fig. 7.25 suggests the austenite fraction may even be lower at around ca. 36 – 38% and that $\bar{\lambda}_\alpha = 34.3 \pm 14.5 \mu\text{m}$. Fig. 7.26 shows optical micrographs of the same sample surface as Fig. 7.27.

Figure 7.27 clearly illustrates that a high amount of substructure has developed in the ferrite phase as well as an overall refined grain size. Along the extensive high angle grain boundary network ($> 15^\circ$ black lines) resulting from this grain refinement, γ_2 has precipitated. Indeed, almost all the high angle boundaries delineating the refinement of ferrite grains appear to be decorated with γ_2 , although notably, these precipitates appear not to have grown into the ferrite grains. Instead, the γ_2 precipitates appear to have taken on an allotriomorphic morphology[5],

[6] after nucleating at the ferrite grain surfaces and forming layers which follow the grain boundary contours. There is evidence of some γ_2 precipitation along the lower angle boundaries delineating the ferritic sub structure (silver lines indicating $> 2^\circ$ misorientation), but this is not as consistent as along the ferrite-ferrite grain boundaries, which uniformly appear to be decorated with γ_2 precipitates.

This allotriomorphic morphology of the γ_2 precipitates decorating the grain boundaries of the ferrite sub-structure is shown schematically in Fig. 7.27. The grain refinement of the ferrite matrix noted above is indicated in Fig. 7.28 where IPF colouring in the sample y -axis has been used to more clearly illustrate presence of discrete ferrite grains. The high angle grain boundary network remains represented by black lines as per Fig. 7.27.

The texture of the ferrite phase from the sample from test # 3 is shown in pole figure representation in Fig. 7.28 where the sharp contours in the $\{100\}$ PF appear to indicate a distribution about, approximately, the $\bar{1}11, 0\bar{1}0$ and 111 poles in general agreement with the classic fibre texture produced from the axisymmetric deformation of BCC metals; $\langle 111 \rangle + \langle 100 \rangle$ duplex, parallel to the wire.

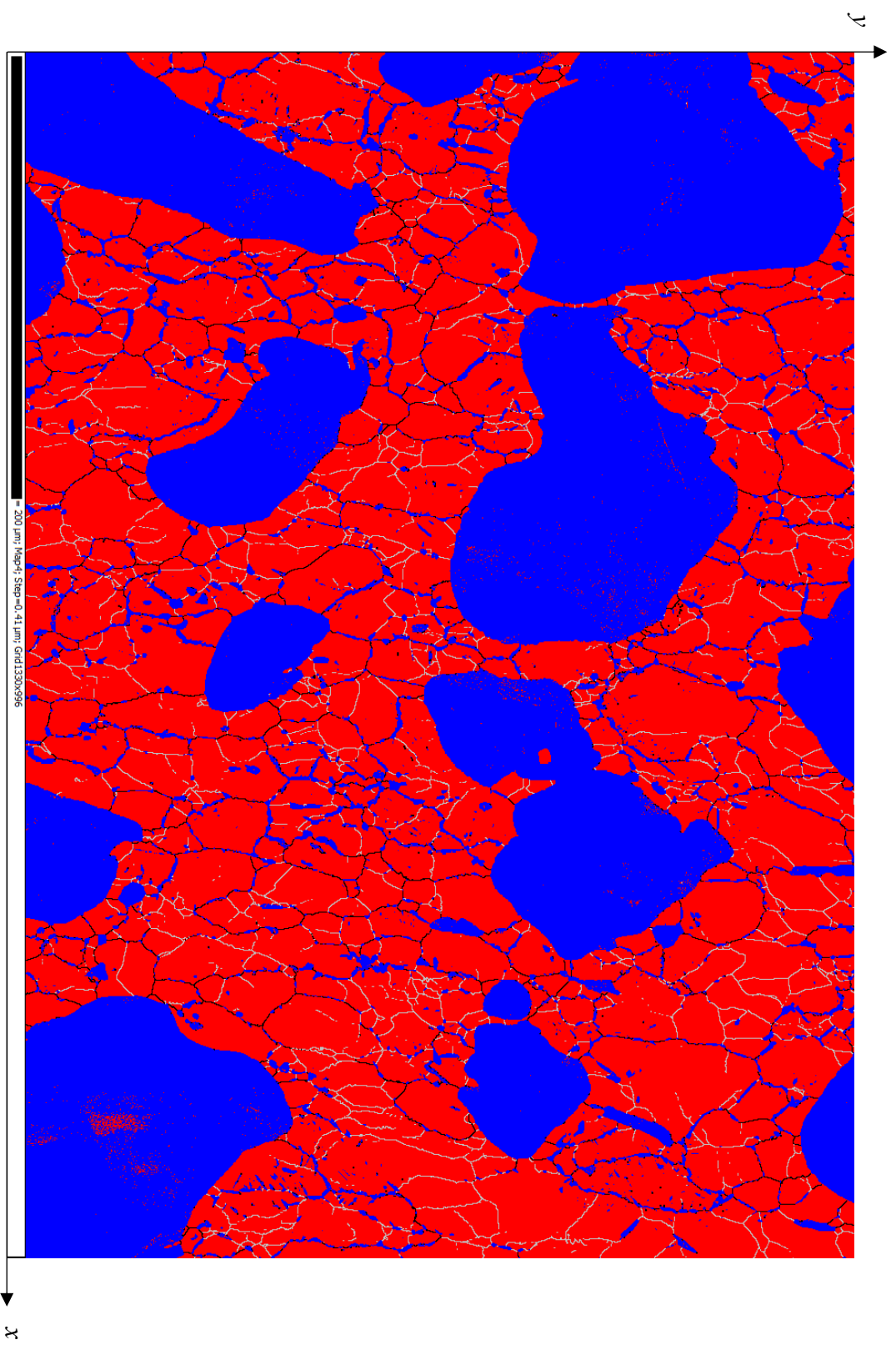


Fig. 7.25 SEM-EBSD phase map of the sample microstructure from test # 3. Ferrite substructure is indicated by the silver and black lines

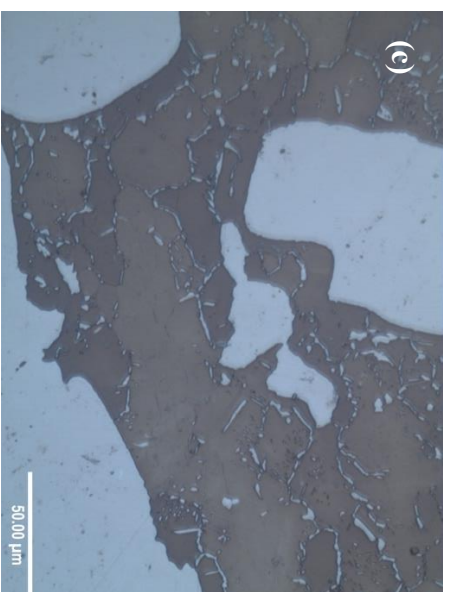
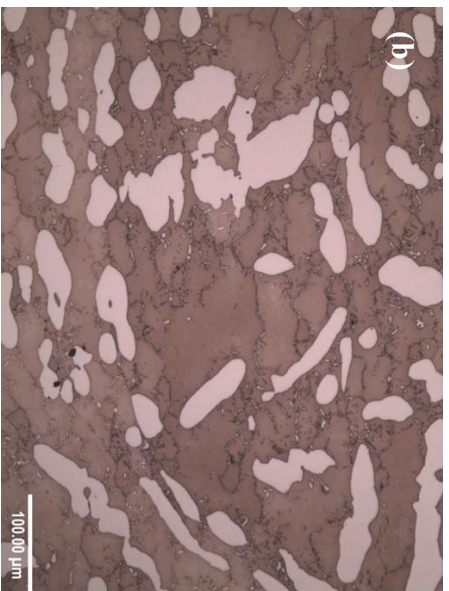
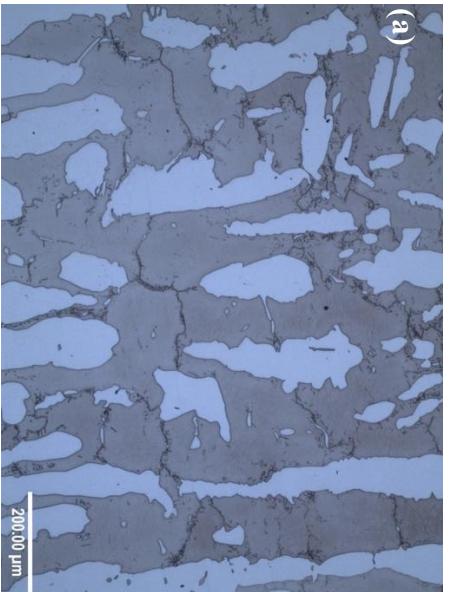


Fig. 7.26 Optical micrographs from test # 3 in the same plane as the SEM-EBSD image above (Fig. 7.27) taken at **a** 5 x **b** 10 x and **c** 20 x magnification

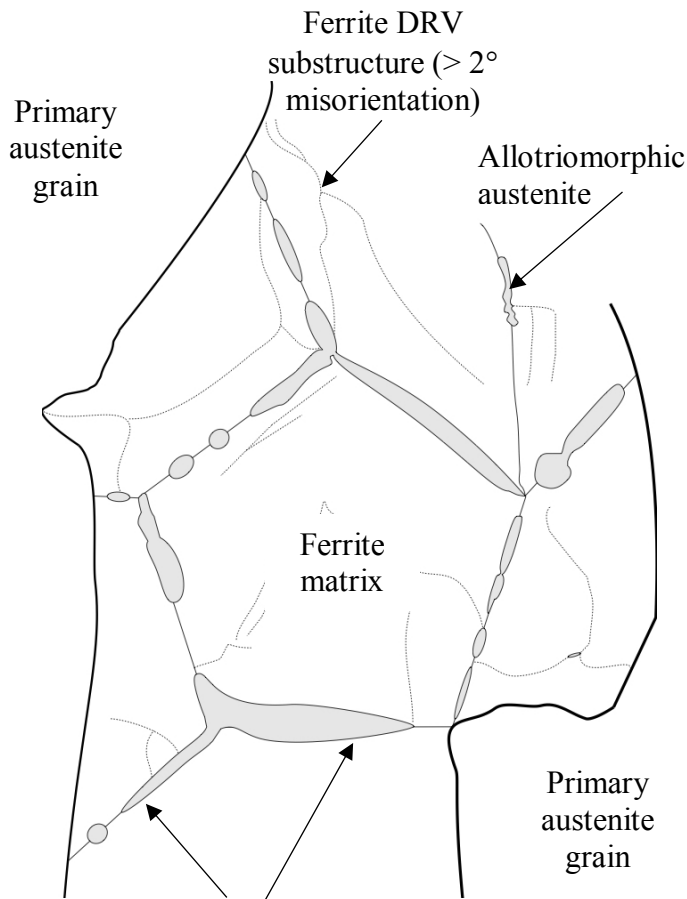
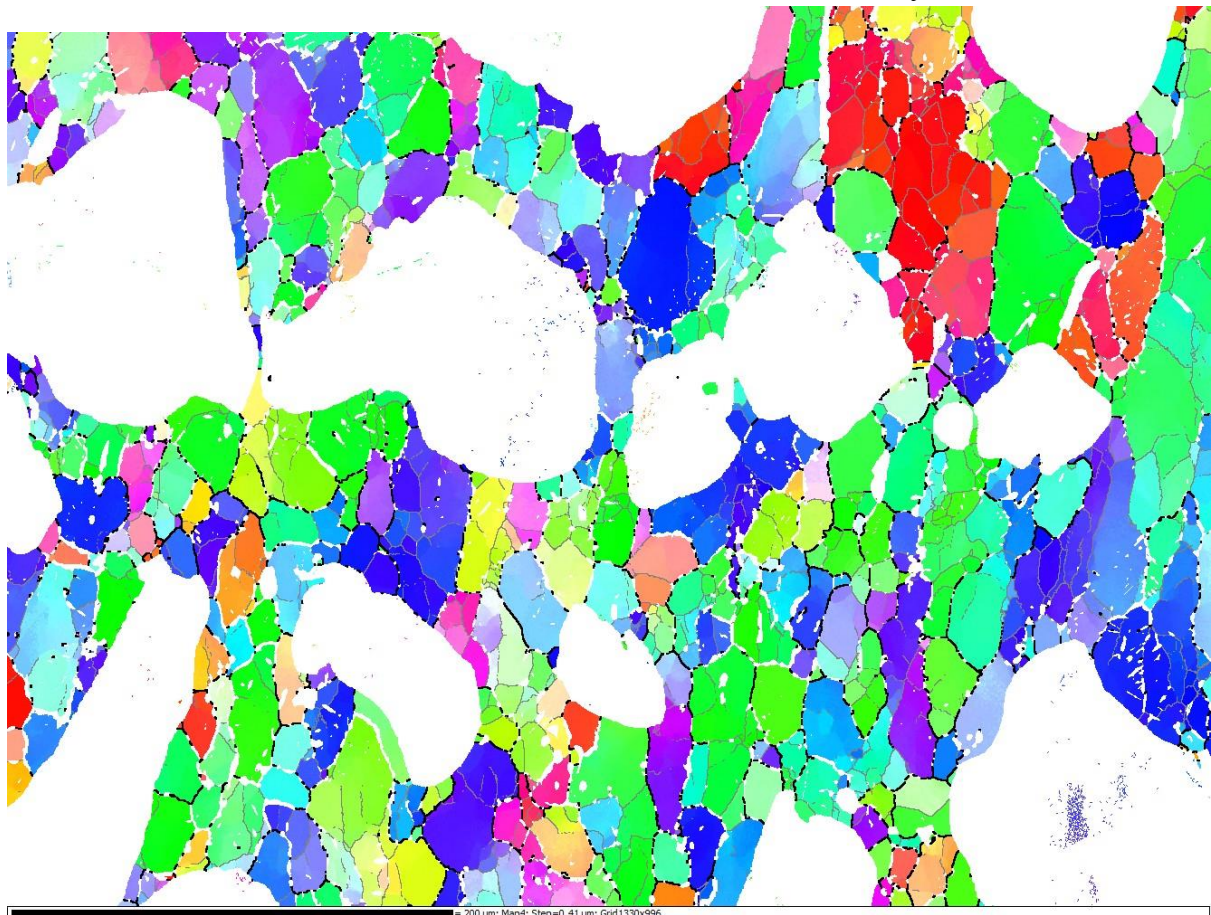


Fig. 7. 27 Schematic representation of the ferrite substructure and austenite precipitation morphology evident in Fig. 7.27

Refined ferrite structure (> 15°) decorated with allotriomorphic γ_2 precipitates

Fig. 7. 28 Ferrite grain refinement as illustrated by IPF colouring in the sample y -axis and high angle (> 15°) boundaries (black lines). The austenite phase is uncoloured for clarity and low angle (> 2°) ferrite sub-grain boundaries are represented by silver lines



Potential distribution around to the (111) and $(\bar{1}\bar{1}\bar{1})$ poles as well as some clustering around to the (010) pole also

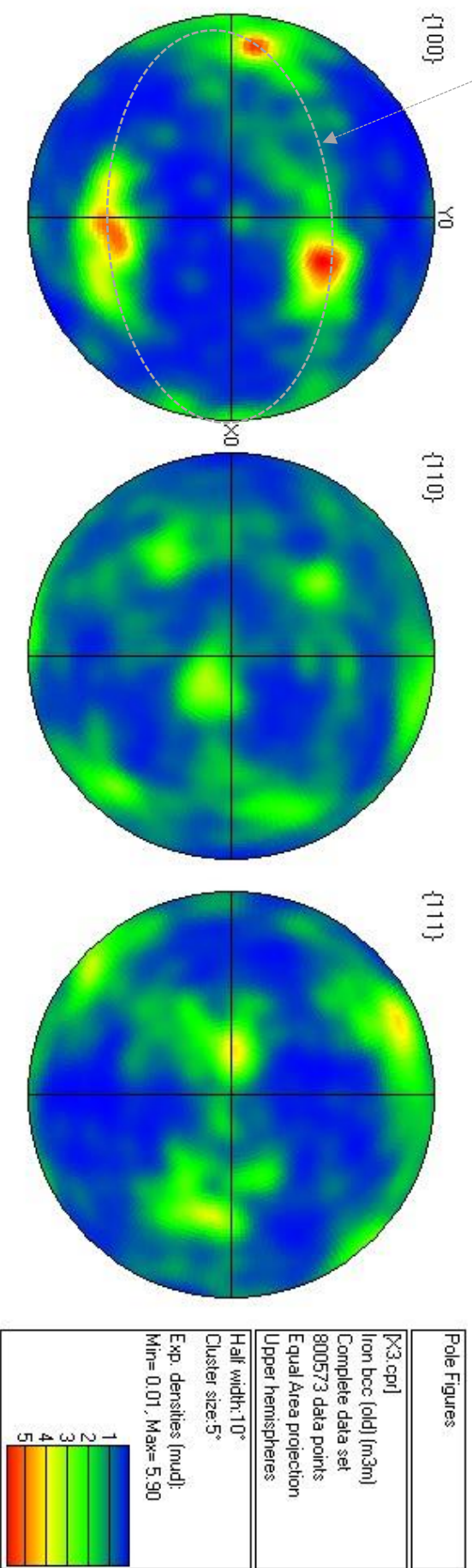


Fig. 7.29 Pole figures constructed with data from the ferrite phase of the sample from test # 3. Despite the suggested existence of the $\langle 111 \rangle + \langle 100 \rangle$ duplex, parallel to the wire in the $\{100\}$ PF, it is important to note the small population size of (relatively large) grains sampled as indicated by the multiple of uniform densities (mud) colour bar suggesting this texture is only ca. 6 x more likely than a random distribution.

The EBSD data from the sample from test # 4 is presented in Fig. 7.30 where in contrast to test # 3, the sample was deformed at a lower temperature. In accordance with the above convention, the ferrite phase is coloured red and the austenite phase blue. Image analysis of several optical micrographs of the same sample surface at lower magnification than Fig. 7.30 suggests the ferrite fraction may be ca. 60.8% and that $\bar{\lambda}_\alpha = 75.2 \pm 12.6 \mu\text{m}$. The indicated phase proportions from these data are broadly similar to the sample from test # 3 at 39.4% austenite and 60.6% ferrite. This correspondence of phase balance between the samples from test # 3 and # 4 is likely to be indicative of the same final QHT temperature used (1080°C) however contradicts the equilibrium molar phase diagram simulation (Fig. 2.4) which suggests austenite should be in the majority at this temperature.

Clearly, comparisons between Figs. 7.25 and 7.30 reveal the production of a much coarser ferrite grain size as a result of lower temperature deformation and additionally that this deformation has not led to the formation of as much low angle substructure (as evidenced by the absence of as many silver lines representing low angle misorientations $> 2^\circ$). Nor too is there evidence of the allotriomorphic γ_2 precipitates seen in Fig. 7.25.

Quantitatively, this difference in the microstructures produced from test # 3 & # 4 is illustrated in Fig. 7.31 where the misorientation angle distribution is presented. The ferrite substructure in the sample from test # 3 is clearly represented by the peak at the low-angle end of the distribution. Optical micrographs (taken in the same plane as the EBSD maps) of the sample from test # 4 are shown in Fig. 7.32.

Equilibrium thermodynamic calculations (Fig. 2.4) predict a greater volume fraction of austenite present in the duplex microstructure at low temperature (1050°C) than at high temperature (1200°C). It is therefore inferred from the data presented in Figs. 7.25, 7.30 and 7.31 that in test # 3 strain has preferentially partitioned into the majority ferrite phase which has dynamically recovered and resulted in the formation of a refined cellular substructure of crystallites constrained (primarily) by low angle boundaries which have created a network along which idiomorphic γ_2 precipitates have nucleated and grown. Contrastingly, in test # 4 where it is assumed austenite occupied the majority volume fraction in the duplex microstructure at T_D , less forming load was carried by the ferrite phase resulting in lower level of dynamic recovery and thus a smaller frequency of low angle misorientations across the

microstructure. At lower temperatures therefore, the effect of deformation should be more obvious in the austenite than at higher temperature and this is demonstrated, again by misorientation distribution, in Fig. 7.33 where data from the austenite phase of the samples from test # 3 and test # 4 is presented. A higher instance of the classic $\langle 111 \rangle 60^\circ$ austenite annealing twin boundaries is evident in the data set from the sample from test # 4 than from test # 3. These annealing twins form as a consequence of grain growth imperfections during the recrystallization of previously deformed FCC metallic materials[7]. Fig. 7.34 shows the EBSD phase map from the sample from test # 4 with the austenite annealing twins illustrated by green lines. Since the post-deformation heat treatment of test # 3 and test # 4 were kept constant, and both samples were immediately water quenched after deformation, it is assumed therefore that this difference in the relative frequency of annealing twins arises as a consequence of the difference in deformation (and consequently degree of recrystallization) experienced by the austenitic phase due to the high and low deformation temperatures, respectively.

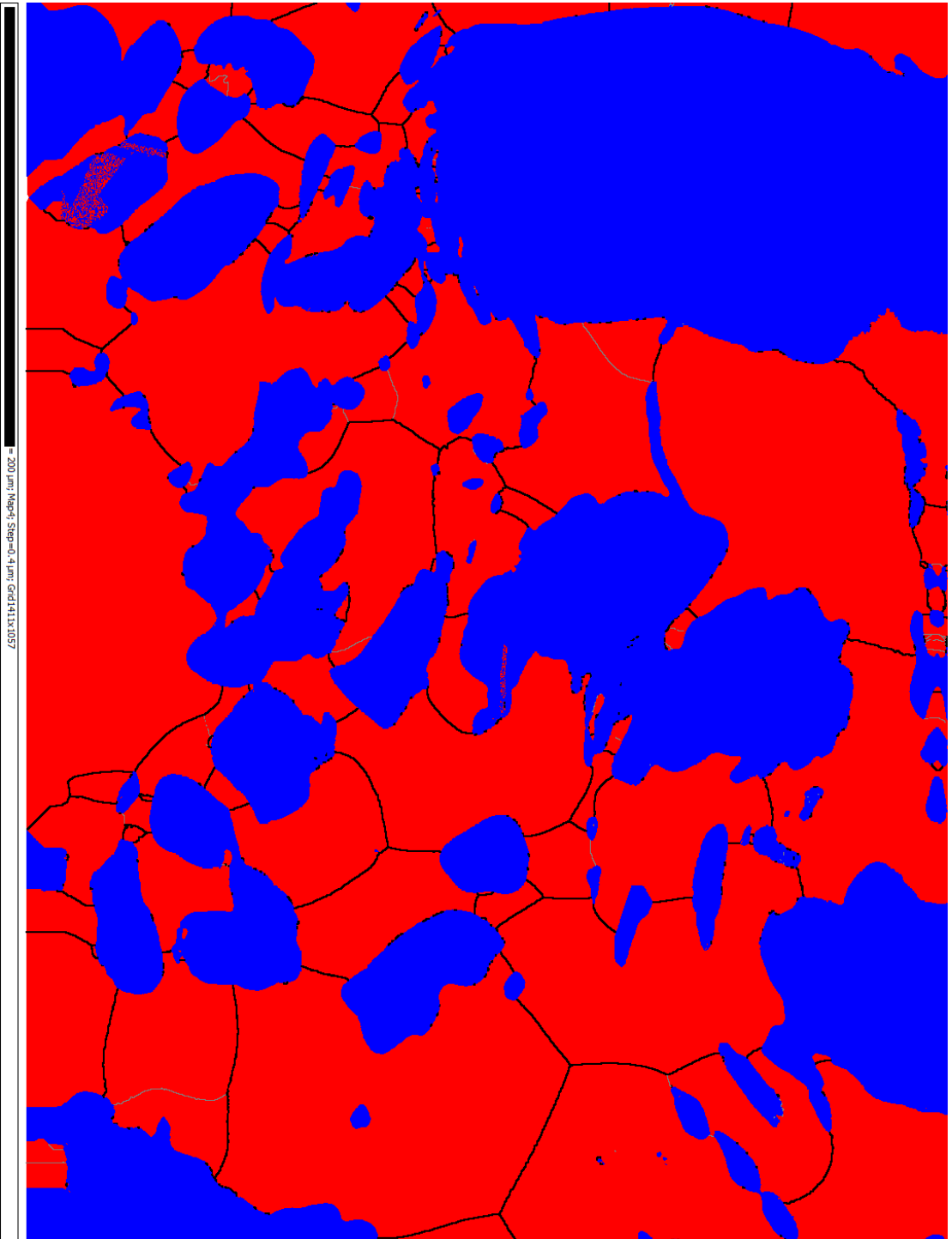


Fig. 7.30 SEM-EBSD phase map of the sample microstructure from test # 4 (low temperature uniaxial compression)

Fig. 7.31 Correlated misorientation angle distributions between neighbouring points in the Fe-BCC phase on the maps in Figs. 7.25 & 7.30. Bin width is set to 0.3°.

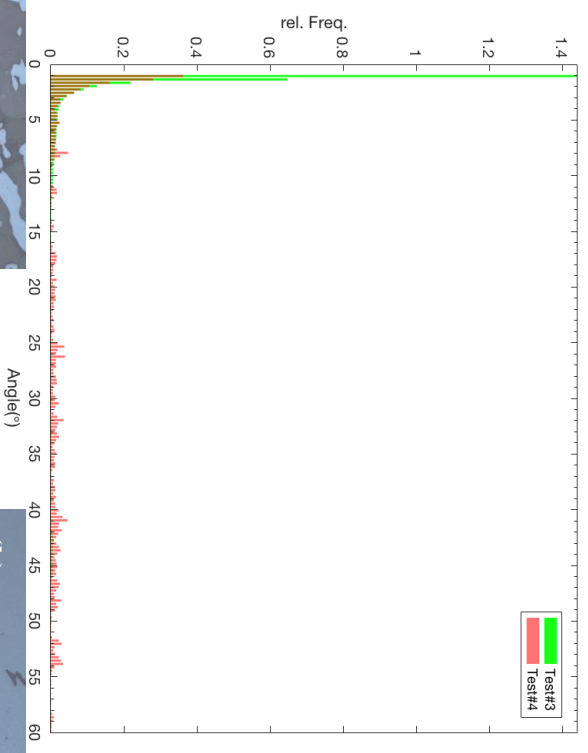
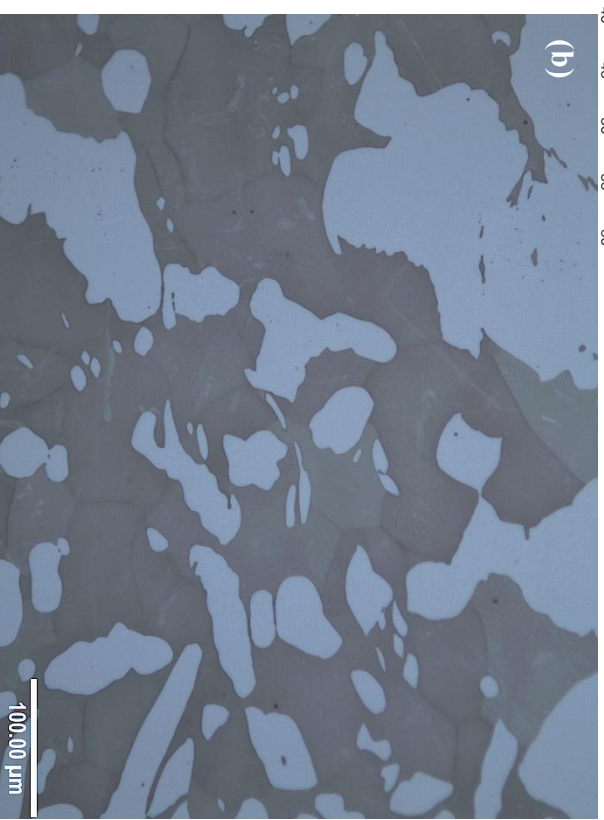


Fig. 7.32 Optical micrographs of the sample form test # 4 taken in the same plane as Fig. 7.32 at **a** 5 and **b** 10 x magnification



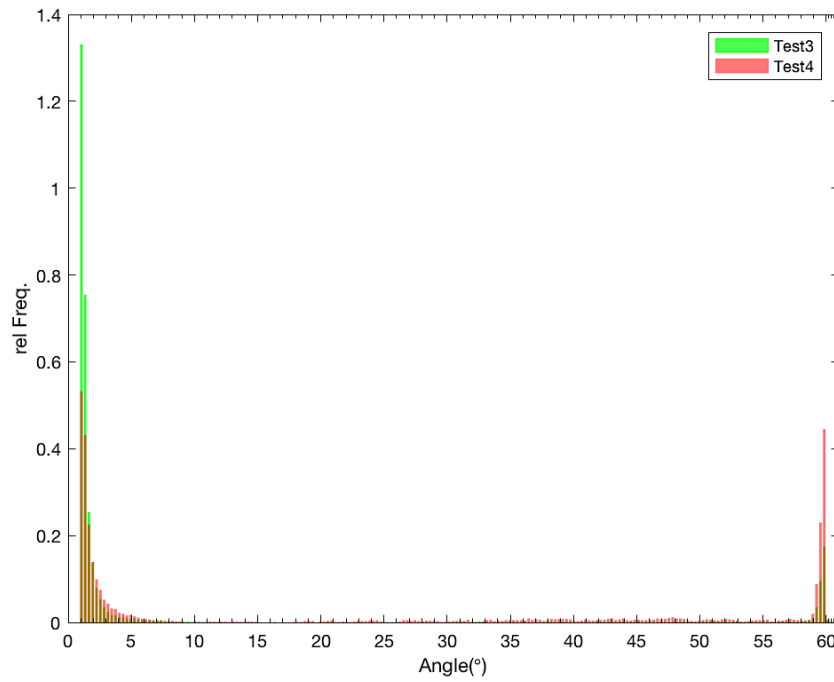


Fig. 7.33 Correlated misorientation angle distributions between neighbouring points in the Fe-FCC phase on the maps in Figs. 7.25 & 7.30. Bin width is set to 0.3° . Note the difference in relative frequency in the two distributions around the 60° angle of misorientation

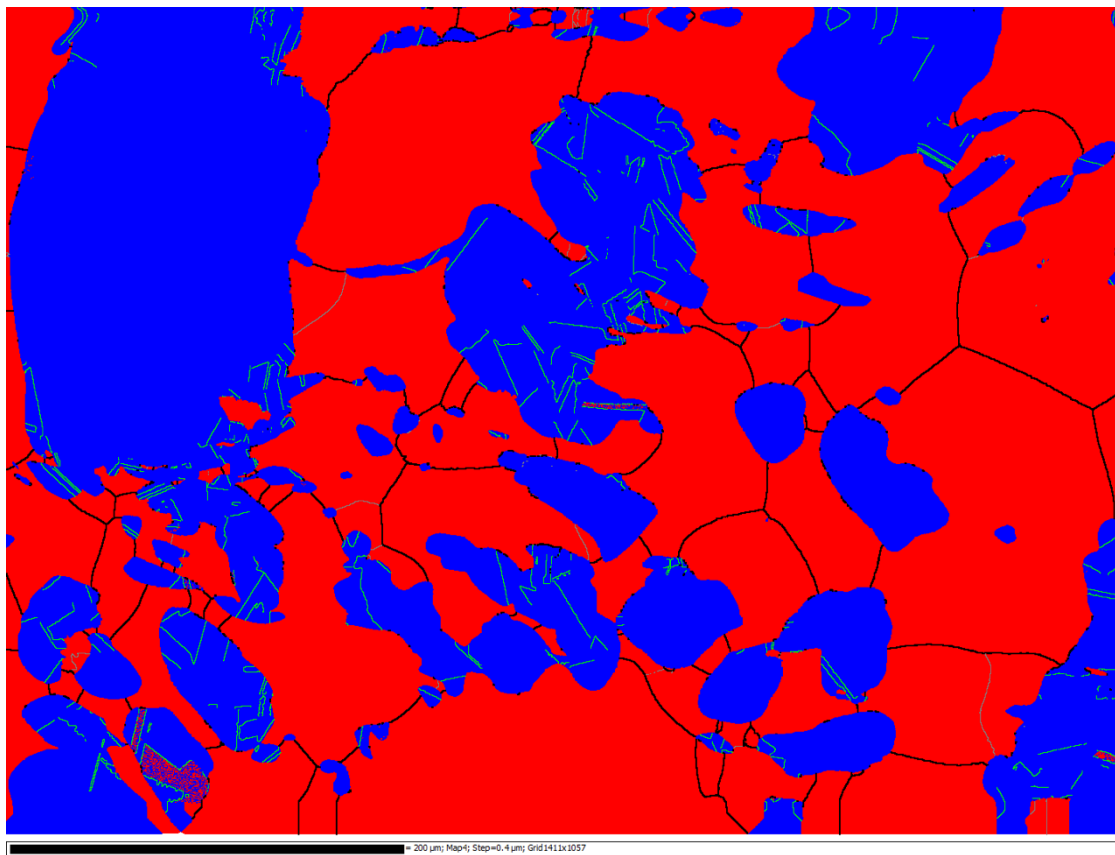


Fig 7.34 $\langle 111 \rangle$ 60° annealing twins in the EBSD phase map of the sample from test # 4, as indicated by the green lines

Comparison of Fig. 7.30 and Fig 7.25 suggests that secondary austenite precipitates appear to nucleate and grow, principally, along the higher angled boundaries (and to a lesser extent the lower angle substructure boundaries) of the refined ferrite structure, itself forming through the DRV response to high temperature deformation. The apparent formation and growth of γ_2 precipitates along the high density of boundaries in the cellular ferrite structure seems to also have a ‘pinning effect’ whereby subsequent grain growth in the following quality heat treatment processing step is resisted and thereby the ferrite grain size from high temperature deformation is retained.

Analysis of the samples from test # 7 and test # 8 allows for the determination of the effect of intermediate air cooling since all other thermo-mechanical processing variables (T_D , $\dot{\epsilon}$, ϵ QHT temperature etc.) were maintained constant with test # 3 and test # 4. The phase map of the sample from test # 7 is presented below in Fig. 7.35 with the EBSD data-indicated phase proportions of 29.8% austenite and 70.2% ferrite. As with previous phase maps in this chapter, the ferrite phase is coloured red and the austenite phase blue. High angle grain boundaries ($>15^\circ$) are coloured black while lower angle misorientations ($> 2^\circ$) defining the ferrite substructure as a result of DRV mechanisms are indicated by the silver lines.

The morphological similarities between the microstructures of the samples from test # 3 and test # 7 are apparent; allotriomorphic γ_2 precipitates decorating the high density of $>15^\circ$ boundaries which form the refined ferritic matrix structure. Lower angle ($>2^\circ$) misorientations are also present in the ferrite phase of both sample microstructures forming a cellular substructure indicative of DRV in response to straining. The misorientation distribution data from the ferrite phase of the samples from test #3 and test #7 is compared in Fig. 7.36 and indicates that a greater proportion of low angle misorientations are present in the microstructure of the sample from test # 3 (high temperature deformation – rapid water quenching to room temperature – reheat to ‘low’ temperature QHT and soak – water quench to room temperature) than in the sample from test # 7 (high temperature deformation – *quasi*-equilibrium air cooling to room temperature – reheat to ‘low’ temperature QHT and soak – water quench to room temperature).

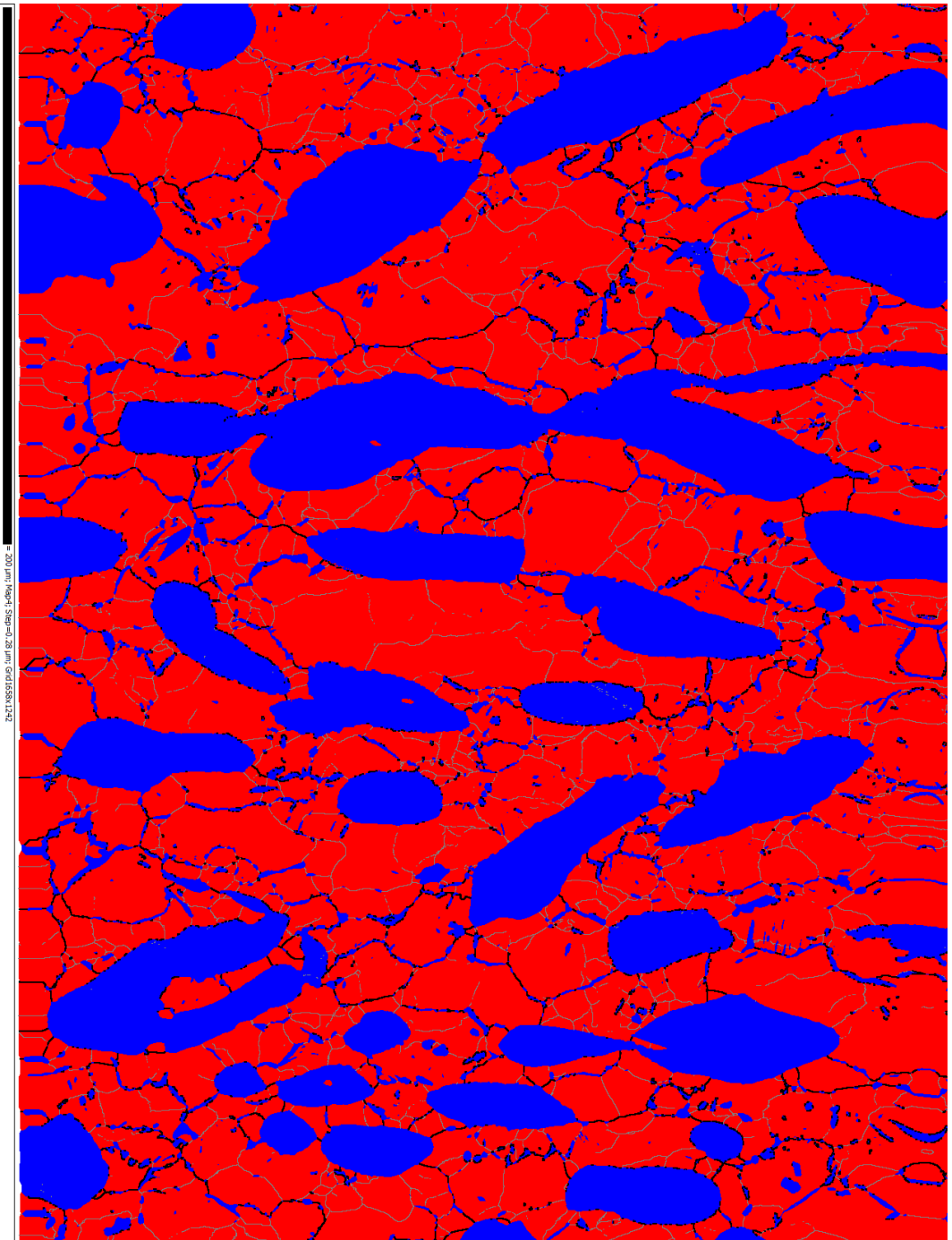


Fig. 7.35 SEM-EBSD phase map of the sample microstructure from test # 7 (high temperature deformation at 1200°C followed by intermediate air cooling then final QHT at 1080°C).

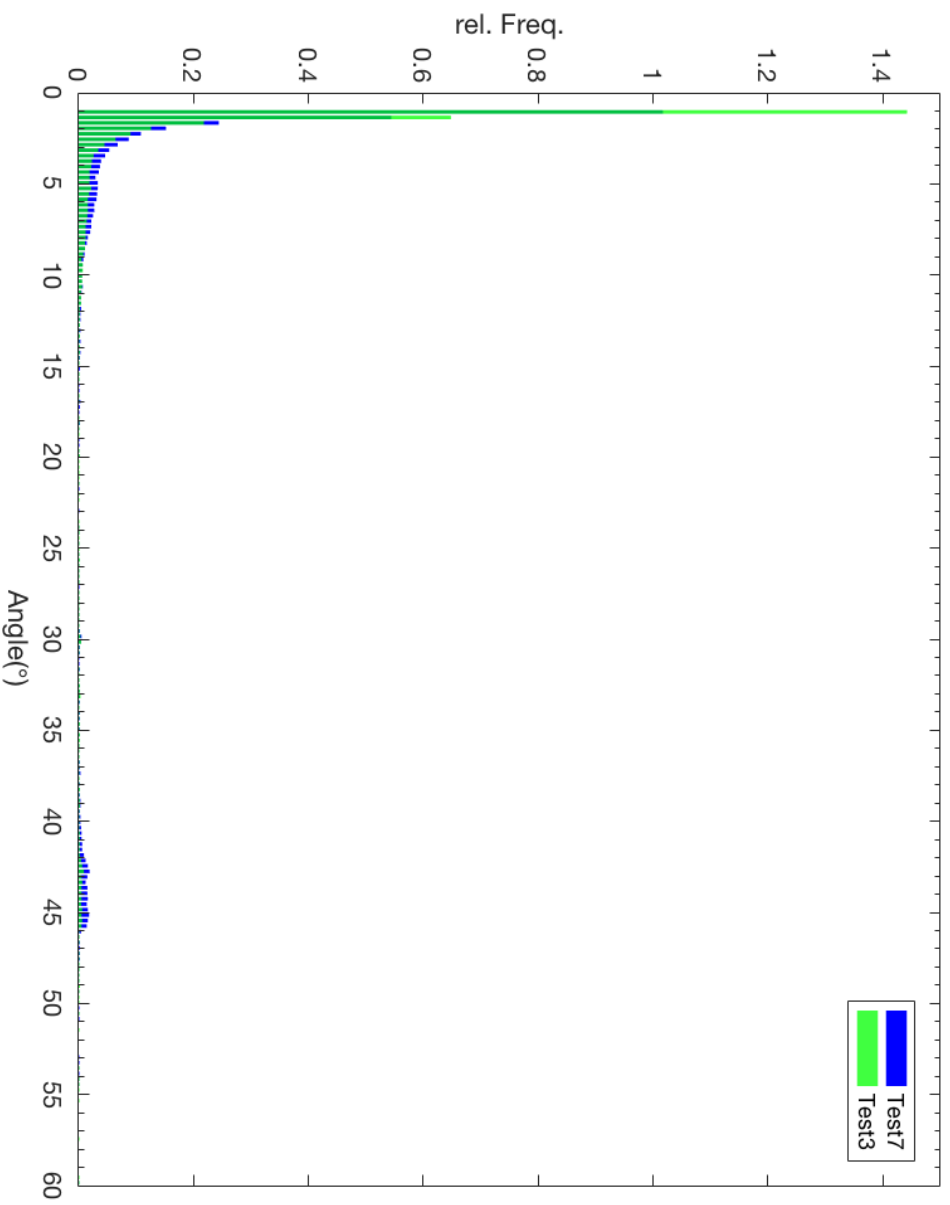


Fig. 7.36 Correlated misorientation angle distributions between neighbouring points in the Fe-BCC phase on the maps in Figs. 7.25 (Test3) & 7.35 (Test7). Angle bin width is set to 0.3°. It should also be noted in Fig 7.36 that there is a slight increase in the number of LAGB for Test #7. This is believed to be because the sample material in Test #3 had significant precipitation of γ_2 along these (prior) LAGBS, thereby reducing their number.

Thermodynamic time-temperature transformation (TTT) modelling using the Thermo-Calc® FEDE6 and MOBFE3 databases has indicated that austenite (FCC_A1) precipitates primarily and rapidly upon the rapid cooling of the ZERON® 100 ferrite matrix (BCC_A2) as illustrated in Fig. 7.37 where the chemical composition of the as received, \varnothing 250 mm AFP ZERON® 100 billet along with specification of grain boundary nucleation sites and a 90° wetting angle were used to set up the simulation.

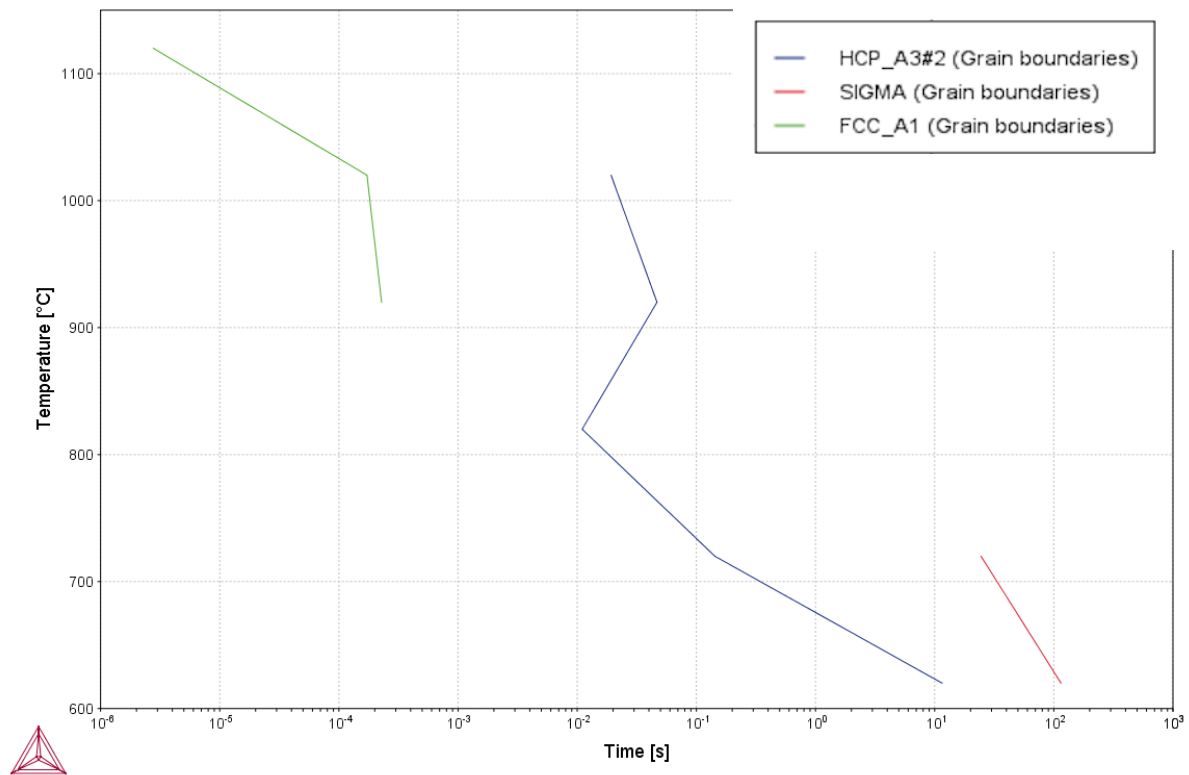


Fig. 7.37 Thermo-Calc® Time-Temperature-Precipitation Diagram for a ZERON® 100-type alloy system

From Figs. 7.25 and 7.35, this rapid precipitation of austenite along BCC matrix grain boundaries appears to occur regardless of cooling rate as the consistent presence of allotropic γ_2 particles decorating high angle grain boundaries (HAGBs) would seem to suggest. Data discussed above from the samples from the high temperature deformation tests (# 3 & # 7) suggested a higher instance of low angle ferritic substructure is formed through rapidly quenching prior to low temperature heat treatment than *quasi*-equilibrium air cooling. It should be noted however that the presence of allotropic γ_2 precipitates on BCC HAGBs presents somewhat of a limitation in terms of assessment of the refined ferrite grain structure through these data; the occurrence of these HAGB precipitates effectively removes the misorientation data in these locations between adjacent points in the ferrite phase. Therefore,

by deleting the precipitates (in fact, the complete FCC phase) from the dataset and iteratively ‘noise reducing’ the resulting zero solutions in the remaining ferrite phase through an averaging filter which determines the misorientation of the zero solutions from the surrounding n -connected data points the immediate neighbourhood (e.g. 3-by-3), the ‘true’ ferrite HAGBs can be reconstructed and their distributions assessed as functions of the thermomechanical testing parameters (Fig. 7.38).

The results of this data reconstruction are illustrated below in Fig. 7.39 where the datasets have been edited to remove the Fe-FCC phase and the remaining Fe-BCC phase subjected to noise reduction filtering and then IPF colouring applied. As previously, black lines are used to indicate the presence of large misorientations, i.e. HAGBs ($>15^\circ$) and silver lines represent the low angle ferritic substructure ($> 2^\circ$ misorientation).

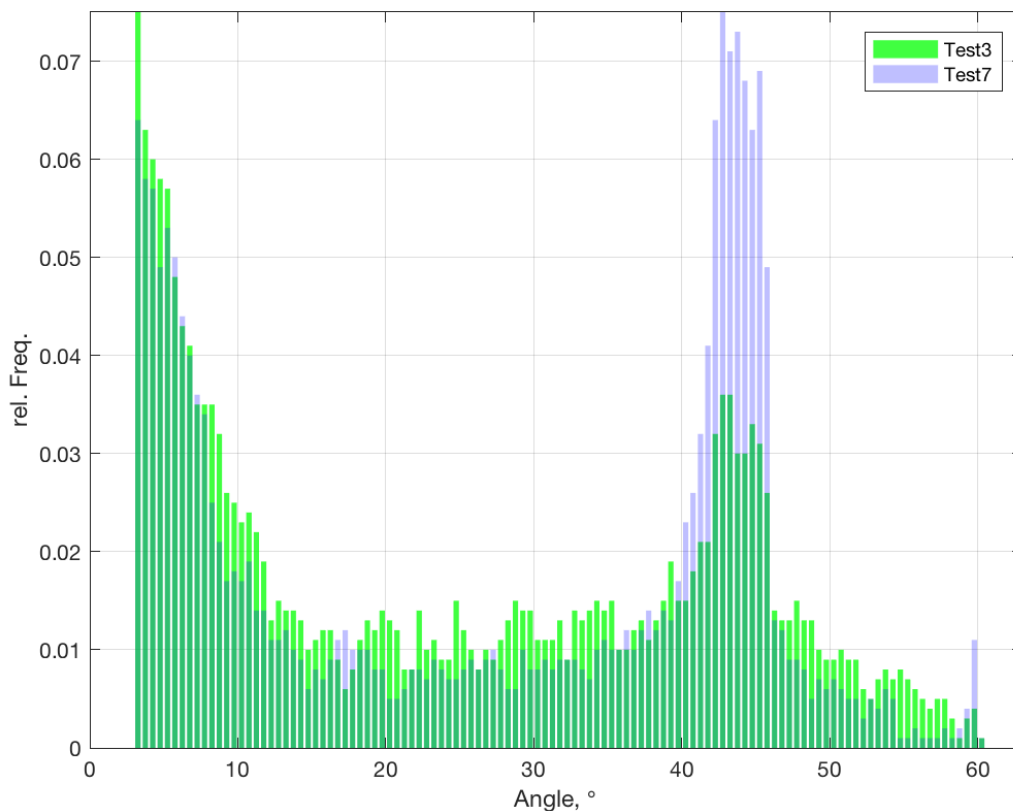
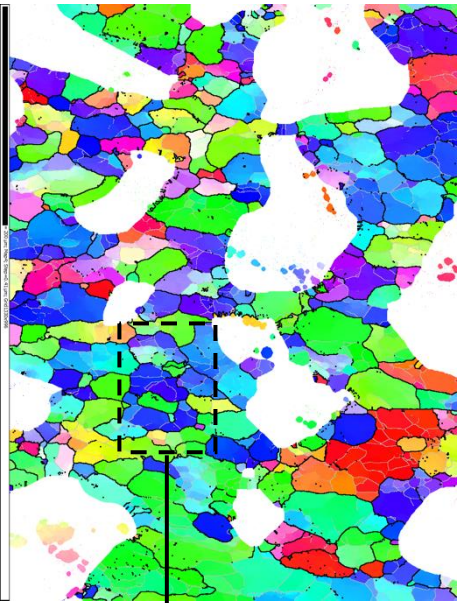
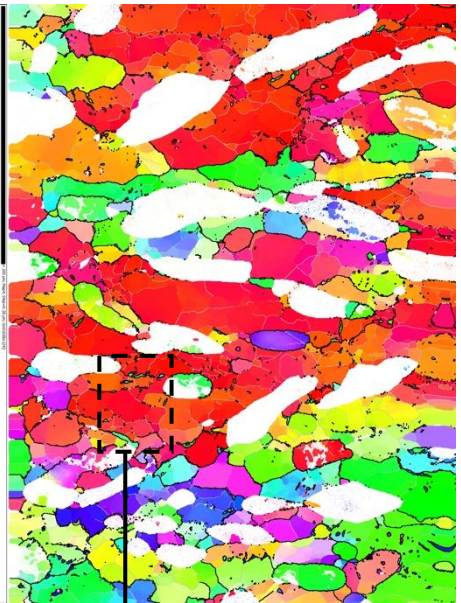
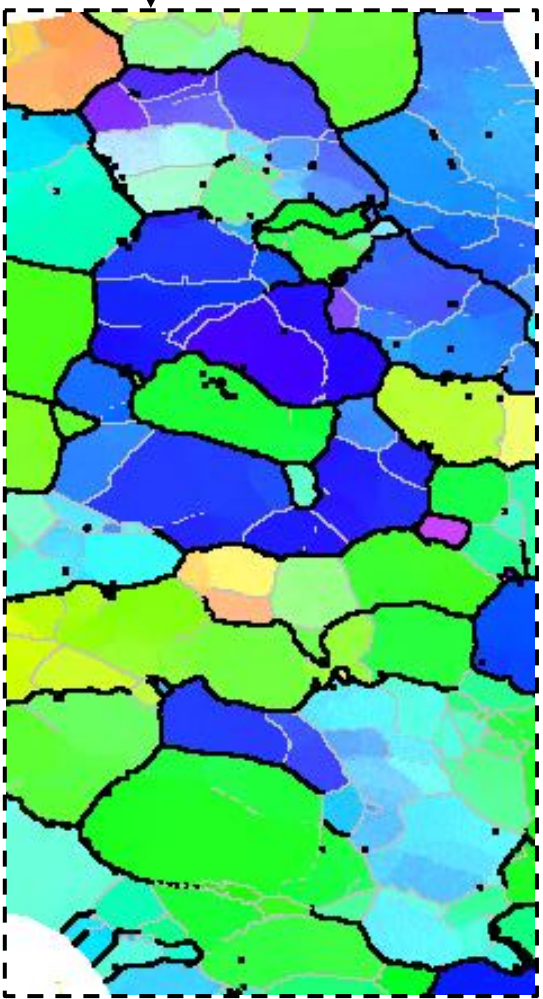


Fig. 7.38 Misorientation angle distribution in the ‘reconstructed’ BCC phase for the samples from test # 3 and test # 7. Note the enlarged bin width in this plot (0.5°) vs. 0.3° used previously. The neighbour-to-neighbour misorientations are also based on minimum angle of 3° here to remove some of the noise present the extreme ends of the distributions in Figs. 7.36, 7.33 & 7.31

Fig. 7.38 indicates that a higher instance of HAGBs, indicative of a potentially more refined ferrite matrix grain structure along which γ_2 precipitates are consequently assumed to form in higher volumes, occurs in the sample allowed to air cool under *quasi*-equilibrium conditions following high-temperature deformation versus the sample that was rapidly water quenched.



(a)



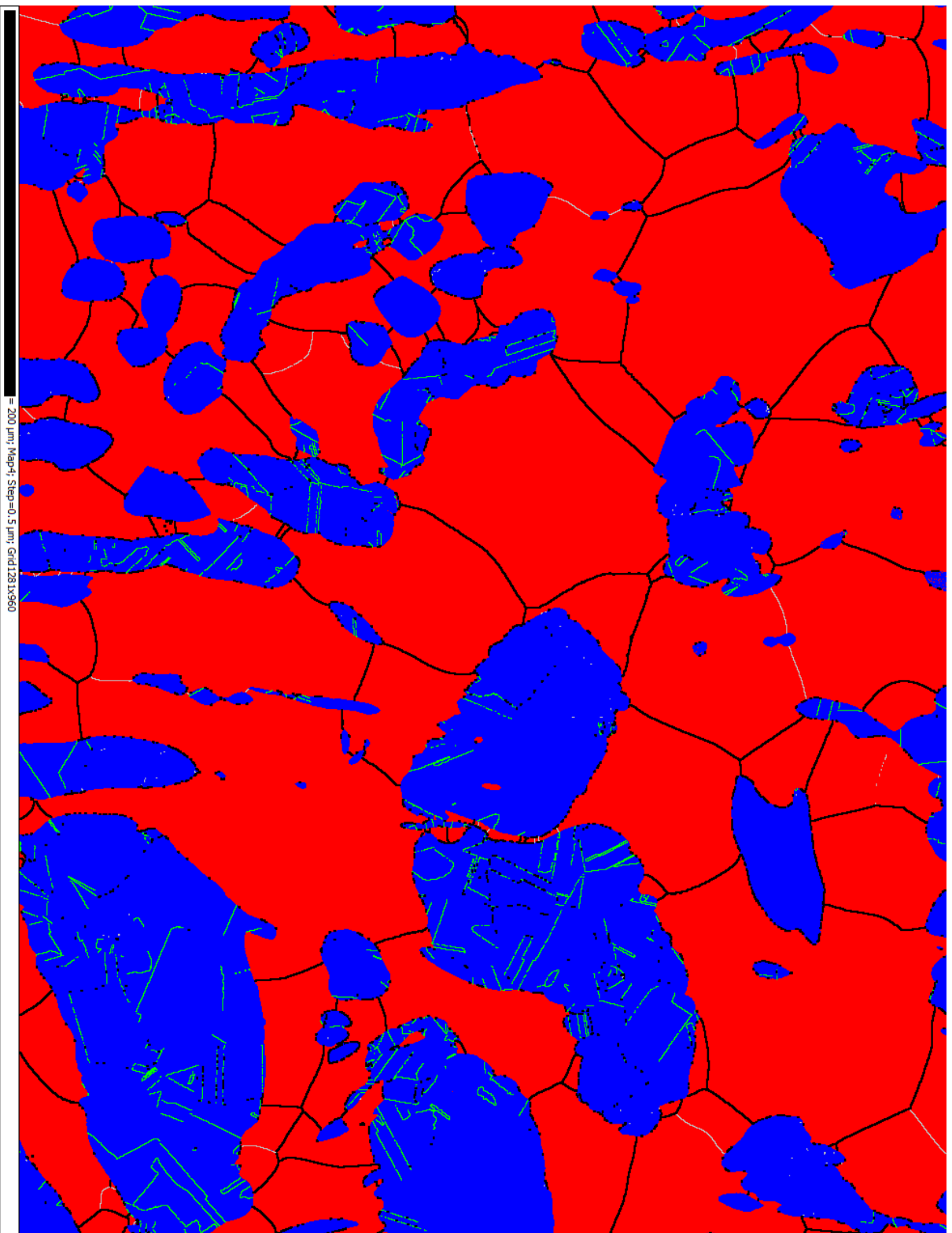
(b)



Fig. 7.39 Reconstructed BCC phase in IPF colouring data showing the 'true' HAGBs & substructure without γ_2 precipitates in the sample microstructures from **a** test # 3 and **b** test # 7

For completeness, the EBSD data from the sample from test # 8 (Fig. 7.24) is presented as a phase map (as previously with the data from test # 4) in Fig. 7.40 along with optical micrographs from the sample and in the same orientation as the EBSD data were gathered. The statistical data indicates that the phase balance is 69.6% ferrite and 30.4% austenite.

In keeping with convention established above, the black and silver lines within the red ferrite phase of Fig. 7.40 indicate misorientations $> 15^\circ$ (grain boundaries) and $> 2^\circ$ (sub-grain boundaries), respectively. The green lines within the blue austenitic phase denote the presence of the characteristic $\langle 111 \rangle 60^\circ$ annealing twins. As with Figs. 7.25, 7.30 & 7.35 the axis along which the sample was compressed is orientated parallel to the page.



= 200 μm ; Map#1; Step=0.5 μm ; Grid128 X850

Fig. 7.40
 SEM-EBSD phase
 map of the sample
 microstructure
 from test # 8

- Black: misorientations > 15°
- Silver: misorientations > 2°
- Green: <111> 60° annealing twins
- Red: ferrite
- Blue: austenite

7.3 Summary

Equilibrium thermodynamics (Fig. 2.4) indicate that at the higher temperatures within the forging window (1050 - 1280°C) the volume fraction of ferrite predominates.

Deformation at lower temperature is suggested to induce greater strain in the austenite, since the volume fraction of this phase should now predominate in the duplex microstructure; evidenced, potentially, by the greater frequency of annealing twin $\langle 111 \rangle 60^\circ$ boundaries (as demonstrated in Fig. 7.33) The exact point of formation these annealing twin, $\langle 111 \rangle 60^\circ$, boundaries within the thermo-mechanical processing cycle remains somewhat unclear (however). Even so, a significant part of the forming load will still be partitioned into the ferrite phase at low temperatures since it remains the continuous matrix phase.

At elevated forging temperatures, it is assumed that a large majority of the load is carried by the ferrite phase, however, the rate of DRV will be increased, versus that at lower temperature. Consequently, a high level of grain refinement and sub-structure may not necessarily result. Therefore, even though as noted above, strain is likely to be increasingly partitioned into the austenite at lower forging temperatures, it is suggested that the ferrite is still highly worked and, in this case, does not recover as quickly so potentially allowing for higher grain refinement and the formation of more substructure.

After deformation the material is then cooled and, as indicated by thermodynamic simulation in Fig. 7.37, grain boundary γ_2 precipitation occurs preferentially and almost instantaneously at temperatures from approximately 1150°C to 900°C. It is proposed that, in all cases, regardless of deformation temperature *or post deformation cooling rate*, an intermediate ferritic structure decorated with allotriomorphic γ_2 precipitates is produced. Indeed, if a more refined and sub-structured ferrite matrix is produced from lower temperature deformation (due to low temperature-suppressed rates of DRV), the greater volume density of low energy nucleation sites on the boundaries may even also allow for more allotriomorphic γ_2 precipitation than in the high deformation temperature microstructure.

Upon reheating to, and soaking at, the QHT temperature (in the case of the samples above, 1080°C) the allotriomorphic γ_2 precipitates tend to dissolve as the stabilizing elements are taken

back into solid solution within the ferrite. However, the test QHT temperature exceeds the 1050°C deformation temperature whereupon the ‘low temperature’ γ_2 precipitates formed, essentially rendering them more thermodynamically unstable than the ‘high temperature’ γ_2 precipitates which formed on the ferritic boundaries after deformation at 1200°C (above QHT temperature) and, crucially, *may even form part of the equilibrium austenite volume fraction at the QHT temperature.*

As a consequence of the dissolution of the ‘low temperature’ γ_2 precipitates, the refined ferritic matrix and DRV substructure is not ‘pinned’ and therefore able to grow resulting in a coarse matrix and the annihilation of low angle misorientations (e.g. Fig. 7.34). Conversely, the ‘high temperature’ γ_2 precipitates are essentially rendered highly stabilized at this ‘low’ QHT temperature and remain undissolved, thereby pinning the ferritic refinement and also acting to block/obstruct the annihilation of the low angle substructure. Resultantly, a more refined ferrite matrix also containing a higher frequency of low angle misorientations appears to be produced as evidenced in Fig. 7.25 & Fig. 7.35.

The classic Hall-Petch relationship (Eqn. 7.1) where k is a material constant, σ_i is the intrinsic yield stress and d is the average grain diameter, describes the inverse root dependence of yield strength on grain size:

$$\sigma_y = \sigma_i + \frac{k}{\sqrt{d}} \quad (\text{Eqn. 7.1})$$

This relationship illustrates the strengthening (and importantly also toughening) effect of grain size refinement and leads to the inference that γ_2 -pinned ZERON® 100 microstructures should perform better mechanically than those which have been free (i.e. ‘unpinned’) to coarsen during QHT due to the dissolution of grain boundary γ_2 . Correspondingly, comparison of Fig. 7.5, Fig. 7.10, Fig. 7.25 & Fig. 7.30 indicates a clear resemblance in the microstructures of the sample taken from the C1 position in the weld neck flange forging and the high temperature compression samples (test # 3 & test # 7). Samples from the C1 position were the only ones to pass the impact toughness specification (Table 7.1) and were ca. 1.8 – 4 times tougher than the C3 and C7 samples. An additional interesting comparative observation is the almost unique presence of intra-granular γ_2 in the C3 and C7 samples. Correspondingly it is also these samples

that bear the closest similarity to the low temperature deformation samples from test # 4 and test # 8. In these tests it is proposed that the dissolution of γ_2 during QHT allows ferrite grain growth to sizes too great for austenitic stabilizing elements to diffuse out of solid solution to the boundaries upon rapid cooling thereby causing the formation of roughly circular, intra-granular γ_2 particles.

The above described process of microstructure evolution as a function of thermo-mechanical processing is illustrated schematically in Fig. 7.43 below with the general conclusion to be drawn that high temperature deformation appears to be required for the production of a refined ferritic matrix, not however because of any great microstructure evolution process, but rather because of the opportunity to form highly stabilised γ_2 grain boundary precipitate 'pins' in whose absence matrix grain coarsening during QHT would otherwise occur. Further, the immediacy of the formation of γ_2 grain boundary precipitates (Fig. 7.39) essentially renders the final duplex microstructure 'product' invariant to post deformation cooling rate.

In reference to the diagrammatic illustration below in Fig. 7.41, soaking at 'high' (red line) and 'low' (blue line) temperatures prior to compression produces the equilibrium thermodynamic duplex phase proportions in the microstructures, biased more towards ferrite and austenite, respectively (Fig. 7.43a).

The softening response to uniaxial compression (the laboratory-scale analogue of the open die forging process detailed previously) at 'high' and 'low' temperatures (Fig. 7.41b) results in unequal strain partitioning between the duplex phases with the majority of the load being carried by the continuous ferrite matrix (at both high and low compression temperature) which consequently dynamically recovers due to its high stacking fault energy. Even though a greater fraction of ferrite is present at higher temperatures the recovery rate will also be increased versus that at lower temperatures where, conversely, austenite occupies a greater fraction. At lower temperature deformation it has been shown how the increased presence of austenite annealing twin $\langle 111 \rangle 60^\circ$ boundaries (Fig. 7.33) may indicate a higher uptake of the forming load, however, critically, this is secondary to the partitioning of strain initially and primarily into the ferrite throughout the whole forging temperature window. The competing and inter-related factors of temperature-varying phase balance, recovery rate and strain partitioning greatly complicate the interpretation (and modelling) of the flow behaviour of duplex material,

however it is somewhat tentatively suggested below that, regardless of deformation temperature, refined ferrite crystallites form as a result of the DRV response to compression and within which are contained a network of low angle sub-grain boundaries constituting the cellular substructure.

Upon post-deformation cooling γ_2 particles precipitate almost immediately (Fig. 7.37) along the grain boundaries of this refined matrix and, to an extent, the lower-angled boundaries of the substructure (Fig. 7.41c). It is however of great importance in the understanding of the effect of thermo-mechanical processing on duplex microstructures to note that *those γ_2 particles precipitated immediately after high temperature deformation, in effect, form part of the equilibrium γ volume fraction at lower temperatures.* Therefore, as illustrated in Fig. 7.41e & 7.41f, they remain undissolved during the QHT (since it is a lower temperature than that at which they precipitated) thereby pinning the ferrite boundaries and acting to retain the refined matrix and low angled substructure.

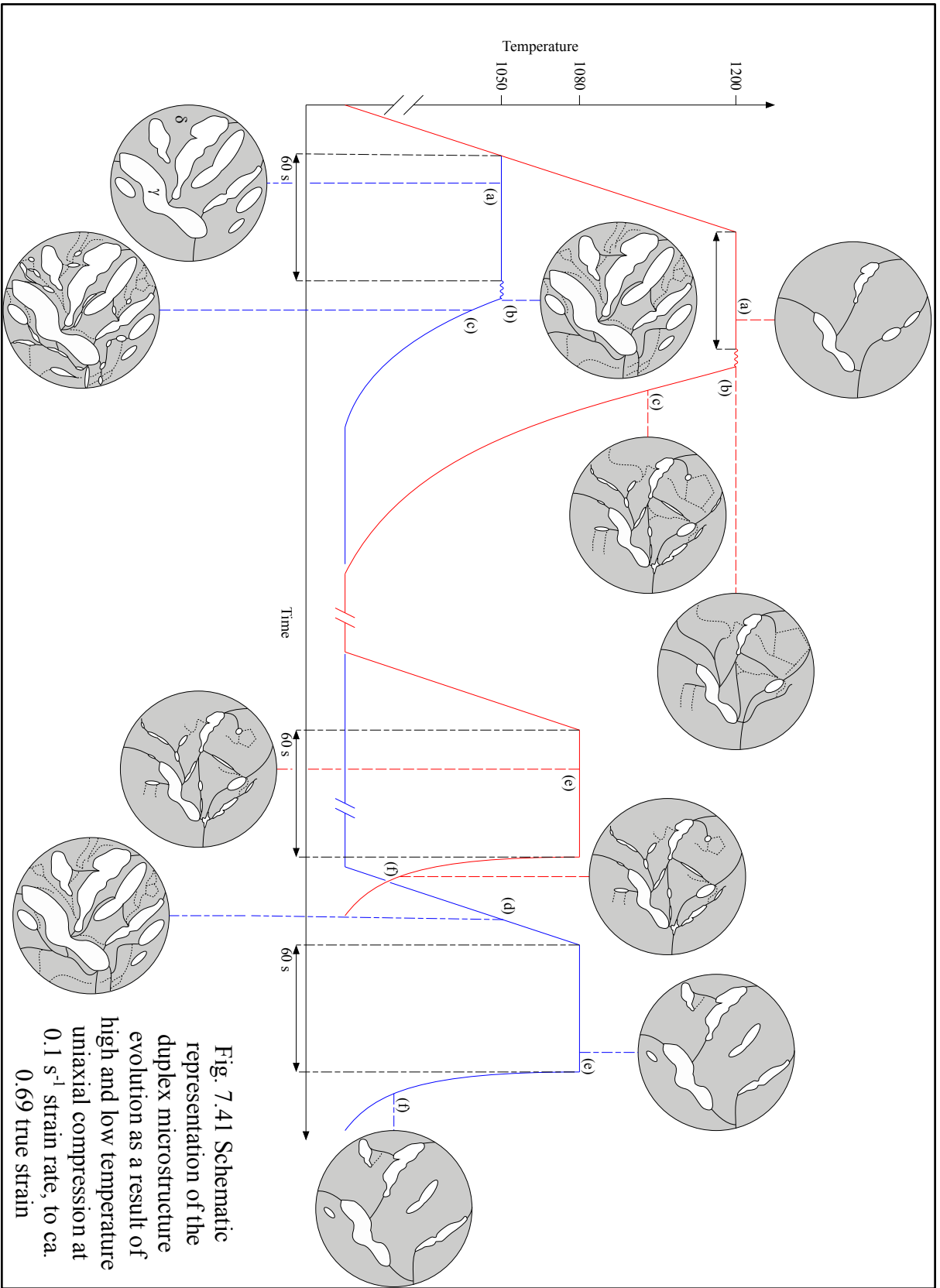


Fig. 7.41 Schematic representation of the duplex microstructure evolution as a result of high and low temperature uniaxial compression at 0.1 s⁻¹ strain rate, to ca. 0.69 true strain

REFERENCES

- [1] “DNVGL-RP-F112 Design of duplex stainless steel subsea equipment exposed to cathodic protection,” Høvik, 2017.
- [2] T. Sourmail, G. Opendacker, G. Hopkin, and H. K. D. H. Bhadeshia, “Annealing Twins.” [Online]. Available: <http://www.phase-trans.msm.cam.ac.uk/abstracts/annealing.twin.html>. [Accessed: 23-Aug-2018].
- [3] T. H. Courtney, *Mechanical Behaviour of Materials*, 2nd ed. Long Grove, IL, 2000.
- [4] H. Kitahara, R. Ueji, N. Tsuji, and Y. Minamino, “Crystallographic features of lath martensite in low-carbon steel,” *Acta Mater.*, vol. 54, no. 5, pp. 1279–1288, Mar. 2006.
- [5] C. H. Lee, H. K. D. H. Bhadeshia, and H.-C. Lee, “Effect of plastic deformation on the formation of acicular ferrite,” *Mater. Sci. Eng. A*, vol. 360, no. 1–2, pp. 249–257, Nov. 2003.
- [6] H. K. D. H. Bhadeshia, “Allotriomorphic Ferrite.” [Online]. Available: <https://www.phase-trans.msm.cam.ac.uk/2000/C9/lectures78.pdf>. [Accessed: 24-Aug-2018].
- [7] R. W. Cahn and P. Haasen, *Physical Metallurgy*. 1996.

Chapter 8: Thermal Simulation & Mechanical Testing

The quality heat treatment (QHT) operation constitutes the second major, and final thermo-mechanical processing operation in the production of a 16" ZERON® 100 weld neck flange forging. As detailed previously in Ch. 4.1.2.2, the QHT operation comprises of loading the forging into, and thermally equilibrating it with, a relatively low temperature furnace ($> 500^{\circ}\text{C}$) then raising the furnace temperature at approximately 150°C/hr up to the soak temperature (1080 or $1120^{\circ}\text{C} \pm 10^{\circ}\text{C}$) and holding for a minimum of 9 hrs. Upon completion of soaking, the component is transferred to an agitated 170m^3 water quench tank (in a witnessed time of 58 s) at, initially, 14°C and in which it is automatically oscillated by a ca. 200 mm-travel cradle for an immersion time calculated from the formulation 600 s/inch section thickness. The reported water temperature upon removal of the forging was 18°C . The temperature of the forging was measured through surface optical pyrometry.

A FE model of the QHT process was constructed using DEFORM™ and from which the time-temperature profiles of the specific Charpy V-notch impact toughness test sample locations within the 16" ZERON® 100 weld neck flange were generated. The simulation engine in DEFORM™ was able to predict the thermal behaviour during the solution treatment and quenching processes of the final quality heat treatment operation using the post-processing test coupon feature whereby specific nodes and elements within the model mesh were identified as corresponding to the respective locations in the forging from which the Charpy V-notch impact toughness test samples were taken. A full range of state variable data (including temperature, mean strain, von Mises strain, effective stress, heat flux, strain rate etc.) were then generated from these specific nodes/elements via the new 'coupon data extraction' command in v.11.1 for each saved time step in the simulation database and output as tab separated value tables at the coupon centre locations. The thermal data outputted from this model, as noted above, was used to create temperature, T – time, t plots of $T = f(t)$ over the transfer and quenching parts of the QHT operation for the three Charpy sample locations within the forging; C1, C3 and C7. Since it was assumed thermal homogeneity at soak temperature in the forging was achieved by the end of furnace soaking, for conciseness these $T = f(t)$ plots for the C1, C3 and C7 locations are presented below as time-scaled from the start of the transfer through air of the forging from the furnace to the quench tank.

8.1 DEFORM™ FEM QHT Model

It is important to note here the parameters (and therefore associated limitations) upon which the FEM model of the QHT process was constructed since these should be considered in the subsequent application of the derived data to the induction heat treatment simulations of the location-specific cooling curves produced and indeed the impact toughness testing of the samples from these induction heat treatment simulations.

The physical properties of the ZERON® 100 alloy, as they pertain to FEM modelling of transient heat transfer are indicated in Fig. 8.1 – Fig. 8.3. These data were converted into user-defined functions during pre-processing setup of the DEFORM™ QHT model to describe the thermal behaviour of ZERON® 100 material as required to solve the governing equations of the heat transfer problem.

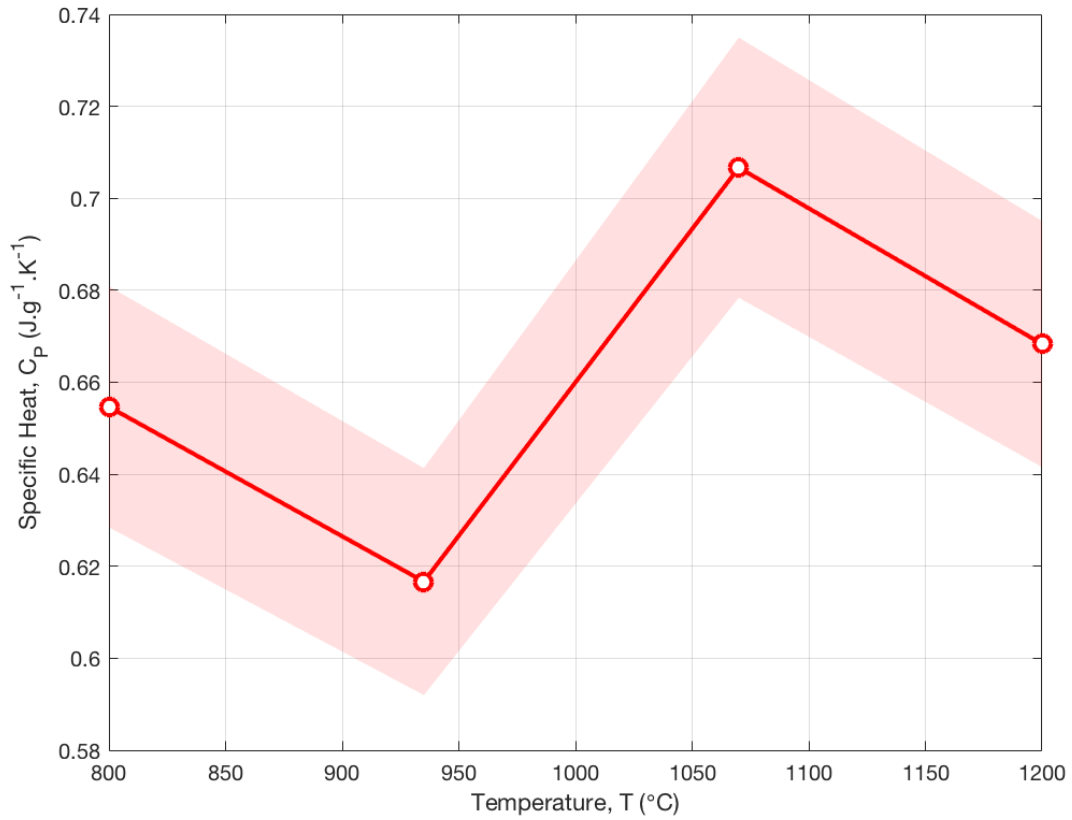


Fig. 8.1 ZERON® 100 heat capacity, $C_p = f(T)$ (averaged data from 1¼'' & 2½'' bar and 15 mm plate samples) \pm 4% uncertainty at the 95% CI indicated by the shaded region

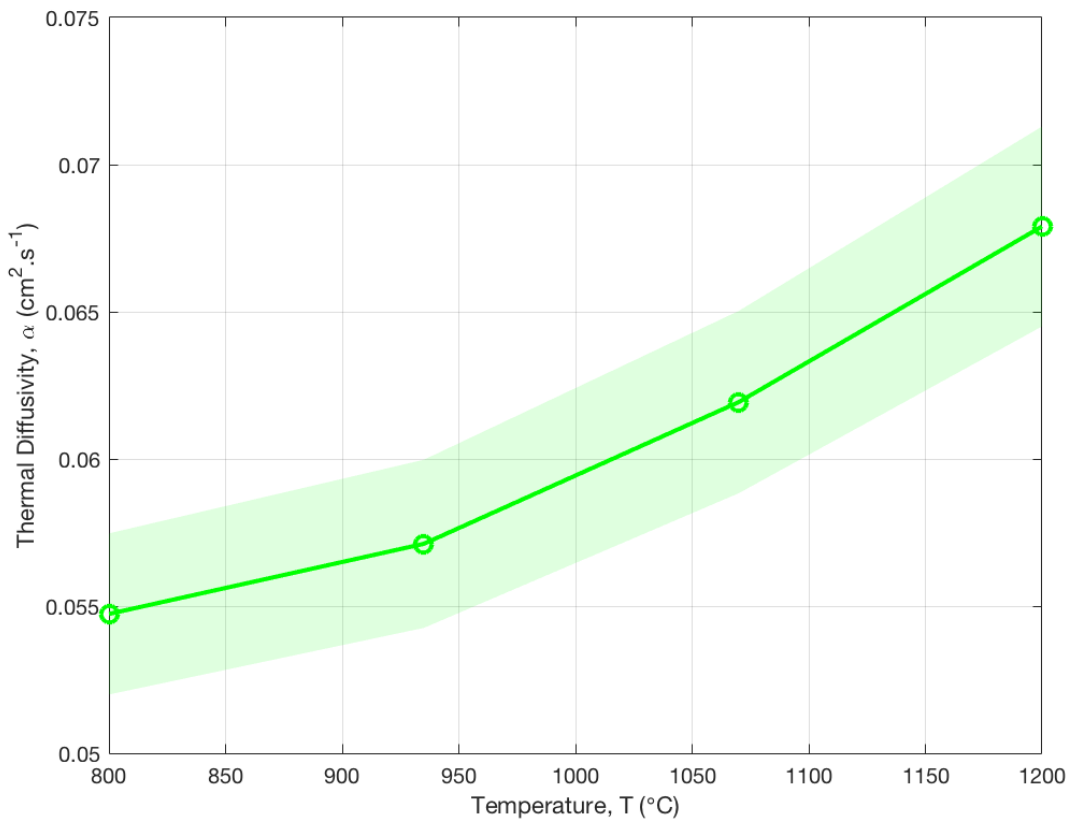


Fig. 8.2 ZERON® 100 thermal diffusivity, $\alpha = f(T)$ (averaged data from 1¼'' & 2½'' bar and 15 mm plate samples) \pm 5 % uncertainty at the 95% CI indicated by the shaded region

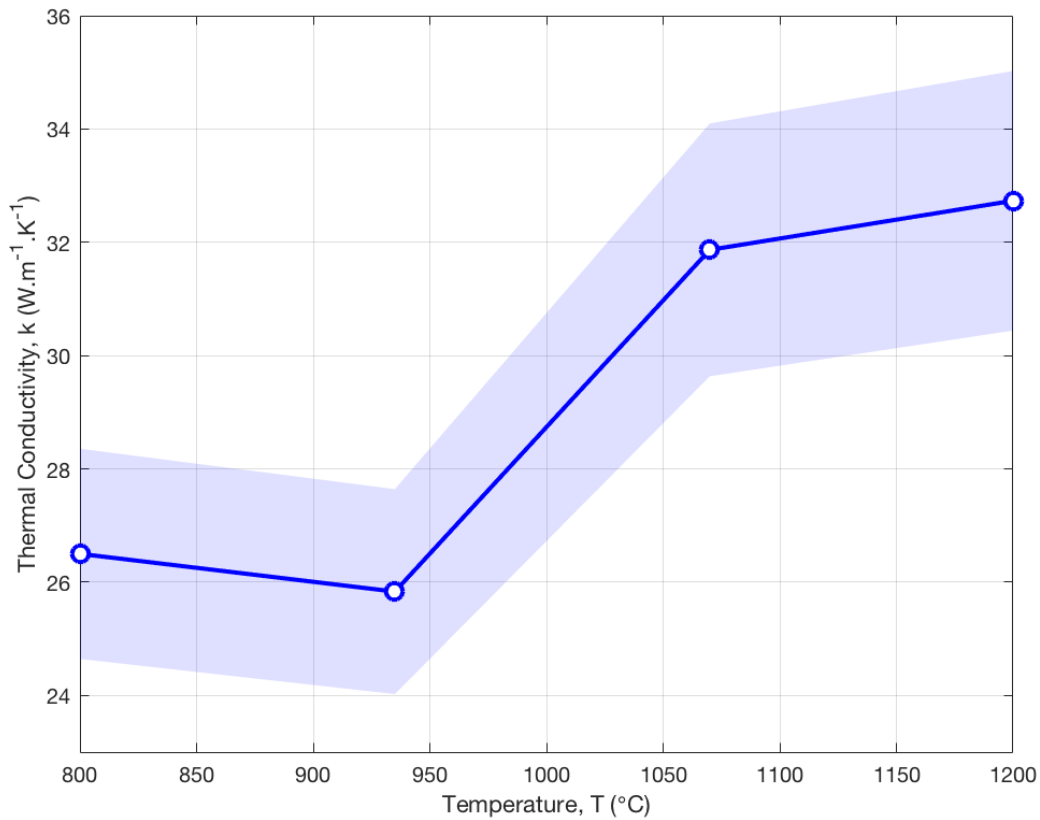


Fig. 8.3 ZERON® 100 $k = f(T)$ (averaged data from 1¼” bar, 2½” bar and 15 mm plate samples) $\pm 7\%$ uncertainty at the 95% CI indicated by the shaded error region

The thermal conductivity function in Fig. 8.3 above was calculated according to the equation:

$$k = \alpha \rho C_p \quad (\text{Eqn. 8.1})$$

Where the density, ρ was derived from the mass, m and volume at room temperature, V_{20} of the ZERON® 100 samples noted above and the measured linear expansion coefficient $\Delta L/L_{20}$ for volume change at high temperature. Density, $\rho = f(T)$ (kg m^{-3}) was then calculated according to:

$$\rho = \frac{m}{V_{20}(1+3(\Delta L/L_{20})/100)} \quad (\text{Eqn. 8.2})$$

For conciseness, the above referenced measured data $\Delta L/L_{20} = f(T)$ is not plotted however, the data measured were fitted to a 3rd degree polynomial whose obtained coefficients were used to derive $\Delta L/L_{20}$ (%), the percentage expansions relative to L_{20} (the sample length at 20°C). Finally, for the purposes of the model, the emissivity (ratio of energy emitted from the domain

surface to that radiated from a perfect, ‘blackbody’, emitter at the same temperature, wavelength etc.) was defined as constant at 0.7.

8.1.1 FEM Transient Heat Transfer Problem Principles and Setup

Discretization of the geometry of the domain into a mesh of finite elements is handled by the Automatic Mesh Generation system in DEFORM™ whereby mesh density is determined by a system defined, weight-based method used to control the size of elements during initial mesh generation. Here mesh density refers to the size of the elements generated (and if necessary, re-generated upon auto-remeshing) within the domain boundary and is principally based on the user-specifiable total number of elements and ‘parameter’ sliding controls, e.g. boundary curvature, temperature distribution, strain and strain rate distribution etc. The mesh generated for the 2-D axisymmetric QHT model is illustrated below in Fig. 8.4.

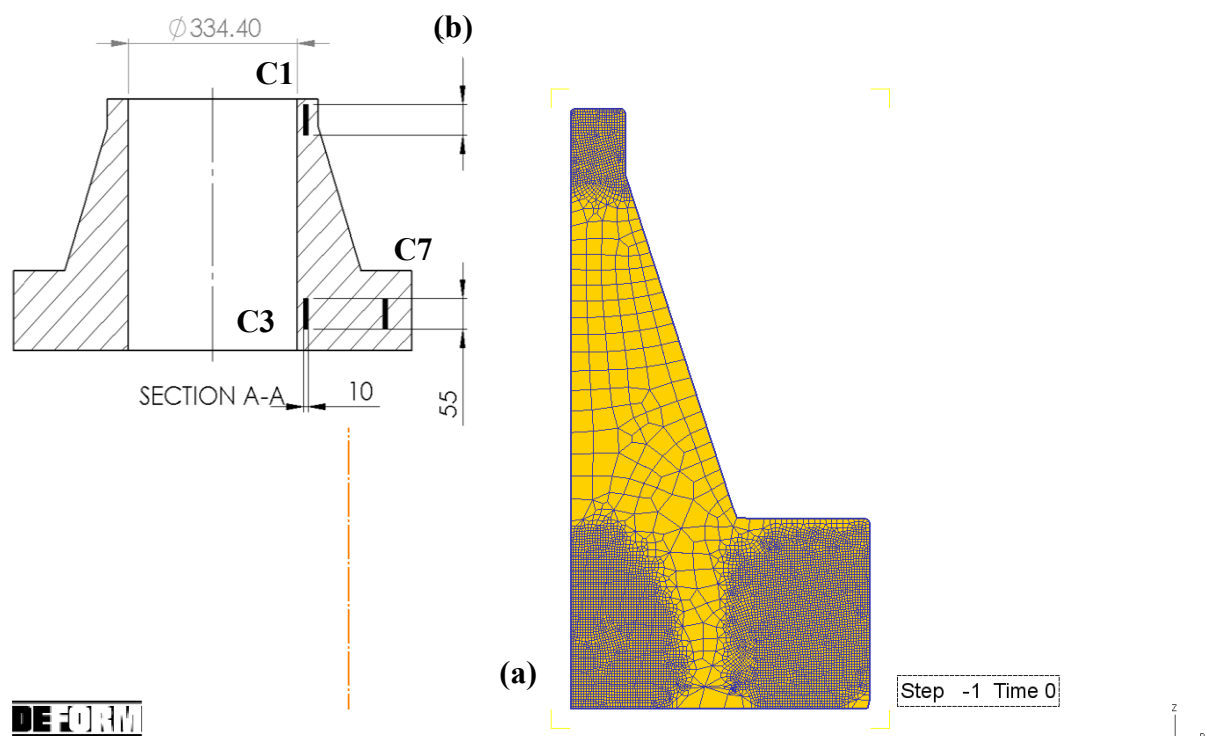


Fig. 8.4 The FE mesh generated in the domain of the 16” ZERON® 100 weld neck flange forging workpiece. The mesh consists of 7947 nodes connecting 7755 quadrilateral elements

Solution of an engineering problem through application of the FEM requires investigation of the convergence of the FE solution and, if necessary, gradually refining the mesh (i.e. increasing the number of elements) and comparing the solution with that obtained by higher-order elements, where the order of the element refers to the polynomial degree used to represent

the solution over the element. Thus, increases in the mesh density (in 2-D, elements/unit area) offer increased solution accuracy and resolution of both state variables (such as temperature) and geometry. Such improvements in solution accuracy however carry an associated penalty and in general the time and computational power required to solve a FE problem increases with number of element nodes. It follows therefore then that a large number of small elements in regions of particular interest in the domain i.e. large temperature gradients in this case, are desirable.

With reference to the mesh generated for the solution of the outlined QHT problem (illustrated in Fig 8.4a) it can clearly be seen that areas of high elemental refinement have been created around the approximate regions in the forging corresponding to the locations from which the Charpy V-notch impact toughness specimens were taken. For reference Fig. 4.12a showing these specimen locations is reproduced as insert Fig 8.4b. User definable areas on the object having higher element densities relative to other areas as illustrated above are specified through mesh density windows in the Advanced Mesh Setting feature of the DEFORMTM pre-processor. Where a mesh window (defined by > 2 connected points) crosses the workpiece border, a specified non-zero rational density value is assigned (as well as an optional velocity for the purposes of a deforming workpiece). The area defined by the window has an associated mesh density which is compared to the unity value of a 'global' window describing an area which covers the whole workpiece.

Transient heat transfer during quenching is a highly non-linear, and thus mathematically complex problem, consisting of primarily; nonlinearities due to the heat source term, Q in the governing equation (Eqn. 8.3), nonlinearities at the domain boundaries arising from the time-dependent convective heat transfer coefficient function, h and non-linearities of the temperature-dependent material properties noted above and illustrated in Fig. 8.1 – Fig. 8.3. Consequently, the thermal load, Q , conductivity, H and heat capacity, C matrices assembled into the system of simultaneous linear element equations to be solved are also temperature dependent[1].

The fundamental approach to FEM numerical analysis of the transient heat transfer problem lies in the reformulation of the unsuitable classical formulation (Eqn. 8.4), which represents a continuous distribution of temperature in both space and time, as an equivalent *variational principle* formulation. Construction of the variational formulation required is very

mathematically involved and covered thoroughly in much more detailed texts specifically related to the application of the FEM to heat transfer analyses[2]. It is therefore more pertinent here, for the purposes of describing the general principles of the FEM transient heat transfer model created, to note that the derivation of the matrix equations referred to above require the definition and integration of appropriate shape functions (defined in Eqn. 8.3 for an example isoparametric quadrilateral axisymmetric element) and/or their derivatives over the elements as a method of providing a temperature field that satisfies the general compatibility requirement of continuity over the entire workpiece,

$$N_i = \frac{1}{4} (1 + s_i s)(1 + t_i t) \quad \text{Eqn. 8.3}$$

Where (s_i, t_i) represents the local elemental co-ordinate system for node i rather than the global $(r-z)$ coordinate system, for ease of evaluation.

In integral form, the generalised shape function for the initial unknown temperature field can be approximated as:

$$T = \sum_{i=1}^n N_i T_i \quad \text{Eqn. 8.4}$$

Where the simultaneous matrix equations (of the form Eqn. 8.3) for the solution of n values of T_i may be obtained by equating to zero the successive weighted residual and integrated residual resulting from substitution of Eqn. 8.5 into Eqn. 8.4[3]. A set of n such simultaneous matrix equations is solved in DEFORMTM through the Newton-Raphson (N-R) iteration method to find the roots and update the temperature field. Once the temperature-update is solved it is applied to the current temperature and the temperature is solved again. Using the N-R method in this way generally allows for solution convergence in fewer iterations versus the direct iteration method and thereby improves the model reliability.

$$[H]\{T\} + [C]\{\dot{T}\} + \{Q\} = 0 \quad \text{Eqn. 8.5}$$

The procedure adopted in the FEM QHT model for solving equations expressed in the general form of Eqn. 8.7 is Gaussian elimination. The solution process of solving linear matrix equations however can take a significant amount of computer time, especially in cases where

a highly refined mesh and time step size are specified. It is necessary therefore to implement an efficiently programmed linear equation solver; the Skyline sparse matrix storage solver chosen for the solution of the QHT model stores the conductivity (analogues of the stiffness matrix in deformation mechanics) and heat capacity matrices column-wise from the diagonal matrix element to the last non-zero element in the column. This reduces the required computer memory storage for the matrix more than for banded matrix form storage[4].

The DEFORMTM system solves time dependent non-linear problems by generating a series of FEM solutions at discrete time increments, the outputted solution from which for the QHT model is illustrated in Fig. 8.5 where the temperature field at various time steps throughout the simulation is displayed. The equation describing the initial condition (necessary for computation of the solution using the FEM) of workpiece thermal homogeneity, $T_i|_{t=0} = T_0$ where, $T_0 = 1120^\circ\text{C}$ is obvious From Fig. 8.5, i.e. all initial nodal temperatures set to soak temperature. Additional boundary conditions (as noted previously) were specified to complete the definition of the thermal problem such that convective heat transfer is set for surface nodes in contact with the quench media, i.e.

$$\Psi(T_s, T_\infty) = h(T_s - T_\infty) \quad \text{Eqn. 8.8}$$

Where Ψ is the surface heat flux, a function of the surface and quenchant temperatures, T_s and T_∞ , respectively.

It is important to note that a $\partial L/\partial t = \rho\Delta H(\partial V/\partial t)$ term (where ΔH is the enthalpy for formation and $\partial V/\partial t$ is the change in the phase transformed) embodying the latent heat effect associated with phase transformation is often included in Eqn. 8.4 when modelling quenching operations, especially when pertaining to ferritic alloys systems[5]. However, in this case, prior *equilibrium* thermodynamic modelling (Fig. 2.4) indicates no ‘major’ volumetric phase change should occur in the ZERON® 100 alloy over the temperature range and cooling rates associated with the QHT operation. Instead, the volume fractions of the duplex phases are shown to change and from which the latent heat released/absorbed is assumed to be negligible and thus undefined here. Further, any latent heat generated from the formation of any tertiary precipitates e.g. σ -phase, Cr-nitrides etc. has also been neglected due to the infinitesimally small indicated molar fraction they occupy (Fig. 2.4). Additionally, the non-equilibrium

cooling conditions have been assumed to largely suppress their formation to extremely small molar fractions and thus omissible ΔH contributions to Q . Since only the volumes of the duplex phases change during cooling and newly nucleated tertiary phases would only occupy extremely small volume fractions, the effects of latent heat may be neglected for this material (see thermodynamic modelling in Ch. 2)

Finally, and most importantly in the evaluation of the applicability of the data derived from this FEM model, two constant convective heat transfer coefficients, h were defined as $100 \text{ W m}^{-2} \text{ K}^{-1}$ and $3100 \text{ W m}^{-2} \text{ K}^{-1}$ to describe the air ($T_0 = 20^\circ\text{C}$) and water ($T_0 = 14^\circ\text{C}$) which surround the forging when it is first transferred out of the furnace to the quench tank and then subsequently immersed in the quench tank, respectively. These values were adapted from reported values in the literature indicated to be appropriate analogues of free convection in air and surface convection for a comparable SAF-2205 alloy bossed connector forging at 1050°C subject to ‘hyper-quenching’ conditions for approximately 30 minutes in water at 16° [6]. The heat transfer coefficient is the constant of proportionality in Newton’s law of cooling (Eqn. 8.9) which provides a general description of convection heat transfer processes, regardless of the particular nature.

$$Q' = h(T_\infty - T_s) \quad \text{Eqn. 8.9}$$

Where Q' is the convective heat flow (W m^{-2}) and proportional to temperature difference between the quench media and body surface. The heat transfer coefficient, h depends upon conditions in the boundary layer (laminar, turbulent fluid motion etc.), themselves influenced by surface geometry and various fluid dynamic properties. Tables of typical $h = f(T)$ values are available for a wide variety of conditions, although these are invariably somewhat coarse estimations at best. It is suggested however[6] that the value of h is stabilized within a few seconds and therefore that to know the cooling profile in the centre of large section forgings, it is only necessary to know the stabilized value of h . Further to this, the influence of surface heat transfer coefficient on rate of cooling decreases with increasing section thickness[7],[8] and therefore since bulk heat transfer is considered in this model, the function $h = f(T)$ during quenching, only becomes significant when consideration of the effects on surface microstructure and residual stresses in steel specimens need to be made[9].

In spite of this, it should be clear that the specification of a constant h in the model (for both of the quench media) limits the ability to account for the complex heat transfer phenomena that occur, for example, upon the formation of an insulative vapour blanket around the forging upon initial immersion in to the quench tank. This vapour blanket should however be rapidly dispersed by the oscillation of the workpiece in agitated water tank[10]. Neither is the model specified such that gradual envelopment by the various quench media is simulated; scheduling setup in the DEFORMTM pre-processor stipulated an initial 58 s ‘transfer through air’ (as can be clear seen from the linear portions of the $T-t$ curves presented in Fig. 8.6 – Fig. 8.8) followed by a complete and instantaneous ca. 1.5 hr water quench.

Clearly limitations in the fidelity of the model presented with the physical QHT process exist. It is important therefore, as noted above, to consider these model limitations and inaccuracies in further evaluation and application of the derived data.

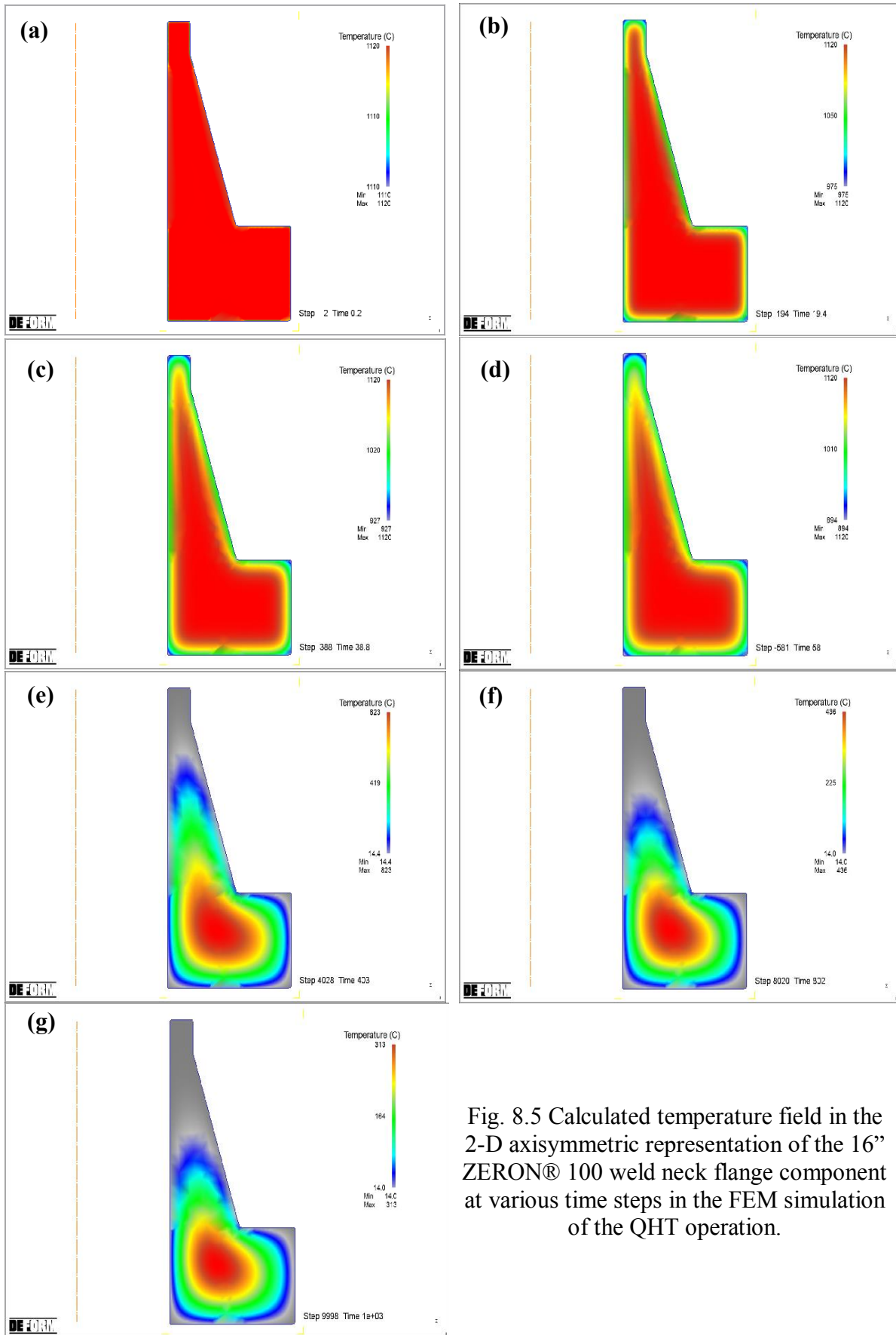


Fig. 8.5 Calculated temperature field in the 2-D axisymmetric representation of the 16” ZERON® 100 weld neck flange component at various time steps in the FEM simulation of the QHT operation.

8.1.2 Derived Cooling Curves

Using the coupon feature in the DEFORMTM post processor, time-temperature data was extracted for the nodal locations in the mesh mapping to the impact toughness specimens as indicated in Fig. 8.4b.

This tabulated data outputted from the simulation of the QHT was interpolated into a series of 20 set-points (or query points, specified as an evenly spaced vector over the time interval defining the end of the soak operation through to attainment of a threshold temperature $< 200^{\circ}\text{C}$ during water quench). This was achieved programmatically through the use of a series of functions available in the MATLAB[®] Curve Fitting and Statistics and Machine Learning Toolboxes based on a piecewise cubic spline interpolation between data points using not-a-knot end conditions (whereby the spline requires that the third derivative of the spline is continuous at x_1 and x_{n-1}).

The interpolated values at the query points are based on a cubic interpolation of the values at neighbouring grid points in each respective dimension. The "not-a-knot" end condition means that, at the first and last interior break in the sequence defined by vector interval noted above, even the third derivative is continuous (up to round-off error). The outputted simulation time-temperature data from DEFORMTM and the interpolated set points are plotted below in Figs. 8.6 – Fig. 8.8 as $T = f(t)$ for the three Charpy V notch impact toughness specimen locations in the forging.

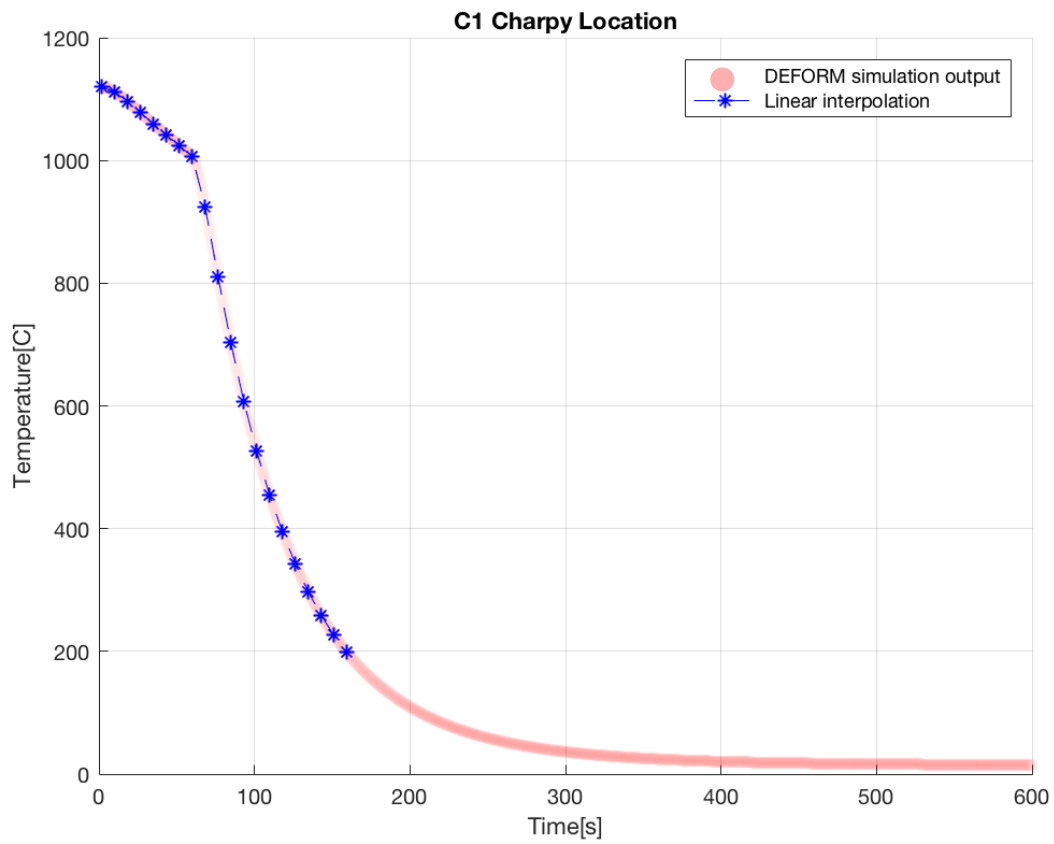


Fig. 8.6 Temperature, T vs. time, t profile for the C1 position time-scaled according to immediate removal from solution annealing in the furnace. The interpolated setpoints defining this continuous cooling curve, as described above, are indicated by the blue markers.

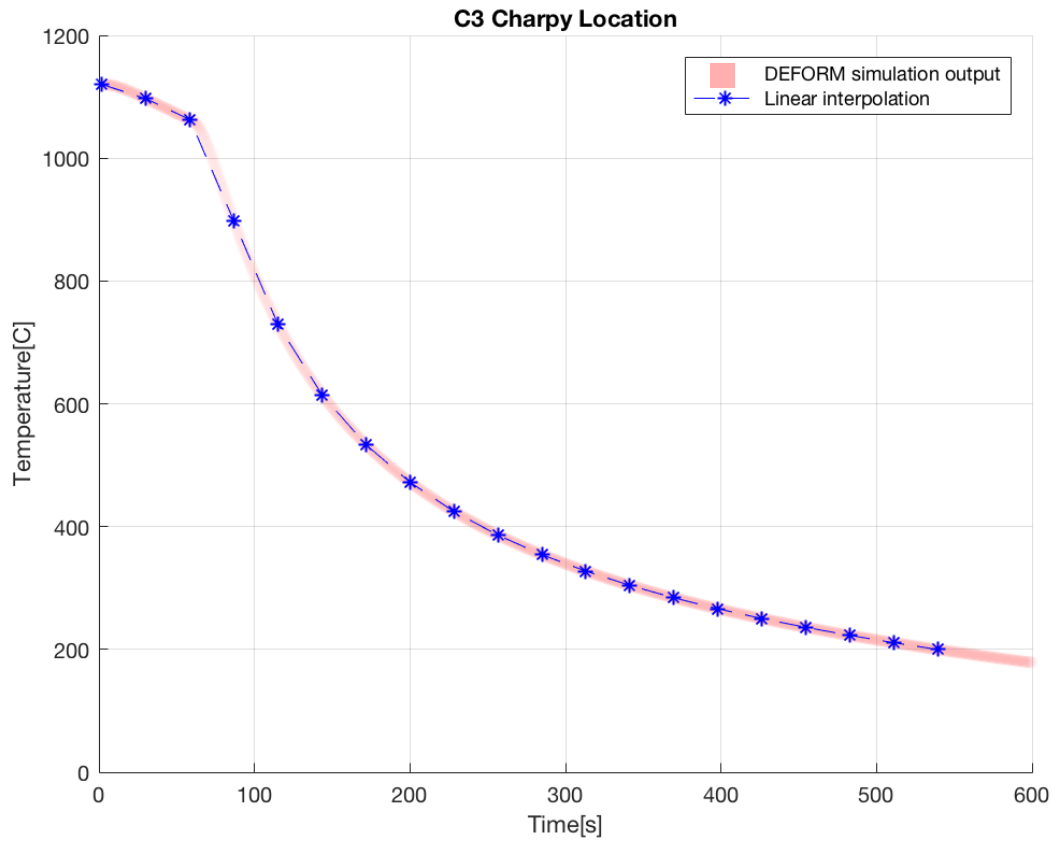


Fig. 8.7 T vs. t profile for the C3 position time-scaled according to Fig. 8.6. Interpolated setpoints defining the continuous cooling curve are again indicated blue star markers.

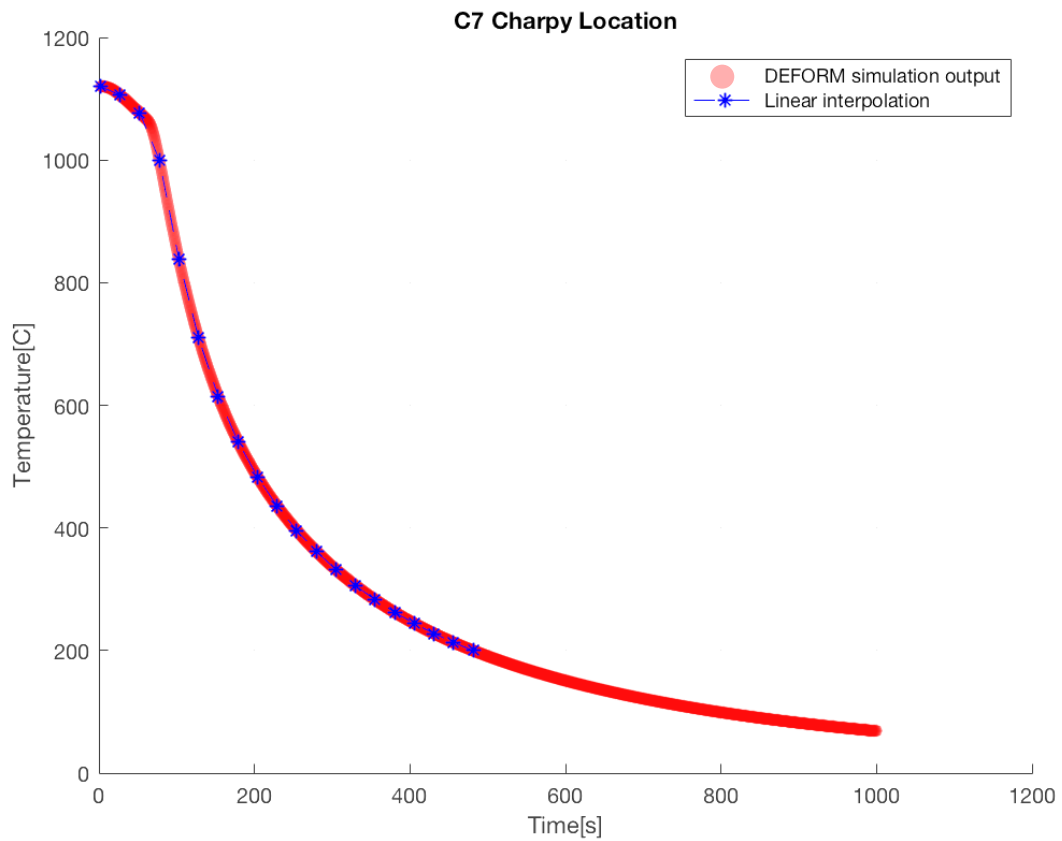


Fig. 8.8 Temperature, T vs. time, t profile for the C7 location formatted etc. according to previous two cooling curves above (Fig. 8.6 & Fig. 8.7)

8.2 Thermal Simulations & Mechanical Testing

The cooling curves produced on the reconfigured ATPU for the C1, C3 and C7 Charpy locations within the forging are presented below. For each location specific thermal simulation, two randomly selected sample bars were tested thus providing a total of four Charpy impact toughness specimens from each test. The full tabulated impact toughness data is presented in Table 8.1. Note full thermal simulations are presented below whereby the samples are ramped (at 10°C/s) to 1120°C, held for 300 s (to thermally homogenise) then cooled according to location specific thermal profiles detailed above (Figs. 8.6 - 8.8).

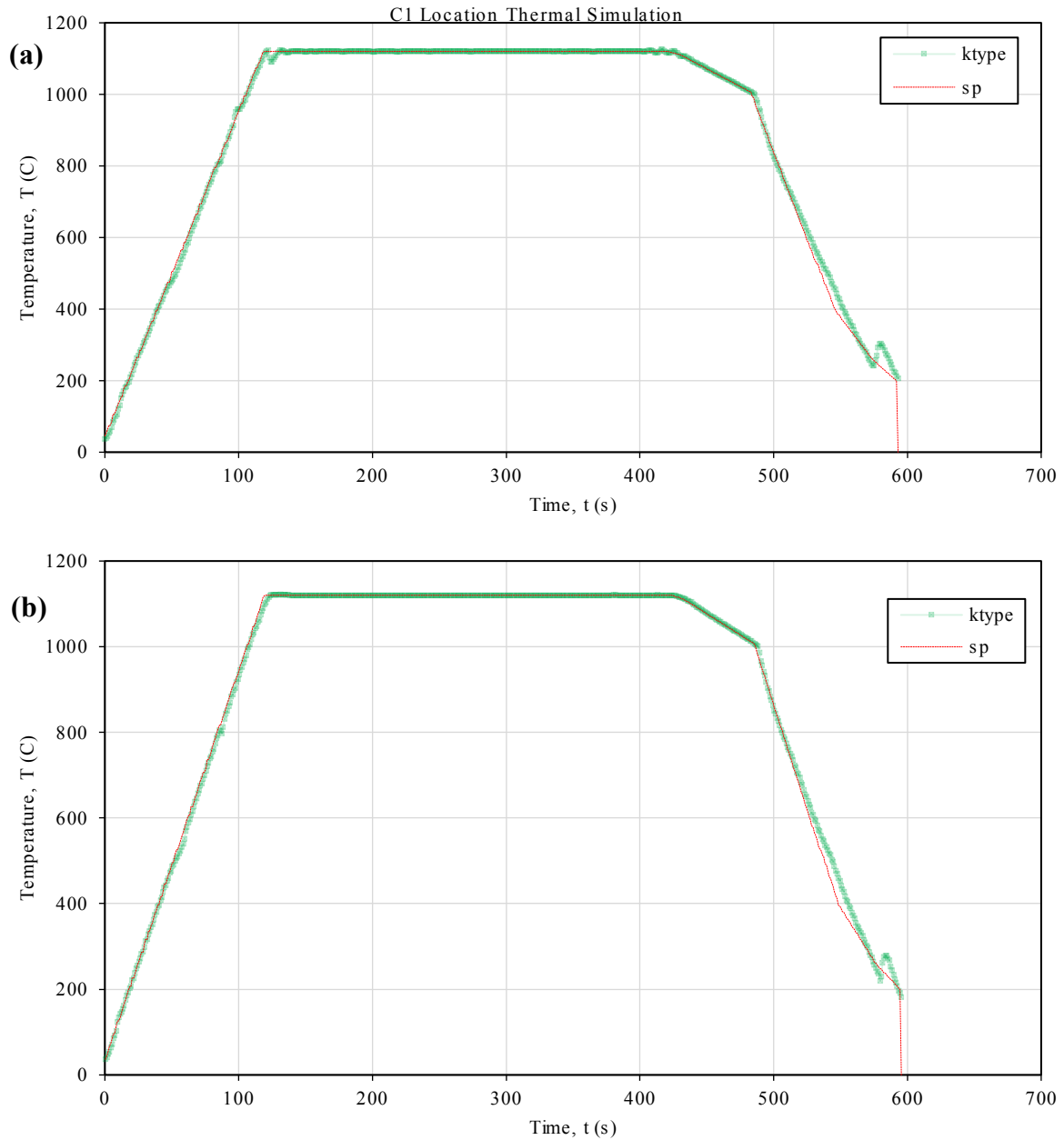


Fig. 8.9 Sample temperature (ktype data series) compared against target setpoints (sp data series) representing the interpolated cooling curve from the FEA QHT model for the C1 location within the forging as tested in the redesigned ATPU on **a** bar 5 and **b** bar)

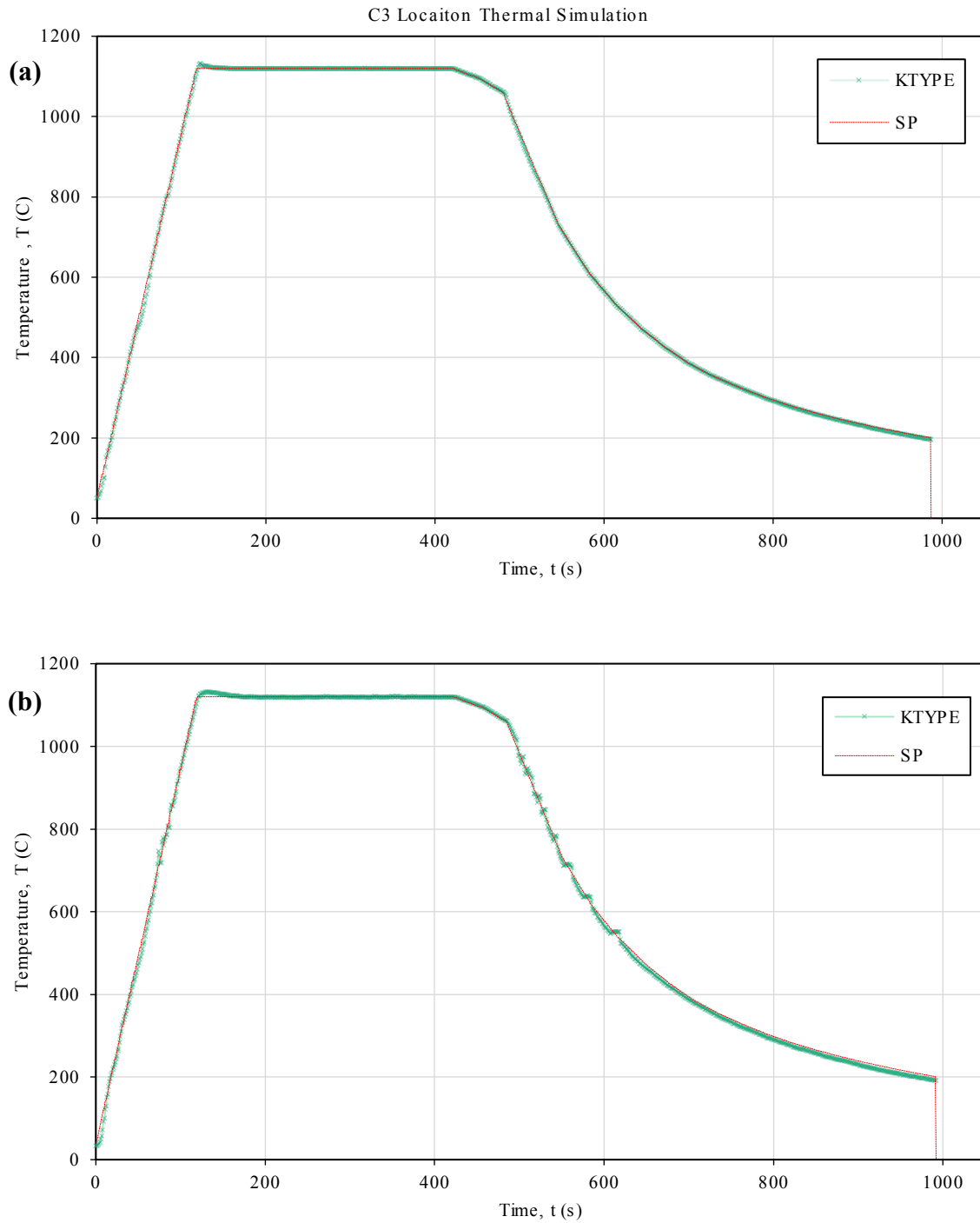


Fig. 8.10 Sample temperature (KTYPE data series) compared against target setpoints (SP data series) representing the interpolated cooling curve from the FEA QHT model for the C3 location within the forging as tested in the redesigned ATPU on **a** bar 4 and **b** bar 6

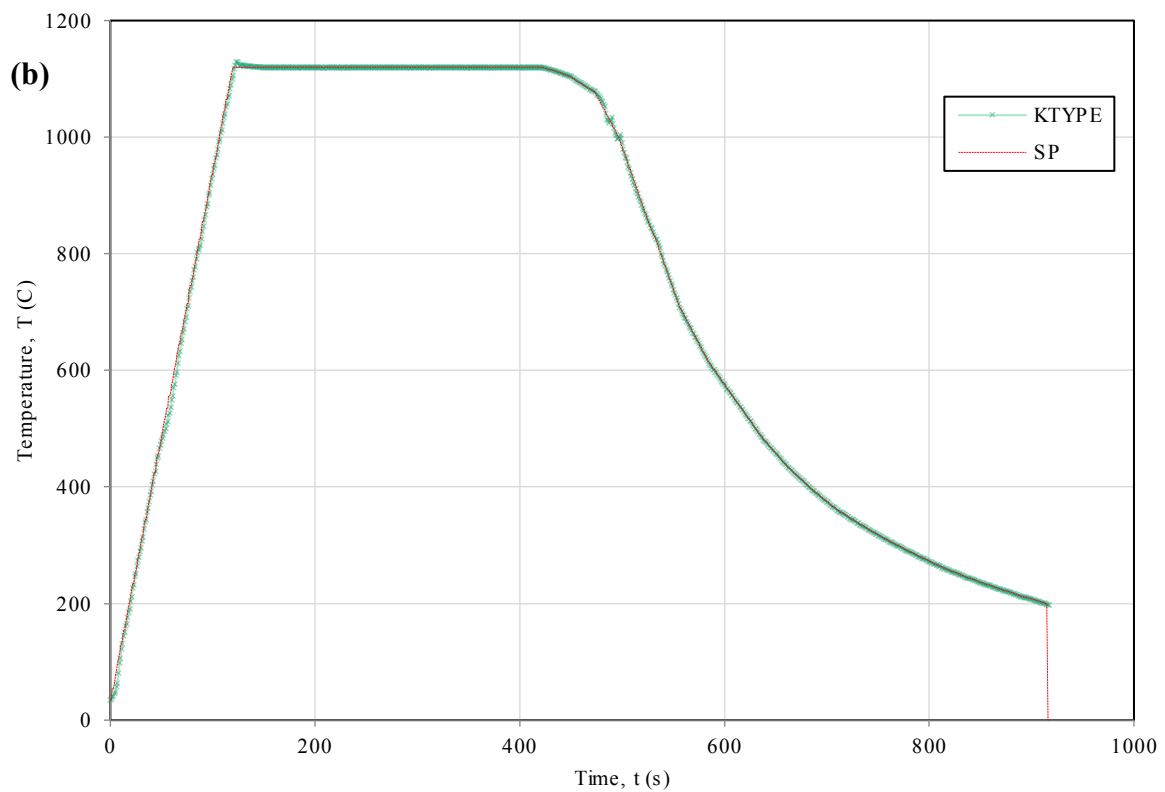
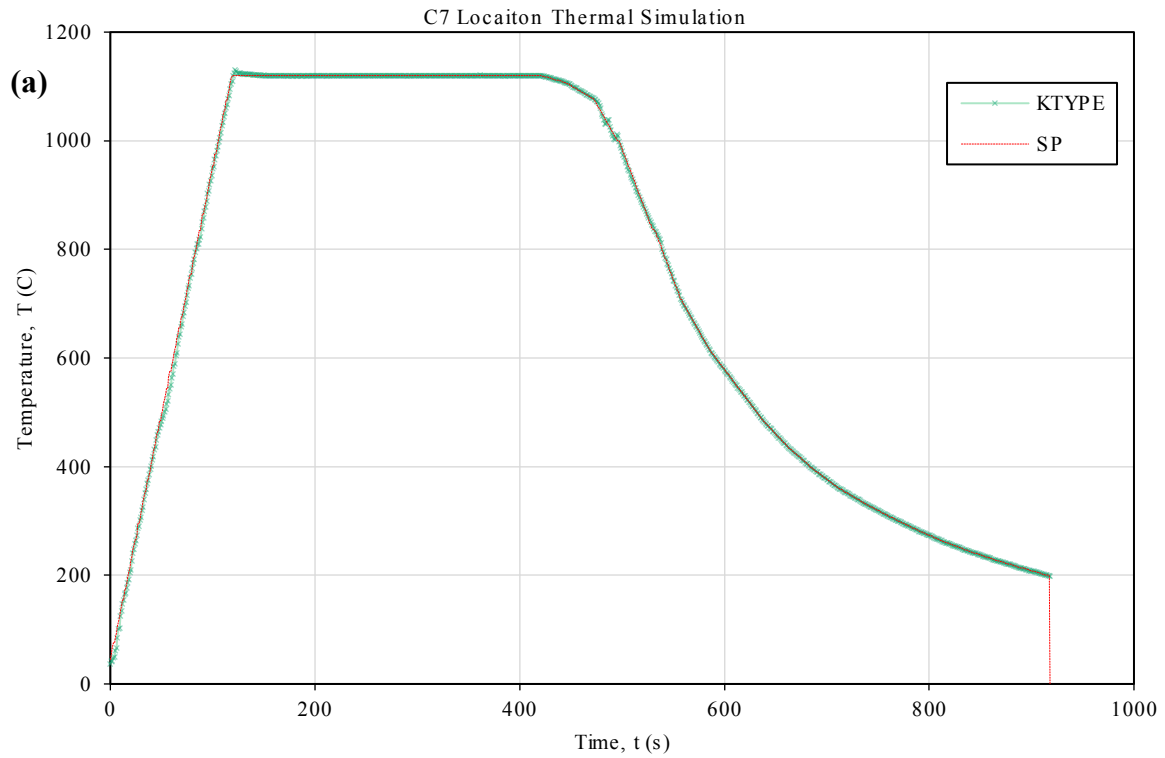


Fig. 8.11 Sample temperature (KTYPE data series) compared against target setpoints (SP data series) representing the interpolated cooling curve from the FEA QHT model for the C7 location within the forging as tested in the redesigned ATPU on **a** bar 3 and **b** bar 9

In addition to simulating the cooling curves from the FEA QHT model, two ‘interrupted’ tests were conducted whereby samples were subject to the same thermal cycles as per Fig. 8.10 & Fig. 8.11 however immediately water quenched with full mist upon reaching the end of the initial ‘linear’ cooling phase of the thermal cycle. In effect these tests aimed to capture the microstructure that had evolved during the transition between leaving the soak furnace and immediately prior to submersion in the quench tank.

‘Interrupted’ tests were carried out according to the thermal profiles for the C1 and C3 locations, however for brevity and general representation, the temperature-time plot for only the interrupted test at the C1 position is illustrated below in Fig. 8.12.

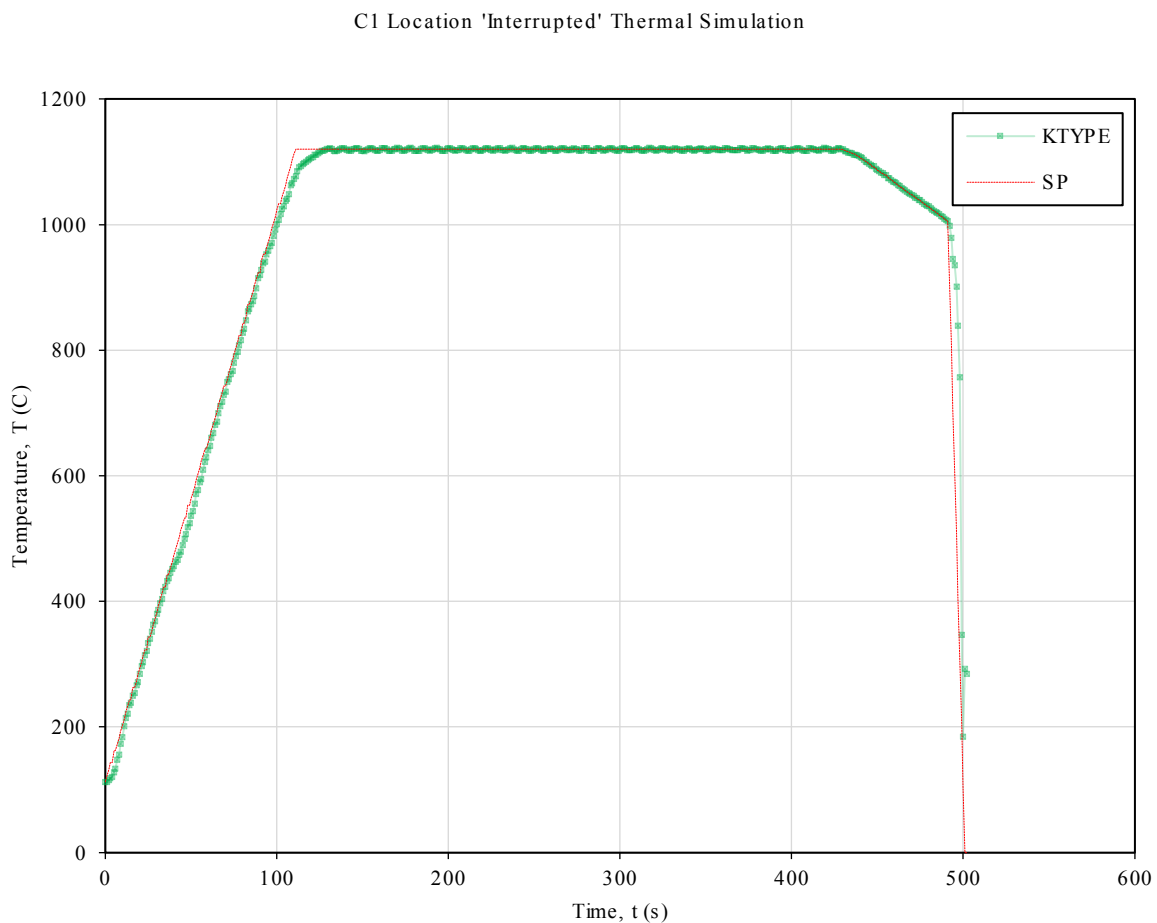


Fig. 8.12 Example of an ‘interrupted’ thermal simulation using the cooling curve for the C1 location. The programmed setpoints (SP) were adjust in this test to simulate a cooling rate of ca. 80°C/s from the temperature reached at the end of the ‘transfer through air’ portion of the thermal cycle to < 200°C. The KTYPE thermocouple data indicates that the cooling of the sample closely approximated this rate.

8.3.1 Impact Toughness & Hardness

The samples subject to thermal simulations as detailed above in Figs. 8.9 – 8.12 were impact toughness tested at -46°C according to ASTM E23 – 16b (Standard Test Method for Notched Bar Impact Testing of Metallic Materials) to maintain consistency with the testing detailed in Table 7.1. The data from these tests is detailed below in Table 8.1

Table 8.1 Charpy V-notch Impact Toughness Data for the Samples Subjected to QHT Simulation as per the Data from the FEA Model

<i>Location in Forging</i>	<i>Sample ID</i>	<i>Results (J)</i>		<i>Mean Toughness (J)</i>	<i>Error (J)</i>
C1	Bar 05	120	115	136.25	± 17.94
	Bar 10	168	142		
C3	Bar 04	88	111	99.50	± 6.85
	Bar 06	88	111		
C7	Bar 03	239	115	182.25	± 42.74
	Bar 09	168	128		
C1 interrupt.	Bar 08	266	96	168.5	± 59.5
	Bar 15	207	282		
C3 interrupt.	Bar 01	242	299	260.5	± 22.61
	Bar 13	270	231		

In addition to Charpy impact toughness testing, the thermal simulation samples were also hardness tested according to ASTM E384 – 17 (Standard Test Method for Microindentation Hardness of Materials) using a 2 kg load and 15 s dwell time. 20 automated linear indents were made per sample using a Struers Durascan 70 G5 and resulting hardness data is presented below in Table 8.2.

Table 8.2 Averaged Hardness Data (HV 2) from the 20 Indents made on each of the Samples Subjected to QHT Simulation as per the Data from the FEA Model

<i>Location in Forging</i>	<i>Sample ID</i>	<i>Mean Hardness (HV 2)</i>	<i>Error</i>
C1	Bar 10	254.2	± 3.86
C3	Bar 04	249.85	± 3.11
C7	Bar 09	250.8	± 3.40
C1 interrupt.	Bar 08	235.15	± 3.68
C3 interrupt.	Bar 13	262.35	± 4.02

The toughness and hardness data presented above in Table 8.1 & Table 8.2 are illustrated graphically in Figs. 8.13 & Fig. 8.14

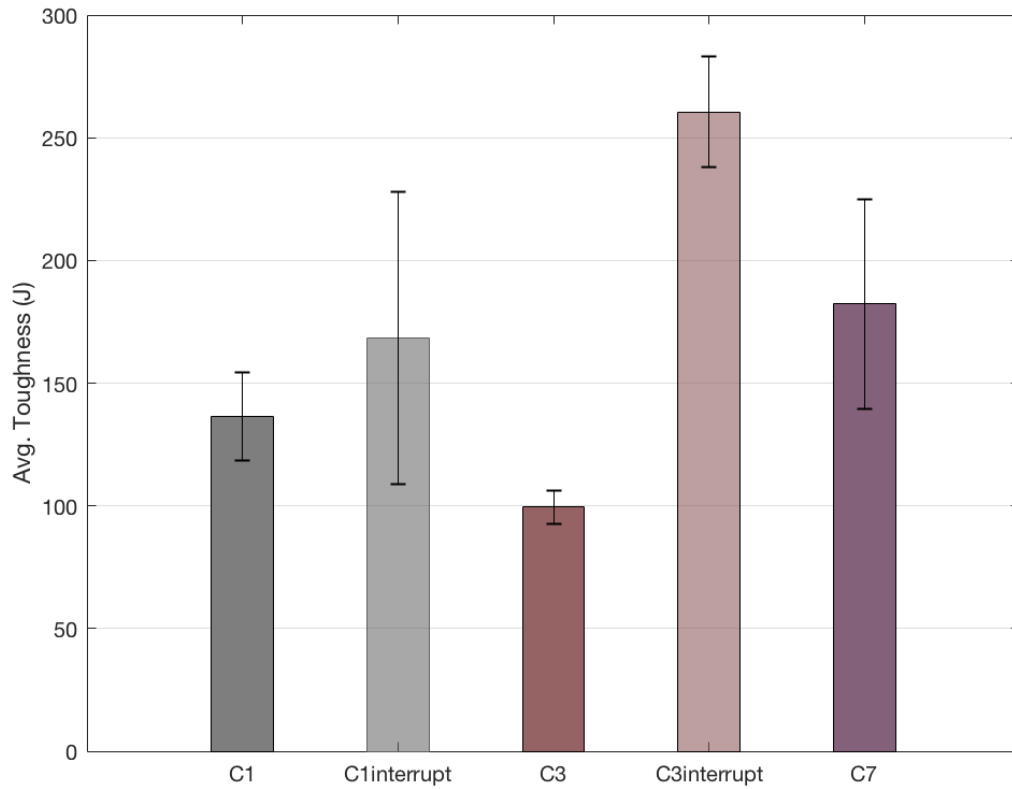


Fig. 8.13 Average toughness of the samples subjected to the thermal simulations detailed in Figs. 8.9 – 8.12

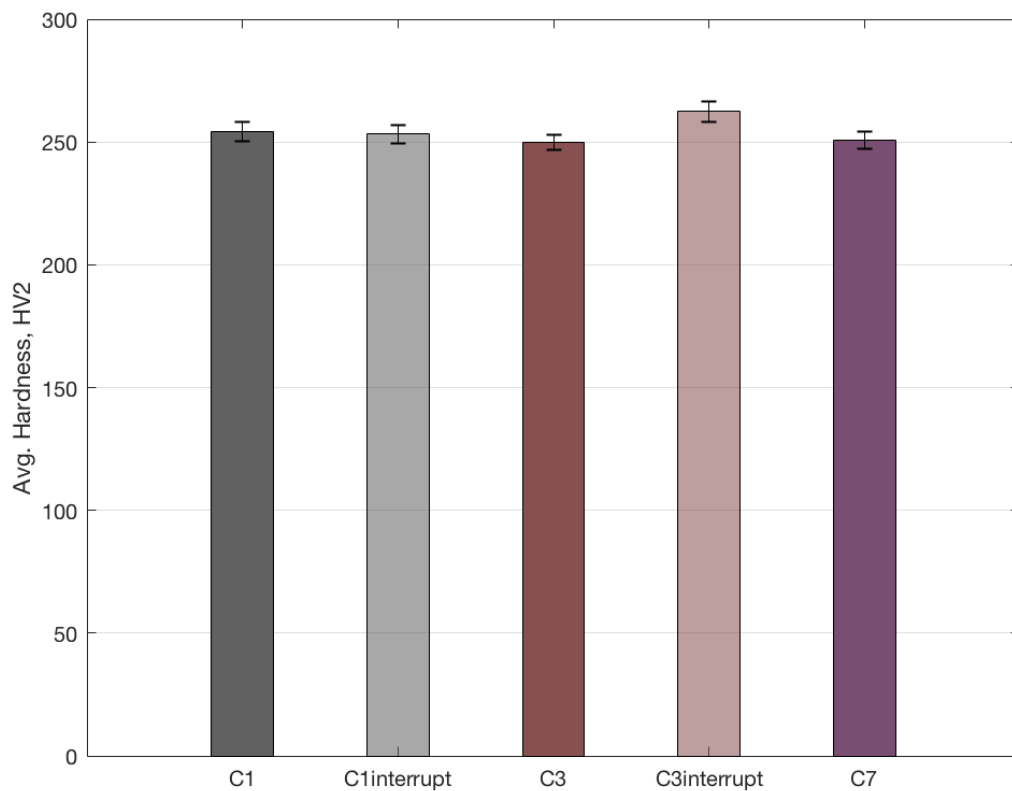


Fig. 8.14 Average harness (HV 2) of the samples subjected to the thermal simulations detailed in Figs. 8.9 – 8.12

While Fig 8.14 seems to suggest a hardness – cooling rate invariance, Fig. 8.13 clearly indicates that the lowest toughness occurs in the sample subjected to the slowest cooling rate (C3). Correspondingly, it is also from the same C3 sample location in the commercial forging where impact toughness properties are the poorest indicating an influence of cooling rate. This is underlined by comparison to the sample subjected to the ‘interrupted’ C3 thermal simulation. Here a marked increase in toughness is achieved by immediately quenching the sample following the simulated initial air cool during transfer from furnace to quench tank, rather than allowing the sample to continue to cool according to the profile of the curve in Fig. 8.7.

All samples were prepared and optically micrographed according to the methodologies outlined in Ch. 4, specifically with the sectioning (and micrography) plane parallel to the orientation of the V-notch and direction of crack propagation as illustrated below in Fig. 8.15. The microstructures of the C3 and C3 interrupted samples are illustrated in Fig. 8.16 & Fig. 8.17 where the direction of crack propagation lies in the plane of the micrographs.

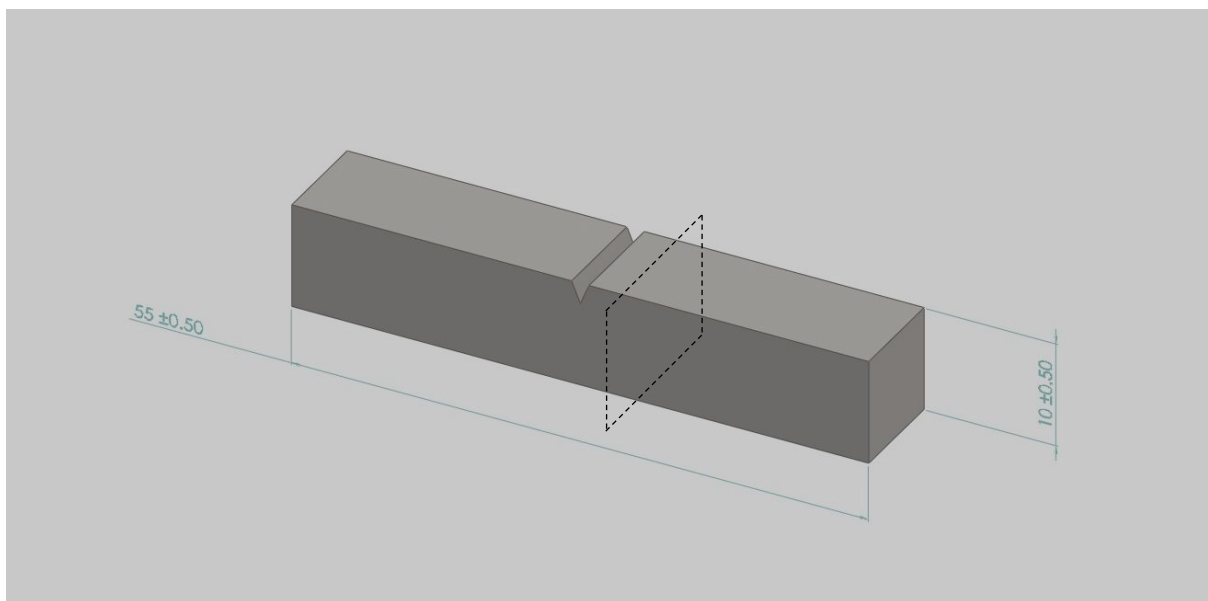


Fig. 8.15 Example Charpy V-notch impact toughness specimen with the sectioning/micrography plane of the C3 and C3 interrupted micrographs shown below in Fig. 8.16 & 8.17 illustrated by the dashed rectangle.

It is important to note that in all cases the samples were taken from the as-received billet, upon which no secondary forging had taken place, in contrast to the Charpy data presented in Ch. 7 which was derived from impact toughness testing of commercially forged material.

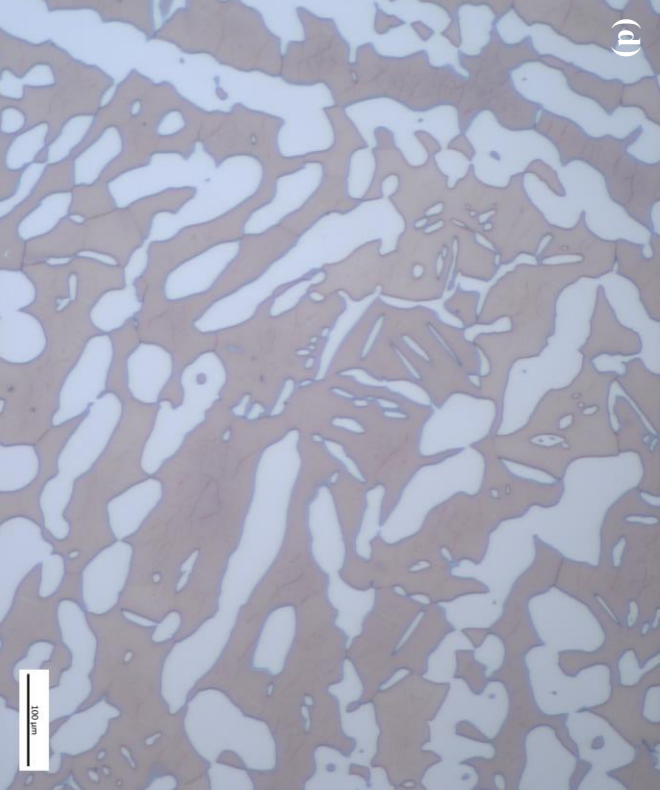
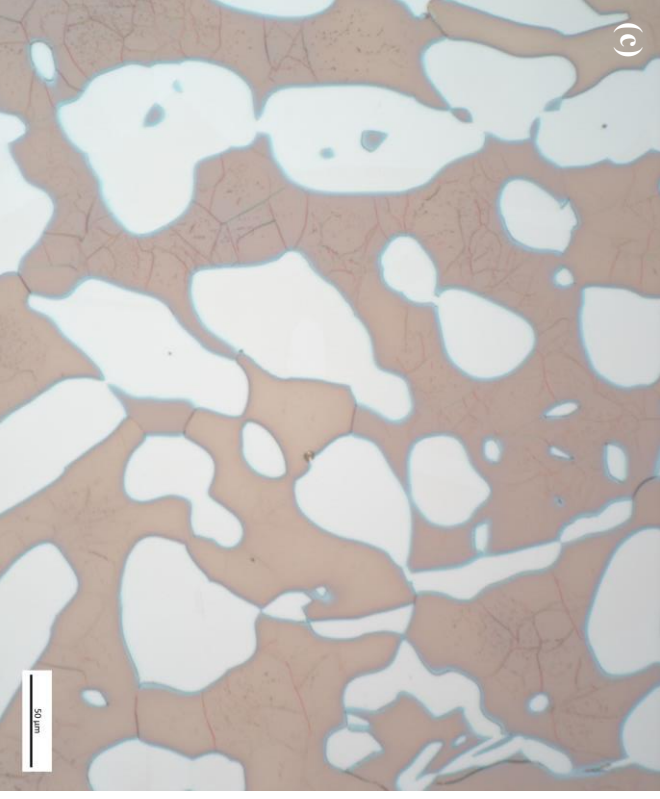
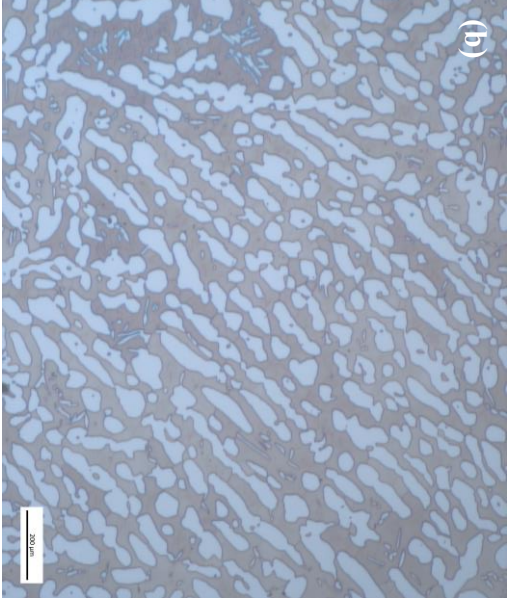
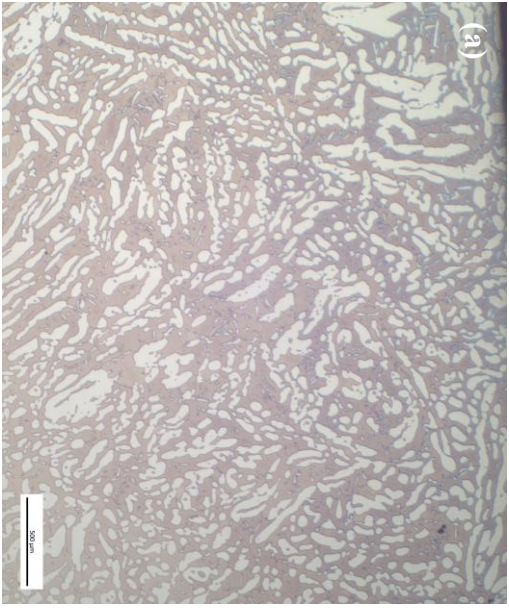


Fig. 8.16 C3 Bar 04 microstructures

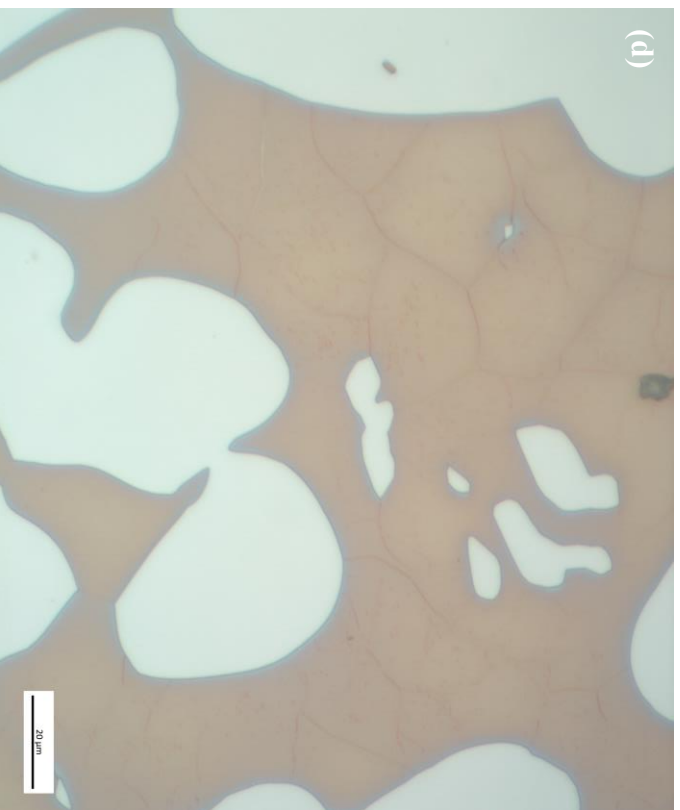
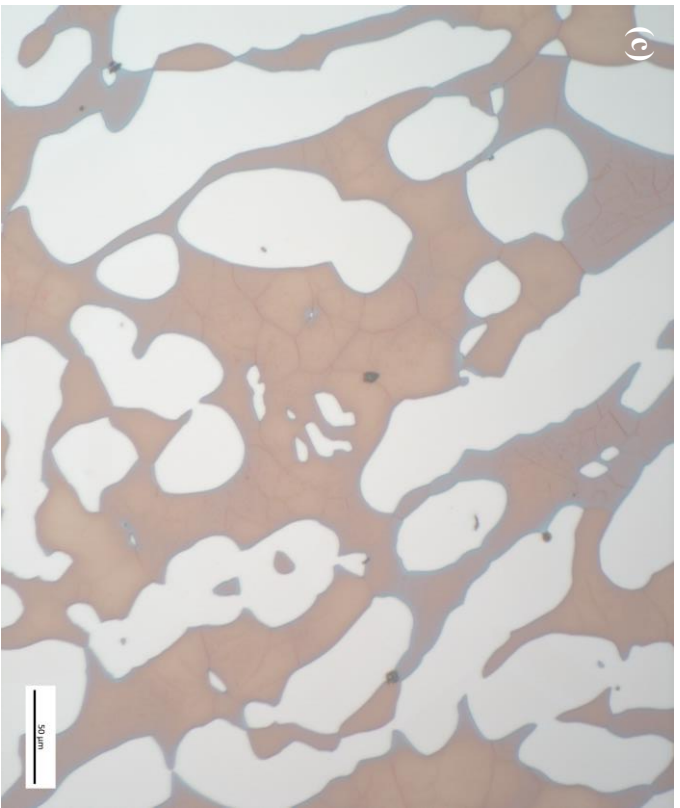
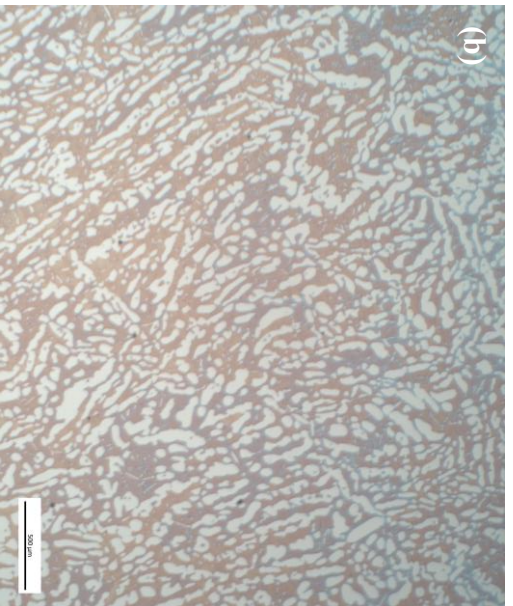
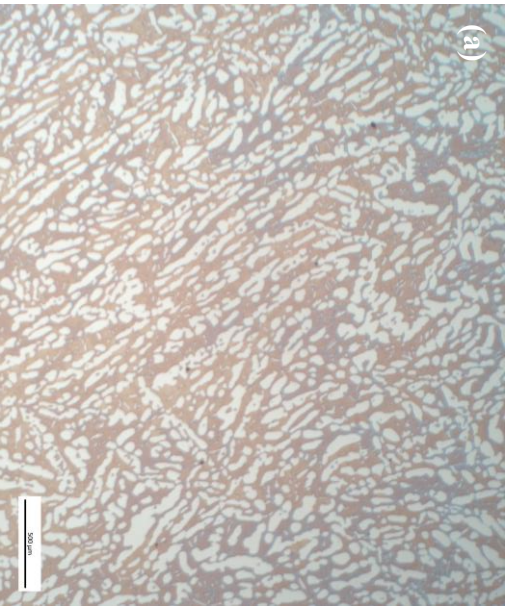


Fig. 8.17 C3 Interrupted Bar 13

8.4 Summary

The thermal simulations and mechanical testing presented in this chapter indicate the applicability of the ATPU, when appropriately configured, to accurately thermally simulate the complex cooling curves arising in industrial thermo-mechanical processing.

It is however important to note at this point that the thermal simulations and mechanical testing in this instance were conducted using sample taken directly from as-received billet starting material, upon which no subsequent industrial secondary working (or indeed their lab-scale analogues) had been carried out. The reason ‘unworked’ starting billet material was used for the ATPU and Charpy samples arose due to the geometric limits imposed by the TMC, whereby the final dimensions of a uniaxially compressed sample would not be compatible with the requisite amount of material required to machine a standard 10 mm² x 55 mm V-notched bar for impact toughness testing.

The thermal simulations and Charpy testing therefore represent close analogues of material from ‘dead-zone’ regions within the component, i.e. positions in which little-to-no strain penetration has occurred as a result of the forging process and consequently there has been limited break-up/refinement of the as received billet microstructure. In effect therefore, the work presented in this chapter represents heat treatment of the ‘most-likely worst-case scenario’ in the forging process in which the as-received microstructure of the billet has been carried through into the near net shaped component.

It should however also be noted that the ‘quality’ of the as received billet is itself subject to significant variation not only in terms of AFP vs. standard product (as discussed in Ch. 2), but also from steelmaker to steelmaker. The billet from which the samples subject to thermal simulation and mechanical testing here were taken was AFP ZEORN® 100 material. Earlier characterisation (Ch. 2) revealed a microstructure in this billet indicative of high temperature cogging of the cast ingot in the GFM RF100 to form the billet, relative to the subsequent solution heat treatment. This is due to the instances of allotriomorphic γ_2 precipitates decorating what appear to be a high density of grain boundaries/sub-structure in the ferritic matrix (Fig. 2.8). Therefore, even though no secondary forming operations had been carried out, the billet

itself represents what is assumed to be ideal starting material for subsequent forging operations where localised areas of little-to-no strain penetration is indicated to occur.

Further evidence of the impact toughness quality of the ‘high temperature forged’ microstructure explored previously in Ch. 7 and displayed in the billet from which the samples experimented upon in this chapter were taken is indicated in the C3 and C3 ‘Interrupted’ toughness data (Fig. 8.13). Even though C3 position represents the slowest cooling Charpy location in the forging, samples in this work subject to (assumed) similarly slow cooling rates registered a mean toughness of ca. 100 J at -46°C. This exceeds the comparable value indicated in Table 7.1. Additionally, when the C3 cooling curve was interrupted and the sample quenched immediately after the initial air cool period during transfer between the soak furnace and quench tank, an improvement in toughness was recorded indicating the potential benefit of ensuring the maximum possible cooling rate.

Finally, and with reference to the billet characterisation in Ch. 2, it is important to also consider the potential effects of billet heterogeneity when interpreting the toughness data presented here. The samples were taken from a range of radial locations through the billet and were therefore unlikely to be identical in terms of microstructure. A lack of homogeneity across the samples tested (as was also noted in the case of the TMC samples) must therefore also be considered in terms of the toughness variation.

REFERENCES

- [1] J. N. Reddy, *An introduction to the finite element method*. McGraw-Hill, 2006.
- [2] R. W. Lewis, K. Morgan, H. R. Thomas, and K. N. Seetharamu, *The finite element method in heat transfer analysis*. Wiley, 1996.
- [3] C. Simsir and C. Gur, “Simulation of Quenching,” in *Handbook of Thermal Process Modeling of Steels*, C. Gur and J. Pan, Eds. Boca Raton: CRC Press, 2009, pp. 341–425.
- [4] S. Kobayashi, S.-I. Oh, and T. Altan, “Metal Forming and the Finite-Element Method,” *J. Mater. Shap. Technol.*, vol. 8, no. 1, p. 377, 1989.
- [5] C. H. Gür and A. E. Tekkaya, “Finite element simulation of quench hardening,” *Steel Res.*, vol. 67, no. 7, pp. 298–306, Jul. 1996.
- [6] P. Jimbert, T. Guraya, A. Torregaray, and P. Bravo, “Metodología para el cálculo de espesores límite libres de fase sigma durante el hipertemple en piezas de aceros dúplex de gran sección,” *Rev. Metal.*, vol. 49, no. 2, pp. 122–130, 2013.
- [7] T.-L. Fu, X.-T. Deng, G.-H. Liu, Z.-D. Wang, and G.-D. Wang, “Experimental study of cooling speed for ultra-thick steel plate during the jet impinging and quenching process,” *Int. J. Precis. Eng. Manuf.*, vol. 17, no. 11, pp. 1503–1514, Nov. 2016.
- [8] H. Wang, W. Yu, and Q. Cai, “Experimental study of heat transfer coefficient on hot steel plate during water jet impingement cooling,” *J. Mater. Process. Technol.*, vol. 212, no. 9, pp. 1825–1831, Sep. 2012.
- [9] B. Bourouga and J. Gilles, “Roles of heat transfer modes on transient cooling by quenching process,” *Int. J. Mater. Form.*, vol. 3, no. 2, pp. 77–88, Jun. 2010.
- [10] M. Sedighi and C. A. McMahon, “The influence of quenchant agitation on the heat transfer coefficient and residual stress development in the quenching of steels,” *Proc. Inst. Mech. Eng. Part B J. Eng. Manuf.*, vol. 214, no. 7, pp. 555–567, Jul. 2000.

Chapter 9: Conclusions & Further Work

During this work, the effects of thermo-mechanical processing on the microstructure and mechanical properties of ZERON® 100 SDSS using processing parameters analogous to the production of 16” dia. weld neck flange components have been investigated.

The preceding chapters have illustrated the various experimental methodologies undertaken to investigate and integrate the micro- and macro-scale effects of these parameters on both as-received starting billet and commercially forged and heat-treated material. During the completion of this work, a number of novel achievements were made as contributions to the field:

1. Axisymmetric compression testing of ZERON® 100 on the University of Sheffield TMC machine and subsequent application of the data to the development of a constitutive flow model.
2. Finite element simulation of the forging and final quality heat treatment operations for the production of weld neck flange components in ZERON® 100.
3. Confirmation of the applicability of identifying γ_2 precipitates in the thermo-mechanically processed duplex microstructure through the presence of the K-S crystallographic orientation relationship with the surrounding ferrite matrix.
4. Calibration, optimisation and verification of the ATPU as a thermal simulator capable of high-fidelity replication of complex, industrially analogous cooling profiles.

Summaries have been presented of each of the main areas of experimental work and these are found at the end of each of Chapters 5, 6, 7 and 8. This final chapter therefore, synthesises the conclusions drawn in the preceding chapters into possible strategies for the optimization of the thermo-mechanical processing route through which the repeatable production of consistently high-quality forged ZERON® 100 engineering components may be achieved. Options for extension of this work, such that these strategies may be investigated further, will be considered at the end of this chapter.

Through the above-mentioned experimental work, it has been possible to characterise the microstructure development through the billet production and subsequent secondary forming operations. This is illustrated schematically below in Fig. 9.1

ZERON® 100 SDSS 'starting material' can be produced through a range of different steelmaking processes, i.e. conventional (EAF + AOD) ingot casting or additional ESR then either radially (GFM) or upset forged to produce billets of demonstrated microstructure inconsistencies (demonstrated in Figs. A-B). It is well established that cogging operations (radial GFM forging) do not impart the same level of strain penetration as upset forging introducing additional variability into the cast product. The secondary forming process can range from the extremes of open die (Figs C-D) to close die forging. The use of, essentially, the cheapest and fastest available suppliers for both billet supply and secondary thermo-mechanical processing must also be considered as further contributing to the reported inconsistencies of final product quality.

For example, in aerospace manufacturing, rotative engine components are only ever made from rotating disk quality material - this is material that has been cogged and/or upset, but not radially forged because the work imparted to the material through GFM operations is not sufficient.

This thesis essentially demonstrated the importance of total manufacturing process control in the assurance of consistent material properties. Additionally, it also demonstrates synoptically how 'un-steel-like' super duplex stainless steels are; the DNA of these alloy (as with most other high-alloy metallic duplex materials) is set early and cannot simply be 'reset' in the final quality heat treatment (as is the case with the ubiquitous Q&T grades steels). What is shown therefore is that this complexity requires, at some point early in the manufacturing process, a standardised operating procedure.

I argue that this work highlights the importance of a 'big picture manufacturing engineering' approach to resolving the issues around reported inconsistencies in the quality of forged SDSS components. Addressing the variability and process control in the manufacturing route, I propose, is likely to yield significantly greater improvements in material performance than for example, small-scale focused efforts on improved identification/reduction of the level of nitriding or academic exercises focused on determination of the average ferrite matrix grain

size. 'Big picture' engineering solutions are however undoubtedly economically driven and, perhaps, in the absence of stringent safety-critical quality assurance (in contrast to the aerospace industry) the use of a variety of primary steelmakers and steelmaking methods as well as secondary forge shops employing a 'quickest way to get shape' approach means inevitable inconsistencies in the mechanical performance of the final product.

This approach may be suitable for single phase, Q&T steels, but when working with duplex alloys, the size, shape and distribution of all the phases within the system are very much a function of the whole processing route.

Key recommendations from this work can be grouped into two categories - those with practical manufacturing engineering applications (perhaps more applicable to the industrial sponsor of the project) as detailed above and those of a more 'fundamentally scientific' nature e.g. the development/validation of the proposed constitutive equation/plastic flow model through further TMC testing, very high resolution SEM-EBSD (or perhaps even TEM) experimentation to positively identify & characterise Cr-nitride precipitates, extension of the thermal simulation work to secondary-forged material with subsequent micro hardness testing, detailed heat treatment and crystallographic investigations into the proposed importance of the secondary austenite solvus temperature etc.

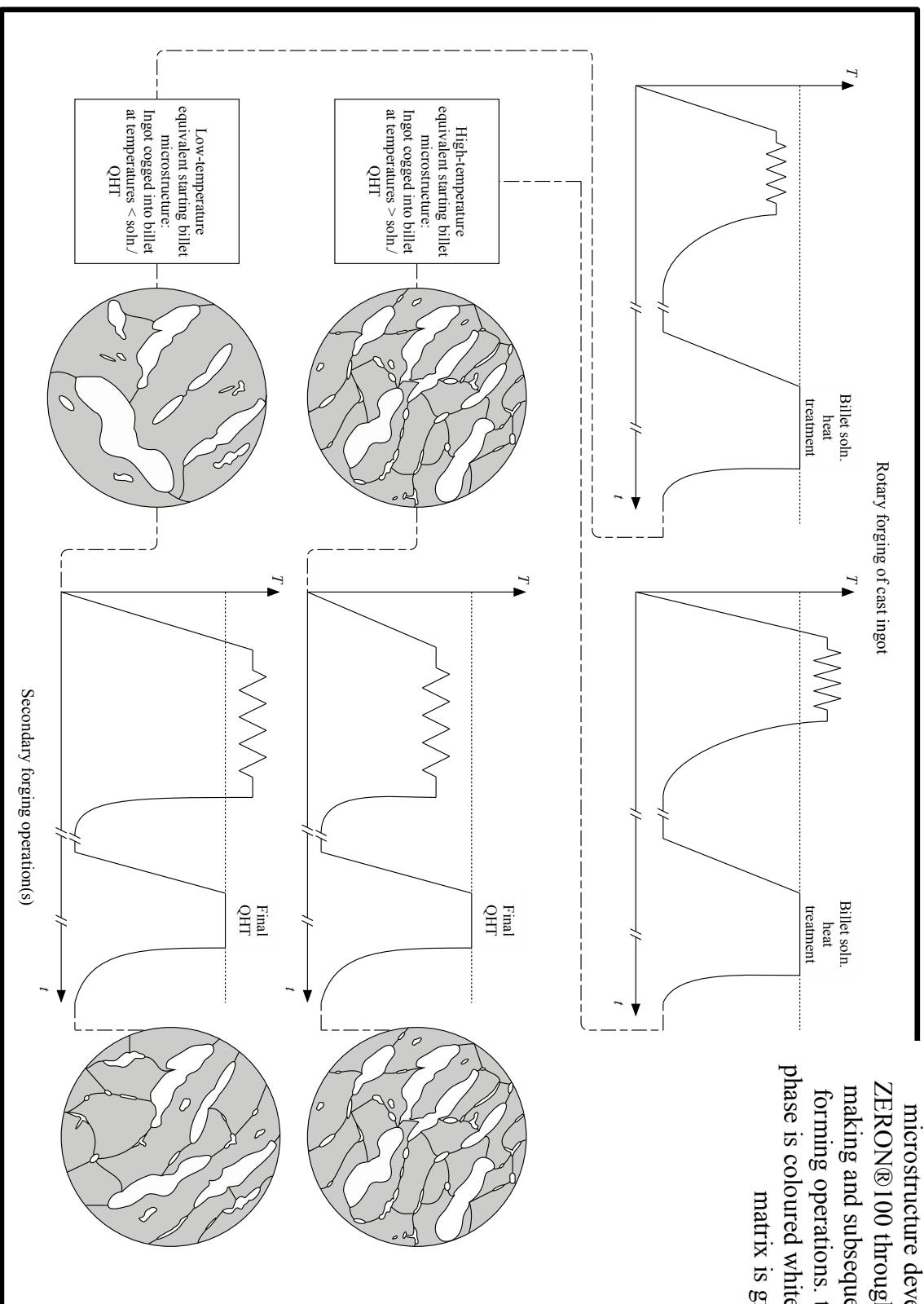


Fig. 9.1 Schematic illustration of the microstructure development in ZERON®100 throughout the billet making and subsequent secondary forging operations. the austenitic phase is coloured white and the ferrite matrix is grey

9.1 Optimisation of the thermo-mechanical processing of ZERON® 100

With reference to Fig. 9.1 above, it is proposed that the ZERON® 100 steel making process produces billet material broadly categorizable as containing ‘equivalent high or low temperature starting microstructures’. It is noted however that billet properties, despite nominally similar chemistry and starting ingot size, can vary from steelmaker to steelmaker, particular transversally.

However, according to the characterisation proposed above and the results from the preceding experimental work, the high temperature equivalent starting billet microstructure is believed to lead to the generation of the best mechanical properties in all areas of the forging. This is because the dead zones, where very little strain penetration occurs, will effectively emerge as heat treated high temperature equivalent starting billet microstructure in the final component (see details in Ch. 8). The ferrite grain size should not coarsen through dissolution of the pinning secondary austenite precipitates as long as the temperature throughout the secondary forming operations is not allowed to exceed the final pass temperature at which the ingot was clogged into billet by the steelmaker. Therefore, even in the low strain, 'unworked' areas of the secondary-forged product, the ferrite grain size refinement associated with improved toughness, will not be lost.

To ensure the retention and incorporation of the preferred, high-temperature equivalent starting billet microstructure in the forged component, it is therefore recommended that verification of the presence of this microstructure morphology is conducted prior to secondary forging (i.e. through sample 'slices' taken from as-received starting billet material). Heat treatments should then be conducted on these billet samples to determine the secondary austenite precipitate *solvus*. Since this is likely to vary from billet to billet due to local chemical inhomogeneities, these heat treatments should be carried out for every billet in a manner similar to the determination of the γ' precipitate *solvus* prior to the thermo-mechanical processing of Ni superalloys for aerospace applications. Upon determination of the dissolution temperature of the ferrite grain boundary-pinning secondary austenite, the upper limit of the secondary forging temperature window can be specified approximately 20°C below this temperature.

In the case of the less suitable, ‘low temperature equivalent’ starting billet microstructure (where an unpinned, coarser ferrite matrix is likely to be expected), the situation becomes more

problematic since the upper limit of the secondary forging window must be specified such that deformation occurs just above the secondary austenite *solvus*. In this scenario it is hoped that sufficient strain penetration can be imparted into the ferrite matrix such that a refined grain size is produced by the precipitation and boundary pinning of secondary austenite particles upon cooling. However, elevated temperature deformation increases the rate of recovery in ferrite and so sufficient working of the material to produce the refined grain size desirable for high toughness will be more difficult.

In a manner very similar to the thermo-mechanical processing of titanium alloys for aerospace applications, the ‘DNA’ of the billet appears to be highly significant in determining the mechanical properties of the final component. The optimum strategy for the generation of high toughness forgings (i.e. through minimisation of ferrite mean free path length) is therefore total thermo-mechanical processing control whereby the high temperature equivalent starting billet microstructure is always specified and the ferrite grain boundaries are pinned by ‘thermally stable’ high temperature secondary austenite and thus restricted from coarsening during secondary forming.

The quality heat treatment (QHT) operation following secondary forming operations is specified by convention in order to dissolve (primarily) any sigma phase formed as a result of the air cooling of the workpiece after forging. However, it may be possible, if sigmatization can be avoided through the rapid quenching of a high temperature forged workpiece, to remove the need for final solution heat treatment since this operation, while dissolving deleterious tertiary precipitates also has the potentially negative effect on toughness of unpinning the deformation-induced matrix refinement (especially if low equivalent temperature starting billet material has been used).

The as-received starting billet has previously always been viewed in industrial practice as a primary material, not a finished product. This work underlines the importance of setting the correct properties at the very outset, during the production of the billet. In certain locations in the forging this primary material is effectively carried through to the finished product.

Thermomechanical processing optimisation through *incremental improvements* is indicated by the work presented here; to produce consistent, homogeneously tough thick-section forged engineering components in ZERON® 100 SDSS an optimum ‘high temperature equivalent’

microstructure in the billet is paramount. It is suggested that this is most likely to be produced via the AFP (P)ESR casting process and subsequent high temperature cogging operations. Closed die forging also appears to induce greater strain penetration (and thus, it is inferred, microstructure refinement) than the equivalent open die operations. Additionally, incorporation of a punching operation into the closed die forging schedule to form the bore in the weld neck flange seeming offers a further incremental improvement in terms of minimising the formation of 'dead zones'. In the case of 'high temperature equivalent' microstructures in the starting billet, secondary forging, a revision down of the upper limit of the temperature processing window may be necessary to ensure retention of intra-granular γ_2 precipitates and thus the pinning of the refined ferrite matrix grain size. For sub-optimal starting material, i.e. 'low temperature equivalent' billet microstructures, secondary forging the lower limit of the temperature processing window may need to be revised up above the subsequent QHT temperature to prefer the formation of the important thermally stable γ_2 precipitates. Although obvious, it is also important to note that complete die fill through adequate lubrication, workpiece alignment and a sufficient number of hammer blows should always be sought during forging and during the QHT operation, the transfer from soak furnace to well agitated quench tank should occur as quickly as possible (note the demonstrated effects on toughness in Ch. 8 of increased cooling rates).

Finally, the optical microscopy and toughness data presented in Figs. 7.21 & 7.22 and Table 7.1 confirm the deleterious effect of Cr-nitride precipitation on toughness, however the primacy of this effect is questionable when combined with unrefined microstructure unit size presenting large ferrite mean free path lengths for crack propagation. The production of such mechanically disadvantageous microstructures was discussed in Ch. 6 and Ch. 7. Positive identification of Cr-nitrides (assumed to be the 'quenched-in' variety in this case) proved extremely problematic however; what appeared to be clear evidence of their presence in the ferrite matrix (or presence prior to electrolytic etching) under the light microscope (Figs. 7.21 & 7.22) is made somewhat more ambiguous when examined in secondary electron mode in the SEM (Fig. 9.2). Here, in the same ferritic matrix there instead appears to be excessive early-state intra-granular precipitation of extremely thin films and discrete particles of (assumed) secondary austenite on substructure boundaries. Since these precipitates were so small SEM-EDS proved to be too coarse of a tool for accurate identification (Fig. 9.3) however, the precipitate morphology, optical evidence of 'etched micro pitting' and occurrence in low toughness material may

provide support for the previously reported essential indistinguishability between early-state precipitation of small Cr-nitride and γ_2 precipitates. This is due to a co-operative precipitation mechanism causing the narrow coexistence and growth of the nitrides and secondary-austenite film together until the diffusion of the heavy nitride-forming elements Cr, Mo, and V limits the nitride growth and allows the secondary austenite to grow alone. In this case it may be even be plausible to also argue that the prevention of further development (possibly through thermal effects, elemental diffusivity range-limiting coarse ferrite grains size or density of DRV structures) of the secondary-austenite films identified in Fig. 9.2 into the type of allotropic precipitates seen in, for example, Figs. 7.27 & 7.37 may have limited toughness since they are believed to act in the retention of a refined basic matrix unit size.

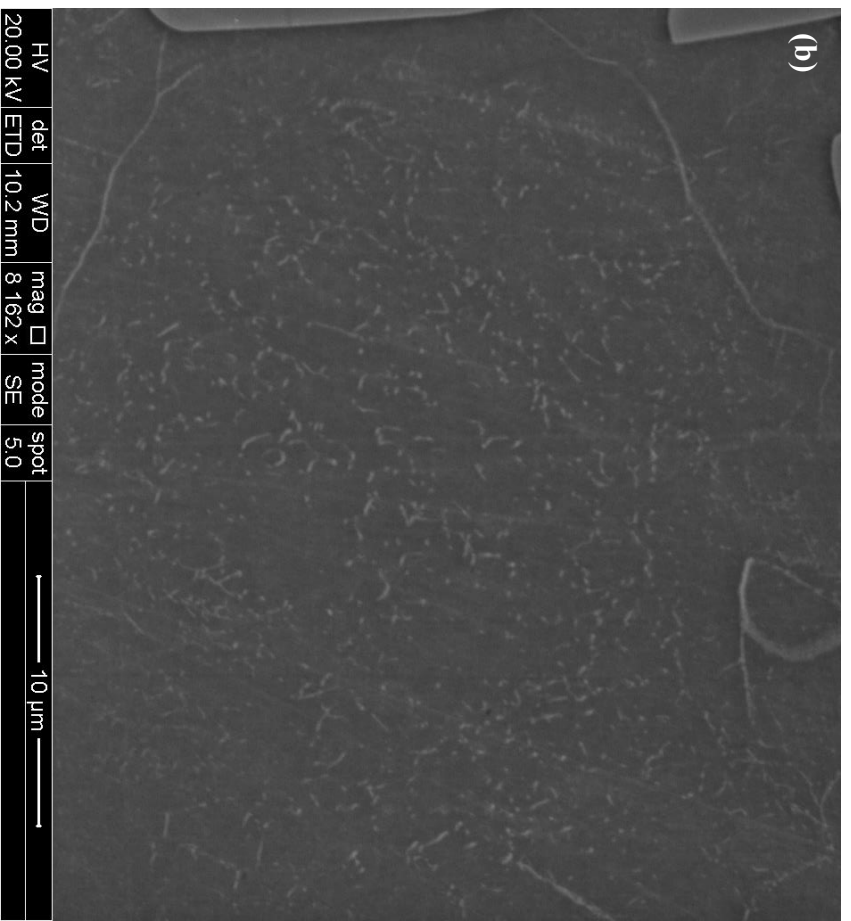
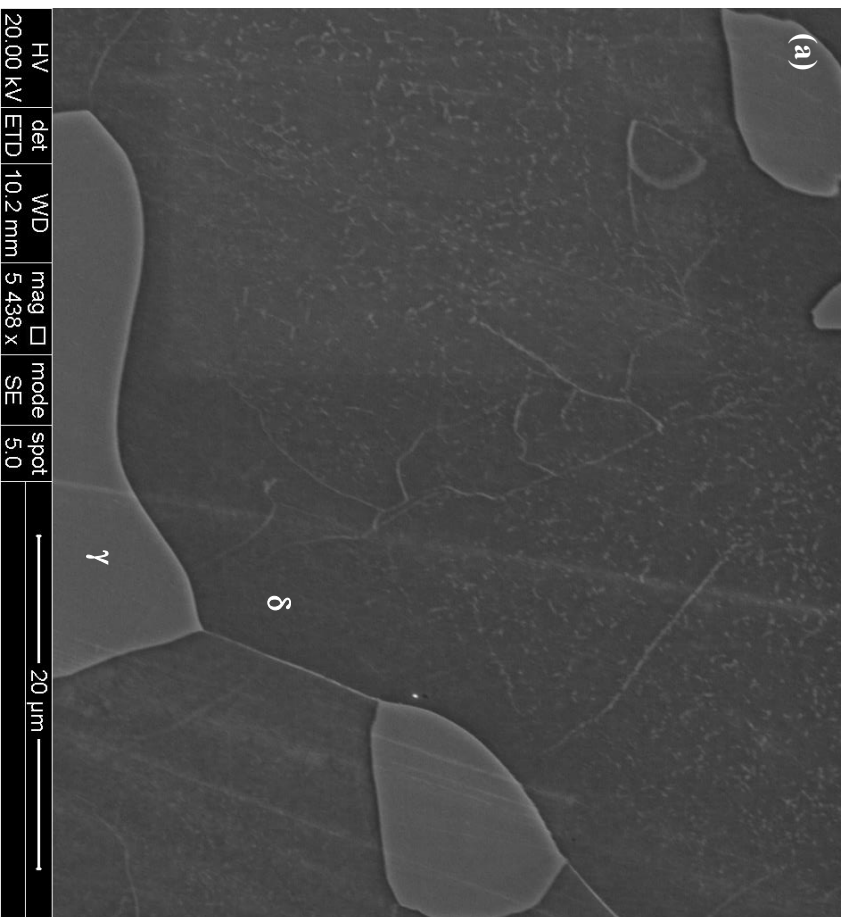


Fig. 9.2 SEM micrographs of the C3 location material detailed in Ch. 7.1.2 Note the previously discussed presence of co-operatively precipitated presumed the nitride and secondary-austenite film

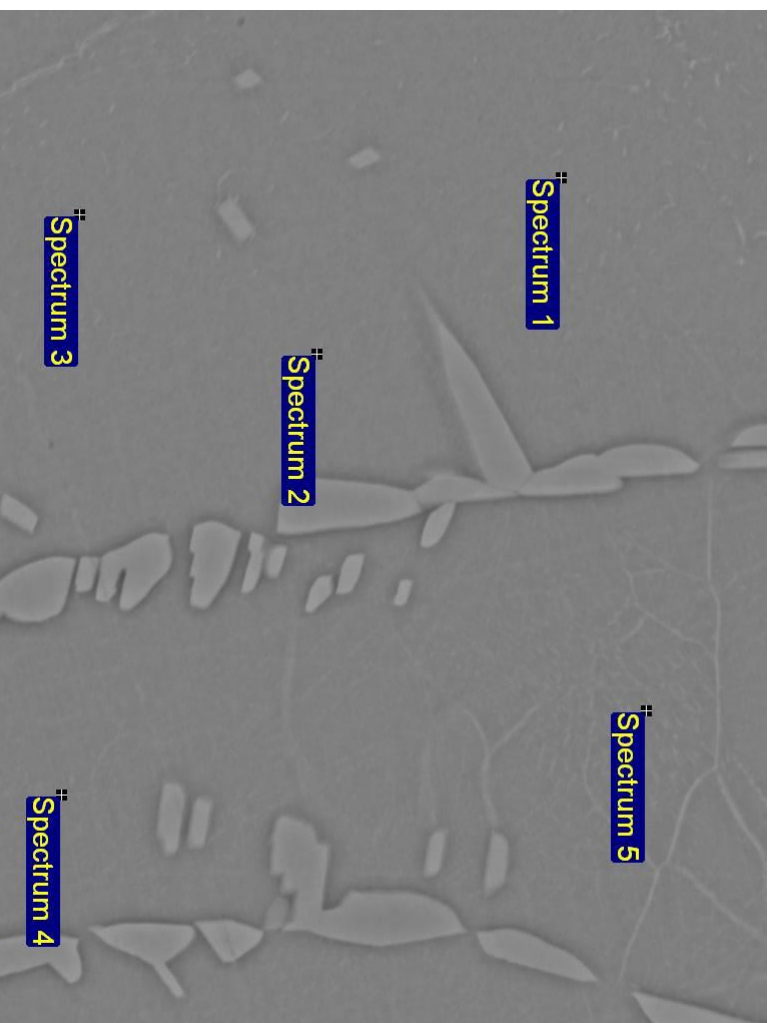


Fig. 9.3 SEM-EDS analysis suggests (relative to the γ_2 particles in Fig. 3.1, taken from the sample) the slight enrichment of Cr and depletion Ni in the ferrite matrix of a ZERON®100 sample exhibiting similar intra-granular nitride and secondary-austenite film as above in Fig. 9.2. The size of the precipitated films means however SEM-EDS cannot resolve adequately at this length scale and instead requires the use of TEM.

Processing option : All elements analysed (Normalised)

Spectrum	In stats	Si	Cr	Mn	Fe	Ni	Cu	Mo	W	Total
Spectrum 1	Yes	0.33	26.68	0.75	60.57	5.69	0.53	4.66	0.79	100.00
Spectrum 2	Yes	0.31	26.96	0.68	60.46	5.64	0.47	4.75	0.74	100.00
Spectrum 3	Yes	0.29	26.68	0.72	60.70	5.78	0.51	4.57	0.75	100.00
Spectrum 4	Yes	0.25	26.77	0.68	60.60	5.47	0.52	4.78	0.94	100.00
Spectrum 5	Yes	0.22	26.78	0.66	60.56	5.67	0.46	4.63	1.03	100.00
Mean		0.28	26.77	0.70	60.58	5.65	0.50	4.68	0.85	100.00
Std. deviation		0.05	0.11	0.04	0.09	0.11	0.03	0.09	0.13	
Max		0.33	26.96	0.75	60.70	5.78	0.53	4.78	1.03	
Min		0.22	26.68	0.66	60.46	5.47	0.46	4.57	0.74	

All results in weight%

9.2 Recommendations for Further Work

Clearly the avoidance of a QHT operation would be dependent upon the achievement of sufficiently fast 'off the press' cooling rates, albeit not so aggressive that thermal cracking results and would need to be verified by detailed mechanical and microstructure investigations on 'as forged and quenched' samples. There is some evidence to suggest the potential viability of this revision to the thermo-mechanical processing route from the micrographs of TMC samples subject to deformation and immediate quenching afterwards (Fig. 5.32). However, the cooling rates achieved in a laboratory scale 10 mm dia. x 15 mm *L* cylindrical sample may not necessarily scale to a commercial 16" forging and would require further detailed heat transfer investigations to determine the threshold section depth in heavy forgings at which an effectively precipitate-free microstructure cannot be achieved due to the physical limits imposed by thermal conductivity and elemental diffusivity ranges.

Fig. 2.32 is assumed to be the starting microstructure of choice; a refined ferrite matrix with a high density of HAGBs acting to increase the toughness, providing of course these boundaries are not acting as sites for the preferential nucleation of embrittling phases such as Cr-nitrides. The intimate precipitation relationship between secondary austenite and Cr-nitrides (REF. Glenn/American welding paper) is such that extremely fine precipitates of either may be essentially indistinguishable. The pinning of the highly refined microstructures in the TMC uniaxial compression samples may therefore be due to such optically unobservable secondary austenite/Cr-nitride precipitates. TEM/high resolution EBSD analysis is therefore needed to reveal their presence (or otherwise) i.e. through the existence of K-S phase relationships.

This work underlines the importance of setting the correct properties at the very outset, during the production of the billet, through total thermo-mechanical process control. Extension of the work in Ch. 2 is therefore also recommended in order to provide a complete characterisation of both AFP and standard product ZERON® 100 material as well confirmation of the suggested equivalent high and low temperature billet microstructures.